Research Topics

Virtual paleobiology – advances in X-ray computed microtomography and 3D visualization of fossils

Edited by
Stergios D. Zarkogiannis, Shinya Iwasaki,
Elizabeth Clark and Pauline Guenser

Published in
Frontiers in Earth Science
Frontiers in Ecology and Evolution

ISSN 1664-8714
ISBN 978-2-8325-4390-0
DOI 10.3389/978-2-8325-4390-0

About Frontiers

Frontiers is more than just an open access publisher of scholarly articles: it is a pioneering approach to the world of academia, radically improving the way scholarly research is managed. The grand vision of Frontiers is a world where all people have an equal opportunity to seek, share and generate knowledge. Frontiers provides immediate and permanent online open access to all its publications, but this alone is not enough to realize our grand goals.

Frontiers journal series

The Frontiers journal series is a multi-tier and interdisciplinary set of open-access, online journals, promising a paradigm shift from the current review, selection and dissemination processes in academic publishing. All Frontiers journals are driven by researchers for researchers; therefore, they constitute a service to the scholarly community. At the same time, the *Frontiers journal series* operates on a revolutionary invention, the tiered publishing system, initially addressing specific communities of scholars, and gradually climbing up to broader public understanding, thus serving the interests of the lay society, too.

Dedication to quality

Each Frontiers article is a landmark of the highest quality, thanks to genuinely collaborative interactions between authors and review editors, who include some of the world's best academicians. Research must be certified by peers before entering a stream of knowledge that may eventually reach the public - and shape society; therefore, Frontiers only applies the most rigorous and unbiased reviews. Frontiers revolutionizes research publishing by freely delivering the most outstanding research, evaluated with no bias from both the academic and social point of view. By applying the most advanced information technologies, Frontiers is catapulting scholarly publishing into a new generation.

What are Frontiers Research Topics?

Frontiers Research Topics are very popular trademarks of the *Frontiers journals series*: they are collections of at least ten articles, all centered on a particular subject. With their unique mix of varied contributions from Original Research to Review Articles, Frontiers Research Topics unify the most influential researchers, the latest key findings and historical advances in a hot research area.

Find out more on how to host your own Frontiers Research Topic or contribute to one as an author by contacting the Frontiers editorial office: frontiersin.org/about/contact

Virtual paleobiology – advances in X-ray computed microtomography and 3D visualization of fossils

Topic editors
Stergios D. Zarkogiannis — University of Oxford, United Kingdom
Shinya Iwasaki — University of Bremen, Germany
Elizabeth Clark — University of California, Berkeley, United States
Pauline Guenser — Université de Bordeaux, France

Citation
Zarkogiannis, S. D., Iwasaki, S., Clark, E., Guenser, P., eds. (2024). *Virtual paleobiology – advances in X-ray computed microtomography and 3D visualization of fossils*. Lausanne: Frontiers Media SA. doi: 10.3389/978-2-8325-4390-0

Table of contents

TYPE Editorial
PUBLISHED 18 January 2024
DOI 10.3389/feart.2024.1357880

EDITED AND REVIEWED BY
Bruce S. Lieberman,
University of Kansas, United States

*CORRESPONDENCE
Stergios D. Zarkogiannis,
✉ stergios.zarkogiannis@earth.ox.ac.uk

RECEIVED 18 December 2023
ACCEPTED 08 January 2024
PUBLISHED 18 January 2024

CITATION
Zarkogiannis SD, Iwasaki S, Clark EG and Guenser P (2024), Editorial: Virtual paleobiology—advances in X-ray computed microtomography and 3D visualization of fossils.
Front. Earth Sci. 12:1357880.
doi: 10.3389/feart.2024.1357880

Editorial: Virtual paleobiology—advances in X-ray computed microtomography and 3D visualization of fossils

Stergios D. Zarkogiannis[1]*, Shinya Iwasaki[2], Elizabeth G. Clark[3] and Pauline Guenser[4]

[1]Department of Earth Sciences, University of Oxford, Oxford, United Kingdom, [2]Graduate School of Environmental Science, Hokkaido University, Sapporo, Japan, [3]Department of Environmental Science, Policy and Management, University of California Berkeley, Berkeley, CA, United States, [4]Universite Claude Bernard Lyon 1, ENSL, UJM, CNRS, LGL-TPE, F-69622, Villeurbanne, France

KEYWORDS

X-ray microcomputed tomography (μCT), virtual paleobiology, virtual paleontology, paleontology-general, paleobiology, X-rays

Editorial on the Research Topic
Virtual paleobiology -advances in X-ray computed microtomography and 3D visualization of fossils

In this issue, the Editors aim to convey the dynamic and evolving nature of the concept of Virtual Paleobiology, capturing the excitement, interest, enthusiasm, and drive that characterize this field. Leveraging the digital nature of X-ray micro-computed tomography (μCT), this approach enables a virtual representation of the analyzed objects. X-ray μCT significantly enhances paleontologists' ability to study and comprehend the biology, evolution, and ecology of organisms, thereby contributing valuable insights to our understanding of the history of life on Earth. The new perspectives offered by μCT into past ecosystems and organism adaptation to environmental dynamics are crucial for advancing our comprehension and prediction of climate and ocean change.

This Research Topic aims to showcase a variety of perspectives of μCT in oceanic and terrestrial paleobiology so as to inspire and promote cutting edge research. It comprises a compilation of original research and methods articles, along with data reports, covering various topics in paleontological research, including virtual paleontology, internal anatomy, taxonomic studies, functional morphology, preservation assessment, paleoecology and taphonomic studies.

Using μCT, Kimoto et al. were able to perform precise bulk density measurements of planktic foraminiferal tests. A notable aspect of their technique lies in the ability to obtain not only nondestructive, highly accurate morphometric measurements of marine calcifiers but also to determine the mass of foraminiferal tests utilizing the X-ray absorption information from the tomographs. This has significant potential to provide quantitative information on the skeletal mass of microfossils in matrices or in situations where microquantities fall below the analytical limits of other techniques.

Similarly, Choquel et al. examined changes in foraminifera calcification resulting from anthropogenic ocean change through the morphological analyses of marine shells acquired via μCT, revealing that modern specimens are thinner and more porous. Their study provided also a post-data routine to analyze entire test parameters such as the average thickness, calcite volume, calcite surface area, number of pores, pore density, and calcite surface area/volume ratio.

Muto et al. demonstrated the power of µCT scanning to resolve biostratigraphic issues in geological context with high deformation caused by tectonics and/or metamorphism. The authors used tomography to visualise conodont microfossils that are too fragile to be sampled with acid dissolution. In particular, they observe Carboniferous-Permian conodont elements from pelagic siliceous sediments from north-eastern Japan. This allowed the authors to identify index species and correlate the studied section to a relative age and describe a faunal turnover around the Carboniferous-Permian boundary.

A major bottleneck in analyzing marine invertebrates using µCT includes the time it takes to segment individual specimens, as well as challenges with differentiating shelly material from a surrounding calcareous matrix. To facilitate the analysis of fossil invertebrates, Edie et al. applied a deep learning interface to a dataset of shelly calcareous fossil material and demonstrated a high-throughput technique that can be used to cut down specimens' extraction time and even improve the morphological fidelity of manual segmentation or physical preparation.

Jacquet et al. illustrated the utilization of µCT in conducting analyses that would be impractical with destructive sampling techniques. The authors employed tomographic imaging to visualize coprolites of mammalian fauna from the Late Eocene to understand the feeding behavior and identities of their producers. They incorporated 3D imaging along with traditional methods of internal specimen visualization, such as thin-section petrography and SEM. Their µCT data supplemented the other means of data acquisition by revealing the porosity and relative proportion of inclusions, which are metrics not permitted to be calculated by traditional destructive sampling techniques.

Herrera et al. performed a precise three-dimensional (3D) morphological analysis of some extraordinarily preserved Middle Pennsylvanian fossil plants obtained from Mazon Creek. In addition, they analysed the mineralogical composition of the fossil plant remnants using elemental maps and Raman spectroscopy. Their results suggest that the X-ray µCT provided excellent information on the 3D morphological structure of fossil plants but that the quality of the reconstruction may be compromised by the mineral filling associated with fossilization. This is an important suggestion for the high-quality, non-destructive analysis of fossils using µCT, which is expected to develop more in the future.

Frosali et al., delved into the previously unexplored realm of paranasal sinus morphology in canids, focusing on both extant and fossil representatives. Employing innovative deformation-based morphometric techniques, the researchers establish a correlation between frontal sinus morphology and ecomorphotypes in extant canids, supporting the link between diet preferences and sinus development. The study underscores the efficacy of combining morphological inspection and deformation-based geometric morphometrics, paving the way for the study of ecological preferences of other fossil carnivorans. In a similar manner, Duhamel et al. conducted a 3D morphological analysis on the skull of Dicynodontia, one of the most successful Permo-Triassic terrestrial tetrapod clades. Their study allowed the examination of the previously unobservable internal anatomy of the skull, leading to the proposal that the holotype specimen of *Eodicynodon oelofseni* belongs to a new genus.

Lastly, X-ray tomography enables the creation of a novel online database featuring exceptionally well-preserved materials. These high-resolution datasets offer versatile utility across various disciplines. Chen et al. exemplify this concept in their paper, providing three-dimensional morphologies of 40 early Pleistocene planktonic foraminifer tests from the western Pacific Ocean. The authors emphasize the database's diverse applications for studying foraminifer evolution and ecology, along with its potential for taxonomic identification automation through machine learning models.

The current compilation of papers represents just a fraction of what promises to be a continuously expanding and developing subject. In addition, the Editors extend their heartfelt gratitude to all the authors and reviewers who have contributed to this Research Topic. Their dedication and efforts have played a crucial role in shaping the content and quality of this Research Topic. Their work reflects a shared commitment to advancing our understanding of virtual paleobiology and contributes to the ongoing growth and vibrancy of this field.

Author contributions

SZ: Conceptualization, Writing–review and editing. SI: Writing–review and editing. EC: Writing–review and editing. PG: Writing–review and editing.

Funding

The author(s) declare that no financial support was received for the research, authorship, and/or publication of this article.

Conflict of interest

The authors declare that the research was conducted in the absence of any commercial or financial relationships that could be construed as a potential conflict of interest.

Publisher's note

frontiers | Frontiers in Ecology and Evolution

TYPE Methods
PUBLISHED 08 March 2023
DOI 10.3389/fevo.2023.1127756

OPEN ACCESS

EDITED BY
Elizabeth Clark,
University of California, Berkeley,
United States

REVIEWED BY
H. David Sheets,
Canisius College,
United States
Daniel Kytyr,
Institute of Theoretical and Applied
Mechanics (ASCR),
Czechia
Janet Burke,
Michigan State University,
United States

*CORRESPONDENCE
Stewart M. Edie
✉ edies@si.edu

SPECIALTY SECTION
This article was submitted to
Paleontology,
a section of the journal
Frontiers in Ecology and Evolution

RECEIVED 20 December 2022
ACCEPTED 15 February 2023
PUBLISHED 08 March 2023

CITATION
Edie SM, Collins KS and Jablonski D (2023)
High-throughput micro-CT scanning and deep learning segmentation workflow for analyses of shelly invertebrates and their fossils: Examples from marine Bivalvia.
Front. Ecol. Evol. 11:1127756.
doi: 10.3389/fevo.2023.1127756

High-throughput micro-CT scanning and deep learning segmentation workflow for analyses of shelly invertebrates and their fossils: Examples from marine Bivalvia

Stewart M. Edie[1]*, Katie S. Collins[2] and David Jablonski[3,4]

[1]Department of Paleobiology, National Museum of Natural History, Smithsonian Institution, Washington, DC, United States, [2]Natural History Museum, London, United Kingdom, [3]Department of the Geophysical Sciences, University of Chicago, Chicago, IL, United States, [4]Committee on Evolutionary Biology, University of Chicago, Chicago, IL, United States

The largest source of empirical data on the history of life largely derives from the marine invertebrates. Their rich fossil record is an important testing ground for macroecological and macroevolutionary theory, but much of this historical biodiversity remains locked away in consolidated sediments. Manually preparing invertebrate fossils out of their matrix can require weeks to months of careful excavation and cannot guarantee the recovery of important features on specimens. Micro-CT is greatly improving our access to the morphologies of these fossils, but it remains difficult to digitally separate specimens from sediments of similar compositions, e.g., calcareous shells in a carbonate rich matrix. Here we provide a workflow for using deep learning—a subset of machine learning based on artificial neural networks—to augment the segmentation of these difficult fossils. We also provide a guide for bulk scanning fossil and Recent shells, with sizes ranging from 1 mm to 20 cm, enabling the rapid acquisition of large-scale 3D datasets for macroevolutionary and macroecological analyses (300–500 shells in 8 hours of scanning). We then illustrate how these approaches have been used to access new dimensions of morphology, allowing rigorous statistical testing of spatial and temporal patterns in morphological evolution, which open novel research directions in the history of life.

KEYWORDS

paleontology, bivalve, 3D morphometrics, high-throughput morphometry, deep learning, computed tomography, CT image segmentation

Introduction

The skeletons of marine invertebrates are a robust system for analyzing patterns of biodiversity, both today and through deep time (Valentine, 1973; Stanley, 1979; Foote, 1997; Seilacher and Gishlick, 2014; Sepkoski, 2015). Bivalvia, the group containing clams, cockles, mussels, oysters and more, contains an estimated 6,000 extant species across the shallow continental shelf (Edie et al., 2017), and shells from across the class are abundantly preserved in the fossil record: tens of thousands of species occur across 520 million years of evolution

(Johnston and Haggart, 1998). These shells are shaped by internal factors such as developmental interactions and modularity (Matsukuma, 1996; Vermeij, 2013; Sherratt et al., 2017; Edie et al., 2022b), and external factors such as selection on life history and ecological function (Stanley, 1970; Vermeij, 1987), providing key insights into questions on the evolution of form (Serb et al., 2011, 2017; Collins et al., 2016), the dynamics of mass extinctions and recoveries (Jablonski, 2005), the tempo and mode of evolution (Jablonski, 2017a), and the origins of spatial diversity gradients (Jablonski et al., 2013). However, such analyses require a wide-ranging inventory of shell form, and much of bivalve diversity is embedded as fossils in consolidated or lithified sediments (Foote et al., 2015; Daley and Bush, 2020). Manual excavation of delicate features, especially those important for taxonomic identification such as the hinge teeth, can require hours to days of preparation (Feldmann et al., 1989; Prôa et al., 2021), and is often impossible.

X-ray computed tomography expands access to and discovery of new diversity in fossil invertebrates (Cunningham et al., 2014; Sutton et al., 2017; Claussen et al., 2019; Reid et al., 2019; Bauer and Rahman, 2021; Collins et al., 2021; Leshno Afriat et al., 2021; Thompson et al., 2021), much like the recent boom in vertebrate paleontology (Racicot, 2016; Schwarzhans et al., 2018; Coates et al., 2019; Goswami et al., 2022). For fossil invertebrates known from molds—the imprints of the original animal left in the surrounding rock—CT scanning can virtually cast the internal or external surfaces of the original animals in bulk, and can recover specimens otherwise inaccessible to manual peels (Reid et al., 2019). Fossils preserved either as primary or remineralized material can be digitally extracted from their enclosing rock or sediments, but to be fair, this virtual preparation sometimes requires as much time as manual preparation given the limited compositional contrast between the materials. Still, unlike physical preparation, digital excavations can "undo" any accidental removal of key features from a fossil, such as the delicate hinge teeth in bivalves. Phase contrast imaging, mostly from synchrotron sources and increasingly in laboratory settings, is improving the separation of fossil material from surrounding matrix (i.e., low attenuation contrast settings, Sutton et al., 2017; Birnbacher et al., 2021), but recent advances in post-processing, namely from deep learning, can also greatly accelerate the "cleaning" of matrix from shell. Deep learning is a powerful tool for image segmentation, helping to denoise X-ray images (Huang et al., 2022) and improve the digital excavation of fossils embedded in matrix (Liu and Song, 2020; Borowiec et al., 2022; Yu et al., 2022 for other applications in evolutionary biology).

Here, we provide a guide for digitally excavating fossil specimens using micro-CT scanning and a workflow for using deep learning to segment calcareous shelly material from calcareous matrix—a situation that inhibits segmentation using material density alone. We walk through bulk scanning fossil and Recent shells, with sizes ranging from 1 mm to 20 cm, which enables the rapid acquisition of large 3D datasets for macroevolutionary and macroecological analyses (300–500 shells in 8 hours of scanning). We then illustrate how these approaches have been used to access new dimensions of morphology, allowing rigorous statistical testing of spatial and temporal patterns in morphological evolution. As with the discoveries of novel morphological and taxonomic observations in vertebrates embedded in nodules, high-throughput X-ray microcomputed tomography (micro-CT) coupled with deep learning segmentation is primed to revolutionize invertebrate evolutionary biology and paleobiology—arguably the largest source of empirical data on the history of life.

Methods

Specimen sampling

Specimen selection and packing

Nearly all specimens sampled to date in the bivalve-3D project ("biv3d") are from museum collections. Sampling strategy will vary according to the arrangement of collections, but the following protocol has been applied in a variety of settings with no loss of specimens. Pulling and preparing specimens for scanning is best practiced with a joint physical and digital paper trail. From a given lot, the selected valve(s) are separated from the remainder of the lot and arranged for a photograph with the lot tag (Figure 1A). A high visibility tag (e.g., neon colored) is placed in the lot noting how many specimens have been pulled. Specimens are then prepped for transport and scanning depending on their size. If larger than 1 cm, the specimen is wrapped in low-density polystyrene foam (often sold as "dish wrapping foam"), which is secured with painter's tape; both materials are transparent to X-rays so that specimens need not leave their packing for scanning, which greatly reduces risk of loss or breakage (Figure 1B). Crumpling the dish foam by hand makes it more pliable, helping to wrap more delicate specimens. Both the specimen's registration number and its physical location are recorded with a pen on the painter's tape. If the specimen is smaller than 1 cm, it is placed inside a gelcap and carefully secured in place with foam. The registration number and the physical location of the specimen (e.g., floor, row, cabinet, and drawer number) in the collection are written on a piece of paper and placed inside the gel cap.

Specimen metadata

At a minimum, we find that databasing the information in Table 1 is crucial to maintaining unique object identifiers and their associated metadata. It is important to record verbatim copies of the ID, locality and stratigraphy info as provided on the museum labels in order to maintain connections back to the museum database, even if those pieces of information are updated for analyses (see "lot photo" in Figure 1A). Each specimen picked for scanning receives a specimen ID (Table 1). In the case of specimens where both valves are to be scanned, a specimen ID refers to both valves, as they are part of the same specimen. This is necessary so that the two digital mesh objects representing those valves can continue to be associated in analyses by their specimen ID (each unique valve is then referenced by a mesh ID, Table 1).

Pre-scan preparation

Grouping specimens

For all scans, the size of the smallest feature of interest determines how specimens are grouped for bulk scanning. In bivalves, a key taxonomic character—the hinge teeth—are often an order of magnitude smaller than the shell, which sets an upper limit on how many specimens may fit into the field of view of the detector. For example, on the GE Phoenix v|tome|x M 240/180 kV Dual Tube µCT

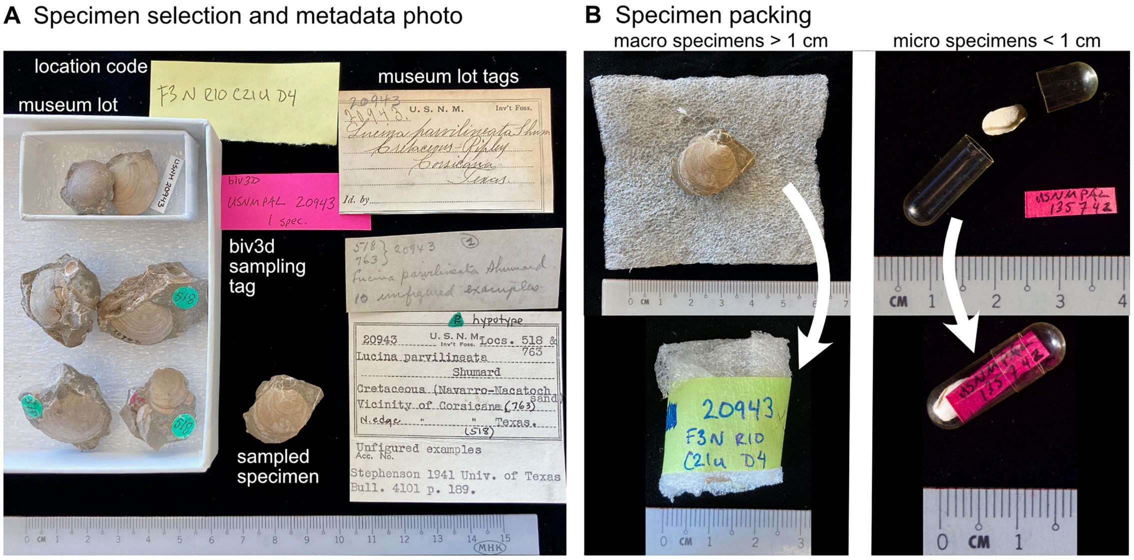

FIGURE 1
Workflow for sampling and packaging specimens from collections for scanning. **(A)** Museum lot with target specimen of Late Cretaceous fossil "*Lucina*" *parvilineata* Shumard 1861 to be imaged and temporary note marking number of specimens or valves sampled (as "biv3d sampling tag"). Location code gives the physical location of the specimen in the museum, here: Floor 3 North, Row 10, Case 21 upper, Drawer 4. **(B)** Macro specimens (>1cm) are wrapped in pliable foam and secured with painter's tape, noting the registration number and the specimen's physical location code in the museum. Micro specimens (<1cm) are placed in gel caps with a tag containing registration number and the specimen's physical location in the museum (on the back of tag in this image).

TABLE 1 Database schema for recording specimen information.

Database field	Value	Field description
Museumid	USNM PAL	Identifier of museum holding specimen (e.g., USNM, NMHUK)
Catalog ID	20943	Registration number for the specimen
Family	Lucinidae	Taxonomic family of specimen
Genus	"*Lucina*"	Taxonomic genus of specimen
Species	*parvilineata*	Taxonomic species of specimen
Species authority	Shumard 1861	Taxonomic authority for species
Locality	In bed of Postoak Creek along the old Dallas highway, half a mile north of Corsicana, Navarro Co. (USGS no. 518, see 17012)	Geographic locality of specimen
Stratigraphy	Late Cretaceous (Early Maastrichtian) Nacatoch Formation (Larina et al., 2016)	Stratigraphic formation, series, group, or other relevant age information of specimen
Specimen ID	4336	Unique integer ID for specimen
Mesh ID	4906	Unique integer ID for part of specimen (for bivalves this is usually a single valve)
Notes	Unfigured examples, Stephenson 1941 Univ. of Texas Bull. 4101 p. 189	General notes on specimen
Location	F3N R10 C21u D4	Physical location code of the specimen in the USNM collection: Floor 3 North Row 10 Case 21 upper Drawer 4

with a DXR250 (16″, 4 M pixel) X-ray detector at the U.S. National Museum of Natural History (NMNH, also USNM), specimens with approximately 1 mm (1,000 μm) features of interest are sufficiently resolved using <20 μm resolution, which would characterize such features with 50 pixels in the image plane. This resolution translates to a 40 mm by 40 mm field of view on a detector 2000 × 2000 pixel detector, which can typically accommodate 4–5 approximately 10–20 mm specimens in a cylindrical arrangement. Larger specimens have larger sizes of their smallest features of interest and can be packed to similar numbers for scanning at lower resolutions; however, most bivalves have scanned best at resolutions finer than 50 μm. Fossil specimens embedded in sedimentary matrix are often scanned alone because multiple fossil specimens, particularly those in dense siliciclastics, can require higher voltage to penetrate the full object; this may exceed the power limits of the micro-CT, and it will likely reduce the contrast between the edges of the specimens and matrix, making segmentation more difficult or virtually impossible (advances in laboratory phase contrast CT could improve segmentation of materials with subtle differences in signal, see Birnbacher et al., 2021). Additionally, scanning fossils embedded in matrix at the highest possible resolution reduces artifacts such as partial volume effects, which arise as the averaging of gray values from materials with different densities in a single voxel (described further in Abel et al., 2012; Racicot, 2016).

Mounting specimens

Once specimens have been grouped for scanning, they can be mounted into cylindrical containers. Straight-sided, thin-walled plastic soda bottles with a flat, level foam insert supporting specimens from the bottom work best for holding specimens (Figure 2A). For macro specimens (>1 cm), arrange in an imbricated fashion with the shell commissure perpendicular to the base of the container (Figure 2A, i.e., mounting with the long-axis perpendicular to the X-ray source as in Sutton et al., 2014, p. 53); this arrangement reduces Feldkamp artifacts and provides the sharpest boundaries between surfaces. Specimens can be mounted in vertical layers up to a height equaling the diameter of the container (i.e., a square field of view), and packed with additional foam to prevent movement during scanning. For micro specimens (<1 cm), use paper or plastic drinking straws to hold gel caps; straws can then be inserted into 50 ml or 15 ml conical centrifuge tubes (Figure 2B), making sure to keep specimens level with each other.

Mapping specimens

To orient the scan, place a marker into the scanning container with lower X-ray density than the specimens, such as an eraser; using markers that are more X-ray dense can shade specimens, which makes them more difficult to segment in post-processing. Draw a plan view "scan map" of the specimens relative to the marker, identifying positions using the unique identification code labeled on the specimen wrap or gel cap (Figure 2). Each scanning "cartridge" can be prepared before scanning, which is a crucial step for maximizing machine time.

Scan settings and reconstruction

Parameter tuning

Once specimens are mounted in the micro-CT, several parameters should be tuned to optimize the X-ray imaging. Each scan can, and often does, have different parameter settings, which vary according to the material density of the specimens and the number of specimens in the scan scene—or, for fossils, by the volume and mineralogy of the surrounding matrix. Because specific scanning parameters will vary by micro-CT system, we emphasize that the tuning process outlined below is intended to be generalizable; nevertheless, the parameters reported here are likely good starting points (for a comprehensive overview of optimizing scanning parameters, see Sutton et al., 2014, pp. 56–60). For all steps that follow, monitor the histogram of gray values in the imaging software; this is the crucial tool for maximizing contrast between materials in the scan.

Because we aim for high throughput, we first set parameters that affect the length of the scan to their lowest values: i.e., set exposure timing to lowest value, frame averaging to 1, and frame skips to 0. Next, we rotate the mounted specimens until viewed through the thickest portion of the scan scene; this will correspond to the lowest intensity gray values in the live image. We increase or decrease the voltage until the minimum gray value intensity recommended for the machine is reached (this ranges between 100 and 200 for the micro-CT at NMNH, trending towards the higher end as the filament ages). We aim for the lowest energy X-rays necessary to penetrate the specimen, which maximizes the contrast between materials (Sutton et al., 2014, pp. 56–57). Next, we adjust the current to maximize the

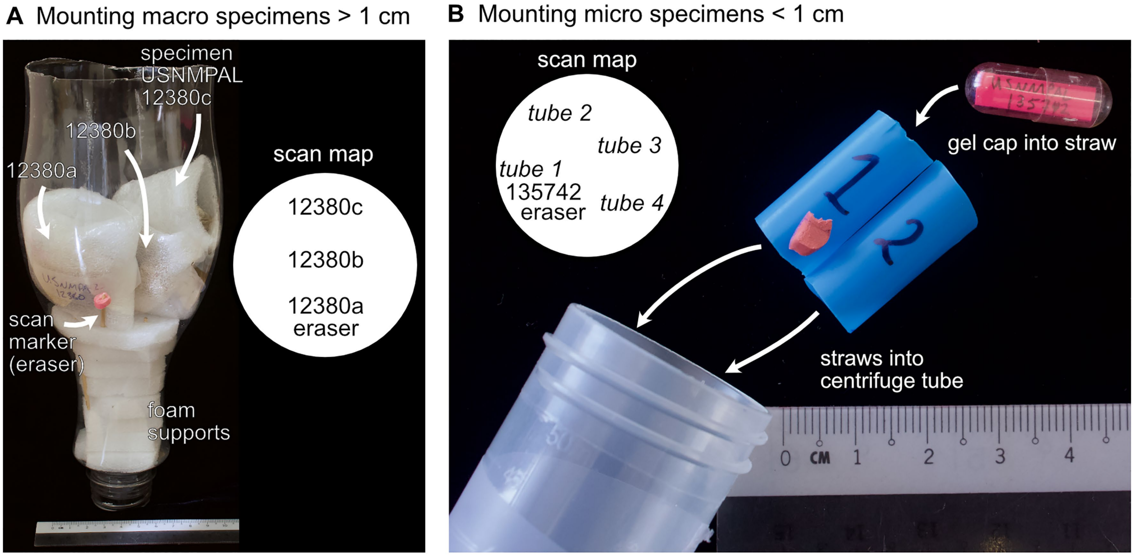

FIGURE 2
Mount of specimens for micro-CT imaging. **(A)** Macro specimens (>1cm) are placed inside a cylindrical plastic container in an imbricated manner, with commissures perpendicular to the foam support at the base of the container. The scan map records the position of specimens in the scan mount using registration numbers or unique specimen IDs relative to the scan marker (e.g., an eraser). **(B)** Micro specimens (<1cm) are placed inside plastic or paper straws, which are then placed inside a 15ml or 50ml centrifuge tube.

total range, contrast ratio, and signal to noise of the histogram (Table 2). Increasing the current also increases the power, and tends to increase the minimum gray value, which can reduce both the signal to noise and contrast ratios (compare values in Table 2); if so, step back to previous settings. If the minimum gray cannot be reached within the power limits of the X-ray tube or without oversaturating the detector, add a physical filter (see next section) or increase the exposure timing, which may require adding frame skips so that the detector panel can discharge between images (this timing can be highly system-dependent). Similarly, it is important to check that the X-ray spot size is not 1.3 times larger than the expected voxel size (i.e., resolution) of the scan. Increasing exposure time and frame averaging will also increase the signal to noise ratio, helping to define sharper boundaries between shell and matrix if needed (often a good setting to adjust when the shell is a calcareous matrix).

Physical filters

Filters can reduce beam hardening, an artifact where soft X-rays are absorbed at the sample surface leaving only the higher energy X-rays to penetrate the sample; this creates streak or cupping artifacts, where gray values grade from high to low intensity towards the interior of the specimen (see Sutton et al., 2014; Wellenberg et al., 2018). Fossil shells in matrix frequently show cupping artifacts, which can complicate simple segmentation on gray value intensity. Metal filters, typically aluminum, copper, or tin sheets ranging from 0.1 to 1 mm in thickness, can minimize this gradient in gray value intensities, but at the cost of diminished compositional contrast. Because many of our fossil shells are in calcareous matrix, meaning there is minimal compositional contrast between specimen and rock, we generally do not use filters in order to maximize what little contrast may exist. For Recent specimens free of matrix, a 0.1 mm copper filter does reduce beam hardening, simplifying segmentation of shell material from air and foam, but segmentation of scans lacking a filter is not any more difficult.

Number of image projections

All of our scans use 360° rotation, and while the rule of thumb for setting the number of projections images is the width of the scan in pixels multiplied by π (Keklikoglou et al., 2019, p. 17), we find that shells with simple, large morphologies (i.e., smooth shells with large hinge teeth) can be scanned with projections equaling the greatest width of the scan scene (for a detector 2000 pixels wide, this would be 2000 projections). This can reduce scan times to as low as 7–10 min, depending also on the exposure time, frame averaging and skips. Thus, it is important to group specimens for bulk scanning according to the desired resolution for their smallest features of interest. For shells with relatively finer details, or for those embedded in matrix, setting a higher number of projections can better resolve those features (Sutton et al., 2014, p. 58; Keklikoglou et al., 2019, p. 7), although we find *N**1.5 to usually be sufficient.

Reconstruction

We have reconstructed all scans using the proprietary software of the micro-CT systems (i.e., GE phoenix datos|x), but alternative solutions are available (Sutton et al., 2014, pp. 149–150). We have always scanned with settings to compensate for any drift in the center of rotation, changes in focal spot size, and any small movement of the specimens (in the GE system, this would be using the Autoscan Optimizer followed by the Automatic Geometry Calibration before reconstruction). Scanning using detector shifts (i.e., small adjustments in the detector panel to reduce hot pixels), can reduce beam hardening (for additional mitigation techniques, see Wellenberg et al., 2018). Streaks, ring artifacts, and beam hardening are often in our scans and could be further mitigated during the reconstruction step—but we find these artifacts to rarely impact the

TABLE 2 Effects of X-ray parameter settings on gray-value histogram for scanning specimen USNM PAL 20943, *"Lucina" parvilineata*.

Parameters			Summary of gray-value histogram						Comments
Filter	Voltage (kV)	Amperage (A)	Min. value	Max. value	Mean value	Range	Contrast	Signal to noise	
None	95	220	330	468	402	123	0.3	16.7	Baseline setting with low voltage and high current.
None	130	110	400	534	470	132	0.3	17.3	Raising voltage and lowering current increases min counts and signal to noise.
None	130	120	444	581	511	145	0.3	19.6	Raise current to spread histogram, increases signal to noise.
None	130	130	470	684	558	201	0.4	24.5	"
None	130	130	470	684	558	201	0.4	24.5	"
None	130	140	517	778	608	270	0.4	31.6	Best histogram spread; settings used for scan.
None	130	150	548	730	630	190	0.3	24.8	Raising current now reduces contrast and signal to noise.
0.1 mm Cu	130	140	282	401	325	121	0.4	14.1	Adding filter reduces min counts and range of histogram.
0.1 mm Cu	140	140	344	468	391	127	0.3	16.6	Increasing voltage improves min contrast and range, but signal to noise still ½ optimal settings above.

final surface mesh for Recent and fossil material that is free of matrix. For fossils in matrix, application of deep learning segmentation below can help to overcome these artifacts.

Scan segmentation

Segmentation with isovalue thresholding

Once reconstructed, Recent and fossil material that is free of matrix can often be isolated from air and packing materials by simply thresholding out the non-target values in the image stack (see a recent list of commercial software and freeware for this operation in Keklikoglou et al., 2019, their Table 15, but also see 3D Slicer Kikinis et al., 2014; we primarily use ORS Dragonfly; Object Research Systems (ORS) Inc., 2022). If the organic content of shells varies within a bulk scan (i.e., nacre vs. calcite), the scan scene may require separate threshold values for generating shell-specific regions of interest (ROIs). These shell ROIs can be further refined using manual segmentation tools, or by removing any pixels isolated from the targeted shells with simple region of interest tools, such as island processing algorithms that remove pixel sets less than a certain value (e.g., "Processing Islands" in ORS Dragonfly). From these refined ROIs, contour meshes can be generated and exported for further cleaning and morphological analysis. For many fossil shells embedded in matrix, particularly those in calcareous matrix, this simple thresholding approach will not work given the limited compositional contrast between the specimen and sediment. Here, deep learning can facilitate segmentation.

Workflow for segmentation with deep learning

Deep learning has become a powerful tool for image segmentation, especially for digital excavation of fossils embedded in matrix (Liu and Song, 2020; Yu et al., 2022). However, we note that to date, our applications of deep learning have yet to perfectly segment a bivalve fossil from matrix (as Yu et al., 2022 also noted for segmenting dinosaur bones from matrix). Thus, we use deep learning as a technique to speed up segmentation, which almost always requires manual tuning to complete; this means finding a compromise between the time spent fitting the model(s) and then manually finalizing the segmentation. We use the deep learning interface developed by ORS Dragonfly (the "Segmentation Wizard," Badran et al., 2020), which creates an interactive session for fitting and refining multiple deep learning models for segmentation. Regardless of the software used, we suggest that this approach is a good, generalizable workflow. Continued research into model architectures will undoubtedly bring faster and more accurate initial segmentations of these low compositional contrast materials, but our emphasis here is on producing sizable datasets of workable 3D models for quantitative evolutionary analysis. Thus, the trade-off in time spent tuning hyperparameters and fitting models in search of a perfect segmentation should be weighed against using an adequate model to provide a strong starting point for manual segmentation.

Within the ORS Dragonfly Segmentation Wizard, we begin segmentation by selecting a slice from the image stack that best represents the full diversity of features; often this is an image slice containing hinge teeth or fine ornamentation (e.g., Figure 3A). We then define the segmentation frame (i.e., a rectangular mask) that brackets the shell and manually set ROIs corresponding to shell material and background (i.e., matrix and/or air, Figure 3A, bottom row). We then train a series of deep learning models using this single frame and visually inspect the predicted segmentation (Figure 3B). Usually, the U-Net architecture (Ronneberger et al., 2015) is the fastest and most accurate approach, but Sensor3D, and variations on the U-Net such as Attention U-Net and U-Net++ can sometimes better separate the boundaries between fossil shell and matrix (hyperparameters for the U-Net fit here are in Figure 3C). The resulting model accuracies provide a general estimate of segmentation performance, but high accuracies can sometimes characterize models with poor definition of the boundary between fossil shell and matrix (e.g., frame 1 in Figure 3B for Round 1 of training, which had an accuracy score of 0.97 Figure 3D). In this example, the model trained for one round cleanly separates shell from air, but confuses parts of the matrix and shell (compare Figures 3A,B for frame 1, particularly around the hinge area). Therefore, the additional training data was labeled, and the model weights updated through continued training.

Subsequent rounds of training improved the segmentation of shell from matrix (compare better capture of the hinge area in rounds 2–4, Figure 3B). The training data in frames 3 and 4 were selected to improve segmentation of shell from matrix where streak artifacts impacted the shell boundary at the edge of the specimen. Frame 5 was selected to improve segmentation of shell from matrix for a region of the hinge area that was not well predicted through the third training round. We could continue to iterate the process at this point, expanding the training set to include image slices with poor predicted segmentation. However, as mentioned above, we weigh the continued time in fine-tuning these segmentation models against manually tuning the segmentation. In general, we find that one or two rounds of creating training data and fitting models is sufficient to produce a strong starting segmentation. From there, we manually segment regions where the model failed to define the boundary between shell and matrix. Without any manual segmentation, the resulting 3D model has noise, but captures nearly all of the relevant taxonomic details (Figure 4). Timing required for segmentation *via* deep learning compared to fully manual operation depends, in part, on compute power. The process described for the fossil in Figure 3 required approximately 3 h, from labeling training data to fitting the model and predicting the segmentation, and half of that time was fitting the initial model (compute power: Intel Xeon Silver 4214R CPU @2.40 GHz with 512 GB RAM and 2 × 16 GB NVIDIA Quadro RTX5000 GPU). Fully manual segmentation of this fossil is estimated to take 8 or more hours of constantly engaged work.

Discussion

New morphological measurements, new macroevolutionary and macroecological insights

Bivalves have been a good model system for testing macroecological and macroevolutionary theories. Aspects of their shell morphologies largely align with molecular phylogenies (Jablonski and Finarelli, 2009; Bieler et al., 2014), allowing morphologically derived phylogenetic analyses of their biogeographic, functional, and morphological evolution through deep time. Three-dimensional micro-CT scans of bivalve shells provide access to previously unseen morphologies and to measurements of morphological dimensions

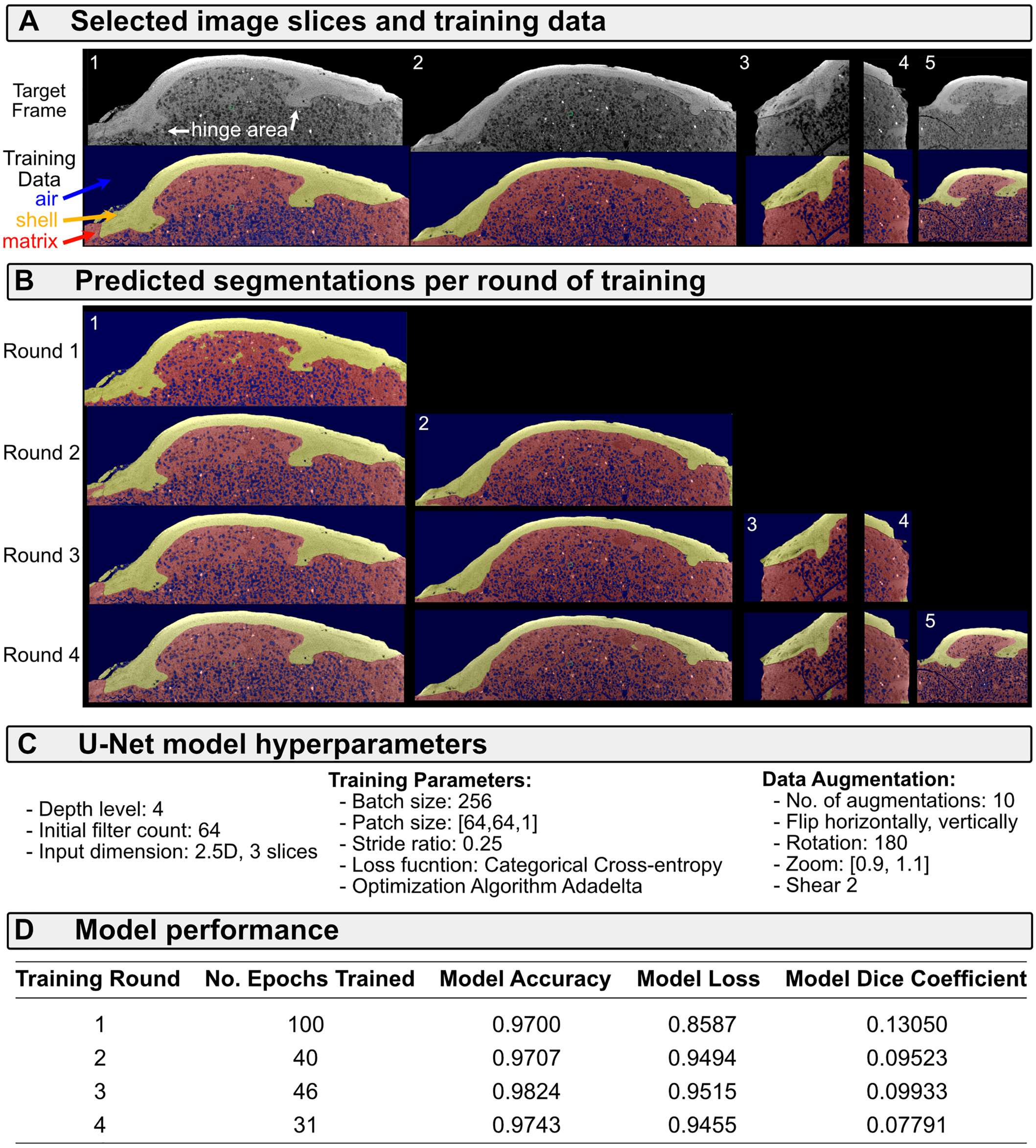

C U-Net model hyperparameters

- Depth level: 4
- Initial filter count: 64
- Input dimension: 2.5D, 3 slices

Training Parameters:
- Batch size: 256
- Patch size: [64,64,1]
- Stride ratio: 0.25
- Loss fucntion: Categorical Cross-entropy
- Optimization Algorithm Adadelta

Data Augmentation:
- No. of augmentations: 10
- Flip horizontally, vertically
- Rotation: 180
- Zoom: [0.9, 1.1]
- Shear 2

D Model performance

Training Round	No. Epochs Trained	Model Accuracy	Model Loss	Model Dice Coefficient
1	100	0.9700	0.8587	0.13050
2	40	0.9707	0.9494	0.09523
3	46	0.9824	0.9515	0.09933
4	31	0.9743	0.9455	0.07791

FIGURE 3
Segmentation of shell from matrix using deep learning for specimen USNM PAL 20943, *"Lucina" parvilineata*. **(A)** Selected image slices cropped to training frames in the top row, with frame number in white text. Bottom row shows ground-truth labeled training data. **(B)** Predicted segmentation for image slices per round of model training, i.e., only frame 1 was trained in round 1, but frames 1 and 2 were used to train round 2, so both have predicted segmentations for this round. Both frames 3 and 4 were included in round 3 of training. Frame 5 was only included in round 4. **(C)** Hyperparameters of the U-Net model. **(D)** Model performance statistics for each round of training.

that have been difficult to quantify at large sample sizes. These new data are helping to address long-standing questions about evolutionary processes within the group, which we example in the following sections. Such approaches add broader phylogenetic context for general tests of ecological and evolutionary processes acting across other model systems such as fishes and birds.

Accessing hidden morphology highlights the termination of an evolutionary pathway following mass extinction

Quantitative analyses of how mass extinctions reorganize the dimensions of biodiversity require rigorous phylogenetic, ecologic, and morphologic hypotheses, and micro-CT will strengthen paleontological efforts on each of these fronts. The bivalve genus *Legumen* was lost in the end-Cretaceous mass extinction around 66 Ma, and its phylogenetic placement and thus the impact of its loss on the subsequent morphological and ecological evolution of its higher clade was uncertain (Collins et al., 2020). This genus is known almost entirely from its external shell shape (as in Figure 5), which is notoriously homoplastic across bivalves (Stanley, 1970; Oliver and Holmes, 2006). Using micro-CT and deep learning segmentation, we were able to segment key fossil specimens from sedimentary matrix, revealing their taxonomically important hinge morphology (Collins et al., 2020). Comparing these digital excavations to the rare specimens with physical preparations of their hinge teeth confirmed the phylogenetic placement of *Legumen* within the most diverse

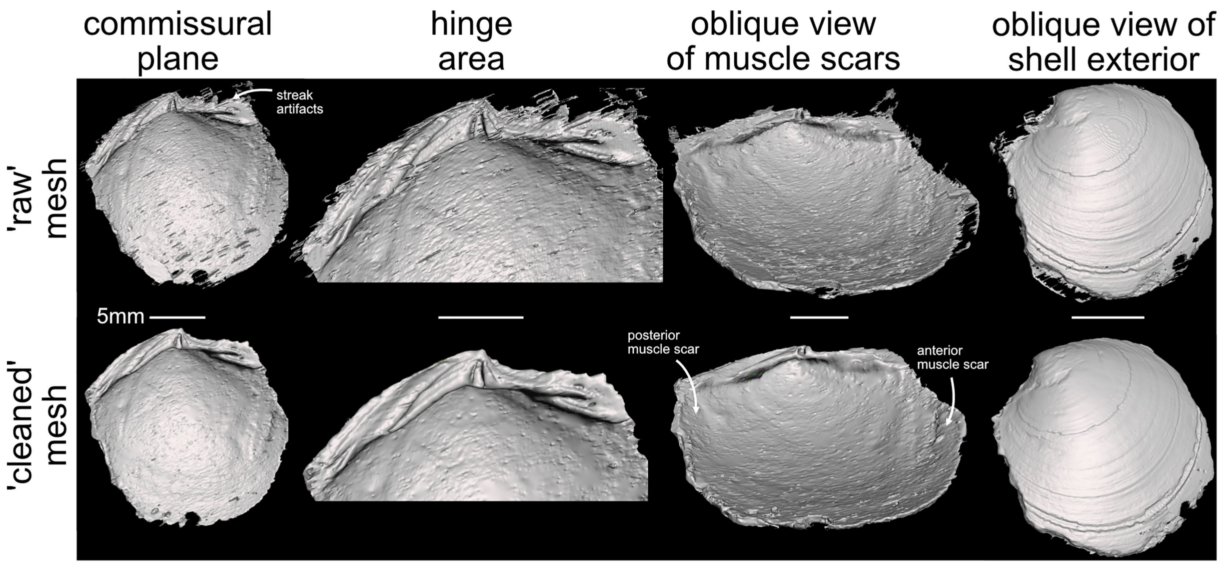

FIGURE 4
Taxonomically important views of the previously inaccessible interior features of Late Cretaceous (Early Maastrichtian) *"Lucina" parvilineata*, USNM PAL 20943. Top row shows the 'raw' mesh surface directly produced by deep learning segmentation after round 4 of training in Figure 3. Bottom row shows the final mesh surface after removal of streak artifacts and manual cleaning of noisy surface data where the model struggled to segment the shell from its surrounding matrix. Considerable care should be taken at this step so as not to erode any genuine, biological features.

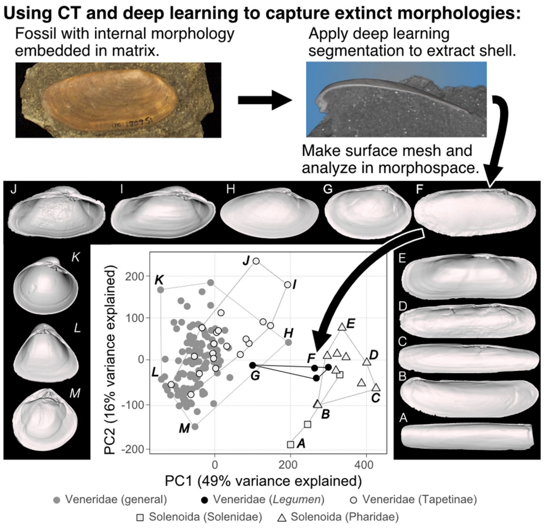

FIGURE 5
Using CT data to capture and analyze extinct morphologies. Fossils embedded in sediment, such as the *Legumen ellipticum* Conrad 1858 photographed here, can be micro-CT scanned and segmented from matrix using the deep learning approach from Figure 3. This analysis showed that the venerid genus *Legumen* (F, G), which was lost at the end-Cretaceous mass extinction, had an atypical shape that has yet to evolve again within the family (adapted from Collins et al., 2020).

bivalve family, Veneridae. Further, 3D morphometrics of its shell shape showed *Legumen* to be atypical for the family, occupying a distinct region of morphospace and ecospace—one that was never regained by the family during its Cenozoic diversification, instead being invaded, and perhaps preempted, by other family-level clades (Figure 5; Collins et al., 2020). Thus, the loss of *Legumen* becomes an important data point in larger analyses of how developmental biases and priority effects from competing clades may interact to shape the re-diversification of biodiversity following mass extinctions.

Volumetric morphometrics and the derivation of the latitudinal diversity gradient

Trade-offs in organismal form can reflect interactions of developmental constraint with ecological and environmental selection. The bivalve shell is a good vehicle for analyzing the relative impact of these factors on the sequence of evolutionary events, and their tempo and mode. For example, the volume of the bivalve's shell compared to its soft-internal anatomy may reflect energetic trade-offs (Collins et al., 2019) and/or may proxy shell strength (Stanley, 1970), but these measurements have required molding the shell and its interior cavity (the space holding the internal soft anatomy; see Stanley, 1970, p. 109). Measuring such volumes from micro-CT-derived 3D models is now computationally simple, where volumes of triangular surface meshes can be approximated by integrating the signed tetrahedral volumes of each triangular face to the centroid of the mesh (Collins et al., 2019). Applying this approach in the comparison of a warm- to cool-temperate fauna has challenged the macroecological hypothesis that lower nutrient availability and decreased aragonite saturation states at high latitudes should filter and/or reduce the volume of the animal that is shell; both large and relatively thick-shelled bivalves are found from the Florida Keys to the Gulf of Maine (Figure 6; Collins et al., 2019). This same high-throughput approach could be used to generate high-precision estimates of intraspecific variation in relative shell volumes for taxa with known responses to gradients in ocean acidification (e.g., bimineralic *Mytilus* species, Bullard et al., 2021).

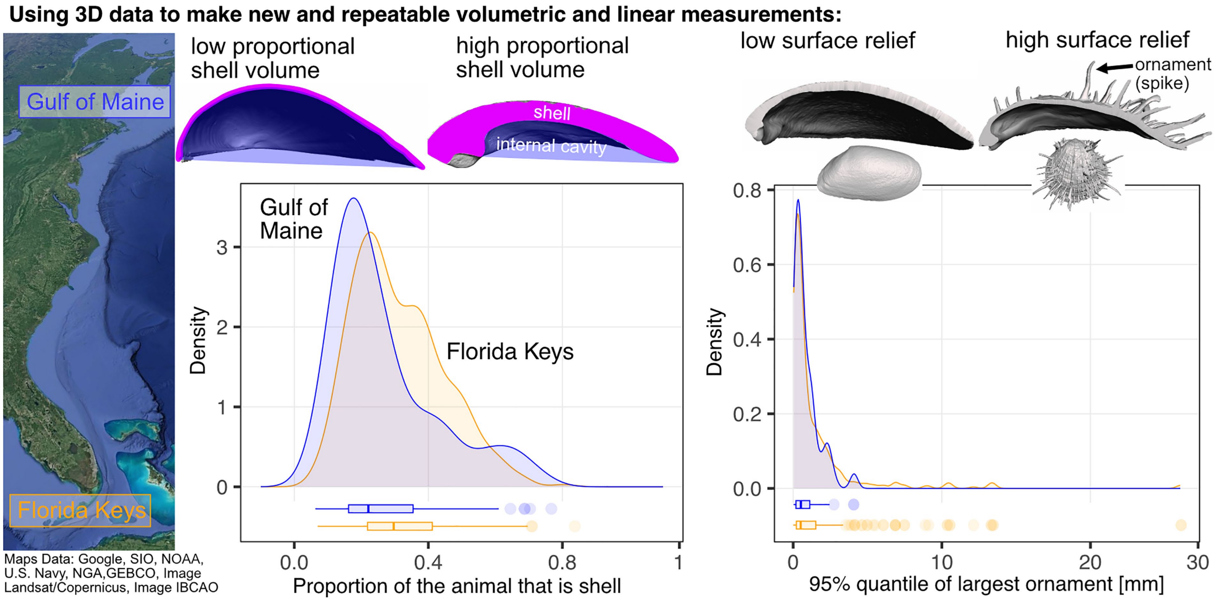

FIGURE 6
Using 3D data to identify latitudinal gradients in shell morphology along the east coast of North America. The proportion of the animal that is shell remains similar between the subtropical Florida Keys and temperate Gulf of Maine, but taxa with the most pronounced ornamentation do not reach the Gulf of Maine (adapted from Collins et al., 2019).

Predation intensity is another factor hypothesized to be a strong determinant of the latitudinal diversity gradient (Vermeij, 1987; Schemske et al., 2009; Freestone et al., 2021). Predation's impact on diversity may operate on longer timescales than can be observed in real-time, and phylogenetically controlled comparative approaches are needed to augment field-based experiments. Some morphological aspects of prey have evidently evolved in direct response to modes and intensities of predation (Vermeij, 1987), and the evolution and variation of bivalve shell spines, ribs, flanges, and other elements of ornamentation are hypothesized to be anti-predatory adaptations (Vermeij, 1987; Harper and Skelton, 1993). Volumetric scans of shells have allowed us to quantify these features and analyze a significant decline in the complexity, or spininess, of shell surfaces among species from low to high latitudes, a shift that occurred by sorting among taxonomic families rather than by evolutionary transformation of genera or species (Figure 6; Collins et al., 2019). While this pattern is consistent with highest predation intensity in the tropics, it primes the investigation of other, potentially underlying factors, such as using fossils to analyze temporal lags in the biogeographic dispersion of species towards higher latitudes, and more generally to analyze regional changes in morphology that might be expected to accompany long-term climate shifts.

3D shape morphometrics and the evolution of disparity

Since the origin of the class more than half a billion years ago, bivalves have evolved in and out of broad swaths of ecological and morphological space, offering many comparative experiments of convergence and divergence. Most analyses of morphological evolution have used 2D morphometrics of the shell, focusing primarily on its outline within the commissural plane (sagittal plane). The commissural profile captures some of the relationship between shell shape and ecological function but misses a key axis of shape variation within the transverse plane—its curvature or inflation. This morphological axis also relates to the shell's interaction with the substratum, from the hydrodynamics of swimming in scallops to the infaunal clam's penetration of substrata, that is, the animal's ability to burrow away from predators and buffer open-water environmental conditions. Analyses of 3D shell shape using surface semi-landmarking capture considerable variation in shell inflation (Collins et al., 2019, p. 9; Edie et al., 2022b, p. 4), which should be taken into account when identifying instances of convergence and divergence. For example, bivalves that bore into rocks—an ecological function that can require excavating substrata that is materially harder than the shell—show a remarkable disparity of shell forms within the usually measured commissural plane, suggesting multiple, divergent evolutionary pathways into the niche. In theory, this function might drive convergence along the "hidden" third axis of variation, shell inflation, but tests including this dimension indicate this is not the case, and that rock-boring is indeed one of the most morphologically disparate functions across the class today (Collins et al., 2023).

Access to phylogenetically and morphologically broad characterizations of shell shape has introduced complications to shape-based morphometrics. For example, aligning specimens on point-based biological homology is complicated by Bivalvia having only one such point across the entire class, the origin of shell growth at the beak (Carter et al., 2012, p. 21; Edie et al., 2022a). Thus, shape-based comparative morphometrics requires alignment using a biomechanical axis that reflects how the animals interact with their environment. The hinge line—the line about which the two valves rotate during the opening and closing of the valves—is functionally analogous across the class, and can be defined using clade-specific features (Edie et al., 2022a). While not strictly adhering to the conventions of geometric morphometrics, this approach gives intuitive gradients and clusters in shell morphology that can be combined with other means of aligning shells to test hypotheses of how tightly coupled form and function are to modes of shell growth (Edie et al., 2022a).

3D morphometrics of shell shape can also address morphological integration and modularity in bivalves, with their simple skeletons that grow by accretion, and how they might contrast with clades exhibiting more complex segmented skeletons (e.g., arthropods and vertebrates). The features of the bivalve shell and the enclosed soft parts might fall into discrete functional or developmental units (Figure 7), e.g., the hinge teeth possibly showing tight covariation with the relative sizes and positions of the muscles and the spring-like ligament that together form the functional complex that opens and closes the shell. Alternatively, the shell may form a discrete, integrated module from the soft-internal anatomy. At least for the most speciose group in today's ocean, the Veneridae, the latter appears to be true (Figure 7; Edie et al., 2022b). Thus, unlike the many modules in segmented invertebrates, the vertebrate skeleton, or even in vertebrate crania, bivalves appear to have tighter integration of their major morphological elements and a lower overall modularity (Sherratt et al., 2017; Edie et al., 2022b). Broader comparisons with other major bivalve groups could reveal a more varied pattern of modularity, integration and disparity, particularly those groups that break bilateral symmetry in shell growth and shape (Jablonski, 2020).

Conclusion

The paleontologist's remit in evolutionary biology has grown substantially since the Modern Synthesis (Gould, 2002; Sepkoski, 2015; Marshall, 2017; Jablonski, 2017a,b). Direct access to evolutionary sequences of morphologies is critical for understanding how innovations and other factors drive diversifications along phylogenetic, functional, and morphological lines, and how the extinction or pruning of forms impacted the trajectories of diversification. Analyses of extant-only data can sometimes proxy the former, particularly for shallow-time radiations, but they cannot address or even approximate the latter. Both patterns of morphological gain *and* loss are needed for robust considerations of how determinism and contingency affect evolutionary trajectories. Still, accessing this library of time-stratified morphologies remains difficult. Discovery of new fossil diversity was once limited by the scale and number of field campaigns, then by "reburial" in under-cataloged and under-digitized museums, and always by physical access to collections. Extensive efforts have steadily grown deep-time biodiversity databases, but many fossils remain locked away in consolidated sediments—in the field and in collections—making them difficult to access without painstaking collection and preparation. X-ray computed tomography overcomes some of these limitations, mobilizing virtual data and spurring substantial discovery and description of new fossils, mostly vertebrates. However, most of life today and in the past belongs to invertebrate phyla, many of which have an abundance of fossilized hard parts. Scanning and digitally excavating these fossils has been a challenge given the compositional similarity between their hard parts and the surrounding sediments, but advances in segmentation using deep learning is speeding up this process. Now, for the first time, we have views into rarely or never seen shell morphologies, such as the previously inaccessible, taxonomically important interior morphology of the "*Lucina*" *parvilineata* segmented here, laying the foundation for more complete phylogenetic consideration. Bivalves, and other invertebrates with strong fossil records including snails, echinoderms, brachiopods, trilobites, sponges, corals, and many more, are ripe for new phylogenetic and morphological evolutionary analyses facilitated by X-ray micro-CT.

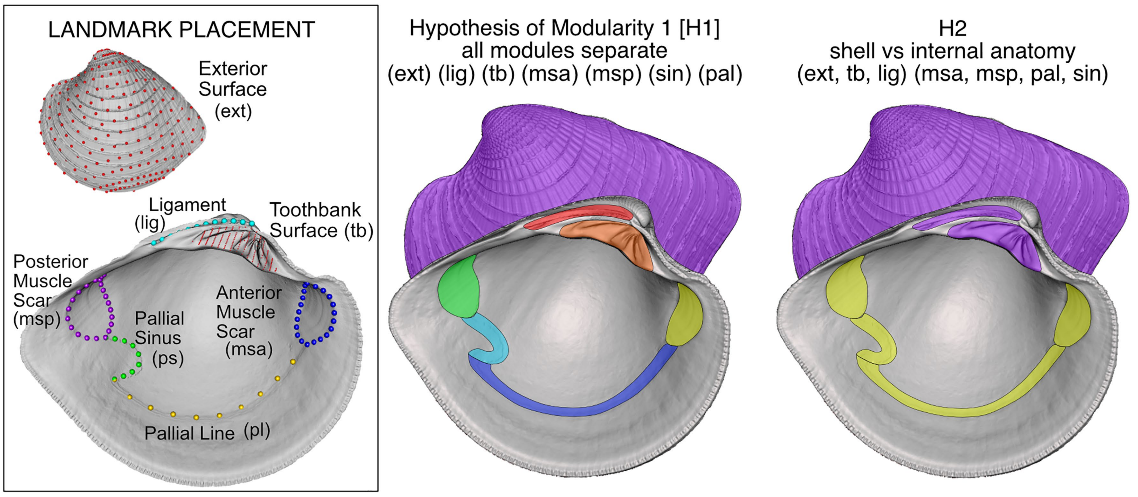

FIGURE 7
Geometric morphometric landmarking of shell features and hypotheses of modularity and integration in the venerid bivalve *Chionopsis amathusia* (Philippi 1844). Hypothesis of modularity "H1" was the working hypothesis, with all potential modules varying independently, but H2, with just two discrete modules, was best supported by morphometric analysis (adapted from Edie et al., 2022a,b).

Data availability statement

The original contributions presented in the study are included in the article. Mesh of USNM PAL 20943 available on Morphosource (ark:/87602/m4/497818). Further inquiries can be directed to the corresponding author.

Author contributions

All authors listed have made a substantial, direct, and intellectual contribution to the work, and approved it for publication.

Funding

The study was supported by National Science Foundation EAR-1633535, DEB 2049627, National Aeronautics and Space Administration EXOB08-0089, and a CDAC Data Science Discovery grant, University of Chicago.

Acknowledgments

We thank the many museums and their staff for access to collections in their care: R. Bieler, J. Gerber, and J. Jones (Field Museum); M. Florence, E. E. Strong, and C. Walters (National Museum of Natural History); R. Portell and J. Slapcinski (University of Florida Museum of Natural History); E. A. Glover, A. Salvador, J. D. Taylor, and T. White (Natural History Museum, London); V. Delvanaz, D. Geiger, P. Valentich-Scott (SBMNH); E. Kools and P. Roopnarine (CAS). For scanning access, we thank A. I. Neander (University of Chicago Paleo-CT micro-CT facility); J. J. Hill and S. Whitaker (NMNH Scientific Imaging Facility). For discussions, we thank F. Goetz and S. Keogh. We thank E. Clark and three reviewers for constructive feedback.

Conflict of interest

The authors declare that the research was conducted in the absence of any commercial or financial relationships that could be construed as a potential conflict of interest.

Publisher's note

References

Abel, R., Laurini, C., and Richter, M. (2012). A palaeobiologist's guide to "virtual" micro-CT preparation. *Palaeontol. Electron.* 15:15.2.6T. doi: 10.26879/284

Badran, A., Marshall, D., Legault, Z., Makovetsky, R., Provencher, B., Piché, N., et al. (2020). Automated segmentation of computed tomography images of fiber-reinforced composites by deep learning. *J. Mater. Sci.* 55, 16273–16289. doi: 10.1007/s10853-020-05148-7

Bauer, J. E., and Rahman, I. A. (2021). *Virtual Paleontology: Tomographic Techniques for Studying Fossil Echinoderms (Elements of Paleontology)*. Cambridge, UK: Cambridge University Press.

Bieler, R., Mikkelsen, P. M., Collins, T. M., Glover, E. A., González, V. L., Graf, D. L., et al. (2014). Investigating the bivalve tree of life–an exemplar-based approach combining molecular and novel morphological characters. *Invertebr. Syst.* 28, 32–115. doi: 10.1071/IS13010

Birnbacher, L., Braig, E.-M., Pfeiffer, D., Pfeiffer, F., and Herzen, J. (2021). Quantitative X-ray phase contrast computed tomography with grating interferometry. *Eur. J. Nucl. Med. Mol. Imaging* 48, 4171–4188. doi: 10.1007/s00259-021-05259-6

Borowiec, M. L., Dikow, R. B., Frandsen, P. B., McKeeken, A., Valentini, G., and White, A. E. (2022). Deep learning as a tool for ecology and evolution. *Methods Ecol. Evol.* 13, 1640–1660. doi: 10.1111/2041-210X.13901

Bullard, E. M., Torres, I., Ren, T., Graeve, O. A., and Roy, K. (2021). Shell mineralogy of a foundational marine species, *Mytilus californianus*, over half a century in a changing ocean. *Proc. Natl. Acad. Sci.* 118:e2004769118. doi: 10.1073/pnas.2004769118

Carter, J. G., Harries, P. J., Malchus, N., Sartori, A. F., Anderson, L. C., Bieler, R., et al. (2012). Illustrated glossary of the Bivalvia. *Treatise Online* Vol 1. (No. 48, Part N), 1–209. doi: 10.17161/to.v0i0.4322

Claussen, A. L., Munnecke, A., Wilson, M. A., and Oswald, I. (2019). The oldest deep-boring bivalves? Evidence from the Silurian of Gotland (Sweden). *Facies* 65:26. doi: 10.1007/s10347-019-0570-7

Coates, M. I., Tietjen, K., Olsen, A. M., and Finarelli, J. A. (2019). High-performance suction feeding in an early elasmobranch. *Sci. Adv.* 5:eaax2742. doi: 10.1126/sciadv.aax2742

Collins, K. S., Crampton, J. S., Neil, H. L., Smith, E. G. C., Gazley, M. F., and Hannah, M. (2016). Anchors and snorkels: heterochrony, development and form in functionally constrained fossil crassatellid bivalves. *Paleobiology* 42, 305–316. doi: 10.1017/pab.2015.48

Collins, K. S., Edie, S. M., Gao, T., Bieler, R., and Jablonski, D. (2019). Spatial filters of function and phylogeny determine morphological disparity with latitude. *PLoS One* 14:e0221490. doi: 10.1371/journal.pone.0221490

Collins, K. S., Edie, S. M., and Jablonski, D. (2020). Hinge and ecomorphology of *Legumen* Conrad, 1858 (Bivalvia, Veneridae), and the contraction of venerid morphospace following the end-Cretaceous extinction. *J. Paleontol.* 94, 489–497. doi: 10.1017/jpa.2019.100

Collins, K. S., Edie, S. M., and Jablonski, D. (2023). Convergence and contingency in the evolution of a specialized mode of life: multiple origins and high disparity of rock-boring bivalves. *Proc. R. Soc. B Biol. Sci.* 290:20221907. doi: 10.1098/rspb.2022.1907

Collins, K. S., Klapaukh, R., Crampton, J. S., Gazley, M. F., Schipper, C. I., Maksimenko, A., et al. (2021). Going round the twist—an empirical analysis of shell coiling in helicospiral gastropods. *Paleobiology* 47, 648–665. doi: 10.1017/pab.2021.8

Cunningham, J. A., Rahman, I. A., Lautenschlager, S., Rayfield, E. J., and Donoghue, P. C. J. (2014). A virtual world of paleontology. *Trends Ecol. Evol.* 29, 347–357. doi: 10.1016/j.tree.2014.04.004

Daley, G., and Bush, A. (2020). The effects of lithification on fossil assemblage biodiversity and composition: an experimental test. *Palaeontol. Electron.* 23:a53. doi: 10.26879/1119

Edie, S. M., Collins, K. S., and Jablonski, D. (2022a). Specimen alignment with limited point-based homology: 3D morphometrics of disparate bivalve shells (Mollusca: Bivalvia). *PeerJ* 10:e13617. doi: 10.7717/peerj.13617

Edie, S. M., Khouja, S. C., Collins, K. S., Crouch, N. M. A., and Jablonski, D. (2022b). Evolutionary modularity, integration and disparity in an accretionary skeleton: analysis of venerid Bivalvia. *Proc. R. Soc. B Biol. Sci.* 289:20211199. doi: 10.1098/rspb.2021.1199

Edie, S. M., Smits, P. D., and Jablonski, D. (2017). Probabilistic models of species discovery and biodiversity comparisons. *Proc. Natl. Acad. Sci.* 114, 3666–3671. doi: 10.1073/pnas.1616355114

Feldmann, R., Chapman, R. E., and Hannibal, J. T. (1989). Paleotechniques. *Paleontol. Soc. Spec. Publ.* 4, f1–f5. doi: 10.1017/S2475262200005360

Foote, M. (1997). The evolution of morphological diversity. *Annu. Rev. Ecol. Syst.* 28, 129–152. doi: 10.1146/annurev.ecolsys.28.1.129

Foote, M., Crampton, J. S., Beu, A. G., and Nelson, C. S. (2015). Aragonite bias, and lack of bias, in the fossil record: lithological, environmental, and ecological controls. *Paleobiology* 41, 245–265. doi: 10.1017/pab.2014.16

Freestone, A. L., Torchin, M. E., Jurgens, L. J., Bonfim, M., López, D. P., Repetto, M. F., et al. (2021). Stronger predation intensity and impact on prey communities in the tropics. *Ecology* 102:e03428. doi: 10.1002/ecy.3428

Goswami, A., Noirault, E., Coombs, E. J., Clavel, J., Fabre, A.-C., Halliday, T. J. D., et al. (2022). Attenuated evolution of mammals through the Cenozoic. *Science* 378, 377–383. doi: 10.1126/science.abm7525

Gould, S. J. (2002). *The Structure of Evolutionary Theory*. Cambridge, MA: Belknap Press of Harvard University Press.

Harper, E., and Skelton, P. (1993). The Mesozoic marine revolution and epifaunal bivalves. *Scr. Geol.* 2, 127–153.

Huang, Z., Liu, Z., He, P., Ren, Y., Li, S., Lei, Y., et al. (2022). Segmentation-guided denoising network for low-dose CT imaging. *Comput. Methods Prog. Biomed.* 227:107199. doi: 10.1016/j.cmpb.2022.107199

Jablonski, D. (2005). Mass extinctions and macroevolution. *Paleobiology* 31, 192–210. doi: 10.1666/0094-8373(2005)031[0192:MEAM]2.0.CO;2

Jablonski, D. (2017a). Approaches to macroevolution: 1. General concepts and origin of variation. *Evol. Biol.* 44, 427–450. doi: 10.1007/s11692-017-9420-0

Jablonski, D. (2017b). Approaches to macroevolution: 2. Sorting of variation, some overarching issues, and general conclusions. *Evol. Biol.* 44, 451–475. doi: 10.1007/s11692-017-9434-7

Jablonski, D. (2020). Developmental bias, macroevolution, and the fossil record. *Evol. Dev.* 22, 103–125. doi: 10.1111/ede.12313

Jablonski, D., Belanger, C. L., Berke, S. K., Huang, S., Krug, A. Z., Roy, K., et al. (2013). Out of the tropics, but how? Fossils, bridge species, and thermal ranges in the dynamics of the marine latitudinal diversity gradient. *Proc. Natl. Acad. Sci.* 110, 10487–10494. doi: 10.1073/pnas.1308997110

Jablonski, D., and Finarelli, J. A. (2009). Congruence of morphologically-defined genera with molecular phylogenies. *Proc. Natl. Acad. Sci. U. S. A.* 106, 8262–8266. doi: 10.1073/pnas.0902973106

Johnston, P., and Haggart, J. (Eds.) (1998). *Bivalves: An Eon of Evolution*. Calgary: University of Calgary Press.

Keklikoglou, K., Faulwetter, S., Chatzinikolaou, E., Wils, P., Brecko, J., Kvaček, J., et al. (2019). Micro-computed tomography for natural history specimens: a handbook of best practice protocols. *Eur. J. Taxon* 522, 1–55. doi: 10.5852/ejt.2019.522

Kikinis, R., Pieper, S. D., and Vosburgh, K. G. (2014). "3d slicer: a platform for subject-specific image analysis, visualization, and clinical support" in *Intraoperative Imaging and Image-Guided Therapy*. ed. F. A. Jolesz (New York, NY: Springer), 277–289.

Larina, E., Garb, M., Landman, N., Dastas, N., Thibault, N., Edwards, L., et al. (2016). Upper Maastrichtian ammonite biostratigraphy of the Gulf coastal plain (Mississippi embayment, southern USA). *Cretac. Res.* 60, 128–151. doi: 10.1016/j.cretres.2015.11.010

Leshno Afriat, Y., Edelman-Furstenberg, Y., Rabinovich, R., Todd, J. A., and May, H. (2021). Taxonomic identification using virtual palaeontology and geometric morphometrics: a case study of Jurassic nerineoidean gastropods. *Palaeontology* 64, 249–261. doi: 10.1111/pala.12521

Liu, X., and Song, H. (2020). Automatic identification of fossils and abiotic grains during carbonate microfacies analysis using deep convolutional neural networks. *Sediment. Geol.* 410:105790. doi: 10.1016/j.sedgeo.2020.105790

Marshall, C. R. (2017). Five palaeobiological laws needed to understand the evolution of the living biota. *Nat. Ecol. Evol.* 1:0165. doi: 10.1038/s41559-017-0165

Matsukuma, A. (1996). Transposed hinges: a polymorphism of bivalve shells. *J. Molluscan Stud.* 62, 415–431. doi: 10.1093/mollus/62.4.415

Object Research Systems (ORS) Inc. (2022). Dragonfly 2022.2 [Computer Software]. Available at: http://www.theobjects.com/dragonfly (Accessed December, 2022).

Oliver, P. G., and Holmes, A. M. (2006). The Arcoidea (Mollusca: Bivalvia): a review of the current phenetic-based systematics. *Zool. J. Linnean Soc.* 148, 237–251. doi: 10.1111/j.1096-3642.2006.00256.x

Prôa, M., Pouit, D., Rouillard, T., Vincent, P., and Mellier, B. (2021). Hidden treasures uncovered: successful detection of fossils below the surface in large limestone blocks using a standard medical X-ray CT scanner. *Foss. Impr.* 77, 36–42. doi: 10.37520/fi.2021.004

Racicot, R. (2016). Fossil secrets revealed: X-ray CT scanning and applications in paleontology. *Paleontol. Soc. Pap.* 22, 21–38. doi: 10.1017/scs.2017.6

Reid, M., Bordy, E. M., Taylor, W. L., le Roux, S. G., and du Plessis, A. (2019). A micro X-ray computed tomography dataset of fossil echinoderms in an ancient obrution bed: a robust method for taphonomic and palaeoecologic analyses. *GigaScience* 8:giy156. doi: 10.1093/gigascience/giy156

Ronneberger, O., Fischer, P., and Brox, T. (2015). "U-Net: convolutional networks for biomedical image segmentation" in *Medical Image Computing and Computer-Assisted Intervention – MICCAI 2015 lecture notes in computer science*. eds. N. Navab, J. Hornegger, W. M. Wells and A. F. Frangi (Cham: Springer International Publishing), 234–241.

Schemske, D. W., Mittelbach, G. G., Cornell, H. V., Sobel, J. M., and Roy, K. (2009). Is there a latitudinal gradient in the importance of biotic interactions? *Annu. Rev. Ecol. Evol. Syst.* 40, 245–269. doi: 10.1146/annurev.ecolsys.39.110707.173430

Schwarzhans, W., Beckett, H. T., Schein, J. D., and Friedman, M. (2018). Computed tomography scanning as a tool for linking the skeletal and otolith-based fossil records of teleost fishes. *Palaeontology* 61, 511–541. doi: 10.1111/pala.12349

Seilacher, A., and Gishlick, A. D. (2014). *Morphodynamics*. Boca Raton, FL: CRC Press.

Sepkoski, D. (2015). *Rereading the Fossil Record: The Growth of Paleobiology as an Evolutionary Discipline*. Chicago, IL: University of Chicago Press.

Serb, J. M., Alejandrino, A., Otárola-Castillo, E., and Adams, D. C. (2011). Morphological convergence of shell shape in distantly related scallop species (Mollusca: Pectinidae). *Zool. J. Linnean Soc.* 163, 571–584. doi: 10.1111/j.1096-3642.2011.00707.x

Serb, J. M., Sherratt, E., Alejandrino, A., and Adams, D. C. (2017). Phylogenetic convergence and multiple shell shape optima for gliding scallops (Bivalvia: Pectinidae). *J. Evol. Biol.* 30, 1736–1747. doi: 10.1111/jeb.13137

Sherratt, E., Serb, J. M., and Adams, D. C. (2017). Rates of morphological evolution, asymmetry and morphological integration of shell shape in scallops. *BMC Evol. Biol.* 17:248. doi: 10.1186/s12862-017-1098-5

Stanley, S. M. (1970). Relation of shell form to life habits of the Bivalvia (Mollusca). *Geol. Soc. Am. Mem.* 125, 1–282. doi: 10.1130/MEM125

Stanley, S. M. (1979). *Macroevolution: Pattern and Process*. San Francisco, CA: W. H. Freeman.

Sutton, M. D., Rahman, I. A., and Garwood, R. J. (2014). *Techniques for Virtual Palaeontology*. Hoboken, NJ: Wiley Blackwell.

Sutton, M., Rahman, I., and Garwood, R. (2017). Virtual paleontology—an overview. *Paleontol. Soc. Pap.* 22, 1–20. doi: 10.1017/scs.2017.5

Thompson, J. R., Cotton, L. J., Candela, Y., Kutscher, M., Reich, M., and Bottjer, D. J. (2021). The Ordovician diversification of sea urchins: systematics of the Bothriocidaroida (Echinodermata: Echinoidea). *J. Syst. Palaeontol.* 19, 1395–1448. doi: 10.1080/14772019.2022.2042408

Valentine, J. W. (1973). *Evolutionary Paleoecology of the Marine Biosphere*. Englewood Cliffs, NJ: Prentice-Hall.

Vermeij, G. J. (1987). *Evolution and Escalation: An Ecological History of Life*. Princeton, NJ: Princeton University Press.

Vermeij, G. J. (2013). Molluscan marginalia: hidden morphological diversity at the bivalve shell edge. *J. Molluscan Stud.* 79, 283–295. doi: 10.1093/mollus/eyt036

Wellenberg, R. H. H., Hakvoort, E. T., Slump, C. H., Boomsma, M. F., Maas, M., and Streekstra, G. J. (2018). Metal artifact reduction techniques in musculoskeletal CT-imaging. *Eur. J. Radiol.* 107, 60–69. doi: 10.1016/j.ejrad.2018.08.010

Yu, C., Qin, F., Li, Y., Qin, Z., and Norell, M. (2022). CT segmentation of dinosaur fossils by deep learning. *Front. Earth Sci.* 9:805271. doi: 10.3389/feart.2021.805271

frontiers | Frontiers in Earth Science

TYPE Original Research
PUBLISHED 03 April 2023
DOI 10.3389/feart.2023.1120170

3D morphological variability in foraminifera unravel environmental changes in the Baltic Sea entrance over the last 200 years

Constance Choquel[1]*, Dirk Müter[2], Sha Ni[1,3], Behnaz Pirzamanbein[4], Laurie M. Charrieau[1,5], Kotaro Hirose[6], Yusuke Seto[7], Gerhard Schmiedl[3] and Helena L. Filipsson[1]*

[1]Department of Geology, Lund University, Lund, Sweden, [2]FORCE Technology, Brøndby, Denmark, [3]Department of Geology, Hamburg University, Hamburg, Germany, [4]Department of Statistics, Lund University, Lund, Sweden, [5]Marine Biogeosciences, Alfred Wegener Institute (AWI), Bremerhaven, Germany, [6]Institute of Natural and Environmental Sciences, University of Hyogo, Kobe, Japan, [7]Department of Geosciences, Osaka Metropolitan University, Kobe, Japan

EDITED BY
Stergios D. Zarkogiannis,
University of Oxford, United Kingdom

REVIEWED BY
Danna Titelboim,
University of Oxford, United Kingdom
Shunichi Kinoshita,
National Museum of Nature and Science, Japan
Ashley Burkett,
Oklahoma State University, United States

*CORRESPONDENCE
Constance Choquel,
✉ constance.choquel@geol.lu.se
Helena L. Filipsson,
✉ helena.filipsson@geol.lu.se

SPECIALTY SECTION
This article was submitted to Paleontology, a section of the journal Frontiers in Earth Science

RECEIVED 09 December 2022
ACCEPTED 15 March 2023
PUBLISHED 03 April 2023

CITATION
Choquel C, Müter D, Ni S, Pirzamanbein B, Charrieau LM, Hirose K, Seto Y, Schmiedl G and Filipsson HL (2023), 3D morphological variability in foraminifera unravel environmental changes in the Baltic Sea entrance over the last 200 years.
Front. Earth Sci. 11:1120170.
doi: 10.3389/feart.2023.1120170

Human activities in coastal areas have intensified over the last 200 years, impacting also high-latitude regions such as the Baltic Sea. Benthic foraminifera, protists often with calcite shells (tests), are typically well preserved in marine sediments and known to record past bottom-water conditions. Morphological analyses of marine shells acquired by microcomputed tomography (µCT) have made significant progress toward a better understanding of recent environmental changes. However, limited access to data processing and a lack of guidelines persist when using open-source software adaptable to different microfossil shapes. This study provides a post-data routine to analyze the entire test parameters: average thickness, calcite volume, calcite surface area, number of pores, pore density, and calcite surface area/volume ratio. A case study was used to illustrate this method: 3D time series (i.e., 4D) of *Elphidium clavatum* specimens recording environmental conditions in the Baltic Sea entrance from the period early industrial (the 1800s) to present-day (the 2010 s). Long-term morphological trends in the foraminiferal record revealed that modern specimens have ~28% thinner tests and ~91% more pores than their historic counterparts. However, morphological variability between specimens and the BFAR (specimens cm^{-2} yr^{-1}) in *E. clavatum* were not always synchronous. While the BFAR remained unchanged, morphological variability was linked to natural environmental fluctuations in the early industrial period and the consequences of anthropogenic climate change in the 21st century. During the period 1940–2000 s, the variations in BFAR were synchronous with morphological variability, revealing both the effects of the increase in human activities and major hydrographic changes. Finally, our interpretations, based on *E. clavatum* morphological variations, highlight environmental changes in the Baltic Sea area, supporting those documented by the foraminiferal assemblages.

KEYWORDS

foraminifera, tomography, 3D reconstructions, synchrotron-light, environmental change, morphological variability

1 Introduction

Over the last 200 years, it has become more and more evident that coastal regions are affected by a range of human-induced environmental stressors (Bijma et al., 2013; Steffen et al., 2015; Reusch et al., 2018). Moreover, atmospheric concentrations of carbon dioxide (CO_2) are increasing and subsequently also increasing oceanic pCO_2, resulting in decreasing oceanic pH, i.e., ocean acidification (OA) (Gattuso and Hansson, 2011; Strong et al., 2014). Increasing atmospheric pCO_2 also contributes to higher temperatures of the atmosphere and surface ocean, increasing vertical water stratification, and reducing the exchange between surface and deep waters (Gruber, 2011). The stratification of the water masses, accentuated with nutrient excess (eutrophication), contributes to the expansion of oxygen-depleted zones $[O_2] <$ 63 µmol L^{-1} or 1.4 ml L^{-1} (i.e., hypoxia or deoxygenation) and degradation of coastal benthic ecosystems (Kroeker et al., 2013; Breitburg et al., 2018). The present-day anthropogenically-induced environmental changes in coastal settings have created a need for a context to understand the severity and potential outcomes of such changes to support evidence-based environmental management strategies. This context can for instance be derived from paleoenvironmental records. In this study, we aim to provide a historical context by using marine sediment archives and their content of calcite ($CaCO_3$) microfossils to improve our understanding of recent environmental changes in coastal areas.

Studies on shell morphology from various marine organisms have a long tradition, but are presently a rapidly expanding field, to a large degree led by the development of high-resolution 3D imaging, acquired through microcomputed tomography (µCT) (e.g. Speijer et al., 2008; Monnet et al., 2009; Liew and Schilthuizen, 2016; Howes et al., 2017; Peck et al., 2018). Our contribution focuses on the morphology of one of the most important calcitic microorganisms in the oceans—the foraminifera. Since the pioneering work of Speijer et al. (2008), the number of studies dealing with 3D reconstructions of foraminiferal shells (tests) is increasing, reaching in 2022 an estimated cumulative number of ~4,000 scanned specimens (Figure 1A). Foraminiferal 3D reconstructions have allowed various topics to be addressed such as taxonomy and ontogeny studies, effects of ocean acidification, effects of temperatures, and micropaleontological time series (see review in Supplementary Table S1). These studies have mainly reconstructed planktonic and tropical large benthic foraminifera (Figure 1B). Small-size benthic foraminiferal species from high-latitude regions have received less attention (Belanger, 2022), despite their rich abundance in these areas (Charrieau et al., 2019), and the ongoing large focus on high-latitude climate change, e.g., in the last IPCC reports (Rhein et al., 2013; Bindoff et al., 2019; Meredith et al., 2019).

To generate 3D time series based on microfossils, it is necessary to scan as many tests as possible to draw statistically valid conclusions and to work at sub-micrometer resolution for measurement accuracy. One way to reach these objectives is to use a synchrotron light-based approach, a developing method to reveal environmental changes through microfossils records (Foster et al., 2013). The scan time per test is considerably shortened at the synchrotron facility (about 10 min/specimen compared to several hours with a conventional µCT scanner) and the image resolution is generally higher (Supplementary Table S1). However, the synchrotron light-based method has been underused compared

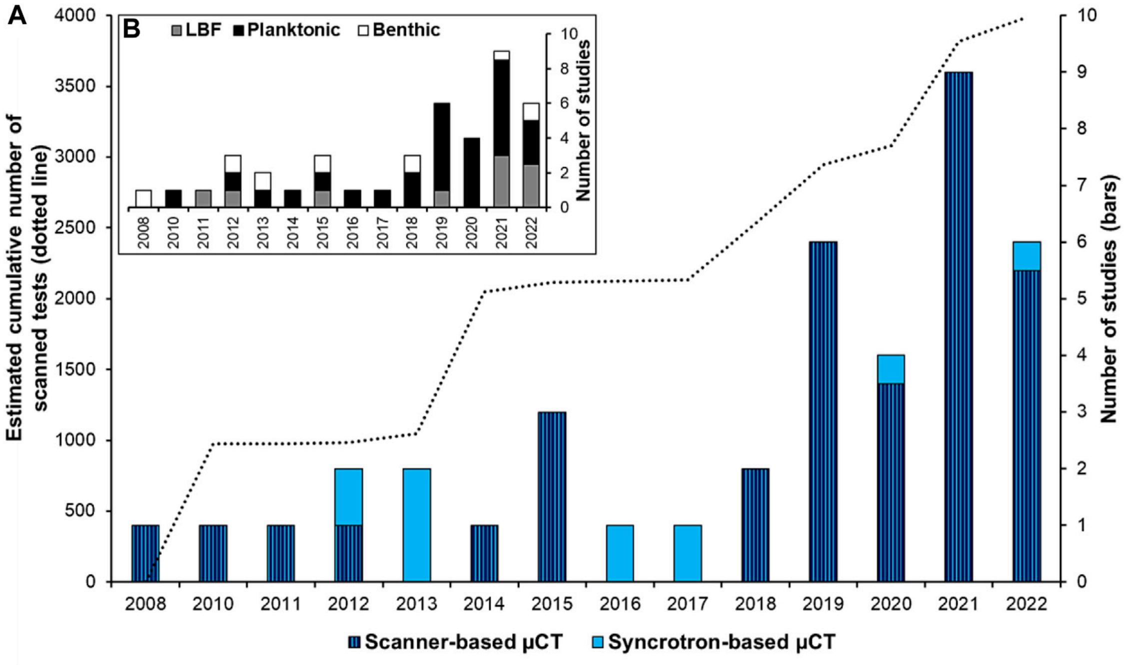

FIGURE 1
(A) Number of studies using 3D foraminifera reconstructions with scanner-based (dark blue with stripes) or synchrotron light-based µCT (light blue), and the estimated number of specimens scanned (dotted line). **(B)** Number of studies using planktonic (black), large benthic foraminifera (LBF, grey), and benthic foraminifera (white). References are in Supplementary Table S1.

to the conventional μCT scanner (Figure 1A). This is probably due to the competitive access to beamtime and the challenge of handling large data sets. In general, morphological parameters such as the thickness and the pore patterns are of great interest for micropaleontological research; the thinning of $CaCO_3$ tests can be related to a decrease in calcification as a consequence of ocean acidification (e.g., Johnstone et al., 2010; Fox et al., 2020), and pore patterns are increasingly attributed to differences in gas exchange, in particular oxygen uptake, interpreted as a proxy of oxygenation conditions (e.g., Burke et al., 2018; Davis et al., 2021). Extracting these two parameters from 3D tests remains difficult due to the limitations of image processing; therefore, optimizing the post-data analysis is also crucial. Moreover, most previous studies were performed with commercially available software (Supplementary Table S1). Consequently, there is an access limitation for image processing, and a lack of harmonized guidelines, especially when using open-source software adaptable to different microfossil shapes.

We focused our case study on an environmentally vulnerable region, affected by a combination of hydrographic changes and human-induced impacts, the Öresund (the Sound, one part of the Danish Straits), a transition zone between the North Sea, the Skagerrak, and the Baltic Sea (Conley et al., 2007; Charrieau et al., 2018a; Carstensen and Conley, 2019; Carstensen and Duarte, 2019; Charrieau et al., 2019; Ljung et al., 2022). Since the 1940 s, the Baltic Sea has been subjected to multiple stressors such as warming of surface seawater, decreasing pH, expansion of hypoxic areas, and massive increases in burial rates of carbonaceous pollutants from biomass burning (Conley et al., 2007; Rutgersson et al., 2014; Reusch et al., 2018; Carstensen and Duarte, 2019; Ljung et al., 2022). Previously, Charrieau et al. (2019) studied environmental changes in the Öresund region from early industrial (the 1800 s) to present-day conditions (the 2010 s), using a combination of climate modeling, sediment geochemistry, and grain-size distribution together with assemblage studies of benthic foraminifera. In particular, the BFAR (specimens $cm^{-2}\,yr^{-1}$) of the species *Elphidium clavatum* (Cushman, 1930) was used to track changes in hydrography. Taking advantage of this historical interesting context and available samples, we extended the analyses on *Elphidium clavatum* specimens to explore potential changes in their calcite test (i.e., external and internal walls) over time, through synchrotron light-based μCT. Here, we also describe a post-data analysis using open-source software, for quantitatively describing the morphological parameters of the entire test such as average thickness, calcite volume, calcite surface area, number of pores, calcite surface area/volume ratio (calcite SV ratio), and pore density (number of pores/calcite surface area).

We hypothesize that changes in the morphological patterns of foraminiferal tests are generated by environmental variations and should be detectable by 3D reconstructions. We first establish the effects on specimen size and relationships between the different morphological parameters of the entire test. Then, we discuss the interpretations of using morphological variability in 3D time series (i.e., 4D; Tudisco et al., 2019) and morphological traits associated with environmental stressors for palaeoecological interpretations. Finally, we compare the BFAR of *Elphidium clavatum* (Charrieau et al., 2019) with its morphological changes, to determine whether 3D morphological test variations can be used as an indicator of recent environmental changes and thus complement foraminiferal assemblages.

2 Materials and methods

2.1 Study area and sampling strategy

The Öresund (the Sound) is one of three pathways making up the Danish Straits and a transitional area between the North Sea, through the Kattegat and the Skagerrak, and the Baltic Sea (Figure 2A). The Öresund is a 118 km long narrow strait with an average depth of 23 m and a maximal depth of 53 m at the northeast of the Island of Ven (Figure 2A). The water column is permanently stratified in a two-layer structure; the salty bottom water (salinity ~29–34; Figure 2B) from the Kattegat penetrates under the brackish layer (salinity ~8–18; Figure 2B) from the Baltic Sea (Carstensen and Conley, 2019; Charrieau et al., 2019). The stratification is dominated by strong advective transports in both water masses driven by freshwater runoffs, westerly and easterly winds, and the North Atlantic Oscillation (NAO) (Hänninen et al., 2000; Charrieau et al., 2019).

Sediment cores were collected in 2013 during a cruise with R/V *Skagerak* at Öresund station DV-1, to the north of the Island of Ven (55°55.59′ N, 12°42.66′ E; Figure 2A). The sampling details and the age-depth model are described by Charrieau et al. (2019). Briefly, two sediment cores 30 and 36 cm long (named DV1-G and DV1-I, respectively), were sliced into 1-cm layers. The first core (DV1-G) was used to establish the age-depth model, using natural (^{210}Pb) and artificial (^{137}Cs) radionuclides, while the second core (DV1-I) was used for benthic foraminiferal fauna analysis. The carbon content profiles, measured on both cores, were used to correlate the two cores and establish the age model. The sedimentation rate ranges between 1 and 5.6 mm yr^{-1} and decreases with depth. Therefore, there is an age uncertainty for the sediment sequence, estimated at ~1.5 years for the first cm-layers and up to ~10 years for the deepest layers.

2.2 Benthic foraminifera

In the work of Charrieau et al. (2018a, 2019), foraminiferal specimens from the upper 2 cm of the DV1-I core were wet-picked, while those from the layers below were dry-picked, and sorted under a Nikon stereomicroscope. The benthic foraminiferal assemblage in the Baltic Sea entrance was composed of 76 species; eleven species had a relative abundance higher than 5% and were considered major species (Charrieau et al., 2018a, 2019). The authors of Charrieau et al. (2019) described the flux of foraminifera also known as benthic foraminiferal accumulation rates or BFAR (specimens $cm^{-2}\,yr^{-1}$) corresponding to the number of specimens per cm^3 multiplied by the sediment accumulation rate (cm yr^{-1}). One of the major species of the assemblage indicating large variations in BFAR over the last 200 years is *Elphidium clavatum* (Charrieau et al., 2019). From the foraminiferal assemblage data, 16 sediment layers were selected, representing the last 200 years (i.e., roughly the years ~2013, ~2010, ~2005, ~2002, ~1993, ~1986, ~1978, ~1960, ~1939, ~1923, ~1906, ~1890, ~1873, ~1857, ~1840, and ~1807). Between five to ten

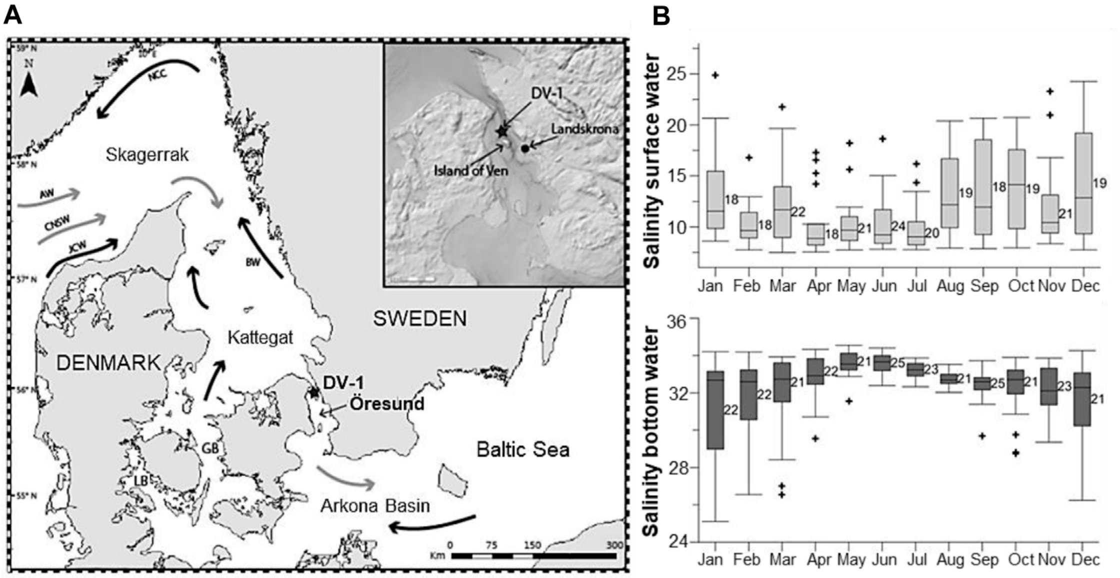

FIGURE 2
(A) Map of the studied area. The star shows the sampling station DV-1 located north of the Island of Ven in the Öresund. GB: Great Belt; LB: Little Belt. General water circulation includes main surface currents (black arrows) and main deep currents (grey arrows). AW: Atlantic Water; CNSW: Central North Sea Water; JCW: Jutland Coastal Water; NCC: Norwegian Coastal Current; BW: Baltic Water. **(B)** Seasonal variability of salinity (PSU) at the surface water (light grey) and the bottom water (dark grey). The numbers next to the bars indicate the number of measurements for each month between 1965 and 2016. Modified from Charrieau et al. (2019).

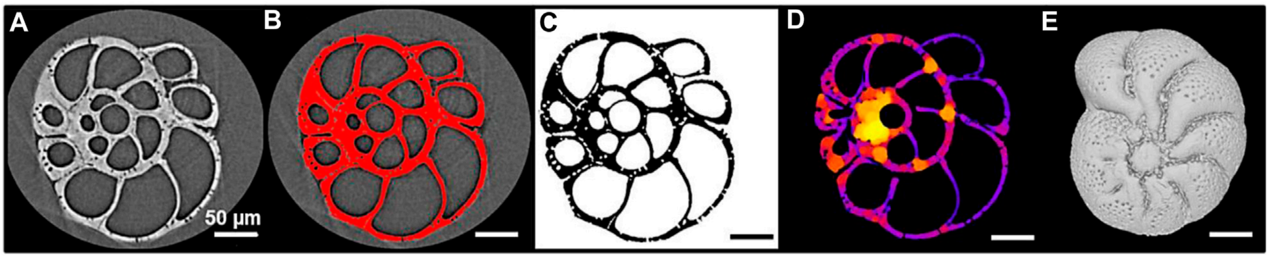

FIGURE 3
Illustration of the stepwise image processing of an *Elphidium clavatum* specimen (DV4-sp1-2005). **(A)** Visualization of a stack of raw images in Fiji. **(B)** Segmentation of the stack in Fiji. **(C)** Stack of binary images resulting from the segmentation. **(D)** Local thickness map generated by the *BoneJ* plugin to calculate automatically the average thickness of the test. **(E)** 3D reconstruction of the test in MeshLab.

Elphidium clavatum specimens from the 150–355 µm size fraction (excluding juveniles/smaller specimens; <150 µm) were selected from each layer. The specimens were picked randomly, although visually pristine/unbroken tests were preferentially selected, and a total of 124 specimens were analyzed within the awarded beamtime.

2.3 Stepwise image processing from 3D stacks

The stepwise image processing is summarized in Figure 3 and the details of the procedure are in Supplementary Appendix S1.

The specimens were scanned at the Beamline BL 47XU, SPring-8 synchrotron facility (Japan). They were mounted on a HiTaCa®, carbon nanotube (CNT) sheet (Hitachi Zosen Corporation; Fujimoto et al., 2018), to avoid damaging the tests during handling, facilitate test recovery, and enable 3D reconstructions. A voxel size of 0.5 µm with 1800 projections and a 150 m exposure time at 23 keV X-ray energy was used. A stack of raw images was generated for each specimen (Figure 3A) and visualized with the open-source software ImageJ/Fiji (Schindelin et al., 2012). The stack was segmented by dividing the images into fore- and background (test selected in red; Figure 3B) to be converted into a stack of binary images, i.e., the test is in black and the background in white (Figure 3C). This segmentation step is crucial since the accuracy of the measurements depends on the delimitation of the test.

The thickness of the foraminiferal tests is one of the most difficult parameters to measure in its entirety, often limited by cross-section observations and local measurements (Bé and Lott, 1964; Hannah et al., 1994; Weinkauf et al., 2020). Previous studies, using 3D reconstructions, estimated the thickness of the entire test indirectly; from the percentage of calcite volume (i.e., external and internal walls) to total volume (i.e., walls plus chamber cavities) of the test (Titelboim et al., 2021), or the ratio of the calcite volume to calcite surface area (e.g., Zarkogiannis et al., 2020). Here another approach was used, from the stack of binary images, the average thickness of the test was automatically calculated from the local thickness map (Figure 3D) using the *BoneJ* plugin in Fiji (Dougherty and Kunzelmann, 2007; Doube et al., 2010). This plugin developed for the biomedical field has already been used to explore the average thickness of echinoids (Müter et al., 2015) and pteropod shells (Peck et al., 2018).

In Fiji, the stacks of binary images were converted into “STL” files suitable for 3D reconstructions. Each 3D test was imported into the open-source software MeshLab (Cignoni et al., 2008). Then, the geometric tool was used to measure automatically the volume and surface area of the calcite. Few studies focus on the pore patterns from 3D tests, however, they are analyzed as a 2D image (Burke et al., 2018; Davis et al., 2021). In MeshLab, a topological tool automatically counts the number of “holes” (pores) in the entire test. Therefore, the detected pores are 1) the pores located at the surface connecting the cell and the surrounding environment, and 2) the pores located in the inner walls if they create a detectable hole (e.g., a pore connecting two chambers).

2.4 Adjusted data and statistical analyses

Morphological parameters are generally dependent on the ontogenetic stage (i.e., size-related). All parameters that were significantly correlated with the maximal diameter of the specimens (MDS) (Pearson correlations with Bonferroni correction applied on *p*-value) were standardized by the average MDS obtained from all specimens. Then, the morphological parameters were adjusted between 0 and one values following the equation:

$$x\_adjusted = \frac{x - xmin}{xmax - xmin}$$

where x is a morphological value for one specimen, $x\_adjusted$ is the standardized value of x which has values between 0 and 1, $xmin$ is the lowest value on all specimens, and $xmax$ is the highest value on all specimens.

To investigate the relationships between the morphological parameters, Pearson linear correlations, and best-fitted polynomial functions were performed when applicable. The significant level for all the tests was $p < 0.05$. Non-parametric Mann-Kendall tests were applied to detect significant monotonic trends over the investigated period (Gilbert, 1987). Because of the small sample sizes, non-parametric Kruskal–Wallis tests were conducted to discriminate the specimens between the different years. In case of significant differences, a Dunn post-hoc test with a Bonferoni correction was applied for two-sample comparisons. The statistical tests and boxplots with individual data points were performed using R software (R version 4.2.1, R Core Team).

3 Results

3.1 Exploration of the morphological patterns

The detailed values of the morphological parameters acquired from the 3D tests are available in Supplementary Table S2.

3.1.1 Effects of specimen size

The maximal diameter of the specimens (MDS) and the number of chambers, both related to test size, are weakly positively correlated (Supplementary Figure S1; $R^2 = 0.17$, $p < 0.0001$). Because this study focuses on the entire test measure, the MDS was rather used than the number of chambers. The MDS varies between 149 and 300 µm (Figure 4). The calcite volume (varying from 2.9 E^{+05} to 2.8 E^{+06} µm^3) and the calcite surface area (varying from 1.4 E^{+05} to 9.1 E^{+05} µm^2) increase sharply with the MDS (Figure 4A; $R^2 = 0.76$, $p < 0.0001$, and Figure 4B; $R^2 = 0.65$, $p < 0.0001$, respectively). Well-fitted polynomial functions are also observed between the calcite volume (Figure 4A) and the calcite surface area (Figure 4B) with the MDS. The number of pores is scattered (varying from 356 to 14,559), but increases significantly with the MDS (Figure 4C; $R^2 = 0.16$, $p < 0.0001$). Most of the specimens have <10,000 pores, except four specimens from the early 21st century showing higher values (Figure 4C; Supplementary Table S2). The average thickness indicates scattered values (varying from 2.71 to 11.71 µm), besides a weak but significant increasing correlation with the MDS is observed (Figure 4D; $R^2 = 0.05$, $p = 0.01$).

3.1.2 Morphological parameters relationships

The calcite volume indicates no significant correlation with the average thickness (Figure 5A; $R^2 = 0.02$, $p = 0.17$). The calcite surface area displays a significant decreasing linear correlation with the average thickness (Figure 5B; $R^2 = 0.36$, $p < 0.0001$). The calcite surface area and calcite volume show a significantly increasing correlation (Figure 5C; $R^2 = 0.21$, $p < 0.0001$). Then, the calcite SV ratio displays a significant decreasing linear correlation with the average thickness (Figure 5D; $R^2 = 0.54$, $p < 0.0001$). Well-fitted polynomial functions are noted between the calcite surface area (Figure 5B; $R^2 = 0.49$, $p < 0.0001$) and the calcite SV ratio (Figure 5D; $R^2 = 0.67$, $p < 0.0001$) with the average thickness. Interestingly, an increasing correlation is found between the average thickness calculated from the *BoneJ* plugin and the calcite VS ratio used as an indicator of thickness by Zarkogiannis et al. (2020) (Supplementary Figure S2; $R^2 = 0.52$, $p < 0.0001$).

The number of pores in the entire test shows a significantly increasing linear correlation with the calcite surface area (Figure 6A; $R^2 = 0.74$, $p < 0.0001$) and a well-fitted polynomial function (Figure 6A; $R^2 = 0.78$, $p < 0.0001$). The pore density indicates a significant decreasing linear correlation with the average thickness (Figure 6B; $R^2 = 0.48$, $p < 0.0001$) and also a well-fitted polynomial function (Figure 6B; $R^2 = 0.65$, $p < 0.0001$). Weak but significant decreasing correlations are found between the pore density and the calcite volume (Figure 6C; $R^2 = 0.04$, $p = 0.03$, and polynomial function; $R^2 = 0.06$, $p = 0.03$), and a highly significant increasing correlation between the calcite SV ratio and the pore density (Figure 6D; $R^2 = 0.69$, $p < 0.0001$).

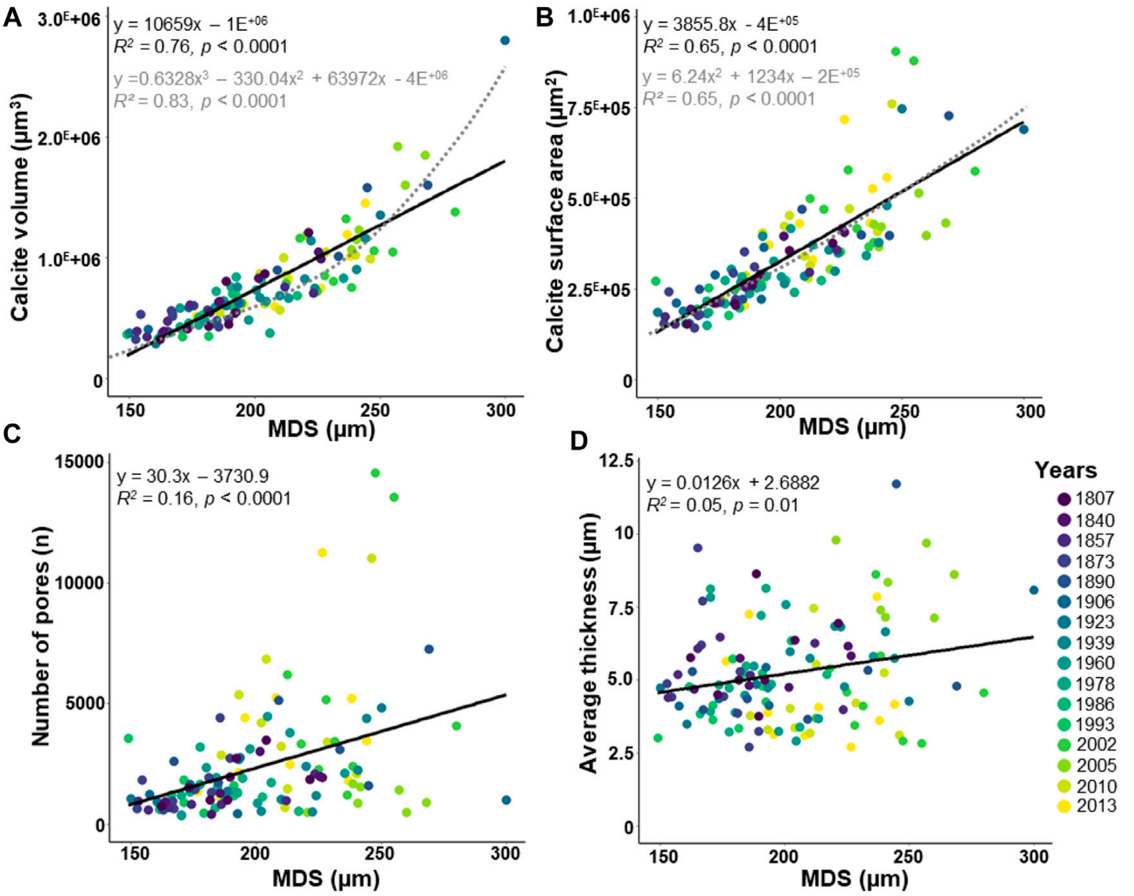

FIGURE 4
Morphological parameters about the maximal diameter of the specimen (MDS). The dataset includes 124 specimens of *Elphidium clavatum* from the Baltic Sea entrance over the last 200 years **(A)** Calcite volume (µm^3). **(B)** Calcite surface area (µm^2). **(C)** Number of pores. **(D)** Average thickness (µm). Linear correlation (black line). Polynomial function (grey dotted line).

3.2 3D time series

The time series of 3D data, based on the average thickness (Figure 7A), number of pores (Figure 7B), calcite volume (Figure 7C), and calcite surface area (Figure 7D), are not normally distributed (Shapiro normality test, p < 0.0001). The average thickness indicates a significant decreasing trend over the last 200 years (Mann-Kendall: z = 3.26, p = 0.001), whereas the number of pores (Mann-Kendall: z = -2.30, p = 0.02), calcite volume (Mann-Kendall: z = -2.36, p = 0.01), and calcite surface area (Mann-Kendall: z = -3.53, p = 0.0004) indicate significant increasing trends.

Significant differences are found between estimated years for the average thickness (Kruskal–Wallis: chi-squared = 32.52, df = 15, p = 0.005), number of pores (Kruskal–Wallis: chi-squared = 40.49, df = 15, p = 0.0003), calcite volume (Kruskal–Wallis: chi-squared = 40.58, df = 15, p = 0.0003), and calcite surface area (Kruskal–Wallis: chi-squared = 43.40, df = 15, p = 0.0001). According to Dunn's post-hoc test, data for ~2005 show thicker tests than ~2002, and ~2010 (Figure 7A). The number of pores is lower for ~2005 (Figure 7B) than ~2013, ~2010, and ~2002, then also lower for ~1986 than ~2002 (Figure 7B). The calcite volume is larger for ~2005 than ~1993, ~1986, ~1978, ~1873, and ~1807 (Figure 7C). Furthermore, the calcite surface area values are higher for ~2002 than ~1986, ~1978, ~1873, and ~1857 (Figure 7D). The statistical values of the posthoc tests are reported in Supplementary Table S3.

The time series of the 3D data for calcite SV ratio (Figure 7E) is non-normally distributed (Shapiro normality test, p = 0.02). The calcite SV ratio time series reveals no significant trend (Mann-Kendall: z = -0.81, p = 0.41). Indeed, most of the boxplots show scattered distributions, such as the years ~1873, ~1960, ~1978, ~1993, ~2002, ~2010, and ~2013, conversely to condensed distributions observed especially for ~1986 and ~2005. Moreover, no significant difference between specimens among years is found (Kruskal–Wallis: chi-squared = 24.98, df = 15, p > 0.05).

The 3D time series of the pore density (Figure 7F) is normally distributed (Shapiro normality test, p = 0.07, and Levene homogeneity of variance test, p = 0.06), but due to the small sample sizes, non-parametric tests are used. The pore density time series indicates no significant trend (Mann-Kendall: z = -1.86, p = 0.06). Except for the years ~1857, ~1923, ~1986, and ~2005, all the boxplots indicate values with scattered distributions. However, significant differences between years are found (Kruskal–Wallis: chi-squared = 42.71, df = 15, p = 0.0001). According to Dunn's post-hoc test, the pore density is lower for ~2005 than ~1890, ~2002, ~2010, and ~2013.

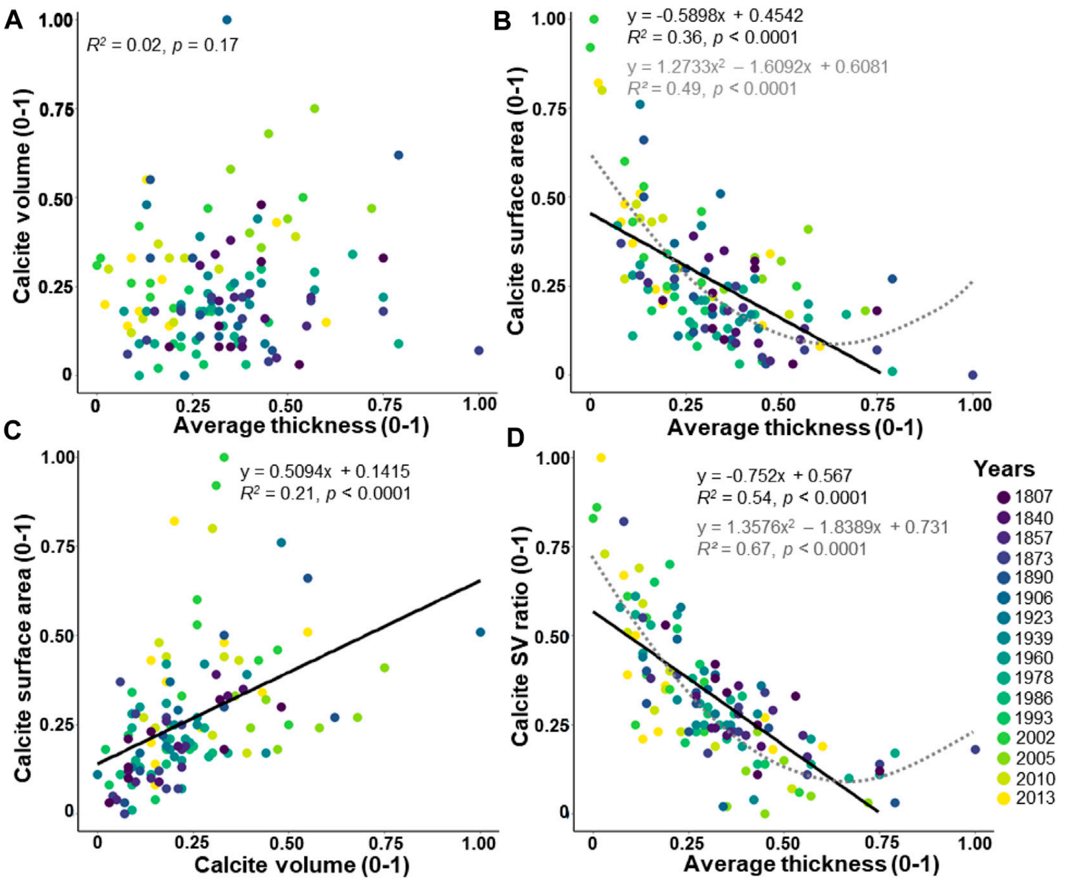

FIGURE 5
Relationships between the average thickness, the calcite volume, and the calcite surface area. The values are adjusted between 0 and 1. The dataset includes 124 specimens of *Elphidium clavatum* from the Baltic Sea entrance over the last 200 years. **(A)** Calcite volume and average thickness. **(B)** Calcite surface area and average thickness. **(C)** Calcite surface area and calcite volume. **(D)** Calcite SV ratio and average thickness. Linear correlation (black line). Polynomial function (grey dotted line).

4 Discussion

The acquisition of morphological parameters such as the average thickness and the number of pores of the entire test was successful, allowing us to reveal the variability of morphological patterns in *Elphidium clavatum*, as well as long-term trends in a past record. Thus, 3D (i.e., 4D) time series are a promising complement for reconstructing environmental changes in the Baltic Sea entrance over the last 200 years. Based on known morphological patterns in foraminifera associated with environmental stressors e.g., ocean acidification, deoxygenation, and warming, we could infer environmental changes occurring in the region. Furthermore, we expanded the environmental interpretations based on the BFAR changes (Charrieau et al., 2019) and morphological variations in *Elphidium clavatum*.

4.1 Managing morphological variability in 3D time series

A large variation in morphological patterns could be the result of mixing two pseudocryptic species with slightly different morphologies. Particularly, *Elphidium clavatum* and *Elphidium selseyense* (Heron-Allen and Earland, 1911) are morphospecies (Darling et al., 2016), often difficult to distinguish visually, which is why some previous studies grouped *E. clavatum* and *E. selseyense* to an *E. clavatum-selseyensis* complex (Groeneveld et al., 2018; Charrieau et al., 2019; Ni et al., 2020). Morphological variations in foraminifera can be explained by external factors such as adaptation to environmental parameters (i.e., phenotypic adaptation) and/or by internal factors such as adaptation of the genome (heritable trait). There is no evidence of high heritability of thickness and pores but they vary in controlled environmental conditions and across environmental gradients (Burke et al. (2018) and references therein). In this study, we assume that the morphological variations observed from the scanned specimens are related to environmental conditions.

Morphological patterns in *Elphidium clavatum* fluctuate broadly over the last 200 years (Figure 7). This variability in test morphology may be explained by the seasonal environmental gradients that occurred in the region in terms of salinity (Figure 2B), pH, temperature, and dissolved oxygen concentrations (Charrieau et al., 2019). Moreover, the increase in human activities since the ~1940 s accentuated the variability range of these environmental

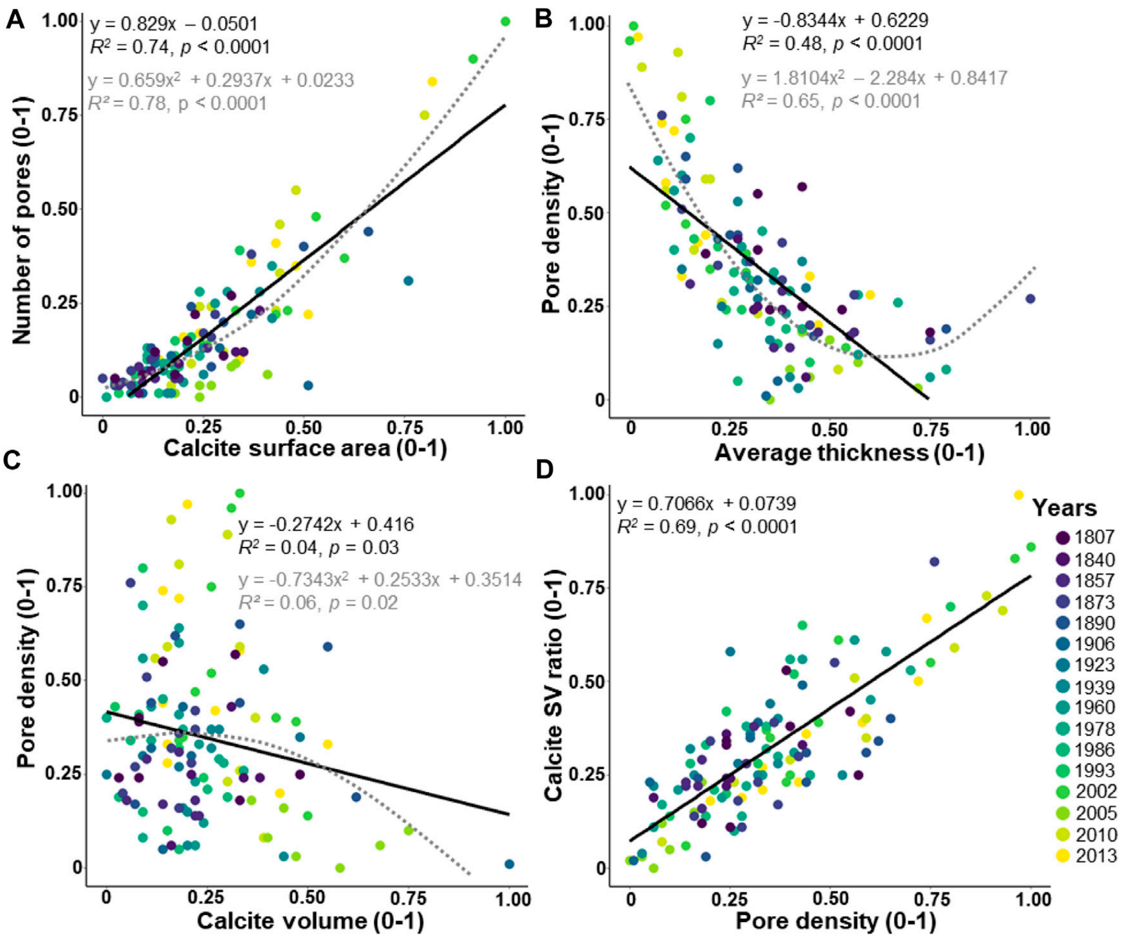

FIGURE 6
Relationships between the pore pattern and the other morphological parameters. The values are adjusted between 0 and 1. The dataset includes 124 specimens of *Elphidium clavatum* from the Baltic Sea entrance over the last 200 years. **(A)** Number of pores and calcite surface area. **(B)** Pore density and average thickness. **(C)** Pore density and calcite volume. **(D)** Calcite SV ratio and pore density. Linear correlation (black line). Polynomial function (grey dotted line).

conditions, such as the expansion and severity of hypoxic zones (Conley et al., 2007; Reusch et al., 2018; Carstensen and Conley, 2019). As the growth rate of benthic foraminifera can be considered rapid (few months), and their morphology reflects the environment they grew in, here, we consider that the test of adult specimens records approximately up to the seasonal resolution of environmental variations. A significant effort has been achieved in this study to analyze as many specimens as possible at a relatively high temporal resolution, however, the representativeness of the scanned specimens may remain limited to capture the full extent of environmental change.

We argue that large variability in morphological patterns (i.e., scattered distribution) indicates that the *Elphidium clavatum* specimens calcified in highly contrasted environmental conditions. Furthermore, Weinkauf et al. (2014) reported that an increase in the morphological variability of foraminiferal tests in geological records may be associated with disruptive selection through a stress response. This stress response may lead to increased diversification of the morphology to a maximized chance of some specimens surviving in unfavorable environments (Weinkauf et al., 2014). Conversely, low variability in morphological patterns (i.e., condensed distribution) should reflect that specimens calcified in less contrasted environmental conditions. Indeed, a decrease in morphological variability of shell traits may be attributed to stabilizing selection often associated with reduced environmental fluctuations, and can also be the result of a gradually changing environment (Weinkauf et al., 2014).

4.2 Specimen size and environmental effects on the morphology of entire tests

4.2.1 Effects of specimen size on thickness and pores

Even if the adult specimens come from the same size fraction, the MDS affects the morphology of the entire test but not to the same extent (Figure 4). The calcite volume (Figure 4A) and calcite surface area (Figure 4B) are highly correlated with the size of the specimens, which was already demonstrated in previous studies (Belanger, 2022 and references therein). Because the average thickness is weakly

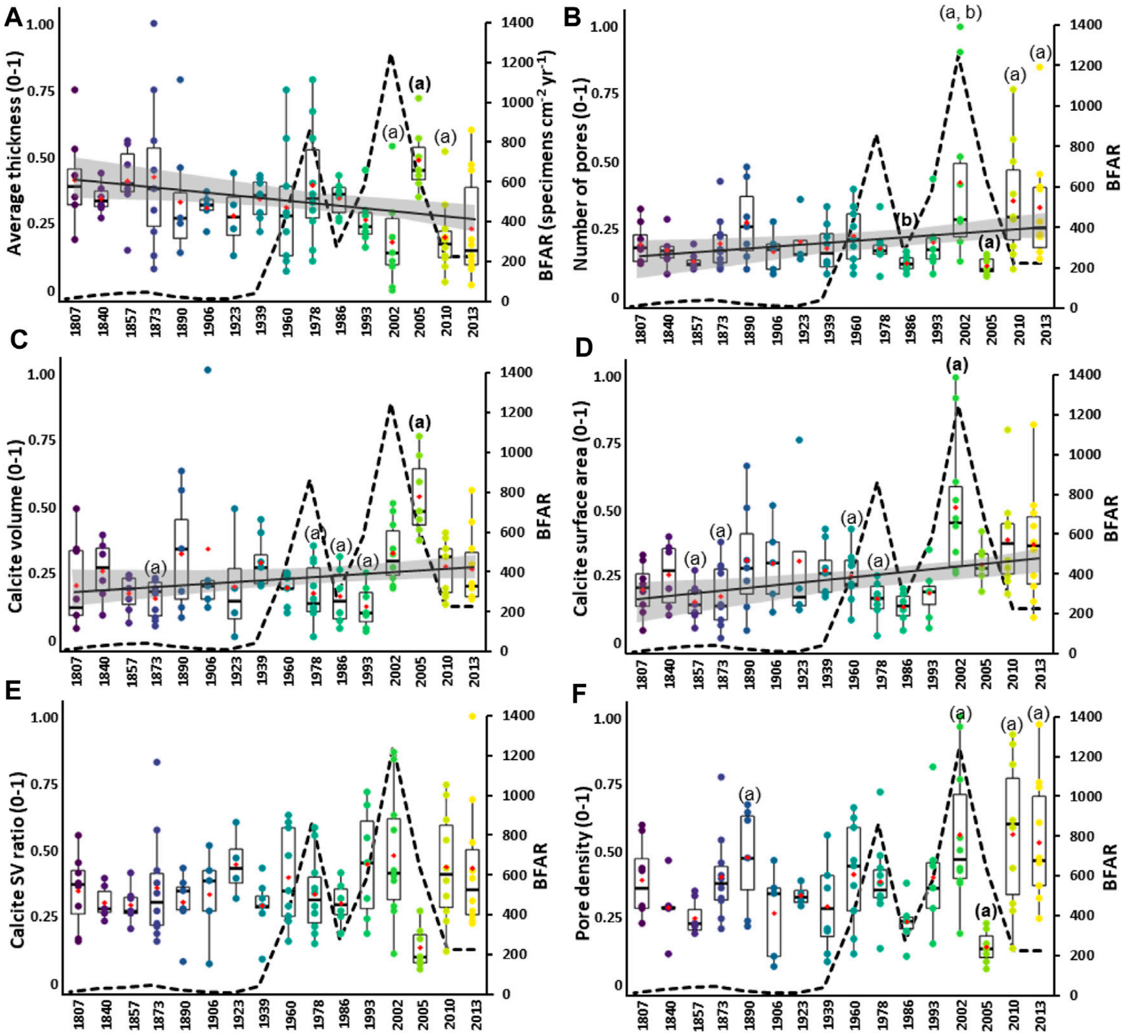

FIGURE 7
3D time series based on the morphological parameters in *Elphidium clavatum* from the Baltic Sea entrance over the last 200 years. **(A)** Average thickness. **(B)** Number of pores. **(C)** Calcite volume. **(D)** Calcite surface area. **(E)** Calcite SV ratio. **(F)** Pore density. Boxplots are shown with colored individual data points per estimated year, the red diamond indicates the mean. The morphological values (y-scale) are adjusted (0–1). The bold letters **(A, B)** indicate significant differences according to Dunn post-hoc test. The dotted line is the BFAR of *E. clavatum* (specimens cm^{-2} yr^{-1}) from Charrieau et al. (2019). A regression line (black line) with a 95% confidence interval (grey area) represents the long-term trend when significant with the Mann-Kendall test.

affected by the MDS (Figure 4D), this parameter could be mainly influenced by environmental factors such as varying salinity, pH, or temperature. Conversely, a non-negligible correlation between the number of pores and the MDS was demonstrated (Figure 4C). Comparisons with previous studies are difficult since the pore pattern is species-specific and has only been performed on small parts of the tests from 2D images (Petersen et al., 2016 and references therein). Interestingly, four specimens from the early 21st century may be considered outliers regarding their very high number of pores (Figure 4C). Several hypotheses may explain these outliers; 1) a threshold value (14,559 pores, Supplementary Table S2) because the number of pores can be limited by the robustness of the test and the metabolic demands of the cell (Richirt et al., 2019), 2) an over-estimated number of pores linked to traces of dissolution in some damaged specimens that may generate additional holes, and 3) taphonomic effects that may increase test porosity (Oakes et al., 2019). This contribution illustrates that 3D reconstructions allow quantifying the morphological parameters of tests that have calcified under different environmental conditions, and highlights the need to standardize specimens by the same MDS for more accurate comparisons.

4.2.2 Morphological traits based on environmental stressors

A wide range of morphological patterns in *Elphidium clavatum* was observed with two distinct patterns; thinner tests have a higher calcite SV ratio (Figure 5D) i.e., a larger surface area (Figure 5B), and a higher pore density (Figure 6B). Conversely, thicker tests have a lower calcite SV ratio and a lower pore density. The well-fitted polynomial functions found between the average thickness and surface calcite area (Figure 5B), calcite SV ratio (Figure 5D), and pore density (Figure 6B), may suggest a compromise between the robustness of the test and the metabolic needs of the cell. This hypothesis can be compared to the scaling laws driving pore patterns described by Richirt et al. (2019). Here, the thickness of the test can have a major role in the pore pattern and the overall shape of the test.

Under natural conditions, it is difficult to associate the variation of morphological patterns with a single environmental factor. However, some morphological traits of foraminifera such as the thickness, SV ratio, and pore density, were previously associated with environmental stressors, allowing us to extrapolate some broad conclusions to *Elphidium clavatum* for palaeoecological interpretations. We expect that *E. clavatum* would decrease calcification (i.e., thickness loss) in response to ocean acidification (OA). Indeed, thinner parts of small benthic foraminiferal tests are commonly observed in culture experiments at lower pH values (Allison et al., 2010; Dissard et al., 2010; Haynert et al., 2011). Moreover, the thinning of the entire test (i.e., outer and inner walls) related to OA is also demonstrated in 3D imaging foraminiferal studies (Supplementary Table S1). Ocean acidification is not the only factor that can lead to test thinning. The combined impact of OA and lower salinity may induce a synergistic effect on the calcification process, decreasing resistance to dissolution (Charrieau et al., 2018a; 2018b). Moreover, thinner walls intensify gas exchange in low-oxygen environments (Bernhard, 1986; Sen Gupta and Machain-Castillo, 1993; Kaiho, 1994). The combined effects of warming and OA may have an antagonist effect on calcification due to the positive effect of increasing temperature on calcification and growth (Haynert and Schönfeld, 2014). Consequently, warmer temperatures may also increase the variability in test thickness.

The assumption would be that *E. clavatum* would have more flattened tests, i.e., a higher calcite SV ratio, in response to deoxygenation and pollution. Some benthic foraminiferal species adapt their tests with flattened shapes to maximize more surface area per unit volume in low-oxygen environments (Bernhard, 1986; Sen Gupta and Machain-Castillo, 1993; Kaiho, 1994). A higher SV ratio can be also associated with a decreasing roundness or an increasing test asymmetry, previously interpreted as an adaptive response toward environmental stress or more variable environmental conditions (Leung et al., 2000; Weinkauf et al., 2014). A decrease in roundness may be also associated with morphological abnormalities. Deformed tests are reported in areas subject to different types of pollution e.g., heavy metals (Alve, 1991), and hydrocarbons (Morvan et al., 2004) but also from areas with a large gradient of salinity such as brackish conditions (Charrieau et al., 2018b). However, lower SV ratios are also observed in benthic foraminifera from high-latitude regions due to the increased volume and size of specimens, probably related to the availability of organic matter even in low-oxygen environments (Belanger, 2022). Therefore, food availability may also increase the calcite SV ratio variability because of a larger calcite volume.

Elphidium clavatum would increase its pore density in response to deoxygenation. In previous studies, correlations are observed between the increase in pore density with lower dissolved oxygen concentrations in the surrounding water (Kuhnt et al., 2013, 2014). Some studies describe that a flattened and thin test facilitates gas exchange by diffusion through the pores by minimizing oxygen consumption and increasing oxygen uptake efficiency (Bradshaw, 1961; Corliss, 1985; Sen Gupta and Machain-Castillo, 1993; Glock et al., 2019). In some benthic foraminifera species from oxygen minimum zones, positive relationships between pore density and temperature, and between pore density and bottom water [NO_3^-] are demonstrated (Glock et al., 2011; Kuhnt et al., 2013). However, these relationships are species-specific and require further investigation in *Elphidium clavatum*. In this study, the thinnest tests have a higher pore density (Figure 6B), thus OA may have a synergistic effect with low-oxygen conditions on the pore density. Some authors argue that deoxygenation could lead to higher porosity, i.e., the percentage of the test surface covered by pores (Richirt et al., 2019). Achieving test porosity with 3D imaging remains a challenge, in this contribution, the pore area is visually highly variable between specimens and cannot be studied without robust statistical methods taking into account the variability in test thickness.

4.3 3D time series to reconstruct recent environmental changes in the Baltic Sea entrance

4.3.1 Long-term trends in morphological changes

Although the morphological variability is large, significant long-term trends in morphological changes over the last 200 years can be noted, especially in the average thickness, number of pores, calcite volume, and calcite surface area (Figure 7). We computed the decrease in average thickness, and the increase in the number of pores, calcite volume, and surface area from the modern foraminifera in ~2013 compared to their historical counterparts in ~1807 (details in Supplementary Table S4). The modern specimens reveal a thickness loss of 28 ± 14% (n = 18), an increase of 35 ± 11% in calcite surface area, an increase of 15 ± 4% in calcite volume, and an increase of 91 ± 67% in the number of pores. These long-term trends can be interpreted as the result of gradual environmental changes in the Baltic Sea entrance. Fox et al. (2020) demonstrate a larger reduction in shell thickness of up to 76% in the planktonic foraminifera *Neogloboquadrina dutertrei* over the last ~140 years in the Pacific ocean. These authors also find a thickness loss of ~20% in *Globigerinoides ruber* (Fox et al., 2020), corresponding to a similar result for *Elphidium clavatum*. *Globigerinoides ruber* is known to display a mechanism of resistance to OA linked to photosynthetic algal symbionts (Fox et al., 2020 and references therein). The same mechanism of resistance for *Elphidium clavatum* cannot be applied, as they are living in the aphotic zone. Putative mechanisms of resistance to OA in non-photosynthetically benthic foraminifera from high-latitude regions need to be further investigated.

4.3.2 Comparisons of environmental interpretations based on BFAR and morphology in *Elphidium clavatum*

During the early industrial period referring to the period from ~1807 to 1939 in our historical context, the BFAR of *Elphidium clavatum* remained stable and low (<44 specimens cm^{-2} yr^{-1}) (Figure 7, Charrieau et al., 2019). From the total foraminiferal assemblage in Charrieau et al. (2019), two subzones were described ~1807–1873 and ~1873–1923, with associated environmental conditions characterized by low oxygen conditions, a salinity of ~30, and the onset of human-induced impacts with various types of pollution (Zillén et al., 2008; Charrieau et al., 2019; Ljung et al., 2022). No significant difference was found in the morphology of the *Elphidium clavatum* specimens between the two subzones, however, the variations in both BFAR and the morphological parameters are not synchronized. Although the BFAR remained unchanged, a large variability in test thickness, calcite SV ratio, and pore density can be observed in ~1873. The relative stability of the morphological patterns excepted in ~1873 indicates a pivotal period, already noted by Charrieau et al. (2019), suggesting wider variability in pH and [O_2] values. In summary, during the early industrial period, although the BFAR of *Elphidium clavatum* remained unchanged, the morphological variations instead reveal the natural variability of environmental conditions in the region.

The ~1939–2002 period corresponds to the intensification of human activities in the region, such as the massive increase of carbonaceous pollution from petroleum products for energy use (Ljung et al., 2022), and excess nutrient loading from terrestrial to marine environments (Gustafsson et al., 2012). This period was marked by favorable growth conditions of *Elphidium clavatum* with two successive sharp increases in the BFAR up to 826 and 1,247 specimens $cm^{-2}\,yr^{-1}$ in ~1939–1978 and ~1986–2002 respectively (Charrieau et al., 2019). These BFAR variations were previously associated with the increase in organic matter as a food source for foraminifera, and major changes in the current and sediment pattern (Charrieau et al., 2019 and references therein). Interestingly, there is a synchronicity between both increases in BFAR and morphological variability, especially for the average thickness, calcite SV ratio, and pore density. Further, the decrease in the BFAR from the short period ~1978–1986 (276 specimens $cm^{-2}\,yr^{-1}$) was associated with the improved environmental conditions to reduce eutrophication in the region (Carstensen et al., 2006; Conley et al., 2007; Charrieau et al., 2019). A decrease in variability for all the morphological parameters is observed in ~1986, suggesting that the specimens calcified in less contrasted environmental conditions. In summary, the historical record of *Elphidium clavatum* reveals the intensification of anthropogenic activities through the synchrony between high reproductive success and broad morphological diversification and conversely reduced variability in test morphology that may be associated with a short event of improved environmental conditions.

The early 21st century foraminiferal record reveals sharp contrasts between the BFAR and morphological variations in *Elphidium clavatum*. The associated environmental conditions during this period were characterized by low oxygen conditions, high organic matter content, and open ocean salinity (Charrieau et al., 2019). Particularly in ~2002, *E. clavatum* dominated the fauna (Charrieau et al., 2019), but the specimens are the most negatively affected over the last 200 years: the average thickness compared to those from ~1807 has decreased by 36 ± 17% (n = 18), the calcite surface area has increased by 63 ± 21%, and the number of pores has increased by 151 ± 120% (Supplementary Table S4). Moreover, in ~2002 the largest variability in the calcite SV ratio and pore density is observed for the whole record (Figure 7). These results can be attributed to the larger seasonal hypoxia event recorded in the Danish Straits in 2002, explained by the combination of bottom water transport, nutrient supply from land, and rising temperature (Conley et al., 2007). By contrast in ~2005, the morphological variability is lower and the specimens significantly differ from the general patterns observed around the 21st century (Figure 7). Especially, the specimens are thicker 11 ± 6% (n= 15), with a larger calcite volume of 77 ± 15% and a lower number of pores of 54 ± 26% compared to those from the ~1807 (Supplementary Table S4). These unexpected results may be related to a massive inflow of highly saline, cold, and extremely oxygen-rich water from the North Sea, called Major Baltic Inflows, affecting occasionally the deep basins of the Baltic Sea and reported in 2003 (Lehmann et al., 2004; Feistel et al., 2006). Then, from the 2010s, a desynchronization is notable between the lower and stable BFAR (~225 specimens $cm^{-2}\,yr^{-1}$) and the large morphological variations of all parameters (Figure 7). The persisting environmental stressors i.e., warming, hypoxia, and OA since the 1940s, in addition to the possible inter-specific competition with opportunistic species such as *Nonionella* sp. T1 and *Nonionoides turgidus* (Charrieau et al., 2019), would not allow *Elphidium clavatum* to combine high reproductive success with a wide diversification of its morphological patterns. Recently, Bernhard et al. (2021) demonstrated in a triple-stressors experiment with propagules that *Elphidium* cf *E. excavatum* indicates high abundance under pre-industrial and cold acidified conditions, low abundance in present-day and cool + OA + hypoxic conditions, and absence in warm + OA + hypoxic conditions, indicating that *Elphidium clavatum* and probably other species from high-latitude regions will be challenged in the next decades.

5 Conclusion

We analyzed 3D time series from 124 foraminiferal specimens, recording the period from early industrial (the 1800 s) to present-day (the 2010 s) conditions in the Baltic Sea entrance. The BFAR (specimens $cm^{-2}\,y^{-1}$) changed profoundly in this vulnerable region subject to natural hydrographic changes and increasing anthropogenic pressures (Charrieau et al., 2019). Here, 3D time series (i.e., 4D) of morphological patterns in *Elphidium clavatum* provide a promising complement to reconstruct the Baltic Sea entrance evaluation over the last 200 years. We demonstrate long-term morphological trends such as the decrease in test average thickness by ~28% (up to 36% in ~2002) and the increase in the number of pores by ~91% (up to 151% in ~2002), revealing that foraminifera are being negatively affected through a multiple stressors situation such as ocean acidification, deoxygenation, and warming. We interpret that a large morphological variability is associated with highly contrasting environmental conditions, and conversely lower morphological variability results from more stable conditions. Over the last two centuries, the variations in the BFAR and the morphological patterns in *E. clavatum* are not always synchronous. In the early industrial period, the BFAR remained unchanged while the variability in pore density fluctuates broadly, suggesting periods with large natural variations in bottom-water oxygenation conditions. From the 1940 s corresponding to the intensification of human activities, increases in BFAR and morphological variability are synchronous, revealing more contrasting seasonal environmental conditions. Finally, in the early 21st century, the BFAR was stable while morphological variations remain large, suggesting a persistent multiple stressors situation. Our project highlights the value of using 3D time series of calcifying microfossils from existing geological archives to quantify the effects of anthropogenic climate change and provide additional information to foraminiferal assemblages studies.

Data availability statement

The original contributions presented in the study are included in the article/Supplementary Material, further inquiries can be directed to the corresponding authors.

Author contributions

HF and LC collected the samples. DM, LC, SN, KH, and YS scanned the samples. CC, DM, and BP worked on the 3D image processing. CC performed the statistical analyses. CC and HF wrote the manuscript. All authors provided manuscript comments and approved the final version.

Funding

This work was supported by the Swedish Research Council Formas (grant 2012-2140) and the Swedish Research Council VR (grant 2017-00671), the Royal Physiographic Society, Crafoord and the Oscar and Lili Lamm Foundations, the Interreg project “MAX4ESSFUN Cross Border Network and Researcher Programme”. We thank SPring-8 for beamtime under proposal numbers 2018A1099, 2018B1241, and 2020A1221.

Acknowledgments

We thank the captain and crew of r/v Skagerak, Karl Ljung, and Petra Schoon for assistance during core collection, and the staff at the SPring-8 synchrotron facility (BL 47XU). We in particular thank Kentaro Uesugi, who was very helpful in the process of foraminifera shells scanning at the synchrotron SPring-8 (Japan). We are very grateful to the editor SZ and the three reviewers.

Conflict of interest

Author DM is employed by the company FORCE Technology.

The remaining authors declare that the research was conducted in the absence of any commercial or financial relationships that could be construed as a potential conflict of interest.

Publisher’s note

Supplementary material

The Supplementary Material for this article can be found online at: https://www.frontiersin.org/articles/10.3389/feart.2023.1120170/full#supplementary-material

References

Allison, N., Austin, W., Paterson, D., and Austin, H. (2010). Culture studies of the benthic foraminifera *Elphidium williamsoni*: Evaluating pH, $\Delta[CO_3^{2-}]$ and inter-individual effects on test Mg/Ca. *Chem. Geol.* 274, 87–93. doi:10.1016/j.chemgeo.2010.03.019

Alve, E. (1991). Benthic foraminifera in sediment cores reflecting heavy metal pollution in Sorfjord, Western Norway. *J. Foraminifer. Res.* 21, 1–19. doi:10.2113/gsjfr.21.1.1

Bé, A. W. H., and Lott, L. (1964). Shell growth and structure of planktonic foraminifera. *Science* 145, 823–824. doi:10.1126/science.145.3634.823

Belanger, C. L. (2022). Volumetric analysis of benthic foraminifera: Intraspecific test size and growth patterns related to embryonic size and food resources. *Mar. Micropaleontol.* 176, 102170. doi:10.1016/j.marmicro.2022.102170

Bernhard, J. M. (1986). Characteristic assemblages and morphologies of benthic foraminifera from anoxic, organic-rich deposits; Jurassic through Holocene. *J. Foraminifer. Res.* 16, 207–215. doi:10.2113/gsjfr.16.3.207

Bernhard, J. M., Wit, J. C., Starczak, V. R., Beaudoin, D. J., Phalen, W. G., and McCorkle, D. C. (2021). Impacts of multiple stressors on a benthic foraminiferal community: A long-term experiment assessing response to ocean acidification, hypoxia and warming. *Front. Mar. Sci.* 8. doi:10.3389/fmars.2021.643339

Bijma, J., Pörtner, H.-O., Yesson, C., and Rogers, A. D. (2013). Climate change and the oceans – what does the future hold? Mar. Pollut. Bull., the global state of the ocean; interactions between stresses, impacts and some potential solutions. *Synthesis Pap. Int. Programme State Ocean 2011 2012 Work.* 74, 495–505. doi:10.1016/j.marpolbul.2013.07.022

Bindoff, N. L., Cheung, W. W. L., Kairo, J. G., Arístegui, J., Guinder, V. A., Hallberg, R., et al. (2019). “Changing ocean, marine ecosystems, and dependent communities,” in *IPCC special report on the ocean and cryosphere in a changing climate*. Editors H.-O. Pörtner, D. C. Roberts, V. Masson-Delmotte, P. Zhai, M. Tignor, E. Poloczanska, et al. (Switzerland: Intergovernmental Panel on Climate Change), 477–587.

Bradshaw, J. S. (1961). Laboratory experiments on the ecology of foraminifera. *Cushman Found. Foram Res. Contr* 12, 87–106.

Breitburg, D., Levin, L. A., Oschlies, A., Grégoire, M., Chavez, F. P., Conley, D. J., et al. (2018). Declining oxygen in the global ocean and coastal waters. *Science* 359, eaam7240. doi:10.1126/science.aam7240

Burke, J. E., Renema, W., Henehan, M. J., Elder, L. E., Davis, C. V., Maas, A. E., et al. (2018). Factors influencing test porosity in planktonic foraminifera. *Biogeosciences* 15, 6607–6619. doi:10.5194/bg-15-6607-2018

Carstensen, J., Conley, D. J., Andersen, J. H., and Ærtebjerg, G. (2006). Coastal eutrophication and trend reversal: A Danish case study. *Limnol. Oceanogr.* 51, 398–408. doi:10.4319/lo.2006.51.1_part_2.0398

Carstensen, J., and Conley, D. J. (2019). Baltic sea hypoxia takes many shapes and sizes. *Limnol. Oceanogr. Bull.* 28, 125–129. doi:10.1002/lob.10350

Carstensen, J., and Duarte, C. M. (2019). Drivers of pH variability in coastal ecosystems. *Environ. Sci. Technol.* 53, 4020–4029. doi:10.1021/acs.est.8b03655

Charrieau, L. M., Filipsson, H. L., Ljung, K., Chierici, M., Knudsen, K. L., and Kritzberg, E. (2018a). The effects of multiple stressors on the distribution of coastal benthic foraminifera: A case study from the skagerrak-baltic sea region. *Mar. Micropaleontol.* 139, 42–56. doi:10.1016/j.marmicro.2017.11.004

Charrieau, L. M., Filipsson, H. L., Nagai, Y., Kawada, S., Ljung, K., Kritzberg, E., et al. (2018b). Decalcification and survival of benthic foraminifera under the combined impacts of varying pH and salinity. *Mar. Environ. Res.* 138, 36–45. doi:10.1016/j.marenvres.2018.03.015

Charrieau, L. M., Ljung, K., Schenk, F., Daewel, U., Kritzberg, E., and Filipsson, H. L. (2019). Rapid environmental responses to climate-induced hydrographic changes in the Baltic Sea entrance. *Biogeosciences* 16, 3835–3852. doi:10.5194/bg-16-3835-2019

Cignoni, P., Callieri, M., Corsini, M., Dellepiane, M., Ganovelli, F., and Ranzuglia, G. (2008). *MeshLab: An open-source mesh processing tool 8.*

Conley, D. J., Carstensen, J., Ærtebjerg, G., Christensen, P. B., Dalsgaard, T., Hansen, J. L. S., et al. (2007). Long-term changes and impacts of hypoxia in Danish coastal waters. *Ecol. Appl.* 17, S165–S184. doi:10.1890/05-0766.1

Corliss, B. H. (1985). Microhabitats of benthic foraminifera within deep-sea sediments. *Nature* 314, 435–438. doi:10.1038/314435a0

Cushman, J. A. (1930). The foraminifera of the atlantic ocean, part 7 – *nonionidae, camerinidae, peneroplidae* and *alveonellidae*. *Bull. U. S. Natl. Mus.* 104, 1–79.

Darling, K. F., Schweizer, M., Knudsen, K. L., Evans, K. M., Bird, C., Roberts, A., et al. (2016). The genetic diversity, phylogeography and morphology of *Elphidiidae* (Foraminifera) in the Northeast Atlantic. *Mar. Micropaleontol.* 129, 1–23. doi:10.1016/j.marmicro.2016.09.001

Davis, C. V., Wishner, K., Renema, W., and Hull, P. M. (2021). Vertical distribution of planktic foraminifera through an oxygen minimum zone: How assemblages and test morphology reflect oxygen concentrations. *Biogeosciences* 18, 977–992. doi:10.5194/bg-18-977-2021

Dissard, D., Nehrke, G., Reichart, G. J., and Bijma, J. (2010). Impact of seawater $p\text{CO}_2$ on calcification and Mg/Ca and Sr/Ca ratios in benthic foraminifera calcite: Results from culturing experiments with *Ammonia tepida*. *Biogeosciences* 7, 81–93. doi:10.5194/bg-7-81-2010

Doube, M., Kłosowski, M. M., Arganda-Carreras, I., Cordelières, F. P., Dougherty, R. P., Jackson, J. S., et al. (2010). BoneJ: Free and extensible bone image analysis in ImageJ. *Bone* 47, 1076–1079. doi:10.1016/j.bone.2010.08.023

Dougherty, R., and Kunzelmann, K.-H. (2007). Computing local thickness of 3D structures with ImageJ. *Microsc. Microanal.* 13, 1678–1679. doi:10.1017/S1431927607074430

Feistel, R., Nausch, G., and Hagen, E. (2006). Unusual Baltic inflow activity in 2002-2003 and varying deep-water properties. *Oceanologia* 48, 21–35.

Foster, L. C., Schmidt, D. N., Thomas, E., Arndt, S., and Ridgwell, A. (2013). Surviving rapid climate change in the deep sea during the Paleogene hyperthermals. *Proc. Natl. Acad. Sci.* 110, 9273–9276. doi:10.1073/pnas.1300579110

Fox, L., Stukins, S., Hill, T., and Miller, C. G. (2020). Quantifying the effect of anthropogenic climate change on calcifying plankton. *Sci. Rep.* 10, 1620. doi:10.1038/s41598-020-58501-w

Fujimoto, N., Maruyama, H., Kawakami, Y., and Yamashita, T. (2018). Development of applications for aligned carbon nanotubes (HiTaCa). *Hitz* 79, 59–63.

Gattuso, J.-P., and Hansson, L. (2011). *Ocean acidification*. Oxford: Oxford University Press.

Gilbert, R. O. (1987). *Statistical methods for environmental pollution monitoring*. New York: van Nostrand Reinhold.

Glock, N., Eisenhauer, A., Milker, Y., Liebetrau, V., Schönfeld, J., Mallon, J., et al. (2011). Environmental influences on the pore density of *Bolivina spissa* (Cushman). *J. Foraminifer. Res.* 41, 22–32. doi:10.2113/gsjfr.41.1.22

Glock, N., Roy, A.-S., Romero, D., Wein, T., Weissenbach, J., Revsbech, N. P., et al. (2019). Metabolic preference of nitrate over oxygen as an electron acceptor in foraminifera from the Peruvian oxygen minimum zone. *Proc. Natl. Acad. Sci.* 116, 2860–2865. doi:10.1073/pnas.1813887116

Groeneveld, J., Filipsson, H. L., Austin, W. E. N., Darling, K., McCarthy, D., Quintana Krupinski, N. B., et al. (2018). Assessing proxy signatures of temperature, salinity, and hypoxia in the Baltic Sea through foraminifera-based geochemistry and faunal assemblages. *J. Micropalaeontology* 37, 403–429. doi:10.5194/jm-37-403-2018

Gruber, N. (2011). Warming up, turning sour, losing breath: Ocean biogeochemistry under global change. *Philos. Trans. R. Soc. Math. Phys. Eng. Sci.* 369, 1980–1996. doi:10.1098/rsta.2011.0003

Gustafsson, B. G., Schenk, F., Blenckner, T., Eilola, K., Meier, H. E. M., Müller-Karulis, B., et al. (2012). Reconstructing the development of Baltic Sea eutrophication 1850–2006. *AMBIO* 41, 534–548. doi:10.1007/s13280-012-0318-x

Hannah, F., Rogerson, R., and Laybourn-Parry, J. (1994). Respiration rates and biovolumes of common benthic Foraminifera (Protozoa). *J. Mar. Biol. Assoc. U. K.* 74, 301–312. doi:10.1017/S0025315400039345

Hänninen, J., Vuorinen, I., and Hjelt, P. (2000). Climatic factors in the Atlantic control the oceanographic and ecological changes in the Baltic Sea. *Limnol. Oceanogr.* 45, 703–710. doi:10.4319/lo.2000.45.3.0703

Haynert, K., and Schönfeld, J. (2014). Impact of changing carbonate chemistry, temperature, and salinity on growth and test degradation of the benthic foraminifer. *Ammon. aomoriensis J. Foraminifer. Res.* 44, 76–89. doi:10.2113/gsjfr.44.2.76

Haynert, K., Schönfeld, J., Riebesell, U., and Polovodova, I. (2011). Biometry and dissolution features of the benthic foraminifer *Ammonia aomoriensis* at high $p\text{CO}_2$. *Mar. Ecol. Prog. Ser.* 432, 53–67. doi:10.3354/meps09138

Heron-Allen, E., and Earland, A. (1911). On recent and fossil foraminifera of the shore sands at Selsey Bill, Sussex. *J. R. Microsc. Soc. Lond. Part.* 8, 436–448.

Howes, E. L., Eagle, R. A., Gattuso, J.-P., and Bijma, J. (2017). Comparison of Mediterranean pteropod shell biometrics and ultrastructure from historical (1910 and 1921) and present day (2012) samples provides baseline for monitoring effects of global change. *PLOS ONE* 12, e0167891. doi:10.1371/journal.pone.0167891

Johnstone, H. J. H., Schulz, M., Barker, S., and Elderfield, H. (2010). Inside story: An X-ray computed tomography method for assessing dissolution in the tests of planktonic foraminifera. *Mar. Micropaleontol.* 77, 58–70. doi:10.1016/j.marmicro.2010.07.004

Kaiho, K. (1994). Benthic foraminiferal dissolved-oxygen index and dissolved-oxygen levels in the modern ocean. *Geology* 22, 719–722. doi:10.1130/0091-7613(1994)022<0719:BFDOIA>2.3.CO;2

Kroeker, K. J., Kordas, R. L., Crim, R., Hendriks, I. E., Ramajo, L., Singh, G. S., et al. (2013). Impacts of ocean acidification on marine organisms: Quantifying sensitivities and interaction with warming. *Glob. Change Biol.* 19, 1884–1896. doi:10.1111/gcb.12179

Kuhnt, T., Friedrich, O., Schmiedl, G., Milker, Y., Mackensen, A., and Lückge, A. (2013). Relationship between pore density in benthic foraminifera and bottom-water oxygen content. *Deep Sea Res. Part Oceanogr. Res. Pap.* 76, 85–95. doi:10.1016/j.dsr.2012.11.013

Kuhnt, T., Schiebel, R., Schmiedl, G., Milker, Y., Mackensen, A., and Friedrich, O. (2014). Automated and manuel analyses of the pore density-to-oxygen relationship in *Globobulimina turgida* (Bailey). *J. Foraminifer. Res.* 44, 5–16. doi:10.2113/gsjfr.44.1.5

Lehmann, A., Lorenz, P., and Jacob, D. (2004). Modelling the exceptional Baltic Sea inflow events in 2002–2003. *Geophys. Res. Lett.* 31. doi:10.1029/2004GL020830

Leung, B., Forbes, M. R., and Houle, D. (2000). Fluctuating asymmetry as a bioindicator of stress: Comparing efficacy of analyses involving multiple traits. *Am. Nat.* 155, 101–115. doi:10.1086/303298

Liew, T.-S., and Schilthuizen, M. (2016). A method for quantifying, visualising, and analysing gastropod shell form. *PLOS ONE* 11, e0157069. doi:10.1371/journal.pone.0157069

Ljung, K., Schoon, P. L., Rudolf, M., Charrieau, L. M., Ni, S., and Filipsson, H. L. (2022). Recent increased loading of carbonaceous pollution from biomass burning in the baltic sea. *ACS Omega* 7, 35102–35108. doi:10.1021/acsomega.2c04009

Meredith, M., Sommerkorn, M., Cassota, S., Derksen, C., Ekaykin, A., Hollowed, A., et al. (2019). Polar Regions. Chapter 3, IPCC special report on the ocean and cryosphere in a changing climate. Available at: https://www.ipcc.ch/srocc/chapter/chapter-3-2/.

Monnet, C., Zollikofer, C., Bucher, H., and Goudemand, N. (2009). Three-dimensional morphometric ontogeny of mollusc shells by micro-computed tomography and geometric analysis. *Palaeontol. Electron.* 12, 1–13. doi:10.5167/uzh-23587

Morvan, J., Cadre, V. L., Jorissen, F., and Debenay, J.-P. (2004). Foraminifera as potential bio-indicators of the “Erika” oil spill in the Bay of Bourgneuf: Field and experimental studies. *Aquat. Living Resour.* 17, 317–322. doi:10.1051/alr:2004034

Müter, D., Sørensen, H. O., Oddershede, J., Dalby, K. N., and Stipp, S. L. S. (2015). Microstructure and micromechanics of the heart urchin test from X-ray tomography. *Acta Biomater.* 23, 21–26. doi:10.1016/j.actbio.2015.05.007

Ni, S., Quintana Krupinski, N. B., Groeneveld, J., Persson, P., Somogyi, A., Brinkmann, I., et al. (2020). Early diagenesis of foraminiferal calcite under anoxic conditions: A case study from the landsort deep, Baltic Sea (iodp site M0063). *Chem. Geol.* 558, 119871. doi:10.1016/j.chemgeo.2020.119871

Oakes, R. L., Peck, V. L., Manno, C., and Bralower, T. J. (2019). Degradation of internal organic matter is the main control on pteropod shell dissolution after death. *Glob. Biogeochem. Cycles* 33, 749–760. doi:10.1029/2019GB006223

Peck, V. L., Oakes, R. L., Harper, E. M., Manno, C., and Tarling, G. A. (2018). Pteropods counter mechanical damage and dissolution through extensive shell repair. *Nat. Commun.* 9, 264. doi:10.1038/s41467-017-02692-w

Petersen, J., Riedel, B., Barras, C., Pays, O., Guihéneuf, A., Mabilleau, G., et al. (2016). Improved methodology for measuring pore patterns in the benthic foraminiferal genus Ammonia. *Mar. Micropaleontol.* 128, 1–13. doi:10.1016/j.marmicro.2016.08.001

Reusch, T. B. H., Dierking, J., Andersson, H. C., Bonsdorff, E., Carstensen, J., Casini, M., et al. (2018). The Baltic Sea as a time machine for the future coastal ocean. *Sci. Adv.* 4, eaar8195. doi:10.1126/sciadv.aar8195

Rhein, M., Rintoul, S. R., Aoki, S., Campos, E., Chambers, D., Feely, R. A., et al. (2013). “Observations: Ocean,” in *Climate change 2013: The physical science basis. Contribution of working group I to the fifth assessment report of the intergovernmental panel on climate change*.

Richirt, J., Champmartin, S., Schweizer, M., Mouret, A., Petersen, J., Ambari, A., et al. (2019). Scaling laws explain foraminiferal pore patterns. *Sci. Rep.* 9, 9149. doi:10.1038/s41598-019-45617-x

Rutgersson, A., Jaagus, J., Schenk, F., and Stendel, M. (2014). Observed changes and variability of atmospheric parameters in the Baltic Sea region during the last 200 years. *Clim. Res.* 61, 177–190. doi:10.3354/cr01244

Schindelin, J., Arganda-Carreras, I., Frise, E., Kaynig, V., Longair, M., Pietzsch, T., et al. (2012). Fiji: An open-source platform for biological-image analysis. *Nat. Methods* 9, 676–682. doi:10.1038/nmeth.2019

Sen Gupta, B. K., and Machain-Castillo, M. L. (1993). Benthic foraminifera in oxygen-poor habitats. *Mar. Micropaleontol.* 20, 183–201. doi:10.1016/0377-8398(93)90032-S

Speijer, R. P., Loo, D. V., Masschaele, B., Vlassenbroeck, J., Cnudde, V., and Jacobs, P. (2008). Quantifying foraminiferal growth with high-resolution X-ray computed tomography: New opportunities in foraminiferal ontogeny, phylogeny, and paleoceanographic applications. *Geosphere* 4, 760–763. doi:10.1130/GES00176.1

Steffen, W., Broadgate, W., Deutsch, L., Gaffney, O., and Ludwig, C. (2015). The trajectory of the anthropocene: The great acceleration. *Anthr. Rev.* 2, 81–98. doi:10.1177/2053019614564785

Strong, A. L., Kroeker, K. J., Teneva, L. T., Mease, L. A., and Kelly, R. P. (2014). ocean acidification 2.0: Managing our changing coastal ocean chemistry. *BioScience* 64, 581–592. doi:10.1093/biosci/biu072

Titelboim, D., Lord, O. T., and Schmidt, D. N. (2021). Thermal stress reduces carbonate production of benthic foraminifera and changes the material properties of their shells. *ICES J. Mar. Sci.* 78, 3202–3211. doi:10.1093/icesjms/fsab186

Tudisco, E., Etxegarai, M., Hall, S. A., Charalampidou, E.-M., Couples, G. D., Lewis, H., et al. (2019). Fast 4-D imaging of fluid flow in rock by high-speed neutron tomography. *J. Geophys. Res. Solid Earth* 124, 3557–3569. doi:10.1029/2018JB016522

Weinkauf, M. F. G., Moller, T., Koch, M. C., and Kučera, M. (2014). Disruptive selection and bet-hedging in planktonic foraminifera: Shell morphology as predictor of extinctions. *Front. Ecol. Evol.* 2. doi:10.3389/fevo.2014.00064

Weinkauf, M. F. G., Zwick, M. M., and Kučera, M. (2020). Constraining the role of shell porosity in the regulation of shell calcification intensity in the modern planktonic foraminifer *Orbulina Universa* d'Orbigny. *J. Foraminifer. Res.* 50, 195–203. doi:10.2113/gsjfr.50.2.195

Zarkogiannis, S. D., Fernandez, V., Greaves, M., Mortyn, P. G., Kontakiotis, G., Antonarakou, A., et al. (2020). X-ray tomographic data of planktonic foraminifera species *Globigerina bulloides* from the Eastern Tropical Atlantic across Termination II. *Gigabyte* 2020, 1–10. doi:10.46471/gigabyte.5

Zillén, L., Conley, D. J., Andrén, T., Andrén, E., and Björck, S. (2008). Past occurrences of hypoxia in the Baltic Sea and the role of climate variability, environmental change and human impact. *Earth-Sci. Rev.* 91, 77–92. doi:10.1016/j.earscirev.2008.10.001

Frontiers in Earth Science

TYPE Original Research
PUBLISHED 21 April 2023
DOI 10.3389/feart.2023.1130107

X-ray tomographic microscopy of Eocene coprolites from Pipestone Springs Main Pocket, southwest Montana

Sarah M. Jacquet[1]*, Jeremy-Louis Webb[1], John Warren Huntley[1], Tara Selly[1,2] and James D. Schiffbauer[1,2]

[1]Department of Geological Sciences, University of Missouri, Columbia, MO, United States, [2]X-ray Microanalysis Laboratory, University of Missouri, Columbia, MO, United States

EDITED BY
Elizabeth Clark,
University of California, Berkeley,
United States

REVIEWED BY
Caleb Gordon,
Yale University, United States
Holger Petermann,
Denver Museum of Nature and Science,
United States

*CORRESPONDENCE
Sarah M. Jacquet,
jacquets@missouri.edu

RECEIVED 22 December 2022
ACCEPTED 06 April 2023
PUBLISHED 21 April 2023

CITATION
Jacquet SM, Webb J-L, Huntley JW, Selly T and Schiffbauer JD (2023), X-ray tomographic microscopy of Eocene coprolites from Pipestone Springs Main Pocket, southwest Montana.
Front. Earth Sci. 11:1130107.
doi: 10.3389/feart.2023.1130107

The Eocene Pipestone Springs Main Pocket (Renova Formation, Jefferson County, Montana, United States of America) is a locality renowned for its diverse Chadronian (late Eocene; ~38–33.9 million years ago) mammalian fauna and abundant coprolites. Two distinct coprolite size classes were previously identified in the trace fossil assemblage from which we selected representatives to investigate feeding behaviors and dietary selection of the producers. A subset of the selected coprolites was analyzed based on their compositional and taphonomic attributes using non-destructive x-ray tomographic microscopy in combination with more traditional methods including thin-section petrography, scanning electron microscopy, and energy dispersive spectroscopy. Among the features extracted in the tomographic data were skeletal fragments, including those showing evidence of bone-crushing; delicate hair molds; encrusted lithic fragments; and several irregular pores and cracks throughout the coprolites. Segmentation and volumetric renders permit quantitative assessment of the relative proportions of inclusions, revealing porosity as a primary volumetric element aside from the matrix and bone inclusions. There was no significant difference in the total volume of bone extracted between coprolite size class, though the smaller coprolites preserved a relatively higher volumetric proportion of undigested skeletal material. This multi-visualization approach provides a means to observe and evaluate differences in the coprolite gross morphology and inclusions across the two size classes, thereby offering valuable insights into the broader paleoecology of the Pipestone Springs Main Pocket coprolite producers and holding promise for comparable paleo-dietary studies of other coprolite-rich deposits.

KEYWORDS

coprolite, taphonomy, μCT, diet, hair

1 Introduction

Coprolites and affiliated trace fossils offer a rare glimpse into the feeding, digestive, and excretory behaviors of their producers whilst simultaneously capturing unique paleoecological and paleoenvironmental information (Hunt et al., 2012; Myhrvold, 2012). Examination of such fossils typically requires sub-sampling of the specimen, often employing destructive sampling techniques (e.g., disaggregation or dissolution) to either a portion of the specimen or its entirety (Bryant, 1970; Fry, 1970; Shillito et al., 2020). Recent studies have utilized non-destructive three-dimensional (3D) imaging techniques, such as x-ray tomographic microscopy (μCT) and synchrotron microtomography, to reveal macroscopic and microscopic inclusions that may otherwise be lost via more traditional methods (Bravo-Cuevas et al., 2017; Qvarnström et al., 2017; 2019; Wang et al., 2018; Romaniuk et al., 2020; Abella et al., 2022). Challenges with x-ray-based methodologies persist, however, often owing to the attributes of the sample. For instance, depending on the preservation of the coprolite, some inclusions may be compositionally similar to the matrix material. In such cases, overlapping intensity ranges will make discerning these features difficult via standard segmentation or thresholding techniques. This lack of phase contrast can be exacerbated by taphonomic processes caused during digestion wherein the bone margins become diffuse, or during diagenesis when remobilization of soluble minerals causes secondary infilling of pores. Diagenesis can also reduce or eliminate phase contrast through secondary remineralization of the entire specimen. Nevertheless, for coprolites and inclusions that have not been substantially altered through taphonomic or diagenetic processes, μCT proves to be a powerful tool in extracting inclusions virtually for qualitative analysis—although its applications for such research at present are in their infancy (but see Huisman et al., 2014; Shillito et al., 2020). Where prior coprolites studies employing μCT have been predominantly qualitative, intent on the description of the types of inclusions, the quantitative analysis of extracted components and associated potential to address testable hypotheses is an area that requires further research.

Herein, we employ non-destructive μCT in conjunction with targeted consumptive sampling to gain a more holistic view of the internal composition and inclusions of a subset of coprolites from a well-documented trace fossil assemblage. Specifically, we targeted coprolite material from the Pipestone Springs Main Pocket (PSMP) assemblage (Renova Formation), Jefferson County, Montana. This site is renowned for its diverse mammalian fauna and associated trace fossils (Lofgren et al., 2017), and previous work has reported on the taxonomy of vertebrate inclusions and the likely identity of at least one taxon of coprolite producer. Lofgren et al. (2017) examined coprolite surface morphology and visible skeletal elements in 358 specimens, including 20 specimens that were mechanically prepared by removing skeletal inclusions. It is worth noting that the regular shape, phosphatic composition, low bone density, and highly digested, fragmented nature of the bones in these specimens supports their interpretation as coprolites, rather than regurgitalites (Myhrvold, 2012; Gordon et al., 2020; Serafini et al., 2022). Analysis of the measurable dimensions of this coprolite assemblage have previously revealed two distinct size classes, including smaller forms ranging from 4 to 15 mm in diameter and larger forms ranging from 16 to 29 mm in diameter (Lofgren et al., 2017). The larger coprolites could not be attributed to any single genus with confidence, and are suggested to have been produced by *Brachyrhynchocyon dodgei*. The producer of the smaller coprolites, with several smaller carnivorous taxa as potential candidates was deduced to be *Hesperocyon gregarius* (Lofgren et al., 2017). This prior work provides an important foundation from which we can both ascertain the broader paleoecological framework for the coprolite assemblage and further build upon it by assessing the taphonomic and diagenetic attributes of the coprolites.

Utilizing computed tomographic techniques provides a novel avenue of investigation to substantiate previous findings on the gross morphology of the PSMP coprolites, as well as to 1) visualize 3D specimen structure and identify the undigested skeletal and keratinous inclusions via virtual segmentation; 2) quantify the relative proportions of bone inclusions and pores to feces matrix; and 3) discern any difference between the two size classes with respect to the shape and volume of bone inclusions. This work further serves to assess the potential applications (and limitations) of μCT techniques in the analysis of coprolites. Finally, corroborating previous findings with data herein, we seek to further elucidate the feeding behavior of these ancient vertebrate producers across coprolite size classes, while also detailing the taphonomic and diagenetic processes found within the PSMP assemblage.

2 Geological setting

Coprolites are derived from the PSMP, which is considered part of the Climbing Arrow Member of the Renova Formation in Jefferson County, Montana (Kuenzi and Fields, 1971; see Hanneman et al., 2022; Figures 1, 2). Specimens documented herein were collected from the upper-most 15 m-thick silty mudstone unit of the Pistone Springs reference section. Outcropping strata are exposed on opposing sides of an erosional gully though both isolated pockets are lithologically and faunally indistinguishable, hence are often referred to as the same bed (Tabrum et al., 1996). Material herein was collected from the RAM V200301 locality which is situated on the dip slope towards the northern end of the Main Pocket exposures, in the same vicinity as MV 5811, MV 5902, and CM 3575 (Orr, 1958; see Hanneman et al., 2022; Figures 3, 4).

Based on prior biostratigraphic correlation and magnetostratigraphy (Prothero, 1984), the PSMP assemblage has been estimated as middle to late Chadronian in age (35.0–35.5 Ma). The deposit is exposed as a 50 cm–4 m thick layer of homogenous tuffaceous mudstone, lacking sedimentary structures or obvious bioturbation (Lofgren et al., 2017). Coprolite and vertebrate remains are randomly distributed (without size-sorting) throughout the deposit, both laterally and vertically, precluding hydrodynamic sorting (Lofgren et al., 2017). Several interpretations concerning the formation of these deposits have been proposed, with initial scenarios involving either repeated ash-rich mud flows or inundated floodplain deposits (Kuenzi and Fields, 1971; Lofgren et al., 2017). However, in the absence of clear debris-flow or fluvial sedimentary features, Hanneman et al. (2022) interpret these deposits as having been formed by predominantly aeolian processes. Paleosols of varying degrees of development and exhibiting extensive bioturbation are intercalated between aeolian events represented by direct and reworked ashfall deposits, and loessites (Hanneman et al., 2022).

3 Materials and methods

The twelve coprolite specimens examined herein (Table 1) are housed in the collections of the Raymond M. Alf Museum of Paleontology (RAM), Claremont, California. The external

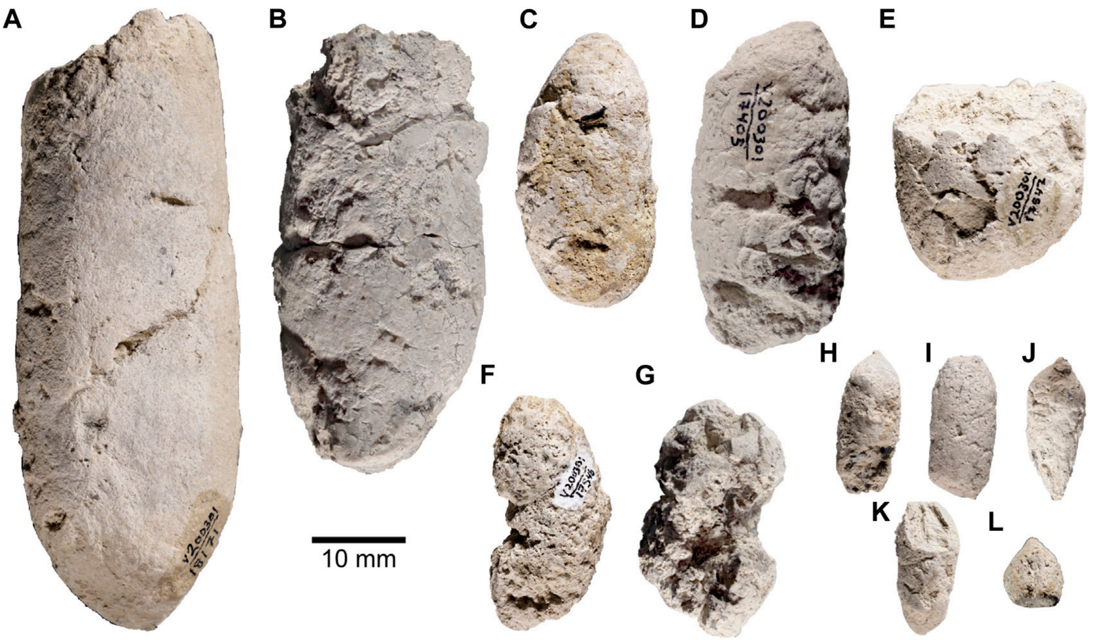

FIGURE 1
Coprolites arranged by mass (g) into Class I **(A–G)** and Class II **(H–L)** **(A)**. RAM 18171 **(B)**. RAM 17517 **(C)**. RAM 17540 **(D)**. RAM 17405 **(E)**. RAM 17547 **(F)**. RAM 17546 **(G)**. RAM 17370 **(H)**. RAM 17557 **(I)**. RAM 31214 **(J)**. RAM 31212 **(K)**. RAM 31211 **(L)**. RAM 31209.

appearance of the coprolites was examined using reflective light microscopy and photographed using a Magnify^2 GIGAMacro Robotic Imaging System with Canon EOS Rebel T6i/T8i DSLR cameras and Nikon ×1 objective to acquire gigapixel resolution photomosaics. Petrographic photomicrographs were captured using a Nikon D3300 DSLR camera mounted to a Nikon Eclipse E200 polarizing microscope. Background illumination was corrected using open-source imaging software FIJI (Schindelin et al., 2012) and the method provided by Landini (2006).

Exterior physical features were described using the methods outlined in Jouy-Avantin et al. (2003), including the identification of color, shape, hardness, texture, the presence or absence of constrictions, and inclusions visible at the surface. Coprolite color was characterized based on the Munsell Color Rock-Color Chart (Munsell Color, 2010). The overall shape and specific morphology of the coprolite extremities were noted (e.g., sharp-ended, rounded, or broken), as were taphonomic modifications including desiccation, abrasion, and surface markings/burrows (Supplementary Table S1). Any inclusions visible on the surface were also noted (i.e., bones, adhering sediment). The surface texture was examined to determine whether the coprolite displayed homogenous or heterogeneous mixtures; compacted aggregates less than 1 mm, compacted aggregates greater than or equal to 1 mm, homogenous mixtures with some aggregates, or many aggregates included in a homogenous mixture.

3.1 Microscopic analyses and visualization

Coprolite samples were scanned using a Zeiss Xradia 510 Versa μCT microscope at the X-ray Microanalysis Laboratory (MizzoμX), University of Missouri, for non-destructive analyses. Optimal scanning parameters for the coprolites varied, with source voltage ranging between 80 and 140 kV, source power between 7 and 10 W, and exposure time between 1 and 5 s(s). All scans captured 1,601 projections through 360° of rotation and used a ×0.4 objective. Two types of Zeiss low-energy filters were used based on sample transmittance values, with 12 scans using the LE5 filter, and two using the LE2 filter. Voxel size ranged from 3.4618 to 30.12 μm. The scanning parameters for each sample are summarized in the Supplementary Table S2.

Visualization of the 3D data was achieved by importing serial tomogram stacks into Dragonfly software v. 2020.2 Build 941–v. 2022.2 for Windows, Object Research Systems (ORS, 2020) Inc., Montreal, Canada, 2018 (http://www.theobjects.com/dragonfly). Segmentation via labeled voxels was performed using upper and lower Otsu thresholding of greyscale values, in combination with other operations such as fill inner areas, Boolean calculations, and in certain cases manual segmentation throughout the image stacks to extract internal constituents and features of the coprolites (e.g., bones and pore spaces) from the matrix. Volume measurements and relative volumetric proportions of pore space and bone inclusions were calculated for each coprolite tomogram. Note for pores, the remaining porosity was measured, which excluded pores that were secondarily infilled. For more delicate features such as the tubular voids inferred to be moldic preservation of hair, a subsample of 300 slices was classified using the Trainable Weka Segmentation Fiji plugin (Arganda-Carreras et al., 2017) to differentiate these features from other volumetric elements, and subsequently imported into ORS Dragonfly for visualization and quantification in 3D. Feret diameters (i.e., caliper diameter, defined as the distance between the two parallel planes restricting the object perpendicular to that

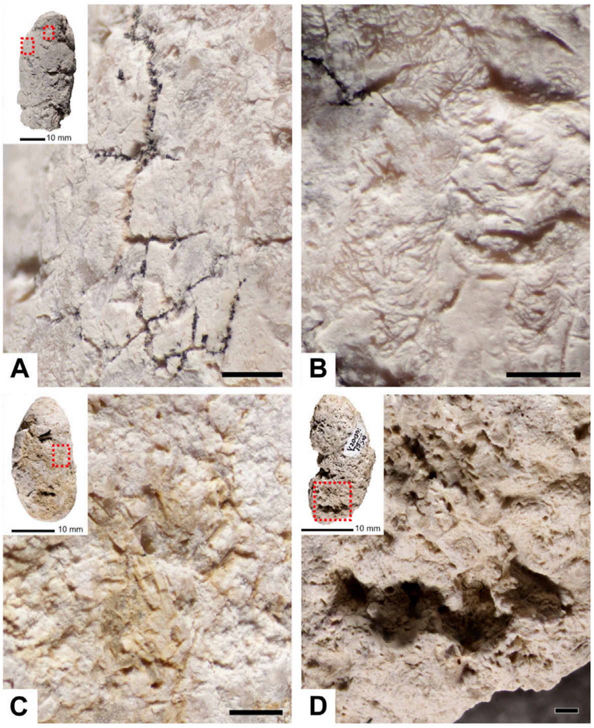

FIGURE 2
Taphonomic and morphological features observed on the surface of coprolite samples. **(A)** Examples of small desiccation cracks (RAM 17517). **(B)**. Shows surface scratches that have no consistent length or pattern to them (RAM 17517). **(C)**. Hair molds (RAM 17540). **(D)**. Large surface pore and likely mold (RAM 17546). Red boxes in overview images represent corresponding zoomed-in images. Scale bars represent 1 mm; insets all 10 mm.

direction) for the bones and pores were measured within Dragonfly. The minimum feret diameter for bones was set at 0.14 mm and the minimum feret diameter for pores set at 0.196 mm. A multi-ROI (Region Of Interest) was extracted from the bone segmentation into group-labeled voxels to identify individual bone components. Select components were then extracted as meshes (.stl files) and smoothed for one iteration in Dragonfly before being exported to Meshmixer, 1995 [Autodesk Meshmixer 3.5, (RRID:SCR_015736)]. The 3D meshes were rendered to remove islands and unrelated material and applied with a shader. Each bone was examined individually for identification and to determine the general shape and signs of fragmentation.

A single specimen (RAM 17540) was prepared and sectioned for examination via optical and scanning electron microscopy (SEM). The coprolite was strengthened with PALEObond Penetrant Stabilizer, embedded in epoxy, and cut diagonally along a section predetermined from observation of the μCT data. One of the two-halves was polished using a Buehler EcoMet250, while the other was left unpolished. Both halves were then analyzed using a Zeiss Sigma 500 VP SEM equipped with a high-definition 5-segment backscattered electron detector at the MizzoμX lab and imaged using the Bruker ATLAS workflow for large-area SEM mosaics. Elemental mapping was conducted on specific regions of interest using dual Bruker XFlash energy dispersive X-ray spectrometers (EDS). All SEM analyses were conducted at their optimal operating conditions of 20 keV beam accelerating voltage, 40 nA beam current, 60 μm aperture for imaging (120 μm aperture for EDS elemental mapping), chamber pressure at 20 Pa, and a working distance of 16.5 mm.

3.2 Statistical analysis

Analyses were conducted and figures produced using software package *R* (R core Team, 2017; Version 4.1.0) and associated R packages *boot, diptest, ggplot2, ggthemes*, *ggpubr* and *mclust* (Davison and Hinkley, 1997; Scrucca et al., 2016; Wickham, 2016; Arnold, 2021; Canty and Ripley, 2021; Maechler, 2021). Raw data is provided in Supplementary Tables S3–S6 along with *R* scripts (Supplementary Scripts S1). Using the volumetric data in Supplementary Table S4, two bar graphs were produced in Microsoft Excel in order to assess the respective contributions of matrix, bones, and pores to total coprolite volume (mm^3) and the relative proportions of these components for each sample.

3.2.1 Testing for size classes of coprolites reported

Size data of coprolites reported in Lofgren et al.'s (2017) Figure 11 were extracted (in 1 mm bins) using plotdigitizer.com (on 8 March 2023, Supplementary Table S6). Gaussian finite mixture modelling of these data was conducted using the *mclust* package in R.

3.2.2 Testing for differences in size classes of our subset of PSMP coprolites

We tested for differences in nine variables by coprolite size class, including measures of length, width, mass, proportion of pore volume, and proportion and size of bone inclusions. We first used the Shapiro test for normality and the Dip test for unimodality (if the data were not normally distributed) to determine if the Wilcoxon Rank-Sum tests were appropriate.

4 Results

4.1 Coprolite external morphology

The coprolites were divided into two different size classes previously defined by Lofgren et al. (2017) based on their diameter, with larger coprolites ranging between 16 and 29 mm and smaller coprolites between 4 and 15 mm. Within our subset we had seven larger class coprolites (Class I; RAM 17370, 17405, 17517, 17540, 17546, 17547, and RAM 18171) and five smaller class coprolites (Class II; RAM 17557, 31209, 31211, 31212, and 31214). Size measurements (i.e., mass, length, and width) are summarized in Table 1. Coprolites exhibited three different colors, including yellow gray (5Y 7/2), grayish yellow (5Y 8/4), or yellowish gray (5Y 8/1), as defined in the Munsell Color Chart (2010). There was no obvious color difference between the classes of coprolites, though all Class II coprolites are yellowish gray, 5Y 8/1.

Most of the examined Class I coprolites (5/7) have a smooth, relatively homogenous surface and tend to share a similar cylinder-like shape, circular in cross-section though occasionally flattened on one side (i.e., RAM 17517) (Figure 1). Notable exceptions include

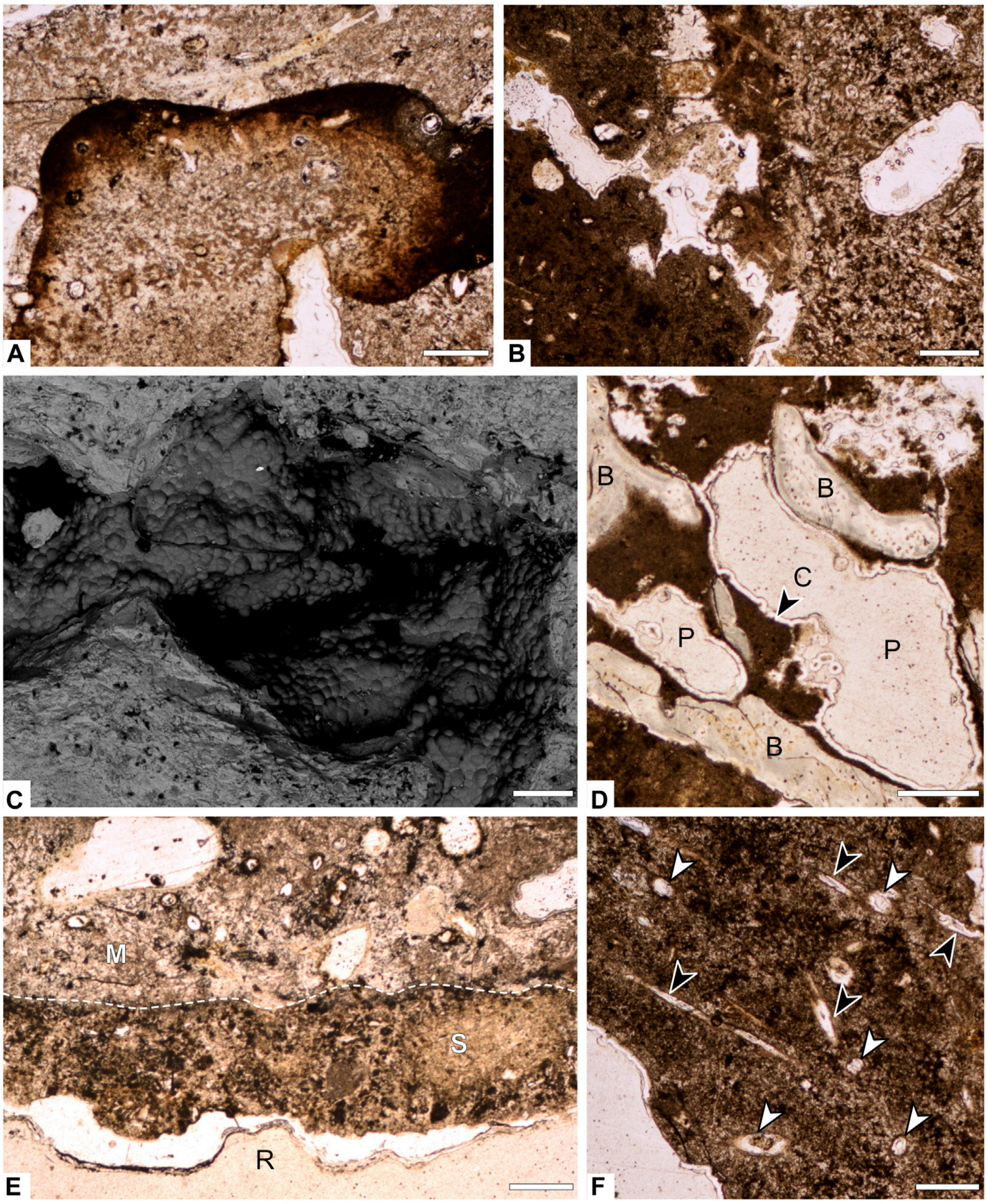

FIGURE 3
Photomicrographs and backscattered electron images of interior composition of specimen RAM 17540. **(A)** Phosphate enriched inclusion embedded within matrix of coprolite. **(B)** Contact between two fabrics of matrix in the interior of the coprolite. **(C)** Backscattered electron image of 3D pore space showing botryoidal silica crust. **(D)** Pore spaces lined with silica crust and bone inclusions. **(E)** Contact (dashed line) between coprolite matrix and adhered layer of sediment. **(F)** Transverse (white arrows) and longitudinal (black arrows) cross sections of hair molds. B= bone; P=pore; C=crust; M=matrix; S=sediment; R=resin. Scale bars represent 250 μm.

RAM 17546 (Figure 1F) and RAM 17370 (Figure 1G), which both display a rough, topographically complex surface, while simultaneously showing signs of constrictions. The examined Class II coprolites also have homogenous, smooth surfaces but are less uniform in shape. As noted by Lofgren et al. (2017), the smaller forms exhibit blunt or tapered ends, and occasionally both. Though few, coprolites within both size classes I and II show small black bone inclusions on their surface visible to the naked eye. In-depth descriptions of each specimen can be found in the Supplementary Text S1.

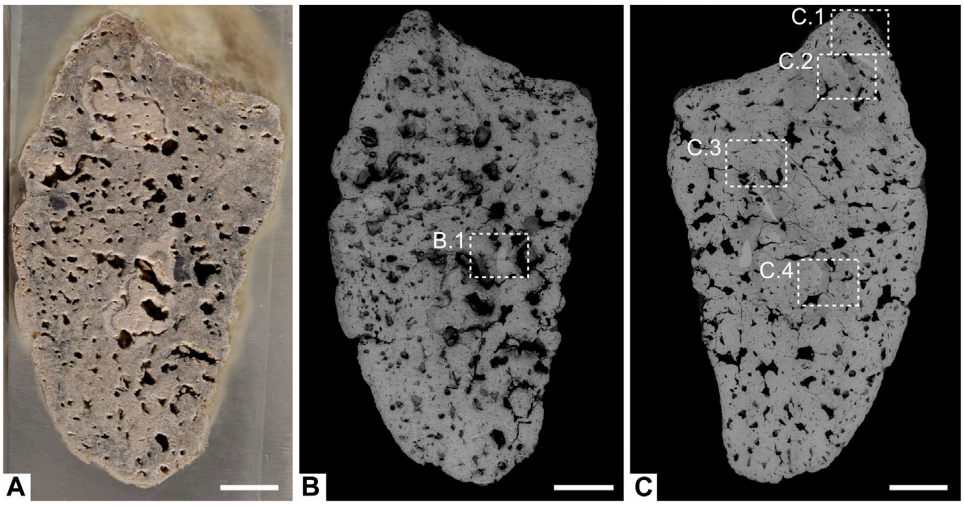

FIGURE 4
Internal and compositional characteristics of RAM 17540 **(A)** Plane view of the unpolished sectioned surface under plain light. **(B)** Backscatter electron image of the same surface figured in **(A)**. **(C)** Back-scatter electron image of polished surface of sectioned sample. Insets shown in Figure 5. Scale bars represent 5 mm.

TABLE 1 Coprolite dimensions and weight arranged by size class and mass (g).

Class	Sample name (RAM)	Length (mm)	Width (mm)	Mass (g)
Class I	17517	50.69	24.11	33.22
Class I	17540	45.94	23.19	27.75
Class I	17405	44.81	22.15	22.00
Class I	17547	28.89	28.90	19.19
Class I	17546	42.50	20.55	17.65
Class I	17370	39.97	21.56	15.97
Class I	18171	64.36	24.03	39.14
Class II	17557	26.14	11.05	3.61
Class II	31214	24.03	10.71	3.27
Class II	31312	26.30	10.63	2.57
Class II	31211	22.65	9.91	2.08
Class II	31209	14.38	11.26	1.68

4.2 Taphonomic surface features

4.2.1 Desiccation cracks

Desiccation cracks occur prior to lithification of the coprolite and are caused as a response to both climate and depositional environment (Northwood, 2005). Several samples displayed desiccation cracks on the exterior coprolite surface (*n* = 6, Supplementary Table S1), varying in size from large, conspicuous cracks with infilled sediment to small hair-line cracks on the surface of the coprolite. An example of these features can be seen on RAM 17517 (Figure 2A), where the cracks appear as small continuous lines that disrupt the specimen surface. RAM 18171 also displays large, infilled cracks approximately midway along the sagittal length that range from 3 to 10 mm in length (Figure 1A). Desiccation cracks were only noted in the larger Class I coprolites where both distinct and finer cracks could be observed together on the same sample.

4.2.2 Abrasion

Abrasion relates to how smooth the surface has become in response to erosion caused by water or wind-born particle scouring following excretion or transport and weathering post

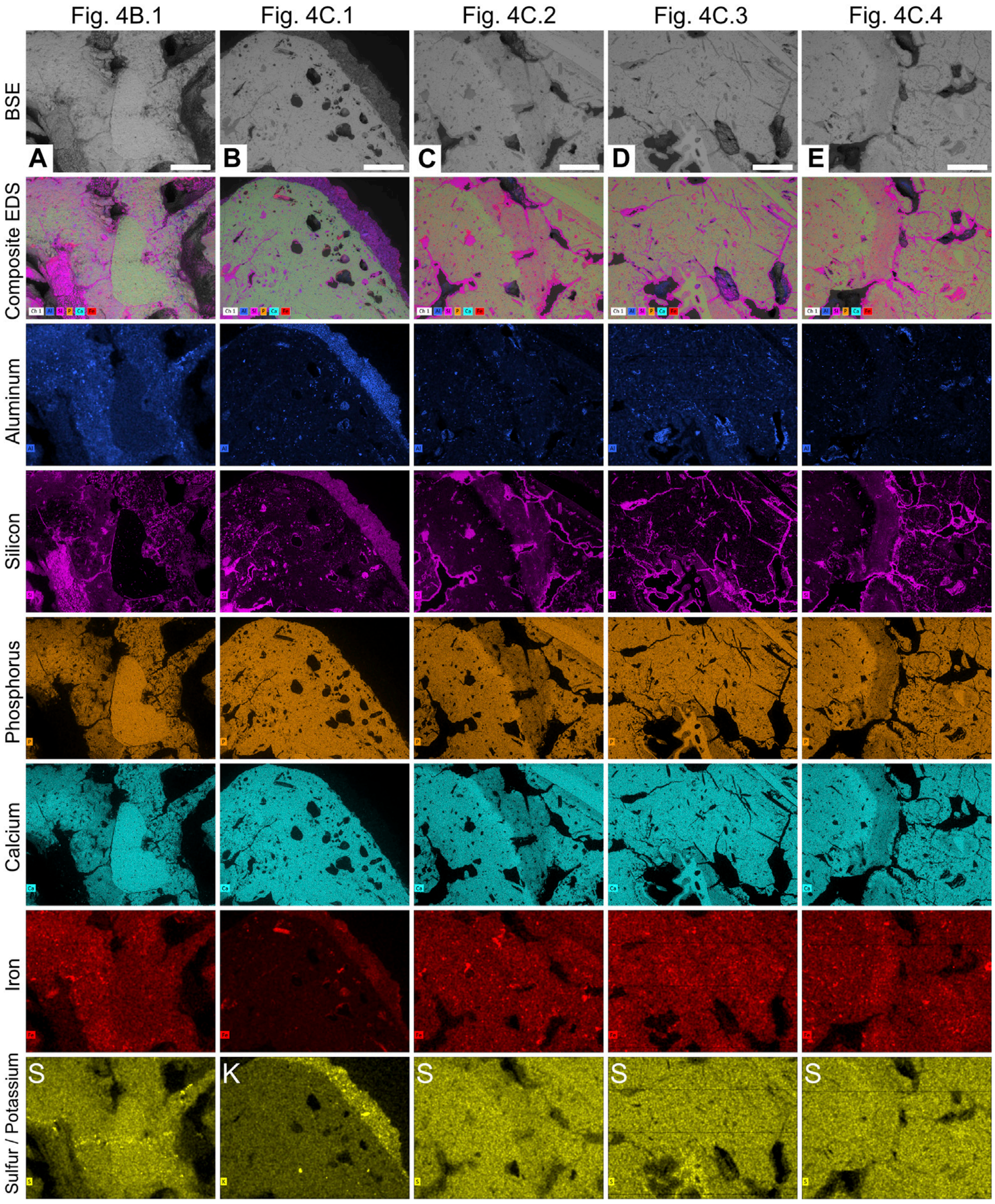

FIGURE 5
EDS elemental maps of areas in specimen RAM 17540 from Figure 4. **(A)**. Well-preserved bone inclusion and surrounding matrix. **(B)** Exterior edge of the coprolite showing sediment adhered to the outer surface. **(C)** Etched bone inclusions with diffuse edges. **(D)** Matrix and hair molds. **(E)** Etched bone inclusions with diffuse edges. Scale bars represent 1 mm.

lithification (Northwood, 2005). We employed the three categories designated by Northwood (2005) to describe the degrees of abrasion including: A. showing no surface abrasions, B. showing little surface abrasion, C. showing significant surface abrasion with a smooth surface. Surface abrasion was common, with most samples (n = 8) displaying evidence of significant abrasion and evenly across the two size classes (SSupplementary Table S1). Two specimens showed evidence of some abrasion (RAM 17517, Figure 1B and RAM 17546, Figure 1F). Those showing no abrasion typically preserved either topographically rough surfaces (RAM 17370, Figure 1G) or delicate features such as radial parallel anal sphincter marks (RAM 31209, Figure 1L). There is no obvious difference in abrasion pattern between coprolite size classes, as both exhibit the full range of abrasion profiles.

4.2.3 Surface marks

Surface marks are more ambiguous in their origin and manifest as some sort of imprint or trace left by either inanimate objects or a biological agent post defecation.

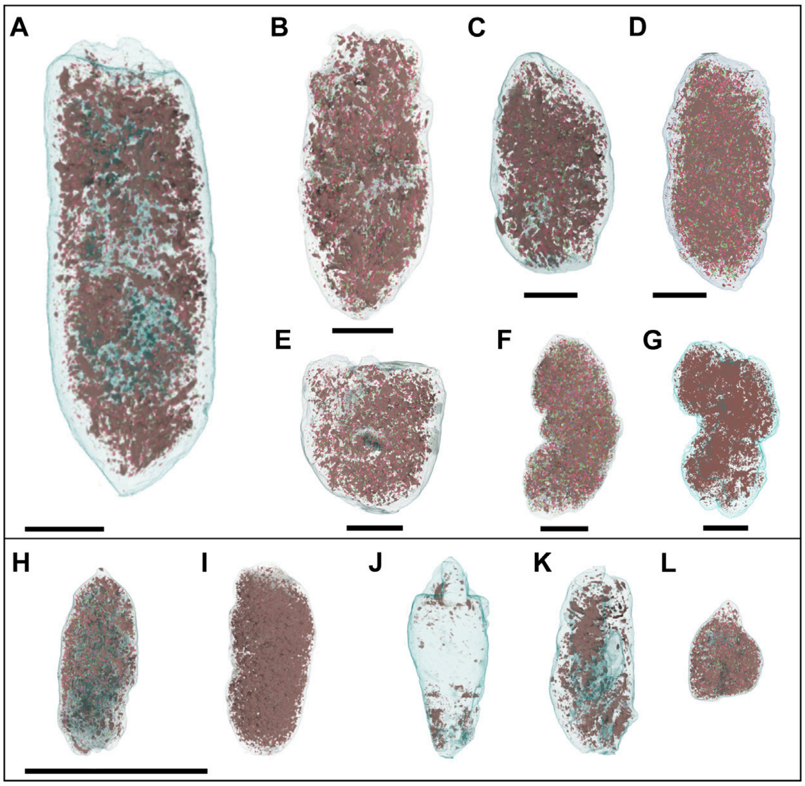

FIGURE 6
Internal view of pores of Class I Coprolites **(A–G)** and Class II **(H–L)**. Pores are colored brown while the external surface of the coprolite is represented by light blue. **(A)** RAM 18171. **(B)** RAM 17517. **(C)** RAM 17540. **(D)** RAM 17405. **(E)** RAM 17547. **(F)** RAM 17546. **(G)** RAM 17370. **(H)** RAM 17557. **(I)** RAM 31214 **(J)** RAM 31212 **(K)** RAM 31211 **(L)** RAM 31209. Scale bars represent 10 mm.

Frequently, these include traces from coprophagous invertebrates as surface scratches or burrows (Northwood, 2005; Eriksson et al., 2011). A few specimens show plausible evidence of invertebrate scratch marks, displayed as short, radiating, unbranching traces with no unified orientation (Figure 2B). Whether these markings are biogenic or abiogenic (i.e., abrasion) is difficult to decern with confidence, though it might be expected that abrasion marks are less localized and more evenly distributed compared to biogenic markings. Notably, the scale of these marks is also comparable to the surface expression of exposed hair molds (i.e., RAM 17403 and 17557), which appear as fine linear impressions on the coprolites' surface (Figure 2C).

4.2.4 Breakage

Breakage in coprolite samples is any sort of mark that shows that the sample has broken after the fossilization process. Breakages are more likely to occur close to surface inclusions within the coprolite, which tend to create weak points (Northwood, 2005). The extent of breakage within the present dataset varies from small parts of the coprolite chipped off (Figures 1H, I, K) to larger portions presumably missing (i.e., RAM 17546; Figure 1E). Some of the coprolite specimens show partially smoothed fracture surfaces, such as RAM 18171 (Figure 1A), indicative of weathering and exposure following the fracture, as compared to fresher, more angular fractures in other specimens such as RAM 17547 (Figure 1E). Breakage was more prevalent in the Class I coprolites than their smaller contemporaries.

4.2.5 Decomposition and distortion

Decomposition of the feces prior to lithification is the main cause of spherical to irregular cavities on the coprolite surfaces, which result from the accumulation of decompositional gasses (Northwood, 2005). Such features were present in both Class I and Class II coprolites and varied in size from sub-millimetric scales to spanning several millimeters. Class I coprolites have larger surface pores, for example best preserved in RAM 17546 and 17370 (Figures 1F, G respectively). The large size of these cavities rules out their representing the remnants of bacterial colonies (described in phosphatic coprolites by, for example, Hollocher et al., 2001). The surface cavities were described based on their relative abundance (Supplementary Table S1). One notable cavity was a linear feature with closely spaced repeated circular depressions (Figure 2F). Select coprolites also display a ventrally flattened surface associated with pre-lithification plasticity of the sample (e.g., RAM 17405 and 18171). This distortion provides some indication of the moisture content of the original scat when excreted and is unique to the larger Class I coprolite samples in the subset observed.

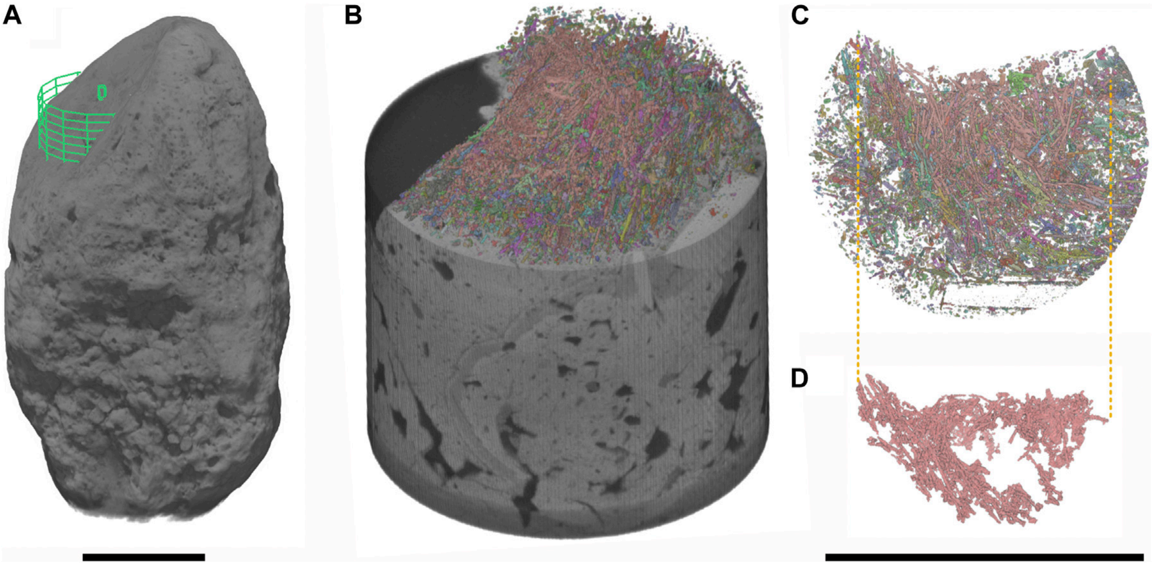

FIGURE 7
Hair molds in RAM 17540. **(A)** Site of targeted ROI for high resolution scan. **(B)** Volume render of targeted region showing a subset of the hair molds within the volume. **(C,D)** Extracted molds using multi-ROI to visualize individual isolated **(C)** and connected **(D)** components. Scale bars represent 10 mm.

4.3 Coprolite internal morphology and inclusions

4.3.1 Matrix

Petrographic analysis reveals a very-fine to medium-grained matrix of predominantly amorphous phosphate interspersed with fine unidentifiable bone fragments (Figure 3). SEM-EDS analysis of RAM 17546 confirms a calcium and phosphorous (carbonated hydroxyapatite) matrix composition, with minor traces of silicon, aluminum, and iron (Figures 4, 5). Evidence of digestive corrosion surfaces and phosphate enrichment are visible along defined boundaries within the matrix (Figure 3A), with some boundaries between different compositional textures notably more diffuse (Figure 3B). There are also conspicuous contacts between the apatite matrix and adhered sediment on the external surface of the coprolite (Figure 3E), characterized by detrital grains and finer sediment containing aluminum and potassium (Figure 5B). Petrographic and μCT analyses additionally demonstrate evidence of desiccation cracks extending inwards from the surface of the coprolite.

4.3.2 Pores

All coprolites examined reveal pores as a major structural element, with voids ranging in volume between 0.001 and 1,389.2 mm^3, and feret diameters of 0.196–50.562 mm. When distinguished from other moldic inclusions (e.g., hair molds, discussed below), no universal pore shapes could be identified, with morphologies ranging from long and thin to large and irregular in shape (Figures 3C, D, 6, 7). Light microscopy and SEM analysis of RAM 17540 reveal that the pores are frequently lined with crusts of botryoidal silica (Figures 3C, D, 5C, D). Interconnected porosity is observed but limited and few pores are in contact with the external surface; instead, most pores are isolated within the matrix (Figure 6). By volume, pores compose the second largest constituent of the coprolite on average after the matrix, comprising between 3.35% and 14.32% across both coprolite size classes (Supplementary Table S4). The number of pores per specimen varied markedly, with their distribution throughout the sample relatively even except when influenced by the position of bone inclusions within the coprolite matrix (Figures 6J, K).

4.3.3 Hair inclusions

Notable features detected using μCT are micron-scale tubules that represent the moldic remains of fossil hair within the coprolite matrix. Unlike the irregular pore spaces or other taphonomic features, these structures have a distinct and consistent morphology that does not display random branching attributed to desiccation cracks, burrows by coprophagous organisms or traces of fungal hyphae (Chin, 2007). Fossilized hair was observable via tomography in 10 of the 12 coprolites. In thin section, hair molds appear as elongated, parallel, straight-edged tubules with circular cross-sections (Figure 3F) and are typically infilled with silica (Figure 5D). Measured cross-sections reveal molds range in width from 0.015 mm to 0.092 mm (n = 60, mean=0.040). Hair molds are also discernible in tomographic slice data; for example, the targeted high-resolution scan (an ~1 cm cylindrical ROI) of specimen RAM 17540 revealed small elongate, tube-like structures, each only a few millimeters in length (Figure 7). While hair molds were distributed relatively evenly throughout the scanned volume (Figures 7B–D), their distribution throughout the entire coprolite was more variable.

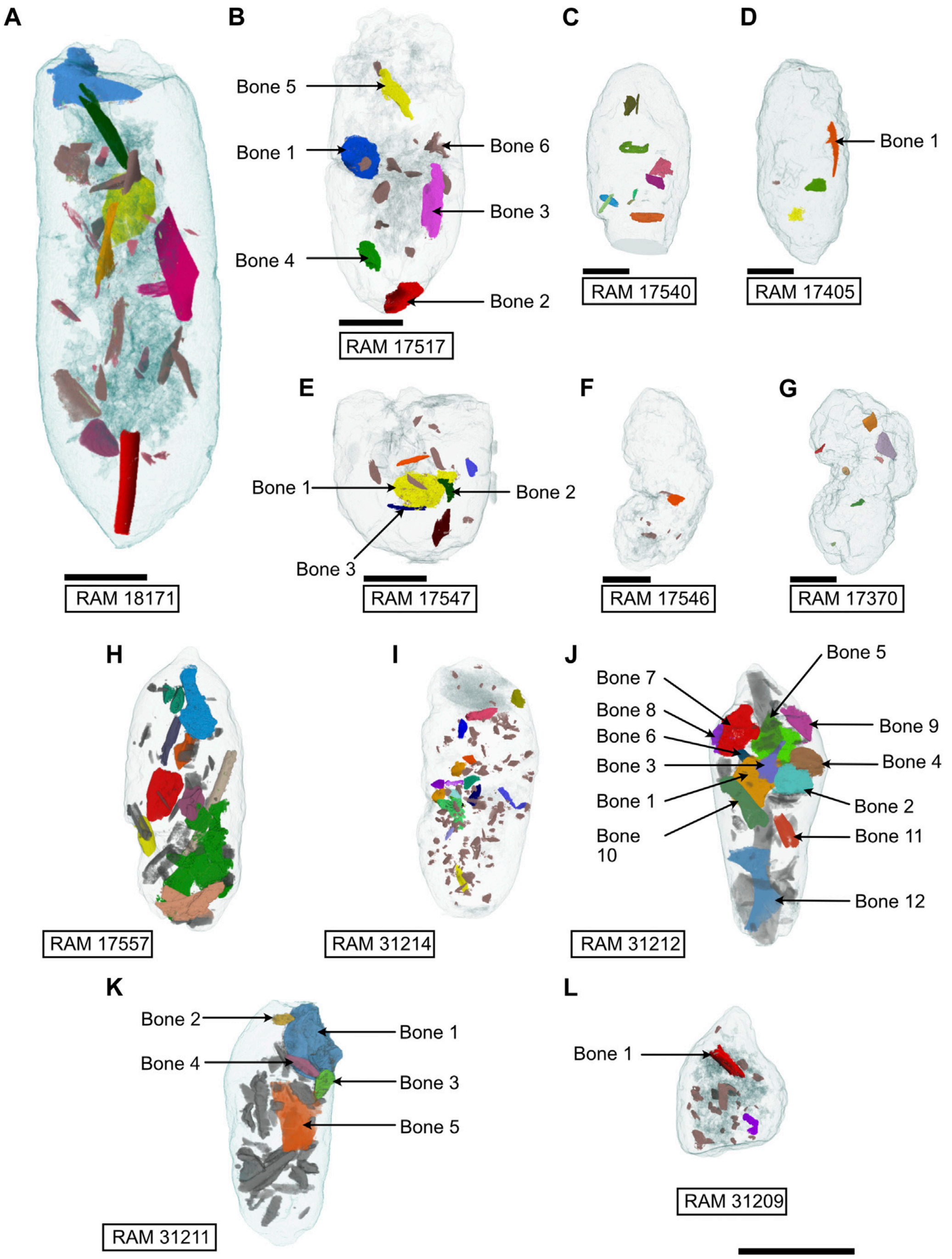

FIGURE 8
Internal view of coprolite bone inclusions divided into size Class I **(A–G)** and Class II **(H–L)**. Bones of interest labeled. Scale bars 10 mm.

4.3.4 Bone inclusions

Bone inclusions visible on the exterior of the coprolites were often dark in color relative to the surrounding matrix. The sectioned surface and corresponding thin section of RAM 17540 shows that bone inclusions varied in their quality of preservation; the better-preserved fragments displayed darker inclusions with clear external margins (Figures 3A, 4A) while poorly preserved, heavily corroded, buff-colored inclusions displayed ill-defined margins (Figure 5E). Compositionally, the bones are similar to the matrix, differing by their increased concentrations of sulfur and decreased concentrations of silicon and iron as compared to the matrix (Figures 5A, E). Virtually extracted material from µCT data shows a considerable variation in the size and degree of fragmentation of bone inclusion, with a maximum bone feret diameter of 16.56 mm for the Class I coprolites and 25.73 mm for Class II. Except for a few coprolites, principally those

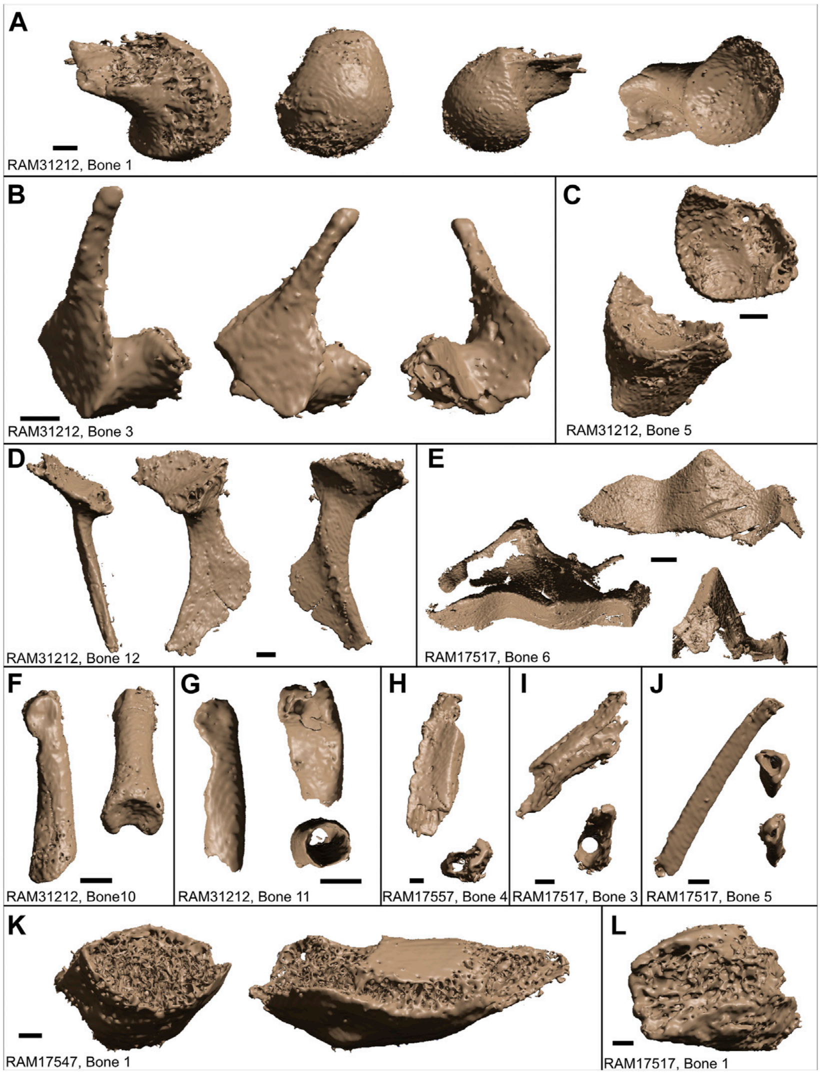

FIGURE 9
Extracted bones with identifiable features. **(A)** Bone 1 of RAM 31212 seen from four different angles. Shows the condyle of a long bone, or capitulum (e.g., femoral head). **(B)** Bone 2 of RAM 17517 seen from three angles showing the zygomatic arch. **(C)** Bone 5 of RAM 31212 seen from two angles, showing acetabulum (socket) of a hipbone. **(D)** Bone 12 of RAM 31212 seen from three different angles, showing potential elements of a pelvic girdle (ischium, or base plate and iliac blade) related to **(C)**. **(E)** Bone 6 of RAM 17517 seen from three angles. Unlikely to be mammal material; unbroken edge and the overall geometry suggest this could be a squamate opisthotic. **(F)** Bone 10 of RAM 31212 seen from two views. Bone identified as a phalange. **(G)** Bone 11 RAM 31212 of RAM 31212 seen from two views. Bone identified as a phalange. **(H,I)** Bone 4 of RAM 17557 and Bone 3 of RAM 17517 each from two views. Potentially ribs; both are flat, hollow short bones with triangular cross-section. **(J)** Bone 5 of RAM 17517 seen in two views. Rib, based on triangular cross-section. **(K,L)** Bone 1 of RAM 17547 and Bone 1 of RAM 17517 show the cancellous structures of the bones contained within the interior. Scale bars represent 1 mm.

preserving parts of long bones (inc. RAM 18171, Figure 8A; RAM 17557; Figure 8H; RAM 31212; Figure 8J), there is limited evidence of preferred bone orientation due to the overly fragmented nature of the inclusions. More typically, smaller bone fragments are visible ‘floating’ around the larger bones within the coprolite matrix.

A total of 437 bone inclusions (excluding volumes of <0.001 mm^3) were virtually extracted from the 12 coprolites examined. Due to their predominantly fragmentary nature (most <1 mm^3), the majority could not be identified to any single taxon, nor categorized anatomically. However, some bones preserved sufficient morphological detail outside of general shape to allow attribution to a particular bone type, i.e., long and short, cancellous, flat and irregular bones. Full descriptions of the most complete extracted bone material figured in Figures 9, 10 are available in the Supplementary Text S2.

4.4 Statistical analyses

The relationships between coprolite volumetric measurements and relative proportion of inclusions (i.e., matrix, pores, bones) are compared for individual coprolite samples (Figures 11A, B, respectively). The proportion of pores within the matrix was consistently greater when compared to that of bone inclusions

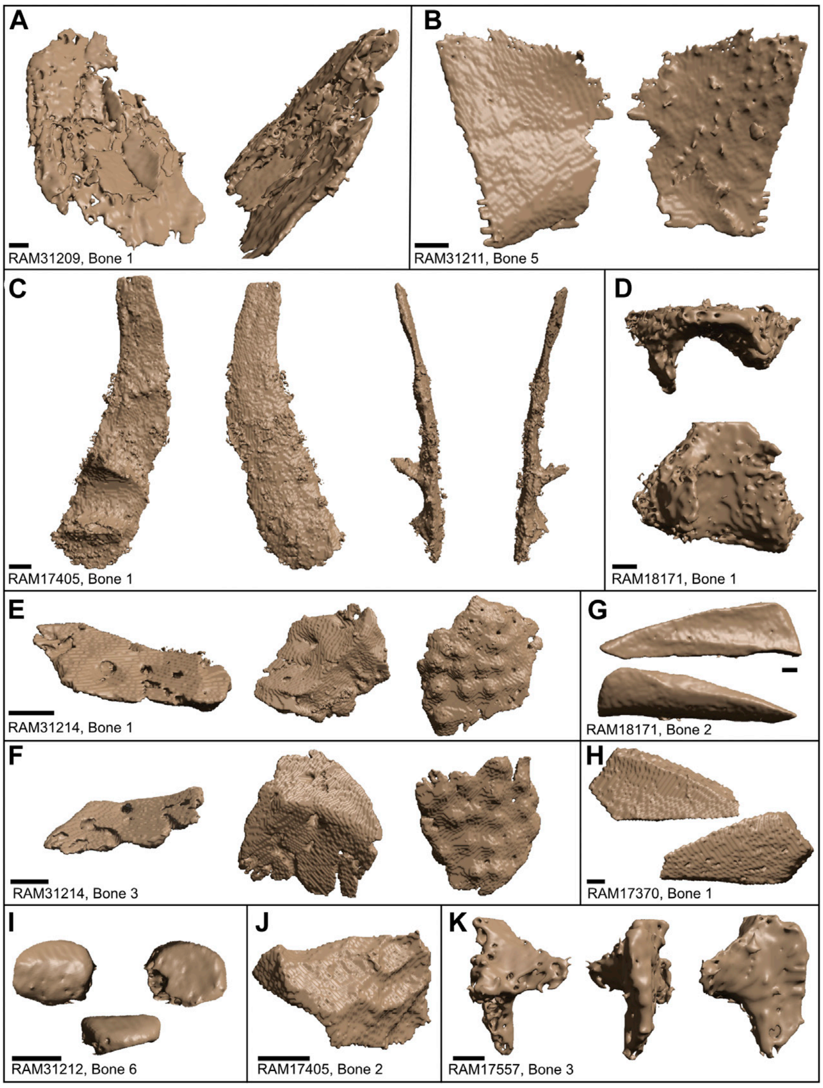

FIGURE 10
Extracted bones based on type. **(A–H)** Flat bones. **(A)** Plane and oblique view of Bone 1 in RAM 31209. **(B)**. Plane views of opposite sides to Bone 5 in RAM 31211. **(C)** Plane and side views of Bone 1 of RAM 17405; possible ilium. **(D)** Plane and side views of Bone 1 in RAM 18171; possible cranial element. **(E–F)** Oblique and plane views of opposite sides to Bone 1 and 3 in RAM 31214. **(G)** Opposing flattened sides of Bone 2 in RAM 18171; resembles fibula. **(H)** Opposing flattened sides in Bone 1 of RAM 17370. **(I–K)** Irregular bones. **(I)** Patella in anterior, lateral, and posterior views of Bone 6 of RAM 31212. **(J)** Plane view of Bone 2 of RAM 17405. **(K)** Plane and side views of Bone 3 of RAM 17557; possible lower jaw joint. Scale bars represent 1 mm.

(Figure 11B). The lowest percentage of pores in any sample was in RAM 17370, with 3.89%, and the highest percentage was 14.32% in RAM 31211. Bone inclusions, on the other hand range from 0.09% in RAM 17546% to 11.64% in RAM 31211.

All 12 coprolites (Class I, $n = 7$; Class II, $n = 5$) were included in statistical analyses to test for differences between the two classes of coprolites. The distribution of coprolite widths based on Lofgren et al.'s (2017) data is best modelled as two Gaussian distributions with unequal variance values. Component 1, the small size class, has a median width of 10.6 mm and comprises 79% of the data. Component 2, the large size class, has a median width of 18.4 mm and comprises 21% of the data. We interpret the coprolite specimens analyzed in this study to cleanly fall into one of the two size categories ($n_{small} = 5$, $n_{large} = 7$) (Supplementary Figure S1).

Coprolite length, width, mass, proportion of pore volume, and proportion of bone volume values for coprolites cannot be shown to not be normally distributed (Supplementary Table S7). The Shapiro tests results for bone volume, maximum feret diameter, mean feret diameter, and minimum feret diameter suggest that these values are not normally distributed, however, the Dip Test for Unimodality results cannot refute unimodality (Supplementary Table S7), therefore the Wilcoxon test is appropriate for these comparisons.

The Wilcoxon Rank-Sum test revealed significant differences in length ($p = 0.003$), width ($p = 0.003$), and mass ($p = 0.003$) between Class I and Class II coprolites (Figure 11C). We bootstraped 95% confidence intervals for the median proportion of pore volume between Class I (0.054 mm^3) and

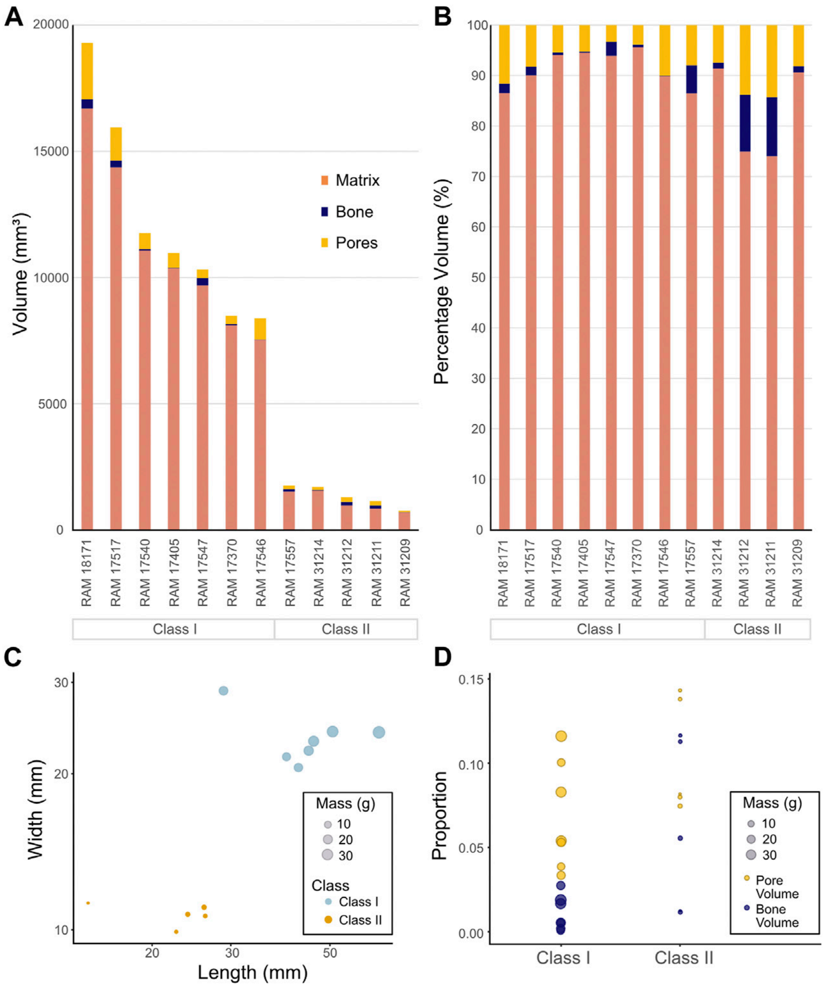

FIGURE 11
Comparison of coprolite shape in addition to volume and proportion of internal components across classes. **(A)** Volumetric analysis of all coprolites, comparing total volume of matrix, bones and pores. **(B)** Volumetric analysis of all coprolites, comparing total percentage of matrix, bones and pores. **(C)** A x-y plot of coprolite samples length vs. width. The size of the dots indicates the mass of the coprolite specimen. **(D)** The proportion of pore and bone material per coprolite specimen between the two classes. Median pore proportion in Class I is 0.054 (95% CI: 0.015, 0.155); and for Class II is 0.082 (95% CI: 0.007, 0.225). Median skeletal proportion in Class I is 0.005 (95% CI: 0.004, 0.024); and for Class II is 0.055 (95% CI: 0.044, 0.172).

Class II (0.082 mm^3) coprolites and found no significant difference. Conversely, bootstrapping for the median proportion of skeletal material between Class I and Class II suggests that there is a significant difference in the median.

Differences in median bone size between the two coprolite classes were tested with a Wilcoxon Rank-Sum test, comparing bone volume, maximum feret diameter, mean feret diameter, and minimum feret diameter (Figures 12A–D; Supplementary Table S7). In total 437 bone values were used in the analysis (Class I, n = 172; Class II, n = 265). There was no significant difference (p = 0.176) between the median bone volumes of Class I (0.1 mm^3) and Class II (0.09 mm^3). The median value of the maximum feret diameters of bones for Class I (1.58 mm) was significantly larger (p = 0.002) than Class II (1.250 mm). Similarly, there was a significant difference ($p < 0.001$) between the median value of mean feret diameters of bones of Class I (1.015 mm) and Class II (0.870 mm). The same result can be seen with the median value of minimum feret diameters of bones, with Class I (0.495 mm) significantly larger (p=0.004) than Class II (0.460 mm).

5 Discussion

5.1 Taphonomic features and internal structures

The PSMP coprolites are well-preserved, excluding extensive surface abrasion, and possess minor diagenetic alteration or secondary mineralization. The limited evidence of adverse taphonomic processes within the subsample conforms to deposition in relatively dry and stable paleoenvironmental conditions. In addition to their in-tact or complete nature, surface features of the coprolites indicate that specimens may have been exposed at the surface for a prolonged period pre-burial due to high degrees of abrasion, likely from wind erosion,

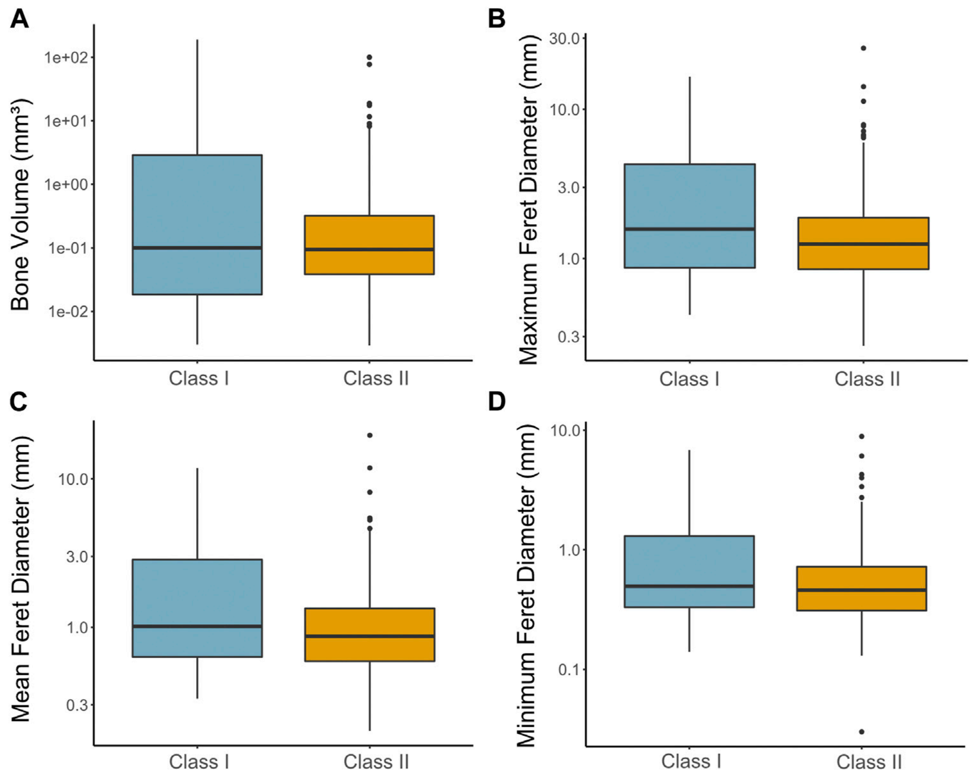

FIGURE 12
Comparison of bone volume and feret diameters across coprolite classes. **(A)** Median difference between Class I and Class II of bone volumes (Class I=0.1 m^3 and Class II=0.09 mm^3). **(B)** Median difference between Class I and Class II maximum feret diameters of bones for coprolites (Class I= 1.575 mm, Class II= 1.25 mm, p=0.001863). **(C)** Median difference between Class I and Class II mean feret diameters of bones for coprolites (Class I= 1.015 mm, Class II= 0.87 mm, p=0.0006583). **(D)** Median difference between Class I and Class II minimum feret diameters of bones for coprolites (Class I= 0.495 mm, Class II= 0.460 mm, p=0.004129).

and the presence of desiccation cracks. Distortion exhibited by flattened ventral surfaces of the coprolites also suggests these rested relatively undisturbed soon after defecation. Desiccation cracks are relatively sparse and are most conspicuous on the larger size Class I specimens. Post-burial diagenesis is similarly limited with minimal evidence of compaction and only minor influence from percolating fluids. Thin botryoidal silica crusts on the surface of internal pores indicate incursion of silica-rich fluids through the porous matrix. Silica is likely derived from adjacent ashfall lapilli tuffs and the coarse fraction (including volcanic glass, quartz, plagioclase, potassium feldspar, and granitic fragments) of the silty mudstone which characterizes the Pipestone Springs strata (Hanneman et al., 2022). Silica infill observed in thin section and SEM data is notably thin, coating pores to a thickness of between ~8 and 354 μm. The lack of homogeneous silica infill or secondary remobilization of phosphate suggests that between phases of burial and exposure, conditions were predominantly devoid of moisture.

The porous nature of the PSMP coprolites is a key morphological attribute that has been overlooked in prior studies. Pores compose the largest percentage of internal structural components after the matrix (Figures 11A, B). Moreover, this represents a minimum estimate of the true porosity, as several pores have been secondarily infilled with silica. As seen in Figure 6, the irregular pores (excluding hair molds) dramatically vary in size from 0.196 to 50.562 mm and are distributed relatively evenly throughout the matrix when not occupied by skeletal remains. Though pores are known to frequently occur within the matrix of coprolites (Horwitz and Goldberg, 1989; Herbig, 1993), their origins remain uncertain, owing to several different processes associated with their formation. One explanation for their formation is decay of some degradable materials within the feces, including smaller bone fragments, soft tissue (muscle, tendons, ligaments, etc.), or insect parts that might not have been digested, and subsequently decayed to form these pores. Given the relatively even distribution of pores throughout the matrix, this seems unlikely. An alternative explanation is that the pores were already present at defecation (including on the surface) caused by trapped gases within the feces—a product of bacterial respiration in the intestine (Herbig, 1993; Magondu, 2021). Gases produced during digestion are typical and varied (Levitt and Bond, 1970); however, reporting the preservation of these gaseous vesicles and their relative abundance within a coprolite is often neglected. As excess gas can relate to bacterial overgrowth within the gut, which may have deleterious consequences for the individual or indicate an intestinal disease (Suarez et al., 2000; Pimentel et al., 2006; Kalantar-Zadeh et al., 2019), the prevalence of such gaseous vesicles may be useful in understanding the gut biome and physiological attributes of coprolite producers. A third explanation for the pores relates to desiccation; as the sample loses moisture, smaller pores (possibly those formed by gases) are enlarged in conjunction with the reduction in overall coprolite volume. As few actualistic studies exist investigating the complete taphonomic processes (from defecation to burial) of modern feces in natural environments, much of this remains speculative (Northwood, 2005; though see Brachaniec et al., 2022).

Another constituent of the porous volumes within the coprolites are the moldic remains of keratinous material, specifically hair. Whilst targeted higher resolution scanning was only performed on one specimen (RAM 17540; Figure 7), other coprolites from this sample subset exhibit similar structures. These small tube-like pores generally fall within the shaft shape and size range of hair, with distinct circular cross-sections. Because these pores are small, isolated, and many terminate without contacting the surface of the coprolite, these tubules can readily be distinguished from desiccation cracks, insect burrows or fungal hyphae. Hair molds can also be observed on the surface of select PSMP coprolites (see RAM 17540, Figure 2C). However, not all small pores exhibit this tube-like form and hence hairs cannot account for all the small topographic depressions observed. Due to keratinous material possessing highly resistant molecules that few extant taxa are able to digest (Leprince et al., 1980), hair is relatively resistant to digestive and early lithification processes (Taru and Backwell, 2013). Though the hair eventually decayed, it was preserved long enough to form molds of the shafts within the interior of the coprolite. This pathway conforms with previous studies where hair tubules have been found as casts and impressions both on the surface and interior of coprolites, often preserving exceptional details of the cuticular surface (Crooper et al., 1997; Taru and Backwell, 2013; Bajdek et al., 2016). Similar to the irregular pores, these molds display a siliceous coating caused by secondary infilling during diagenesis.

5.2 Insights into feeding behavior

Qualitative and quantitative analyses of the two coprolite size classes observed reveal notable differences with respect to the morphology of the inclusions, which may inform about feeding habits and physiological differences of their respective producers. Results of our analyses reveal a discernable statistical difference in the relative proportions of bone inclusions to total coprolite volume between Classes I and II. Notably, the proportion of bone volume was greater in the smaller Class II coprolites by comparison to the larger Class I coprolites (Figure 12A). However, there was no significant difference in the extracted bone volumes between the two classes indicating that, despite the relative size of the smaller Class II coprolites, the bone constituent was comparable to that observed in larger Class I coprolites.

In the case of Class I coprolites, bones tended to be larger overall with respect to their feret diameters (Figures 12B–D). Bone inclusions within the Class I coprolites also showed more degradation and evidence of intense fragmentation from mastication, such that few bones could be reliably identified. This implies that the Class I producers were capable of consuming larger prey compared to the Class II producers. Bones extracted from the Class I coprolites, including Bone 1 of RAM 17547 (Figure 9K) and Bone 1 of RAM 17517 (Figure 9L), lacked an identifiable shape but revealed internal features such as cancellous tissue associated with larger bones (e.g., pelvic bones, vertebrae, etc.). The ambiguous shapes, incomplete condition of the bones, and preponderance of homogeneous phosphatic matrix contained within Class I coprolites, aligns with specific feeding habits and digestive processes. Principally, the evidence presented herein supports a durophagous carnivorous producer with a bone crushing habit, which is comparable to previous findings in relation to late Miocene carnivoran coprolites from California (Wang et al., 2018). The producers of these latter coprolites are inferred to have been borophagine canids that filled a unique ecological niche in North America, comparable to extant hyenas, until their disappearance approximately 2 million years ago (Lofgren et al., 2017; for further discussion see section 2.4.2 below). Like the California specimens, the PSMP coprolites also exhibit a powdered homogenous matrix of bone residues (Figures 3A, B) indicative of a producer with a highly acidic gastrointestinal system (Wang et al., 2018). Examples of corrosion are visible in Bone 1 RAM 17547 (Figure 9K) where internal thin trabecular material is revealed. Bone dissolution could also account for the diffuse boundaries exhibited by several bone inclusions during the segmentation process.

Class II coprolites overall have a statistically larger proportion of bones compared to total coprolite volume than Class I, though there is notable variation within the sampled dataset (Figure 11D). Such variation is also evident in the condition of extracted inclusions. Most identifiable bones in the PSMP material are associated with specimens in Class II, though this is slightly skewed as most of these bones were also recovered from a single specimen, RAM 31212 (Figure 8J). This coprolite has the second largest amount of bone inclusions of those examined here (Supplementary Table S4, 11.28%), while RAM 31211 has the highest overall proportion (Supplementary Table S4, 11.64%). Three of the Class II coprolites (RAM 31211, 31212, and 17557) are more densely packed with larger bone inclusions suggesting that the producers were capable of consuming the bones whole, with limited mastication of prey items compared to the producers of the Class I coprolites. In this case, producers of these Class II coprolites were able to extract nutrients with minimal bone-crushing required to consume the prey item. Most likely, this is attributed to the smaller size of the prey item itself for which durophagous mastication was not necessary (Pokines and Tersigni-Tarrant, 2012). On the other hand, the Class II coprolites also preserve smaller bones compared to Class I coprolites, as seen by the significantly smaller median values in feret diameters in Class II compared to Class I coprolites (Figures 12B–D). These smaller bones show evidence of intense fragmentation (RAM 31209, Figure 8I and RAM 31214, Figure 8L) which lends support to the capacity for bone-crushing when required for larger prey items, or once the higher-return nutrient-rich organs had been eaten (Pokines and Tersigni-Tarrant, 2012). More direct evidence for a bone-crushing habit is displayed in Bone 1 of RAM 31209 (Figure 10A) which features a clear indent on the flat surface of the bone where the bone has been partially crushed, as well as tooth marks in Bone 6 of RAM 17517 (Figure 9E). There is also some tentative evidence to suggest gnawing or bone cracking in Bone 12 of RAM 31212 (Figure 9D) exhibited by the somewhat rounded edges on the proximal base plate. It is worth noting that the degree to which stomach acids have caused shrinkage or subsequent breakage of the ingested bone material in the Class II coprolites is difficult to discern and could potentially further account for some reduction in bone fragment size (Fernández-Jalvo et al., 2014). However, the clear boundaries visible between the matrix and the bone material via the CT tomogram

TABLE 2 Summary of the main carnivorous species found in the PSMP. Data derived from LaGarry (2004)[a]; Lofgren et al. (2017)[b]; Christison et al. (2022)[c].

Taxon	Family	Body Mass (kg)	Mean prey mass (kg)
Hyaenodon microdon	Hyaenodontidae	1.6[b]/27.2[c]	49.1[b]
Hyaenodon crucians	Hyaenodontidae	~17[a]/3.3[b]	NA
Hesperocyon gregarius	Canidae	3[a]/~2.9[b]/3.5[c]	6.4[b]
Mustelavus priscus	Mustelidae	1.9[b]	NA
Brachyrhynchocyon dodgei	Amphicyonidae	13.9[c]	25.1[b]
Daphoenictis tedfordi	Amphicyonidae	NA	NA
Paristis montanus	Ursidae	2.5[b]	NA
Palaeogale sectoria	Palaeogalidae	1.7[b]	NA

slices might attest to the relative resistance of these bone fragments to acid dissolution.

In a previous study employing comparable μCT methods, evidence of an osteophagous diet was inferred from two carnivoran coprolites of discrete sizes from the late Miocene, Spain (Abella et al., 2022). Evidence of osteophagy was based on abundant skeletal inclusions including fragments that appeared to belong to larger bones while others display depressions resembling partial tooth marks. Similar to the Class I PSMP coprolites, the larger specimen of the Spanish coprolites (specimen BAT-3′9.178) preserves irregular bone fragments not identifiable to a specific anatomical bone but does show evidence of digestive corrosion (Abella et al., 2022). The smaller coprolite (BAT-3′10.153), which is comparable in length to the PSMP Class I coprolites exhibits more complete skeletal elements and has a greater proportion of bone inclusions relative to the larger coprolite at the same locality (Abella et al., 2022; Figures 4, 6). Several medium-sized carnivores were suggested as the producer of the smaller coprolite though the most probable was *Protictitherium crassum*, a member of Hyaenidae.

These findings conform with the borophagine canids interpretation of Lofgren et al. (2017), to the extent that 1) some of the predators consumed whole bones; 2) there was a degree of bone fracturing that occurred, especially in the smaller coprolites; and 3) evidence of digestive corrosion was present.

5.3 Identity of the producer

In previous work, Lofgren et al. (2017) hypothesize that the relationship between the diameter of a producer's feces and its body mass, in conjunction with the relative abundance of the respective carnivore species in the PSMP could be applied to determine the likelihood of the producer itself. Several different mammalian predators have been recovered from the PSMP site, belonging to eight different species (Lofgren et al., 2017) including *Hyaenodon microdon* (Mellett, 1977), *Hyaenodon crucians* (Leidy, 1853), *H. gregarius* (Cope, 1873), *Mustelavus priscus* (Clark, 1936, in Scott and Jepsen, 1936), *B. dodgei* (Scott, 1898), *Parictis montanus* (Clark and Guensburg, 1972), *Daphoenictis tedfordi* (Hunt, 1974), and *Palaeogale sectoria* (Gervais, 1848). After estimating the overall body mass of the predators and their mean prey mass (see Table 2), Lofgren et al. (2017) deduced that the range in diameters of larger coprolites may have represented multiple species, concluding that *B. dodgei* was most likely due to the abundance of dentigerous elements in the deposit (77% of the larger species). Similarly, the smaller coprolites could have been produced by *P. sectoria, P. montanus, Hyaenodon crucians, H. microdon,* and *H. gregarius* (Lofgren et al., 2017). Although the body mass estimates are congruent with *Hy. crucians* as a likely producer, the bone alteration observed in the smaller coprolites is more consistent with extant canids and hence *Hes. gregarius* was inferred as the main producer of the smaller coprolites (Lofgren et al., 2017).

While the coprolite interior volumes and bone inclusions observed herein did not reveal any unambiguous details as to which taxon might have excreted the coprolites, they did show that at least the Class I producers had aggressive gastrointestinal environments that could digest bone material and cartilage. This is presumably comparable to the bone-crushing habits of modern spotted hyaenas (*Crocuta*), which are also known to consume (and occasionally regurgitate) indigestible materials such as hair (Kruuk, 1972; Di Silvestre et al., 2000). However, as noted by Wang et al. (2018) in their assessment of the California carnivoran coprolites, there is a paucity of literature investigating gastric pH across broader Carnivora, and hence it is highly speculative to make further inferences as to the identity of the producer based on broad assumptions of a bone-dissolving gastrointestinal system alone.

5.4 Evaluation of μCT for analysis of PSMP coprolites

The value of using μCT as a non-destructive method in extracting information on the internal inclusions of coprolite samples has been well-demonstrated (Qvarnström et al., 2017; 2019). However, specific advantages, limitations, and implicit biases encountered herein are worthy of discussion. We note that while X-ray microscopy can certainly add value to the study of coprolites, results depend on the resolution of the CT scan and the nature of the specimen. In some cases, using μCT alone may not be sufficient to fully describe the internal constituents of bromalites for a particular investigation, and it is recommended to use it in conjunction with other techniques for a more comprehensive analysis. The difficulty of identifying bone inclusions within the PSMP coprolites using μCT to a level beyond generic bone type was not a limitation of μCT itself, but rather a consequence of how much the bones were masticated and digested. Similar results were documented by Abella et al. (2022), wherein they solely used μCT, but found many of the bones were not identifiable to a certain anatomical bone or taxon, and instead the authors relied on describing the general shape and features. Studies comparing the results of mechanical extraction and μCT analysis have encountered similar difficulties. For example, investigations of neolithic midden deposits from Swifterbant, Netherlands, used paired μCT and physical extraction methods to examine phytoliths and bone fragments from finely layered and coprolite-hosting deposits (Huisman et al., 2014). Results showed that many bone features were visible using both methods, though comparably more recognizable bone elements were identified in the sieved material (n = 32) compared to μCT (n = 7 with confidence, 5 unable to be attributed to species level) (Huisman et al., 2014). The benefit of using μCT in the case of the Swifterbant material, was the ability to provide microstratigraphic context as well as recognize articulated remains and material too small to appear in the sieved fraction (Huisman et al., 2014). A noteworthy finding comparable to observations made in the material herein was that identification of the skeletal components was not dependent on how the bones were extracted, but rather on how completely the bones were preserved (Huisman et al., 2014). Bones with few distinguishable features as a consequence of mastication and digestive processes are going to appear almost identical whether observed virtually or as physically extracted material. In the case of the present study, surface renders of select bones were blurred by ill-defined edges and significant degradation due to the digestive processes which reduced the phase contrast between bone inclusions and the surrounding phosphatic matrix. This further emphasizes that potential limitations on μCT are associated with the degree of preservation of the inclusions and not solely the imaging technique.

The primary advantage of using μCT in this study was the ability to reveal volumes, including pores and moldic remains of fossil hair, that would not otherwise be attainable via traditional disaggregation methods. These structures were readily visible in tomographic slices, in both standard and targeted higher resolution scans, and could be extracted to display their morphology as well as their distribution in 3D space (Figure 7). Because hair tubules represent external molds, mechanical or chemical extraction of inclusions would impede the detection of such features at all. Even thin sectioning only provides a very shallow 3D view of these fossil hair follicles and may preclude unambiguous identification of the elongate molds from other potential explanations (i.e., burrows, desiccation cracks). Hair imprints in phosphate aggregates from a Palaeolithic cave site in Western Slovenia have similarly been revealed by μCT methods (Turk et al., 2015). Though the PSMP hair molds could not be attributed to any specific taxon, their prevalence throughout the coprolite may provide insight into the higher taxonomic affiliation to prey items (i.e., mammalian), or alternatively could allude to the affinity of the consumer (e.g., if they ingested their own hair while grooming). Based on analysis of modern vertebrate carnivore scat, the digestibility of hair varies between predator and prey item, however, under most circumstances, it is significantly less digestible compared to bone (Ackerman et al., 1984; Baker et al., 1993; Gamberg and Atkinson, 2016). The presence of hair in feces also can persist for several days after initial consumption depending on the rate of passage through the intestine (Helm, 1984; Kelly and Garton, 1997; Pires et al., 2011). Consequently, we hypothesize that coprolites have a higher likelihood of preserving hair remains when compared to body fossils, and introduce taphonomic bias toward bromalites as a source of information on hair structures and morphology. This supports previous studies that demonstrate the potential of bromalites to facilitate exceptional preservation of soft tissues (Chin et al., 2003; Qvarnstrom et al., 2017; Gordon et al., 2020).

Internal porosity and associated characteristics of the pores were overlooked in previous examination of this material (Lofgren et al., 2017) and are easily removed via consumptive sampling methods. Though it is difficult to ascertain whether such original features were considered or overlooked in other coprolite studies (Wang et al., 2018; Romaniuk et al., 2020; Abella et al., 2022), this raises concern for a potential reporting bias in the visualization of segmented volume renders in isolation to tomographic slice data. Ideally, pairing cross-sectional tomographic data directly with volumetric reconstructions (e.g., Turk et al., 2015; figures 4, 5; Shillito et al., 2020; figure 3) promotes transparency in documenting coprolite internal composition. Moreover, tomographic slices should be made available upon publication (whether via the journal or repository institution) to facilitate reproducibility of the analysis. Porosity of coprolites is likely an important primary and taphonomic feature. The presence of pores may have broader implications for gut function and health, hence understanding pore morphology, abundance, and distribution is relevant to revealing both palaeobiological data of the producer and the diagenetic history of the overall coprolite specimen.

6 Conclusion

X-ray tomographic microscopy of twelve coprolites examined herein provides key insights into the diet, feeding behavior, and physiology of the producers from the Miocene Pipestone spring Main Pocket, Montana. The application of μCT was a viable alternative to consumptive sampling and was able to differentiate internal inclusions and volumes, including bones and pores, from the overall matrix. Across the two coprolite size classes, several different bone types of varying quality are preserved. Although μCT methods were able to extract the skeletal inclusions in detail, the condition of the bones as a result of the overall digestive process precluded taxonomic identification and hence limited descriptions to general bone type. A primary benefit to employing μCT methods is the ability to extract details of internal structures that would be unattainable via consumptive sampling methods. Foremost is the presence of pores and tubular hair molds within the coprolite matrix, which we describe in coprolites of this locality for the first time.

The size, shape, and abundance of bone inclusions in conjunction with hair impressions demonstrate these predators consumed vertebrate prey. Depending on the size of the prey, the respective producers of the coprolite size classes may have adapted different feeding habits to maximize the return on nutrients. The larger coprolites contained comparatively fewer complete bones but were highly fragmented suggesting bone-crushing habits. Alternatively, the variability in the smaller coprolites containing both complete bone morphologies in greater proportions as well as fragmented bone implies both whole consumption and bone-crushing behavior.

Overall, application of μCT methodologies will allow for further standardization of coprolite studies. With the growth of virtual paleontology, an opportunity has presented itself for the expansion of coprolite research and the integration of novel qualitative and quantitative analyses. Where coprolite samples were once damaged or destroyed via traditional methods, μCT provides a valuable means to preemptively survey specimens to target regions of interest that maximize data return whilst minimizing consumptive sampling for thin sectioning, SEM and elemental analyses. Within the sample subset described here, certain coprolites possess minimal inclusions and consequently would offer a limited view of the internal heterogeneity present within the sample population. Moreover, it is desirable that prior to destructive sampling, a virtual record of the coprolite is retained for reference. To this end, μCT may be instrumental in the long-term preservation and curation of coprolite samples, and simultaneously promote sharing 3D datasets via online repositories. Ultimately, this facilitates opportunities to share qualitative and quantitative μCT datasets via digital repositories. Such methodologies enable greater standardization of methods and allow for more comparative analyses to expand the field of coprolite research.

Data availability statement

The datasets presented in this study can be found in online repositories. The names of the repository/repositories, accession numbers and DOIs can be found in the article/Supplementary Material.

Author contributions

SJ: conceptualization, methodology, supervision, writing—review and editing, investigation, resources, visualization, project administration, data curation, funding acquisition. J-LW: writing—original draft, software, investigation, visualization. JH: formal analysis, visualization, editing. TS: visualization, funding acquisition. JS: visualization, resources, funding acquisition. All authors contributed toward edits to the final submitted manuscript.

Funding

Research presented herein was supported by the University of Missouri Research Council Award (URC-20-046), which provided funds for CT scanning and SEM imaging. SJ and J-LW were supported by NSF Sedimentary Geology and Paleobiology Award (EAR-SGP) 1917031. J-LW was also supported by the Department of Geological Sciences, University of Missouri. JS and the X-ray Microanalysis Core were supported by NSF Instrumentation and Facilities (EAR/IF) 1636643. JH and JS were supported by NSF EAR CAREER 1650745 and 1652351 respectively.

Acknowledgments

We appreciate the valuable comments made by two reviewers which greatly improved the overall quality of the manuscript. We would like to thank Dr. Andrew Farke, Dr. Gabriel Santos, and Bailey Jorgensen from the Raymond M. Alf Museum of Paleontology at the Webb School (Claremont, California, United States) for gathering and loaning the specimens that were used in this study. We appreciate the assistance of Drs Lee Lyman and Casey Holliday for helpful discussions on the identification of select extracted bones from the CT data.

Conflict of interest

The authors declare that the research was conducted in the absence of any commercial or financial relationships that could be construed as a potential conflict of interest.

Publisher's note

Supplementary material

The Supplementary Material for this article can be found online at: https://www.frontiersin.org/articles/10.3389/feart.2023.1130107/full#supplementary-material

References

Abella, J., Martín-Perea, D. M., Valenciano, A., Hontecillas, D., Montoya, P., and Morales, J. (2022). Coprolites in natural traps: Direct evidence of bone-eating carnivorans from the late Miocene batallones-3 site, madrid, Spain. *Lethaia* 54, let.12438–774. doi:10.1111/let.12438

Ackerman, B. B., Lindzey, F. G., and Hemker, T. P. (1984). Cougar food habits in southern Utah. *J. Wildl. Manage.* 48, 147–155. doi:10.2307/3808462

Arganda-Carreras, I., Kaynig, V., Rueden, C., Eliceiri, K. W., Schindelin, J., Cardona, A., et al. (2017). Trainable Weka segmentation: A machine learning tool for microscopy pixel classification. *Bioinformatics* 33, 2424–2426. doi:10.1093/bioinformatics/btx180

Arnold, J. (2021). "ggthemes: Extra themes, scales and geoms for 'ggplot2'. R package,". version 4.2.4.

Bajdek, P., Qvarnström, M., Owocki, K., Sulej, T., Sennikov, A. G., Golubev, V. K., et al. (2016). Microbiota and food residues including possible evidence of pre-mammalian hair in Upper Permian coprolites from Russia. *Lethaia* 49 (4), 455–477. doi:10.1111/let.12156

Baker, L. A., Warren, R. J., and James, W. E. (1993). Bobcat prey digestibility and representation in scats. *Proc. Annu. Conf. Southeast. Assoc. Fish Wildl. Agencies* 47, 71–79.

Brachaniec, T., Środek, D., Surmik, D., Niedźwiedzki, R., Georgalis, G. L., Płachno, B. J., et al. (2022). Comparative actualistic study hints at origins of alleged Miocene coprolites of Poland. *PeerJ* 10, e13652. doi:10.7717/peerj.13652

Bravo-Cuevas, V. M., Morales-García, N. M., Barrón-Ortiz, C. R., Theodor, J. M., and Cabral-Perdomo, M. A. (2017). Canid coprolites from the late pleistocene of hidalgo, central Mexico: Importance for the carnivore record of North America. *Ichnos Int. J. Plant Animal Traces* 24, 239–249. doi:10.1080/10420940.2016.1270209

Bryant, V. M. J. (1970). "Late full-glacial and postglacial pollen analysis of Texas sediments," in *Unpublished PhD thesis* (Austin: University of Texas).

Canty, A., and Ripley, B. (2021). "boot: Bootstrap R (S-plus) functions,". R package version 1.

Chin, K., Eberth, D. A., Schweitzer, M. H., Rando, T. A., Sloboda, W. J., and Horner, J. R. (2003). Remarkable preservation of undigested muscle tissue within a late cretaceous tyrannosaurid coprolite from Alberta, Canada. *Palaios* 18, 286–294. doi:10.1669/0883-1351(2003)018<0286

Chin, K. (2007). The paleobiological implications of herbivorous dinosaur corprolites from the Upper Cretaceous two medicine formation of Montana: Why eat wood? *Palaios* 22, 554–566. doi:10.2110/palo.2006.p06-087r

Christison, B. E., Gaidies, F., Pineda-Munoz, S., Evans, A. R., Gilbert, M. A., and Fraser, D. (2022). Dietary niches of creodonts and carnivorans of the late Eocene cypress hills formation. *J. Mammal.* 103 (1), 2–17. doi:10.1093/jmammal/gyab123

Clark, J. (1936). Diagnosis of *metacodon* and description of *M. magnus*. Scott, W. B. and G. L. Jepsen *The mammalian fauna of the white river oligocene: Part 1. Insectivora and Carnivora* (Pennsylvania: Transactions of the American Philosophical Society).

Clark, J., and Guensburg, T. E. (1972). Arctoid genetic characters as related to the genus. *Parictis Fieldiana Geol.* 26, 1–76.

Cope, E. D. (1873). Third notice Of extinct vertebrata from the tertiary of the plains. *Paleontological Bulletin* 16, 1–8.

Davison, A. C., and Hinkley, D. V. (1997). *Bootstrap methods and their applications*. Cambridge: Cambridge University Press.

Di Silvestre, I., Novelli, O., and Bogliani, G. (2000). Feeding habits of the spotted hyaena in the niokolo koba national park, Senegal. *Afr. J. Ecol.* 38 (2), 102–107. doi:10.1046/j.1365-2028.2000.00220.x

Eriksson, M. E., Lindgren, J., Chin, K., and Månsby, U. (2011). Coprolite morphotypes from the upper cretaceous of Sweden: Novel views on an ancient ecosystem and implications for coprolite taphonomy. *Lethaia* 44, 455–468. doi:10.1111/j.1502-3931.2010.00257.x

Fernández-Jalvo, Y., Andrews, P., Sevilla, P., and Requejo, V. (2014). Digestion versus abrasion features in rodent bones. *Lethaia* 47 (3), 323–336. doi:10.1111/let.12061

Fry, G. F. (1970). "Preliminary analysis of the hogup cave coprolites," in *Hogup cave ed. Aikens* (Salt Lake City: University of Utah Press, University of Utah Anthropological Papers).

Gamberg, M., and Atkinson, J. L. (2016). Prey hair and bone recovery in ermine scats. *J. Wildl. Manage.* 52, 657–660. doi:10.2307/3800926

Gervais, P. M. P. (1848). Zoologie et paléontologie françaises (animaux vertébrés): ou nouvelles recherches sur les animaux vivants et fossiles de la France. *Libraire de la Société de Géographie, Paris*, 271. doi:10.5962/bhl.title.39473

Gordon, C. M., Roach, B. T., Parker, W. G., and Briggs, D. E. G. (2020). Distinguishing regurgitalites and coprolites: A case study using a triassic bromalite with soft tissue of the pseudosuchian archosaur revueltosaurus. *Palaios* 35, 111–121. doi:10.2110/palo.2019.099

Hanneman, D. L., Lofgren, D., Hasiotis, S. T., and Mcintosh, W. C. (2022). Late Eocene (Priabonian) chronostratigraphy, depositional environment, and paleosol-trace fossil associations, Pipestone Springs, southwest Montana. *Acta Palaeontol. Pol.* 67 (1), 5–20. doi:10.4202/app.00901.2021

Helm, R. C. (1984). Rate of digestion in three species of pinnipeds. *Can. J. Zool.* 62, 1751–1756. doi:10.1139/z84-258

Herbig, H. G. (1993). First upper devonian crustacean coprolites: *Favreina prima* n. sp. from northern Morocco. *J. Paleontol.* 67 (1), 98–103. doi:10.1017/s002233600002120x

Hollocher, T. C., Chin, K., Hollocher, K. T., and Kruge, M. A. (2001). Bacterial residues in coprolite of herbivorous dinosaurs: role of bacteria in mineralization of feces. *Palaios* 16, 547–565. doi:10.1669/0883-1351(2001)016<0547:BRICOH>2.0.CO;2

Horwitz, L. K., and Goldberg, P. (1989). A study of Pleistocene and Holocene hyaena coprolites. *J. Archaeol. Sci.* 16, 71–94. doi:10.1016/0305-4403(89)90057-5

Huisman, D. J., Ngan-Tillard, D., Tensen, M. A., Laarman, F. J., and Raemaekers, D. C. M. (2014). A question of scales: studying Neolithic subsistence using micro CT scanning of midden deposits. *Journal of Archaeological Science*. doi:10.1016/j.jas.2014.05.006

Hunt, A. P., Lucas, S. G., Milàn, J., and Spielmann, J. A. (2012). Vertebrate coprolite studies: Status and prospectus. *NMMNH&S* 57, 5–24.

Hunt, R. M. (1974). *Daphoenictis*, a cat-like carnivore (mammalia, amphicyonidae) from the oligocene of North America. *J. Paleontology* 48 (5), 1030–1047.

Jouy-Avantin, F., Debenath, A., Moigne, A. M., and Moné, H. (2003). A standardized method for the description and the study of coprolites. *J. Archaeol. Sci.* 30 (3), 367–372. doi:10.1006/jasc.2002.0848

Kalantar-Zadeh, K., Berean, K. J., Burgell, R. E., Muir, J. G., and Gibson, P. R. (2019). Intestinal gases: Influence on gut disorders and the role of dietary manipulations. *Nat. Rev. Gastroenterology Hepatology* 16, 733–747. doi:10.1038/s41575-019-0193-z

Kelly, B. T., and Garton, E. O. (1997). Effects of prey size, meal size, meal composition, and daily frequency of feeding on the recovery of rodent remains from carnivore scats. *Can. J. Zool.* 75, 1811–1817. doi:10.1139/z97-810

Kruuk, H. (1972). *The spotted hyena: A study of predation and social behavior*. Chicago: University of Chicago Press.

Kuenzi, W. D., and Fields, R. W. (1971). Tertiary stratigraphy, structure, and geologic history, Jefferson Basin, Montana. *Geol. Soc. Am. Bull.* 82, 3373–3394. doi:10.1130/0016-7606(1971)82[3373:TSSAGH]2.0

LaGarry, H. E. (2004). "Taphonomic evidence of bone processing from the Oligocene of northwestern Nebraska," in *School of natural Resources, institute of agriculture and natural Resources* (United States: University of Nebraska-Lincoln).

Landini, G. (2006). Background illumination correction. https://blog.bham.ac.uk/intellimic/background-illumination-correction (Accessed March 21, 2021).

Leidy, J. (1853). Remarks on a collection of fossil Mammalia from Nebraska. *Proc. Acad. Nat. Sci. Phila.* 6, 392–394.

Leprince, P., Dandrifosse, G., Goffinet, G., and Schoffeniels, E. (1980). How are feathers digested by raptors? *Biochem. Syst. Ecol.* 8, 211–219. doi:10.1016/0305-1978(80)90014-9

Levitt, M. D., and Bond, J. H. (1970). Volume, composition, and source of intestinal gas. *Gastroenterology* 59, 921–929. doi:10.1016/s0016-5085(19)33654-6

Lofgren, D. L., Shen, C. Y., Buday, N. N., Ylagan, C. A., Lofgren, K. K., Lai, R., et al. (2017). Coprolites and mammalian carnivores from Pipestone Springs, Montana, and their paleoecological significance. *Ann. Carnegie Mus.* 84 (4), 265–285. doi:10.2992/007.084.0402

Maechler, M. (2021). "diptest: Hartigan's dip test statistic for unimodality - corrected,". R package version 0.76-0.

Magondu, B. W. (2021). "Fracture mechanics of pelleted feces within mammals," in *Undergraduate research option thesis* (Georgia: Georgia Institute of Technology).

Mellett, J. S. (1977). Paleobiology of North American Hyaenodon (Mammalia, Creodonta). *Paleobiology of North American Hyaenodon (Mammalia, Creodonta)* 1, 1–134.

Meshmixer, A. (1995). *Autodesk, inc.* USA: San Rafal.

Munsell Color (Firm) (2010). *Munsell soil color charts: With genuine Munsell color chips*. Grand Rapids, MI: Munsell Color.

Myhrvold, N. P. (2012). A call to search for fossilised gastric pellets. *Hist. Biol.* 24, 505–517. doi:10.1080/08912963.2011.631703

Northwood, C. (2005). Early Triassic coprolites from Australia and their palaeobiological significance. *Palaeontology* 48 (1), 49–68. doi:10.1111/j.1475-4983.2004.00432.x

Orr, J. B. (1958). "The tertiary of Western Montana," in Society of vertebrate paleontology, 8th annual field conference guidebook , 25–33.

ORS: Object Research Systems (2020). *Dragonfly software v. 2020.2 Build 941–v. 2022.2*. Montréal, Canada: ORS: Object Research Systems, Inc. Available at: http://www.theobjects.com/dragonfly.

Pires, M. M., Widmer, C. E., Silva, C., and Setz, E. Z. F. (2011). Differential detectability of rodents and birds in scats of ocelots, *Leopardus pardalis* (Mammalia: Felidae). *Zoologia* 28, 280–283. doi:10.1590/S1984-46702011000200019

Pokines, J. T., and Tersigni-Tarrant, M. A. (2012). "Forensic anthropology: An introduction," in *Forensic anthropology: An introduction*. Editors M. A. Tersigni-Tarrant and N. R. Shirley (Boca Raton (FL): CRC Press).

Prothero, D. R. (1984). Magnetostratigraphy of the early oligocene Pipestone Springs locality, Jefferson county, Montana. *Contributions Geol. Univ. Wyo.* 23 (1), 33–36.

Qvarnström, M., Niedźwiedzki, G., Tafforeau, P., Žigaite, Ž., and Ahlberg, P. E. (2017). Synchrotron phase-contrast microtomography of coprolites generates novel palaeobiological data. *Sci. Rep.* 7, 2723. doi:10.1038/s41598-017-02893-9

Qvarnström, M., Wernström, J. V., Piechowski, R., Tałanda, M., Ahlberg, P. E., and Niedźwiedzki, G. (2019). Beetle-bearing coprolites possibly reveal the diet of a Late Triassic dinosauriform. *R. Soc. Open Sci.* 6, 181042. doi:10.1098/rsos.181042

Pimentel, M., Lin, L. N., Enayati, P., Van Den Burg, B., Lee, H. R., Chen, J. H., et al. (2006). Methane, a gas produced by enteric bacteria, slows intestinal transit and augments small intestinal contractile activity. *American Journal of Physiology-Gastrointestinal and Liver Physiology* 290, 1089–1095. doi:10.1152/ajpgi.00574.2004

R Core Team (2017). *R: A language and environment for statistical computing*. Vienna, Austria: R Foundation for Statistical Computing.

Romaniuk, A. A., Panciroli, E., Buckley, M., Pal Chowdhury, M., Willars, C., Herman, J. S., et al. (2020). Combined visual and biochemical analyses confirm depositor and diet for Neolithic coprolites from Skara Brae. *Archaeol. Anthropol. Sci.* 12, 274. doi:10.1007/s12520-020-01225-9

Schindelin, J., Arganda-Carreras, I., Frise, E., Kaynig, V., Longair, M., Pietzsch, T., et al. (2012). Fiji: An open-source platform for biological-image analysis. *Nat. methods* 9, 676–682. doi:10.1038/nmeth.2019

Scott, W. B., and Jepsen, G. L. (1936). The mammalian fauna of the white river oligocene: Part I. Insectivora and Carnivora. *Trans. Am. Philos. Soc.* 28 (1), 1–153. doi:10.2307/1005507

Scott, W. B. (1898). Notes on the canidae of the white river oligocene. *Proc. Am. Philos. Soc.* 19, 325–415. doi:10.2307/1005497

Scrucca, L., Fop, M., Murphy, T. B., and Raftery, A. E. (2016). Mclust 5: Clustering, classification and density estimation using Gaussian finite mixture models. *R J.* 8 (1), 289–317. doi:10.32614/rj-2016-021

Serafini, G., Gordon, C. M., Foffa, D., Cobianchi, M., and Giusberti, L. (2022). Tough to digest: first record of Teleosauroidea (Thalattosuchia) in a regurgitalite from the Upper Jurassic of north-eastern Italy. *Papers in Palaeontology* 8, 1–22. doi:10.1002/spp2.1474

Shillito, L. M., Blong, J. C., Green, E. J., and van Asperen, E. N. (2020). The what, how and why of archaeological coprolite analysis. *Earth Sci. Rev.* 207, 103196. doi:10.1016/j.earscirev.2020.103196

Suarez, F. L., and Levitt, M. D. (2000). An understanding of excessive intestinal gas. *Curr. Gastroenterol. Rep.* 2, 413–419. doi:10.1007/s11894-000-0042-8

Tabrum, A. R., Prothero, D. R., Garcia, D., and Emry, R. J. (1996). "Magnetostratigraphy and biostratigraphy of the Eocene-Oligocene transition, southwestern Montana"," in *The terrestrial eocene-oligocene transition in North America*. Editors D. R. Prothero and R. J. Emry (Cambridge: Cambridge University Press).

Taru, P., and Backwell, L. (2013). Identification of fossil hairs in *Parahyaena brunnea* coprolites from Middle Pleistocene deposits at Gladysvale cave, South Africa. *J. Archaeol. Sci.* 40 (10), 3674–3685. doi:10.1016/j.jas.2013.04.031

Turk, J., Čretnik, J., Turk, M., and Mladenovič, A. (2015). Hair imprints in Pleistocene cave sediments and the use of X-ray micro-computed tomography for their reconstruction. *Facies* 61 (422). doi:10.1007/s10347-014-0422-4

Wang, X., White, S. C., Balisi, M., Biewer, J., Sankey, J., Garber, D., et al. (2018). First bone-cracking dog coprolites provide new insight into bone consumption in *Borophagus* and their unique ecological niche. *Elife* 7, e34773. doi:10.7554/eLife.34773

Wickham, H. (2016). *ggplot2: Elegant graphics for data analysis*. New York: Springer-Verlag.

frontiers | Frontiers in Ecology and Evolution

TYPE Original Research
PUBLISHED 19 May 2023
DOI 10.3389/fevo.2023.1173341

OPEN ACCESS

EDITED BY
Stergios D. Zarkogiannis,
University of Oxford, United Kingdom

REVIEWED BY
George Lyras,
National and Kapodistrian University of Athens, Greece
Emmanuel Paul Gilissen,
Royal Museum for Central Africa, Belgium
Alejandro Pérez Ramos,
Malaga University, Spain

*CORRESPONDENCE
Saverio Bartolini-Lucenti
✉ saverio.bartolinilucenti@unifi.it
Lorenzo Rook
✉ lorenzo.rook@unifi.it

RECEIVED 24 February 2023
ACCEPTED 24 April 2023
PUBLISHED 19 May 2023

CITATION
Frosali S, Bartolini-Lucenti S, Madurell-Malapeira J, Urciuoli A, Costeur L and Rook L (2023) First digital study of the frontal sinus of stem-Canini (Canidae, Carnivora): evolutionary and ecological insights throughout advanced diagnostic in paleobiology.
Front. Ecol. Evol. 11:1173341.
doi: 10.3389/fevo.2023.1173341

First digital study of the frontal sinus of stem-Canini (Canidae, Carnivora): evolutionary and ecological insights throughout advanced diagnostic in paleobiology

Samuele Frosali[1], Saverio Bartolini-Lucenti[1,2]*, Joan Madurell-Malapeira[1,3], Alessandro Urciuoli[2,4,5], Loïc Costeur[6] and Lorenzo Rook[1,7]*

[1]Department of Earth Science, University of Florence, Florence, Italy, [2]Institut Català de Paleontologia Miquel Crusafont, Universitat Autònoma de Barcelona, Cerdanyola del Vallès, Spain, [3]Department of Geology, Universitat Autònoma de Barcelona, Cerdanyola del Vallès, Spain, [4]Universitat Autònoma de Barcelona, Cerdanyola del Vallès, Spain, [5]Division of Palaeoanthropology, Senckenberg Research Institute and Natural History Museum Frankfurt, Frankfurt am Main, Germany, [6]Naturhistorisches Museum Basel, Basel, Switzerland, [7]Changes Foundation, Sapienza Università di Roma, Roma, Italy

Introduction: The phylogenetic and ecological importance of paranasal sinuses in carnivorans was highlighted by several previous authors, mostly in extant species. Nevertheless, no specific study on this feature on extant canids, and no one on fossil representatives of the family, has been published up to now. Here, we analyze for the first time the paranasal sinus of extant and fossil canids through computed tomographic techniques to characterize them morphologically and morphometrically, making ecological inferences.

Methods: To do so, we applied for the first time an innovative deformation-based morphometric approach.

Results: The results obtained for extant species highlight a remarkable correlation between morphology and ecomorphotypes previously defined by some scholars (namely hypercarnivorous group-hunters; small-prey hypercarnivores, mesocarnivores, hypocarnivores). Our results thus support the direct relationship between diet preferences and the development of frontal sinus in canids. Regarding fossil specimens, we reconstructed for the first time the frontal sinus of three *Eucyon* species and compared it to those of living forms.

Discussion: The best-preserved specimen, the only known cranium of *Eucyon adoxus* dated to the Late Pliocene of Saint-Estève (France), displayed similarities with hypercarnivorous group-hunter canids by the large sinus prominences. Given that the overall craniodental morphology of *E. adoxus* suggests that it acted as a small prey hypercarnivore—similar to extant *Canis simensis*—the aforementioned affinities might have evolved independently, in relation to high stresses during feeding. Overall, our study demonstrates that morphological inspection and deformation-based geometric morphometrics complement each other and allow a thorough investigation of sinus shape variability, thus enabling the study of sinus morphology in other fossil carnivorans with the ultimate goal of inferring their ecological preferences.

KEYWORDS

innovative morphometrics, sustainable cultural heritage, Canidae, paranasal sinuses, paleoecology, *Eucyon*

1. Introduction

1.1. Dispersal of the tribe Canini in Eurasia

Currently, the members of the family Canidae are widely distributed across Eurasia and Africa, but geologically speaking this is just a recent achievement. Throughout most of their history, the distribution of canids was restricted to North America (Wang and Tedford, 2008; Tedford et al., 2009; Sotnikova and Rook, 2010). The major biotic events related to the dispersal of the subfamily Caninae (to which all extant canids belong to) and their evolution in Eurasia coincided with faunal turnovers that, in these continents, occurred between 5.5 and 0.5 Ma. One of the two major events of the Canini dispersal in Eurasia was the "*Eucyon* event" (*sensu* Sotnikova and Rook, 2010) that took place at the end of the Miocene (the other main event was the so-called "*Canis* event" at the beginning of the Late Pliocene; Sotnikova and Rook, 2010). Species of the genus *Eucyon* (Tedford and Qiu, 1996) indeed appeared in Central Asia, Europe, and Africa by the latest Miocene (Figure 1). For instance, the remarkable Late Miocene occurrences of *Eucyon monticinensis* (Rook, 1992) in Europe, *Eucyon davisi* (Merriam, 1911) in Asia, and *Eucyon intrepidus* (Morales et al., 2005) in Africa, were roughly contemporaneous. The genus then experienced multiple radiations in Eurasia and Africa, reaching a relatively high diversity in the Pliocene of Eurasia (Rook, 2009; Figure 1). The diversification of the Canini in Asia peaked at the beginning of the Early Pliocene, as evidenced by the appearance of *Nurocyon chonokhariensis* (Sotnikova, 2006) and *Eucyon zhoui* (Tedford and Qiu, 1996), and by the increase in number of *E. davisi* finds (Sotnikova and Rook, 2010). The European diversity peaked later with the arrival of "*Canis*" *michauxi* (Martin, 1973), *Eucyon adoxus* (Martin, 1973), and *Eucyon odessanus* (Odintzov, 1967) in the Late Ruscinian (Late Pliocene; Sotnikova and Rook, 2010) (Figure 1). In the Early Pleistocene, after the "*Canis* event," there was a species turnover on the continent and the species of the genus *Eucyon* went almost completely extinct, being limited to the Chinese *Eucyon minor* (Teilhard de Chardin and Piveteau, 1930) and "*Canis*" *kuruksaensis* (Sotnikova, 1989), while *Canis sensu* lato underwent a wide diversification. This turnover included *Canis teilhardi* (Qiu et al., 2004), *Canis longdanensis* (Qiu et al., 2004), *Canis chihliensis* (Teilhard de Chardin and Piveteau, 1930), *Canis* (*Xenocyon*) *brevicephalus* (Qiu et al., 2004), and *Canis* (*Xenocyon*) *dubius* (Teilhard de Chardin, 1940) in China, and the western forms like the renown *Canis etruscus* (Forsyth-Major, 1877), *Canis arnensis* (Del Campana, 1913), *Canis borjgali* (Bartolini-Lucenti et al., 2020), *Canis* (*Xenocyon*) *falconeri* (Forsyth-Major, 1877), and *Canis accitanus* (Garrido and Arribas, 2008; Sotnikova and Rook, 2010). The diversity of the *Canis* s.l. group decreased in the second half of the Early Pleistocene of Eurasia, becoming mostly limited to the large hypercarnivorous form *Canis* (*Xenocyon*) *lycaonoides* (Kretzoi, 1938) and small wolf *Canis mosbachensis* (Soergel, 1925) (and its possible zoogeographic extreme *Canis variabilis* Pei, 1934) (Rook et al., 2023).

1.2. Brief overview of biomechanics of the frontal sinus in carnivorans

The frontal sinus is an often-overlooked anatomical structure. Nevertheless, recent studies unveil the renovated interest for this paranasal cavity in paleontological and paleoanthropological research, for its potential at different levels, e.g., evolutionary, biomechanical, ecological one (Balzeau et al., 2022).

In carnivorans, the first introduction of the frontal sinus as a taxonomic-useful character was proposed by Huxley (1880) and is today widely recognized by the scientific community as a diagnostic feature in the phylogenetic analysis of Canidae. The basal state (lack of the sinus) is manifested externally by a shallow depression or a groove, creasing the dorsal surface of the postorbital process (Tedford et al., 1995): this condition is present in almost all the living species of the tribe Vulpini and it is indeed known as the "vulpine crease." In members of the tribe Canini, this cavity inflates and expands its size: the most derived condition is shown by *Canis*, where the sinus penetrates the postorbital process to its tip and expands posteriorly along the rostrodorsal surface of the braincase, ultimately reaching the frontoparietal suture (Tedford et al., 1995). This enlargement of the frontal region produces a deeply convex morphology of the dorsal surface of the cranium above the orbits and an enlargement, in width, of the postorbital constriction.

Among other cranial features, like dentition morphology or snout length, the development of the frontal sinus is linked to the type of diet the species evolved. Particularly, large canids with hypercarnivorous diets tend to have more developed sinuses and enlarged, domed frontals. In durophagous carnivorans, both in Hyaenidae and Borophaginae, the frontal sinus extends backward toward the posterior tip of the skull and, as a result, there is a large air space between the braincase and the parietal bones above it (Paulli, 1900; Joeckel, 1998; Vinuesa et al., 2015). Werdelin (1989) and Joeckel (1998) proposed that such a domed head in bone-cracking hyaenids and canids serves to transmit the great stresses from the premolars to the back of the skull, thereby reducing the bending stress of the rostrum. The main hypothesis to explain the presence of the frontal sinus in carnivorans is indeed that these structures are useful for the even dissipation of stresses linked to feeding mechanics. Some studies (among others Curtis and Van Valkenburgh, 2014) also pointed out a relationship between the intraspecific variations of the morphology and size of the frontal sinus and the diet of the individual (the softer the food eaten, the smaller the frontal sinus; Curtis et al., 2018; Pérez-Ramos et al., 2020; Ruiz et al., 2023). Other hypotheses have been suggested to explain the function of these structures, among others the idea that frontal sinuses are useful for brain cooling, olfaction, potential sensory enhancement ability, or for the maximization of muscle attachment areas, or even hibernation (Joeckel, 1998; McGreevy et al., 2004; Vinuesa et al., 2015, 2016; Vinuesa, 2018; Pérez-Ramos et al., 2020). However, none of these explanations is entirely satisfactory and one hypothesis does not necessarily exclude another. The present paper offers the first in-depth study of the frontal sinus of extant and fossil canids using computed tomography and innovative 3D methodologies (never applied to these structures) to characterize and analyze them and, eventually, draw ecological inferences on the considered fossil taxa.

2. Materials and methods

2.1. Studied and comparative material

This study reports the first digital analysis of the frontal sinuses of three stem-Canini of the genus *Eucyon*: the only known cranium

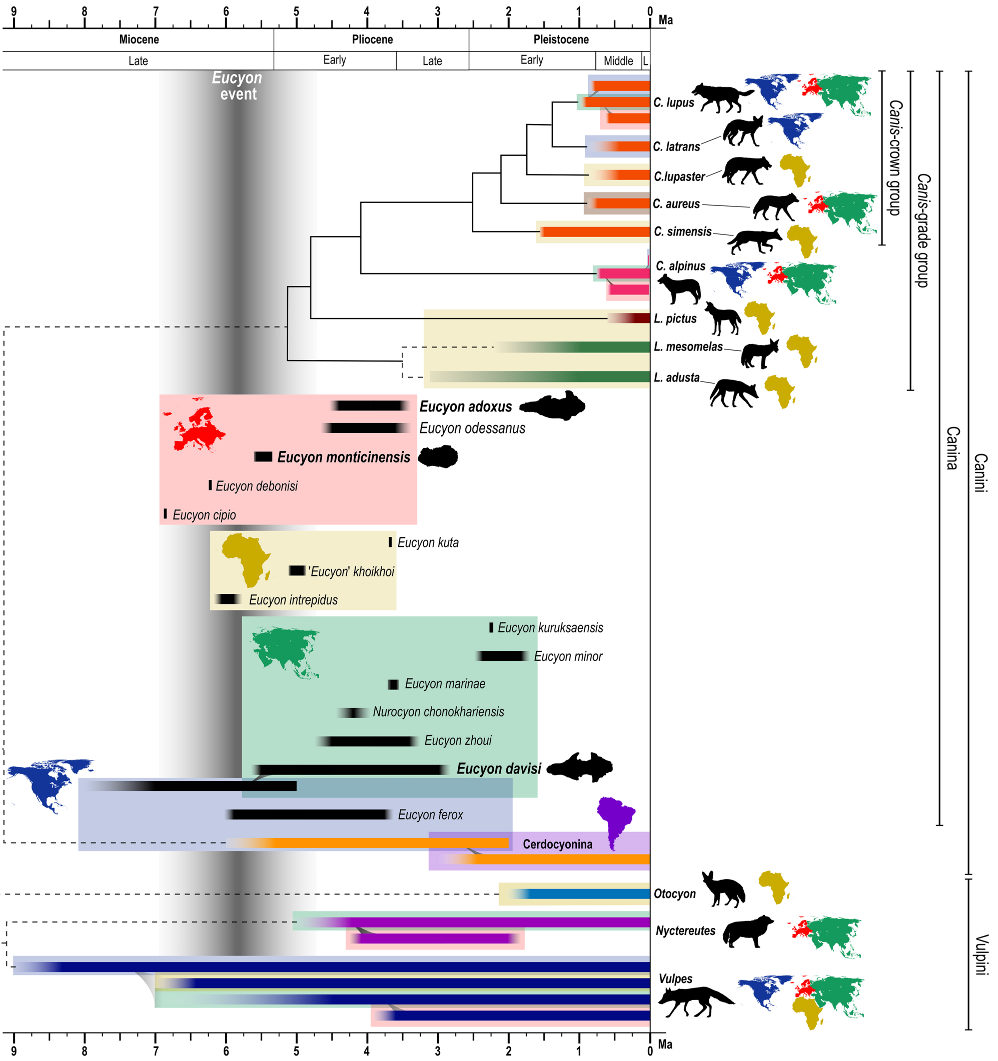

FIGURE 1
Stratigraphic, phylogenetic, and geographical scheme of *Eucyon* spp. in the framework of extant canids evolution and zoogeography from Miocene to modern times. The phylogenetic relationships are compiled using widely accepted and recent molecular and total evidence analyses (e.g., Zrzavý et al., 2018; Perri et al., 2021). Solid lines represent undisputed patterns of affinities; divergence between solid-lines groups are time-calibrated using average time of divergence expressed in these works (e.g., Perri et al., 2021). Dashed lines account for disputed topologies of trees (e.g., paraphyly of *Lupulella*; relationship among Vulpini; *cf.* Wayne and Ostrander, 2007 and Zrzavý et al., 2018). Time of the nodes in the dashed-lined groups should not be taken as significative. Considering the disputed nature of several *Eucyon* spp. (as expressed in the text) we reported only their chronological and geographic distribution. Data are taken from: Tedford and Qiu (1996), Sotnikova (2006), Spassov and Rook (2006), De Bonis et al. (2007), Montoya et al. (2009), Rook (2009), Tedford et al. (2009), Werdelin et al. (2015), Bartolini-Lucenti and Rook (2021), Valenciano et al. (2022). '*Eucyon* event' is taken from Sotnikova and Rook (2010). Colors of the chronological ranges represents clades. Ranges of other canids are taken from previously cited literature and also from: Stiner et al. (2001), Boudadi-Maligne (2010), Werdelin and Sanders (2010), Bartolini-Lucenti et al. (2018), Marciszak et al. (2021), Tamvakis et al. (2022), Martínez-Navarro et al. (2023). Color continents maps next to specific names represent presence of the species in one/more than one continent(s), following the color code of the boxes in the figure.

of the species *Eucyon adoxus*, from the Late Pliocene of Saint-Estève (France; Rook, 2009) and stored at the Natural History Museum of Basel (NMB Rss.45); a cranium (F:AM 97057) of *Eucyon davisi* from the Early-Late Pliocene of Xiakou, Yushe Basin (China; Tedford and Qiu, 1996), currently stored at the American Museum of Natural History of New York (U.S.A.); and, the only known cranial specimen of *Eucyon monticinensis*, from the latest Late Miocene of Cava Monticino (Italy, Bartolini-Lucenti et al., 2022) and stored in the Civic Museum of Natural Sciences of Faenza. The objective of the study is the comparison of the sinus of these fossil species to that of selected extant Canidae. The extant comparative specimens used here are held at the "La Specola" Zoology Museum of Florence (MZUF), the Giacomo Doria Natural History Museum of Genoa (CE) and the Earth Science Department of the University of Florence (DST). Additional specimens were downloaded from the digital repository MorphoSource.[1] The considered comparative sample includes (Supplementary Table S1) four specimens of *Canis lupus*, Linnaeus (1758), four of *Canis lupaster* (Hemprich and Ehrenberg, 1828/1834), three of *Canis simensis* Rüppell (1835/1840), two of *Canis aureus* (Linnaeus, 1758), one of *Canis latrans*

---

[1] www.morphosource.org

Say (1823), one of *Lupulella adusta* (Sundevall, 1847), four of *Lupulella mesomelas* (Schreber, 1775), two of *Lycaon pictus* (Temminck, 1820), and one of *Vulpes lagopus* (Linnaeus, 1758). To compare morphologically and morphometrically the specimens we used the digital analysis of images derived from CT scans via the software Amira (ver. 5.4.5, Thermo Fisher). Tomographic scans of the material from Florence and Faenza were acquired at the Medical Radiology ward ("SOS Radiologia") of the San Giovanni di Dio Hospital (Florence, Italy) using a Siemens Somatom Definition AS scanner. *Eucyon adoxus* was scanned at the Biomaterials Science Center of the University of Basel, Switzerland using a Phoenix Nanotom (GE). The specimen of *Eucyon davisi* was scanned at the University of Texas high-resolution X-ray Computed Tomography Facility (Austin, Texas, U.S.A.). For the specimens downloaded from Morphosource, we report the info included in the metadata and accompanying files of the raw data: m-81.001, *Canis simensis*, originally held at the AMNH Mammal Collection, was scanned by the University of Texas high-resolution X-ray Computed Tomography Facility (Austin, Texas, U.S.A.). 80-50-290, *Canis latrans*, kept at the University of Arkansas Museum and was scanned by the MicroCT Imaging Consortium for Research and Outreach (Fayetteville, Arkansas, U.S.A.). 368.443, *Lycaon pictus* was scanned by the University of Texas high-resolution X-ray Computed Tomography Facility (Austin, Texas, U.S.A.), while the original sample comes from NMNH – Division of Mammals. The data obtained from these images made the reconstruction of the frontal sinuses of all the specimens possible. We decided to use the left sinus only to ease the alignment of the surfaces and, consequently, their analysis with deformation-based geometric morphometric methods.

2.2. Nomenclature and abbreviations

2.2.1. Proposed nomenclature of the frontal sinuses

We propose for the first time a nomenclature to describe the frontal sinus in canids and carnivorans (Figure 2). The sinus is divided into three regions: rostral, caudal, and ventral ones. The rostral and caudal regions are characterized by specific features on their dorsal, medial, lateral, and ventral surfaces. The ventral region is generally described for its medial and lateral sides and its rostral and caudal margins. The features, although variable, can be recognized on the outer surface. Here we report the names and abbreviations for the analyzed specimens. Abbreviations and their definition, in alphabetical order: **ci**, caudal incision (if more than one: medial ci, lateral ci, etc.); **dcll**, dorsocaudal lateral lobe; **dcml**, dorsocaudal medial lobe; **ds**, dorsal sulcus (if the sulcus is simple it may be named "longitudinal ds"; if it branches, it can have "a transverse part of the ds"; etc.); **l**, lobe (a large inflated portion of the sinus), **lb**, lobule (a smaller and less prominent lobe); **p**, prominence (general term to describe an inflation of the surface of the sinus); **pol**, postorbital lobe; **ri**, rostral incision (generally divides the rostral region of the sinus in two sides: the rostrolateral lobe and the rostromedial one); **rll**, rostrolateral lobe; **rml**, rostromedial lobe; **vl**, ventral lobe (the tip of the ventral region); **vlp**, ventrolateral prominence.

2.2.2. Other abbreviations used in the text

List of abbreviations used in the paper, in alphabetical order: BM, body mass; CBL, condylobasal length of the cranium (prosthion-occipital condyles); LmaxS, maximum rostrocaudal length of the frontal sinus; TL, total length of the cranium (measured from prosthion-akrokranion); Vol, volume of the frontal sinuses.

2.2.3. Morphometric variables and ecomorphogroups

We used Autodesk Meshmixer (ver. 3.5.474, Autodesk) and Artec Studio 15 Professional (ver. 15.0.3.425, Artec) software to ameliorate and regularize the mesh structure, as well as to measure the sinus volume (Vol), sinus maximum rostrocaudal length (LmaxS), the cranial length (TL) and the condylobasal length (CBL). The latter was used to estimate the body mass of each specimen, using the regression formula proposed by Van Valkenburgh (1990). Van Valkenburgh and Koepfli (1993), studying extant canids dietary preferences, established four distinct ecological groups. The differed for their morphological features and the proportional amount of vertebrate prey in their diet: Group 1 and 2 have >70% of vertebrate meat in their diet, thus are considered hypercarnivore canids. They are distinguished by the fact that Group 1 canids cooperatively hunt large prey, whereas Group 2 are hypercarnivorous specialized in small prey. Group 3 canids are mesocarnivorous, with an income of 70–50% of vertebrate meat in their diet. Group 4 represent the hypocarnivorous dogs with <50% of meat. We used these well attested groups to investigate the ecological implication of the development of the frontal sinus.

To assess the presence of correlation among the variables considered in the analysis, we performed ordinary least squares (OLS) regressions on natural log-transformed linear variables (ln TL, ln LmaxS, in mm), natural log-transformed cube root of the left sinus volume (ln Vol, in mm^3), and on the natural log-transformed body mass (ln BM, in kg). The regressions were performed for the whole Canidae sample, as well as for two subsets based on ecological preferences (group hunters vs. non-group hunters) due to the difference noted in one of the ecological groups. We also checked the homogeneity of the slopes and intercepts between group hunters and the rest of the sample via analysis of the covariance (ANCOVA). All regressions were performed in R Studio (v. 2023.03.0 + 386 "Cherry Blossom" release 3c53477afb13ab959aeb5b34df1f10c237b256c3, 2023-03-0936; RStudio Team, 2021) for R (v. 4.1.2; R Core Team, 2021) using the lm() function of the base package 'stats', whereas we used the anova() function of the 'car' v. 3.0–11 (Fox and Weisberg, 2019) to perform the ANCOVA.

2.2.4. Diffeomorphic surface matching analyses

To further inspect the shape variation in the canid sinus, we employed a diffeomorphic surface matching (DSM) approach, which is a recently-developed landmark-free geometric morphometrics method that allows the direct comparison between continuous surfaces by relying on their geometrical correspondence (Glaunès and Joshi, 2006; Durrleman et al., 2014). This method takes into account all data points at the same time and does not require point-to-point correspondence, thus allowing the use of surfaces composed by a different number of faces (Durrleman et al., 2012). From an operational viewpoint, DSM first estimates the average shape for the considered sample and identifies its most variable portions, attaching a number of initial control points to them. The deformations from the average to each of the analyzed specimens are then modeled as smooth and invertible functions (that are, diffeomorphisms) and compiled to build an atlas for the entire sample. Compared with

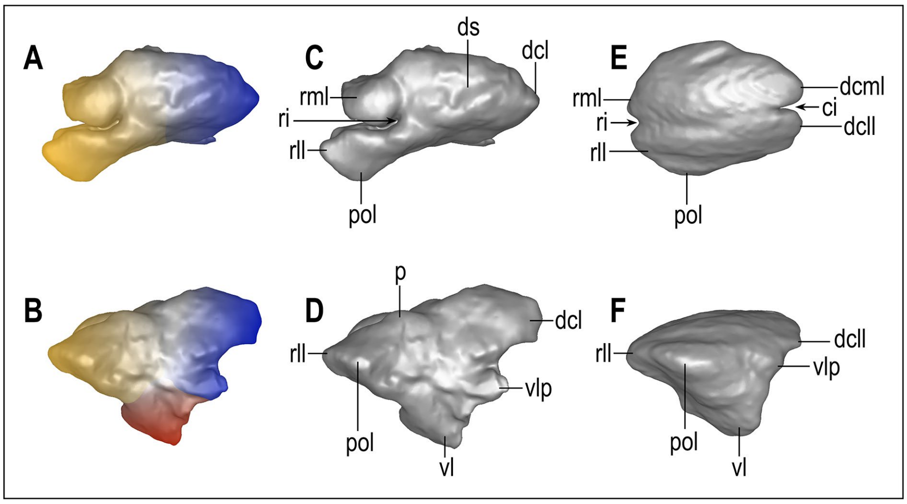

FIGURE 2
Nomenclature of the main parts of the frontal sinus of Canidae. *Eucyon adoxus* (NMB Rss.45, **A–D**) and *C. lupaster* (MZUF-2714, **E,F**) were taken as models because their sinuses represent, respectively, a quite complex and one of the simplest versions of this paranasal structure (not to scale). The color map **(A,B)** represents the principal areas of the sinus: yellow, rostral region; blue, caudal region; red, ventral region. ci, caudal incision; dcll, dorsocaudal lateral lobe; dcml, dorsocaudal medial lobe; ds, dorsal sulcus; l, lobe; lb., lobule; p: prominence; pol, postorbital lobe; ri, rostral incision; rll, rostrolateral lobe; rml, rostromedial lobe; vl, ventral lobe; vlp, ventrolateral prominence.

landmarks, correspondence between surfaces is not strictly homologous, which is particularly convenient for structures with a very complex 3D morphology that does not allow to identify a large number of homologous points, as in the case of frontal sinuses and of other craniodental structures (e.g., semicircular canals and enamel/dentine junction; Urciuoli et al., 2020; Zanolli et al., 2022).

Prior to performing DSM analyses, the surfaces required a number of preparatory steps. First the 3D models of the left sinus of each specimen were decimated to 40,000 triangles (±100 triangles) in Amira and saved in PLY format. Given the complexity and variability of the sinus, the alignment methods used for preprocessing the surfaces in other DSM analyses (Beaudet et al., 2016; Urciuoli et al., 2020) did not yield satisfactory results. To circumvent this issue, we defined a number of landmarks (see Table 1) that allowed us to generally describe its morphology and orientation. The aforementioned landmarks were placed on each individual in Amira software and used to perform a General Procrustes alignment in R using the procSym() function of the 'Morpho' v. 4.1.3 (Schlager, 2017) package. The obtained aligned configurations were then used to extract the rotational matrix and scaling factor for each individual, which were then applied to the corresponding surface using two functions, computeTransform() and applyTransform(), of the 'Morpho' package. The aligned surfaces were then converted into legacy VTK files using the open-source software Paraview v. 5.6.0.[2] The VTK files were then analyzed with Deformetrica ver. 4.3 (Bône et al., 2018) using the 'DeterministicAtlas' analysis with Kernel size = 0.10, resulting in the identification of 7,800 control points. The *V. lagopus* individual was not included in the analysis due to its very reduced sinus morphology. R scripts and data used here for the analyses are available at the following link http://dx.doi.org/10.5281/zenodo.7836886.

TABLE 1 List of landmarks (LM) used in the analysis and their number and definition.

LM number	Definition
1	Rostralmost (Anteriormost) point on the rostromedial lobe.
2	Caudalmost (Posteriormost) point of the incision between rostromedial and lateral lobe.
3	Lateralmost point of the lateral lobe.
4	Medialmost point on the medial side of the sinus.
5	Caudalmost (Posteriormost) point of the sinus.
6	Ventralmost point of the frontal sinus.

The obtained deformation fields (i.e., the output of the DSM analyses) were then inspected with different multivariate methods to identify the possible presence of patterns of shape variation in the data. First, we computed a principal component analysis (PCA), which allows to reduce the high dimensionality of the data and to concentrate the variance in the first axes (components). The resulting components were then used to perform a canonical variate analysis (CVA)—with the CVA() function of the 'Morpho' package—using hunting and dietary preferences (group hunters, hypercarnivory of small prey, and mesocarnivory) as grouping factor, thus enabling us to assess the presence of a group structure within the data. We included only the first seven components (accounting for the 71.9% of total variance) as these returned the best classification results, a practice commonly used in high-dimensional shape data (e.g., Zanolli et al., 2022). The fossil specimens (*E. adoxus* NMB Rss.45, *E. davisi* F:AM 97057) and the hypocarnivore *Lupulella adusta* (MZUF-8496) were plotted *a posteriori* onto the shape space. For these specimens, we also computed cross-validated posterior probabilities and typicality probabilities using their CVA scores. Posterior probabilities assume that an individual must belong to one of the *a priori* defined groups and are expressed as a percentage. In contrast, the interpretation of

---

[2] www.paraview.org

typicality probabilities is less intuitive, as they test the null hypothesis of group membership for a given specimen and return a *p*-value, which allows to reject the null hypothesis (i.e., the specimen is an outlier for the considered group) at $p < 0.05$. Finally—as for the morphometric variables—we assessed the possible presence of allometric trends in the shape data by regressing each of the obtained PCs and CVs against the log-transformed body mass (in kg) in R.

3. Results

3.1. Description of the sinuses of *Eucyon*

The three species of the genus *Eucyon* considered in this study show quite different morphologies of the frontal sinuses. The cranium of *E. monticinensis* MSF 466, at present the only cranium of the species ever recovered and described, is extremely deformed due to taphonomic processes. The deformation affecting the fossil involved a dorsoventral compression, with a left lateral component, so that the cranium seems to lie on the left side. The left sinus, the only one preserved in MSF 466, is thus heavily deformed (Figure 3). Despite this problematic, the 3D model shows that this species presents quite a small sinus, with reduced lobes. Further comments on its development are hindered by the deformation: it is indeed hard to understand the dorsoventral extension of the sinus, as well as the development of its ventral lobe. The other species of the genus, also shown in Figure 3, show instead a very different morphology of this paranasal cavity. *Eucyon adoxus* possesses instead a well-developed frontal sinus with a marked rostral incision that identifies two prominent rostral lobes. On the dorsal surface, the sinus of *E. adoxus* shows evident prominences along the main axis of the sinus, marked by a dorsal sulcus. The ventral lobe is elongated ventrally, giving the frontal sinus a triangular-like outline, in lateral view. The postorbital lobe is developed, resembling in shape the morphology of the process of the frontal bone: indeed, the sinus visibly invades the whole length of the process (Figure 3). This species shows also a trigonal dorsocaudal lobe and a marked ventrolateral prominence jutting caudally. The sinus of *Eucyon davisi* is rostrocaudally elongated but with fairly inflated generalized structures (Figure 3). The rostrocaudal elongation is remarkable: even if they do not reach the frontoparietal suture, the sinus covers a fair portion of the endocranial cavity. There is no rostromedial lobe, whereas the rostrolateral one is prominent, in dorsal and lateral views (Figure 3). In lateral view, the ventral lobe is slender compared to the inflated and rounded dorsocaudal lobe. The postorbital lobe is reduced and sharp, jutting pointily on the lateral plane.

3.2. Morphological and morphometric comparison of the frontal sinuses in Canidae

Figure 4 shows the final reconstruction of the frontal sinuses of a single specimen for each fossil and extant species, considered in

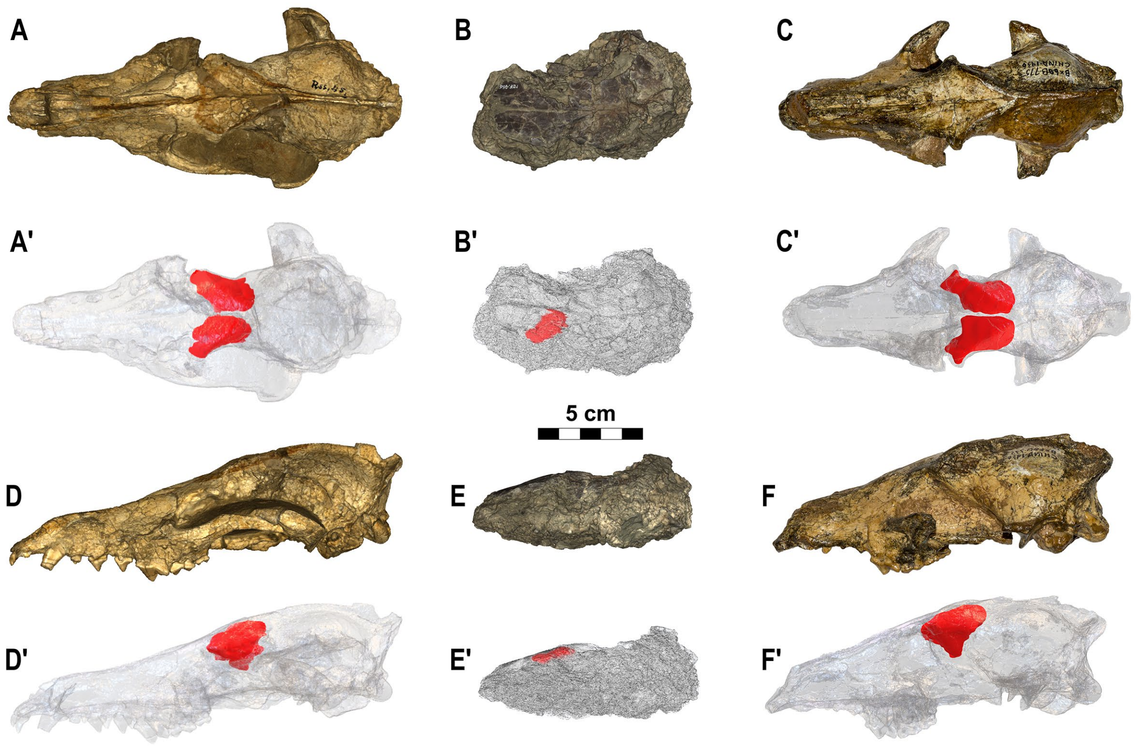

FIGURE 3
Crania of the three species of *Eucyon* here analyzed. **(A–A′,D–D′)** *Eucyon adoxus* (NMB Rss.45) from St. Estève (Late Pliocene, MN 15; southern France), in dorsal **(A–A′)** and in left lateral **(D–D′)** views. **(B–B′,E-E′)** *Eucyon monticinensis* (MSF 466) from Cava Monticino (latest Miocene, 5.61–5.33 Ma; Emilia-Romagna, Italy), in dorsal **(B–B′)** and left lateral **(D–D′)** views. **(C–C′,F-F′)** *Eucyon davisi* (F:AM 97057) from near Xiakou (late Early-Late Pliocene, ~4.0–3.0 Ma; Yushe Basin, Shanxi, China), in dorsal **(C–C′)** and left lateral **(F–F′)** views. **(A′–F′)** Highlight the position of the frontal sinuses within the crania.

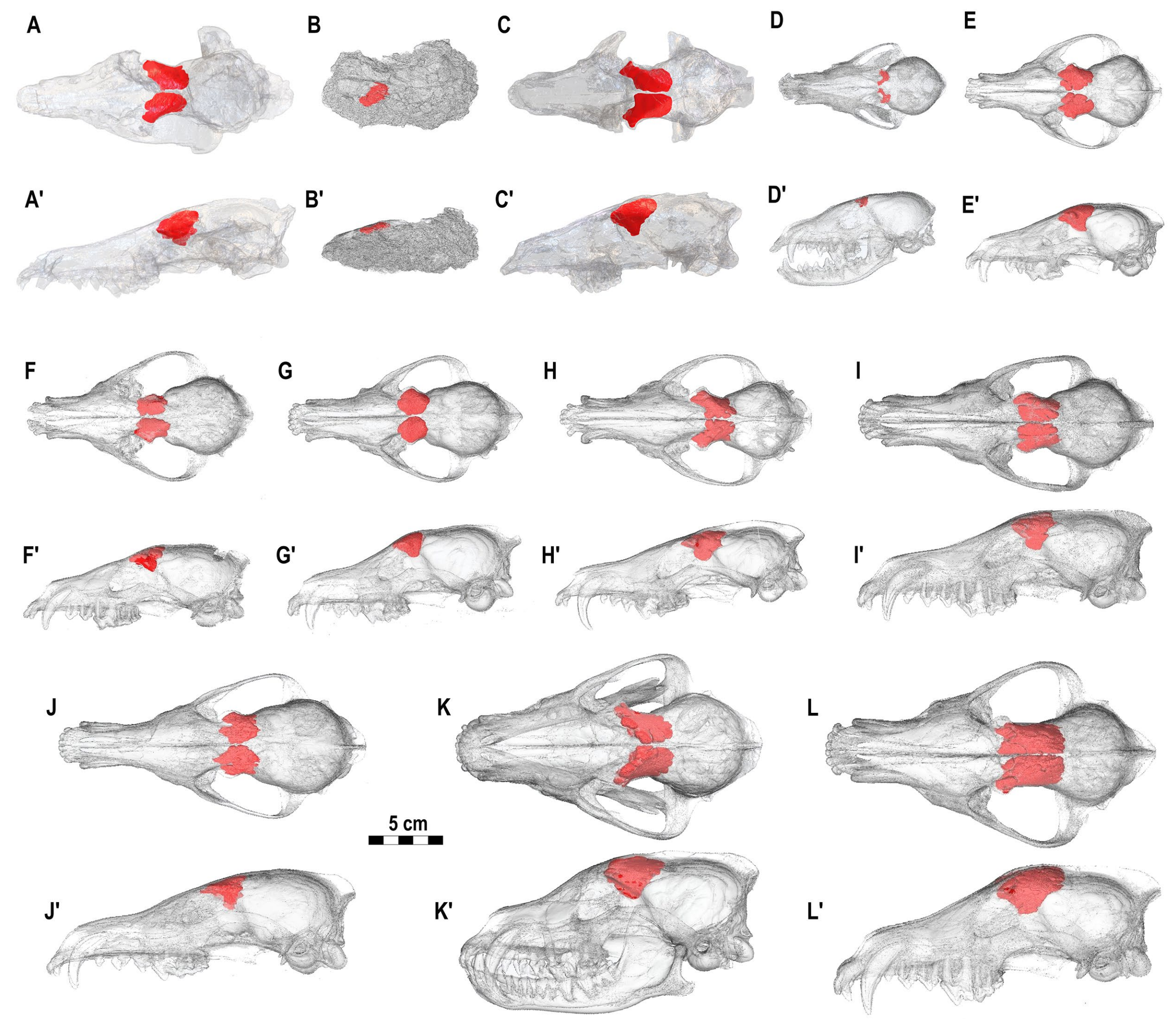

FIGURE 4
Dorsal and left lateral views of the crania of fossil and extant Canidae analyzed here, with the frontal sinuses in their natural position. **(A–A′)** NMB Rss.45, *E. adoxus*. **(B–B′)** MSF 466, *E. monticinensis*. **(C–C′)** F:AM 97057, *E. davisi*. **(D–D′)** MZUF-1474, *V. lagopus*. **(E–E′)** MZUF-1715, *L. mesomelas*. **(F–F′)** MZUF-11878, *C. aureus*. **(G–G′)** MZUF-1851, *C. lupaster*. **(H-H′)** MZUF-8496, *L. adusta*. **(I–I′)** 88-50-290, *C. latrans*. **(J–J′)** MZUF-13781, *C. simensis*. **(K–K′)** 368.443, *L. pictus*. **(L–L′)** MZUF-11874, *C. lupus*.

relationship to the cranium. Figure 5 shows the morphology of the left sinus of a single specimen for each species considered. As it is visible from Figures 4, 5, the frontal sinus is a fairly variable structure, showing a wide range of dimensions and morphologies in the members of the family Canidae. The analysis shows the almost total lack of sinus in *V. lagopus*, which are not well defined nor possess proper lobes, rather many small chambers barely connected to each other. On the contrary, all the other specimens analyzed possessed well-formed sinus, distinguished from one another for their degree of external complexity. Despite these differences all species shared a rounded three-sided outline in lateral view and the presence of at least one rostral lobe. In all the species of *Canis*, two rostral lobes separated by the rostral incision are visible, despite their different degree of development in the various species. *Canis aureus* and *C. lupaster* show very similar frontal sinuses with a shallow rostral incision and a small rostromedial and rostrolateral lobes, while *C. latrans* and *L. mesomelas*, despite still having two fairly small rostral lobes, show a deeper rostral incision (which in the case of *L. mesomelas* is also wider). The postorbital lobe in *C. aureus*, *C. lupaster* and *L. mesomelas* is reduced and barely diversified on the lateral side of the rostrolateral lobe. It also has comparable position in rostrocaudal length of the sinus. The similarity between *L. mesomelas* and *C. aureus* and *C. lupaster* also extends in lateral view: a three-sided outline, with no or modestly developed ventrolateral prominence. *Canis latrans* has a deeper and more developed sinus, in both dorsal and lateral views. *Canis simensis* has a deep, wide, and rounded rostral incision, with two well-formed rostral lobes, especially the rostrolateral one. In general terms, the sinus of the Ethiopian wolf is characterized by a relatively poor rostrocaudal elongation but a proportionally dorsoventrally deep extension. Indeed, in lateral view the sinus shows an angulated and

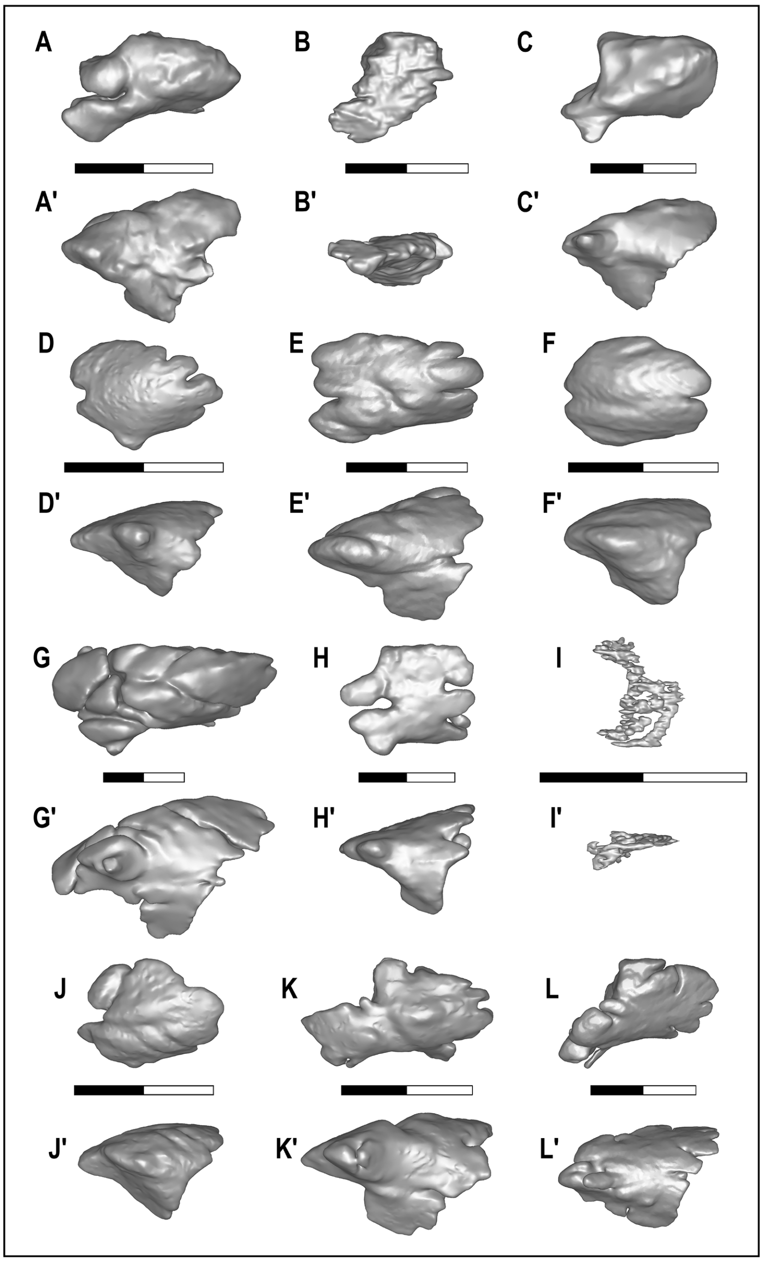

FIGURE 5
Dorsal and lateral views of the left frontal sinus of the examined species. Each model has been reported to same width (and true scale, i.e., 2cm, is reported per each specimen between dorsal and lateral view). **(A–A′)** NMB Rss.45, *E. adoxus*. **(B–B′)** MSF 466, *E. monticinensis*. **(C–C′)** F:AM 97057, *E. davisi*. **(D–D′)** MZUF-11880, *C. aureus*. **(E–E′)** 88-50-290, *C. latrans*. **(F–F′)** MZUF-2714, *C. lupaster*. **(G–G′)** MZUF-2032, *C. lupus*. **(H–H′)** MZUF-13781, *C. simensis*. **(I–I′)** MZUF-1474, *V. lagopus*. **(J–J′)** MZUF-3293, *L. mesomelas*. **(K–K′)** MZUF-8496, *L. adusta*. **(L–L′)** 368.443, *L. pictus*.

wide ventral lobe. Moreover, it displays a series of caudal incisions which denote multiple caudal lobes. *Canis lupus* possesses the most complex sinus in the genus *Canis*, rivaled only by that of *L. pictus*. In addition to a deep rostral incision, *C. lupus* shows two well-developed and domed rostral lobes and a dorsal sulcus that branches medially and laterally, shaping different prominences. The African hunting dog, *L. pictus*, have a complex and lobose sinus, marked by the developed rostrolateral lobe and a reduced rostromedial one. In this species, the postorbital lobe is rostrally advanced and further pneumatized in two separated lobules. The degree of complexity and of additional prominences of the dorsal surface is similar to that of the wolf. Caudally, the sinus of *L. pictus* is rounded and subdivided into different smaller lobules by evident incisions, similarly but more than in *C. lupus*. In *L. adusta*, the sinus is particularly proportionally elongated rostrocaudally and marked by the absence of the rostromedial lobe. Furthermore, it possesses an enlarged rostrolateral lobe. Despite the breadth of this part, the postorbital lobe is not so expanded, yet invading the zygomatic process of the frontal. The postorbital lobe is parted in two lobules in the considered specimen. Despite the generic attribution, the sinuses of *L. adusta* and

L. mesomelas differ greatly from one another. This is evident in the dorsal shape of the sinuses (slender in *L. adusta*, in dorsal view, and characterized by prominences visible, in lateral view), the morphology of the rostral region and in the development of the caudal lobe and of the ventrocaudal promincence of *L. adusta* (the latter almost in as proper lobe). The morphology of the sinus of *E. davisi* and *E. monticinensis* resembles that of *L. adusta* for the absence of a rostromedial lobe and a developed rostolateral one. Nevertheless, the sinus of *E. monticinensis* is rostrocaudally shorter compared to the one of *L. adusta*. The reduction in rostrocaudal length is similar to *C. aureus*, *C. lupaster*, and *L. mesomelas*. Nevertheless, the taphonomic deformation of the cranium (thus of the sinus) hinders proper comparison with the other extant canids. *Eucyon davisi* instead shows a proportionally reduced rostrolateral lobe when compared to the large and inflated one of *L. adusta*. Furthermore, the sinus of the fossil species is more inflated with almost no subdivisions, whereas *L. adusta* shows numerous lobules individualized by sulci and incisions. Despite these differences the sinus of *L. adusta* is closest in terms of general resemblance to that of *E. davisi*. The sinus of *E. adoxus* differs from that of medium-sized canids (*C. aureus*, *C. lupaster*, *C. latrans*, *C. simensis*, and *L. mesomelas*) for its rostrocaudal elongated and pointed shape, in dorsal view. In this regard, it resembles *C. lupus*, though proportionally smaller. Even in lateral view, *E. adoxus* has a proportionally deep sinus, unlike previous taxa. The dorsal surface shows some prominences identified by a branched sulcus resembling those of *C. latrans* and, to minor extent, *C. lupus*. The presence of a bulging and inflated rostromedial sulcus marks a sharp difference with *L. adusta*.

Another feature used to describe the morphology and development of these paranasal cavities is their caudal extension, in particular relative to the frontoparietal suture. As visible in Figure 4, only in *C. lupus* and *L. pictus* the frontal sinus reaches the frontoparietal suture, whereas in the other species, despite their difference, it never extends further caudally. Other species that have well-developed frontal sinuses with a considerable caudal extension, i.e., close to the frontoparietal suture, are *C. latrans*, *C. simensis*, and *L. adusta*. If the cranium is observed in lateral view (Figure 4), it is relevant to note the relationship between the frontal sinus and the endocranium. The frontal sinus in *V. lagopus* is evidently reduced. In *C. lupus* the frontal sinus covers a good portion of the cranial cavity, whereas in the other species it covers different portions of the braincase. In *C. aureus* the overlap between the frontal sinus and the brain is the smallest (Figure 4). The second is *C. lupaster*, and then *C. simensis* and *C. latrans* which have similar parts of the braincase covered by the frontal sinus. *Lycaon pictus* has a large portion of the braincase topped by the frontal sinus even if the overlapping region is not as large as in *C. lupus*. In *Lupulella* spp., *L. adusta* seems to possess a longer region of the braincase covered by the frontal sinus compared to *L. mesomelas*. As mentioned above, in the fossil species the sinus expands caudally into a modest portion of the endocranial cavity. This extension is comparable in both *E. adoxus* and *E. davisi*. The preservation of *E. monticinensis* specimen (MSF 466) does not allow any comparison.

As far as the morphometric analyses are concerned, the study considered in particular the relationship between different parameters extrapolated by the tridimensional renderings of the frontal sinus (e.g., sinus volume, maximum rostrocaudal length of the sinus) and characteristics of the considered specimens/species (e.g., total length of the cranium, body mass) (Table 2). The results are reported in Table 3 and Figures 6, 7. The sinus of *E. monticinensis* was not considered because it was too deformed for this kind of analysis.

The bivariate regressions for the considered morphometric variables show that they are highly correlated with one another and with the body mass (Figures 6, 7; Table 3). Both ln LmaxS and ln Vol show a strong correlation with ln BM, which explains a similarly large amount of the variance of the two variables (*ca.* 70–75%) and follows a negative allometry relationship (i.e., the body mass grows slower than either volume or the maximum sinus length) (Figures 6A,B). The correlation between ln LmaxS and ln Vol with ln TL is similarly strong, explaining approximately 70% of total variance, yet shows a positive allometry relationships (i.e., the skull length increases faster than both volume and maximum sinus length) (Figures 6C,D). In all plots of Figure 6, *V. lagopus* and *C. lupus* lie at the two extremes of variability, as the former has an extremely reduced sinus, whereas the latter has the largest and most developed sinus of all the considered species. Between these two extremes lie all the other extant species. *Eucyon adoxus* is located close to the variability of *C. simensis*, for its similar values of ln Vol and ln LmaxS, and to the lower ranges of Groups 1 hypercarnivores. *Eucyon davisi* lies a bit apart from the ecomorphological groups. The comparable values of ln LmaxS and ln TL, *E. davisi* is often close to *L. adusta* (as in Figures 6A,C,D). Considering the relationship between ln LmaxS and ln Vol (Figure 7) we have seen an interesting pattern of distribution. Group-hunters canids (Group 1 of Van Valkenburgh and Koepfli, 1993) are separated from the other canids, especially mesocarnivores (Group 3) and small-prey hypercarnivores (Group 2). This is highlighted by the regression lines with different R^2 plotted in the graph (Figure 7; Table 3). The distinction in the lines suggests the presence of an allometric grade shift between group-hunter taxa and the rest of Canidae. This is further confirmed by the ANCOVA results, showing the homogeneity of the allometric slopes ($F = 0.005$, $p = 0.947$) and the presence of significant differences between the intercepts ($F = 136.03$, $p = <0.001$) of the two groups. Hence, group hunters appear to possess a more voluminous sinus for a similar sinus length when compared to non-group hunter canid taxa. Apparently, *L. adusta* lies together with the large-prey hypercarnivores, unlike *E. davisi* or *E. adoxus*, which clustered close, almost overlapped, to *C. simensis*.

3.3. Diffeomorphic analyses

The principal component analysis (PCA) performed on the deformation fields obtained from the DSM analyses performed on the left sinus (Figure 8; Table 3; see Supplementary Material) allows discerning the four different ecological groups included in the study, particularly when the first three principal components (PCs; 46.2% of total variance) are considered at the same time. The bivariate regressions between the PCs and log-transformed BM identify the presence of a significant allometric relationship only for PC2 (Table 3), where the body mass explains half ($R^2 = 0.429$, $p < 0.001$) of its total variance, thus suggesting that BM differences play a limited role in explaining the separation observed between the analyzed taxa. The PC1 accounts for the 20.7% of the variability. Along this axis the groups fail to separate properly, with the majority of the specimens located on the positive side of the axis

TABLE 2 Results of the measurements of the specimens examined.

Species	Cat. Num.	Vol (mm^3)	LmaxS (mm)	TL (mm)	BM (kg)
Eucyon adoxus	NMB Rss.45	2692.9	28.8	182	15.5
Eucyon davisi	F:AM 97057	3014.6	30.6	167.3	11.4
Eucyon monticinensis	MSF 466	985.3*	22.1*	-	12.0^{+}
Canis aureus	MZUF-11880	1640.2	24.1	154.2	7.4
	MZUF-11878	1517.8	20.3	151.5	9.2
Canis latrans	88-50-250	3469.3	29.5	197.0	19.6
Canis lupaster	MZUF-1851	1683.4	21.6	156.4	9.6
	MZUF-2140	675.2	15.5	156.3	8.7
	MZUF-2110	712.8	18.4	150.5	8.5
	MZUF-2714	1549.1	20.4	146.5	8.5
Canis lupus	MZUF-2032	11406.5	50.7	220.1	26.0
	MZUF-11874	8772.2	46.5	223.2	26.5
	MZUF-16534	9342.2	44.8	231.5	29.2
	DST-N01	4437.5	39.6	212.6	22.3
Canis simensis	m-81.001	2579.7	28.4	208.4	22.3
	CE818	1789.9	24.3	187.2	16.3
	MZUF-13781	2935.8	28.8	203.4	21.7
Lupulella adusta	MZUF-8496	1920.9	31.4	166.5	13.2
Lupulella. mesomelas	MZUF-1843	1000.1	19.3	-	-
	MZUF-1898	1755.5	24.0	150.1	9.4
	MZUF-1128	942.2	19.7	153.6	9.8
	MZUF-1715	2382.4	26.8	147.1	-
	MZUF-3293	1293.6	22.9	132.3	6.5
Lycaon pictus	368.443	5913.1	44.1	204.0	21.4
	MZUF-1127	3323.3	36.0	192.9	20.0
Vulpes lagopus	MZUF-1474	29.5	9.5	113.1	4.4

*these measures must be taken with caution; $^{+}$estimation taken from Bartolini-Lucenti and Rook (2021), based on the regression formula by Van Valkenburgh (1990) based on length of the lower carnassial.

TABLE 3 Results of ordinary least-squares (OLS) regressions between natural log-transformed metric variables, natural log-transformed body mass, principal components (PCs), and canonical variates (CVs) used to assess the correlation between the used variables.

	R^2	*p*	Slope	SE	95% CI		Intercept	SE	95% CI	
Canidae (n = 25)										
ln LmaxS vs. ln Vol	**0.887**	**<0.001**	**0.936**	**0.071**	**0.788**	**1.084**	**0.904**	**0.181**	**0.527**	**1.281**
ln Vol vs. ln BM	**0.699**	**<0.001**	**0.638**	**0.088**	**0.454**	**0.821**	**0.883**	**0.233**	**0.398**	**1.368**
ln LmaxS vs. ln BM	**0.738**	**<0.001**	**0.652**	**0.082**	**0.481**	**0.823**	**1.6**	**0.217**	**1.154**	**2.056**
ln Vol vs. ln TL	**0.695**	**<0.001**	**1.767**	**0.242**	**1.266**	**2.269**	**−6.564**	**1.247**	**−9.149**	**−3.979**
ln LmaxS vs. ln TL	**0.718**	**<0.001**	**1.788**	**0.232**	**1.307**	**2.268**	**−5.912**	**1.195**	**−8.390**	**−3.434**
PC1 vs. ln BM	0.122	0.062	−0.402	0.204	−0.827	0.022	1.07	0.546	−0.069	2.209
PC2 vs. ln BM	**0.429**	**<0.001**	**0.554**	**0.135**	**0.272**	**0.837**	**−1.426**	**0.363**	**−2.183**	**−0.668**
PC3 vs. ln BM	0.016	0.567	0.096	0.165	−0.249	0.441	−0.264	0.443	−1.188	0.661
CV1 vs. ln BM	**0.317**	**0.004**	**−4.742**	**1.448**	**−7.763**	**−1.722**	**11.853**	**3.883**	**3.753**	**19.952**
CV2 vs. ln BM	**0.281**	**0.007**	**−2.409**	**0.793**	**−4.063**	**−0.754**	**6.492**	**2.128**	**2.054**	**10.931**
Group hunters (n = 6)										
ln LmaxS vs. ln Vol	**0.091**	**0.002**	**0.731**	**0.104**	**0.443**	**1.0187**	**1.628**	**0.304**	**0.783**	**2.472**
Non-group hunters (n = 19)										
ln LmaxS vs. ln Vol	**0.86**	**<0.001**	**0.75**	**0.075**	**0.59**	**0.91**	**1.304**	**0.181**	**0.919**	**1.689**

Significant correlations are in bold.

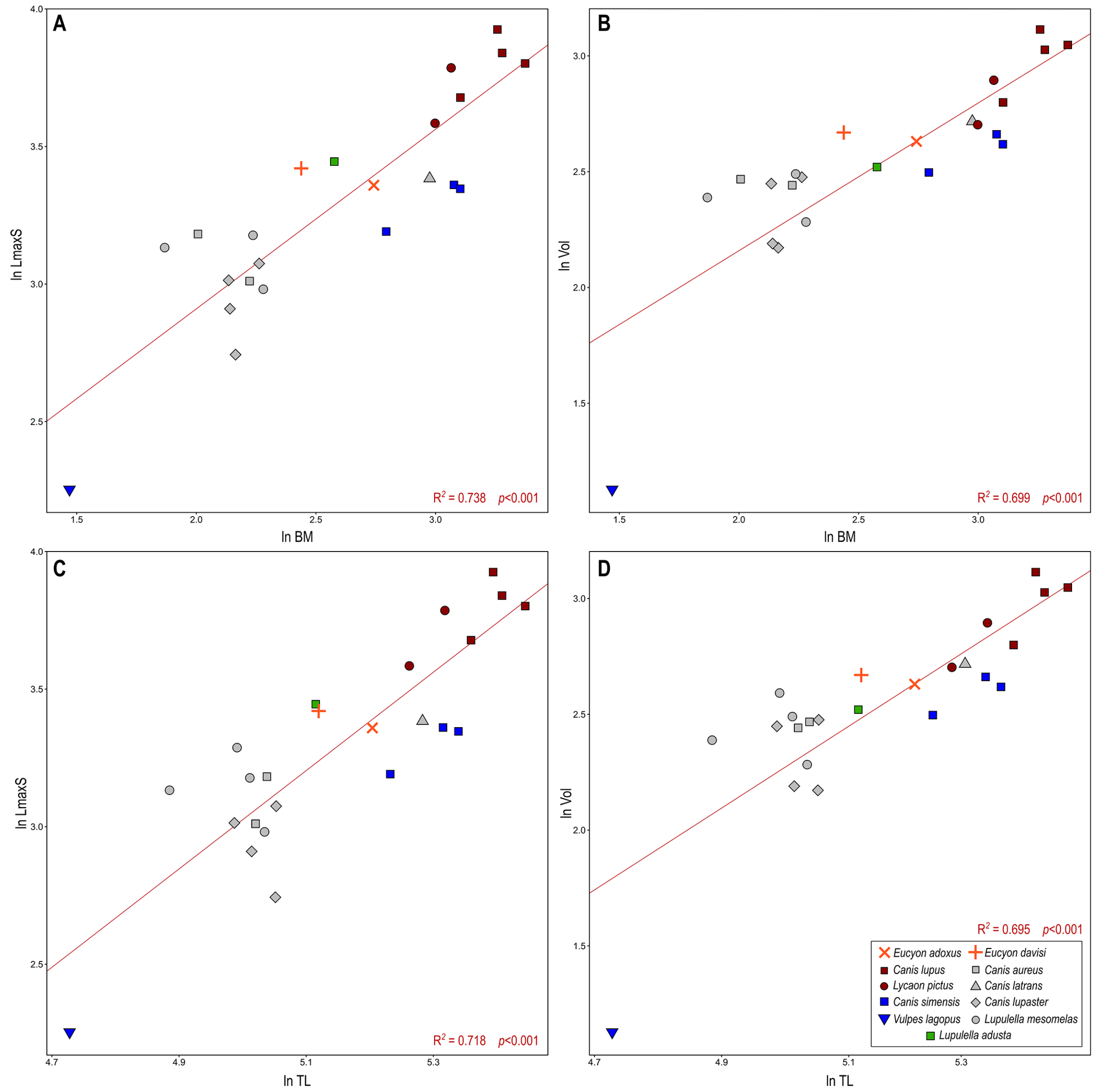

FIGURE 6
Bivariate regressions between **(A)** the natural log-transformed body mass (ln BM) vs. the log-transformed maximum rostrocaudal length of sinus (ln LmaxS). **(B)** The log-transformed body mass (ln BM) vs. the log-transformed of cubic root of volume of the sinus (ln Vol). **(C)** The natural log-transformed total length of the cranium (ln TL) vs. the log-transformed maximum rostrocaudal length of sinus (ln LmaxS). **(D)** the natural log-transformed total length of the cranium (ln TL) vs. the log-transformed of cubic root of volume of the sinus (ln Vol). Lines represent OLS (ordinary least squares regressions) best-fit lines for the whole canid sample. There is a significant correlation between all the variables (see Table 3 for further details).

and very few on negative values. *Canis lupus* and *L. pictus* (Group 1) show a wide-range variability along PC1. Apart from one specimen of *L. mesomelas*, both *Canis simensis* (Group 2) and canids of Group 3 placed in the positive side of PC1. This position corresponds to proportionally inflated (especially laterolaterally and dorsoventrally) but rostrocaudally shortened sinuses – see Figure 8C. This pattern is confirmed by their morphology (see Figure 5). *Eucyon adoxus* lies close to *C. simensis*, with a slightly low negative value of PC1. *Eucyon davisi* falls within the variability of Groups 1 and 3. PC2 accounts for 14.7% of the morphological variability. Along this axis the ecological groups are almost separated, with Groups 2 placed on the positive side of PC2, whereas the majority of Group 3 and the specimen of *L. adusta* have the negative values of the axis. Most of the specimens of Group 1 canids have high positive values of PC2. The fossil species have small positive values of PC2. The PC3 accounts for the 10.8% of the variability. Along this axis the groups are almost all clustered together toward positive values (between −0.25 and 0.5). *Eucyon* spp. lie within this cluster of extant species.

The canonical variate analysis (CVA; Figure 9) performed on the first four principal components achieves good classification results after cross-validation, with 95.2% of correctly classified individuals. A visual inspection of the bivariate plot of CV1 and CV2 confirms this result and shows a very good separation between the *a priori* identified ecological groups, with no overlap among them (Figure 9) along CV1 (80.5% of total variance). Notably, CV1 and CV2 show a strong and

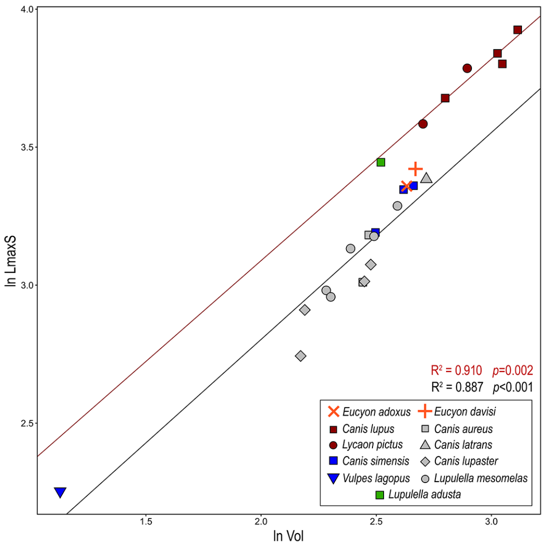

FIGURE 7
Bivariate regressions between the natural log-transformed of cubic root of volume of the sinus (ln Vol) and log-transformed maximum rostrocaudal length of sinus (ln LmaxS). Lines represent OLS (ordinary least squares regressions) best-fit lines for the whole canid sample (black) and hypercarnivorous group-hunting canids (red). There is a significant correlation between volume and the length of the sinus (see Table 3 for further details).

significant correlation with the body mass (Table 3), which explains less than half (CV1: $R^2 = 0.317$, $p = 0.004$; CV2: $R^2 = 0.281$, $p = 0.007$) of its variance. Thus implying that BM plays a role in the shape differences captured by these axes, while not being the main driver of shape variation. This is also partially reflected by the distribution of the groups along the CV1, all clearly separated from one another. Specimens of Groups 1, 2 and 3 cluster fairly well and lie at the opposite sides of the axis, respectively in its negative (Group 1) and positive (Groups 2–3) portion. The two extremes are related to completely different shapes of the sinus: the lowest values of the CV1 coincide with rostrocaudally elongated and narrow sinus, with strong rostrolateral lobes; on the contrary, the high values of CV1 correspond to laterolaterally inflated and short sinus, see Figure 9B. In between them lies the single specimen of *L. adusta*. The fossil species are located in the negative side of the axis: *E. adoxus* is enclosed in the variance of Group 1 canids, whereas the *E. davisi* has the lowest value of CV1. On the CV2 (19.5% of variance) the specimens do not separate greatly and most of them are rather comprised between −2 and 2. Only *C. simensis* lies far, with peculiarly negative low values. Along this axis, *E. adoxus* confirms its position close to Group 1 canids. *Eucyon davisi* has very high values, lying far from any group. This corresponds to fairly rostrocaudal short sinuses with developed rostral lobes. The posterior probabilities computed for *E. adoxus*, *E. davisi* and *L. adusta* on the basis of CVA scores classify these taxa as group-hunters, with a posterior probability of 100% for both fossil species and 94% for *L. adusta* (Table 4). In contrast, the typicality probabilities—which do not imply that each specimen must belong to at least one of the groups as posterior probabilities do— show that *L. adusta* and *E. davisi* represent outliers for all the considered ecological groups ($p < 0.05$). In turn, *E. adoxus* matches the variability of group-hunters ($p = 0.30$; Table 4) confirming the result of posterior probabilities.

4. Discussion

4.1. Frontal sinus: phylogenetic signal and ecological relevance

Among carnivorans, the frontal sinus as anatomical structure has been deeply studied in Hyaenidae (Vinuesa et al., 2016) and recently in Ursidae (Pérez-Ramos et al., 2020). Frontal sinus in fossil hyaenids were firstly described by Joeckel (1998), evidencing that bone-cracking forms like *Adcrocuta* possessed very enlarged frontal sinus overlapping the whole brain cavity and other jackal-like, wolf-like and transitional bone-cracker forms with lesser enlarged sinus which only overlap from 70 to 80% of the brain cavity like *Hyaenotherium*, *Palinhyaena* (Qiu et al., 1979) or *Ictitherium* (Joeckel, 1998; see also Vinuesa et al., 2015, 2016; Vinuesa, 2018, for further discussion). Despite the interesting convergent evolution between hyaenas and canids (see Supplementary Material), even in terms of frontal sinus development, that of fossil canids was never studied in detail, except for a few cases. For instance, some scholars hypothesized a posteriorly enlarged frontal sinus in some hypercarnivorous and durophagous American fossil canids like *Borophagus* (Cope, 1892) and *Epicyon* (Leidy, 1858) (see Werdelin, 1989; Tseng and Wang, 2010).

In Caninae, i.e., extant canids, the features of the frontal sinus were described for the first time by Huxley (1880), who used them as one of the main characteristics to differentiate between "Alopecoid" and "Thooid" canids. In his view, the division is justified by the lack of the frontal sinus in the former and their retention in the latter. Some scholars discarded this interpretation relating it to an increasing size (e.g., Matthew, 1924), whereas others maintained the unrelatedness between frontal sinus development and body size (we will discuss this further on). The latter interpretation favored the validity of frontal sinus features for phylogenetic interpretations such as those of Berta (1988) or Tedford et al., (1995, 2009). The studies of the late R.H. Tedford, together with X. Wang and B.E. Taylor, are among the most relevant analyses of the frontal sinus in extant and fossil Caninae. In their papers, the authors studied the absence or presence of the sinus, and its development in terms of expansion toward the postorbital process of the frontal, in lateral sense, and the frontoparietal suture, in caudal sense. Anatomical and paleontological evidence supports the interpretation of a phylogenetic information in the expansion of the frontal sinus: the early forms of Caninae (e.g., *Leptocyon* Matthew, 1918) lack a developed sinus (Tedford et al., 2009), as does most of the extant and fossil representatives of the genus *Vulpes* and *Urocyon* (Baird, 1858). In juxtaposition to this condition, *Canis* spp. have inflated sinuses that always invade the postorbital process and, in some taxa, extends toward the frontoparietal suture. The similarities between *Leptocyon*, *Urocyon* and *Vulpes* in terms of morphological features and the timing of their paleontological record (the genus *Leptocyon* is the oldest of the subfamily Caninae known since the Oligocene, whereas *Vulpes* and *Urocyon* are the oldest of extant canids to appear in the fossil record; Tedford et al., 2009) suggest the primitive nature of the absence/reduction of the frontal sinus in Caninae (confirmed also in Canidae by other observations, e.g., Wang, 1994; Wang et al., 1999). And at the same time the development in *Canis* apparently marks the derivate state of these taxa. This observation is corroborated by empirical evidence and was often used also with a systematic purpose. Tedford and Qiu (1996) included the lateral inflation of the sinus into the

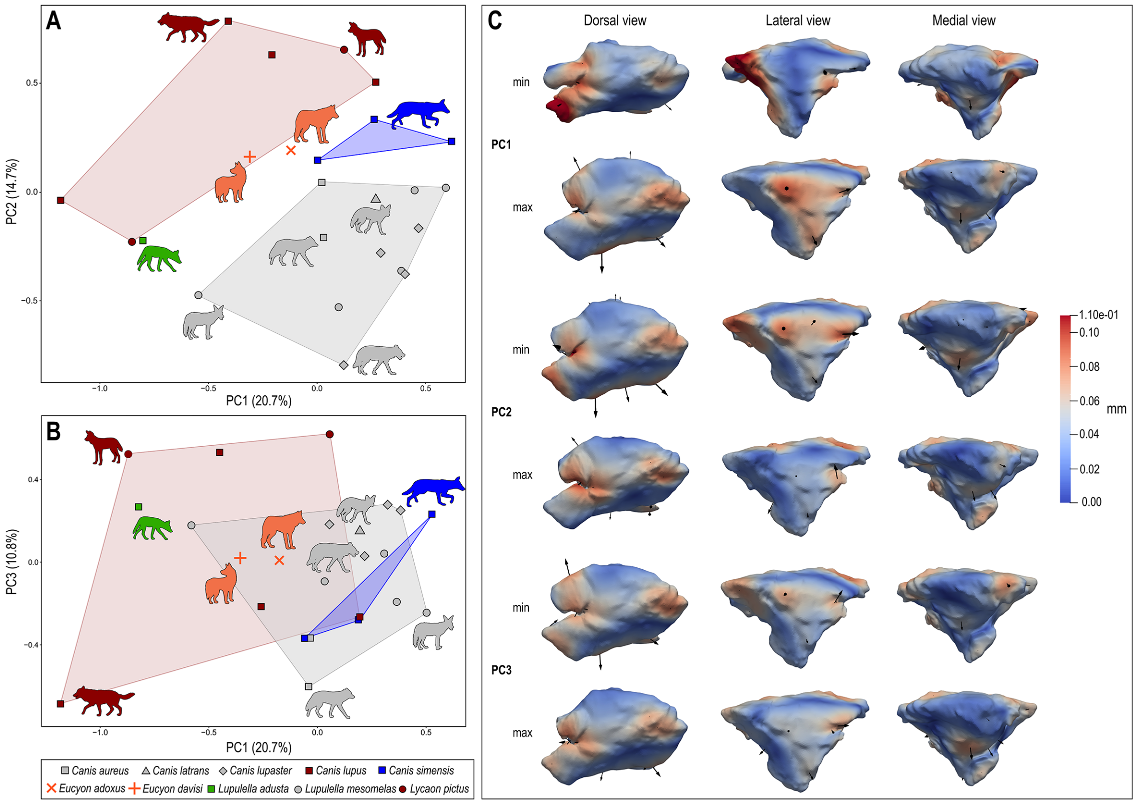

FIGURE 8
Bivariate scatterplots of PCA results performed on the deformation fields obtained from DSM analysis of sinus shape (variance for each component included within parentheses): **(A)** PC2 vs. PC1; **(B)** PC3 vs. PC1. **(C)** Maximum (below) and minimum (above) extreme conformations of shape variation are shown in dorsal (left), lateral (middle), and medial (right) views for each PC: PC1, PC2, and PC3. Cumulative deformations from mean shape are mapped on the surface by means of a pseudocolor scale ranging from dark blue (no displacement) to dark red (0.11mm). Black arrows correspond to the vectors identifying the direction and amount of displacement. Symbols and convex hulls are colored group-wise as follows: dark red – hypercarnivorous group hunters; grey – mesocarnivores; blue – hypercarnivores on small prey; green – hypocarnivores.

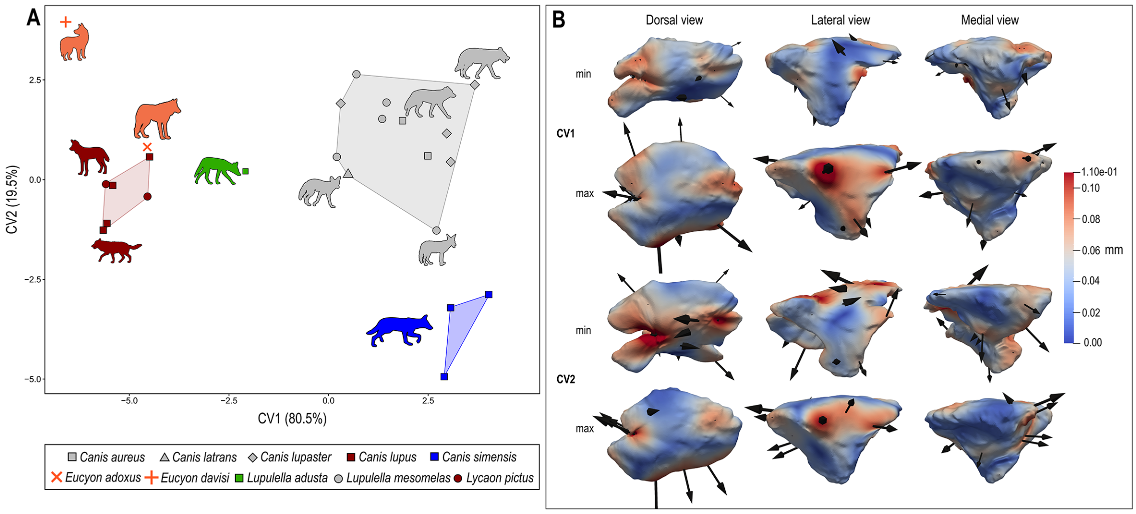

FIGURE 9
(A) Bivariate scatterplots of CVA results performed on the deformation fields obtained from DSM analysis of sinus shape (variance for each canonical variate included within parentheses). **(B)** Maximum (below) and minimum (above) extreme conformations of shape variation are shown in dorsal (left), lateral (middle), and medial (right) views for each CV: CV1 and CV2. Cumulative deformations from mean shape are mapped on the surface by means of a pseudocolor scale ranging from dark blue (no displacement) to dark red (0.11mm). Black arrows correspond to the vectors identifying the direction and amount of displacement. Symbols and convex hulls are colored group-wise as follows: dark red – hypercarnivorous group hunters; grey – mesocarnivores; blue – hypercarnivores on small prey; green – hypocarnivores.

TABLE 4 **Posterior and typicality probabilities computed for *E. adoxus*, *E. davisi*, and *L. adusta* based on canonical variate analysis (CVA) scores obtained using hunting strategy as a grouping factor.**

	Group hunters	Hypercarnivores	Mesocarnivores
Posterior probabilities			
E. adoxus NMB Rss.45	100%	0%	0%
E. davisi F:AM 97057	100%	0%	0%
L. adusta MZUF-8496	94%	0%	6%
Typicality probabilities			
E. adoxus NMB Rss.45	**0.38**	<0.001	<0.001
E. davisi F:AM 97057	<0.001	<0.001	<0.001
L. adusta MZUF-8496	0.01	<0.001	<0.001

Note that while posterior probabilities represent the likelihood of belonging to a group (expressed as a percentage), typicality probabilities are given as *p*-values for the null hypothesis of group membership so that for $p < 0.05$, the specimen can be considered an outlier for a given group. Highest posterior probabilities and significant typicality probabilities are in bold.

postorbital process as one of the diagnostic features of the genus *Eucyon*, a synapomorphy shared with *Canis*. Sotnikova (2006) described a peculiar Canini from the Pliocene of Mongolia as *Nurocyon chonokhariensis* thanks to a combination of primitive and derived features, among which sharing a large frontal sinus that invades the postorbital process with *Canis* and *Eucyon*.

Nevertheless, the information from the structure and development of the frontal sinus has also led to some phylogenetic reconstructions that contrast with molecular evidence. One of the most striking probably is relationship between the crab-eating fox (*Cerdocyon* Smith, 1839) and the raccoon dog (*Nyctereutes*): some morphological analyses (Tedford et al., 2009) include the two taxa within the Cerdocyonina (subtribe erected by Tedford et al., 2009 to include the clade of South American Caninae) whereas the molecular and total-evidence phylogenies show the distance between them (see also Figure 1). While the position of *Cerdocyon* is confirmed, *Nyctereutes* is deeply rooted within the tribe Vulpini, well separated from Canini (among others, Lindblad-Toh et al., 2005; Wayne and Ostrander, 2007; Chen and Zhang, 2012; Zrzavý et al., 2018; Figure 1). This incongruence can be explained by observing the numerous similarities that the crab-eating fox and the raccoon dog show in their cranial and dentognathic features. Among these comparable features there are the prominent subangular lobe, the expanded angular process, the reduced canines, and the development of the frontal sinus, clearly visible from a direct study of cranial specimens (Tedford et al., 1995). These characteristics are linked to diet and ecological preferences and thus most probably they represent convergent features evolved in two distantly related groups, in different context (Eurasia for *Nyctereutes* and South America for *Cerdocyon*) (Bartolini-Lucenti et al., 2018). Indeed, the development of sinuses in *Nyctereutes* has been related by some authors to the possibility of producing relatively large bite forces while feeding (Curtis, 2014; Curtis and Van Valkenburgh, 2014), just like in larger canids (Slater et al., 2009; Tseng and Wang, 2010). Similar ecological interpretation, rather than phylogenetic one, was applied to the Late Miocene taxon *Eucyon ferox* (Miller and Carranza-Castañeda, 1998). Once considered the first member of the genus *Canis*, also due to the development of its frontal sinus, a recent reassessment of its general features suggests a more plausible interpretation of the taxon to the genus *Eucyon* and with a hypercarnivorous diet (Bartolini-Lucenti and Rook, 2021). As in the case of *Nyctereutes*, the development of the sinus of *E. ferox* is thus plausibly related to its diet.

4.2. Frontal sinus and inferred diet preferences

Despite the variability displayed by this structure, the comparison of different morphologies of the frontal sinus possessed by the different canids has shown some patterns (Figure 5). Most of the features discussed above seem to correspond to an ecological affinity rather than a phylogenetic relationship between species with similar sinus morphologies. Indeed, in some cases, phylogenetically related taxa differ more than with distantly related ones. For instance, the species identified as mesocarnivorous (*C. aureus*, *C. latrans*, *C. lupaster* and *L. mesomelas*; n.b., all members of Group 3) have comparable general shapes of the sinuses. They show, e.g., shallower rostral incisions and modest and simple rostrolateral lobes, less developed compared to the hypercarnivorous ones, like *C. lupus* (Group 1) and *C. simensis* (Group 2). Moreover, mesocarnivorous species share fairly smooth dorsal surface of the sinus, without marked sulci on it. The only exception to this smooth pattern is *C. latrans*, which shows a particularly evident caudal prominence, identified by a transverse dorsal sulcus (Figure 5). As far as hypercarnivorous species are concerned, it should be noted that Groups 1 and 2 show a great difference between them: the former has simpler lobes in the rostral region whereas the latter has more developed and more complex rostral lobes. Furthermore, the sinus of *C. simensis* has low prominences on its dorsal side, although some sulci are still visible on its surface, and, in general terms, are deeper than those of mesocarnivorous canids. On the contrary, the sinus of *C. lupus* is considerably more complex and marked by deep sulci and evident prominences (Figure 5). A great complexity and pneumatization is evident also in *L. pictus*. *Lupulella adusta*, here represented by a single specimen, has its own peculiarities. Unlike the mesocarnivorous species, the sinus is developed, elongated rostrocaudally and possesses relatively high prominences on its dorsal surface. The grouping of taxa according to ecological affinity is testified also by the morphometric analyses here carried out (Figures 6–9). Independently from the methodology and the application (i.e., log-transformed measures or 3D meshes), the results coherently point out two distinct groups, separated from one another. All this evidence fits with the inferences of other scholars (e.g., Curtis and Van Valkenburgh, 2014) on the degree of pneumatization and the development of the frontal sinus according to feeding ecology. The grade shift between group hunters (Group 1) and the others, despite their diet (namely Group 2–3) add further support to this interpretation (Figure 7). Interestingly, the position of *L. adusta* matches the hypothesis: larger stresses during feeding (whether from food items or prey hunting) seem to result in comparably larger and convoluted sinuses in group hunters and hypocarnivorous canids. If such inference can be easily drawn from Group 1 species, in the case of Group 4 ones (though here represented by a single specimen), at the very least, the results corroborate the observation by Curtis and Van Valkenburgh (2014) regarding *N. procyonoides* (another typical hypocarnivorous, i.e., Group 4, taxon, following Van Valkenburgh and Koepfli, 1993).

Therefore, our analyses confirm how relevant frontal sinus is as an anatomical structure and yet the numerous parameters that influence its development. Surely, like Matthew (1924) hypothesized, body mass has an influence on the development of the sinus. Nevertheless, the influence of phylogeny pointed out by several scholars (e.g., Berta, 1988; Tedford et al., 2009; see above) is undeniable. Generally, members of the tribe Vulpini do not have frontal sinus, whereas, on the contrary, Canini always do possess the sinus, with different development (Figures 4, 5). When comparing the morphology of the sinus within Canini, some phylogenetically controlled features seem to be present (e.g., an expanded rostromedial lobe in *Canis* s.s. unlike *Lupulella*). Nevertheless, other smaller scale differences or peculiar similarities between the species here considered cannot be easily explained with phylogeny. The third parameter with a relevant role in shaping the frontal sinus of canids is their ecology, in terms of dietary habits. Indeed, this structure is linked to a complex and interrelated set of characteristics which must be simultaneously taken into consideration when studying fossil species. Despite the deformation that hinders morphometric analyses, the sinus of *E. monticinensis* is modestly developed and characterized by a similarity with the genus *Lupulella*, rather than *Canis*. This similarity is shared also by *E. davisi*. In both fossil taxa, the developed rostrolateral lobe marks this similarity, especially with *L. adusta*. Despite the mild deformations, the similarity of the sinus of *E. monticinensis* with the species of the African *Lupulella* is interesting for its timing. *Eucyon monticinensis* represents one of the oldest undisputed records of Canidae in western Eurasia (age of the type locality: *ca* 5.6–5.3 Ma; Rook, 1992; Bartolini-Lucenti et al., 2022; Figure 1), part of the '*Eucyon* event' of the Late Miocene (Sotnikova and Rook, 2010). The time of divergence of the genus *Lupulella* from the *Canis*-clade following recent molecular analyses (e.g., Perri et al., 2021) is estimated around 5.1 Ma. There are Late Miocene records of *Eucyon* in Africa (e.g., *E. intrepidus* from Kenya), which nevertheless were recently disputed by some authors for the scanty nature and the inconsistency of their features (see Werdelin et al., 2015 for a deeper discussion on the issue). Taxa typical of '*Eucyon* event', e.g., *E. monticinensis* and *E. davisi* from Asia (Sotnikova and Rook, 2010), could be at the base of the radiation of this jackal-like canids in Eurasia but also in Africa. *Lupulella* might be the extant descendant of such dispersal and radiation. The interpretation does not contrast with present phylogenetic hypotheses (e.g., Zrzavý et al., 2018) and finds support in the patterns of morphological and morphometric affinities obtained here. Regarding *E. davisi*, linear morphometric parameters were not conclusive in classifying the diet of this fossil taxa with any of extant dietary groups, if not for a similarity with Group 3 species (Bartolini-Lucenti and Rook, 2021). Dentognathic features do not hint at any peculiar dietary specialization to hypo- or hypercarnivory (Rook, 2009). Our results show certain degree of peculiarity of *E. davisi* compared to other species, which lies close to *L. adusta* in the linear models (Figure 6) but does not follow the allometric grade shift between natural log-transformed volume and maximum length (Figure 7) and clearly differs from all other groups when total shape is considered (Figures 8, 9).

Different is the case of *E. adoxus*. The development of the rostromedial lobe, or the prominent convoluted dorsal morphology does not support a similarity to mesocarnivorous species (Group 3). This interpretation can be disregarded also considering the results of the morphometric analyses (Figures 6–9). It also differs from the proportionally wider and shallower sinus of *C. simensis*. Morphologically and morphometrically, our results suggest that *E. adoxus* was subject to a relevant amount of stress, comparable, proportionally, to that experienced by Group 1 canids. Such a similarity contrasts with its cranial and dentognathic features, which do not support an ascription to this ecomorphogroup (see also Bartolini-Lucenti and Rook, 2021). It could be argued that even the single specimen of *L. adusta* falls close to hypercarnivorous group-hunters in some analyses (Figures 7, 8; Table 4) and yet the morphological features of this canid are clearly hypocarnivorous. Even in this case, an ascription of *E. adoxus* to hypocarnivorous group can be easily excluded for its dentognathic features. The elongated cranium, the diastemata between premolars, with their pointy cusps, and sharp molars are more definitely close to those of *C. simensis*. Nevertheless, as reminded above, the distinction in terms of frontal sinus development between *E. adoxus* and *C. simensis* is significant. Studying the frontal sinus of Group 2 species is difficult as three out of four species ascribed at this ecomorphogroup are of the genus *Vulpes*, with virtually no sinus [*V. lagopus*, see the 'protosinus' in Figure 5; *Vulpes macrotis* (Merriam, 1888) and *Vulpes corsac* (Linnaeus, 1768)]. The only representant that possesses a sinus is *C. simensis*, and even in this species it is not particularly expanded nor so convoluted (see Figure 5). Almost resembling the condition of Group 3 canids (e.g., *C. aureus* or *C. lupaster*). The hypercarnivorous diet of this canid, based primarily on rodents like the big-headed African mole-rat (*Tachyoryctes macrocephalus* Rüppell, 1842) (Kingdon, 1989), does not imply elevated stresses for their masticatory apparatus. This explains the morphology and modest development of *C. simensis* sinus, despite the degree of carnivory especially in comparison with mesocarnivorous (Group 3). Much evidence supports this: for instance, Van Valkenburgh and Koepfli (1993) showed that, indeed, mesocarnivorous species have more robust mandibles compared to Group 2 species. The cranial and dental morphology of *E. adoxus* fit with the interpretation of this taxon as small-prey hypercarnivorous (Group 2). The more convoluted sinus of *E. adoxus* cannot be explained suggesting that it was capable of hunting large prey, like some Group 3 taxa, as neither its linear morphometric parameters (Bartolini-Lucenti and Rook, 2021) nor the tridimensional morphology of the sinus support it. More plausibly the preferred prey of this canid was larger than those of *C. simensis*. Bartolini-Lucenti and Rook (2021) used the least regression equation of Van Valkenburgh et al. (2003) to estimate typical prey size of *E. adoxus*, obtaining a prey weight of 5 kg. This estimation greatly exceeds the average size of the larger typical prey of *C. simensis* (*T. macrocephalus*: ~400–900 g, Yalden, 1985) and it is close to extant leporid lagomorphs like hares (genus *Lepus* Linnaeus, 1758). A connection between elongated cranium and mandible, characterized by diastemata, and a lagomorph-based diet was proposed for other fossil canids, e.g., *Cynotherium sardous* (Studiati, 1857) from Sardinia (see Lyras et al., 2006; Lyras and Van der Geer, 2006; Madurell-Malapeira et al., 2015). Lagomorphs experienced a moment of great radiation at the beginning of the Pliocene (Lopez-Martinez, 2008) and dispersal events characterizing different regions and bioprovinces of Eurasia (Maridet et al., 2007). Among the large rodents and lagomorphs of the Early-Late Pliocene of western Europe, several taxa were present, e.g., *Castor* (Linnaeus, 1758); *Trogontherium* (von Waldheim, 1809); *Hystrix* (Linnaeus, 1758); *Hypolagus* (Dice, 1917); and *Oryctolagus* (Lilljeborg, 1874) (see Hugueney, 2004; Lopez-Martinez, 2008). Of these, the former three are generally of large size (Hugueney, 2004), despite the presence of a small-sized *Trogontherium minus* (Newton, 1890) that was found in Red Crag (MN15, UK, Fostowicz-Frelik, 2008) and Perrier-Les Etouaries (Hugueney et al., 1989). Although the latter site is younger than type locality of *E. adoxus*, St. Estève (Roussillon Basin; France; Nomade et al., 2014), the former site is one of the few other occurrences of *E. adoxus* in Europe (Rook, 2009). The Pliocene leporine lagomorph *Hypolagus* (extinct) and *Oryctolagus* were surely smaller compared to the larger rodents before mentioned, but still robust forms compared to the extant species, like *Oryctolagus laynensis* (López Martínez, 1977) (see López-Martínez, 1989; Lopez-Martinez, 2008). They were recorded in the late Early and Late Pliocene of western Europe, also in the Roussillon basin (Mein and Aymar, 1984) together with *Trischizolagus* (Radulesco and Samson, 1967) (another leporine lagomorph). *Eucyon davisi* apparently fed on smaller prey, since the estimated prey size is around 2 kg (Bartolini-Lucenti and Rook, 2021). Interestingly even for *E. monticinensis* the estimated prey size is around 5 kg

FIGURE 10
Restoration of the three *Eucyon* species studied here with their fossil crania highlighting the position of the frontal sinuses, in red. Top: *Eucyon davisi* and the cranium F:AM 97057, on the right. Centrum: *Eucyon adoxus* and the specimen NMB Rss.45, on the left. Bottom: *Eucyon monticinensis* with fragmented cranium MSF 466. Artwork by Cecilia Loddi.

(Bartolini-Lucenti and Rook, 2021). Nevertheless, neither the latter two *Eucyon* spp. possess a specialized dentition nor mandibular features allowing us to narrow down a preferred diet. The morphology of their sinuses seems non-conclusive either.

5. Concluding remarks

Despite the known relevance of the frontal sinus for the phylogeny and ecology of Carnivora, no previous work has ever focused specifically on the morphology of this structure in extant and fossil canids nor described it in detail. This study represents the first attempt to characterize the frontal sinus of Canidae, using CT and micro-CT scans to assess its 3D shape via an innovative 3D geometric morphometric method (i.e., diffeomorphic surface matching analysis), which allows the direct comparison between continuous surfaces in a landmark-free fashion.

The results for extant Caninae show a great correspondence between morphology and renowned ecomorphotype (see Van Valkenburgh and Koepfli, 1993) supporting previous interpretations on the direct influence of diet and feeding behavior on the relative development of frontal sinus in the different canid species. Regarding the fossil species, we were able to reconstruct for the first time the whole sinuses of three *Eucyon* spp. (Figure 10) and compare them with the extant species. The deformation of the specimen of *E. monticinensis* from Cava Monticino does not allow a proper study of the sinus. On the contrary, *E. adoxus*, one of the most enigmatic canids of the Pliocene of the western Eurasia, show a sinus with developed prominences testifying to a relevant stress during feeding, proportionally like hypercarnivorous canids, if not even group-hunters. The dentognathic features of *E. adoxus* do not support an interpretation of this early Canini as a hunter of large prey but more of small prey specialist, like *C. simensis*. The resemblance between these two species can also be retraced to the cranial and mandibular characteristics.

The novel combination of morphological, linear and 3D morphometric analyses has allowed the first rigorous characterization of the frontal sinus of fossil canids of the genus *Eucyon* (Figure 10), revealing the importance of such anatomical structure and its deep connection with size, phylogeny, and ecology of the considered species. The methodology and the analyses here carried out for the first time could be useful tools to help characterizing the frontal sinus and investigating the dietary preferences of fossil carnivorans.

Data availability statement

Publicly available datasets were analyzed in this study. This data can be found at: http://dx.doi.org/10.5281/zenodo.7836886.

Author contributions

SF segmented the tomographic data and prepared a preliminary draft of the text with the help of SB-L and LR. SB-L prepared the linear and 3D data and performed statistical analyses. AU carried out the geometric morphometric analysis. SB-L, JM-M, and AU prepared the manuscript with the contribution of SF, LR, and LC. All author revised and approved the final version of the text.

Funding

SB-L is supported by the Tuscany Region funds for young researchers "Giovanisì" (www.giovanisi.it): "POR FSC 2014–2020" funds for "Progetti di alta formazione attraverso l'attivazone di Assegni di Ricerca." LR acknowledges the support of CHANGES Foundation to the University of Florence (Earth Sciences Department), funded by the Italian Ministry of University and Research, PNRR, Missione 4 Componente 2, "Dalla ricerca all'impresa," Investimento 1.3, Project PE_0000020.

Acknowledgments

The authors are thankful to the kindness of the curators who allowed us to scan the specimens in their collections or to access them online: Paolo Agnelli, curator of the Zoological Museum "La Specola" (Museum of Natural History of the University of Florence, Italy); Enzo Bagnaresi and Marco Sami of the Civic Museum of Natural Sciences of Faenza (Italy); Laurel Lamb of the University of Arkansas Museum (Fayetteville, Arkansas, U.S.A.); Neil Duncan, Collections Manager of the American Museum of Natural History (New York, U.S.A.); Jessie Maisano, Department of Geological Sciences, Jackson School of Geosciences, University of Texas at Austin (U.S.A.). They are indebted to the staff of the San Giovanni di Dio Hospital (Florence, Italy), especially to Elisabetta Peruzzi and Giovanni Dedola and all the technicians of Medical Radiology ward ("SOS Radiologia") for granting us access to their CT-scanner and support while processing raw data. We thank greatly Georgios Lyras for kindly providing us the scan of *E. davisi*. They thank Georg Schulz and Bert Müller for access to the CT-scanner at the Biomaterials Science Center of the University of Basel. We thank Cecilia Loddi for the gorgeous restoration of our *Eucyon* species.

Conflict of interest

The authors declare that the research was conducted in the absence of any commercial or financial relationships that could be construed as a potential conflict of interest.

Publisher's note

Supplementary material

The Supplementary material for this article can be found online at: https://www.frontiersin.org/articles/10.3389/fevo.2023.1173341/full#supplementary-material

References

Baird, S.F. (1858). *Mammals: Upon the zoology of the several Pacific railroad routes. Reports, explorations and surveys for railroad route from Mississippi River to Pacific Ocean 8*: xix–xlviii, 1–757. Washington, DC: Tucker.

Balzeau, A., Albessard-Ball, L., Kubicka, A. M., Filippo, A., Beaudet, A., Santos, E., et al. (2022). Frontal sinuses and human evolution. *Sci. Adv.* 8:eabp9767. doi: 10.1126/sciadv.abp9767

Bartolini-Lucenti, S., Bukhsianidze, M., Martínez-Navarro, B., and Lordkipanidze, D. (2020). The wolf from Dmanisi and augmented reality: review, implications, and opportunities. *Front. Earth Sci.* 8:131. doi: 10.3389/feart.2020.00131

Bartolini-Lucenti, S., Madurell-Malapeira, J., and Rook, L. (2022). The carnivorans from cava Monticino (Faenza, Italy; Messinian) revisited. *Hist. Biol.* 34, 1458–1470. doi: 10.1080/08912963.2022.2042806

Bartolini-Lucenti, S., and Rook, L. (2021). "*Canis*" *ferox* revisited: diet ecomorphology of some long gone (late Miocene and Pliocene) fossil dogs. *J. Mamm. Evol.* 28, 285–306. doi: 10.1007/s10914-020-09500-1

Bartolini-Lucenti, S. B., Rook, L., and Morales, J. (2018). *Nyctereutes* (Mammalia, Carnivora, Canidae) from Layna and the Eurasian raccoon-dogs: an updated revision. *Riv. Ital. Paleontol. Stratigr.* 124, 597–616. doi: 10.13130/2039-4942/10739

Beaudet, A., Dumoncel, J., Thackeray, J. F., Bruxelles, L., Duployer, B., Tenailleau, C., et al. (2016). Upper third molar internal structural organization and semicircular canal morphology in Plio-Pleistocene south African cercopithecoids. *J. Hum. Evol.* 95, 104–120. doi: 10.1016/j.jhevol.2016.04.004

Berta, A. (1988). Quaternary evolution and biogeography of the large south American Canidae (Mammalia, Carnivora). *Geol. Sci.* 132:149.

Bône, A., Louis, M., Martin, B., and Durrleman, S. (2018). "Deformetrica 4: an open-source software for statistical shape analysis" in *Shape in medical imaging. Shape MI 2018*. eds. M. Reuter, C. Wachinger, H. Lombaert, B. Paniagua, M. Lüthi and B. Egger (Cham: Springer), 3–13.

Boudadi-Maligne, M. (2010). Les Canis pleistocenes du sud de la France: approche biosystematique, evolutive et biochronologique. Available at: https://tel.archives-ouvertes.fr/tel-00908031/ (Accessed April 21, 2023).

Chen, L., and Zhang, H. (2012). The complete mitochondrial genome and phylogenetic analysis of *Nyctereutes procyonoides*. *Acta Ecol. Sin.* 32, 232–239. doi: 10.1016/j.chnaes.2012.07.003

Cope, E. D. (1892). A hyena and other Carnivora from Texas. *Am. Nat.* 26, 1028–1029.

Curtis, A. A. (2014). A three-dimensional quantitative investigation of frontal sinus morphology and function in mammalian carnivores. Available at: https://escholarship.org/uc/item/2ts7c0b1 (Accessed April 21, 2023).

Curtis, A. A., Orke, M., Tetradis, S., and Van Valkenburgh, B. (2018). Diet-related differences in craniodental morphology between captive-reared and wild coyotes, *Canis latrans* (Carnivora: Canidae). *Biol. J. Linnean Soc.* 123, 677–693. doi: 10.1093/biolinnean/blx161

Curtis, A. A., and Van Valkenburgh, B. (2014). Beyond the sniffer: frontal sinuses in carnivora. *Anat. Rec.* 297, 2047–2064. doi: 10.1002/ar.23025

De Bonis, L., Peigné, S., Likius, A., Mackaye, H. T., Vignaud, P., and Brunet, M. (2007). The oldest African fox (Vulpes riffautae n. sp., Canidae, Carnivora) recovered in late Miocene deposits of the Djurab desert, Chad. *Naturwissenschaften* 94, 575–580. doi: 10.1007/s00114-007-0230-6

Del Campana, D. (1913). Cani pliocenici della Toscana. *Palaeontogr. Ital.* 19, 189–254.

Dice, L.R. (1917). *Systematic position of several American Tertiary lagomorphs*. Berkeley, CA: University of California Press

Durrleman, S., Pennec, X., Trouvé, A., Ayache, N., and Braga, J. (2012). Comparison of the endocranial ontogenies between chimpanzees and bonobos via temporal regression and spatiotemporal registration. *J. Hum. Evol.* 62, 74–88. doi: 10.1016/j.jhevol.2011.10.004

Durrleman, S., Prastawa, M., Charon, N., Korenberg, J. R., Joshi, S., Gerig, G., et al. (2014). Morphometry of anatomical shape complexes with dense deformations and sparse parameters. *NeuroImage* 101, 35–49. doi: 10.1016/j.neuroimage.2014.06.043

von Waldheim, G. F. (1809). Sur l'*Elasmotherium* et le *Trogontherium*, deux animaux fossils et inconnus de la Russie. *Memoirs de l'Academie Imperiale des Sciences de Moscou* 2, 250–268.

Forsyth-Major, C. I. (1877). Considerazioni sulla fauna dei mammiferi pliocenici e post-pliocenici della Toscana. *Atti Soc. Tosc. Sci. Nat. Mem.* 3, 207–227.

Fostowicz-Frelik, Ł. (2008). First record of *Trogontherium cuvieri* (Mammalia, Rodentia) from the middle Pleistocene of Poland and review of the species. *Geodiversitas* 30, 765–778.

Fox, J., and Weisberg, S. (2019). *An R companion to applied regression, 3rd*. Sage, Thousand Oaks CA

Garrido, G., and Arribas, A. (2008). *Canis accitanus* nov. sp., a new small dog (Canidae, Carnivora, Mammalia) from the Fonelas P-1 Plio-Pleistocene site (Guadix basin, Granada, Spain). *Geobios* 41, 751–761. doi: 10.1016/j.geobios.2008.05.002

Glaunès, J. A., and Joshi, S. (2006). "Template estimation form unlabeled point set data and surfaces for computational anatomy" in *MICCAI 2006 workshop proceedings. MFCA'06 workshop. Mathematical foundations of computational anatomy: Geometrical and statistical methods for modelling biological shape variability*. eds. X. Pennec and S. Joshi (Copenhagen: INRIA/MICCAI), 29–39.

Hemprich, F. G., and Ehrenberg, C. G. (1828/1834). "Symbolae Physicae" in *Seu Icones et Descriptiones Corporum Naturalium Novorum aut minus Cognitorum quae ex Itineribus per Libyam, Aegyptium, Nubiam, Dongalam, Syriam, Arabiam et Habessiniam, pars Zoologica II, Anima* (Berlin: Officina Academica).

Hugueney, M. (2004). Large rodents from the upper Pliocene of saint-Vallier (Drôme, France): Castoridae, Hystricidae (Mammalia, Rodentia). *Geobios* 37, S126–S132. doi: 10.1016/S0016-6995(04)80012-3

Hugueney, M., Guérin, C., and Poidevin, J.-L. (1989). Découverte de *Trogontherium minus* Newton, 1890 (Rodentia: Castoridae) dans le Villafranchien inférieur de Perrier-Étouaires (Puy-de-Dôme, France): implications phylogénétiques. *Comptes Rendus de l'Académie des Sciences, série II* 309, 763–768.

Huxley, T. H. (1880). On the cranial and dental characters of the Canidæ. *Proc. Zool. Soc. London* 48, 238–288. doi: 10.1111/j.1469-7998.1880.tb06558.x

Joeckel, R. M. (1998). Unique frontal sinuses in fossil and living hyaenidae (Mammalia, Carnivora): description and interpretation. *J. Vertebr. Paleontol.* 18, 627–639. doi: 10.1080/02724634.1998.10011089

Kingdon, J. (1989). *Island Africa: The evolution of Africa's rare plants and animals*, Princeton, NJ: Princeton University Press. ISBN 0–691–08560-9.

Kretzoi, M. (1938). Die Raubtiere von Gombaszög nebst einer Übersicht der Gesamtfauna. *Ann. Musei Natl. Hungarici Pars Mineral. Geol. Palaeontol.* 31, 88–157.

Leidy, J. (1858). Notice of remains of extinct Vertebrata, from the valley of the Niobrara River, collected during the exploring expedition of 1857, in Nebraska, under the command of Lieut. G. K. Warren, U.S. top. Eng., by Dr. F. V. Hayden, geologist to the expedition. *Proc. Acad. Nat. Sci. Philadelphia* 1858, 20–29.

Lindblad-Toh, K., Wade, C. M., Mikkelsen, T. S., Karlsson, E. K., Jaffe, D. B., Kamal, M., et al. (2005). Genome sequence, comparative analysis and haplotype structure of the domestic dog. *Nature* 438, 803–819. doi: 10.1038/nature04338

Lilljeborg, W. (1874). *Fauna Ofver Sveriges och Norges Ryg- gradsdjur I. Daggdjuren*. Uppsala: W. Schultz.

Linnaeus, C. (1758). *Systema Naturae per regna Tria Naturae, Secundum classes, ordines, genera, species, cum Characteribus, Differentiis. Synonymis, Locis. Tomus I. Editio Decima, Reformata* Stockholm: Laurentius Salvius

Linnaeus, C. (1768). *Systema naturae per regna tria naturae, secundum classes, ordines, genera, species, cum characteribus, differentiis synonymis, locis. Regum animale. Class I, Mammalia. 12th*. Stockholm: Laurentius Salvius.

López Martínez, N. (1977). Nuevos lagomorfos (Mamma- lia) del Terciario y Cuaternario de España. *Trab Neógeno-Cuaternario* 8, 7–45.

López-Martínez, N. (1989) Revisión sistemática y bioestratigráfica de los Lagomorpha (Mammalia) del Terciario y Cuaternario inferior de España. PhD Univ. Madrid 1977, published in mem. Museo Paleont., Univ. Zaragoza, Madrid.

Lopez-Martinez, N. (2008). "The Lagomorph Fossil Record and the Origin of the European Rabbit," in *Lagomorph Biology*, eds. P. C. Alves, N. Ferrand and K. Hackländer (Berlin, Heidelberg: Springer-Verlag Berlin Heidelberg), 27–46

Lyras, G., and Van Der Geer, A. (2006). Adaptations of the Pleistocene Island canid *Cynotherium sardous* (Sardinia, Italy) for hunting small prey. *Cranium* 23, 51–60.

Lyras, G. A., van der Geer, A. A. E., Dermitzakis, M. D., and De Vos, J. (2006). *Cynotherium sardous*, an insular canid (Mammalia: Carnivora) from the Pleistocene of Sardinia (Italy), and its origin. *J. Vertebr. Paleontol.* 26, 735–745. doi: 10.1671/0272-4634(2006)26[735:CSAICM]2.0.CO;2

Madurell-Malapeira, J., Palombo, M. R., and Sotnikova, M. (2015). *Cynotherium malatestai*, sp. nov. (Carnivora, Canidae) from the early middle Pleistocene deposits of Grotta dei Fiori (Sardinia, Western Mediterranean). *1. J. Vertebr. Paleontol.* 35:e943400. doi: 10.1080/02724634.2014.943400

Marciszak, A., Kropczyk, A., and Lipecki, G. (2021). The first record of *Cuon alpinus* (Pallas, 1811) from Poland and the possible impact of other large canids on the evolution of the species. *J. Quat. Sci.* 36, 1101–1121. doi: 10.1002/jqs.3340

Maridet, O., Escarguel, G., Costeur, L., Mein, P., Hugueney, M., and Legendre, S. (2007). Small mammal (rodents and lagomorphs) European biogeography from the late Oligocene to the mid Pliocene. *Glob. Ecol. Biogeogr.* 16, 529–544. doi: 10.1111/j.1466-8238.2006.00306.x

Martin, R. (1973). Trois nouvelles especes de Caninae (Canidae, Carnivora) des gisements plio-villafranchiens d'Europe. *Doc. des Lab Géologie la Fac. des Sci. Lyon* 57, 87–96.

Martínez-Navarro, B., Gossa, T., Carotenuto, F., Bartolini-Lucenti, S., Palmqvist, P., Asrat, A., et al. (2023). The earliest Ethiopian wolf: implications for the species evolution and its future survival. *Commun. Biol.* 6:350. doi: 10.1038/s42003-023-04908-w

Matthew, W. D. (1918). Contributions to the Snake Creek Fauna. *Bull. Am. Mus. Nat. Hist.* 38, 183–229.

Matthew, W. D. (1924). Third contribution to the Snake Creek fauna. *Bull. Am. Mus. Nat. Hist.* 50, 59–210.

McGreevy, P., Grassi, T. D., and Harman, A. M. (2004). A strong correlation exists between the distribution of retinal ganglion cells and nose length in the dog. *Brain. Behav. Evol.* 63, 13–22. doi: 10.1159/000073756

Mein, P., and Aymar, J. (1984). Decouvertes recentes de mammiferes dans le Pliocene du Roussillon. Note preliminaire. *Publications du Mus. Confluences* 22, 69–71.

Merriam, C.H. (1888). *Description of a new fox from Southern California: Vulpes macrotis sp. nov. long-eared fox*. Gibson Bros.

Merriam, J. C. (1911). Tertiary mammal beds of Virgin Valley and Thousand Creek in north-western Nevada. Part 2. Vertebrate faunas. *Bull. Depart. Geol. Univ. Califor.* 11, 199–304.

Miller, W. E., and Carranza-Castañeda, O. (1998). Late tertiary canids from Central Mexico. *J. Paleontol.* 72, 546–556. doi: 10.1017/S002233600002432X

Montoya, P., Morales, J., and Abella, J. (2009). Eucyon debonisi n. sp., a new Canidae (Mammalia, Carnivora) from the latest Miocene of Venta del Moro (Valencia, Spain). *Geodiversitas* 31, 709–722. doi: 10.5252/g2009n4a709

Morales, J., Pickford, M., and Soria, D. (2005). Carnivores From the Late Miocene and Basal Pliocene of the Tugen Hills, Kenya. *Rev. la Soc. Geol. Espana* 18, 39–61.

Newton, E. T. (1890). On some new mammals from the red and Norwich crags. *Quart. J. Geol. Soc. London* 46, 444–453. doi: 10.1144/GSL.JGS.1890.046.01-04.29

Nomade, S., Pastre, J. F., Guillou, H., Faure, M., Guérin, C., Delson, E., et al. (2014). 40Ar/39Ar constraints on some French landmark late Pliocene to early Pleistocene large mammalian paleofaunas: paleoenvironmental and paleoecological implications. *Quat. Geochronol.* 21, 2–15. doi: 10.1016/j.quageo.2012.12.006

Odintzov, I. A. (1967). New species of Pliocene Carnivora, *Vulpes odessana* sp. nov. from the karst cave of Odessa. *Paleontolog Sbornik, L'vov University* 4, 130–137. (in Russian)

Paulli, S. (1900). Über die Pneumaticität des Schädels bei den Säugetieren. Eine morphologische Studie III. Über die Morphologie des Siebbeins und Pneumaticität bei den Insectivoren, Hyracoideen, Chiropteren, Carnivoren, Pinnipedien, Edentates, Rodentiern, Prosimien und Primaten. *Gegenbaurs Morphologisches Jahrbuch* 28, 483–564.

Pei, W. (1934). On the Carnivora from locality 1 of Choukoutien. *Palaeontol. Sin. Ser. C* 8, 1–216.

Pérez-Ramos, A., Tseng, Z. J., Grandal-D'Anglade, A., Rabeder, G., Pastor, F. J., and Figueirido, B. (2020). Biomechanical simulations reveal a trade-off between adaptation to glacial climate and dietary niche versatility in European cave bears. *Sci. Adv.* 6:eaay9462. doi: 10.1126/sciadv.aay9462

Perri, A. R., Mitchell, K. J., Mouton, A., Álvarez-Carretero, S., Hulme-Beaman, A., Haile, J., et al. (2021). Dire wolves were the last of an ancient New World canid lineage. *Nature* 591, 87–91. doi: 10.1038/s41586-020-03082-x

Qiu, Z., Deng, T., and Wang, B. (2004). Early Pleistocene mammalian fauna from Longdan, Dongxiang, Gansu, China. *Paleontol. Sin.* 27:198.

Qiu, Z., Huang, W.-L., and Cuo, Z.-H. (1979). Hyaenidae of the Qingyang (K'ingyang) *Hipparion* fauna. *Vertebr. Palasiat.* 17, 200–221.

R Core Team (2021). *R: A language and environment for statistical computing*. R Foundation for Statistical Computing, Vienna, Austria

Radulesco, C., and Samson, P. (1967). Contribution à la connaissance du complexe faunistique de Malusteni-Beresti (Pléistocène inférieur), Roumanie I. Ord. Lagomorpha, Fam. Leporidae. Neues Jahrb. für Mineral. Geol. und Paläontologie. *Monatshefte* 9, 544–563.

Rook, L. (1992). "*Canis*" *monticinensis* sp. nov., a new Canidae (Carnivora, Mammalia) from the late Messinian of Italy. *Boll. della Soc. Paleontol. Ital.* 31, 151–156.

Rook, L. (2009). The wide-ranging genus *Eucyon* Tedford & Qiu, 1996 (Mammalia, Carnivora, Canidae, Canini) in the Mio-Pliocene of the Old World. *Geodiversitas* 31, 723–741. doi: 10.5252/g2009n4a723

Rook, L., Bartolini-Lucenti, S., Cirilli, O., Delfino, M., Ferretti, M. P., and Pando, L. (2023). "Vertebrate records," in *Reference Module in Earth Systems and Environmental Sciences*. (Elsevier Inc.), 1–11.

RStudio Team (2021). *RStudio: Integrated development environment for R*. RStudio, PBC, Boston, MA

Ruiz, J. V., Ferreira, G. S., Lautenschlager, S., de Castro, M. C., and Montefeltro, F. C. (2023). Different, but the same: inferring the hunting behaviour of the hypercarnivorous bush dog (*Speothos venaticus*) through finite element analysis. *J. Anat.* 242, 553–567. doi: 10.1111/joa.13804

Rüppell, E. (1835/1840). *Neue Wirbelthiere zu der Fauna von Abyssinien gehorig, Saugethiere*. Siegmund Schmerber, Frankfurt am Main

Rüppell, E. (1842). Saugethiere aus der Ordnung der Nager, beo- bachtet in Nordostlichen Africa. *Mus. Senckenbergianum* 3, 99–116.

Say, T. (1823). Account of an expedition from Pittsburgh to the Rocky Mountains, performed in the years 1819 and '20, by order of the hon. J. C. Calhoun, Sec'y of war: under the command of Major Stephen H. long. From the notes of Major long, Mr. T. Say, and other gentlemen of the exploring party, ed. E. James (Philadelphia, PA: H.C. Carey and I. Lea), 503.

Schlager, S. (2017). "Morpho and Rvcg e shape analysis in R: R-packages for geometric morphometrics, shape analysis and surface manipulations" in *Statistical Shape and Deformation Analysis, Methods, Implementation and Applications*. eds. G. Zheng, S. Li and G. Székely (London: Academic Press), 217–256.

Schreber, J. C. D. (1775). *Die Säugethiere in Abbildungen nach der Natur mit Beschreibungen*. Erlangen: Wolfgang Walther.

Slater, G. J., Dumont, E. R., and Van Valkenburgh, B. (2009). Implications of predatory specialization for cranial form and function in canids. *J. Zool.* 278, 181–188. doi: 10.1111/j.1469-7998.2009.00567.x

Smith, C. H. (1839). "The canine family in general or the genus *Canis*" in *The naturalist's library, vol. 18. Natural history of dogs*. ed. W. Jardine, vol. *1* (Edinburgh: W. H. Lizars), 267.

Soergel, W. (1925). Die Säugetierfauna des altdiluvialen Tonlages von Jockgrim. *Pfalz. Zeits. Deut. Geol. Ges.* 77, 405–438.

Sotnikova, M.V. (1989). The carnivore mammals from the Pliocene to the Early Pleistocene. Stratigraphic significance. *Trans. Geol Inst RAS* 440, 1–122. (in russian)

Sotnikova, M. (2006). A new canid *Nurocyon chonokhariensis* gen. et sp. nov. (Canini, Canidae, Mammalia) from the Pliocene of Mongolia. *CFS Cour. Forschungsinstitut Senckenb.*, 11–21.

Sotnikova, M., and Rook, L. (2010). Dispersal of the Canini (Mammalia, Canidae: Caninae) across Eurasia during the late Miocene to early Pleistocene. *Quat. Int.* 212, 86–97. doi: 10.1016/j.quaint.2009.06.008

Spassov, N., and Rook, L. (2006). *Eucyon marinae* sp. nov. (Mammalia, Carnivora), a new canid species from the Pliocene of Mongolia, with a review of forms referable to the genus. *Riv. Ital. di Paleontol. e Stratigr.* 112, 123–133.

Stiner, M. C., Howell, F. C., Martínez-Navarro, B., Tchernov, E., and Bar-Yosef, O. (2001). Outside Africs: middle Pleistocene *Lycaon* from Hayonim cave, Israel. *Boll. della Soc. Paleontol. Ital.* 40, 293–302.

Studiati, C. (1857) "Description des fossiles de la brèche osseuse de Monreale de Bonaria près de Cagliari", in *Voyage en Sardeigne 3*, ed. MarmoraA. La, Turin: Arthus Bertrand, 651–704.

Sundevall, C. J. (1847). Nya Mammalia från Sydafrika. *Ofv. K. Svenska Vet.-Akad. Forhandl. Stockholm* 3, 118–121.

Tamvakis, A., Savvidou, A., Spassov, N., Youlatos, D., Merceron, G., and Kostopoulos, D. S. (2022). New insights on early Pleistocene *Nyctereutes* from the Balkans based on material from Dafnero-3 (Greece) and Varshets (Bulgaria). *Palaeoworld* 3. doi: 10.1016/j.palwor.2022.09.006

Tedford, R. H., and Qiu, Z. (1996). A new canid genus from the Pliocene of Yushe, Shanxi Province. *Vertebr. Palasiat.* 34, 27–40.

Tedford, R. H., Taylor, B. E., and Wang, X. (1995). Phylogeny of Caninae (Carnivora: Canidae): the living taxa. *Am. Museum Novit.* 3146, 1–40.

Tedford, R. H., Wang, X., and Taylor, B. E. (2009). Phylogenetic systematics of the north American fossil Caninae (Carnivora: Canidae). *Bull. Am. Museum Nat. Hist.* 325, 1–218. doi: 10.1206/574.1

Teilhard de Chardin, P. (1940). The fossils from locality 18 near Peking. *Palaeontol. Sin. Ser. C* 9, 1–95.

Teilhard De Chardin, P., and Piveteau, J. (1930). Les mammifères fossiles de Nihowan (Chine). *Ann. Paleontol.* 19, 1–134.

Temminck, C. J. (1820). Sur le genre Hyène, et description d'une espèce nouvelle, découverte en Afrique. *Ann. Gen. Sci. Phys.* 3, 46–57.

Tseng, Z. J., and Wang, X. (2010). Cranial functional morphology of fossil dogs and adaptation for durophagy in *Borophagus* and *Epicyon* (Carnivora, Mammalia). *J. Morphol.* 271, 1386–1398. doi: 10.1002/jmor.10881

Urciuoli, A., Zanolli, C., Beaudet, A., Dumoncel, J., Santos, F., Moyà-Solà, S., et al. (2020). The evolution of the vestibular apparatus in apes and humans. *elife* 9:e51261. doi: 10.7554/eLife.51261

Valenciano, A., Morales, J., and Govender, R. (2022). *Eucyon khoikhoi* sp. nov. (Carnivora: Canidae) from Langebaanweg "E" quarry (early Pliocene, South Africa): the most complete African canini from the Mio-Pliocene. *Zool. J. Linnean Soc.* 194, 366–394. doi: 10.1093/zoolinnean/zlab022

Van Valkenburgh, B. (1990). "Skeletal and dental predictors ofbodymass in carnivores" in *Body size in mammalian Paleobiology: Estimation and biological implications*. eds. J. Damuth and B. MacFadden (Cambridge: Cambridge University Press), 181–205.

Van Valkenburgh, B., and Koepfli, K.-P. (1993). Cranial and dental adaptations to predation in canids. *Symp. Zool. Soc. London* 65, 15–37.

Van Valkenburgh, B., Sacco, T., and Wang, X. (2003). Pack hunting in Miocene borophagine dogs: evidence from craniodental morphology and body size. *Vertebr. Foss. Their Context Contrib. Honor Richard H. Tedford*. 279, 147–162.

Vinuesa, V. (2018). Bone-cracking hyenas (Carnivora, Hyaenidae) from the European Neogene and quaternary: taxonomy. *Paleobiol. Evolut.* Unpublished PhD Thesis

Vinuesa, V., Iurino, D. A., Madurell-Malapeira, J., Liu, J., Fortuny, J., Sardella, R., et al. (2016). Inferences of social behavior in bone-cracking hyaenids (Carnivora, Hyaenidae) based on digital paleoneurological techniques: implications for human–carnivoran interactions in the Pleistocene. *Quat. Int.* 413, 7–14. doi: 10.1016/j.quaint.2015.10.037

Vinuesa, V., Madurell-Malapeira, J., Fortuny, J., and Alba, D. M. (2015). The Endocranial morphology of the Plio-Pleistocene bone-cracking hyena *Pliocrocuta perrieri*: behavioral implications. *J. Mamm. Evol.* 22, 421–434. doi: 10.1007/s10914-015-9287-8

Wang, X. (1994). Phylogenetic systematics of the Hesperocyoninae (Carnivora, Canidae). *Bull. Am. Museum Nat. Hist.* 221, 1–207.

Wang, X., and Tedford, R. H. (2008). *Dogs and their fossil relatives*. New York: Columbia University Press

Wang, X., Tedford, R. H., and Taylor, B. E. (1999). Phylogenetic systematics of the Borophaginae (Carnivora. Canidae). *Bull. Am. Mus. Nat. Hist.* 243, 1–391.

Wayne, R. K., and Ostrander, E. A. (2007). Lessons learned from the dog genome. *Trends Genet.* 23, 557–567. doi: 10.1016/j.tig.2007.08.013

Werdelin, L. (1989). Constraint and adaptation in the bone-cracking canid *Osteoborus* (Mammalia: Canidae). *Paleobiology* 15, 387–401. doi: 10.1017/S009483730000957X

Werdelin, L., Lewis, M. E., and Haile-Selassie, Y. (2015). A critical review of African species of *Eucyon* (Mammalia; Carnivora; Canidae), with a new species from the Pliocene of the Woranso-mille area, Afar region, Ethiopia. *Pap. Palaeontol.* 1, 33–40. doi: 10.1002/spp2.1001

Werdelin, L., and Sanders, W. J. (2010). *Cenozoic Mammals of Africa*. Berkeley: University of California Press.

Yalden, D. W. (1985). Tachyoryctes macrocephalus. *Mamm. Species* 237, 1–3. doi: 10.2307/3503827

Zanolli, C., Kaifu, Y., Pan, L., Xing, S., Mijares, A., Kullmer, O., et al. (2022). Further analyses of the structural organization of *Homo luzonensis* teeth: evolutionary implications. *J. Hum. Evol.* 163:103124. doi: 10.1016/j.jhevol.2021.103124

Zrzavý, J., Duda, P., Robovský, J., Okřinová, I., and Pavelková Řičánková, V. (2018). Phylogeny of the Caninae (Carnivora): combining morphology, behaviour, genes and fossils. *Zool. Scr.* 47, 373–389. doi: 10.1111/zsc.12293

frontiers | Frontiers in Earth Science

TYPE Original Research
PUBLISHED 22 June 2023
DOI 10.3389/feart.2023.1162023

OPEN ACCESS

EDITED BY
Pauline Guenser,
Université de Bordeaux, France

REVIEWED BY
Andrey Zhuravlev,
Institute of Biology, Russia
Li Tian,
China University of Geosciences Wuhan,
China

*CORRESPONDENCE
Shun Muto,
✉ s-muto@aist.go.jp
Satoshi Takahashi,
✉ stakahashi@eps.nagoya-u.ac.jp

RECEIVED 09 February 2023
ACCEPTED 12 June 2023
PUBLISHED 22 June 2023

CITATION
Muto S, Takahashi S and Murayama M (2023), Conodont biostratigraphy of a Carboniferous–Permian boundary section in siliceous successions of pelagic Panthalassa revealed by X-ray computed microtomography.
Front. Earth Sci. 11:1162023.
doi: 10.3389/feart.2023.1162023

Conodont biostratigraphy of a Carboniferous–Permian boundary section in siliceous successions of pelagic Panthalassa revealed by X-ray computed microtomography

Shun Muto[1]*, Satoshi Takahashi[2]* and Masafumi Murayama[3,4]

[1]Geological Survey of Japan, National Institute of Advanced Industrial Science and Technology, Tsukuba, Japan, [2]Department of Earth and Environmental Sciences, Nagoya University, Nagoya, Japan, [3]Department of Marine Resource Science, Faculty of Agriculture and Marine Science, Kochi University, Nankoku, Japan, [4]Center for Advanced Marine Core Research, Kochi University, Nankoku, Japan

Pelagic deep-sea siliceous successions in accretionary complexes preserve precious records of a vast deep seafloor that is now lost due to plate subduction. Microfossils are the key means of age assignment of these successions, but poor preservation due to tectonic deformation and metamorphism at the subduction zone hamper biostratigraphic records. X-ray computed microtomography, while not widely used in biostratigraphic studies until now, allows us to visualize fossils that are impossible or difficult to extract from host rocks due to poor preservation. In this study, we applied this method on conodonts from a pelagic chert–claystone succession in Okoshizawa, Iwaizumi Town, Northeast Japan, using a laboratory-based X-ray microscope. This work is a first close look at conodont biostratigraphy across the Carboniferous–Permian boundary in pelagic deep Panthalassa. We identified conodonts including ten species that are used as zonal markers in intensely studied areas such as around the East European Platform and Midcontinent United States. Based on the occurrence of conodonts, the studied section in Okoshizawa was correlated to the lower Moscovian to middle Artinskian. Confirmation of Moscovian to Artinskian age diagnostic conodonts from pelagic Panthalassa strengthens their role as global biostratigraphic indicators. By identifying more numerous specimens compared to the conventional hydrofluoric acid dissolution method, we were able to obtain information about conodont faunal characteristics around the Carboniferous–Permian boundary in pelagic deep areas of Panthalassa. The dominant taxa changed from *Streptognathodus* to *Mesogondolella* in the middle Asselian, probably reflecting an ecological takeover by the latter in the deep waters.

KEYWORDS

accretionary complex, chert, deep-sea, North Kitakami Belt, X-ray microscope

1 Introduction

1.1 X-ray computed microtomography on microfossils from deep-sea rocks

Pelagic deep-sea siliceous successions in accretionary complexes are records of the deep seafloor that are now lost due to subduction (e.g., Isozaki et al., 1990; Wakita and Metcalfe, 2005). Due to the lack of macrofossils and datable tuff beds, microfossils are the key means of age assignment of these successions. In particular, conodonts have proved to be vital in age assignment and correlation with various Palaeozoic to Triassic marine facies in other regions (Isozaki and Matsuda, 1980; Yao et al., 1980; Yamakita et al., 2007; Hori et al., 2011; Yamashita et al., 2018; Muto et al., 2019; Tomimatsu et al., 2020). Pelagic deep-sea sections dated by conodonts are used as sedimentary records of a unique oceanic realm, which also has the advantage of covering extremely long time intervals (millions to tens of millions of years) without receiving strong local effects (Takahashi et al., 2009; Sano et al., 2010; Sano et al., 2012; Nakada et al., 2014; Takahashi et al., 2014; Muto et al., 2018; Muto et al., 2020; Tomimatsu et al., 2020; Grasby et al., 2021; Muto, 2021; Takahashi et al., 2021).

The drawback in biostratigraphic research of conodonts in pelagic deep-sea sedimentary rocks within accretionary complexes is the poor preservation of conodonts due to deformation and metamorphism at the subduction zone that hamper biostratigraphic records. Conodonts in these rocks are obtained by dissolving the host rock with dilute HF acid (introduced in Hayashi, 1968) or less commonly by observing rock pieces split parallel to the bedding plane (Yamakita et al., 1999). The former method allows extraction of conodont elements, but the yield of conodont elements is usually quite low. The latter can obtain a larger number of elements because altered and cracked specimens can be observed, but the direction of observation of the specimens is limited. In the face of these limitations, Muto et al. (2021) proposed the use of X-ray computed microtomography (X-ray µCT) as a method that offers more consistency.

X-ray computed tomography can image fossils that are buried within the host rock, and the development of X-ray microscopes and synchrotron facilities allowed application to microfossils (Ketcham and Carlson, 2001; Mees et al., 2003; Cnudde and Boone, 2013; Cunningham et al., 2014). X-ray µCT on conodonts have been introduced in recent years mainly for the purpose of morphological and palaeontological analyses, taking advantage of the high-quality 3D-morphological data and their versatility (Goudemand et al., 2011; Goudemand et al., 2012; Jones et al., 2012; Mazza and Martínez-Pérez, 2015; Martínez-Pérez et al., 2016; Zhuravlev, 2017; Guenser et al., 2019; Huang et al., 2019; Sun et al., 2020). However, the method is not widely used in biostratigraphic studies. The reason is because conodonts can be extracted relatively easily from most types of rocks containing these fossils. Hence, acquisition and rapid identification of large quantities of specimens by extraction and observation using scanning electron microscopes (SEMs) is generally the most accessible and efficient method. On the other hand, in the case of some rare types of rocks such as pelagic deep-sea siliceous rocks in accretionary complexes, X-ray µCT can be a powerful tool to visualize fossils that are not extractable using chemicals or not identifiable in limited angle of observation on rock surfaces. Zhuravlev and Gerasimova (2016) successfully used X-ray µCT to search and observe conodonts in basinal siliceous rocks. Recently, we applied X-ray µCT to siliceous rocks in accretionary

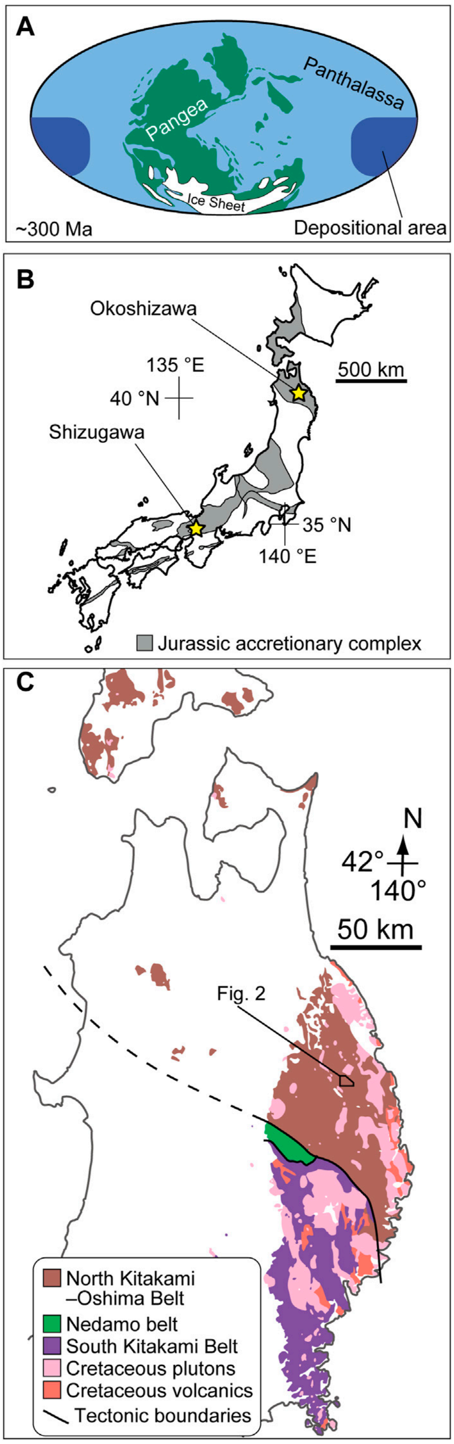

FIGURE 1
(A) Palaeogeorgaphic map by Mei and Henderson (2001) based on Ziegler et al. (1997). The depositional area of pelagic deep-sea sedimentary rocks preserved within Jurassic accretionary complexes of Japan is shown. **(B)** Distribution of the Jurassic accretionary complex in the Japanese islands in the basement rocks (based on Isozaki et al., 2010) and the location of Okoshizawa (this study; Ehiro et al., 2008) and Shizugawa (Kusunoki et al., 2004). **(C)** Exposure of pre-Paleogene rocks in northern Tohoku of Northeast Japan (modified from Geological Survey of Japan, AIST, 2020).

complexes that have undergone greater diagenesis and showed that it is in many cases the most consistent means to observe conodonts in these rocks (Muto et al., 2021).

1.2 The Carboniferous–Permian boundary

This study focuses on the Carboniferous–Permian boundary (CPB) in deep-sea sedimentary rocks deposited in pelagic Panthalassa. Conodont biostratigraphy was used for age assignment of stratigraphic intervals around the CPB in classic sections around the East European Platform centred in western Russia (Barskov et al., 1981; Chernykh and Reshetkova, 1987; Sobolev and Nakrem, 1996; Chernykh and Ritter, 1997) and Midcontinent United States (von Bitter, 1972; Perlmutter, 1975; Ritter, 1995). The Global Stratotype Section and Point (GSSP) of the CPB was ratified in Aidaralash Creek, Aktöbe, northern Kazakhstan which is situated in the marginal area of the East European Platform, and the first appearance datum of the conodont *Streptognathodus isolatus* was chosen as the definition of the boundary (Davydov et al., 1998). The conodont-based boundary definition and age correlation was adopted in other regions including South China (Wang and Qi, 2003), Japan (Kusunoki et al., 2004) and South America (Suárez-Riglos et al., 1987). Monographic studies following the ratification of the CPB both around the East European Platform (Chernykh, 2005; Chernykh, 2006) and Midcontinent United States (Boardman et al., 2009) lead to the description of various new species, many of which were considered useful in improving the temporal resolution of conodont zonal schemes. However, conodont studies were conducted rather independently in the two regions for both the Pennsylvanian (upper Carboniferous) and Cisuralian (lower Permian). Therefore, establishment of a global scheme was, and partly remains, hampered by both endemism of conodonts and taxonomic issues (Henderson, 2018; Barrick et al., 2022).

Due to the above circumstances, accumulation of data on conodont biostratigraphy from a wide range of palaeogeographic regions is required for the establishment of a globally applicable biostratigraphic framework across the CPB. Such data will provide information on which taxa can be found universally and which are endemic to a certain region or confined to particular environments. In this sense, pelagic sedimentary rocks accumulated in Panthalassa (Figure 1A) are one of the critical pieces of information. These pelagic rocks, now only found in circum-Pacific accretionary complexes (e.g., Isozaki et al., 1990), represent a unique oceanic realm of an extremely open-marine environment. Two types of rocks represent this oceanic realm: limestone deposited on seamounts and siliceous rocks deposited on abyssal plains (e.g., Isozaki et al., 1990). The latter preserves a more long-ranging record (up to 150 million years) and also represents an oceanic environment with extremely deep bathymetry, not found in sedimentary records elsewhere (e.g., Matsuda and Isozaki, 1991).

Pelagic deep-sea successions of Carboniferous to Permian age deposited in Panthalassa are found almost exclusively in accretionary complexes in Japan. Conodont occurrences across the CPB have been reported from two localities in the Jurassic accretionary complex: Shizugawa in south Kyoto (Kusunoki et al., 2004) and Okoshizawa in north Iwate (Ehiro et al., 2008) (Figure 1B). Carboniferous to Permian conodonts were also reported from deep-sea chert in the Ashio Mountains in east Japan (Hayashi et al., 1990), but these are based on erroneous identification of Permian and Triassic conodonts (Muto and Ito, 2021). The confirmation of rocks as old as the Carboniferous from the Jurassic accretionary complex was a valuable report by itself when the works in Shizugawa and Okoshizawa were published, and efforts were not concentrated on narrowing down the CPB in both localities. In addition, these studies were published before the monographic studies around the CPB in the Urals (Chernykh, 2005, 2006) and Midcontinent United States (Boardmann et al., 2009), which means that the species concepts in the previous works in Japan are not directly comparable with that adopted today. Therefore, there is a need to refine the information on conodont biostratigraphy in the CPB interval in Panthalassic pelagic deep-sea successions based on higher sampling resolution and updated taxonomic concepts. In this study, we focus on the Okoshizawa section, which is observed in outcrops from which Ehiro et al. (2008) reported Carboniferous and Permian conodonts (locality “Ref.1” therein). This is one of the fossil localities in which Muto et al. (2021) confirmed the applicability of X-ray μCT on conodonts in pelagic deep-sea siliceous rocks. By applying the method on more samples across the CPB, we establish a correlation of this boundary interval in pelagic deep-sea sections of Panthalassa with the modern biostratigraphic schemes adopted around the East European Platform, Midcontinent United States and elsewhere.

2 Geological setting

The Okoshizawa section is exposed in a roadcut along a logging road traversing the east bank of Okoshi Stream (Okoshizawa in Japanese) in the northwest part of Iwaizumi Town, Iwate Prefecture, Tohoku, Northeast Japan (40°0′14″N 141°36′17″E) (Figures 1C, 2). We studied pelagic deep-sea sedimentary rocks (mostly bedded chert) that belong to the Jurassic accretionary complex of the North Kitakami Belt (Ehiro et al., 2008). These sedimentary rocks were deposited in the Superocean Panthalassa (Figure 1A) then transported and accreted at the subduction zone along its western margin by plate motion during the Jurassic to earliest Cretaceous (Isozaki et al., 1990; Wakita and Metcalfe, 2005; Ehiro et al., 2008; Uchino and Suzuki, 2020).

The geology of the area around Okoshizawa is detailed in Ehiro et al. (2008) and Muto et al. (2023) (Figure 2). The pelagic deep-sea sedimentary rocks in Okoshizawa mostly comprise bedded chert and siliceous claystone of the Otori Unit of Takahashi et al. (2016) (revised by Muto et al., 2023). The Otori Unit is mainly composed of stacked sheets of coherent sequences of pelagic deep-sea chert and hemipelagic siliceous mudstone in the structurally lower part (Okoshizawa Subunit), and mixed rock facies in the structurally upper part (Osakamoto Subunit) (Figure 2; Muto et al., 2023). The Okoshizawa section belongs to the Okoshizawa Subunit and corresponds to the stratigraphically lowermost part of a coherent succession of chert and siliceous mudstone (Muto et al., 2023). The confirmed age of chert ranges from Pennsylvanian to Upper Triassic (Ehiro et al., 2008; Takahashi et al., 2009; Muto et al., 2021; Muto et al., 2023), and its youngest limit likely extends into the Lower Jurassic based on the Middle Jurassic age of the conformably overlying siliceous mudstone (Suzuki et al., 2007; Muto et al., 2023).

The Okoshizawa section is composed of brownish yellow dolostone with greenish grey chert interbeds, greenish grey chert,

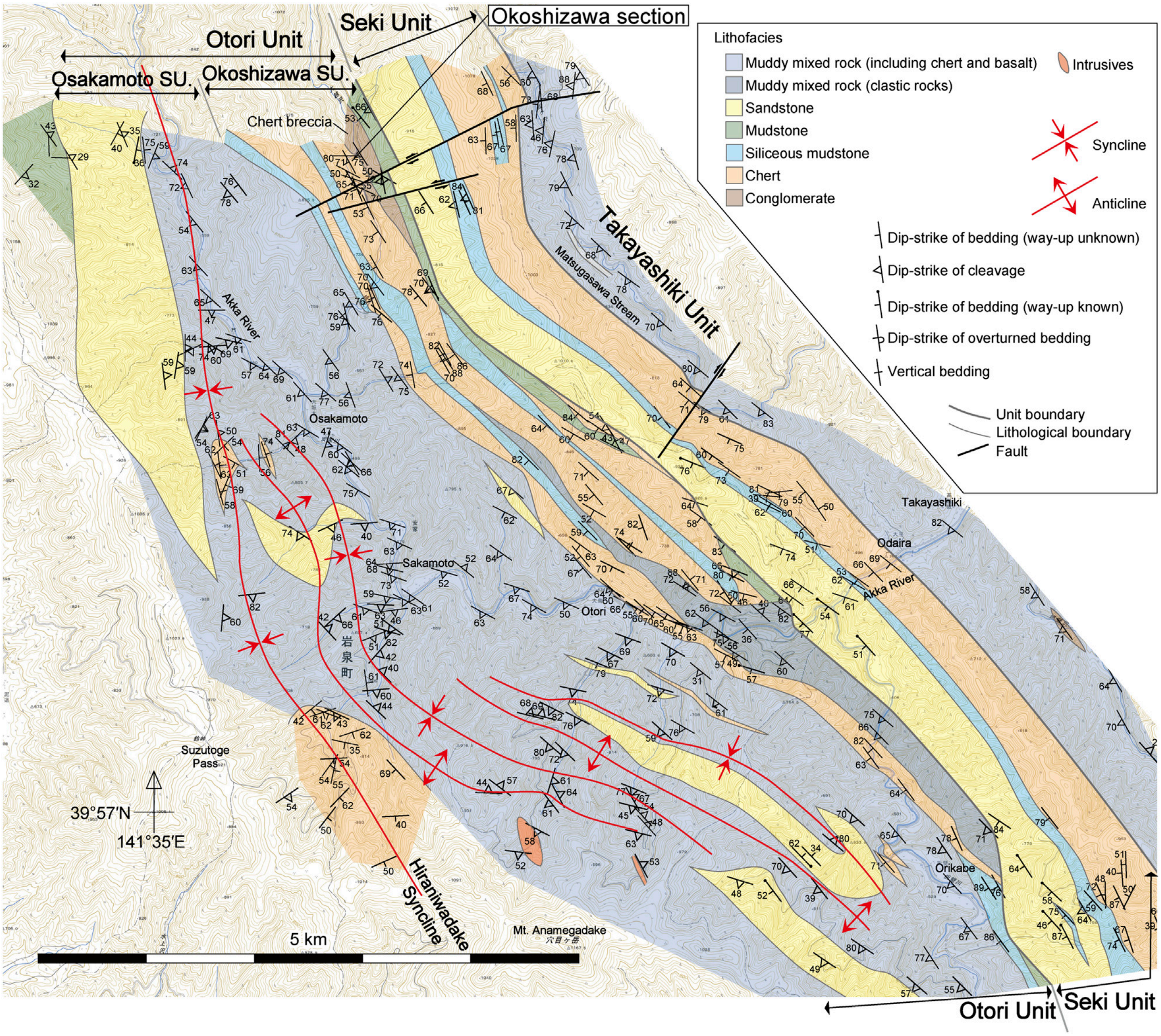

FIGURE 2
Geological map of the Akka area (Muto et al., 2023). The Okoshizawa section is situated in the Okoshizawa Subunit composed mainly of stacked sheets of coherent chert–siliceous mudstone sequences. Base map from 1: 25,000 topographic map "Akkamori", "Rikuchu-Itsukaichi", "Hashigami" and "Akka" by the Geospatial Authority of Japan. SU. Subunit.

green claystone, dark red siliceous claystone with grey and white chert interbeds and grey bedded chert in ascending order, consistent with the brief report by Ehiro et al. (2008) (Figure 3). Basaltic volcaniclastics are exposed in a separated outcrop apparently ~40 m below the base of the section, but the stratigraphic relationship between the basaltic rocks and dolostone at the base of the Okoshizawa section is unknown. The lithologies that constitute the Okoshizawa section have been described by Muto et al. (2023), and this study presents a detailed lithostratigraphy (Figure 4).

The lowermost part of the section is composed of mostly1–5 cm-thick dolostone beds with 1–10 cm-thick greenish grey chert interbeds with a total thickness of ~2 m. The thickest dolostone bed is 40 cm thick. Overlying this is greenish grey chert, separated by a covered area from the underlying strata. It is approximately 1.6 m thick and is well-bedded with single bed thickness of generally 2–5 cm. Green siliceous claystone is in contact with the greenish grey chert with a fault and has a total thickness of approximately 1 m. It is somewhat weakly bedded (i.e., the bedding plane is not laterally traceable in some cases) with single bed thickness of generally 2–5 cm. Greyish cherty layers are present within the green siliceous claystone, although not conspicuous at the outcrop surface. Dark red siliceous claystone conformably overlies the green siliceous claystone and attains approximately 10.3 m in total thickness. There are three bedding parallel slip planes of which one diminishes within the observed area of the outcrop, whereas two ("fault?" in Figures 3C,D) extend further and may cause gaps in the lithostratigraphy. One of the bedding parallel slip planes are accompanied by an isoclinal fold pair. The red siliceous claystone is also somewhat weakly bedded with single bed thickness of generally 2–5 cm. White chert layers, often laterally

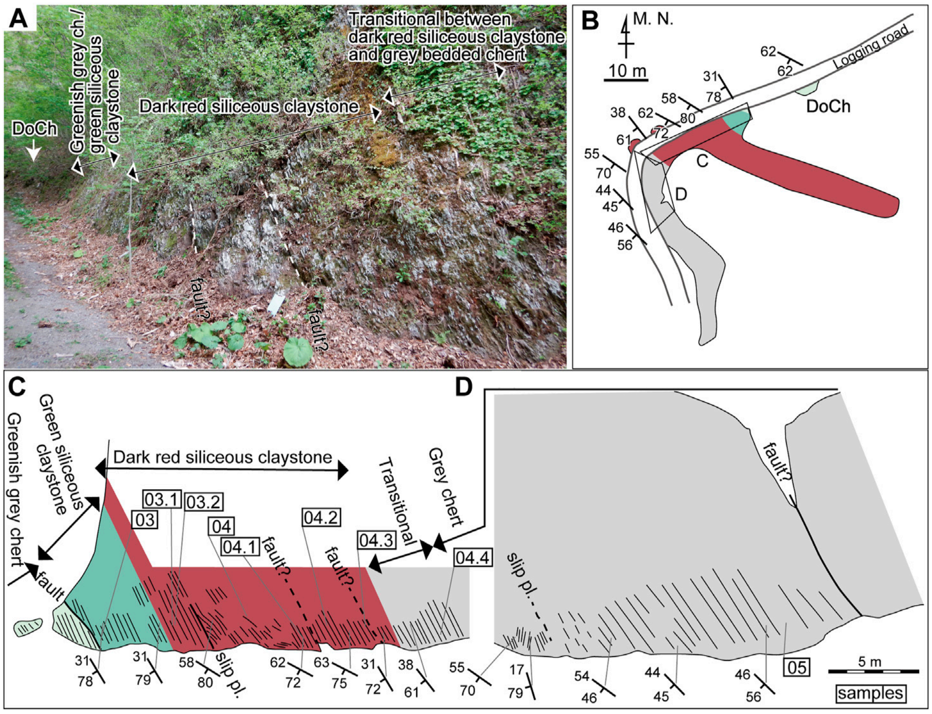

FIGURE 3
(A) Photograph of the roadcut where the Okoshizawa section is exposed. DoCh: outcrop of dolostone with greenish grey chert interbeds. The blue board in the centre is 20 cm × 30 cm. The fault and slip plane in the left side of **(C)** is not shown in here. **(B)** Sketch of the outcrops of the Okoshizawa section in plan view. See **(C)** for legends for colour. **(C, D)** Sketch of the outcrop of the main part of the Okoshizawa section. Sampled horizons are indicated by sample IDs ("Okz-CO-" is abbreviated) enclosed in rectangles.

discontinuous and nodule-like, occur within the red siliceous claystone. The lithofacies changes upsection to grey bedded chert with a transitional zone approximately 2.2 m thick. The grey chert is 8 m thick measured to the fault at the top of the logged interval and is well-bedded with single bed thickness of mostly 3–10 cm. There is an isoclinal fold pair in the lower part, above which a bedding-parallel slip plane occurs (Figure 3D). Grey bedded chert south of the fault that marks top of the section (Figure 3D) is not logged in detail in this study. The presence of dolomite accompanied by minor basaltic fragments in the lowermost part (Muto et al., 2023) implies inputs from topographic highs such as oceanic islands, whereas the total lack of silt-size or larger detrital grains indicate deposition in a remotely pelagic setting.

Ehiro et al. (2008) previously reported *Mesogondolella clarki*, *Gondolella gymna*, *Idiognathodus delicatus*, *Idiognathoides sinuatus*, *Diplognathodus atetsuensis* and *Diplognathodus coloradoensis* from the greenish grey chert intercalated in dolostone, and *Streptognathodus elongatus*, *Gondolella* cf. *bella* sensu Clark and Mosher (1966), *Mesogondolella bisselli* and *Sweetognathus* cf. *whitei* from the red siliceous claystone (their "tuffaceous chert"), but with no illustrations. Muto et al. (2021) used X-ray µCT on specimens on rock pieces and identified *St. elongatus* and *Streptognathodus bellus*. These conodonts indicate a Moscovian to Artinskian (middle late Carboniferous to middle early Permian) age. However, *M. bisselli* and *Sw. whitei* are now considered to have ranges that do not overlap (e.g., Henderson, 2018; Petryshen et al., 2020). The apparent discrepancy with the occurrence of conodonts reported by Ehiro et al. (2008) may be due to taxonomic issues or because the two species were obtained from different levels in the red siliceous claystone. The absence of lithostratigraphic columns in Ehiro et al. (2008) precludes further discussions on the age of the section including the exact position of the CPB.

3 Methods

Methods to obtain conodont specimens from deep-sea siliceous rocks and perform X-ray µCT scanning is described in detail in Muto et al. (2021). The following is a brief summary. Conodont elements were found by observing cleaved rock pieces under a stereoscopic microscope (Muto et al., 2019). Rock pieces containing well-preserved specimens were selected and trimmed down to blocks of a few millimetres. The specimens on the rock pieces were enclosed in a "hedge" of concrete mortar to avoid effects of surface refraction in the CT images, glued onto the end of a pencil lead and scanned using a ZEISS Xradia 410 versa X-ray microscope equipped with a L8121-03 SEL X-ray source of Hamamatsu Photonics K.K. at the Center for Marine Core Research, Kochi University. Scans for imaging of conodont elements were conducted with spatial resolutions of 1 µm^3/voxel, 1.5 µm^3/voxel or 2 µm^3/voxel depending on the size of the specimens (see Supplementary Table S1 for details). Three-dimensional images of the fossils were produced by Amira Software (Thermo Fisher Scientific).

We also performed the conventional extraction method of conodonts using dilute hydrofluoric (HF) acid; 16 cycles (8 or 16 h per cycle) using 5–10wt% HF acid (following the method of

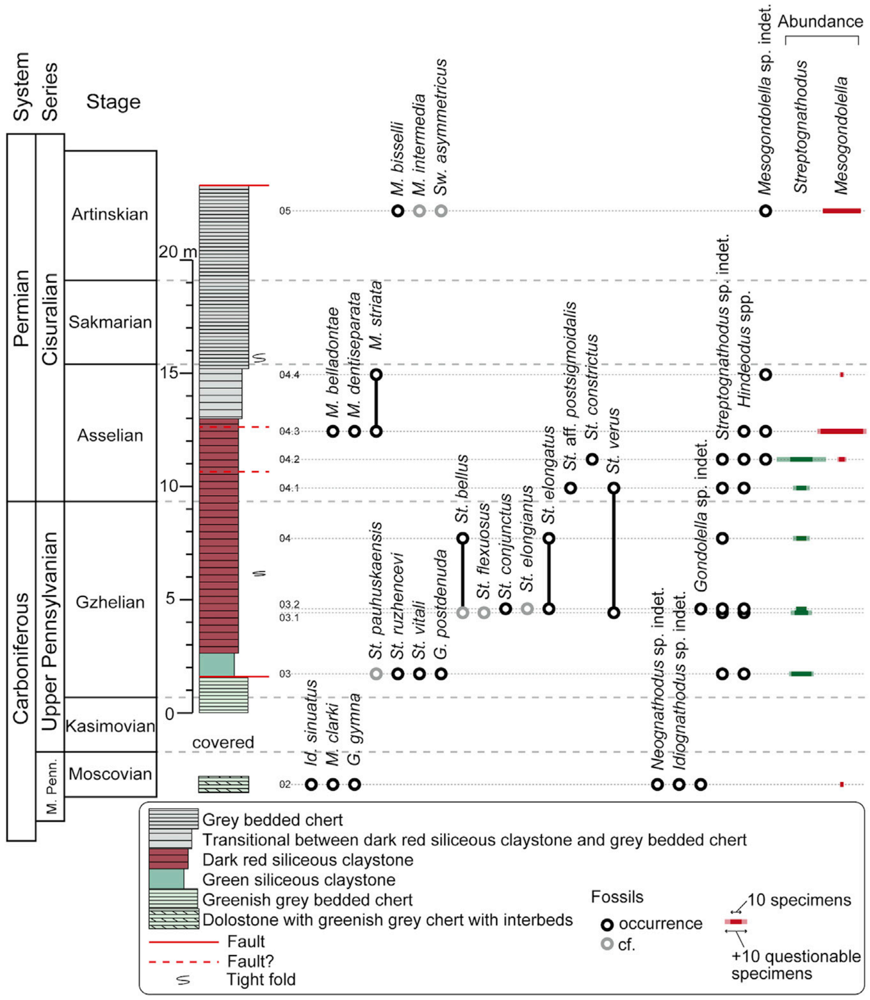

FIGURE 4
Lithostratigraphic column and conodont occurrence of the Okoshizawa section. Sample Okz-CO-04 was studied in Muto et al. (2021). M. Penn. Middle Pennsylvanian; *Id. Idiognathoides*; *M. Mesogondolella*; *G. Gondolella*; *St. Streptognathodus*; *Sw. Sweetognathus*. The prefix "Okz-CO-" is abbreviated from sample IDs. Absolute abundance of *Streptognathodus* and *Mesogondolella* is represented by the width of horizontal bars on the far right. See Supplementary Table S2 for more details on conodont occurrence. Note that the vertical position of stage boundaries on the leftmost column is not showing their precise level in the lithostratigraphic column and uncertainties exist between samples horizons.

Nishikane et al., 2011). Greenish grey chert and green siliceous claystone yielded a number of conodont elements, but these were mostly broken fragments. Red siliceous claystone and grey chert yielded no elements. Conodonts extracted by dilute HF acid were mounted on carbon tapes and photographed by a scanning electron microscope (SEM; Hitachi SU3500) at the Geological Survey of Japan. In addition, some "clean" moulds (see results section for detail) were photographed using SEM.

4 Results

4.1 Occurrence and preservation of the conodont fossils

Conodonts in the studied section were black coloured in the greenish grey chert intercalated in dolostone and the lower part of the grey chert, dark grey in the green siliceous claystone, white to orange in the red siliceous claystone and moulds in the upper part of the grey chert (Figure 5). Of these, the black and dark grey fossils were dense material with high CT values, while the white and orange fossils were composed of material with high CT values but were less dense, probably due to recrystallization, in accordance with Muto et al. (2021). Due to this, the surface of white and orange fossils was less sharply recognized and had greater noise compared with the black and dark grey varieties. "Clean" moulds with no secondary precipitate inside were easily recognized from the host rock. When secondary precipitate was present, which was the case in many of the moulds, the surface of the fossil specimens produced from X-ray μCT was somewhat noisy. Despite some difficulties, images produced from X-ray μCT were adequate to identify many of the specimens to the species level and most to the genus level (Figures 6–8). In general, idiognathodontids were more difficult to identify compared to gondolellids because species distinctions are based on morphological features of smaller sizes.

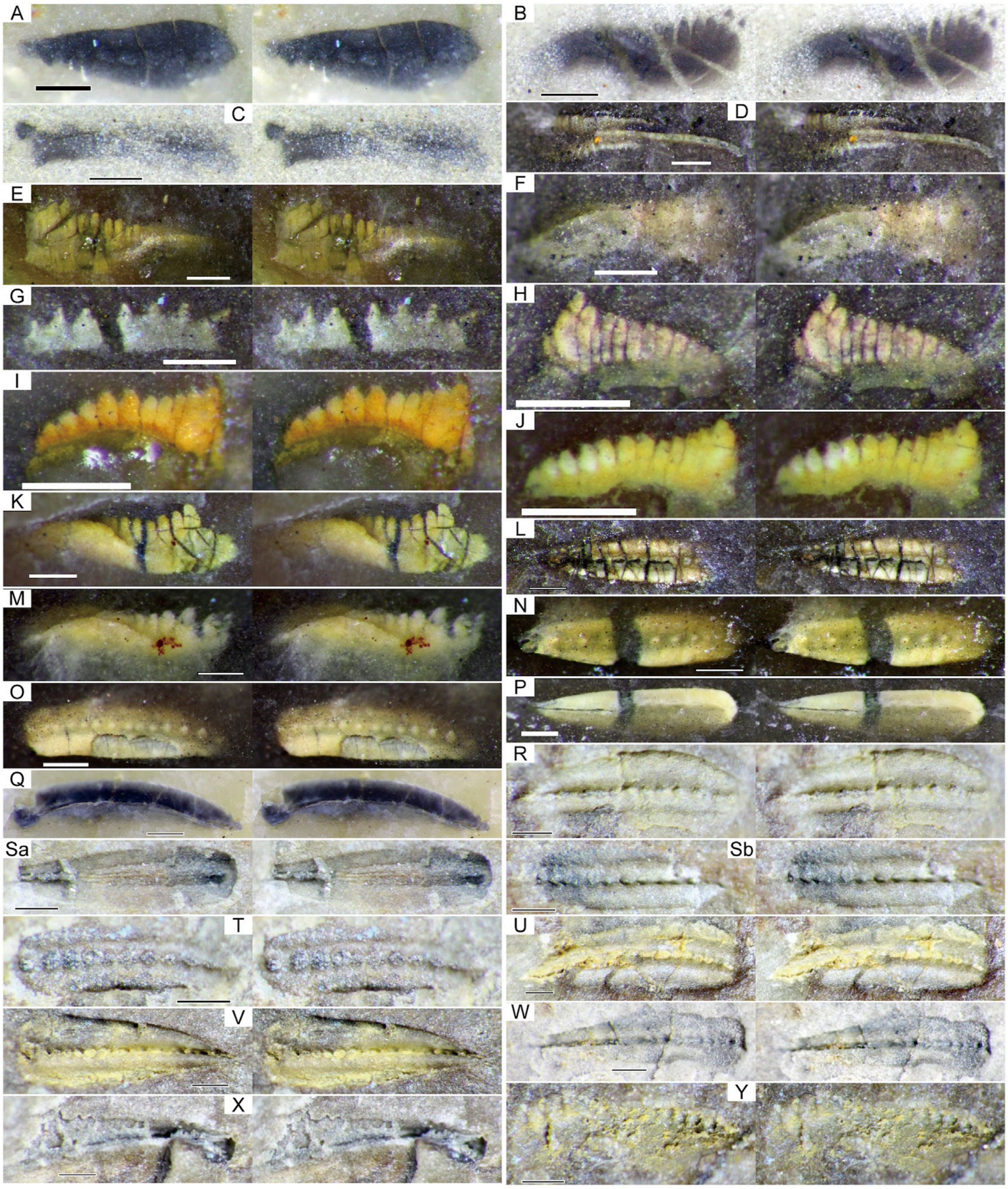

FIGURE 5
Stereographic photographs of conodonts obtained from the Okoshizawa section (parallel viewing). Note that most specimens were identified based on X-ray μCT scans (Figures 6–8) and SEM photography (Figure 9). **(A)** *M. clarki*, Okz-CO-02. **(B)** *St. vitali*, Okz-CO-03. **(C)** *G. postdenuda*, Okz-CO-03. **(D)** *St.* cf. *bellus*, Okz-CO-03.1. **(E)** *St.* cf. *flexuosus*, Okz-CO-03.1. **(F)** *St. conjunctus*, Okz-CO-03.2. **(G)** *Gondolella* sp. indet., Okz-CO-03.2. **(H)** *H. minutus*, Okz-CO-03.2. **(I, J)** *H. minutus*, Okz-CO-04.1. **(K)** *St.* aff. *postsigmoidalis*, Okz-CO-04.1. **(L)** *Mesogondolella* sp. indet., Okz-CO-04.2. **(M)** *St. constrictus*, Okz-CO-04.2. **(N, P)** *M. dentiseparata*, Okz-CO-04.3. **(O)** *M. dentiseparata* transitional to *M. striata*. **(Q)** *M. striata*, Okz-CO-04.4. **(R–T)** *M.* cf. *bisselli*, Okz-CO-05, (Sa) and (Sb) are counterparts. **(U–X)** *M.* cf. *intermedia*, Okz-CO-05. **(Y)** *Sw.* cf. *asymmetricus*. *H.*: *Hindeodus*. See Figure 4 for abbreviation of other genera. Scale bars are 200 μm.

Of the investigated samples, greenish grey chert and green siliceous claystone which contained black and dark grey conodont fossils also yielded conodont elements by dilute HF acid treatment. Samples with white and orange fossils were completely unproductive after 16 cycles of HF acid treatment. We did not perform HF acid treatment for sample Okz-CO-05,

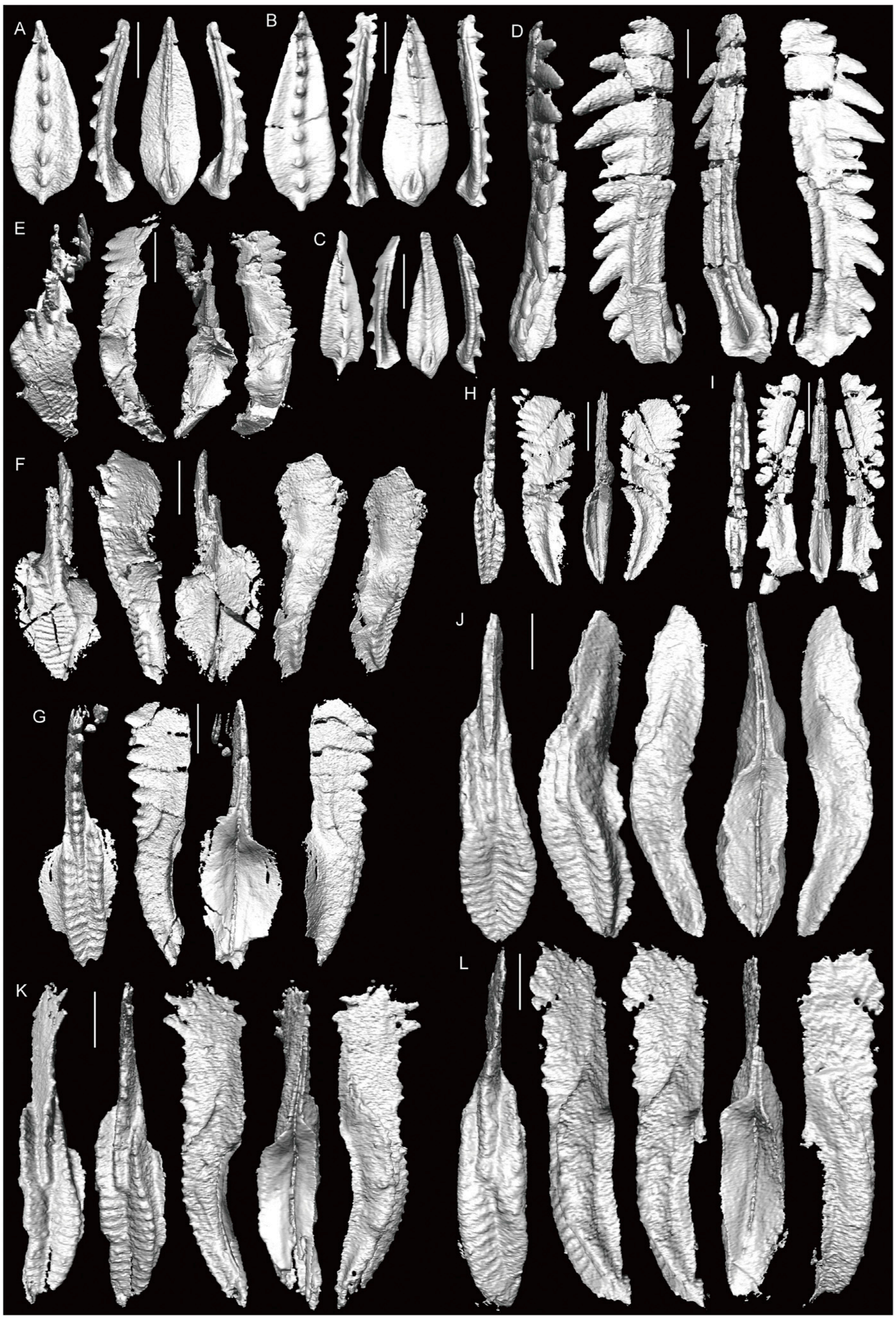

FIGURE 6
3D-images of conodonts obtained by X-ray μCT (part one). **(A–C)** *M. clarki*, Okz-CO-02; **(B)** shown in Figure 5A. **(D)** *G. gymna*, Okz-CO-02. **(E)** *Idiognathodus* sp. indet., Okz-CO-02. **(F)** *Id. sinuatus*, Okz-CO-02 **(G, H)** *St. vitali*, Okz-CO-03; **(H)** shown in Figure 5B. **(I)** *G. postdenuda*, Okz-CO-03; shown in Figure 5C. **(J, K)** *St.* cf. *bellus*, Okz-CO-03.1; **(J)** shown in Figure 5D. **(L)** *St.* cf. *flexuosus*; shown in Figure 5E. Scale bars are 200 μm.

in which conodonts were preserved as moulds. As stressed in Muto et al. (2021), the results indicate that X-ray μCT is the most consistent method of observing conodonts in the deep-sea siliceous rocks, because it enables us to observe altered specimens and cracked specimens. Altered specimens that are white or orange coloured and specimens preserved as moulds can only be observed by this method. In the case of grey or black specimens that have suffered minimal alteration, extraction by dilute HF acid is possible, but the number of identifiable conodonts obtained in the same time period is inferior compared to the method using X-ray μCT, probably because the majority of these conodonts are cracked. Indeed, most of the conodonts extracted using dilute HF acid in this study were unidentifiable fragments. In the case of the present study, X-ray μCT was absolutely crucial, because the state of preservation of conodonts in most of the investigated samples did not allow extraction using dilute HF acid.

We also performed SEM photography on some specimens preserved as "clean" moulds (Figures 9I–L). SEM photography was

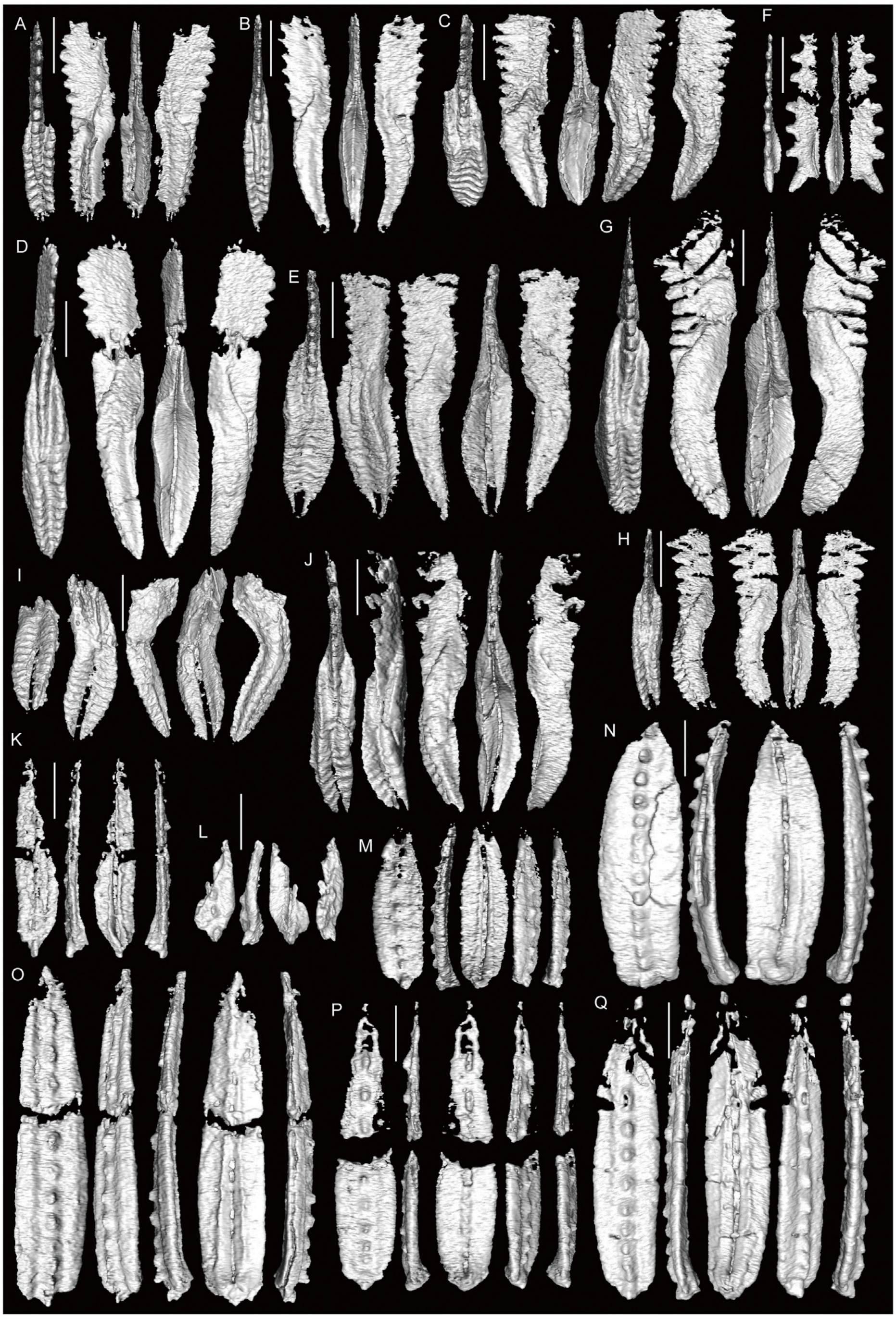

FIGURE 7
3D-images of conodonts obtained by X-ray µCT (part two). **(A)** *St. verus*, Okz-CO-03.1. **(B)** *St.* cf. *elongianus*, Okz-CO-03.2. **(C)** *St. conjunctus*, Okz-CO-03.2, shown in Figure 5F. **(D)** *St. elongatus*, Okz-CO-03.2. **(E)** *St. bellus*? Okz-CO-03.2. **(F)** *Gondolella* sp. indet., Okz-CO-03.2; shown in Figure 5G. **(G)** *St.* aff. *postsigmoidalis*, Okz-CO-04.1; shown in Figure 5K **(H)** *St. verus*, Okz-CO-04.1 **(I, J)** *St. constrictus*, Okz-CO-04.2; **(J)** shown in Figure 5M **(K, L)** *Mesogondolella* sp. indet., Okz-CO-04.2; **(K)** shown in Figure 5L. **(M, O–Q)** *M. dentiseparata*, Okz-CO-04.3; (O) shown in Figure 5P; **(P)** shown in Figure 5N. **(N)** *M. dentiseparata* transitional to *M. striata*; shown in Figure 5O. Scale bars are 200 µm.

not as effective as when performed on extracted conodonts. Compared with images based on X-ray µCT, the latter is more useful in allowing unlimited direction of observation. On the other hand, SEM has higher special resolution allowing observation of more subtle features. Sample preparation is also easier for SEM photography, in which the rock pieces need not be trimmed down to millimetre-size. However, taking SEM photographs usually requires some degree of trimming as well, and cannot be recommended for very fragile specimens. To sum up, SEM photography of moulds may be preferred over X-ray µCT when the moulds are "clean" (no precipitate on the mould walls that obscure surface topography), when trimming down the sample down to millimetre-size causes risks

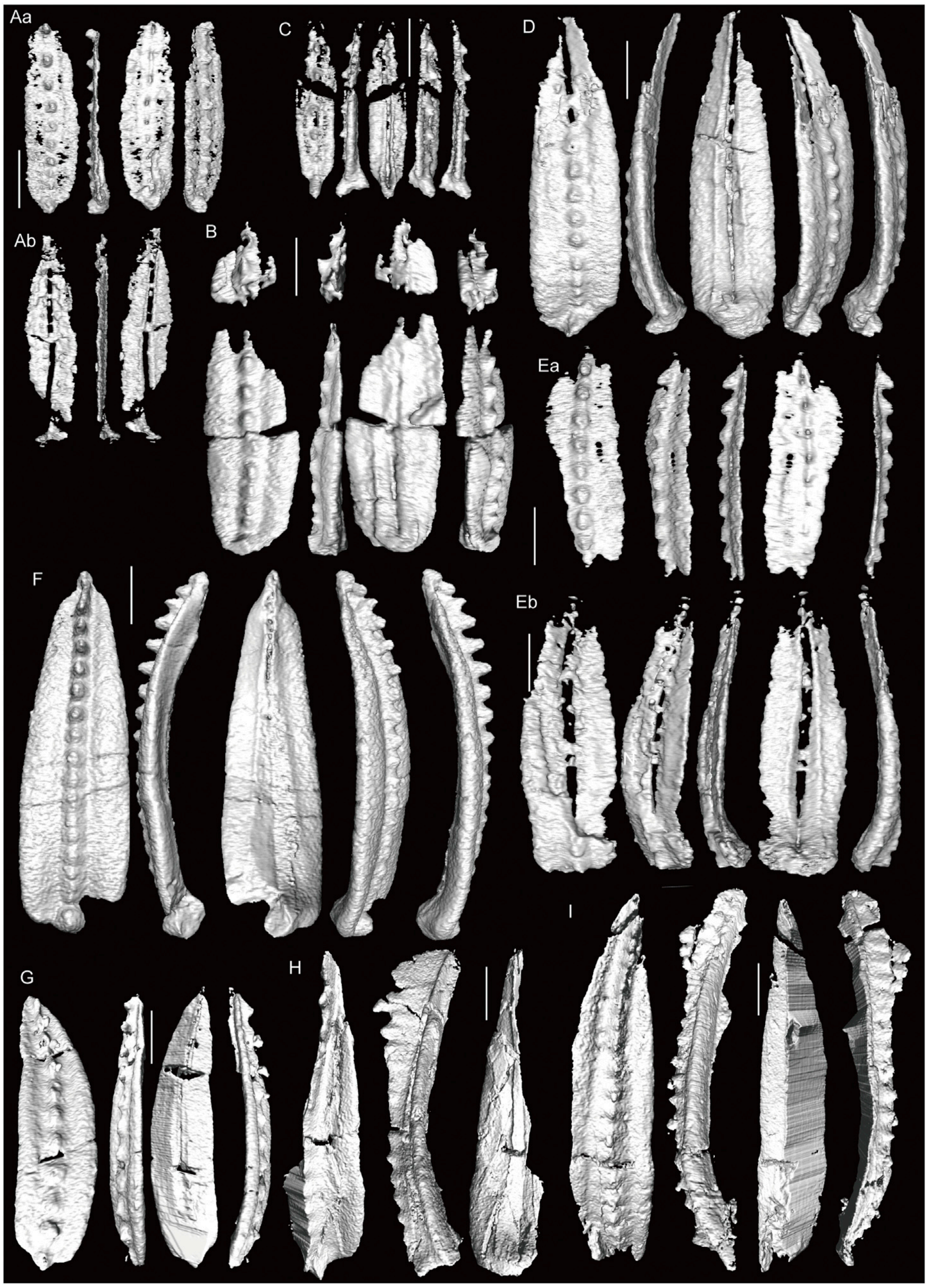

FIGURE 8
3D-images of conodonts obtained by X-ray µCT (part three). **(A, B)** *M. dentiseparata*, Okz-CO-04.3; (Aa) and (Ab) are counterparts of an element split in half. **(C, D)** *M. belladontae*, Okz-CO-04.3. **(E)** *M. striata*, Okz-CO-04.3; (Ea) and (Eb) are counterparts of an element split in half. **(F)** *M. striata*, Okz-CO-04.4; shown in Figure 5Q. **(G)** *M. bisselli*, Okz-CO-05. **(H)** *M.* cf. *intermedia*, Okz-CO-05, shown in Figure 5X. **(I)** *M. intermedia*? Okz-CO-05. Scale bars are 200 µm.

of breaking it or when the targeted morphological feature is too subtle to be obtained by X-ray µCT.

4.2 Conodont biostratigraphy of the okoshizawa section

We identified 22 conodont species belonging to six genera from a total of ten samples (Figure 4; Supplementary Table S2). In this section, the occurrence of conodonts in the Okoshizawa section is described in ascending order. The age assignment of the section is discussed in the next chapter.

Sample Okz-CO-02 which is from a greenish grey chert bed intercalated in dolostone yielded a number of segminiplanate gondolellids and carminiscaphate idiognathodontids. Gondolellid elements with a lanceolate platform outline, low, discrete denticles and a terminally located cusp with a base that creates a protrusion beyond the dorsal side of the platform were identified as *Mesogondolella clarki* (Koike) (Figures 6A–C). A gondolellid element with a blade of sharp denticles fused at the base, a

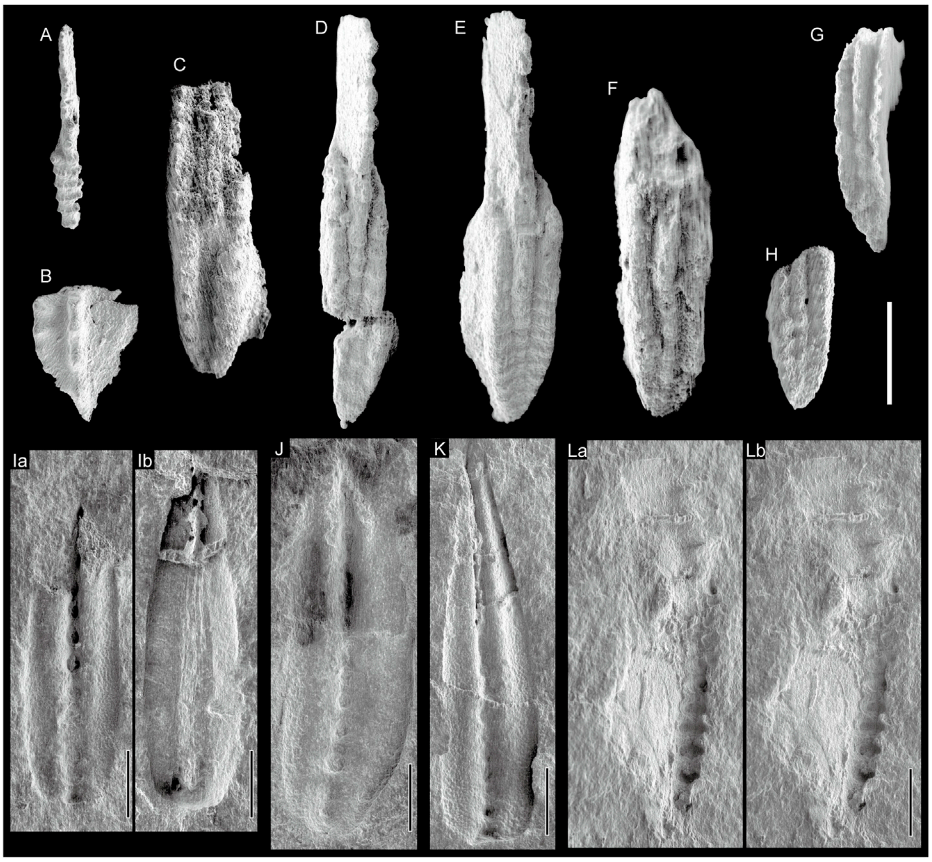

FIGURE 9
SEM photographs of conodonts obtained using dilute HF acid **(A–H)** and conodonts preserved as "clean" moulds **(I–L)** **(A)** *Idiognathoides* sp. indet., Okz-CO-02; juvenile specimen. **(B)** *Neognathodus* sp. indet., Okz-CO-02 **(C)** *St.* cf. *pauhuskaensis*, Okz-CO-04.3. **(D)** *St. ruzhencevi*, Okz-CO-03 **(D)** *St. vitali*, Okz-CO-03. **(F–H)** *St. ruzhencevi*? Okz-CO-03 **(I, J)** *M.* cf. *bisselli*, Okz-CO-05; **(Ia, Ib)** are counterparts; **(I)** shown in Figure 5S; **(J)** shown in Figure 5R **(K)** *M.* cf. *intermedia*, Okz-CO-05; shown in Figure 5W **(L)** *Sw.* cf. *asymmetricus*, Okz-CO-05; shown in Figure 5Y; (La) and (Lb) are parallel viewing stereographic pairs.

narrow platform, a wide basal cavity and a cusp broken at its thick base was identified as *Gondolella gymna* Merril and King (Figure 6D). An asymmetric carminiscaphate element with a platform crossed by uninterrupted transverse ridges that joins the blade on one side and declines into an adcarinal parapet on the other was identified as a dextral element of *Idiognathoides sinuatus* Harris and Hollingsworth (single element form species *Idiognathoides corrugatus* (Harris and Hollingsworth)) (Figure 6F). An idiognathodontid lacking a trough on the platform was identified as *Idiognathodus* sp. (Figure 6E). A juvenile element of *Idiognathoides* and a fragmented element of *Neognathodus* were extracted by treatment with dilute HF acid (Figures 9A,B). The former is distinguished by an asymmetric carminiscaphate form with the blade connecting on one lateral side of a platform covered by transverse ridges. The latter is distinguished by the carina that reaches the end of a platform with asymmetrically elevated and ornamented parapets.

Samples from the green siliceous claystone and the red siliceous claystone excluding the uppermost part (samples Okz-CO-03.1, -03.2, -04.1 and -04.2) were characterized by the dominance of carminiscaphate idiognathodontids (Figure 4). All specimens of idiognathodontids identified to the genus level belong to *Streptognathodus*, which possesses a platform with a longitudinal trough in the medial position and a carina and blade standing between adcarinal parapets.

From sample Okz-CO-03 in the green siliceous claystone, a segminiplanate gondolellid and several *Streptognathodus* elements were identified by X-ray μCT. A gondolellid element with a blade of fused stubby denticles, a moderately large terminal cusp, a narrow platform and wide basal cavity was identified as *Gondolella postdenuda* von Bitter and Merril (Figure 6I). Carminiscaphate elements with a blade that passes into a carina of nodes extending more than half the platform and short transverse ridges interrupted by a median groove was identified as *Streptognathodus vitali* Chernykh (Figures 6G,H). In addition, some *Streptognathodus* elements were extracted by dilute HF acid. Of these, one is *St. vitali*, while two others were identified as *Streptognathodus ruzhencevi* (Kozur) and *Streptognathodus* cf. *pawhuskaensis* (Harris and Hollingsworth) (Figures 9C–H). The former is distinguished by a symmetric narrow platform with carinal nodes extending to the dorsal end, and the latter by a wide and U-shaped (flat-based) median groove.

Streptognathodus from Sample Okz-CO-03.1 from the lower part of the red siliceous claystone that possess a shallow V-shaped median groove is comparable to *Streptognathodus bellus* Chernykh and Ritter (Figures 6J,K). One of these specimens is broken on the rostral side (Figure 6K), but the 3D image is not resolved enough to show the broken part as a sharp structure. *Streptognathodus bellus* was also reported from the middle part of the red siliceous claystone (sample Okz-CO-04) by Muto et al. (2021). Sample Okz-CO-03.1 yielded two other *Streptognathodus* species. An asymmetric *Streptognathodus* element with a platform oral surface that declines more steeply in the caudal side in the dorsal portion and the median groove bending towards the caudal side is comparable to *Streptognathodus flexuosus* Chernykh and Ritter (Figure 6L). A *Streptognathodus* element with a narrow platform that has a concave caudal margin and is widest in the ventral portion was identified as *Streptognathodus verus* Chernykh (Figure 7A). This form was found again in the middle part of the red siliceous claystone (sample Okz-CO-04.1; Figure 7H). Sample Okz-CO-03.2 contained three *Streptognathodus* species. A narrow *Streptognathodus* with an irregular median groove was identified as *Streptognathodus* cf. *elongianus* Boardman et al. (Figure 7B). A narrow *Streptognathodus* with a deep median groove and moderately long carina was identified as *Streptognathodus elongatus* Gunnell (Figure 7D). A *Streptognathodus* element with a platform covered by transverse ridges that are continuous across the median groove is comparable to *Streptognathodus conjunctus* Reshetkova and Chernykh (Figure 7C). Of these, *St. elongatus* was reported from the middle part of the red siliceous claystone (sample Okz-CO-04) by Muto et al. (2021). In addition, sample Okz-CO-03.2 contained a segminate element with low discrete denticles and a wide basal cavity identified as *Gondolella* sp. (Figure 7F). Sample Okz-CO-04.1 in the upper part of the red siliceous claystone yielded a *Streptognathodus* element with a blade and carina slightly offset from the median groove that was identified as *Streptognathodus* aff. *postsigmoidalis* Chernykh (Figure 7G). Approximately 1.2 m higher (sample Okz-CO-04.2), a narrow *Streptognathodus* with a constriction of the platform around the termination of the carina was found. This form was identified as *Streptognathodus constrictus* Reshetkova and Chernykh (Figures 7I,J). In addition, this sample yielded segminiplanate elements with low discrete denticles, a small basal cavity and terminal cusp, which we place in *Mesogondolella* (Figures 7K,L).

The uppermost part of the red siliceous claystone and overlying grey bedded chert (samples Okz-CO-04.3, -04.4, -05) were dominated by segminiplanate P1 elements of *Mesogondolella* (Figure 4). The uppermost part of the red siliceous claystone (sample Okz-CO-04.3) yielded three species. Narrow *Mesogondolella* elements with a small cusp and low node-like denticles that are widely spaced particularly in the ventral portion were identified as *Mesogondolella dentiseparata* (Reshetkova and Chernykh) (Figures 7M–Q; Figure 8A). Segminiplanate elements with low widely spaced denticles and a cusp outstandingly thicker and taller than the preceding denticles were identified as *Mesogondolella belladontae* (Chernykh) (Figures 8C,D). Segminiplanate elements with low discrete denticles and a cusp that is distinguishable but not dominant were identified as *Mesogondolella striata* (Chernykh and Reshetkova) (Figure 8E). The last species also occurred from the lower part of the grey bedded chert (sample Okz-CO-04.4) (Figure 8F). A higher horizon of the grey bedded chert (sample Okz-CO-05) yielded different forms of *Mesogondolella*. Forms with low generally node-like denticles and platform margins that are sub-parallel in the middle portion, tapers in the ventral area and rounded in the dorsal margin were identified as *Mesogondolella bisselli* (Clark and Behnken) (Figure 8G) and *M.* cf. *bisselli* (Figures 5R–T; Figures 9I, J). Forms with denticles that form a fused blade in the ventral portion, a cusp that is distinguishable from the preceding denticles in thickness and height and a rounded square dorsal platform margin are comparable to *Mesogondolella intermedia* (Igo) (Figures 5V–X, 8H, 9K). In addition, this sample yielded a carminiscaphate element with a ventral blade and dorsal dome-like platform with carinal nodes that are connected by a narrow medial ridge, which was identified as *Sweetognathus* cf. *asymmetricus* Sun and Lai (*sensu* Petryshen et al., 2020) (Figures 5Y, 9L).

Carminiscaphate P1 elements of *Hindeodus* were found throughout the red siliceous claystone. Some of these specimens are identifiable as *H. minutus* (Ellison) referring to the detailed morphological study of this species by Merril (1973) (Figures 5H–J). Unfortunately, all specimens of *Hindeodus* were very poorly preserved and, although the fossils were vaguely distinguishable in individual tomographic sections from the X-ray μCT scans, it was impossible to produce accurate 3D images. This is probably due to the small size and thin nature of the *Hindeodus* elements that made them susceptible to damage by alteration.

5 Discussion

5.1 Age correlation

Classic studies on conodont biostratigraphy around the CPB were conducted around the East European Platform that includes the GSSP (e.g., Barskov et al., 1981; Akhmetshina et al., 1984; Chernykh and Retshekova, 1987; Davydov et al., 1994) and Midcontinent United States (e.g., Ritter, 1995). Detailed works on conodont biostratigraphy of intervals including the CPB have also been published from South China (e.g., Wang and Qi, 2003), western United States (Lucas et al., 2017; Ritter., 2020; Beauchamp et al., 2022b) and Arctic Canada (Beauchamp et al., 2022a). Below, we compare the occurrence of conodonts mainly with these regions to assign the age of the Okoshizawa section. Because the basal part of the Okoshizawa section yielded distinctly older conodonts compared to the rest, the basal part (sample Okz-CO-02) and the main part (all other samples) are discussed separately.

The combination of all three species from the lowermost part of the Okoshizawa section (Okz-CO-02) is not reported from other regions. Of these, *Id. sinuatus* is the most widely recognized species, occurring from around the East European Platform, central and western United States, South China (references below), Europe (Nemyrovskaya et al., 2011), Japan (Takahashi et al., 2020) and South America (Nascimento et al., 2005; Cardoso et al., 2017). It occurs in the Bashkirian to lower Moscovian in the Donets Basin (Nemyrovskaya, 1999; Nemyrovskaya et al., 1999; Fohrer et al., 2007) and the Bashkirian Mountains (Nemirovskaya and Alekseev, 1994) around the East European Platform and South China (Wang and Qi, 2003; Qi et al., 2014, 2016; Hu et al., 2017). In the United States, the range of this species ends lower, covering most of the Morrowan regional stage, which correlates with most of the Bashkirian (Dunn, 1970; Lane and Straka, 1974; Baesemann and Lane, 1985). *Mesogondolella clarki* occurs from the upper Moscovian in the Donets Basin (Nemyrovskaya, 2011; Nemyrovskaya, 2017) and lower to middle Moscovian in South China (Wang and Qi, 2003; Qi et al., 2014; Qi et al., 2016; Hu et al., 2017). Thus, *Id. sinuatus* disappears before the appearance of *M. clarki* in the Donets Basin, while it cooccurs with *M. clarki* in the lower Moscovian in South China. *Mesogondolella clarki* is also reported from strata correlated to the upper Bashkirian and middle Moscovian in Alaska (Savage and Barkeley, 1985), but the stratigraphic distribution of conodont species used as age indicators therein appears to contradict with more intensely studied regions, suggesting that the biostratigraphy may require reconsideration. *Gondolella gymna* is recorded from the Seville limestone in Illiois (Merril and King, 1971; von Bitter and Merril, 1980), which is correlated to the middle Moscovian (Barrick et al., 2022). This species is not documented around the East European Platform or South China, although a similar form of *Gondolella* with a reduced platform and a large cusp is reported in the upper Bashkirian to lower Moscovian in the latter (Qi et al., 2016). The three species from Okoshizawa occur from seamount limestones in the Permian accretionary complex of the Akiyoshi Belt in Japan, which were also deposited in pelagic Panthalassa (Atetsu limestone, Koike, 1967; Ko-yama limestone, Ishida et al., 2013; Omi limestone, Takahashi et al., 2020). *Idiognathoides sinuatus* is only known from the Bashikirian of the Atetsu limestone, *M. clarki* is reported from the lower Moscovian in all three studied areas, and *G. gymna* is only known from the upper Bashkirian to lower Moscovian of the Omi limestone (*Gondolella*? sp. A of Koike, 1967).

Putting an emphasis on conodont occurrences around the East European Platform, Midcontinent United States and South China, it is most parsimonious to correlate the basal part of the Okoshizawa section to the lower Moscovian (Supplementary Figure S1, Supplementary Datasheet 3). This age assignment assumes that in Okoshizawa the range of *Id. sinuatus* is similar to that in South China, the Donets Basin and Bashkirian Mountains, that of *M. clarki* is similar to that in South China and that of *G. gymna* is similar to Midcontinent United States. On the other hand, the range of *M. clarki* extends lower than the Donets Basin and the range of *Id. sinuatus* extends higher than the United States in Okoshizawa.

In strata of Late Pennsylvanian age, species of *Idiognathodus* and *Streptognathodus* are used to define conodont biozones both around the East European Platform typified by sections in the Ural region (Chernykh and Ritter, 1997; Chernykh, 2005; Chernykh, 2006; Goreva and Alekseev, 2010) and in Midcontinent United States (Ritter, 1995; Barrick et al., 2004; Barrick et al., 2013; Barrick et al., 2022). In the lower Cisuralian, species of *Streptognathodus*, *Sweetognathus* and *Mesogondolella* are considered as key age indicators in the Ural region (Chernykh, 2005, 2006), while the former two genera are mainly used in Midcontinent United States (Boardman et al., 2009). *Steptognathodus*-based zones of the Upper Pennsylvanian to lowermost Cisuralian have been reproduced in South China (Wang and Qi, 2003; Hu et al., 2020). A number of stratigraphically important species of *Streptognathodus* have been confirmed as widely distributed, including *Streptognathodus isolatus*, which defines the CPB (Davydov et al., 1998). Earliest Permian species of *Mesogondolella* were originally known only from the Ural region (Chernykh and Reshetkova, 1987; Chernykh, 2005; Chernykh, 2006), but have recently been found from Nevada (Wardlaw et al., 2015; Beauchamp et al., 2022b) and the Sverdrup Basin (Beauchamp et al., 2022a), confirming the validity of this group as correlation markers.

Streptognathodus vitali from sample Okz-CO-03 in the green siliceous claystone of the Okoshizawa section is a zonal marker species for the lower Gzhelian both around the East European Platform (Chernykh, 2005, 2006; Goreva and Alekseev, 2010) and in Midcontinent United States (Barrick et al., 2013; Barrick et al., 2022). This species also occurs in the lower Gzhelian of South China (Hu et al., 2020). *Streptognathodus pauhuskaensis* and *St. ruzhencevi* are species that respectively have lowest occurrences (LOs) below and above that of *St. vitali*, and cooccur in the lower Gzhelian *St. vitali* Zone around the East European Platform (Goreva and Alekseev, 2010) and in Midcontinent United States (Barrick et al., 2013; Barrick et al., 2022). In South China, *St. pauhuskaensis* occurs from the upper Kasimovian to lower Gzhelian (Wang and Qi, 2003; Hu et al., 2020). The sample from Okoshizawa also yielded *G. postdenuda*, a species that occurs from the lower Gzhelian with *St. vitali* (von Bitter and Merril, 1980; Heckel, 2013). Thus, conodonts from sample Okz-CO-03 indicate the lower Gzhelian.

The lower to middle part of the red siliceous claystone in Okoshizawa (samples Okz-CO-03.1, -03.2 and -04) yielded *St. bellus* and comparable specimens. This is a zonal marker species of the upper Gzhelian around the East European Platform (Chernykh, 2005; Chernykh, 2006; Goreva and Alekseev, 2010) as well as Midcontinent United States (Barrick et al., 2013; Barrick et al., 2022). This species also occurs from the upper Gzhelian of South China (Wang and Qi, 2003). In Okoshizawa, the range of *St. bellus* and comparable specimens parallel the range of *St. elongatus*, which appears in the upper part of the range of *St. bellus* in the Urals (Schmitz and Davydov, 2012), Midcontinent United States (Boardman et al., 2009) and South China (Wang and Qi, 2003). *Streptognathodus elongatus* is also known from the upper Gzhelian in western United States (Ritter, 2020). *Streptognathodus* cf. *flexuosus* and *St. conjunctus* occurred in the lower samples containing *St. bellus* in Okoshizawa. *Streptognathodus flexuosus* occurs in the upper part of the range of *St. bellus* in the Urals (Schmitz and Davydov, 2012) and Midcontinent United States (Boardman et al., 2009) and *St. conjunctus* occurs from the uppermost Gzhelian with *St. elongatus* in the Urals (Barskov et al., 1981; Chernykh and Reshetkova, 1987), Midcontinent United States (Boardman et al., 2009) and western United States (Ritter, 2020). Hence, the lower to middle part of the red siliceous claystone is correlated to the upper Gzhelian.

Sample Okz-CO-04.2 from the upper part of the red siliceous claystone yielded *St. constrictus*. This species characterizes the Asselian in the Urals (Chernykh, 2005, 2006; Chernykh et al., 2020), Novaya Zemlya (Sobolev and Nakrem, 1996), Midcontinent United States (Boardman et al., 2009), Nevada (Beauchamp et al., 2022b) and the Sverdrup Basin (Beauchamp et al., 2022a). Due to its wide distribution, *St. constrictus* has been proposed as a marker species for an international zonation (Henderson, 2018). From the top of the red siliceous claystone in Okoshizawa (sample Okz-CO-043), we obtained *M. belladontae*, *M. dentiseparata* and *M. striata*, the lattermost of which also occurred higher in the grey bedded chert (sample Okz-CO-04.4). These three species occur from the Asselian in the Urals (Chernykh, 2005; Chernykh, 2006; Chernykh et al., 2020), Novaya Zemlya (Sobolev and Nakrem, 1996), Nevada (Beauchamp et al., 2022b) and the Sverdrup Basin (Beauchamp et al., 2022a), with the LOs of *M. belladontae* and *M. dentiseparata* in the lower Asselian (except for Nevada where the latter appears in the middle Asselian), and the LO of *M. striata* and the highest occurrence of *M. belladontae* in the middle Asselian. The conodonts indicate that the upper part of the red siliceous claystone to the lower part of the grey chert is correlated to the Asselian.

The highest sample in Okoshizawa yielded *M. bisselli*, *M.* cf. *bisselli*, *M.* cf. *intermedia* and *Sw.* cf. *asymmetricus*. The cooccurrence of *M. bisselli*, *M. intermedia* and *Sw. asymmetricus* is recorded in the middle Artinskian of Nevada (Beauchamp et al., 2022b) and the Sverdrup Basin (Beauchamp et al., 2022a). *Mesogondolella intermedia* has not been reported from the Urals, but this absence is interpreted as a result of the disappearance of *Mesogondolella* in the middle Artinskian in the Urals due to shallowing of the depositional environment (Henderson, 2018). The three species also cooccur in Artinskian limestone deposited on Panthalassic seamounts (Igo, 1981; *Sw. asymmetricus* is referred to as *Sweetognathus whitei* therein). Hence, the conodonts from this sample indicate the middle Artinskian.

To summarize the above, the main part of the Okoshizawa section is correlated to the Geologic Time Scale as follows: the green siliceous claystone is correlated to the lower Gzhelian, the lower to middle part of the red siliceous claystone to the upper Gzhelian, the upper part of the red siliceous claystone to the lower to middle Asselian, the lower part of the grey bedded chert to the upper Asselian and the upper part of the grey chert to the middle Artinskian (Figure 4). Kasimovian and Sakmarian strata have not been confirmed by conodonts, which is probably a result of insufficient sampling density in these deep-sea rocks with very low sedimentation rates. Regarding the position of the CPB, *St. isolatus*, which defines the boundary, was not found in the present study. The most important species that constrain the CPB in the Okoshizawa section are *St. bellus* and *St. constrictus*. The former is restricted to the Gzhelian in the Ural region (Chernykh and Ritter, 1997; Schmitz and Davydov, 2012) and Midcontinent United States (Boardman et al., 2009), while it enters the basal Asselian in South China (Wang and Qi, 2003). The latter species occurs above the CPB in the lower Asselian in the Urals (Chernykh, 2005, 2006; Chernykh et al., 2020), Novaya Zemlya (Sobolev and Nakrem, 1996), Midcontinent United States (Boardman et al., 2009), Nevada (Beauchamp et al., 2022b) and the Sverdrup Basin (Beauchamp et al., 2022a). Therefore, we place the CPB between the occurrence of these two species in the Okoshizawa section. Sample Okz-CO-04.1 is positioned within this interval, but unfortunately did not yield conodonts that allow further robust age constraints. A specimen from this sample that offers an additional hint for the placement of the CPB is *St.* aff. *postsigmoidalis*, which has a weakly sigmoidal alignment of the blade, carina and median groove. In the above features it has an affinity with Asselian lineages from *Streptognathodus cristellaris* to *St. postsigmoidalis* or to *Streptognathodus plenus* (Chernykh, 2006). If our specimen belongs to this lineage, the CPB should be placed below this sample, but this argument remains highly speculative at this point.

Two *Streptognathodus* species from Okoshizawa do not show the same stratigraphic distribution as other regions. *Streptognathodus* cf. *elongianus* was found in sample Okz-CO-03.2 with *St. conjunctus* and *St. elongatus*. *Streptognathodus elongianus* was described from the basal part of the range of *St. bellus* in Midcontinent United States, and below the LO of *St. flexuosus* and *St. conjunctus* (Boardman et al., 2009) and is also known from below the LO of the latter two species in New Mexico (Lucas et al., 2017). This species is not reported outside the United States, and its stratigraphic distribution on the global scale may need further consideration. We identified *St. verus* in two samples. This species is known to occur above *St. constrictus* in the Urals (Chernykh, 2005, 2006) and Midcontinent United States (Henderson, 2018), and the occurrence in Okoshizawa is considerably older. Therefore, our specimens may represent a separate species.

5.2 Faunal characteristics

Out of all conodont elements found in the Okoshizawa section, only a minor portion was identified to the species level due to the paucity of well-preserved specimens. This situation generally prohibits discussions about the faunal characteristics of the section at the species level. On the other hand, inferences can be made on faunal characteristics at higher taxonomic levels (e.g., *Streptognathodus* vs. *Mesogondolella*).

As explained above, the basal part of the Okoshizawa section is correlated to the lower Moscovian. In the well-studied sections in the Donets Basin, Bashikirian Mountains, western and central United States and South China, lower Moscovian strata are generically rich, and yield species of *Adetognathus*, *Declinognathodus*, *Diplognathodus*, *Hindeodus*, "*Streptognathodus*" and *Swadelina* in addition to *Idiognathoides*, *Idiognathodus*, *Neognathodus*, *Mesogondolella* and *Gondolella* (Lane and Straka, 1974; Baesemann and Lane, 1985; Nemyrovskaya et al., 1999; Stamm and Wardlaw, 2003; Qi et al., 2014; Qi et al., 2016). Despite the fact that the number of identified conodont elements in the Okoshizawa sample is not so large, we recognized the latter five genera. Although not confirmed in this study, Ehiro et al. (2008) reported *Idiognathodus delicatus*, *Diplognathodus atetsuensis* and *Diplognathodus coloradoensis* from the same interval of the Okoshizawa section. Lower Moscovian seamount limestones of pelagic Panthalassa, also yield diverse conodonts consisting of *Idiognathoides*, *Idiognathodus*, *Neognathodus*, *Mesogondolella*, *Hindeodus* and "*Streptognathodus*" (Koike, 1967; Ishida et al., 2013; Takahashi et al., 2020). Thus, the early Moscovian conodont fauna in pelagic Panthalassa was diverse at the generic level both in shallow and deep areas, and many of the genera known from peri-continental regions were also present in the ocean thousands of kilometres away from the nearest continents. An exception may be *Adetognathus*, which is regarded to be a nearshore taxon (Driese et al., 1984; Davis and Webster, 1985), consistent with the fact that it has not been recovered from Okoshizawa or the seamount limestones.

The most striking feature in the faunal character of the Okoshizawa section is the abrupt change from a *Streptognathodus*-dominated fauna to a *Mesogondolella*-dominated fauna in the Asselian (Figure 4; Supplementary Table S2). Although *Mesogondolella*-like platform elements do occur below this transition, their abundance is inferior compared to *Streptognathodus*. The shift in dominant taxon from *Streptognathodus* to *Mesogondolella* is also suggested in another pelagic deep-sea section in Shizugawa, Kyoto, Southwest Japan, although details on their abundance is not mentioned (Kusunoki et al., 2004). *Mesogondolella* is regarded as a deep-water taxon and their abundance is controlled by fluctuations in sea-levels as well as "actual" origination and extinction (Henderson, 2018; Beauchamp et al., 2022b). For example, the disappearance of this genus in the Artinskian in the Urals is considered as a result of shallowing, while its complete absence in the Midcontinent United States is attributed to the consistently shallow setting (Henderson, 2018). On the other hand, the strata of the Okoshizawa section were deposited on a pelagic deep seafloor that received little or no effect of sea level changes, reflected in the constantly very fine-grained and carbonate-lacking lithology of the main part of the section. Therefore, the sudden faunal change in the Okoshizawa section is unrelated to sea level change and is rather attributed to ecological replacement of *Streptognathodus* by *Mesogondolella* in pelagic Panthalassa, perhaps as a result of competition. *Mesogondolella* appeared in the lower Asselian in the Urals (Chernykh, 2005; Chernykh, 2006; Chernykh et al., 2020), western United States (Wardlaw et al., 2015; Beauchamp et al., 2022b) and the Sverdrup Basin (Beauchamp et al., 2022a), but were not yet abundant in pelagic Panthalassa, where *Streptognathodus* remained dominant. By the middle Asselian, *Mesogondolella* proliferated and spread into pelagic Panthalassa, apparently forcing *Streptognathodus* into demise. Early Cisuralian *Mesogondolella* was long unreported from outside the Urals, but were recently shown to be present in western United States and the Sverdrup Basin (see references above). The result of this study extends the confirmed palaeogeographic domain of *Mesogondolella* and further strengthens the basis for using the taxon for global correlation of the lower Cisuralian. Since the stratigraphic range of *Mesogondolella* species is sometimes difficult to deduce from peri-continental sections due to the effect of sea level changes, pelagic deep-sea sections such as the Okoshizawa section would be important reference sections to elucidate the timing of origination and extinction of these taxa.

The genus *Streptognathodus*, along with *Idiognathodus*, includes species that are found ubiquitously in various environments, while some of its members are thought to have environmentally restricted habitats (Merril and von Bitter, 1984). In particular, Henderson (2018) pointed out that *Streptognathodus* was ecologically replaced by *Sweetognathus*, which is a shallow-water taxon (Petryshen et al., 2020; Beauchamp et al., 2022b). This is seemingly contradictory with the dominance of *Streptognathodus* in the pelagic deep-sea sedimentary rocks in Okoshizawa in the Gzheian to lower Asselian and its replacement not by *Sweetognathus* but by *Mesogondolella* in the middle Asselian. However, we draw attention to the fact that the youngest members of *Streptognathodus* are known from the upper Asselian in peri-continental regions (Boardman et al., 2009; Chernykh et al., 2020; Beauchamp et al., 2022a, b) and that they have not been recovered in Okoshizawa. We infer that these late Asselian *Streptognathodus* holdovers were generally restricted to shallow seas near landmasses similar to its ecological successor, *Sweetognathus*, as Henderson (2018) stated. On the other hand, *Streptognathodus* of ecological niche in deeper waters were probably driven into extinction by proliferating *Mesogondolella* in the middle Asselian.

The conodont *Streptognathodus isolatus*, which defines the CPB in the GSSP in Aidaralash, Kazakhstan, was not recovered in this study. This is partly contributing to the difficulty in placing the CPB in the Okoshizawa section. The diagnostic feature of *St. isolatus* is the presence of accessory nodes on the caudal lobe of the platform, separated from the platform by a narrow groove. In the Okoshizawa section, we found no *Streptognathodus* with accessory nodes or lobes on the platform. Thus, not only *St. isolatus*, but all *Streptognathodus* species possessing accessory nodes and lobes are absent. This is also the case with the pelagic deep-sea section in Shizugawa, Kyoto (Kusunoki et al., 2004). While the absence of *St. isolatus* may be a result of insufficient sampling density, the total absence of lobed or node-bearing *Streptognathodus* throughout the Okoshizawa section cannot be explained simply by sparsity of sampled horizons. For example, *Streptognathodus wabaunsensis*, a species that bears accessory nodes on the caudal lobe that cooccurs with *St. elongatus* in the upper Gzhelian in both Kazakhstan (Chernykh and Ritter, 1997) and Midcontinent United States (Boardman et al., 2009), was not found in our samples, nor were any *Streptognathodus* with accessory nodes found within the corresponding interval. Although further research on more numerous specimens of this genus is desired, *Streptognathodus* with accessory nodes and lobes seem to be rare or absent in the Gzhelian to middle Asselian pelagic deep areas of Panthalassa and may have been members of this genus that have a somewhat restricted distribution.

Finally, a noteworthy specimen is *Gondolella* sp. in the upper Gzhelian sample. This specimen has a widely inflated, thin-walled and ventrally extended basal cavity and a completely reduced platform showing similarities with the Gzhelian genus *Solkognathus* and the Permian genus *Vjalovognathus* (Figures 5G, 7F). It has been proposed that both *Vjalovognathus* and *Solkognathus* developed from *Gondolella* with reduced or no platforms (Nicoll and Metcalfe, 1998; Yuan et al., 2016). *Solkognathus* is only represented by one species in the upper Gzheian of the Urals (Chernykh, 2005), while *Vjalovognathus* is a genus restricted to peri-Gondwana seas that appeared in the Sakmarian (Nicoll and Metcalfe, 1998; Mei and Henderson, 2001; Yuan et al., 2016). Similar forms are also reported from Gzhelian or Asselian chert deposited in pelagic deep Panthalassa (Plate 2, Figures 8, 9 in Kusunoki et al., 2004). Present knowledge on this group in the Gzhelian to Asselian interval is limited, but they may have originated in the Ural region and spread elsewhere in the Gzhelian, then became restricted to peri-Gondwanan regions by the Sakmarian.

6 Conclusion

We investigated a siliceous deep-sea section (the Okoshizawa section) in Northeast Japan that was accumulated in pelagic Panthalassa. While some conodont fossils were obtained by conventional dilute HF acid dissolution, a large number of conodonts were observed using a laboratory-based X-ray microscope on specimens found on rock pieces by an optic microscope. The increase in efficiency of observing conodonts from these rocks made it possible to identify enough specimens to make correlations with other regions and make inferences on the faunal characteristics of conodonts in pelagic deep areas of Panthalassa. Based on the obtained conodonts, the section was dated as early Moscovian to middle Artinskian. Important age indicators such as *Id. sinuatus*, *St. vitali*, *St. bellus*, *St. elongatus*, *St. constrictus*, *M. belladontae*, *M. dentiseparata*, *M. striata* and *M. bisselli* were recognized by images obtained by X-ray μCT. The CPB is placed between the occurrences of *St. bellus* and *St. constrictus*. Asselian species of *Mesogondolella* were documented for the first time in pelagic Panthalassa, supporting the validity of these species for global correlation. In the Okoshizawa section, the conodont fauna changes drastically from a *Streptognathodus*-dominated one to a *Mesogondolella*-dominated one in the middle Asselian. This turnover probably reflects an ecological replacement of *Streptognathodus* by *Mesogondolella* in pelagic deep areas of Panthalassa.

Data availability statement

The original contributions presented in the study are included in the article/Supplementary Material, further inquiries can be directed to the corresponding authors.

Author contributions

SM designed the research, carried out the field investigation, sample collection, sample processing, X-ray scans, SEM phtotography and wrote the manuscript. ST took part in initiating the research and manuscript editing. MM collaborated in the initiation of the research, took care of X-ray scanning and edited the manuscript. All authors contributed to the article and approved the submitted version.

Funding

This study was supported by JSPS Grant-in-Aid for Research Activity Start-up Grant Number 19K23470.

Acknowledgments

The authors are deeply indebted to Kazuko Yoshizawa for helping us with finding references and producing illustrations, to Masanori Ozeki for assistance in laboratory work and illustrations, to Shinsuke Yagyu and Takuya Matsuzaki for their support during X-ray scans, to Noritoshi Suzuki for sharing his collection of literature and to Koji Seike for his help in 3D-visualization of conodonts using Amira Software. We are grateful to two reviewers Andrey Zhuravlev and Li Tian and editor Pauline Guenser who helped improve the manuscript. This study was performed under the cooperative research program of Center for Advanced Marine Core Research (CMCR), Kochi University, Accept Nos. 22A048 and 22B043.

Conflict of interest

The authors declare that the research was conducted in the absence of any commercial or financial relationships that could be construed as a potential conflict of interest.

Publisher's note

Supplementary material

The Supplementary Material for this article can be found online at: https://www.frontiersin.org/articles/10.3389/feart.2023.1162023/full#supplementary-material

References

Akhmetshina, L. Z., Barskov, I. S., and Isakova, T. N. (1984). Gzhelian, asselian, and sakmarian conodonts from the Russian platform, southern Urals, and pre-caspian basin. *Trans. Mosc. State Univ.* 13, 51–54. (in Russian).

Baesemann, J. F., and Lane, H. R. (1985). Taxonomy and evolution of the genus Rhachistognathus Dunn (conodonta; late Mississippian to early middle Pennsylvanian). *Cour. Forsohungsinstitut Senckenb.* 74, 93–136.

Barrick, J. E., Alekseev, A. S., Blanco-Ferrera, S., Goreva, N. V., Hu, K., Lambert, L. L., et al. (2022). Carboniferous conodont biostratigraphy. *Geol. Soc. Lond. Spec. Publ.* 512, 695–768. doi:10.1144/sp512-2020-38

Barrick, J. E., Lambert, L. L., Heckel, P. H., and Boardman, D. R. (2004). Pennsylvanian conodont zonation for midcontinent north America. *Rev. Española Micropaleontol.* 36, 231–250.

Barrick, J. E., Lambert, L. L., Heckel, P. H., Rosscoe, S. J., and Boardman, D. R. (2013). Midcontinent Pennsylvanian conodont zonation. *Stratigraphy* 10, 55–72.

Barskov, I. S., Isakova, T. N., and Schastlivcheva, N. P. (1981). Conodonts of the gzelian and asselian boundary beds, southern Urals. *Izvesiya Acad. Nauk. SSR, Seriya Geol.* 5, 78–87. (in Russian).

Beauchamp, B., González, D. C., Henderson, C. M., Baranova, D. V., Wang, H., and Pelletier, E. (2022a). Late pennsylvanian–early permian tectonically driven stratigraphic sequences and carbonate sedimentation along northern margin of Sverdrup Basin (otto fiord depression, arctic Canada). *SEPM Spec. Publ.* 113, 226–254. doi:10.2110/sepmsp.113.12

Beauchamp, B., Henderson, C. M., Dehari, E., Von Bassenheim, D. W., Elliot, S., and González, D. C. (2022b). Carbonate sedimentology and conodont biostratigraphy of late pennsylvanian–early permian stratigraphic sequences, carlin canyon, Nevada: New insights into the tectonic and oceanographic significance of an iconic succession of the Basin and range. *SEPM Spec. Publ.* 113, 34–71. doi:10.2110/sepmsp.113.14

Boardman, D. R., II, Wardlaw, B. R., and Nestell, M. K. (2009). *Stratigraphy and conodont biostratigraphy of the uppermost carboniferous and lower permian from the North American midcontinent [also on CD]*. Lawrence: Kansas Geological Survey, 42.

Cardoso, C. N., Sanz-López, J., and Blanco-Ferrera, S. (2017). Pennsylvanian conodonts from the tapajós group (amazonas basin, Brazil). *Geobios* 50, 75–95. doi:10.1016/j.geobios.2017.02.004

Chernykh, V. V., Chuvashov, B. I., Shen, S. Z., Henderson, C. M., Yuan, D. X., and Stephenson, M. H. (2020). The global stratotype section and point (GSSP) for the base-sakmarian stage (cisuralian, lower permian). *Episodes* 43, 961–979. doi:10.18814/EPIIUGS/2020/020059

Chernykh, V. V. (2006). Lower permian conodonts in the Urals. *Ekaterinburg Inst. Geol. Geochem. Uralian Branch Russ. Acad. Sci*, 130.

Chernykh, V. V., and Reshetkova, N. P. (1987). The biostratigraphy and conodonts from Carboniferous–Permian boundary deposits on the west slope of the Urals. *Sverdlovsk Uralian Branch, USSR Acad. Sci*, 53.

Chernykh, V. V., and Ritter, S. M. (1997). Streptognathodus (conodonta) succession at the proposed carboniferous–permian boundary stratotype section, Aidaralash Creek, northern Kazakhstan. *J. Paleontol.* 71, 459–474. doi:10.1017/s0022336000039470

Chernykh, V. V. (2005). *Zonal method in biostratigraphy, zonal conodont scale of the Lower Permian in the Urals*. Ekaterinburg: Institute of Geology and Geochemistry of RAN. (in Russian), 217.

Clark, D. L., and Mosher, L. C. (1966). Stratigraphic, geographic, and evolutionary development of the conodont genus Gondolella. *J. Paleontol.* 40, 376–394.

Cnudde, V., and Boone, M. N. (2013). High-resolution X-ray computed tomography in geosciences: A review of the current technology and applications. *Earth-Sci. Rev.* 123, 1–17. doi:10.1016/j.earscirev.2013.04.003

Cunningham, J. A., Rahman, I. A., Lautenschlager, S., Rayfield, E. J., and Donoghue, P. C. J. (2014). A virtual world of paleontology. *Trends Ecol. Evol.* 29, 347–357. doi:10.1016/j.tree.2014.04.004

Davis, L. E., and Webster, G. D. (1985). Late mississippian to early pennsylvanian conodont biofacies in central Montana. *Lethaia* 18, 67–72. doi:10.1111/j.1502-3931.1985.tb00685.x

Davydov, V. I., Barskov, I. S., Bogoslovskaya, M. F., Leven, E. Y., Popov, A. V., Akhmetshina, L. Z., et al. (1994). The carboniferous–permian boundary in stratotype sections of the south Urals and its correlation. *Stratigr. Geol. Correl.* 2, 889–906. doi:10.1080/00206819209465643

Davydov, V. I., Glenister, B. F., Spinosa, C., Ritter, S. M., Chernykh, V. V., Wardlaw, B. R., et al. (1998). Proposal of Aidaralash as global stratotype section and point (GSSP) for base of the permian system. *Episodes* 21, 11–18. doi:10.18814/epiiugs/1998/v21i1/003

Driese, S. G., Carr, T. R., and Clark, D. L. (1984). Quantitative analysis of Pennsylvanian shallow-water conodont biofacies, Utah and Colorado. *Geol. Soc. Am. Mem.* 196, 233–250.

Dunn, D. L. (1970). Middle Carboniferous conodonts from Western United States and phylogeny of the platform group. *J. Paleontol.*, 312–342.

Ehiro, M., Yamakita, S., Takahashi, S., and Suzuki, N. (2008). Jurassic accretionary complexes of the North Kitakami Belt in the akka-kuji area, Northeast Japan. *J. Geol. Soc. Jpn.* 114, 121–139. (in Japanese). doi:10.5575/geosoc.114.s121

Fohrer, B., Nemyrovska, T. I., Samankassou, E., and Ueno, K. (2007). The pennsylvanian (moscovian) izvarino section, Donets Basin, Ukraine: A multidisciplinary study on microfacies, biostratigraphy (conodonts, foraminifers, and ostracodes), and paleoecology. *Mem. (The Paleontol. Soc.* 69, 1–85. doi:10.1666/06-121.1

Geological Survey of Japan, AIST (2020) Seamless digital geological map of Japan 1: 200,000. Geological Survey of Japan, AIST.

Goreva, N. V., and Alekseev, A. S. (2010). Upper carboniferous conodont zones of Russia and their global correlation. *Stratigr. Geol. Correl.* 18, 593–606. doi:10.1134/S086959381006002X

Goudemand, N., Orchard, M. J., Tafforeau, P., Urdy, S., Brühwiler, T., Brayard, A., et al. (2012). Early Triassic conodont clusters from South China: Revision of the architecture of the 15 element apparatuses of the superfamily Gondolelloidea. *Palaeontology* 55, 1021–1034. doi:10.1111/j.1475-4983.2012.01174.x

Goudemand, N., Orchard, M. J., Urdy, S., Bucher, H., and Tafforeau, P. (2011). Synchrotron-aided reconstruction of the conodont feeding apparatus and implications for the mouth of the first vertebrates. *Proc. Natl. Acad. Sci. U. S. A.* 108, 8720–8724. doi:10.1073/pnas.1101754108

Grasby, S. E., Bond, D. P. G., Wignall, P. B., Yin, R., Strachan, L. J., and Takahashi, S. (2021). Transient Permian-Triassic euxinia in the southern Panthalassa deep ocean. *Geology* 49, 889–893. doi:10.1130/G48928.1

Guenser, P., Souquet, L., Dolédec, S., Mazza, M., Rigo, M., and Goudemand, N. (2019). Deciphering the roles of environment and development in the evolution of a Late Triassic assemblage of conodont elements. *Paleobiology* 45, 440–457. doi:10.1017/pab.2019.14

Hayashi, S., Iijima, S., Nakajima, T., Sawaguchi, T., Tanaka, H., and Yoshida, H. (1990). Late paleozoic to mesozoic formations in the southwestern Ashio mountains. *Bull. Gunma Prefect. Mus. Hist.* 11, 1–34. (in japanese with English abstract).

Hayashi, S. (1968). The permian conodonts in chert of the adoyama formation, Ashio mountains, central Japan. *Earth Sci. (Chikyu Kagaku)* 22, 63–77. (in Japanese with English abstract and description).

Heckel, P. H. (2013). Pennsylvanian stratigraphy of northern Midcontinent Shelf and biostratigraphic correlation of cyclothems. *Stratigraphy* 10, 3–39.

Henderson, C. M. (2018). Permian conodont biostratigraphy. *Geol. Soc. Spec. Publ.* 450, 119–142. doi:10.1144/SP450.9

Hori, R. S., Yamakita, S., Ikehara, M., Kodama, K., Aita, Y., Sakai, T., et al. (2011). Early triassic (induan) radiolaria and carbon-isotope ratios of a deep-sea sequence from waiheke island, north island, New Zealand. *Palaeoworld* 20, 166–178. doi:10.1016/j.palwor.2011.02.001

Hu, K., Qi, Y., Qi, W., and Wang, Q. (2020). Carboniferous conodont zonation of China. *Newsletters Stratigr.* 53, 141–190. doi:10.1127/nos/2019/0498

Hu, K. Y., Qi, Y. P., Wang, Q. L., Nemyrovska, T. I., and Chen, J. T. (2017). Early pennsylvanian conodonts from the luokun section of luodian, guizhou, south China. *Palaeoworld* 26, 64–82. doi:10.1016/j.palwor.2015.12.003

Huang, J., Martínez-Pérez, C., Hu, S., Zhang, Q., Zhang, K., Zhou, C., et al. (2019). Apparatus architecture of the conodont Nicoraella kockeli (Gondolelloidea, Prioniodinina) constrains functional interpretations. *Palaeontology* 62, 823–835. doi:10.1111/pala.12429

Igo, H. (1981). Permian conodont biostratigraphy of Japan. *Palaeontol. Soc. Jpn. Spec. Pap.* 24, 1–51.

Ishida, K., Suzuki, S., and Inada, N. (2013). Visean – moscovian conodont biostratigraphy of the ko-yama limestone group, Akiyoshi Belt, SW Japan. *Natral Sci. Res. Univ. Tokushima* 27, 29–52.

Isozaki, Y., Maruyama, S., Aoki, K., Nakama, T., Miyashita, A., and Otoh, S. (2010). Geotectonic subdivision of the Japanese islands revisited: Categorization and definition of elements and boundaries of pacific-type (Miyashiro-type) orogen. *Chigaku Zasshi (Jounal Geogr.* 119, 999–1053. (in Japanese with English abstract). doi:10.5026/jgeography.119.999

Isozaki, Y., Maruyama, S., and Furuoka, F. (1990). Accreted oceanic materials in Japan. *Tectonophysics* 181, 179–205. doi:10.1016/0040-1951(90)90016-2

Isozaki, Y., and Matsuda, T. (1980). Age of the tamba group along the hozugawa "anticline". *West. hills Kyoto, Southwest Jpn. J. Geosci. Osaka City Univ.* 23, 115–134.

Jones, D., Evans, A. R., Siu, K. K. W., Rayfield, E. J., and Donoghue, P. C. J. (2012). The sharpest tools in the box? Quantitative analysis of conodont element functional morphology. *Proc. R. Soc. B Biol. Sci.* 279, 2849–2854. doi:10.1098/rspb.2012.0147

Ketcham, R. A., and Carlson, W. D. (2001). Acquisition, optimization and interpretation of X-ray computed tomographic imagery: Applications to the geosciences. *Comput. Geosci.* 27, 381–400. doi:10.1016/S0098-3004(00)00116-3

Koike, T. (1967). A Carboniferous succession of conodont faunas from the Atetsu Limestone in southwest Japan (Studies of Asiatic conodonts, Part 4). *Tokyo Kyoiku Daigaku Sci. Rep. Sect. C Geol. Mineral. Geogr.* 92, 279–318.

Kusunoki, T., Ohara, M., and Musashino, M. (2004). Carboniferous-Permian microbiostratigraphy in chert sequence from the southeastern part of the Tamba Belt, Shizugawa district, Uji City (Outline note). *Earth Sci. (Chikyu Kagaku)* 58, 37–54. (in Japanese with English abstract).

Lane, H. R., and Straka, J. J. (1974). *Late Mississippian and early pennsylvanian conodonts, Arkansas and Oklahoma*. Boulder: Geological Society of America.

Lucas, S. G., Krainer, K., Barrick, J. E., Vachard, D., and Ritter, S. M. (2017). Lithostratigraphy and microfossil biostratigraphy of the pennsylvanian-lower permian horquilla formation at new well peak, big HatchetMountains, new Mexico, USA. *Stratigraphy* 14, 223–246. doi:10.29041/strat.14.1-4.223-246

Martínez-Pérez, C., Rayfield, E. J., Botella, H., and Donoghue, P. C. J. (2016). Translating taxonomy into the evolution of conodont feeding ecology. *Geology* 44, 247–250. doi:10.1130/G37547.1

Matsuda, T., and Isozaki, Y. (1991). Well-documented travel history of Mesozoic pelagic chert in Japan: From remote ocean to subduction zone. *Tectonics* 10, 475–499. doi:10.1029/90tc02134

Mazza, M., and Martínez-Pérez, C. (2015). Unravelling conodont (Conodonta) ontogenetic processes in the Late Triassic through growth series reconstructions and X-ray microtomography. *Boll. della Soc. Paleontol. Ital.* 54, 161–186. doi:10.4435/BSPI.2015.10

Mees, F., Swennen, R., Van Geet, M., and Jacobs, P. (2003). Applications of X-ray computed tomography in the geosciences. *Geol. Soc. London, Spec. Publ.* 215, 1–6.

Mei, S., and Henderson, C. M. (2001). Evolution of Permian conodont provincialism and its significance in global correlation and paleoclimate implication. *Palaeogeogr. Palaeoclimatol. Palaeoecol.* 170, 237–260. doi:10.1016/S0031-0182(01)00258-9

Merrill, G. K., and King, C. W. (1971). Platform conodonts from the lowest Pennsylvanian rocks of northwestern Illinois. *J. Paleontol.*, 645–664.

Merrill, G. K. (1973). Pennsylvanian nonplatform conodont genera I: Spathognathodus. *J. Paleontol.* 47, 289–314.

Merrill, G. K., and von Bitter, P. H. (1984). Facies frequencies among Pennsylvanian conodonts: Apparatuses and abundances. *Geol. Soc. Am. Spec. Pap.* 196, 251–261.

Muto, S., and Ito, T. (2021). Conodont fossils from the kiryu and ashikaga district (quadrangle series 1:50,000), central Japan with emphasis on the reexamination of "Carboniferous" conodonts from the Ashio Belt. *Bull. Geol. Surv. Jpn.* 72, 325–344. doi:10.9795/bullgsj.72.325

Muto, S., Ito, T., and Murayama, M. (2023). Geology and accretionary age of the Otori unit, North Kitakami Belt. *Bull. Geol. Surv. Jpn.* 74, 1–40. doi:10.9795/bullgsj.74.1_1

Muto, S. (2021). Recurrent deposition of organic-rich sediments in Early Triassic pelagic Panthalassa and its relationship with global oceanic anoxia: New data from Kyoto, Southwest Japan. *Glob. Planet. Change* 197, 103402. doi:10.1016/j.gloplacha.2020.103402

Muto, S., Takahashi, S., Yamakita, S., and Onoue, T. (2020). Scarcity of chert in upper Lower Triassic Panthalassic deep-sea successions of Japan records elevated clastic inputs rather than depressed biogenic silica burial flux following the end-Permian extinction. *Glob. Planet. Change* 195, 103330. doi:10.1016/j.gloplacha.2020.103330

Muto, S., Takahashi, S., Yamakita, S., Soda, K., and Onoue, T. (2019). Conodont-based age calibration of the Middle Triassic Anisian radiolarian biozones in pelagic deep-sea bedded chert. *Bull. Geol. Surv. Jpn.* 70, 43–89. doi:10.9795/bullgsj.70.43

Muto, S., Takahashi, S., Yamakita, S., Suzuki, N., Suzuki, N., and Aita, Y. (2018). High sediment input and possible oceanic anoxia in the pelagic Panthalassa during the latest Olenekian and early Anisian: Insights from a new deep-sea section in Ogama, Tochigi, Japan. *Palaeogeogr. Palaeoclimatol. Palaeoecol.* 490, 687–707. doi:10.1016/j.palaeo.2017.11.060

Muto, S., Yagyu, S., Takahashi, S., and Murayama, M. (2021). Identification of conodont fossils in pelagic deep-sea siliceous sedimentary rocks using laboratory-based X-ray computed microtomography. *Lethaia* 54, 687–699. doi:10.1111/let.12432

Nakada, R., Ogawa, K., Suzuki, N., Takahashi, S., and Takahashi, Y. (2014). Late Triassic compositional changes of aeolian dusts in the pelagic Panthalassa: Response to the continental climatic change. *Palaeogeogr. Palaeoclimatol. Palaeoecol.* 393, 61–75. doi:10.1016/j.palaeo.2013.10.014

Nascimento, S., Scomazzon, A., Moutinho, L., Lemos, V., and Matsuda, N. (2005). Conodont biostratigraphy of the lower itaituba formation (atokan, penssylvanian), amazonas basin, Brazil. *Rev. Bras. Paleontol.* 8, 193–202.

Nemirovskaya, T., and Alekseev, A. S. (1994). The bashkirian conodonts of the askyn section bashkirian mountains, Russia. *Bull. Société Belge. Géologie* 103, 109–133.

Nemyrovska, T. I. (1999). Bashkirian conodonts of the Donets Basin, Ukraine. *Scr. Geol.* 25, 1–115.

Nemyrovska, T. I. (2017). Late mississippian-middle pennsylvanian conodont zonation of Ukraine. *Stratigraphy* 14, 299–318. doi:10.29041/strat.14.1-4.299-318

Nemyrovska, T. I. (2011). Late moscovian (carboniferous) conodonts of the genus Swadelina from the Donets Basin, Ukraine. *Micropaleontology* 57, 491–505. doi:10.47894/mpal.57.6.03

Nemyrovska, T. I., Perret-Mirouse, M.-F., and Alekseev, A. S. (1999). On moscovian (late carboniferous) conodonts of the Donets Basin, Ukraine. *Neues Jahrb. Geol. Palaontol. Abh.* 214, 169–194. doi:10.1127/njgpa/214/1999/169

Nemyrovska, T. I., Wagner, R. H., Winkler Prins, C. F., and Montañez, I. (2011). Conodont faunas across the mid-carboniferous boundary from the barcaliente formation at la lastra (Palentian Zone, Cantabrian mountains, Northwest Spain); geological setting, sedimentological characters and faunal descriptions. *Scr. Geol.*, 127–175.

Nicoll, R. S., and Metcalfe, I. (1998). Early and middle permian conodonts from the canning and southern carnarvon basins, western Australia: Their implications for regional biogeography and palaeoclimatology. *Proc. R. Soc. Victoriaety Vic.* 110, 419–461.

Nishikane, Y., Kaiho, K., Takahashi, S., Henderson, C. M., Suzuki, N., and Kanno, M. (2011). The Guadalupian-Lopingian boundary (Permian) in a pelagic sequence from Panthalassa recognized by integrated conodont and radiolarian biostratigraphy. *Mar. Micropaleontol.* 78, 84–95. doi:10.1016/j.marmicro.2010.10.002

Perlmutter, B. (1975). Conodonts from the uppermost wabaunsse group (pennsylvanian) and the admire and council grove groups (permian) in Kansas. *Geol. Palaeontol.* 9, 95–115.

Petryshen, W., Henderson, C. M., De Baets, K., and Jarochowska, E. (2020). Evidence of parallel evolution in the dental elements of Sweetognathus conodonts: Sweetognathus Evolutionary Mechanisms. *Proc. R. Soc. B Biol. Sci.* 287, 20201922. doi:10.1098/rspb.2020.1922

Qi, Y., Hu, K., Wang, Q., and Lin, W. (2014). Carboniferous conodont biostratigraphy of the dianzishang section, Zhenning, Guizhou, South China. *Geol. Mag.* 151, 311–327. doi:10.1017/S0016756813000344

Qi, Y. P., Lambert, L. L., Nemyrovska, T. I., Wang, X. D., Hu, K. Y., and Wang, Q. L. (2016). Late bashkirian and early moscovian conodonts from the naqing section, luodian, guizhou, south China. *Palaeoworld* 25, 170–187. doi:10.1016/j.palwor.2015.02.005

Ritter, S. M. (2020). Improved conodont biostratigraphic constraint of the Carboniferous/Permian boundary in south-central New Mexico, USA. *Stratigraphy* 17, 39–56. doi:10.29041/strat.17.1.39-56

Ritter, S. M. (1995). Upper Missourian–Lower Wolfcampian (Upper Kasimovian–Lower Asselian) conodont biostratigraphy of the midcontinent, U.S.A. *U.S.A. J. Paleontol.* 69, 1139–1154. doi:10.1017/S0022336000038129

Sano, H., Kuwahara, K., Yao, A., and Agematsu, S. (2010). Panthalassan Seamount-Associated Permian-Triassic Boundary Siliceous Rocks, Mino Terrane, Central Japan. *Paleontol. Res.* 14, 293–314. doi:10.2517/1342-8144-14.4.293

Sano, H., Kuwahara, K., yao, A., and Agematsu, S. (2012). Stratigraphy and Age of the Permian-Triassic Boundary Siliceous Rocks of the Mino Terrane in the Mt. Funabuseyama Area, Central Japan. *Paleontol. Res.* 16, 124–145. doi:10.2517/1342-8144-16.2.124

Savage, N. M., and Barkeley, S. J. (1985). Early to middle Pennsylvanian conodonts from the Klawak Formation and the Ladrones Limestone, southeastern Alaska. *J. Paleontol.* 59, 1451–1475.

Schmitz, M. D., and Davydov, V. I. (2012). Quantitative radiometric and biostratigraphic calibration of the Pennsylvanian-Early Permian (Cisuralian) time scale and pan-Euramerican chronostratigraphic correlation. *Bull. Geol. Soc. Am.* 124, 549–577. doi:10.1130/B30385.1

Sobolev, N. N., and Nakrem, H. A. (1996). Middle Carboniferous-Lower Permian conodonts of Novaya Zemlya. *Nor. Polarinst. Skr.* 199, 1–129.

Stamm, R. G., and Wardlaw, B. R. (2003). *Conodont faunas of the late middle pennsylvanian*. USA: Desmoinesian) lower Kittanning cyclothem, 95–121.

Suárez-Riglos, M., Hünicken, M. A., and Merino-Redo, D. A. (1987). "Conodont biostratigraphy of the Upper Carboniferous-Lower Permian rocks of Bolivia," in *Conodont-Investigative techniques and applications-*. Editor R. L. Austin (Chichester: Ellis Horwood Ltd), 317–325.

Sugimoto, M. (1974). Stratigraphical Study in the Outer Belt of the Kitakami Massif, Northeast Japan. *Tohoku Univ. Inst. Geol. Paleontol. Contrib.* 74, 1–60. (in Japanese with English abstract).

Sun, Z.-Y., Liu, S., Ji, C., Jiang, D.-Y., and Zhou, M. (2020). Gondolelloid multielement conodont apparatus (Scythogondolella) from the Lower Triassic of Jiangsu, East China, revealed by high-resolution X-ray microtomography. *Palaeoworld* 30, 286–295. doi:10.1016/j.palwor.2020.06.001

Suzuki, N., Yamakita, S., Takahashi, S., and Ehiro, M. (2007). Middle Jurassic radiolarians from carbonate manganese nodules in the Otori Formation in the eastern part of the Kuzumaki-Kamaishi Subbelt, the North Kitakami Belt, Northeast Japan. *J. Geol. Soc. Jpn.* 113, 274–277. (in japanese with English abstract). doi:10.5575/geosoc.113.274

Takahashi, S., Ehiro, M., Suzuki, N., and Yamakita, S. (2016). Subdivisional scheme of the North Kitakami Belt, Northeast Japan and its tectonostratigraphic correlation to the Oshima and South Chichibu belts: an examination of the Jurassic accretionary complex in the west Akka area. *J. Geol. Soc. Jpn.* 122, 1–22. (in japanese with English abstract). doi:10.5575/geosoc.2015.0034

Takahashi, S., Hori, R. S., Yamakita, S., Aita, Y., Takemura, A., Ikehara, M., et al. (2021). Progressive development of ocean anoxia in the end-Permian pelagic Panthalassa. *Glob. Planet. Change* 207, 103650. doi:10.1016/j.gloplacha.2021.103650

Takahashi, S., Yamakita, S., Suzuki, N., Kaiho, K., and Ehiro, M. (2009). High organic carbon content and a decrease in radiolarians at the end of the Permian in a newly discovered continuous pelagic section: A coincidence? *Palaeogeogr. Palaeoclimatol. Palaeoecol.* 271, 1–12. doi:10.1016/j.palaeo.2008.08.016

Takahashi, S., Yamasaki, S. ichi, Ogawa, Y., Kimura, K., Kaiho, K., Yoshida, T., et al. (2014). Bioessential element-depleted ocean following the euxinic maximum of the end-Permian mass extinction. *Earth Planet. Sci. Lett.* 393, 94–104. doi:10.1016/j.epsl.2014.02.041

Takahashi, Y., Agematsu, S., and Sashida, K. (2020). Bashkirian–Moscovian (Pennsylvanian) conodonts from the pelagic atoll carbonate of the Omi Limestone, Akiyoshi Terrane, central Japan. *Micropaleontology* 66, 351–367. doi:10.47894/mpal.66.4.06

Tomimatsu, Y., Nozaki, T., Sato, H., Takaya, Y., Kimura, J.-I., Chang, Q., et al. (2020). Marine osmium isotope record during the Carnian "pluvial episode" (Late Triassic) in the pelagic Panthalassa Ocean. *Glob. Planet. Change* 197, 103387. doi:10.1016/j.gloplacha.2020.103387

Uchino, T., and Suzuki, N. (2020). Late Jurassic radiolarians from mudstone near the U–Pb-dated sandstone of the North Kitakami Belt in the northeastern Shimokita Peninsula, Tohoku, Japan. *Bull. Geol. Surv. Jpn.* 71, 313–330. doi:10.9795/bullgsj.71.313

von Bitter, P. H. (1972). Environmental control of conodont distribution in the Shawnee Group (Upper Pennsylvanian) of eastern Kansas. *Univ. Kans. Paleontol. Contrib.* 59, 1–105.

von Bitter, P. H., and Merrill, G. K. (1980). *Naked species of* Gondolella *(Conodontophorida): Their distribution, taxonomy, and evolutionary significance.* Germany: Royal Onta. Royal Ontario Museum.

Wakita, K., and Metcalfe, I. (2005). Ocean plate stratigraphy in East and Southeast Asia. *J. Asian Earth Sci.* 24, 679–702. doi:10.1016/j.jseaes.2004.04.004

Wang, Z., and Qi, Y. (2003). Upper Carboniferous (Pennsylvanian) conodonts from South Guizhou of China. *Riv. Ital. Paleontol. Strat.* 109, 379–397.

Wardlaw, B. R., Gallegos, D. M., Chernykh, V. V., and Snyder, W. S. (2015). Early Permian conodont fauna and stratigraphy of the Garden Valley Formation, Eureka County, Nevada. *Micropaleontology* 61, 369–387. doi:10.47894/mpal.61.4.07

Yamakita, S., Kadota, N., Kato, T., Tada, R., Ogihara, S., Tajika, E., et al. (1999). Confirmation of the Permian/Triassic boundary in deep-sea sedimentary rocks; earliest Triassic condonts from black carbonaceous claystone of the Ubara section in the Tamba Belt, Southwest Japan. *J. Geol. Soc. Jpn.* 105, 895–898. doi:10.5575/geosoc.105.895

Yamakita, S., Takemura, A., Kamata, Y., Aita, Y., Hori, S. R., and Campbell, H. J. (2007). A conodont biostratigraphic framework of a Permian/Triassic ocean-floor sequence in the accretionary Waipapa Terrane at Arrow Rocks, Northland, New Zealand. *GNS Sci. Monogr.* 24, 69–85.

Yamashita, D., Kato, H., Onoue, T., and Suzuki, N. (2018). Integrated Upper Triassic Conodont and Radiolarian Biostratigraphies of the Panthalassa Ocean. *Paleontol. Res.* 22, 167–197. doi:10.2517/2017pr020

Yao, A., Matsuda, T., and Isozaki, Y. (1980). Triassic and Jurassic radiolarians from the Inuyama area, central Japan. *J. Geosci. Osaka City Univ.* 23, 135–154.

Yuan, D. X., Zhang, Y. C., Shen, S. Z., Henderson, C. M., Zhang, Y. J., Zhu, T. X., et al. (2016). Early Permian conodonts from the Xainza area, central Lhasa Block, Tibet, and their palaeobiogeographical and palaeoclimatic implications. *J. Syst. Palaeontol.* 14, 365–383. doi:10.1080/14772019.2015.1052027

Zhuravlev, A. V., and Gerasimova, A. I. (2016). XMT micropalaeontological study of the silicites. *Vestn. Inst. Geol. Komi Sci. Cent. Ural. Branch Ras.* 3, 26–32. doi:10.19110/2221-1381-2016-3-26-32

Zhuravlev, A. V. (2017). Histological application of X-ray computed microtomography of conodonts. *Vestn. Inst. Geol. Komi Sci. Cent. Ural. Branch Ras.* 2, 41–44. doi:10.19110/2221-1381-2017-2-41-44

Ziegler, A. M., Hulver, M. L., and Rowley, D. B. (1997). "Permian world topography and climate," in *Late glacial and postglacial environmental changes-quaternary, carboniferous±Permian and proterozoic*. Editor I. P. Martini (New York: Oxford University Press), 111–146.

frontiers | Frontiers in Earth Science

TYPE Methods
PUBLISHED 14 July 2023
DOI 10.3389/feart.2023.1200976

Check for updates

OPEN ACCESS

EDITED BY
Shinya Iwasaki,
University of Bremen, Germany

REVIEWED BY
Saverio Bartolini Lucenti,
University of Florence, Italy
Vivi Vajda,
Swedish Museum of Natural History,
Sweden

*CORRESPONDENCE
Fabiany Herrera,
fherrera@fieldmuseum.org

RECEIVED 05 April 2023
ACCEPTED 23 June 2023
PUBLISHED 14 July 2023

CITATION
Herrera F, Hotton CL, Smith SY, Lopera PA, Neander AI, Wittry J, Zheng Y, Heck PR, Crane PR and D'Antonio MP (2023), Investigating Mazon Creek fossil plants using computed tomography and microphotography.
Front. Earth Sci. 11:1200976.
doi: 10.3389/feart.2023.1200976

Investigating Mazon Creek fossil plants using computed tomography and microphotography

Fabiany Herrera[1]*, Carol L. Hotton[2,3], Selena Y. Smith[4], Paula A. Lopera[5], April I. Neander[6], Jack Wittry[7], Yuke Zheng[1,8,9], Philipp R. Heck[1,8,9], Peter R. Crane[10,11] and Michael P. D'Antonio[1]

[1]Earth Sciences, Negaunee Integrative Research Center, Field Museum of Natural History, Chicago, IL, United States, [2]National Center for Biotechnology Information, National Library of Medicine, National Institutes of Health, Bethesda, MD, United States, [3]Department of Paleobiology, National Museum of Natural History, Smithsonian Institution, Washington, DC, United States, [4]Department of Earth and Environmental Sciences and Museum of Paleontology, University of Michigan, Ann Arbor, MI, United States, [5]Smithsonian Tropical Research Institute, Panama, Panama, [6]Department of Organismal Biology and Anatomy, The University Chicago, Chicago, IL, United States, [7]Gantz Family Collections Center, Field Museum of Natural History, Chicago, IL, United States, [8]Robert A. Pritzker Center for Meteoritics and Polar Studies, Negaunee Integrative Research Center, Field Museum of Natural History, Chicago, IL, United States, [9]Department of the Geophysical Sciences, The University of Chicago, Chicago, IL, United States, [10]Yale School of Environment, Yale University, New Haven, CT, United States, [11]Oak Spring Garden Foundation, Upperville, VA, United States

More than 20,000 siderite concretions from the Mazon Creek area of northern Illinois, United States are housed in the paleobotanical collections of the Field Museum. A large proportion contain fossil plants of Middle Pennsylvanian age that often have excellent three-dimensional morphology and sometimes anatomical detail. Approximately eighty plant taxa have been recognized from the Mazon Creek Lagerstätte, but few have been studied in detail, and in some cases the systematic affinities of these fossils need reevaluation. The three-dimensional (3D) preservation of Mazon Creek fossil plants makes them ideal candidates for study using x-ray micro-computed tomography (μCT), and here we apply these techniques to more accurately reconstruct the morphology of specimens of *Tetraphyllostrobus* Gao et Zodrow and *Crossotheca* Zeiller. The mineralogical composition of the fossil plant preservation was studied using elemental maps and Raman spectroscopy. *In-situ* spores were studied with differential interference contrast, Airyscan confocal super-resolution microscopy, and scanning electron microscopy, which reveal different features of the spores with different degrees of clarity. Our analyses show that μCT can provide excellent detail on the three-dimensional structure of Mazon Creek plant fossils, with the nature of associated mineralization sometimes enhancing and sometimes obscuring critical information. Results provide guidance for selecting and prioritizing fossil plant specimens preserved in siderite concretions for future research.

KEYWORDS

Paleozoic, *Tetraphyllostrobus*, *Crossotheca*, micro-computed tomography, MeshLab, differential interference contrast, airyscan confocal superresolution microscopy

1 Introduction

The Paleozoic Mazon Creek Lagerstätte is one of the richest fossil assemblages and many thousands of specimens preserved in sideritic concretions have been recovered from the Francis Creek Shale of the Carbondale Formation in the Illinois Basin, United States, which is of Moscovian (~307–311 Ma), Middle Pennsylvanian age. The concretions preserve impressions, casts, and molds of a wide variety of organisms from a broad spectrum of estuarine marine to freshwater environments (Johnson and Richardson, 1966; Nitecki, 1979; Baird et al., 1985; 1986; Clements et al., 2019). The Mazon Creek biota includes many terrestrial animals and plant remains (e.g., Wittry, 2006; 2020) that were evidently washed into coastal and marine depocenters suitable for the formation of siderite concretions in the Mazonian delta (e.g., Cotroneo et al., 2016; McCoy et al., 2016; Clements et al., 2019). Fossils in the concretions exhibit exquisite preservation which reflects the early formation of the nodules prior to significant sediment compaction and decomposition. Fossil metazoans often have the remains of soft tissues preserved. Fossil plants often contain spores (e.g., Drinnan and Crane, 1994) and also have excellent details of external morphology, which is sometimes complemented by the preservation of anatomical details (Drinnan et al., 1990). Among the many metazoans from the deposit are fossil jellyfish, polychaete worms, and the "Tully Monster" (*Tullimonstrum gregarium*) (Johnson and Richardson, 1966; Richardson, 1966). The latter has been studied especially intensively and the quality of preservation provides information on the probable notochord and other structures, as well as eye pigmentation, which has engendered vigorous debate on the likely systematic affinities of this enigmatic organism (e.g., Clements et al., 2016; McCoy et al., 2016; 2020; Sallan et al., 2017).

Like the fossil invertebrates and vertebrates, the floral component of the Mazon Creek biota is also diverse (Darrah, 1969; Drinnan and Crane, 1994). It includes plant parts of lycopsids, sphenopsids, ferns, pteridosperms, cordaites, as well as fossils of uncertain relationship. The fossil assemblage is dominated by leaves of ferns, sphenopsids, and pteridosperms (Locatelli et al., 2016), with lycopsids as secondary contributors (Wittry, 2006; 2020). Fossil plants in the Mazon Creek sideritic concretions exhibit excellent 3D morphology but most studies of plants from these nodules have focused on their appearance in two-dimensions and what can be seen on the surfaces of casts and molds. The first plant fossil from the Mazon Creek flora to be reconstructed in 3D was *Stephanospermum konopeonus* Langford, a medullosan pteridosperm ovule (Drinnan et al., 1990). Using a combination of longitudinal splitting, transverse cutting, serial sectioning and peels, Drinnan et al. (1990) characterized the histology of the ovule and reconstructed its three-dimensional form. Advanced imaging techniques including µCT now provide the opportunity to conduct similar studies non-destructively and more efficiently (Sutton, 2008), but despite the recent widespread use of µCT for reconstructing the anatomy and systematics of Mesozoic and Cenozoic plants (e.g., Friis et al., 2007; 2014; Smith et al., 2009a; Smith et al., 2009b; Collinson et al., 2013; 2016; Manchester et al., 2019; 2022; Matsunaga et al., 2019; 2021; Shi et al., 2021; Smith et al., 2021), this state-of-the-art technology has been barely applied to Mazon Creek plant fossils. To our knowledge, the only Mazon Creek plant that has been studied using a combination of light microscopy and µCT scanning is the medullosan pteridosperm ovule *Stephanospermum braidwoodensis* Spencer et Hilton (Spencer et al., 2013), which is very similar to *Stephanospermum konopeonus*.

Here, we apply these, and other advanced visualization techniques to exceptionally well-preserved fossils of *Tetraphyllostrobus* Gao et Zodrow and *Crossotheca* Zeiller from the Mazon Creek flora to determine their structure and elucidate general principles for the study of Mazon Creek fossil plants using µCT scanning.

2 Materials and methods

The Mazon Creek fossil specimens studied here are housed in the paleobotanical collections of the Field Museum (FM). Three specimens recently identified as cf. *Tetraphyllostrobus broganensis* in Mazon Creek siderite nodules (Wittry, 2020) were examined in this study. Two (PP54628, PP58471) were scanned using a GE dual tube µCT scanner at the PaleoCT lab in the Department of Organismal Biology and Anatomy at the University of Chicago. The third (PP34514) was scanned using a Nikon XT H 225ST industrial µCT system with a Perkin Elmer 1620 X-ray detector panel and a tungsten reflection target at the University of Michigan, CTEES facility.

For PP54628 (Figure 1) both part and counterpart were scanned together separated by a thin piece of wrapping foam. The scan used a 240 kV micro-focus tube at 150kV and 250 µA at 500 m exposure timing, using filter of 0.5 mm Cu. Resolution of voxel x=y=z= 31.8520 µm with 1,200 projection images was achieved. For PP5847 (Figure 2) both part and counterpart were scanned as for PP54628, but a with 180 kV nano-focus tube at 150kV and 250 µA at 500 m exposure timing, using filter of 0.5 mm Cu. Resolution of voxel x=y=z= 20.8280 µm with 1600 projection images was achieved. PP34514 (Figure 3) was physically sectioned with a Hi-Tech Diamond 6″trim saw. Sections were scanned at 113kV and 105 µA at 500 m exposure timing, using filter of 0.5 mm Cu. Resolution of voxel x=y=z= 12.0 µm with 3,141 projection images was achieved. Anatomical details were obtained from acetate peels (Galtier et al., 1999) taken from the surfaces of individual sections and mounted on slides with Eukitt. Light photographs and microphotographs of acetate peels were obtained at the Field Museum. Macrophotography was with a digital Canon EOS R digital camera (MP-E 65 mm f/2.8 1–5x macro lens) attached to a Stackshot system, with the digital photographs merged using Helicon Focus software. Microphotography was with a ZEISS Axio Imager.A2 microscope using differential interference contrast (DIC) and a Jenoptik Gryphax NAOS digital camera.

The part and counterpart of *Crossotheca* (PP58059; Figure 4) were scanned together as for PP54628 and PP58471, but with a 180 kV nano-focus tube, at 150 kV and 250 µA at 500 m exposure timing, using filter of 0.2 mm Cu. Resolution of voxel x=y=z= 32.2230 µm with 1,800 projection images was achieved.

The µCT volumes were visualized mainly using Avizo Software 3D 2022.1 (Thermo Fisher Scientific, Waltham, MA, United States). A volume thresholding tool in Avizo was used to demarcate the digitized 3D volume of the fossil specimens from the surrounding matrix of the concretion. Multiple functions were applied to the data

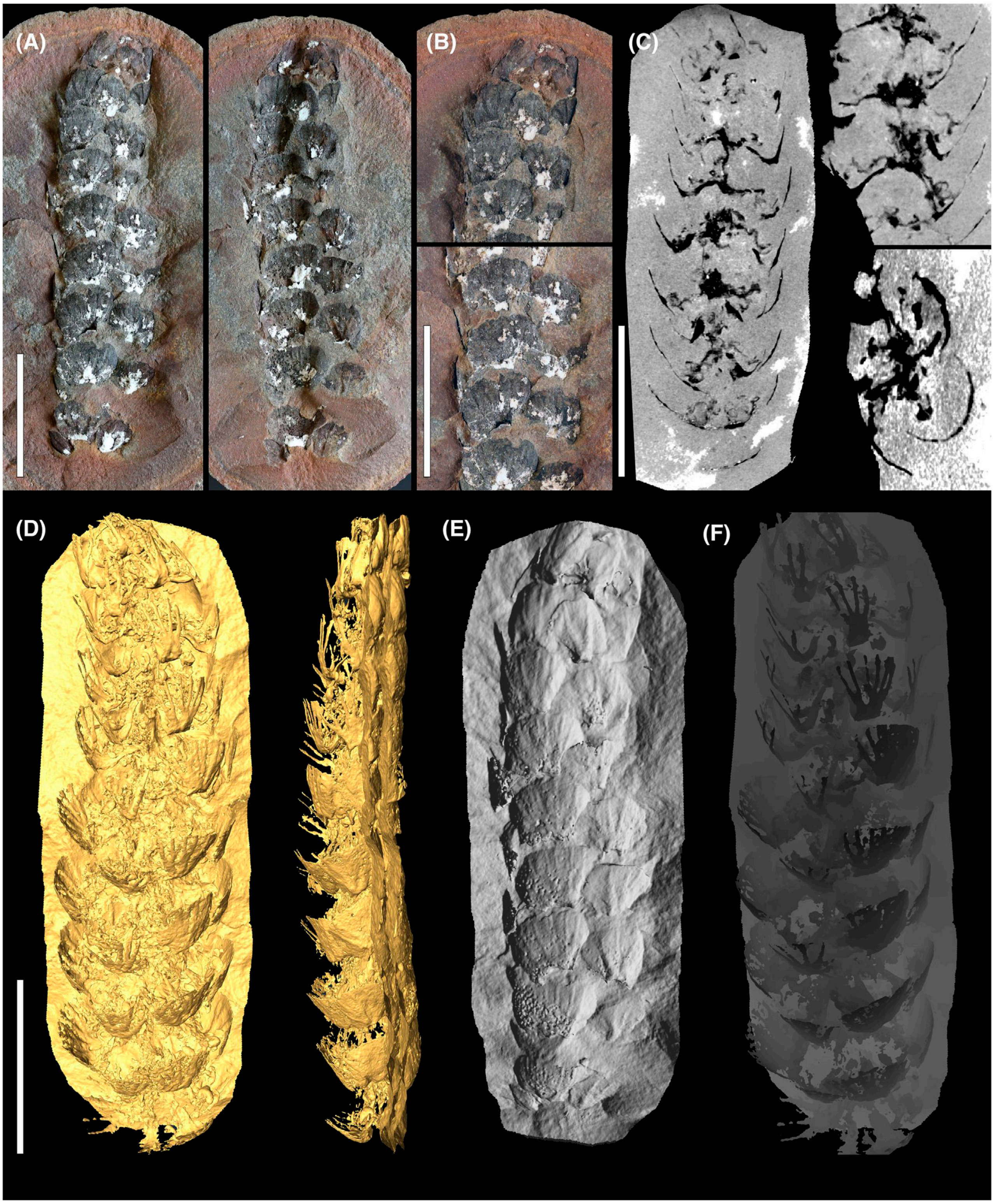

FIGURE 1
Strobilus of cf. *Tetraphyllostrobus broganensis* (PP54628). **(A)** Light photographs of part and counterpart of strobilus in a sideritic concretion. **(B)** Detail of top and middle portion of strobilus in A (left) showing two orthostichies that suggest a decussate arrangement of the sporophylls. Note the white patches of aluminosilicates on the surface of the strobilus. **(C)** Computed tomography images showing longitudinal (left and top right) and transverse (bottom right) sections. Note the V-shaped sporophylls in lateral view that are directed downwards proximally and upwards distally, and the curved sporophyll outlines in transverse section. **(D)** Reflective isosurface renderings showing buried surface of the strobilus in A (left) and a lateral view of that portion of the strobilus embedded in the matrix. Note four of six sporophylls in each apparent whorl which complement the pair of sporophylls visible on the surface in A (left). **(E)** Surface rendering from A (left) processed with MeshLab (shader: slicingplane) and highlighting the ribbed external surface of

(*Continued*)

FIGURE 1 (Continued)
sporophylls. **(F)** Surface rendering from D (left) processed with MeshLab (shader: depthmap) showing the four buried sporophylls at each whorl. Scale bars: 10 mm.

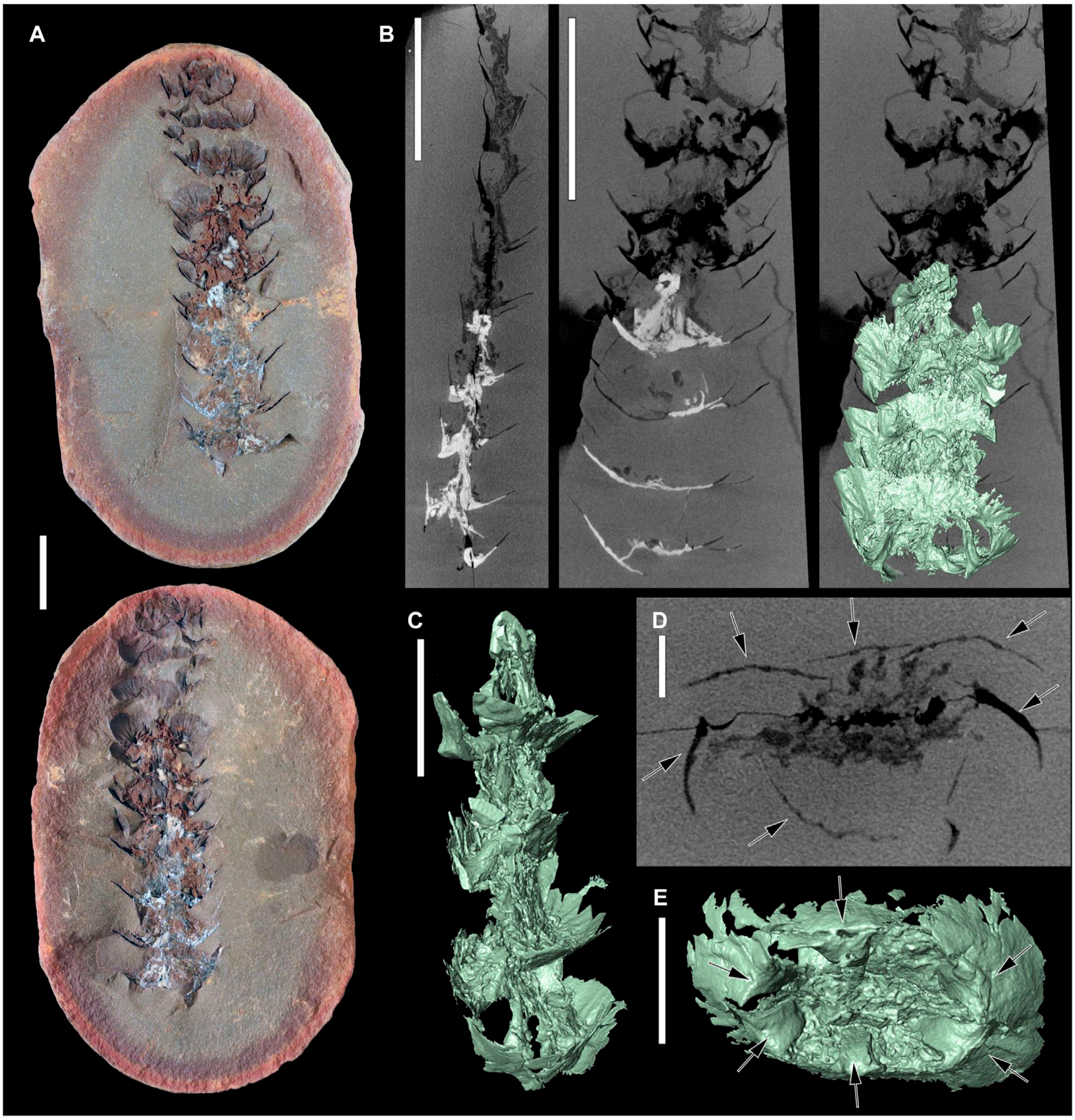

FIGURE 2
Strobilus of cf. *Tetraphyllostrobus broganensis* (PP58471). **(A)** Light photographs of part and counterpart of strobilus embedded in a sideritic concretion showing the variable mineralogical composition with predominantly iron oxides (upper half) and predominantly sulfide minerals (lower half). **(B)** Computed tomography images in lateral (left) and frontal (middle, right) sections showing the conspicuous mineralogical transition from predominantly iron oxides (upper half) to sulfide minerals (lower half). Note partial compression of strobilus in left image. Right image shows a superimposed isosurface rendering from the sulfide-rich zone. **(C)** Isolated isosurface rendering of sulfide-rich zone from B in lateral view showing V-shaped sporophylls in longitudinal section and the separation between successive whorls. **(D)** Computed tomography image in transverse section showing six sporophylls (arrows). **(E)** Basal view of surface rendering from C showing the broad proximal shafts of six sporophylls (arrows). Scale bars: 10 mm **(A and B)**; 5 mm **(C and E)**; 2 mm **(D)**.

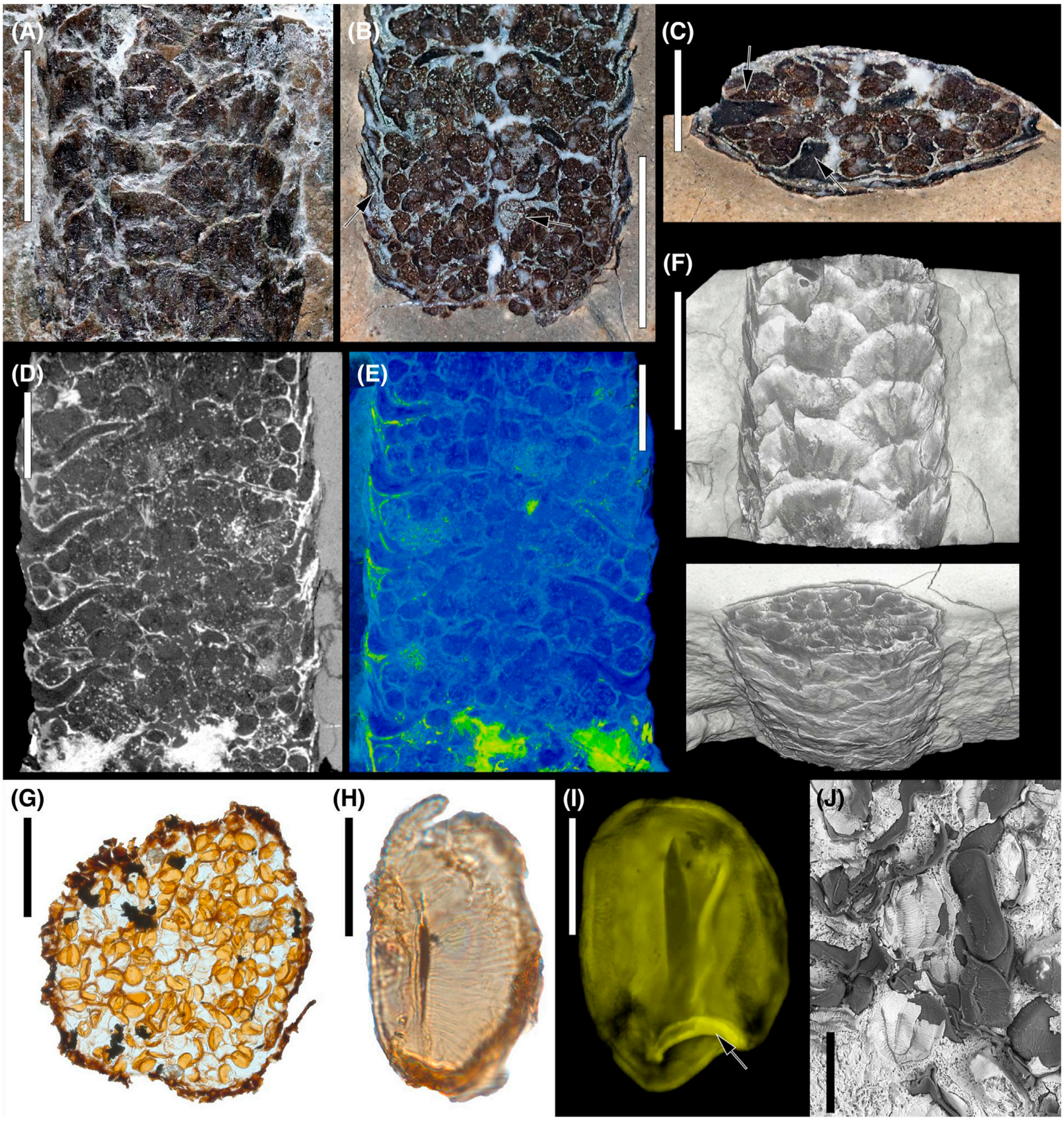

FIGURE 3
Strobilus and spores of cf. *Tetraphyllostrobus broganensis* (PP34514). **(A)** Light photograph of strobilus within sideritic matrix showing two orthostichies that suggest a decussate arrangement of the sporophylls. **(B)**. Light photograph of strobilus in oblique longitudinal section showing spheroidal sporangia (arrows) each containing numerous spores. **(C)** Light photograph of strobilus in transverse section showing abundant spheroidal sporangia and the broad proximal shafts of two sporophylls (arrows). **(D)** Computed tomography image in oblique longitudinal section showing the V-shaped sporophylls with broad proximal shafts and numerous spheroidal sporangia. White and bright patches indicate areas of pyritization. **(E)** Volren image from D showing reflective differential composition of pyrite (light green) *versus* the rest of the strobilus (blue-purple). **(F)** Volren images in frontal and oblique views from A and C, respectively showing clear orthstichies of overlapping sporophylls. **(G)** Light micrograph of a peel of an isolated sporangium showing abundant spores. **(H)** Light micrograph (DIC) of a *Columinisporites* spore showing closely spaced ridges approximately perpendicular to the monolete suture. The longitudinal ridges paralleling the monolete suture are not visible. **(I)** Airyscan confocal image of monolete *Columinisporites* showing the spore wall, longitudinal monolete suture, very faint perpendicular ridges (left) and longitudinal and oblique folds (arrow) in the spore wall. **(J)** SEM image of several *Columinisporites* spores showing the characteristic, partially detached, laterally striate perispore. Scale bars: 5 mm **(A, B and F)**; 2 mm **(C–E)**; 200 µm **(G)**; 40 µm **(J)**; 20 µm **(H, I)**.

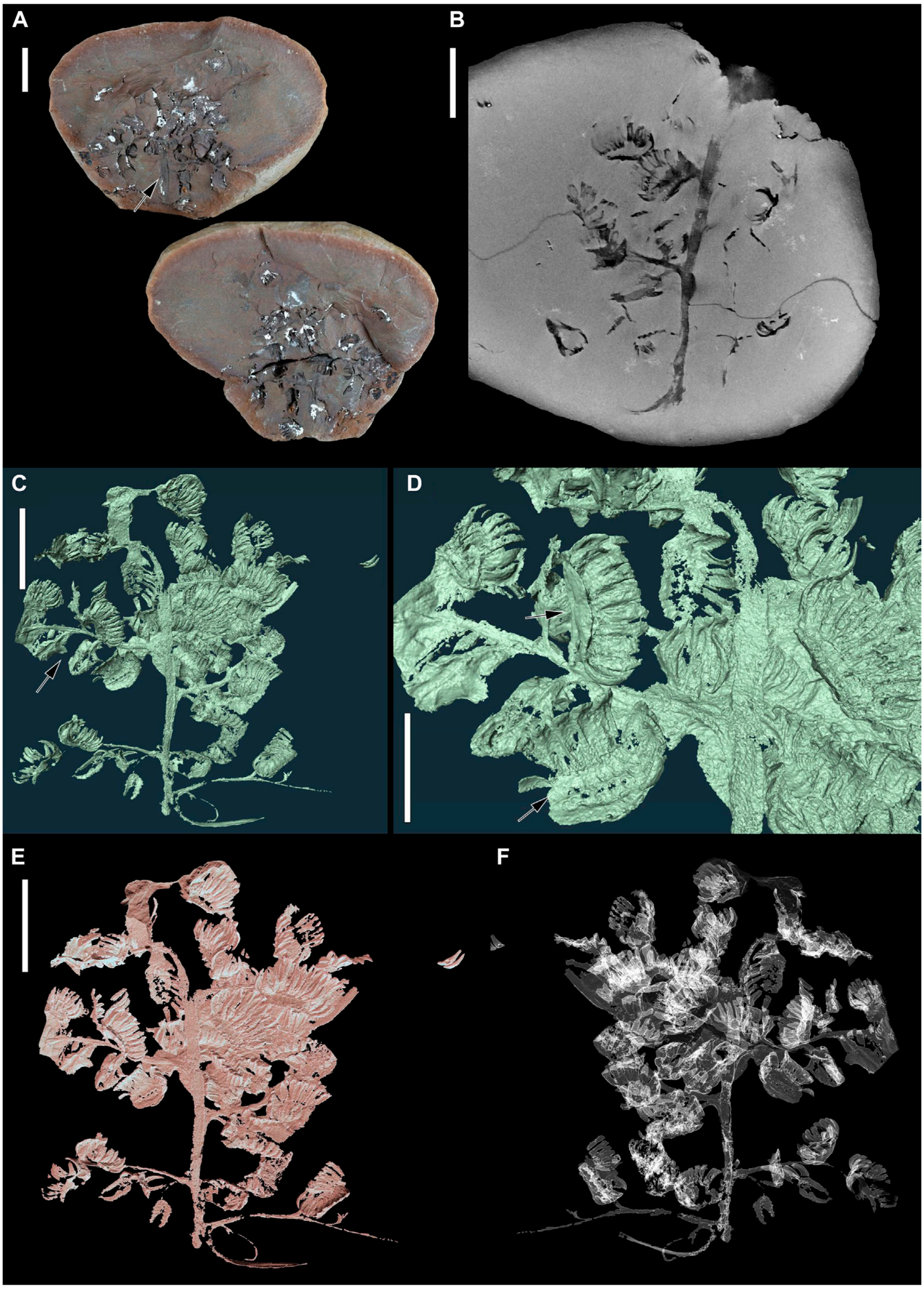

FIGURE 4
Branching axis cf. *Crossotheca trisecta* (PP58059). **(A)** Light photographs of part and counterpart in a sideritic concretion. Note the stout central axis (arrow) and white patches of aluminosilicates on surface of the fossil. **(B)** Computed tomography image showing the stout axis and two secondary axes with attached synangia. **(C)** Isolated virtual rendering showing the 3D architecture of the branching axis. **(D)** Detail from C (arrow) showing a synangia in lateral view attached to a simple lamina (upper arrow) and view from below showing the arrangement of the sporangia in two rows (lower arrow). **(E)** Virtual surface rendering from C processed with MeshLab (shader: radiancescaling, lit sphere effect). **(F)** Mirror image of virtual cast surface rendering from C processed with MeshLab (shader: x-ray). Scale bars: 10 mm **(A, B, C, E and F)**; 5 mm **(D)**.

to briefly evaluate the quality of the scans and the 3D preservation using volrens, isosurfaces, isosurface renderings, and volume renderings. An isosurface was first created to reconstruct the buried surface of the parts and counterparts (draw style: shaded) with the "back face" function selected. Once the desired surface models were achieved, each volume was exported as a .ply file for further analysis or visualization in MeshLab 2022.02 (Cignoni et al., 2008). Additional filters in MeshLab were helpful for removal of isolated surface fragments. MeshLab rendering-shaders functions, for example, depthmap, slicingplane, radiancescaling (lit-sphere effect), and x-ray were applied to improve the visualization of the surface models.

In-situ spores from the permineralized cone of specimen PP34514 (Figure 3) were examined directly on polished specimens attached to a stub and scanned at the National Museum of Natural History with a Zeiss EVO MA15 scanning electron microscope (EHT = 12 kv, WD = 7.5 mm, I probe = 1.2 nA, signalA = CZBSD). The spores were also imaged using a Zeiss LSM 980 with Airyscan 2 confocal superresolution microscope at the Smithsonian Tropical Research Institute. Images were taken at ×630 magnification (×63/NA 1.4 oil DIC) with fluorescence contrast, using 561 and 639 nm laser wavelengths and an intensity of 40% and 16% respectively. A total of 147 axial images were taken at 0.19 μm increments to capture the 3D morphology of each spore. Images were analyzed using Zeiss Zen 3.4.

To evaluate the response to μCT of specimens preserved in different minerals we acquired *in situ* and *ex-situ* elemental maps (Oxford Instruments AZTec) of the fossil concretions (Supplementary Material). *In-situ* and *ex-situ* Raman microspectroscopy was performed at FM with a WITec alpha 300 R system equipped with a 532 nm laser (Supplementary Material). Data was analyzed using WITec Project Plus software.

2 Results

2.1 Tetraphyllostrobus

Since its original description the systematic placement of *Tetraphyllostrobus* has been problematic. The genus was described based on approximately thirty compression specimens from the Late Carboniferous of Canada that were assigned to the only species of the genus, *Tetraphyllostrobus broganensis* Gao and Zodrow (Gao and Zodrow, 1990). The new morphological and anatomical information on the strobili and *in situ* spores of three specimens identified as cf. *Tetraphyllostrobus broganensis* in Mazon Creek siderite nodules (Wittry, 2020) confirms their assignment *Tetraphyllostrobus.* A detailed systematic and nomenclatural treatment of these fossils will be the subject of a separate study.

The three μCT scans of the Mazon Creek specimens of cf. *Tetraphyllostrobus broganensis* (Figures 1–3) all reveal excellent 3D preservation of the strobili. Some compaction of the original plant material is evident, but the visualizations reveal whorls of six sporophylls at each node (Figures 1C, F; Figures 2D, E) rather than pairs of sporophylls in a decussate arrangement, as was initially described based on the compression specimens of *Tetraphyllostrobus* (Gao and Zodrow, 1990). This aspect of the morphology is best seen in a combination of digital transverse sections (Figure 1C, 2D), isosurface images of the buried surface (Figure 1D), internal depth map visualizations (Figure 1F), and volume renderings (Figures 2B, C, E). The μCT data from all three strobili also show that each sporophyll has a V-shaped appearance in longitudinal section (Figures 1C, 2B, 3D). This results from the downward orientation of the proximal sporophyll stalk at an angle of ca. 45°, with the distal lamina then turned prominently upwards. The seemingly decussate organization of the sporophylls noted in compression fossils (Gao and Zodrow, 1990) is also apparent in the Mazon Creek specimens (Wittry, 2020) as two distinct orthostichies. This is a result of the facture plane that passes across the surface of the cone clearly exposing only two of the six sporophylls in each whorl (e.g., Figure 2B, left).

Specimen PP34514 shows excellent preservation of sporangia, which are well seen in both longitudinal and transverse sections (Figures 3B–E, G–J). DIC microscopy, Airyscan, and SEM all show that the spores in specimen PP34514 are attributable to the Carboniferous dispersed spore genus *Columinisporites* (Figures 3G–J) (Peppers, 1964). Isolated *Columinisporites* spores have been found in late Pennsylvanian deposits across the Illinois basin (Peppers, 1964; 1970), but this is the first *in situ* record in the Mazon Creek flora. The genus was described as an elliptical to reniform spore with sculpture characterized by several to numerous prominent ridges running roughly parallel to the long axis of the spore and a network of smaller (secondary) ridges extending approximately transverse to the longitudinal ridges (Peppers, 1964). This distinctive sculpture is in a layer external to the spore wall that is readily detached and is generally interpreted as a perispore (Taylor, 1986). Perispore remnants often remain attached to the spore wall.

The proximal monolete aperture is clearly visible with DIC and Airyscan imaging (Figures 3H, I). DIC also resolves the anastomosing network of transverse secondary ridges on the spore wall, although the primary ridges are not visible (Figure 3H). In the Airyscan images this transverse ornamentation is barely noticeable but a two-layered spore wall is visible (Figure 3I). SEM is the most effective for demonstrating the longitudinal ridges (visible as grooves in the micrograph) as well as the monolete apertures and secondary ridges (Figure 3J). SEM also clearly illustrates the detachable nature of the perispore, showing some portions embedded within the tissue of the sporangium and other portions adhering to the spore wall. Primary ridges appear as grooves, indicating that they are in negative relief, that is, the underside of the perispore is imaged. These observations support interpretations that view the perispore was derived from tapetal tissue as in modern ferns and sphenopsids (Wallace et al., 2011). The marked contrast in the SEM image between the spore wall (dark) and the perispore and embedding tissue (light) also points to compositional differences between the sporopollenin exine and the presumed tapetally-derived perisporial tissues.

2.2 Crossotheca

Crossotheca includes over a dozen described species of microsporangiate fertile units (Taylor et al., 2009; McLoughlin, 2021) that have been interpreted both as a lyginopterid pollen organ (Sellards, 1902; Darrah, 1937; Andrews and Mamay, 1948; Millay and Taylor, 1979) and the fertile frond of a eusporangiate fern (Danzé, 1955; Brousmiche, 1982).

The μCT scan of the nodule of cf. *Crossotheca trisecta* (Sellards, 1902; Wittry, 2020) provides an excellent illustration of the utility of combining digital sections (Figure 4B), virtual cast surface renderings (Figures 4C, D) with Meshlab processing (Figures 4E, F) for reconstructing complex 3D plant parts such as *Crossotheca*. The specimen is mainly preserved as a mold with some organic material remaining along the synangia walls (Figure 4A). This style of preservation allowed almost instantaneous reproduction of a virtual cast surface rendering, which is less time-consuming, and likely more accurate, than manual and interpretative standard segmentation techniques. The virtual cast surface renderings and MeshLab (Figures 4C–F) visualizations also reveal detailed external and internal morphological features of the synangia that are not clearly visible on the uneven surfaces of the concretion with standard reflected light microscopy (Figure 4D). Additional μCT scans of other *Crossotheca* specimens will be needed for more detailed assessment of the systematic affinities of these fertile units but the results presented here illustrate the potential of μCT scanning for the efficient analysis of the 3D structure in *Crossotheca* and similar specimens with complex morphologies from the Mazon Creek Lagerstätte.

2.3 Mineralogy of Mazon Creek plant concretions and computed tomography visualization

A recent study (Cotroneo et al., 2016), and the SEM chemical maps and *in situ* and *ex-situ* Raman microspectroscopy results presented here, confirm that the non-fossiliferous part of Mazon Creek concretions is mainly sideritic in composition, as has long been recognized. The four specimens analyzed reveal that the plant fossils often preserve a high-fidelity impression of their external surface, with the resulting void created by the loss of the original plant material infilled by various minerals that precipitate in the space. Based on these results, we group the minerals involved in a similar manner to Cotroneo et al. (2016) (Supplementary Material): 1) replacement by calcite and aluminosilicates (likely kaolinite, illite), 2) replacement by iron oxides, 3) replacement by sulfide minerals (e.g., sphalerite), and 4) pyritization with silicates and calcite present (Supplementary Table S1).

The three concretions containing *Tetraphyllostrobus* show that infilling minerals can either facilitate or obscure μCT visualization and 3D reconstruction of the original plant organ. In μCT images of strobilus PP54628 (Figure 1) mainly shows organic exterior walls with abundant aluminosilicates, which are visible as white patches on the surface of both part and counterpart of the concretion or bright areas with poor resolution (e.g., scattering artifacts) (Figure 1C). The organic exterior walls of the strobilus also display sufficient contrast for easy visualization in μCT images resulting in correspondingly less time-consuming and more straightforward renderings of complex 3D morphology (Figures 1D–F) than manual and exhaustive standard segmentation techniques (e.g., Matsunaga et al., 2021; Herrera et al., 2022).

Strobilus PP58471 (Figure 2) preserves thinner organic exterior walls than PP54628 (Figure 1), but there are distinct mineralogical domains in the upper and lower halves of the specimen. The upper half is mainly replaced by iron oxides while the lower portion is replaced mainly by sulfides (i.e., sphalerite). Other areas are empty, perhaps due to loss of the mineral infilling when the concretion was split or no infiltration of precipitates, for example, near the tips of the sporophylls. Both mineralogical domains (Figures 2B, D) exhibit good contrast in μCT images, but sulfides gave better conditions for creating and rapidly isolating 3D renderings using different volume threshold values and tools (Figures 2C, E).

Strobilus PP34514 (Figure 3) shows the greatest mineralogical diversity of the three *Tetraphyllostrobus* concretions. The central axis and sporophylls are primarily organic, whereas the sporangia appear filled with calcite and silicates. This specimen also presents various degrees of pyritization along the walls of the axis, sporophylls and sporangia, and there are also small pyrite crystals scattered throughout the strobilus. White patches of calcite crystals also fill the empty spaces in the strobilus and sporophylls, and also between sporangia. Overall, the predominantly organic nature of the strobilus provides good contrast in μCT images, but scattered pyritization results in disruptive scattering artifacts (Figure 3D). However, where small pyrite crystals occur along the edges of morphological features, they become helpful in recognizing sporophylls and sporangia in volren images (Figure 3E).

The branching system of cf. *Crossotheca trisecta* (PP58059) (Figure 4) is mainly preserved as a mold with some organic material remaining along the central axis and the walls of the synangia. The μCT images and renderings show excellent 3D preservation and minimal compressional deformation of synangia. As in the *Tetraphyllostrobus* strobilus PP54628 (Figure 1), white patches of aluminosilicates result in low resolution and poor contrast in CT images. However, the 3D preservation as a mold yields a high-fidelity impression of the external surface of the original plant organ facilitating the 3D rendering and isolation of the specimen from the sideritic matrix (Figures 4C, D). The surface models obtained with MeshLab (Figures 4E, F) also show the utility of 3D mesh processing software for visualizing complex 3D structures.

3 Discussion

Biomarkers and macromolecular biosignatures obtained with *in situ* Raman spectra studies on vertebrates, invertebrates, and coprolites from Mazon Creek have recently provided exciting results for reevaluating the affinity of problematic fossil organisms (McCoy et al., 2020) and the reconstruction of trophic relationships in this Carboniferous ecosystem (Tripp et al., 2022). Raman analyses showed the potential utility of this technique for recognizing the mineralogical composition of Mazon Creek fossil plants, but future biomarker analyses could also help elucidate the deep relationships among vascular plants and other unexplored trophic plant dynamic processes.

Approximately eighty plant taxa have been recognized from the Mazon Creek Lagerstätte, and there are more than 20,000 plant fossil specimens in the Field Museum collections. However, many of the plant taxa require careful structural analysis and systematic revaluation, including the specimens of *Tetraphyllostrobus* and *Crossotheca* studied here. A previous study by Drinnan et al. (1990) on ovules of *Stephanospermum konopeonus* demonstrated the potential for extracting high quality 3D information from plant fossils preserved in Mazon Creek ovules. More recently a study by Spencer et al. (2013) on a similar medullosan ovule, *Stephanospermum braidwoodensis*, showed that non-destructive μCT further enhanced the opportunities to develop 3D reconstructions of fossil plants preserved in siderite nodules. The current study on other kinds of plant fossils in Mazon Creek nodules further demonstrates the value of μCT scanning and the resulting visualizations for understanding the 3D structure of Paleozoic plants. However, the quality of results will be influenced by the composition of the minerals filling the voids left by the decomposing plant material, with calcite, aluminosilicates, iron oxides, sulfides, and pyrite all potentially involved. For 3D renderings of Mazon Creek plants, specimens with high amounts of organic preservation and more homogeneous mineralization should be prioritized, with sulfides preferred over iron oxides. Specimens in which the voids are filled in part by aluminosilicates are likely to give the least helpful results. Excellent preservation of spores studied with DIC, SEM, and Airyscan confocal super-resolution microscopy also provides useful high-quality information for the correct identification of *in situ* palynomorphs.

Data availability statement

The raw data supporting the conclusions of this article will be made available by the authors, without undue reservation.

Author contributions

FH designed the outline of this work. PRC initially studied and prepared specimen PP34514. FH, CLH, SYS, PAL, AIN, and MPD processed μCT, SEM, and Airyscan data. JW identified fossil specimens. FH, YZ, and PRH obtained elemental maps and conducted Raman microspectroscopy. FH wrote the manuscript and discussed the contents with CLH, SYS, PAL, AIN, JW, YZ, PRH, PRC, and MPD. All authors contributed to the article and approved the submitted version.

Funding

This work was funded by the Negaunee Integrative Research Center (to FH, MPD, and PRH) A. Susman (to FH), and the NSF grant 1802352 (The Pteridological Collections Consortium: An integrative approach to pteridophyte diversity over the last 420 million years) for the digitization of the Mazon Creek Flora at the Field Museum. MPD was supported by the Negaunee Integrative Postdoctoral Scientist Fellowship, Field Museum of Natural History.

Acknowledgments

The authors would like to thank Carlos Jaramillo at the Smithsonian Tropical Research Institute for providing the Airyscan confocal microscope and Zhe-Xi Luo for assistance with micro-CT scanning at University of Chicago. This study includes data produced in the CTEES facility at University of Michigan, supported by the Department of Earth and Environmental Sciences and College of Literature, Science, and the Arts. The authors would also like to thank Akiko Shinya and reviewers for their helpful comments.

Conflict of interest

The authors declare that the research was conducted in the absence of any commercial or financial relationships that could be construed as a potential conflict of interest.

Publisher's note

Supplementary material

The Supplementary Material for this article can be found online at: https://www.frontiersin.org/articles/10.3389/feart.2023.1200976/full#supplementary-material

References

Andrews, H. N., and Mamay, S. A. (1948). A *Crossotheca* from northern Illinois. *Ann. Mo. Bot. Gard.* 35 (3), 203–205. doi:10.2307/2394529

Baird, G. C., Shabica, C. W., Anderson, J. L., and Richardson, E. S., Jr. (1985). Biota of a Pennsylvanian muddy coast: Habitats within the Mazonian delta complex, northeast Illinois. *J. Paleontol.* 59 (2), 253–281.

Baird, G. C., Sroka, S. D., Shabica, C. W., and Kuecher, G. J. (1986). Taphonomy of middle Pennsylvanian Mazon Creek area fossil localities, northeast Illinois: Significance of exceptional fossil preservation in syngenetic concretions. *Palaios* 1, 271–285. doi:10.2307/3514690

Brousmiche, C. (1982). Sur la synonymie de *Crossotheca boulayi* Zeiller, 1886–88 et *Crossotheca bourozii* Danzé, 1956 avec l'espéce-type du genre: *Crossotheca crepinii* Zeiller, 1883: Une nouvelle interprétation de la fructification. *Geobios* 15 (5), 679–703. doi:10.1016/S00166995(82)80002-8

Cignoni, P., Callieri, M., Corsini, M., Dellepiane, M., Ganovelli, F., and Ranzuglia, G. (2008). *MeshLab: An open-source mesh processing tool* in Sixth Eurographics Italian Chapter Conference, Salerno, Italy, July 2nd - 4th, 2008, 129–136.

Clements, T., Dolocan, A., Martin, P., Purnell, M., Vinther, J., and Gabbott, S. E. (2016). The eyes of *Tullimonstrum* reveal a vertebrate affinity. *Nature* 532, 500–503. doi:10.1038/nature17647

Clements, T., Purnell, M., and Gabbott, S. (2019). The Mazon Creek Lagerstätte: A diverse late Paleozoic ecosystem entombed within siderite concretions. *J. Geol. Soc.* 176 (1), 1–11. doi:10.1144/jgs2018-088

Collinson, M. E., Smith, S. Y., van Konijnenburg-van Cittert, J. H., Batten, D. J., van der Burgh, J., Barke, J., et al. (2013). New observations and synthesis of Paleogene heterosporous water ferns. *Int. J. Plant Sci.* 174 (3), 350–363. doi:10.1086/668249

Collinson, M. E., Adams, N. F., Manchester, S. R., Stull, G. W., Herrera, F., Smith, S. Y., et al. (2016). X-Ray micro-computed tomography (micro-CT) of pyrite-permineralized fruits and seeds from the London Clay Formation (Ypresian) conserved in silicone oil: A critical evaluation. *Botany* 94 (9), 697–711. doi:10.1139/cjb-2016-0078

Cotroneo, S., Schiffbauer, J., McCoy, V., Wortmann, U., Darroch, S., Peng, Y., et al. (2016). A new model of the formation of Pennsylvanian iron carbonate concretions hosting exceptional soft-bodied fossils in Mazon Creek, Illinois. *Geobiology* 14 (6), 543–555. doi:10.1111/gbi.12197

Danzé, J. (1955). Le genre *Crossotheca* Zeiller C. *R.* Aci. Sc. 241, 1616–1618.

Darrah, W. C. (1937). *Codonotheca* and *Crossotheca*: Polliniferous structures of pteridosperms. *Bot. Mus. Leafl. Harv. Univ.* 4 (9), 153–172. doi:10.5962/p.295102

Darrah, W. C. (1969). *A critical review of the Upper Pennsylvanian floras of eastern United States with notes on the Mazon Creek flora of Illinois*. Gettysburg, PA, USA: Privately published, 220.

Drinnan, A. N., Schramke, J. M., and Crane, P. R. (1990). *Stephanospermum konopeonus* (Langford) Comb. Nov.: A medullosan ovule from the middle Pennsylvanian Mazon Creek flora of northeastern Illinois, USA. *Bot. Gaz.* 151 (3), 385–401. doi:10.1086/337839

Drinnan, A. N., and Crane, P. R. (1994). A synopsis of medullosan pollen organs from the middle Pennsylvanian Mazon Creek flora of northeastern Illinois, USA. *Rev. Palaeobot. Palynol.* 80 (3-4), 235–257. doi:10.1016/0034-6667(94)90003-5

Friis, E. M., Crane, P. R., Pedersen, K. R., Bengtson, S., Donoghue, P. C., Grimm, G. W., et al. (2007). Phase-contrast X-ray microtomography links Cretaceous seeds with Gnetales and Bennettitales. *Nature* 450 (7169), 549–552. doi:10.1038/nature06278

Friis, E. M., Marone, F., Pedersen, K. R., Crane, P. R., and Stampanoni, M. (2014). Three-dimensional visualization of fossil flowers, fruits, seeds, and other plant remains using synchrotron radiation X-ray tomographic microscopy (SRXTM): New insights into Cretaceous plant diversity. *J. Paleontol.* 88 (4), 684–701. doi:10.1666/13-099

Galtier, J., Phillips, T. L., Jones, T. P., and Rowe, N. P. (1999).*The acetate peel technique" in Fossil plants and spores: Modern techniques*. Editors T. P. Jones and N. P. Rowe (London: Geological Society of London), 67–70.

Gao, Z., and Zodrow, E. L. (1990). A new strobilus *Tetraphyllostrobus broganensis* gen. et sp. nov. from the Upper Carboniferous, Sydney Coalfield, Nova Scotia, Canada. *Rev. Palaeobot. Palynol.* 66 (1-2), 3–11. doi:10.1016/0034-6667(90)90025-E

Herrera, F., Testo, W. L., Field, A. R., Clark, E. G., Herendeen, P. S., Crane, P. R., et al. (2022). A permineralized Early Cretaceous lycopsid from China and the evolution of crown clubmosses. *New Phyto.* 233, 2310–2322. doi:10.1111/nph.17874

Johnson, R. G., and Richardson, E. S., Jr (1966). A remarkable Pennsylvanian fauna from the Mazon Creek area, Illinois. *J. Geol.* 74, 626–631. doi:10.1086/627194

Locatelli, E. R., Krajewski, L., Chochinov, A. V., and Laflamme, M. (2016). Taphonomic variance between marattialean ferns and medullosan seed ferns in the Carboniferous Mazon Creek Lagerstätte, Illinois, USA. *Palaios* 31 (3), 97–110. doi:10.2110/palo.2015.073

Manchester, S. R., Kapgate, D. K., Ramteke, D. D., Patil, S. P., and Smith, S. Y. (2019). Morphology and anatomy of the angiosperm fruit *Baccatocarpon*, incertae sedis, from the Maastrichtian Deccan Intertrappean Beds of India. *Acta Palaeobot.* 59 (2), 241–250. doi:10.2478/acpa-2019-0019

Manchester, S. R., Zhang, X., Hotton, C. L., Wing, S., and Crane, P. R. (2022). Two-seeded cones of probable gnetalean affinity from the Morrison Formation (Late Jurassic) of Utah and Colorado, USA. *Acta Palaeob.* 62 (2), 77–92. doi:10.35535/acpa-2022-0006

Matsunaga, K. K. S., Herendeen, P. S., Herrera, F., Ichinnorov, N., Crane, P. R., and Shi, G. (2021). Ovulate cones of *Schizolepidopsis ediae* sp. nov. provide insights into the evolution of Pinaceae. *Int. J. Plant Sci.* 182 (6), 490–507. doi:10.1086/714281

Matsunaga, K. K. S., Manchester, S. R., Srivastava, R., Kapgate, D. K., and Smith, S. Y. (2019). Fossil palm fruits from India indicate a Cretaceous origin of Arecaceae tribe Borasseae. *Bot. J. Linn. Soc.* 190 (3), 260–280. doi:10.1093/botlinnean/boz019

McCoy, V. E., Saupe, E. E., Lamsdell, J. C., Tarhan, L. G., McMahon, S., Lidgard, S., et al. (2016). The 'Tully monster' is a vertebrate. *Nature* 532, 496–499. doi:10.1038/nature16992

McCoy, V. E., Wiemann, J., Lamsdell, J. C., Whalen, C. D., Lidgard, S., Mayer, P., et al. (2020). Chemical signatures of soft tissues distinguish between vertebrates and invertebrates from the Carboniferous Mazon Creek Lagerstätte of Illinois. *Geobiology* 00, 560–565. doi:10.1111/gbi.12397

McLoughlin, S. (2021). *Gymnosperms" in Encyclopedia of Geology*. Editors D. Alderton and S. A. Elias Second Edition (Cambridge: Academic Press), 476–500. doi:10.1016/B978-0-08-102908-4.00068-0

Millay, M. A., and Taylor, T. N. (1979). Paleozoic seed fern pollen organs. *Bot. Rev.* 45, 301–375. doi:10.1007/BF02860858

Nitecki, M. H. (1979). in *Mazon Creek fauna and flora: A hundred years of investigation" in Mazon Creek fossils*. Editor M. H. Nitecki (New York: Academic Press), 1–12.

Peppers, R. A. (1964). Spores in strata of late Pennsylvanian cyclothems in the Illinois basin. *Ill. State Geol. Surv. Bull.* 90, 1–89.

Peppers, R. A. (1970). Correlation and palynology of coals in the Carbondale and Spoon Formations (Pennsylvanian) of the northeastern part of the Illinois basin. *Ill. State Geol. Surv. Bull.* 93, 1–173.

Richardson, E. S., Jr (1966). Wormlike fossil from the Pennsylvanian of Illinois. *Science* 151 (3706), 75–76. doi:10.1126/science.151.3706.75.b

Sallan, L., Giles, S., Sansom, R. S., Clarke, J. T., Johanson, Z., Sansom, I. J., et al. (2017). The 'Tully Monster' is not a vertebrate: Characters, convergence and taphonomy in Palaeozoic problematic animals. *Palaeontology* 60 (2), 149–157. doi:10.1111/pala.12282

Sellards, E. H. (1902). On the fertile fronds of *Crossotheca* and *Myriotheca*, and on the spores of other Carboniferous ferns from Mazon Creek, Illinois. *Am. J. Sci.* 14 (81), 195–202. doi:10.2475/ajs.s4-14.81.195

Shi, G., Herrera, F., Herendeen, P. S., Clark, E. G., and Crane, P. R. (2021). Mesozoic cupules and the origin of the angiosperm second integument. *Nature* 594 (7862), 223–226. doi:10.1038/s41586-021-03598-w

Smith, S. Y., Collinson, M. E., Rudall, P. J., Simpson, D. A., Marone, F., and Stampanoni, M. (2009a). Virtual taphonomy using synchrotron tomographic microscopy reveals cryptic features and internal structure of modern and fossil plants. *Proc. Natl. Acad. Sci. U. S. A.* 106 (29), 12013–12018. doi:10.1073/pnas.0901468106

Smith, S. Y., Collinson, M. E., Simpson, D. A., Rudall, P. J., Marone, F., and Stampanoni, M. (2009b). Elucidating the affinities and habitat of ancient, widespread Cyperaceae: *Volkeria messelensis* gen. et sp. nov., a fossil mapanioid sedge from the Eocene of Europe. *Am. J. Bot.* 96 (8), 1506–1518. doi:10.3732/ajb.0800427

Smith, S. Y., Kapgate, D. K., Robinson, S., Srivastava, R., Benedict, J. C., and Manchester, S. R. (2021). Fossil fruits and seeds of Zingiberales from the late Cretaceous—early Cenozoic Deccan Intertrappean Beds of India. *Int. J. Plant Sci.* 182 (2), 91–108. doi:10.1086/711474

Spencer, A. R. T., Hilton, J., and Sutton, M. D. (2013). Combined methodologies for three-dimensional reconstruction of fossil plants preserved in siderite nodules: *Stephanospermum braidwoodensis* nov. sp. (Medullosales) from the Mazon Creek Lagerstätte. *Rev. Palaeobot. Palynol.* 188, 1–17. doi:10.1016/j.revpalbo.2012.09.001

Sutton, M. D. (2008). Tomographic techniques for the study of exceptionally preserved fossils. *Proc. R. Soc. B* 275 (1643), 1587–1593. doi:10.1098/rspb.2008.0263

Taylor, E. L., Taylor, T. N., and Krings, M. (2009). *Paleobotany: The biology and evolution of fossil plants*. Burlington, Massachusetts: Academic Press.

Taylor, W. A. (1986). Ultrastructure of sphenophyllalean spores. *Rev. Palaeobot. Palynol.* 47 (1–2), 105–128. doi:10.1016/0034-6667(86)90009-6

Tripp, M., Wiemann, J., Brocks, J., Mayer, P., Schwark, L., and Grice, K. (2022). Fossil biomarkers and biosignatures preserved in coprolites reveal carnivorous diets in the Carboniferous Mazon Creek ecosystem. *Biology* 1289, 1289. doi:10.3390/biology11091289

Wallace, S., Fleming, A., Wellman, C. H., and Beerling, D. J. (2011). Evolutionary development of the plant and spore wall. *AoB Plants* plr027, plr027. doi:10.1093/aobpla/plr027

Wittry, J. (2006). *The Mazon Creek fossil flora*. Illinois, USA: Earth Science Club of Northern Illinois, 164.

Wittry, J. (2020). *A comprehensive guide to the fossil flora of Mazon Creek*. Illinois, USA: Earth Science Club of Northern Illinois, 275.

Frontiers in Ecology and Evolution

TYPE Data Report
PUBLISHED 25 August 2023
DOI 10.3389/fevo.2023.1171891

Check for updates

OPEN ACCESS

EDITED BY
Pauline Guenser,
Université de Bordeaux, France

REVIEWED BY
Miriam Cobianchi,
University of Pavia, Italy
Adriane Lam,
Binghamton University, United States

*CORRESPONDENCE
Li Lo
lilo115@ntu.edu.tw

RECEIVED 22 February 2023
ACCEPTED 01 August 2023
PUBLISHED 25 August 2023

CITATION
Chen W-L, Kang J-C, Kimoto K, Song Y-F, Yin G-C, Swisher RE, Lu C-H, Kuo L-W, Huang J-JS and Lo L (2023) μ-Computed tomographic data of fossil planktonic foraminifera from the western Pacific Ocean: a dataset concerning two biostratigraphic events during the Early Pleistocene.
Front. Ecol. Evol. 11:1171891.
doi: 10.3389/fevo.2023.1171891

μ-Computed tomographic data of fossil planktonic foraminifera from the western Pacific Ocean: a dataset concerning two biostratigraphic events during the Early Pleistocene

Wei-Lun Chen[1,2,3], Jia-Cih Kang[1,2,3], Katsunori Kimoto[4], Yen-Fang Song[5], Gung-Chian Yin[5], Robert E. Swisher[1], Chen-Han Lu[6], Li-Wei Kuo[7], Jyh-Jaan Steven Huang[3,8] and Li Lo[1,2,3]*

[1]Department of Geosciences, National Taiwan University, Taipei, Taiwan, [2]Laboratory of Paleoceanography, National Taiwan University, Taipei, Taiwan, [3]Research Center for Future Earth, National Taiwan University, Taipei, Taiwan, [4]Research Institute for Global Change, Japan Agency for Marine-Earth Science and Technology (JAMSTEC), Yokosuka, Japan, [5]National Synchrotron Radiation Research Center, Hsinchu, Taiwan, [6]Taichung Municipal Taichung Girl's Senior High School, Taichung, Taiwan, [7]Department of Earth Sciences, National Central University, Taoyuan, Taiwan, [8]Institute of Oceanography, National Taiwan University, Taipei, Taiwan

KEYWORDS

planktonic foraminifera, morphometric analysis, Pacific Ocean (equatorial west), X-ray tomographic imaging, biostratigraphy

Introduction

Planktonic foraminifera first became prevalent during the Mesozoic marine revolution event (Tappan and Loeblich, 1988), quickly becoming one of the most diversified calcareous microplanktons (Bown et al., 2004). These eukaryotic organisms secret a biomineralized test that forms a dominant constituent of marine sediments across open marine ecosystems. Almost 70% of the modern seafloor is covered by the calcareous remains of planktonic foraminifera (Neil et al., 2005), providing abundant materials for systematic and quantitative analyses. Due to their widespread distribution regionally and globally across different geographical zones, planktonic foraminifera are exceptionally useful as a geochemical proxy and are commonly utilized in various paleoclimatological/paleoceanographic studies (Liu et al., 2015; Lo et al., 2022). Furthermore, evolution and modifications in the test morphology of planktonic foraminifera are highly susceptible and responsive to shifting environmental conditions, with observed morphological variations often triggered by the everchanging environment (Hecht and Savin, 1972; Renaud and Schmidt, 2003; Schmidt et al., 2004). This leads to high observed taxonomic turnover and rapid evolution rates in planktonic foraminifera, subsequently providing exceptional analytical utility, with researchers favoring their use as a dominant index fossil in Mesozoic and Cenozoic marine biostratigraphy (Berggren et al., 1995; Wade et al., 2011; Fraass et al., 2015). Based on these assets and advantages, the study of planktonic foraminifera has shown promise in biostratigraphy, in clarifying the environmental changes, and for understanding the evolutionary importance of the species.

Traditionally, the morphological analysis of planktonic foraminifera, regardless of qualitative or quantitative aspects, remains two-dimensional and limited under the restrictions and constraints of optical microscopes and imaging techniques that flatten a complex three-dimensional morphology, introducing biases into systematic and analytical studies. Traditional techniques and methodologies to explore the complicated three-dimensional test geometry and internal structures of planktonic foraminifera necessitates and requires invasive procedures such as serial dissection, which can be both time-consuming and labor-intensive, as well as reliant on the expertise of the researchers (Görög et al., 2012). An alternative and less destructive method utilizes a scanning electron microscope (SEM), first introduced in the 1960s for higher resolution photography of external structures (Hay and Sandberg, 1967). Nevertheless, despite the advantages, sample preparation procedures, such as Au/C coating and holder fixation, often led to the limitation of reusing the samples for further studies and have restricted the application of SEM analyses of planktonic foraminifera tests (Görög et al., 2012). These conventional two-dimensional methods have contributed significantly in measuring linear, simple geometric, and numeric parameters such as length, width, the radius of the chamber, degree of whorl (Olsson, 1972), test area (Poole and Wade, 2019), the roundness of the periphery, and aperture shape (Wei, 1987). However, regarding the analysis of semi-three-dimensional features (e.g., surface area, chamber size, and geometrical/spatial relationships), measurements can often be inaccurate and biased because of the complex configuration of planktonic foraminifera and the difficulty in properly quantifying these data with traditional methodologies and techniques.

The development of new three-dimensional analytical methods, including projection X-ray microscopy (PXM) and microfocus X-ray CT (MXCT) and their application toward the study of planktonic foraminifera, dramatically changes how researchers can assess morphological variation within the group. Importantly, new methodologies and techniques provide an avenue to avoid the shortcomings and inconveniences that have plagued studies reliant on conventional two-dimensional methods. The application of these modern techniques towards planktonic foraminifer has been attempted to examine a variety of morphological aspects including: ontogeny (Schmidt et al., 2013; Caromel et al., 2016; Caromel et al., 2017; Burke et al., 2020; Duan et al., 2021), speciation (Vanadzina and Schmidt, 2022), shell density (Ofstad et al., 2021), and buoyancy reconstruction (Zarkogiannis et al., 2019). These recent advances in technology and analysis can provide more accurate and thoroughgoing insight into the body plan and geometry of fossil specimens, allowing the computation of parameters such as chamber cavity volume and surface area that were previously impractical or impossible to quantify otherwise. Other applications formerly not possible, including the reconstruction of the early developed chambers (including proloculus and the subsequent ~10 chambers, which are usually covered by the late developed ones) (Duan et al., 2021) and the estimation of shell density with CT numbers (Iwasaki et al., 2019), can now be utilized for analysis. Lastly, but most crucially, these new techniques are non-invasive and non-destructive towards the analyzed foraminifera test, allowing for the scanned sample to still be available for further studies (e.g., stable isotope analysis). As the recovered three-dimensional data is digital, this provides for the long-term storage, archiving, and even reassessment of acquired specimen data in perpetuity.

Despite the wide range of research conducted to date that has contributed towards a better understanding of many different morphological aspects of planktonic foraminifera, these initial studies have mostly used datasets compromising a relatively small number of specimens. This limits the current scope of potential research that can be conducted, with present studies tending to focus on developmental changes and growth variation across stages within a species and/or within a short time period, assuming the specimens used are representative of their population (Schmidt et al., 2013; Caromel et al., 2016; Caromel et al., 2017; Burke et al., 2020; Duan et al., 2021; Vanadzina and Schmidt, 2022). Broader, more complex, and even more scientifically relevant evolutionary, paleoecological, and paleoclimatic topics, such as morphological and evolutionary change across biostratigraphic events and the interactions between the organism and the Earth's evolving climate system, remain currently under explored, and the required datasets are non-existent. Therefore, further works examining three-dimensional morphology, with datasets of expanded size and scope, will help to shed new light on both evolutionary and environmental interactions and their combined effects on evolution and adaptive responses in organisms.

Here we present a dataset comprising twenty three-dimensional reconstruction models of planktonic foraminifera from two distinctive biostratigraphic events from the Early Pleistocene in the western Pacific Ocean. This record contains samples from different timings both before and within the two biostratigraphic events, the LAD event of *Globigerinoidesella fistulosa* with its presumed relative *Trilobatus sacculifer* (1.76–1.72 Ma), and the fifth left-coiling event (L5) of *Pulleniatina* spp. (2.15–1.93 Ma). Important questions regarding the development of environmental adaptations and the morphological criteria for the diagnosis and distinguishing of species are still left to be answered, e.g., what specimens can truly be called *G. fistulosa*? This is a critical question to determine the horizon of the LAD event. *Globigerinoidesella fistulosa* currently lacks a clear morphological rule to enable its differentiation from *T. trilobatus*, as there are transitional morphologies with inconspicuous protuberance. Despite Poole and Wade (2019) addressing the question, the solution still lacks quantitative standards. This fact leads to questions about whether *G. fistulosa* is just an ontogenetic stage or a taxonomic synonym of *T. trilobatus* (Chen, 2008). In addition, more studies are required to understand the paleoecological significance of the digitate structures present on *G. fistulosa*. These structures may be highly related to its extinction, coinciding with a dramatic environment shift recorded in a mixed layer-thermocline depth transition event that occurred at ~1.7 Ma (Wara et al., 2005; Chen, 2008). With expanded morphological analyses regarding novel parameters (e.g., skeleton volume, cavity volume, total volume, surface area, and chamber centroid position)

(Schmidt et al., 2013; Caromel et al., 2016; Caromel et al., 2017; Burke et al., 2020; Duan et al., 2021; Vanadzina and Schmidt, 2022), in the future, clues or even postulates can be provided to further studies and improve our knowledge of the important evolutionary and paleoecological interactions. Moreover, these datasets will build a foundation and assist with efforts to correlate biostratigraphic and evolutionary data with paleoceanographic data; data that would provide great insight and further our understanding of paleoenvironment–organism interactions. Broadly, the development of larger CT datasets, like the one presented in here, helps further a variety of research goals dependent on a substantial dataset for analysis and implementation, including the advancement of potential machine learning models for species-level identification or to conduct auto-chamber segmentation (Ge et al., 2017; Mitra et al., 2019).

Datasets

This study develops a three-dimensional μ-CT reconstruction dataset of planktonic foraminifera collected from marine sediments of the Ocean Drilling Program (ODP) Hole 1115B (9°11'S; 151°34'E, water depth 1,149 m). Sediment samples were washed over a 63 μm screen and planktonic foraminifera tests were hand-picked at the Department of Geosciences, National Taiwan University, Taiwan. The foraminifera tests were picked from six size fractions (250–300, 300–355, 355–425, 425–500, 500–600 and >600 μm). ODP 1115B's age model was reconstructed utilizing high-resolution planktonic foraminiferal oxygen isotope stratigraphy with support from paleomagnetic reversal and calcareous organisms biostratigraphic events (Chuang et al., 2018). The samples were then scanned at the Japan Agency for Marine-Earth Science and Technology (JAMSTEC; Yokotsuka, Japan) and the National Synchrotron Radiation Research Center (NSRRC; Hsinchu, Taiwan). The files presented in the dataset are divided into two sub-datasets: the *Trilobatus sacculifer* plexus (comprising 9 "normal" *T. sacculifer*, defined by the spherical last chamber, and 11 *Globigerinoidesella fistulosa*) during 1.76–1.72 Ma and 20 dextral/sinistral morphotypes of *Pulleniatina* spp. during 2.15–1.93 Ma. The list of samples provided in this dataset, along with associated information for depth of the core, age, and species of the *Trilobatus sacculifer* plexus and *Pulleniatina* spp. can be found in Figure 1 and Tables 1 and 2.

We have applied image processing procedures to the data to remove the impurities (e.g., sediments and materials used for holding the sample during the scanning procedures) by using the functions including Select Region and Remove through ImageJ software (available at https://imagej.nih.gov/ij/) (Schindelin et al., 2012). The files can be opened in various CT analysis software such as VG studio, ORS dragonfly, and Amira/Avizo, with the scale according to the voxel size/pixel size of the JAMSTEC and NSRRC reconstructions (1.0 μm/voxel and 1.3 μm/voxel, respectively).

Protocols of microfocus X-ray CT (MXCT) analysis

Morphometry of planktic foraminiferal tests was performed using microfocus X-ray CT (ScanXmateD160TSS105, Comscantechno Co. Ltd., Yokohama, Japan) at JAMSTEC. A high-resolution setting (X-ray focus spot size: 0.8 μm; X-ray source voltage: 80 kV; X-ray source current: 60 μA; target current: 10.5 μA; detector array size of 1024 × 1024 pixels; 1,800 projections in 360° rotations) was applied. Geometric resolution of isotropic voxel size was 1.0 μm/voxel. We used ConeCTexpress (White Rabbit Corp., Tokyo, Japan) for corrections and the reconstruction of tomography data; the general principle of Feldkamp cone beam reconstruction was followed to reconstruct

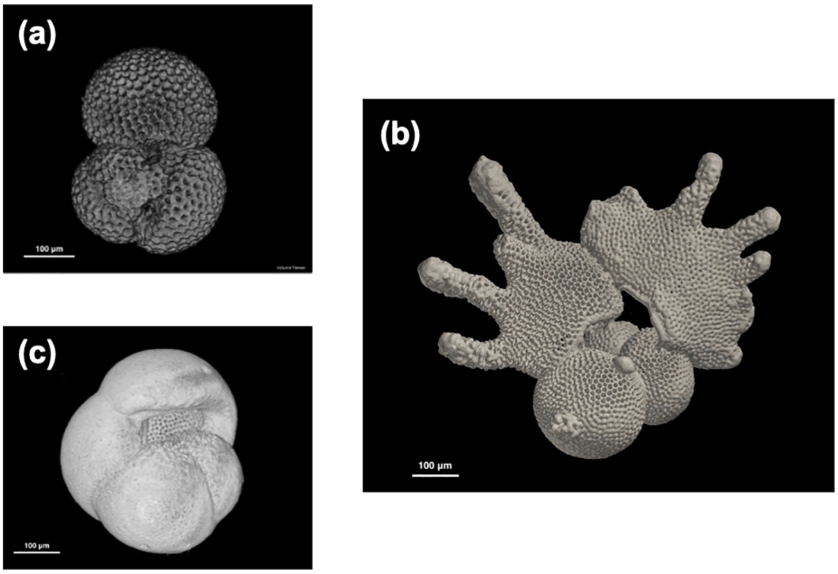

FIGURE 1
Examples of reconstructed planktonic foraminifera 3D images from ODP Hole 1115B, Solomon Sea, using the dataset. **(A)** *Trilobatus sacculifer* (10H2W 95–97 cm, 1.72 Ma), **(B)** *Globigerinodesella fistulosa* (10H4W 65–67 cm, 1.75 Ma), and **(C)** *Pulleniatina obliquiloculata* (left coiling, 12H6W 65–37 cm, 2.04 Ma). Note that all the scales are in 100 μm.

TABLE 1 Information of planktonic foraminifera *Trilobatus sacculifer* plexus and *Globigerinoidesella fistulosa* samples in this dataset.

Site	Core	Section	Level	Age (Ma)[#]	Species	File name	CT method
ODP1115B	10H	2W	95–97 cm	1.72 Ma	*Trilobatus sacculifer*	TW_ODP1115B_10H2W_95-97cm_TsacN1	MXCT
ODP1115B	10H	2W	95–97 cm	1.72 Ma	*Trilobatus sacculifer*	A1_nor_05	PXM
ODP1115B	10H	4W	5–7 cm	1.739 Ma	*Globigerinoidesella fistulosa*	TW_ODP1115B_10H4W_5-7cm_Gfis3	MXCT
ODP1115B	10H	4W	5–7 cm	1.739 Ma	*Trilobatus sacculifer*	TW_ODP1115B_10H4W_5-7cm_TsacN1	MXCT
ODP1115B	10H	4W	65–67 cm	1.745 Ma	*Globigerinoidesella fistulosa*	TW_ODP1115B_10H4W_65-67cm_Gfis1	MXCT
ODP1115B	10H	4W	65–67 cm	1.745 Ma	*Globigerinoidesella fistulosa*	TW_ODP1115B_10H4W_65-67cm_Gfis5	MXCT
ODP1115B	10H	4W	65–67 cm	1.745 Ma	*Trilobatus sacculifer*	TW_ODP1115B_10H4W_65-67cm_TsacN1	MXCT
ODP1115B	10H	4W	65–67 cm	1.745 Ma	*Trilobatus sacculifer*	TW_ODP1115B_10H4W_65-67cm_TsacN2	MXCT
ODP1115B	10H	4W	70–72 cm	1.745 Ma	*Globigerinoidesella fistulosa*	A22_fis_03	PXM
ODP1115B	10H	4W	70–72 cm	1.745 Ma	*Globigerinoidesella fistulosa*	A22_fis_05	PXM
ODP1115B	10H	4W	70–72 cm	1.745 Ma	*Globigerinoidesella fistulosa*	A22_fis_06	PXM
ODP1115B	10H	4W	70–72 cm	1.745 Ma	*Globigerinoidesella fistulosa*	A22_fis_07	PXM
ODP1115B	10H	4W	70–72 cm	1.745 Ma	*Globigerinoidesella fistulosa*	A22_fis_08	PXM
ODP1115B	10H	4W	95–97 cm	1.748 Ma	*Trilobatus sacculifer*	A19_nor_01	PXM
ODP1115B	10H	4W	95–97 cm	1.748 Ma	*Trilobatus sacculifer*	A19_nor_02	PXM
ODP1115B	10H	4W	95–97 cm	1.748 Ma	*Trilobatus sacculifer*	A19_nor_03	PXM
ODP1115B	10H	4W	125–127 cm	1.753 Ma	*Globigerinoidesella fistulosa*	TW_ODP1115B_10H4W_125-127cm_Gfis3	MXCT
ODP1115B	10H	4W	125–127cm	1.753 Ma	*Globigerinoidesella fistulosa*	TW_ODP1115B_10H4W_125-127cm_Gfis4	MXCT
ODP1115B	10H	4W	125–127 cm	1.753 Ma	*Trilobatus sacculifer*	TW_ODP1115B_10H4W_125-127cm_TsacN1	MXCT
ODP1115B	10H	5W	5–7 cm	1.758 Ma	*Globigerinoidesella fistulosa*	A17_fis_01	PXM

[#] Age model is based on Chuang et al. (2018).

image cross sections based on a filtered back projection algorithm. The reproducibility of CT number (density), volume, and average thickness is 0.9%, 1.5%, and 1.9% (in 31 analyses), respectively.

Protocols of projection X-ray microscopy

We utilized projection X-ray microscopy (PXM) at beamline TPS31A of the Taiwan Photon Source at the NSRRC, Taiwan, to reveal the 3-dimensional internal morphological structure of the specimens. The energy of the X-ray is tunable from 5–30 keV by using a double crystal monochromator (DCM). The X-ray size at the sample position is 25.0 × 1.4 mm^2. The spatial resolution of an image is 0.5–6.5 μm according to various magnifications of the objective lens. The pixel number, pixel size, and total area of the image detector are 2,560 × 2,160, 1.3 μm, and 16.6 × 14.0 mm^2, respectively. The temporal resolution can approach 20 ms/frame and 40 sec/tomography. We adopted X-ray energy of 22 keV in PXM-DCM mode. The spatial resolution of the image is 2.6 μm by using a 10× objective lens and bin2 reconstruction. The field of view of an image is 1.7 × 1.4 mm^2. The standard deviation (%) of width, height, thickness, and absorption of one sample in 20 analysis is 0.09%, 0.18%, 0.01%, and 2.9%, respectively. Tomography was implemented by performing azimuthal rotations at intervals of 0.25 degrees over the full range of ±90 degrees, resulting in a total

TABLE 2 Information of planktonic foraminifera *Pulleniatina* spp. samples in this dataset.

Site	Core	Section	Level	Age (Ma)[#]	Species	File name	CT method
ODP 1115B	11 H	7 W	5–7 cm	1.93 Ma	*Pulleniatina obliquiloculata*	*P. obliquiloculata*_11_7_01	PXM
ODP 1115B	11 H	7 W	5–7 cm	1.93 Ma	*Pulleniatina obliquiloculata*	*P. obliquiloculata*_11_7_02	PXM
ODP 1115B	11 H	7 W	5–7 cm	1.93 Ma	*Pulleniatina obliquiloculata*	*P. obliquiloculata*_11_7_03	PXM
ODP 1115B	11 H	7 W	5–7 cm	1.93 Ma	*Pulleniatina obliquiloculata*	*P. obliquiloculata*_11_7_04	PXM
ODP 1115B	12 H	6 W	65–67 cm	2.04 Ma	*Pulleniatina finalis*	*P. finalis*_12_6_01	MXCT
ODP 1115B	12 H	6 W	65–67 cm	2.04 Ma	*Pulleniatina finalis*	*P. finalis*_12_6_02	MXCT
ODP 1115B	12 H	6 W	65–67 cm	2.04 Ma	*Pulleniatina praecursor*	*P. praecursor*_12_6	MXCT
ODP 1115B	12 H	6 W	65–67 cm	2.04 Ma	*Pulleniatina obliquiloculata*	*P. obliquiloculata*_12_6_01	MXCT
ODP 1115B	12 H	6 W	65–67 cm	2.04 Ma	*Pulleniatina obliquiloculata*	*P. obliquiloculata*_12_6_02	MXCT
ODP 1115B	13 H	2W	65–67 cm	2.08 Ma	*Pulleniatina obliquiloculata*	*P. obliquiloculata*_13_2_01	PXM
ODP 1115B	13 H	2W	65–67 cm	2.08 Ma	*Pulleniatina obliquiloculata*	*P. obliquiloculata*_13_2_02	PXM
ODP 1115B	13 H	4 W	5–7 cm	2.10 Ma	*Pulleniatina finalis*	*P. finalis*_13_4	MXCT
ODP 1115B	13 H	4 W	5–7 cm	2.10 Ma	*Pulleniatina praecursor*	*P. praecursor*_13_4_01	MXCT
ODP 1115B	13 H	4 W	5–7 cm	2.10 Ma	*Pulleniatina praecursor*	*P. praecursor*_13_4_02	MXCT
ODP 1115B	13 H	4 W	5–7 cm	2.10 Ma	*Pulleniatina obliquiloculata*	*P. obliquiloculata*_13_4_01	MXCT
ODP 1115B	13 H	4 W	5–7 cm	2.10 Ma	*Pulleniatina obliquiloculata*	*P. obliquiloculata*_13_4_02	MXCT
ODP 1115B	13 H	6 W	95–97 cm	2.15 Ma	*Pulleniatina obliquiloculata*	*P. obliquiloculata*_13_6_01	PXM
ODP 1115B	13 H	6 W	95–97 cm	2.15 Ma	*Pulleniatina obliquiloculata*	*P. obliquiloculata*_13_6_02	PXM
ODP 1115B	13 H	6 W	95–97 cm	2.15 Ma	*Pulleniatina obliquiloculata*	*P. obliquiloculata*_13_6_03	PXM
ODP 1115B	13 H	6 W	95–97 cm	2.15 Ma	*Pulleniatina obliquiloculata*	*P. obliquiloculata*_13_6_04	PXM

[#] Age model is based on Chuang et al. (2018).

of 721 projection images, which were then reconstructed using a filtered-back-projection algorithm.

Research potential estimation and discussion

The LAD of *G. fistulosa* has been considered a useful index event in marine biostratigraphy, marking the ~1.7 Ma interval. However, due to the strong morphological resemblance of *G. fistulosa* to its close relative *T. sacculifer*, accurate identification of this important index event can be problematic. The existence of some transitional morphotypes can further complicate the recognition of *G. fistulosa*, potentially obscuring the biostratigraphic utility of the species. Previous studies have proposed several criteria to fix this problem; however, most of the solutions remain qualitative and subjective in nature, based on two-dimensional observations that lack more robust quantitative support for species-level distinction (the synthetic review is included in Pool and Wade, 2019). Secondly, we are keen to understand the ecological significance of the digitate structures present on *G. fistulosa* prior to its extinction event as well as the left coiling event of *Pulleniatina* spp., which are unique occurrences and events that could be related to the paleoceanographic shifting in the Pacific Ocean (Wara et al., 2005).

Data presentation

The dataset is organized into two sub-datasets for μ-CT data of foraminifer tests. One sub-dataset is presented as a zipped folder and contains a group of TIFF image stacks (*Pulleniatina* spp.), while the other is a group of TIFF image stacks (*T. sacculifer* and *G. fistulosa*). Each image stack contains 200–500 TIFF images for each individual foraminifer sample. A whole image stack needs to be imported into the CT analysis software to obtain integrated 3D foraminifer reconstruction (Figures 1A–C). Scales need to be set up manually with the pixel size (1 μm for MXCT and 1.3 μm for PXM).

Data availability statement

The datasets presented in this study can be found in online repositories. A link to the data can be found below: https://zenodo.org/record/7874195#.ZEs4AnZByUk.

Author contributions

LL designed and generated the planktonic foraminifera samples. KK performed the MXCT analysis. Y-FS and G-CY performed PXM analyses. W-LC, J-CK, and C-HL processed the data, reconstructed the 3D models, and prepared the first draft. L-WK and J-JSH generously provided support for image analyses software and data processing protocols. RS significantly revised the structure of the manuscript and direction of paleontological discussions. All authors contributed to the article and approved the submitted version.

Funding

The authors would like to thank the following grants and institutions that supported this research: the Science Vanguard Research Program of the Ministry of Science and Technology (MOST) (110-2636-M-002- 011 to LL) and National Taiwan University (109L892603 to LL).

Acknowledgments

This research used samples provided by the International Ocean Discovery Program (IODP). The authors thank Mr. Chien-Yu Lee, Dr. Pei-Tzu Lee, and Mr. Shih-Ting Lo of the NSRRC Experimental Technique Group for PXM data execution.

Conflict of interest

Publisher's note

References

Berggren, W. A., Kent, D. V., Swisher, C. C., and Aubry, M.-P. (1995). "A revised Cenozoic geochronology and chronostratigraphy", in *Geochronology, time scales and global stratigraphic correlation*. Eds. W. A. Berggren, D. V. Kent, M.-P. Aubry and J. Hardenbol. *SEPM Special Publication 54*. Claremore, OK: Society for Sedimentary Geology.

Bown, P. R., Lees, J. A., and Young, J. R. (2004). "Calcareous nannoplankton evolution and diversity through time", in *Coccolithophores*. Eds. H. R. Thierstein and J. R. Young. Berlin: Springer.

Burke, J. E., Renema, W., Schiebel, R., and Hull, P. M. (2020). Three-dimensional analysis of inter-and intraspecific variation in ontogenetic growth trajectories of planktonic foraminifera. *Mar. Micropaleontology.* 155, 101794. doi: 10.1016/j.marmicro.2019.101794

Caromel, A. G., Schmidt, D. N., Fletcher, I., and Rayfield, E. J. (2016). Morphological change during the ontogeny of the planktic foraminifera. *J. Micropalaeontology.* 35 (1), 2–19. doi: 10.1144/jmpaleo2014-017

Caromel, A. G., Schmidt, D. N., and Rayfield, E. J. (2017). Ontogenetic constraints on foraminiferal test construction. *Evol. Dev.* 19 (3), 157–168. doi: 10.1111/ede.12224

Chen, C.-Y. (2008). *A study on the disappearance of* Globigerinoides fistulosus *and its relationship to the hydrological change of the tropical Pacific*. Master's thesis: National Taiwan University.

Chuang, C.-K., Lo, L., Zeeden, C., Chou, Y.-M., Wei, K.-Y., Shen, C.-C., et al. (2018). Integrated stratigraphy of ODP Site 1115 (Solomon Sea, southwestern equatorial Pacific) over the past 3.2 Ma. *Mar. Micropaleontology* 144, 25–37. doi: 10.1016/j.marmicro.2018.09.003

Duan, B., Li, T., and Pearson, P. N. (2021). Three dimensional analysis of ontogenetic variation in fossil globorotaliiform planktic foraminiferal tests and its implications for ecology, life processes and functional morphology. *Mar. Micropaleontology.* 165, 101989. doi: 10.1016/j.marmicro.2021.101989

Fraass, A. J., Kelly, D. C., and Peters, S. E. (2015). Macroevolutionary history of the planktic foraminifera. *Annu. Rev. Earth Planetary Sci.* 43 (1), 139–166. doi: 10.1146/annurev-earth-060614-105059

Ge, Q., Zhong, B., Kanakiya, B., Mitra, R., Marchitto, T., and Lobaton, E. (2017). "Coarse-to-fine foraminifera image segmentation through 3D and deep features," in *2017 IEEE Symposium Series on Computational Intelligence (SSCI)*. Piscataway, NJ: IEEE.

Görög, Á, Szinger, B., Tóth, E., and Viszkok, J. (2012). Methodology of the micro-computer tomography on foraminifera. *Palaeontologia Electronica.* 15 (1), 15. doi: 10.26879/261

Hay, W. W., and Sandberg, P. A. (1967). The scanning electron microscope, a major break-through for micropaleontology. *Micropaleontology*, 13 (4), 407–418. doi: 10.2307/1484718

Hecht, A. D., and Savin, S. M. (1972). Phenotypic variation and oxygen isotope ratios in Recent planktonic foraminifera. *J. Foraminiferal Res.* 2 (2), 55–67. doi: 10.2113/gsjfr.2.2.55

Iwasaki, S., Kimoto, K., Sasaki, O., Kano, H., and Uchida, H. (2019). Sensitivity of planktic foraminiferal test bulk density to ocean acidification. *Sci. Rep.* 9 (1), 9803. doi: 10.1038/s41598-019-46041-x

Liu, Y., Lo, L., Shi, Z., Wei, K.-Y., Chou, C.-J., Chen, Y.-C., et al. (2015). Obliquity pacing of the western Pacific Intertropical Convergence Zone over the past 282,000 years. *Nat. Commun.* 6 (1), 1–7. doi: 10.1038/ncomms10018

Lo, L., Shen, C.-C., Zeeden, C., Tsai, Y.-H., Yin, Q., Yang, C.-C., et al. (2022). Orbital control on the thermocline structure during the past 568 kyr in the Solomon Sea, southwest equatorial Pacific. *Quaternary Sci. Rev.* 295, 107756. doi: 10.1016/j.quascirev.2022.107756

Mitra, R., Marchitto, T., Ge, Q., Zhong, B., Kanakiya, B., Cook, M., et al. (2019). Automated species-level identification of planktic foraminifera using convolutional neural networks, with comparison to human performance. *Mar. Micropaleontology.* 147, 16–24. doi: 10.1016/j.marmicro.2019.01.005

Neil, H., Cooke, P., and Northcote, L. (2005). The life and death of planktonic foraminifera. *Water Atmosphere.* 13 (1), 18–19.

Ofstad, S., Zamelczyk, K., Kimoto, K., Chierici, M., Fransson, A., and Rasmussen, T. L. (2021). Shell density of planktonic foraminifera and pteropod species *Limacina helicina* in the Barents Sea: relation to ontogeny and water chemistry. *PloS One* 16 (4), e0249178. doi: 10.1371/journal.pone.0249178

Olsson, R. (1972). Growth changes in the *Globorotalia fohsi* lineage. *Eclogae Geologicae Helvetiae.* 65 (1), 165–184. doi: 10.5169/seals-164083

Poole, C. R., and Wade, B. S. (2019). Systematic taxonomy of the *Trilobatus sacculifer* plexus and descendant *Globigerinoidesella fistulosa* (planktonic foraminifera). *J. Systematic Palaeontology.* 17 (23), 1989–2030. doi: 10.1080/14772019.2019.1578831

Renaud, S., and Schmidt, D. N. (2003). Habitat tracking as a response of the planktic foraminifer *Globorotalia truncatulinoides* to environmental fluctuations during the last 140 kyr. *Mar. Micropaleontology* 49 (1-2), 97–122. doi: 10.1016/S0377-8398(03)00031-8

Schindelin, J., Arganda-Carreras, I., Frise, E., Kaynig, V., Longair, M., Pietzsch, T., et al. (2012). Fiji: an open-source platform for biological-image analysis. *Nat. Methods* 9 (7), 676–682. doi: 10.1038/nmeth.2019

Schmidt, D. N., Rayfield, E. J., Cocking, A., and Marone, F. (2013). Linking evolution and development: Synchrotron Radiation X-ray tomographic microscopy of planktic foraminifers. *Palaeontology.* 56 (4), 741–749. doi: 10.1111/pala.12013

Schmidt, D. N., Thierstein, H. R., Bollmann, J., and Schiebel, R. (2004). Abiotic forcing of plankton evolution in the Cenozoic. *Science.* 303 (5655), 207–210. doi: 10.1126/science.1090592

Tappan, H., and Loeblich, A. R. Jr. (1988). Foraminiferal evolution, diversification, and extinction. *J. Paleontology*, 62 (5), 695–714.

Vanadzina, K., and Schmidt, D. N. (2022). Developmental change during a speciation event: evidence from planktic foraminifera. *Paleobiology.* 48 (1), 120–136. doi: 10.1017/pab.2021.26

Wade, B. S., Pearson, P. N., Berggren, W. A., and Pälike, H. (2011). Review and revision of Cenozoic tropical planktonic foraminiferal biostratigraphy and calibration to the geomagnetic polarity and astronomical time scale. *Earth-Science Rev.* 104 (1–3), 111–142. doi: 10.1016/j.earscirev.2010.09.003

Wara, M. W., Ravelo, A. C., and Delaney, M. L. (2005). Permanent El Niño-like conditions during the Pliocene warm period. *Science* 309 (5735), 758–761. doi: 10.1126/science.1112596

Wei, K.-Y. (1987). Multivariate morphometric differentiation of chronospecies in the late Neogene planktonic foraminiferal lineage *Globoconella*. *Mar. Micropaleontology.* 12, 183–202. doi: 10.1016/0377-8398(87)90020-X

Zarkogiannis, S. D., Antonarakou, A., Tripati, A., Kontakiotis, G., Mortyn, P. G., Drinia, H., et al. (2019). Influence of surface ocean density on planktonic foraminifera calcification. *Sci. Rep.* 9 (1), 1–10. doi: 10.1038/s41598-018-36935-7

frontiers | Frontiers in Earth Science

TYPE Original Research
PUBLISHED 21 December 2023
DOI 10.3389/feart.2023.1184671

OPEN ACCESS

EDITED BY
Stergios D. Zarkogiannis,
University of Oxford, United Kingdom

REVIEWED BY
Constance Choquel,
Lund University, Sweden
Georg Schulz,
University of Basel, Switzerland
Shunichi Kinoshita,
National Museum of Nature and Science,
Japan

*CORRESPONDENCE
Katsunori Kimoto,
✉ kimopy@jamstec.go.jp

RECEIVED 12 March 2023
ACCEPTED 22 November 2023
PUBLISHED 21 December 2023

CITATION
Kimoto K, Horiuchi R, Sasaki O and Iwashita T (2023), Precise bulk density measurement of planktonic foraminiferal test by X-ray microcomputed tomography.
Front. Earth Sci. 11:1184671.
doi: 10.3389/feart.2023.1184671

Precise bulk density measurement of planktonic foraminiferal test by X-ray microcomputed tomography

Katsunori Kimoto[1]*, Rika Horiuchi[1], Osamu Sasaki[2] and Tomohiro Iwashita[3]

[1]Japan Agency for Marine-Earth Science and Technology (JAMSTEC), Yokosuka, Japan, [2]Tohoku University Museum, Sendai, Japan, [3]White Rabbit, Corp., Tokyo, Japan

X-ray Microcomputed Tomography (μCT) is rapidly becoming an important analytical technique for examining the precise morphometry of small objects. The most notable feature of this technique is that it enables nondestructive, highly accurate morphometric measurements at micrometer-order resolution. In the Earth sciences, this makes μCT extremely useful for clarifying how genetic associations and the surrounding environment affect the morphology of micro-sized organisms. However, the actual analytical methods and the points that must be considered to produce reliable data have rarely been discussed in detail. Here, to address this lack of discussion, we describe in detail our methodology for precise μCT-based morphometry by using a test of the planktonic foraminifer and marine calcifier *Globorotalia inflata*. In addition to demonstrating the long-term stability of our μCT setup and analytical approach, we also propose a new methodology for test bulk density calibration using artificial carbonate phantoms. We expect that μCT together with our artificial phantom-based methodology will be useful for calculating accurate test bulk densities of micro-sized marine calcifiers.

KEYWORDS

X-ray microcomputed tomography (μCT), CT number, planktonic foraminifera, test bulk density, artificial calcite phantoms

1 Introduction

μCT is a CT technique that allows precise morphological analysis of microfossils and other geological materials. This technique offers a notable advantage in the study of microfossils by allowing the simultaneous, nondestructive examination of their morphologies at both the outer surface and the internal structure, all on micrometer scales. Furthermore, this technique also allows for the quantification of morphological information, facilitating comparisons between different specimens or cryptic species and more accurate identification of species compared with stereomicroscope and scanning electron microscope (SEM) techniques (e.g., Briguglio et al., 2014; Ikenoue et al., 2016; Shimizu et al., 2017; Xiao et al., 2017; Kachovich et al., 2019).

Planktonic foraminiferal tests have traditionally been used as a tool to reconstruct past and present marine environmental conditions. Many planktonic foraminifera develop a secondary crust layer as they reproduce, covering the thinner primary layer they formed at the end of growth (Brummer et al., 1987; Erez, 2003). This secondary calcification is primarily a mature characteristic and is formed in deeper water during growth (e.g., Arikawa, 1983; Lohmann, 1995). The theoretical model of Lohmann (1995), which addresses the effects of secondary layer formation and selective dissolution of the primary layer on the isotope composition of the test, subsequently led to the development of two new proxies of carbonate chemistry of seawater in the past ocean (e.g., Broecker and Clark, 2001); Size-normalized shell weight (SNW; e.g., Barker and Elderfield, 2002; Bijma et al., 2002; Moy et al., 2009; Beer et al., 2010; Aldridge et al., 2012; Naik et al., 2013) and area-normalized shell weight (ANW; e.g., Marshall et al., 2013; Osborne et al., 2016; Weinkauf et al., 2020) are representative proxies of [CO_3^{2-}] of sea water. These proxies are obtained by normalizing the test weight (mass) by the test length or test area determined from a SEM image of the test. However, such images are two-dimensional projection images, which makes it difficult to assess the accuracy of these proxies. Because the test of planktonic foraminifera has a curvature shape and its walls consist of a dense and complex structure composed of multiple layers with organic matter and calcium carbonate (Schiebel and Hemleben, 2017). Thus, SNW and ANW are indirect measurements of test density.

Three-dimensional morphometry with μCT has the potential to solve the above problems. The application of μCT for estimating the carbonate solubility and calcification capacity of marine calcareous materials has recently been widely discussed (Johnstone et al., 2010; Iwasaki et al., 2015; 2019a; Todd et al., 2020; Zarkogiannis et al., 2020; Kinoshita et al., 2021; Kuroyanagi et al., 2021; Ofstad et al., 2021; Charrieau et al., 2022). Furthermore, ambitious attempts have been made to estimate the concentration of carbonate ions in past seawater by quantifying the dissolution of foraminifera tests (e.g., Iwasaki et al., 2019b; 2022), habitat depth (Zarkogiannis et al., 2022), and to detect the biological effects of anthropogenic environmental changes since the Industrial Revolution (Fox et al., 2020).

To date, the methodology, accuracy, and reproducibility of densitometry of microfossil using μCT are yet to be discussed in detail. Here, we set out to describe in detail the collection of measurements by μCT analysis and precautions that must be considered. In addition, we also discuss the stability of μCT measurements for the analysis of foraminiferal tests, as well as the development and application of new reference materials for density measurement of calcium carbonate.

2 Methodology

2.1 Samples

The target specimen was a single test of the planktonic foraminifer *Globorotalia inflata* that was recovered from water pumped from the surface of the Kuroshio Current in the western North Pacific. The reference material for μCT measurement was a single grain of limestone crystal formed from stable oxygen and carbon isotopes (NBS19, NIST RM8544) (Iwasaki et al., 2015). The grains of this material are uniform in density, are readily available, and are used as a reference material in Earth-science laboratories around the world (currently unavailable, but extant in labs around the world). The reference material was analyzed at the same time as the target specimen, which allowed for later adjustments to be made to offset energy fluctuations in the X-ray radiation produced from the X-ray tube. To prepare the standard material, the limestone grain was gently dissolved in a weak acid (0.01 M HCl), molded with a brush into a spherical-to-subspherical shape, and used as a standard sample to average the X-ray transmission distance.

In μCT analyses, objects exposed to X-ray irradiation generate heat on their surface, which may cause the adhesive used to fix the object to the rotation stage to melt and the sample to become loose and move during analysis. For this reason, the exposure time should be set as short as possible, and complete fixation of the object is important. Tragacanth and other similar adhesives that are commonly used for fixing microfossils easily become flexible under heat; therefore, here we used a urethane adhesive with much better heat resistance (Jellafin; SEC Seaprex, Co., Ltd., Hakodate, Japan).

2.2 X-ray irradiation

The principal equipment and analytical parameters used in this study are shown in Table 1. In this study, the tube voltage and current were set at 80 kV and 50 μA, respectively, and the target current was 10.5 μA. Multiple stacking (averaging multiple images acquired at the same projective position) is an effective way to increase the signal-to-noise ratio when acquiring transmission images; in particular, the effect of noise generated by the air around objects can be markedly reduced. In consideration of the balance between image acquisition time and improvement of the signal-to-noise ratio, four images were averaged to obtain a single image. The projection number was set at 1,200 for an X-ray detector size of 992 × 992 pixels (1 × 1 binning).

2.3 Beam hardening

When an object is irradiated with white X-rays with a wide energy distribution, the X-rays with high energy preferentially penetrate through the object, whereas those with low energy are absorbed at the outer surface of the object or by surfaces inside the material and reach the detector only after attenuation. This selective absorption of X-rays is called beam hardening (BH), and it often adversely affect for density measurements of microfossils made using μCT (Briguglio et al., 2014). To reduce the intensity of BH artifacts, a metal filter can be inserted in front of the X-ray source. In a simulation examining the transmitted X-ray energy distribution obtained with various metal filters at an X-ray tube voltage of 80 kV, the greatest suppression of X-ray transmission in the low-energy region less than 20 kV, which is the primary cause of BH, was obtained with 200-μm-thick, high-grade aluminum (>99.0% Al). In the present study, we therefore used a 200-μm-thick Al filter in front of the X-ray detector (Ay et al., 2012). This filter was used for all of the test bulk density measurements.

To evaluate the effect of BH, it is useful to monitor the gray values of the reconstructed image of a homogeneous reference material (phantom) made of the same material as the target and measured at the same time as the target. If BH artifacts do not appear in the cross-section of the reference material at a similar transmission distance to the target specimen, it is safe to assume that the BH effect is weak in the target specimen. Conversely, if BH does appear in the cross-section, we

TABLE 1 Principal equipment and analytical parameters used in the study.

X-ray tube	L10711-03 (hamamatsu photonics)
X-ray detector	PaxScan 1313DX (1024x1024 pixels, Varex Imaging)
Tube Voltage (kV)	80
Tube current (μA)	50
Target current (μA)	10.5
X-ray focal point size (μm)	0.8
Cumlative number of images	2
Number of image acquisition/sec	3
Projection number	1,200
Resolution (μm)/pixel	1.00
Binning	1 x 1 (992x992)

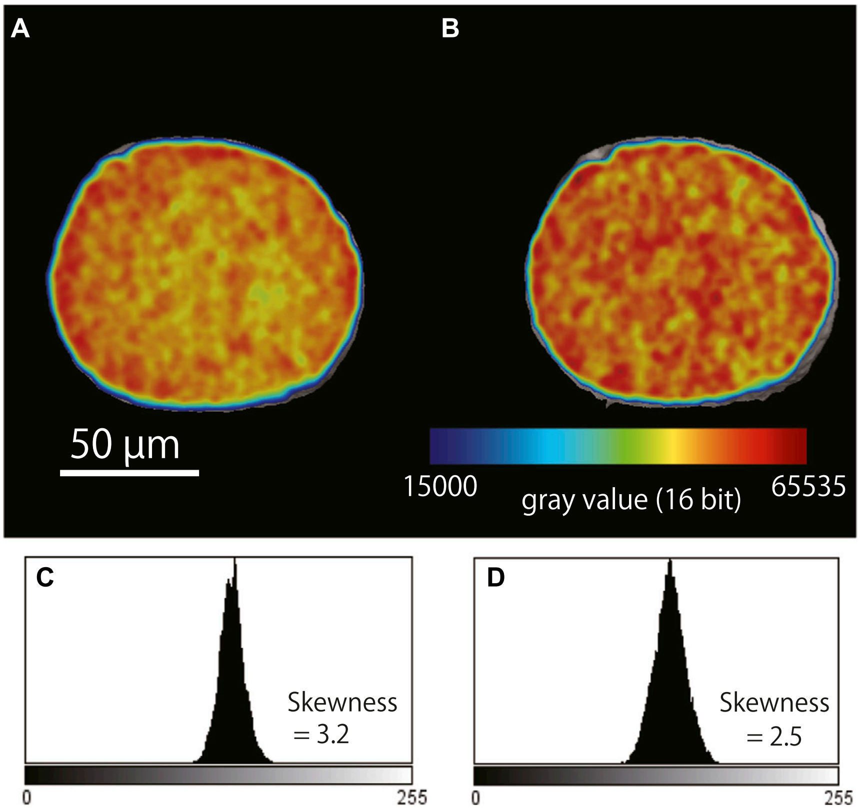

FIGURE 1
Examples of beam hardening artifacts in a cross-section of the limestone reference material (NBS19) before and after correction. **(A)** Cross-section image of the reference material obtained without a metal filter. High gray values (red) are seen around the edge of the reference material, and lower values (yellow) are seen at the center. **(B)** Cross-section image of the same reference material obtained with a 0.2-mm thick aluminum filter placed in front of the X-ray detector; the gray values are overall more homogeneous compared with what was observed without the filter. **(C)** Frequency distribution of the gray values in **(A)**. **(D)** Frequency distribution of the gray values in **(B)**.

should assume that the target specimen at transmission distances greater than the diameter of the reference material are affected by BH. In the present study, the diameter of the limestone reference material was selected to match the total length of the X-ray transmission distance through the foraminiferal tests; the presence or absence of BH artifacts was evaluated by examining the gray values of a cross-section image of the limestone. Thus, a limestone grain with a diameter of 100–300 μm was used, and the difference of the gray value between approximately 100 pixels at the outer edges or in the center was within 2% on average and was reduced to 10%–20% of that obtained without the metal filter (Figure 1). Thus, in this study, BH up to a calcium carbonate thickness of 100–300 μm was considered to be corrected by the aluminum filter. In practice, the total X-ray transmission length of planktonic foraminiferal walls is less than 300 μm, and many species have high porosity due to the presence of pores in the wall. Therefore, the above method should be applicable for test bulk density analysis of almost all planktonic foraminiferal tests.

In this study, a grain of limestone (NBS 19; ~130 μm in diameter; 2.71 g/cm^3 in true density; 1,000 in mean CT number) was used to normalize the CT number of foraminiferal tests. (Iwasaki et al., 2019a).

2.4 CT number as an index of the relative density of calcium carbonate

In analyses of human bone density, the following CT numbers are often used: −1,000 (air), 0 (water), and 1,000 (highest bone density) (Hounsfield, 1980). CT number is calculated in Hounsfield units (HU; named after the proponent of this number) by using the following equation:

$$\text{CT number} = \frac{\mu(\text{tissue}) - \mu(\text{water})}{\mu(\text{water}) - \mu(\text{air})} \times 1000, \qquad (1)$$

where μ is the attenuation coefficient for each material.

The same concept can be applied to the calculation of the test bulk density of a foraminiferal sample. Although the attenuation coefficient and the gray value are not exactly the same physical quantity, they are both parameters related to the attenuation of X-rays, and the relative relationship holds. Therefore, they can be made dimensionless and expressed as a relative density by normalizing by the gray value of the standard sample (Iwasaki et al., 2015).

The relative number of gray values between the sample and standard material is called the calcite CT number (hereafter simply CT number), defined by the following equation:

$$\text{CT number} = \frac{\mu(\text{foram}) - \mu(\text{air})}{\mu(\text{standard}) - \mu(\text{air})} \times 1000, \qquad (2)$$

where μ(foram), μ(air), and μ(standard) are the gray values of the foraminiferal test, the surrounding air, and the standard material, respectively. In the present study, the values of μ(air) and μ(standard) were set to 0 and 1,000, respectively. CT number refers to the value related to density only when the sample is composed of a homogeneous material and when the effect of BH is eliminated. In the case of foraminiferal tests composed of a single material, the bulk density of the test can be calculated from the CT number.

3 Calibration of accurate test bulk density: external calibration with artificial phantoms

In X-ray CT scanning, a reference sample (e.g., air or water) and a target sample are scanned simultaneously, and the CT numbers of the tomographic image (e.g., Hounsfield scale of medical CT) are calibrated from the grayscale of the image based on the gray values of the reference sample. The development of a suitable CT number calibration method is the most important issue in the application of μCT. There are currently no commercially available reference materials (phantoms) that mimic the bulk density of small grains of calcium carbonate such as the foraminiferal tests. To maintain the external accuracy of the measured bulk density, independent comparative calibration phantoms are needed. Therefore, we produced our own calibration phantoms as follows.

1) Pure artificial calcium carbonate powder (~5 μm particle diameter; >99.9% purified, chemical analysis grade) was used to make the phantoms. Calcium carbonate powder was placed in a die set and exposed to pressures from 1.5 to 10 tons for 20 min to solidify the carbonate powder. These solidified calcium carbonate samples were named "die samples".
2) The die samples were gently removed from the die set and weighed to three decimal places in milligrams on a microbalance (Sartorius ME5; Sartorius Lab Inst. GmbH and Co., Germany). Then, the volume of the die samples was measured by μCT.
3) The test bulk density of the die samples was obtained by dividing the weight by the volume.
4) The die samples were molded into smaller pieces (<300 μm in diameter) by hand using a surgical knife under a binocular stereomicroscope and then used as the reference material in the foraminiferal test bulk density analysis.

This method yielded carbonate phantoms with various porosities (i.e., bulk densities) because different pressures result in different states of crimping between the calcium carbonate particles. To develop a calibration equation between test bulk density and CT number, we analyzed these phantoms and a single NBS19 grain by μCT under the same conditions as those used for the subsequent analysis of the foraminiferal test (Table 2).

To verify the stability of the CT number under the present experimental conditions, test bulk density analysis of a single foraminiferal test was repeated every 2 days for 2 months (Nov. To Dec. 2022). The reason for this period is that the tungsten filament in the X-ray tube runs out after about 2 months (ca. 300 h of operation) at the rate at which we operate our instrument; therefore, we needed to complete the experiment within 2 months so that all of the measurements were performed under the same conditions.

To evaluate the objectivity of this method for test bulk density, multiple weight measurements of single foraminifera were performed using electronic microbalances and the differences between the μCT and conventional methods were evaluated. A Cubis II MCA6.6S electronic microbalance (Sartorius Lab Instruments GmbH and Co., Germany) was used for the measurement of the single specimens. The measurements were performed at room temperature (25.7°C–26.0 °C) and humidity from 29% to 34%.

The μCT instrument used in this experiment was a ScanXmateDF160TSS105 (Comscantechno Co., Ltd., Yokohama, Japan) installed at the Japan Agency for Marine-Earth Science and Technology (JAMSTEC, Kanagawa, Japan). The same tungsten filaments and tungsten targets were used throughout the experiment. The same experimental settings were used for all the analyses. Reconstructions and drawings of images were obtained by using the coneCTexpress and Molcer Plus 3D image visualization

TABLE 2 Data of die samples and calibration phantoms used in this study.

Die samples				
#ID	Volume (×10^3 µm^3)	Weight (µg)	Weight STD	Remarks
P2	125.58	229.682*	0.007	*5 times average
P4	56.23	111.675*	0.004	*5 times average
P8	25.81	54.114*	0.012	*5 times average
Calibration phantoms				
ID	Volume (×10^3 µm^3)	CT number	CT number STD	Bulk density
P2-1	16.29	692.8	13.3	1.83
P4-1	9.45	745.4	10.3	1.99
P8-1	15.11	780.0	12.1	2.10
NBS19	0.32	1,000	-	2.71 (in theory)

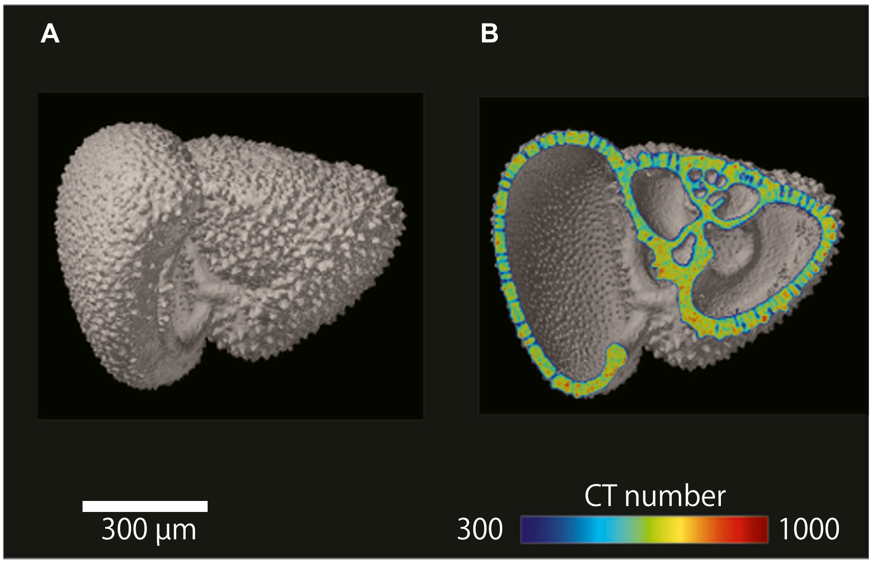

FIGURE 2
µCT images of a single shell of the planktonic foraminifer *Globorotalia inflata*. **(A)** Isosurface image of *G. inflata*. **(B)** Cross-sectional image of *G. inflata* with a color overlay showing CT number.

and processing software (White Rabbit, Corp., Tokyo, Japan), respectively. The general principle of Feldkamp cone-beam reconstruction was followed to reconstruct image cross-sections based on the filtered back-projection algorithm.

4 Results

4.1 Histogram and determination of the threshold of the 3D image

A single test of the planktonic foraminifer *G. inflata* was subjected to µCT to obtain isosurface and cross-sectional images (Figure 2). Segmentation is an important concept for making an isosurface image because it directly affects not only the quality of the reconstructed 3D image but also that of the subsequent analyses. Segmentation can be described as "thresholding" to distinguish regions of interest from other unwanted regions: areas higher than the threshold are displayed, whereas areas below it are ignored. Generally, 3D image processing software performs an automatic segmentation (e.g., by using Otsu's formula (Otsu, 1980)). However, in our method, since the threshold value changes with the shape of the histogram, the range of variation is large for low test bulk density samples with severe dissolution. To minimize measurement errors due to variations in threshold values, we clarified the relationship between the gray values of the air and

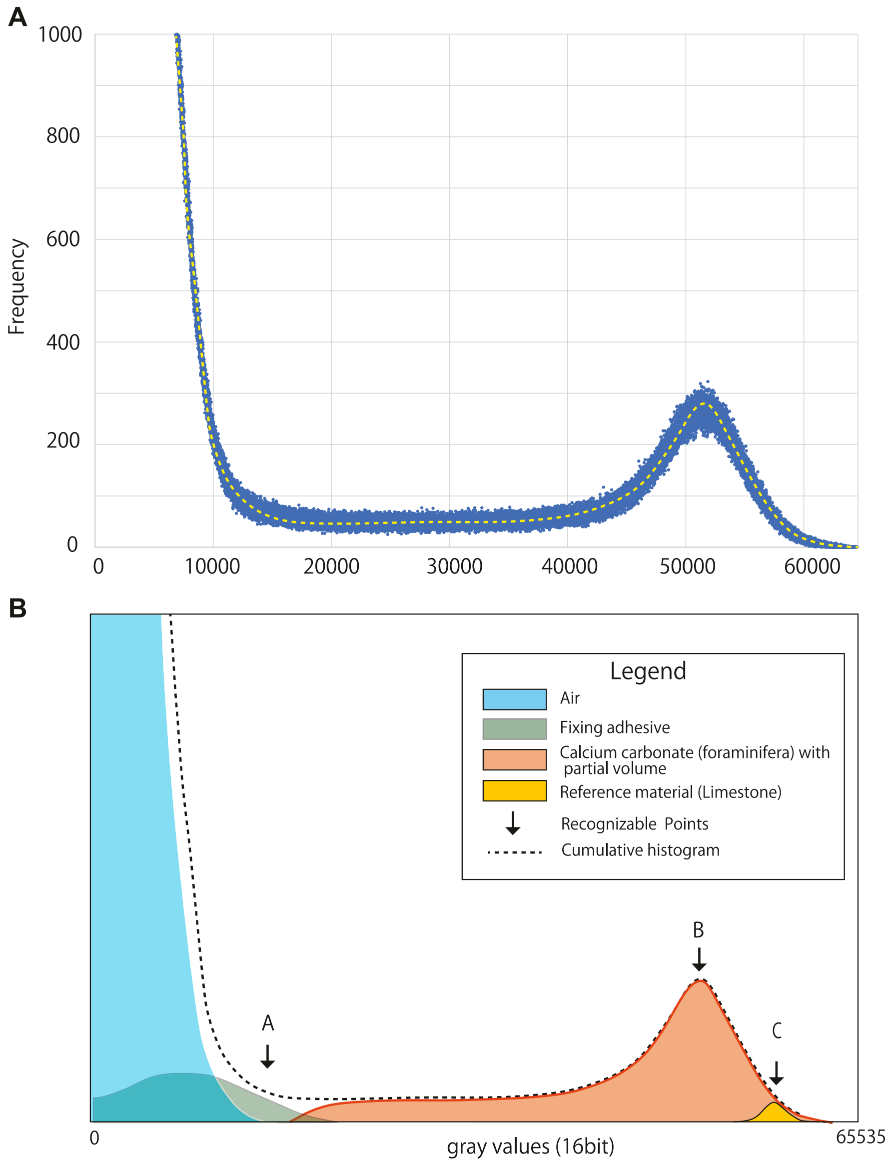

FIGURE 3
Histograms obtained for a 16-bit image of a single shell of the planktonic foraminifer *Globorotalia inflata*. **(A)** Original gray value histogram. **(B)** Diagram showing the peaks comprising the gray value histogram and recognizable control points. (A): maximum gray value of the air surrounding the specimen, (B): peak gray value for the foraminiferal shell, (C): peak gray value for the limestone reference material. The histogram was obtained by reconstructing each component separately after the μCT measurement.

the reference material, which are constantly visible during the measurement is in progress, and then calculated the threshold value.

Figure 3 shows the gray value histogram obtained for a 16-bit image of the foraminiferal test. The 16-bit image comprised grayscale voxels each with a value between 0 (lowest) and 65,535 (highest) (Figure 3A). The histogram contains four component peaks, one each for the air surrounding the foraminiferal test, the fixing adhesive, the foraminiferal test (calcium carbonate) including partial volumes, and the reference material (i.e., limestone) (Figure 3B). In the present study, the peak value of the air was set at a gray value of 0.

The peak attributed to the adhesive was almost fully contained within the peak for the air, which was expected because the adhesive used to fix the samples was purposely selected because of its low X-ray absorption, which greatly eases differentiation between the adhesive and the specimen during image processing.

A partial volume is defined as a voxel that contains both the specimen and the surrounding air. Therefore, the peak attributed to foraminiferal calcium carbonate represents a combination of the voxels only containing the foraminiferal test as well as the voxels containing partial volumes.

There was a marked difference in gray values between air and calcium carbonate because of the large difference in their densities,

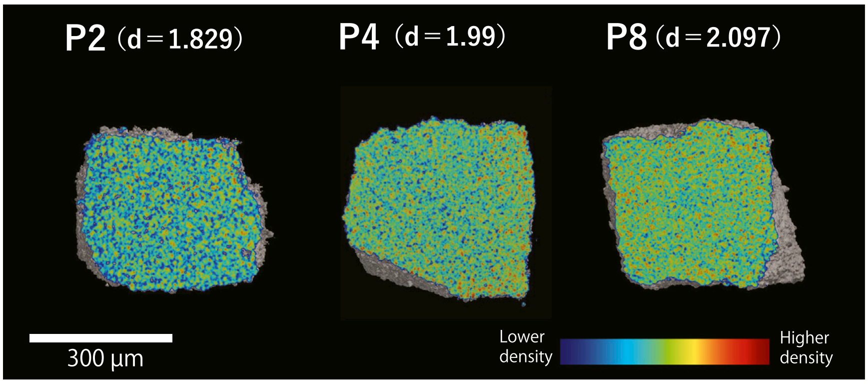

FIGURE 4
Cross-sectional images showing the density differences of the artificial calcite phantoms developed in the present study. Phantoms P2, P4, and P8 were each pressed for 10 min with weights of 2, 4, and 8 tons, respectively. Colors represent the relative density. D = bulk density.

which means they are well separated in the histogram of gray values (Figure 3B). The relative position between the upper gray value limit of air and the peak of the reference material depends on the sensitivity of the X-ray detector when the X-ray energy is constant; therefore, the relative location between the two should be constant under the same X-ray irradiation conditions. This relationship can be shown as a simplified ratio, response factor k, which indicates the relationship between the upper limit of air and the peak value of calcium carbonate (limestone) and can be calculated as follows:

$$k = \frac{\mu(\mathrm{CC})\,peak}{\mu(\mathrm{Air})\,max} \tag{3}$$

where μ(Air)max is the maximum gray value of the air and μ(CC) peak is the modal gray value of the reference material. Ideally, k should be constant, so if the peak position for the reference material can be identified, the lower boundary limit can be automatically determined. In the present study, all voxels with a value higher than the maximum gray value of air (i.e., the threshold value for binarization) were considered to contain calcium carbonate, and CT numbers were calculated.

The above concepts were used to investigate the long-term stability and reliability of the CT numbers obtained using the present μCT setup as well as to calculate the physical parameters related to test bulk density.

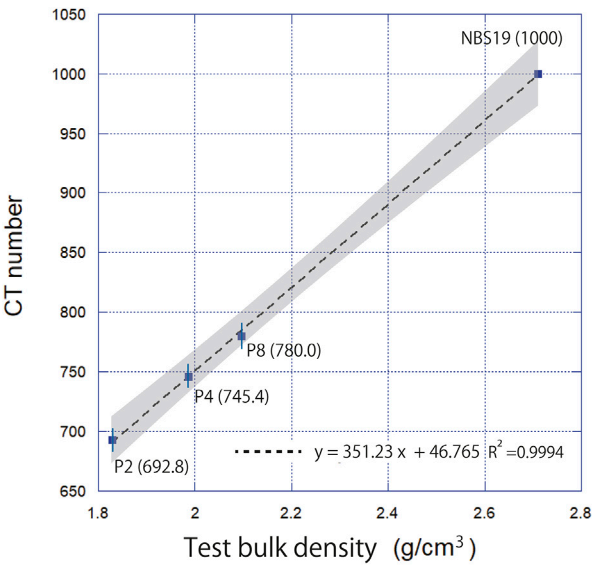

FIGURE 5
Relationship between test bulk density and CT number for the artificial carbonate phantoms (P2, P4, P8 with each CT number in parentheses) and reference material NBS19. The dotted line indicates the linear regression line (R^2 = 0.9994). The gray shading indicates the 95% confidence interval.

4.2 Calibration with our artificial carbonate phantoms

Based on the cross-sectional images (Figure 4), our artificial carbonate phantoms observed by μCT were considered to be sufficiently homogeneous for use as calibration phantoms. The relationship between the bulk density and CT number of the calibration phantoms is shown in Figure 5. For each calibration phantom, the CT number was measured 10 times, and the average value and relative standard deviation were calculated. The relationship between CT number and bulk density is described by the following linear regression equation:

$$\text{CT number} = 351.23 \times \text{test bulk density} + 46.765 \ (R^2 = 0.9994). \tag{4}$$

Thus, the response of the X-ray detector was proportional to the X-ray attenuation by the sample.

4.3 CT number and other physical properties of planktonic foraminifera

Over the 2-month investigation period, the CT number and other physical properties of a single foraminiferal test were

TABLE 3 **µCT analysis results and physical properties of *Globorotalia inflata* shells for the 2-month investigation period.**

#Run	Air	NBS peak	*k*	CT number	Shell bulk denisty (g/cm^3)	Volume ($\times10^6\mu m^3$)	Surface area ($\times10^6\mu m^2$)	Average thickness (µm)	Calculated weight (µg)
1	15,421	49,234	3.2	853.7	2.30	9.3	1.344	13.9	21.4
2	15,400	48,822	3.2	863.4	2.32	9.4	1.348	14.0	21.9
3	14,192	48,314	3.4	851.5	2.29	9.6	1.359	14.2	22.0
4	14,602	48,859	3.4	856.7	2.30	9.5	1.334	14.2	21.8
5	15,953	49,507	3.1	854.5	2.30	9.3	1.323	14.1	21.5
6	14,862	48,218	3.2	867.1	2.33	9.5	1.339	14.1	22.1
7	15,011	48,909	3.3	849.5	2.28	9.4	1.353	13.8	21.4
8	14,581	49,992	3.4	853.5	2.30	9.4	1.344	14.0	21.6
9	15,687	49,298	3.1	853.1	2.29	9.5	1.337	14.3	21.9
10	14,602	48,000	3.3	865.0	2.33	9.5	1.355	14.0	22.0
11	14,786	49,589	3.4	845.0	2.27	9.5	1.313	14.4	21.5
12	14,540	49,858	3.4	851.6	2.29	9.5	1.332	14.2	21.7
13	13,915	49,568	3.6	839.6	2.26	9.6	1.335	14.3	21.6
14	14,458	48,447	3.4	857.6	2.31	9.4	1.352	13.9	21.7
15	13,690	48,544	3.6	850.3	2.29	9.6	1.341	14.3	21.9
16	13,147	48,610	3.7	842.8	2.26	9.7	1.318	14.8	22.1
17	12,461	48,424	3.9	847.9	2.28	9.8	1.345	14.5	22.3
18	11,714	48,642	4.2	845.7	2.27	9.8	1.410	13.9	22.3
19	12,779	49,048	3.8	850.2	2.29	9.8	1.355	14.4	22.3
20	14,233	48,418	3.4	865.9	2.33	9.4	1.360	13.9	22.0
21	14,520	48,482	3.3	853.8	2.30	9.5	1.339	14.2	21.8
22	14,356	48,920	3.4	847.5	2.28	9.5	1.351	14.1	21.6
23	14,049	42,499	3.0	856.9	2.30	9.4	1.398	13.4	21.6
24	14,888	48,249	3.2	853.9	2.30	9.3	1.328	14.0	21.3
25	13,905	48,249	3.5	854.3	2.30	9.6	1.359	14.1	22.1
26	14,735	48,644	3.3	858.5	2.31	9.4	1.352	13.9	21.7
27	14,509	47,443	3.3	869.9	2.34	9.5	1.327	14.3	22.2
28	15,564	47,744	3.1	853.5	2.30	9.5	1.360	14.0	21.8
29	15,851	50,039	3.2	857.3	2.31	9.3	1.357	13.8	21.5
30	15,759	49,771	3.2	862.0	2.32	9.3	1.351	13.8	21.6
31	16,516	48,000	2.9	871.0	2.35	9.4	1.346	13.9	22.0
Mean	14,538	48,592	3.4	854.9	2.30	9.5	1.347	14.08	21.8
STD	1,047.299	1,313	0.26	7.72	0.02	0.14	0.02	0.26	0.28
RSD%	7.2	2.7	7.8	0.9	1.0	1.5	1.5	1.9	1.3

examined a total of 31 times by µCT (Table 3). The mean upper gray value for the air was 14,538 (range, 14,538–16,516). The mean value of *k*, which indicates the responsiveness of the X-ray detector, was 3.4 (range, 2.91–4.15).

The average CT number was 854.9 (range, 839.6–871.0; standard deviation, 7.7; variability, 0.90%). The variability of CT number showed no clear trend over the 2-month investigation period (Figure 6).

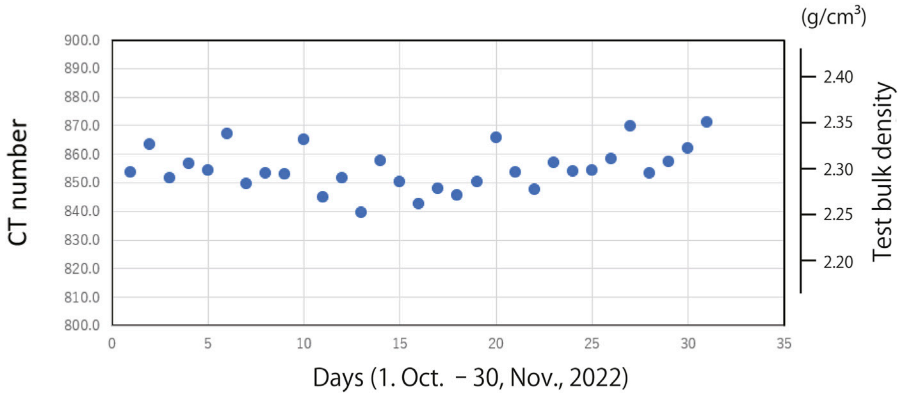

FIGURE 6
Distribution of CT number for the 31 analyses conducted over the 2-month investigation period.

TABLE 4 Average weight of a single *Globorotalia inflata* specimen measured 20 times using an electronic microbalance.

	Aluminum boat weight (mg)	*G. inflata* weight (mg)	Calculated shell bulk density (g/cm^3)
Mean (20 measurements)	1.946	0.029	3.244
STDEV	0.002	0.002	0.266
RSD (%)	0.11	8.21	8.21
			Room temp: 25.7 °C
			Humidity: 29% (26.0 °C)

4.4 Stability of weight measured by electronic microbalance

Table 4 shows the weight of one individual test of *G. inflata* measured 20 times by using an electronic microbalance. The average weight was 0.029 mg and the standard deviation was 0.002 mg (8.21%). The weights of the individual tests fell within the range of already published values (9.65–59.59 µg; Haarmann et al., 2011). However, the calculated test bulk density was 3.24 g/cm^3, which was slightly higher than the theoretical density of limestone (2.71 g/cm^3). A possible reason for this discrepancy was that cytoplasm was still present in the test chamber, which was confirmed by examination of the transparent µCT image. It is difficult to estimate the weight of dried cytoplasm from a µCT image; however, assuming that the average test bulk density (2.30 g/cm^3) calculated by µCT is correct, the weight of dried cytoplasm in a *G. inflata* test is estimated to be 0.0085 mg. The total chamber volume of the *G. inflata* examined in this experiment was calculated to be 0.015 mm^3. Assuming that the density of the cytoplasm is almost equal to that of seawater, its weight is almost half the weight of the seawater that fills this volume. Thus, this experiment shows that using the weights of single individuals measured on an electronic microbalance does not provide accurate estimates of test bulk density due to the effect of the cytoplasm inside the foraminiferal test. Thus, the measurement of test bulk density by microbalance may not be appropriate for all contexts.

5 Discussion

5.1 Bulk density calibration by using artificial carbonate phantoms

Although artificial phantoms exist to calculate human bone density, measuring the bulk density of carbonate particles using an artificial phantom of pure calcium carbonate has never been investigated. In the present study, the relationship between artificial carbonate phantoms and CT number showed a clear relationship, indicating that there is a linear relationship between the bulk density of calcium carbonate particles and the responsiveness of the X-ray detector (Figure 5). Thus, our findings show that test bulk density measurement using artificial carbonate phantoms is feasible. Furthermore, this approach identifies and eliminates impurities present in the foraminiferal test from the image, allowing only the volume of the test to be measured. This provides a new methodology for obtaining accurate test weights for samples that may contain sediment or cytoplasm.

Based on above methodology, test bulk density was calculated. Using Eq. 4, the mean test bulk density and weight of single test of *G. inflata* calculated from the CT number was 2.3 ± 0.02 g/cm^3 and 21.8 ± 0.28 µg, respectively. This value was close to the average bulk density reported for several species of planktonic foraminifera in the western North Pacific (Iwasaki et al., 2019a) and was within the weight range reported for individual *G. inflata* in modern water (Haarmann et al., 2011).

The average volume and surface area of the foraminiferal test calculated from the isosurface image was 9.5 × 10^6 μm^3 and 1.347 × 10^6 μm^2, respectively; variability was 1.5% for both. The average thickness, calculated by dividing the volume of the foraminieral test by one-half the surface was 14.1 μm, with a variability of 1.9%. No long-term trends over the 2-month investigation period were observed for the three observed parameters.

5.2 Long-term stability and reliability of CT number and other parameters

The CT number determined for the foraminiferal test was very stable over the 2-month investigation period (Figure 6). Variability remained within 0.9%, and no systematic fluctuations were observed. The volume and surface area also had a high reproducibility of 1.5% each. The calculated weight averaged 21.8 μg with an STD of 0.28 μg. This variability is comparable to and/or slightly better than those reported by others for the weights of planktonic foraminifera (e.g., Marshall et al., 2013; Iwasaki et al., 2019a). This means that weights can be obtained with comparable accuracy without the use of an electronic microbalance. The stability of an electronic microbalance is generally affected by the surrounding environment, including environmental vibration, air temperature changes, electromagnetic interference, and static electricity, which tend to increase the measurement error. In the present study, we used an electronic ultra-microbalance, but the obtained variability was 8.2%, which was much greater than that obtained with μCT (1.3%). Our results suggest that our μCT approach is reliable and objective, and that it can be used for highly accurate analysis of the test bulk density of carbonate test.

The variation of the thresholds determined by the upper limit of air was relatively larger throughout the 2-month analysis period (STD = 7.2%). The cause of this variation is not well understood at this time but it may be related to day or long-term fluctuations in tube current or voltage, or changes in noise. The variation may affect not only the threshold for segmentation but also the *k* value, which is the relative position of the air and the peak value of the standard material (limestone). Further investigation is needed to determine the cause.

5.3 Aspects related to micropaleontology and paleoceanography

The weight of foraminifera and other marine calcifiers is a fundamental indicator of marine carbonate production through the Earth history. Therefore, obtaining accurate test bulk densities of marine calcifiers is extremely important from micropaleontology and paleoceanography perspectives. Furthermore, calculation of weight is important because it can be converted to carbon mass. Weak dissolution of foraminiferal tests in shallow water and at the sediment/water interface has been reported in only a few papers (e.g., Archer and Maier-Reimer, 1994; Schiebel et al., 2007). Although earlier studies have reconstructed carbonate ion concentrations from test fragmentation rates and weight changes of foraminifera (e.g., Broecker and Clark, 2001; de Villiers, 2005), direct measurement of test bulk density measurements are expected to further improve the accuracy of this method.

Traditionally, it has been extremely difficult to obtain information for the quantification of carbonate dissolution and reconstruction of [CO_3^{2-}] from poorly preserved deep-sea samples because of high fragmentation of the foraminiferal tests contained within the samples. Our μCT approach could potentially be applied to such fragmentated samples. In the past, attempts have been made to estimate the chemical properties of seawater, particularly its corrosiveness to calcium carbonate, from the extent of the fragmentation and morphological characteristics of the fragments of fossil tests (e.g., Adelseck, 1977; Ku and Oba, 1978). If the fragmentation is due to carbonate dissolution rather than physical destruction, then indications of the process of dissolution should remain in the fragments. If the fragmentation history can be identified through dissolution experiments in the laboratory, possible applications include elucidation of the intensity of carbonate dissolution and the resulting carbonate ion concentration by measuring the density of the fragments. As already mentioned, the major advantage of μCT analysis is that it is a nondestructive analysis, which allows geochemical analysis to be performed after morphometric measurements. After μCT measurements, stable isotope ratios and trace element analyses can be performed to reveal post-depositional alteration that occur with carbonate dissolution.

However, there are some points to note when using test bulk density as an index of carbonate dissolution. For example, when foraminiferal tests with two-layered structures are strongly affected by carbonate dissolution (Lohmann, 1995), the layer most vulnerable to carbonate dissolution is removed first, leaving behind the less-vulnerable layer (Berger, 1975; Johnstone et al., 2010; 2011; Iwasaki et al., 2015). A test that has undergone strong dissolution could still have a high CT number, which may lead to the erroneous conclusion that the individual test has not undergone dissolution. Therefore, when CT number is used as an index of the dissolution of marine calcifiers, it should be applied to species for which the dissolution process is known, and the CT numbers should always be considered together with the microstructure revealed by SEM, CT images, or both. This is also true when examining the thickness and volume of foraminiferal tests.

5.4 Aspects related to ocean acidification and modern oceanography

The progress of ocean acidification is an urgent global environmental issue. Quantifying test bulk density is extremely important for considering changes in the carbonate system under ocean acidification and its impacts on marine calcifiers. Many studies examining the changes in coastal water carbonate systems and their biological impacts have been conducted; however, few have been conducted on pelagic ecosystems. In particular, the relationships between ocean acidification and low-trophic level ecosystems are poorly understood. Orr et al. (2005) were the first to suggest the biological impacts of ocean acidification on shelled pteropods, and others have subsequently reported the impacts on thecosomatous pteropods, the tests of which contain aragonite, in the modern ocean (e.g., Doney et al., 2009; Bednaršek et al., 2014; Howes et al., 2017; Peck, et al., 2018; Bednaršek et al., 2021; Mekkes, et al., 2021; Niemi et al., 2021).

To understand the impact of ocean acidification on marine life, it is becoming increasingly important to undertake studies to observe test formation in marine organisms. For example, Wakita et al. (2013) have suggested that the total alkalinity of the western North Pacific in winter has remained unchanged in the last decade due to limited production of calcium carbonate species. Calcification by marine calcifiers might also be suppressed in the northwestern North Pacific (e.g., Riebesell et al., 2000). Test bulk density measurements using µCT may help us to understand these phenomena. However, moving forward, long-term accumulation of data for the modern ocean will be needed, and for this an international framework that facilitates cooperation and expansion of analytical facilities will have to be established.

6 Conclusion

Here, we repeatedly measured the morphology (volume and CT number) of planktonic foraminifer by using µCT over a period of 2 months. Our findings demonstrate that µCT systems can be used to measure the test bulk density of calcareous tests and to examine their morphology with high accuracy.

In addition, the CT numbers of our novel artificial carbonate phantoms showed excellent linearity with independently measured bulk density, indicating their potential for use as reference materials to measure test bulk density of marine calcifiers. By calibrating CT numbers using these phantoms, we expect to be able to standardize measurement results between laboratories.

Data availability statement

The original contributions presented in the study are included in the article/Supplementary Material, further inquiries can be directed to the corresponding author.

Author contributions

KK and RH performed all experimental design and µCT analysis; OS and TI provided technical guidance and scientific advice on the CT analysis. All authors contributed to the article and approved the submitted version.

Funding

The author(s) declare financial support was received for the research, authorship, and/or publication of this article. This work was supported by JSPS KAKENHI grants (JP19H03037 and JP15H05712) and JAMSTEC operating grants.

Acknowledgments

Keisuke Shimizu contributed to the statistical evaluation and discussion of the data. Nina Bednaršek provided fruitful discussions regarding µCT analysis of marine calcifiers.

Conflict of interest

Author TI was employed by White Rabbit Corp.

The remaining authors declare that the research was conducted in the absence of any commercial or financial relationships that could be construed as a potential conflict of interest.

Publisher's note

References

Adelseck, J. C. G. (1977). Dissolution of deep-sea carbonate: preliminary calibration of preservational and morphologic aspects. *Deep-Sea Res.* 24 (12), 1167–1185. doi:10.1016/0146-6291(77)90520-3

Aldridge, D., Beer, C. J., and Purdie, D. A. (2012). Calcification in the planktonic foraminifera *Globigerina bulloides* linked to phosphate concentrations in surface waters of the North Atlantic Ocean. *Biogeosciences* 9, 1725–1739. doi:10.5194/bg-9-1725-2012

Archer, D., and Maier-Reimer, E. (1994). Effect of deep-sea sedimentary calcite preservation on atmospheric CO2 concentration. *Nature* 367, 260–263. doi:10.1038/367260a0

Arikawa, R. (1983). Distribution and taxonomy of globigerina pachyderma (ehrenberg) off the sanriku coast, northeast Japan. *Sci. Rep. Tohoku Univ. 2nd Ser. Geol.* 53, 103–157.

Ay, M. R., Mehranian, A., Maleki, A., Ghadiri, H., Ghafarian, P., and Zaidi, H. (2012). Experimental assessment of the influence of beam hardening filters on image quality and patient dose in volumetric 64-slice X-ray CT scanners. *Phys. Med.* 28, 249–260. doi:10.1016/j.ejmp.2012.03.005

Barker, S., and Elderfield, H. (2002). Foraminiferal calcification response to glacial-interglacial changes in atmospheric CO2. *Science* 297, 833–836. doi:10.1126/science.1072815

Bednaršek, N., Feely, R. A., Reum, J. C. P., Peterson, B., Menkel, J., Alin, S. R., et al. (2014). *Limacina helicina* shell dissolution as an indicator of declining habitat suitability owing to ocean acidification in the California Current Ecosystem. Proc. R. Soc. *B* 281, 20140123. doi:10.1098/rspb.2014.0123

Bednaršek, N., Naish, K.-A., Feely, R. A., Hauri, C., Kimoto, K., Hermann, A. J., et al. (2021). Integrated assessment of ocean acidification risks to pteropods in the northern high latitudes: regional comparison of exposure, sensitivity and adaptive capacity. *Front. Mar. Sci.* 8, 671497. doi:10.3389/fmars.2021.671497

Beer, C. J., Schiebel, R., and Wilson, P. A. (2010). Testing planktic foraminiferal shell weight as a surface water $[CO_3^{2-}]$ proxy using plankton net samples. *Geology* 38, 103–106. doi:10.1130/G30150.1

Berger, W. H. (1975). "Dissolution of deep-sea carbonates: an introduction," in *Dissolution of deep-sea carbonates*. Editors W. V. Sliter, A. W. H. Bé, and W. H. Berger (Lawrence, KS, USA: Cushman Found. Foram. Res., Spec. Publ.), 13, 7–10.

Bijma, J., Hönisch, B., and Zeebe, R. E. (2002). Impact of the ocean carbonate chemistry on living foraminiferal shell weight: comment on "Carbonate ion concentration in glacial-age deep waters of the Caribbean Sea" by W. S. Broecker and E. Clark. *Geochem. Geophys. Geosyst.* 3, 1–7. doi:10.1029/2002GC000388

Briguglio, A., Woger, J., Wolfgring, E., and Hohenegger, J. (2014). "Changing investigation perspectives: methods and applications of computed tomography on larger benthic foraminifera," in *Approaches to study living foraminifera: collection, maintenance and experimentation*. Editors H. Kitazato and J. Bernhard (Springer), 55–70. doi:10.1007/978-4-431-54388-6_4

Broecker, W., and Clark, E. (2001). Reevaluation of the $CaCO_3$ size index paleocarbonate ion proxy. *Paleoceanogr* 16, 669–671. doi:10.1029/2001pa000660

Brummer, G.-J. A., Hemleben, C., and Spindler, M. (1987). Ontogeny of extant spinose planktonic foraminifera (Globigerinidae): a concept exemplified by *Globigerinoides sacculifer* (Brady) and *G. ruber* (d'Orbigny). *Mar. Micropaleontol.* 12, 357–381. doi:10.1016/0377-8398(87)90028-4

Charrieau, L. M., Nagai, Y., Kimoto, K., Dissard, D., Below, B., Fujita, K., et al. (2022). The coral reef-dwelling *Peneroplis* spp. shows calcification recovery to ocean acidification conditions. *Sci. Rep.* 12, 6373. doi:10.1038/s41598-022-10375-w de Villiers, S. (2005). Foraminiferal shell-weight evidence for sedimentary calcite dissolution above the lysocline. *Deep Sea Res. Part I Ocean. Res. Pap.* 52 (5), 671–680. doi:10.1016/j.dsr.2004.11.014

Doney, S. C., Fabry, V., Feely, R. A., and Kleipas, J. A. (2009). Ocean acidification: the other CO2 problem. *Annu. Rev. Mar. Sci.* 1, 169–192. doi:10.1146/annurev.marine.010908.163834

Erez, J. (2003). The source of ions for biomineralization in foraminifera and their implications for paleoceanographic proxies. *Rev. Mineral. Geochem* 54 (1), 115–149. doi:10.2113/0540115

Fox, L., Stukins, S., Hill, T., and GilesMiller, C. (2020). Quantifying the effect of anthropogenic climate change on calcifying plankton. *Sci. Rep.* 10, 1620. doi:10.1038/s41598-020-58501-w

Haarmann, T., Hathorne, E. C., Mohtadi, M., Groeneveld, J., Kölling, M., and Bickert, T. (2011). Mg/Ca ratios of single planktonic foraminifer shells and the potential to reconstruct the thermal seasonality of the water column. *Paleoceanog* 26, PA3218. doi:10.1029/2010PA002091

Hounsfield, G. N. (1980). Computed medical imaging. *J. Comput. Assist. Tomogr.* 4, 665–674. doi:10.1097/00004728-198010000-00017

Howes, E. L., Eagle, R. A., Gattuso, J.-P., and Bijma, J. (2017). Comparison of mediterranean pteropod shell biometrics and ultrastructure from historical (1910 and 1921) and present day (2012) samples provides baseline for monitoring effects of global change. *PLoS ONE* 12, e0167891. doi:10.1371/journal.pone.0167891

Ikenoue, T., Bjørklund, K. R., Dumitrica, P., Krabberød, A. K., Kimoto, K., Matsuno, K., et al. (2016). Two new living Entactinaria (Radiolaria) species from the Arctic province: *Joergensenium arcticum* n. sp. and *Joergensenium clevei* n. sp. *Mar. Micropaleont* 124, 75–94. doi:10.1016/j.marmicro.2016.02.003

Iwasaki, S., Kimoto, K., Okazaki, Y., and Ikehara, M. (2019a). X-ray micro-CT scanning of tests of three planktic foraminiferal species to clarify dissolution process and progress. *Geochem Geophys* 20. doi:10.1029/2019GC008456

Iwasaki, S., Kimoto, K., Sasaki, O., Kano, H., Honda, M. C., and Okazaki, Y. (2015). Observation of the dissolution process of Globigerina bulloides tests (planktic foraminifera) by X-ray microcomputed tomography. *Paleoceanogr* 30, 317–331. doi:10.1002/2014PA002639

Iwasaki, S., Kimoto, K., Sasaki, O., Kano, H., and Uchida, H. (2019b). Sensitivity of planktic foraminiferal test bulk density to ocean acidification. *Sci. Rep.* 9, 9803. doi:10.1038/s41598-019-46041-x

Iwasaki, S., Lembke-Jene, L., Nagashima, K., Arz, H. W., Harada, N., Kimoto, K., et al. (2022). Evidence for late-glacial oceanic carbon redistribution and discharge from the Pacific Southern Ocean. *Nat. Comm.* 13, 6250. doi:10.1038/s41467-022-33753-4

Johnstone, H., Schulz, M., Barker, S., and Elderfield, H. (2010). Inside story: an X-ray computed tomography method for assessing dissolution in the tests of planktonic foraminifera. *Mar. Micropaleont* 77, 58–70. doi:10.1016/j.marmicro.2010.07.004

Johnstone, H., Yu, J., Elderfield, H., and Schulz, M. (2011). Improving temperature estimates derived from Mg/Ca of planktonic foraminifera using X-ray computed tomography–based dissolution index, XDX. *Paleoceanog* 26, PA1215. doi:10.1029/2009PA001902

Kachovich, S., Sheng, J., and Aitchison, J. C. (2019). Adding a new dimension to investigations of early radiolarian evolution. *Sci. Rep.* 9, 6450. doi:10.1038/s41598-019-42771-0

Kinoshita, S., Kuroyanagi, A., Kawahata, H., Fujita, K., Ishimura, T., Suzuki, A., et al. (2021). Temperature effects on the shell growth of a larger benthic foraminifer (*Sorites orbiculus*): results from culture experiments and micro X-ray computed tomography. *Mar. Micropaleont* 163, 101960. doi:10.1016/j.marmicro.2021.101960

Ku, T., and Oba, T. (1978). A method for quantitative evaluation of carbonate dissolution in deep-sea sediments and its application to paleoceanographic reconstruction. *Quat. Res.* 10 (1), 112–129. doi:10.1016/0033-5894(78)90016-9

Kuroyanagi, A., Irie, T., Kinoshita, S., Kawahata, H., Suzuki, A., Nishi, H., et al. (2021). Decrease in volume and density of foraminiferal shells with progressing ocean acidification. *Sci. Rep.* 11, 19988. doi:10.1038/s41598-021-99427-1

Lohmann, G. P. (1995). A model for variation in the chemistry of planktonic foraminifera due to secondary calcification and selective dissolution. *Paleoceanog* 10 (3), 445–457. doi:10.1029/95pa00059

Marshall, B. J., Thunell, R. C., Henehan, M., Astor, Y., and Wejnert, K. E. (2013). Planktonic foraminiferal area density as a proxy for carbonate ion concentration: a calibration study using the Cariaco Basin ocean time series. *Paleoceanogr* 28, 363–376. doi:10.1002/palo.20034

Mekkes, L., Renema, W., Bednaršek, N., Alin, S. R., Feely, R., Huisman, J., et al. (2021). Pteropods make thinner shells in the upwelling region of the California Current Ecosystem. *Sci. Rep.* 11, 1731. doi:10.1038/s41598-021-81131-9

Moy, A., Howard, W., Bray, S., and Trull, T. (2009). Reduced calcification in modern Southern Ocean planktonic foraminifera. *Nat. Geosci.* 2, 276–280. doi:10.1038/ngeo460

Naik, S. S., Godad, S. P., Naidu, P. D., and Ramaswamy, V. (2013). A comparison of *Globigerinoides ruber* calcification between upwelling and non-upwelling regions in the Arabian Sea. *J. Earth Syst. Sci.* 122, 1153–1159. doi:10.1007/s12040-013-0330-y

Niemi, A., Bednaršek, N., Michel, C., Feely, R. A., Williams, W., Azetsu-Scott, K., et al. (2021). Biological impact of ocean acidification in the Canadian arctic: widespread severe pteropod shell dissolution in amundsen gulf. *Front. Mar. Sci.* 8, 600184. doi:10.3389/fmars.2021.600184

Ofstad, S., Zamelczyk, K., Kimoto, K., Chierici, M., Fransson, A., and Rasmussen, T. L. (2021). Shell density of planktonic foraminifera and pteropod species *Limacina helicina* in the Barents Sea: relation to ontogeny and water chemistry. *PloS one* 16 (4), e0249178. doi:10.1371/journal.pone.0249178

Orr, J., Fabry, V., Aumont, O., Bopp, L., Doney, S., Feely, R. A., et al. (2005). Anthropogenic ocean acidification over the twenty-first century and its impact on calcifying organisms. *Nature* 437, 681–686. doi:10.1038/nature04095

Osborne, E. B., Thunell, R. C., Marshall, B. J., Holm, J. A., Tappa, E. J., Benitez-Nelson, C., et al. (2016). Calcification of the planktonic foraminifera *Globigerina bulloides* and carbonate ion concentration: results from the Santa Barbara Basin. *Paleoceanog Paleoclim* 31 (8), 1083–1102. doi:10.1002/2016PA002933

Otsu, N. (1980). Automatic threshold selection method based on discriminant and least squares criteria. *IEICE Trans.* J63-D (4), 349–356.

Peck, V. L., Oakes, R. L., Harper, E. M., Manno, C., and Tarling, G. A. (2018). Pteropods counter mechanical damage and dissolution through extensive shell repair. *Nat. Commun.* 9, 264. doi:10.1038/s41467-017-02692-w

Riebesell, U., Zondervan, I., Rost, B., Tortell, P. D., Zeebe, E. E., and Morel, F. M. M. (2000). Reduced calcification of marine plankton in response to increased atmospheric CO_2. *Nature* 407, 364–367. doi:10.1038/35030078

Schiebel, R., Barker, S., Lendt, R., Thomas, H., and Bollmann, J. (2007). Planktic foraminiferal dissolution in the twilight zone. *Deep-Sea Res. II* 54, 676–686. doi:10.1016/j.dsr2.2007.01.009

Schiebel, R., and Hemleben, C. (2017). Planktic foraminifers in the modern ocean. *Springer Berl. Heidelb.* doi:10.1007/978-3-662-50297-6

Shimizu, K., Kimoto, K., Noshita, K., Wakita, M., Fujiki, T., and Sasaki, T. (2017). Phylogeography of the pelagic snail *Limacina helicina* (gastropoda: thecosomata) in the subarctic western North Pacific. *J. Mollusc. Stud.* 84, 30–37. doi:10.1093/mollus/eyx040

Todd, C. L., Schmidt, D. N., Robinson, M. M., and De Schepper, S. (2020). Planktic foraminiferal test size and weight response to the late Pliocene environment. *Paleoceanog Paleoclim* 35, e2019PA003738. doi:10.1029/2019PA003738

Wakita, M., Watanabe, S., Honda, M., Nagano, A., Kimoto, K., Matsumoto, K., et al. (2013). Ocean acidification from 1997 to 2011 in the subarctic western North Pacific Ocean. *Biogeosciences* 10, 7817–7827. doi:10.5194/bg-10-7817-2013

Weinkauf, M. F. G., Zwick, M. M., and Kucera, M. (2020). Constraining the role of shell porosity in the regulation of shell calcification intensity in the modern planktonic foraminifer *Orbulina universa* d'Orbigny. *J. Foram Res.* 50 (2), 195–203. doi:10.2113/gsjfr.50.2.195

Xiao, Y., Suzuki, N., and He, W. (2017). Applications and limitations of Micro-XCT imaging in the studies of Permian radiolarians: a new genus with bi-polar main spines. *Acta Palaeontol. Pol.* 62 (3). doi:10.4202/app.00367.2017

Zarkogiannis, S., Fernandez, V., Greaves, M., Mortyn, P. G., Kontakiotis, G., and Antonarakou, A. (2020). X-ray tomographic data of planktonic foraminifera species *Globigerina bulloides* from the eastern tropical atlantic across termination II. *Gigabyte* 1, 1–10. doi:10.46471/gigabyte.5

Zarkogiannis, S. D., Iwasaki, S., Rae, J. W. B., Schmidt, M. W., Mortyn, P. G., Kontakiotis, G., et al. (2022). Calcification, dissolution and test properties of modern planktonic foraminifera from the central atlantic ocean. *Front. Mar. Sci.* 9, 864801. doi:10.3389/fmars.2022.864801

frontiers | Frontiers in Earth Science

TYPE Original Research
PUBLISHED 14 February 2024
DOI 10.3389/feart.2023.1220341

OPEN ACCESS

EDITED BY
Shinya Iwasaki,
University of Bremen, Germany

REVIEWED BY
Jörg Fröbisch,
Museum of Natural History Berlin (MfN), Germany
Saverio Bartolini Lucenti,
University of Florence, Italy

*CORRESPONDENCE
Alienor Duhamel,
✉ alienor.duhamel@ens-lyon.org

RECEIVED 10 May 2023
ACCEPTED 18 July 2023
PUBLISHED 14 February 2024

CITATION
Duhamel A, Benoit J, Wynd B, Wright AM and Rubidge B (2024), Redescription of three basal anomodonts: a phylogenetic reassessment of the holotype of *Eodicynodon oelofseni* (NMQR 2913). *Front. Earth Sci.* 11:1220341. doi: 10.3389/feart.2023.1220341

Redescription of three basal anomodonts: a phylogenetic reassessment of the holotype of *Eodicynodon oelofseni* (NMQR 2913)

Alienor Duhamel[1,2]*, Julien Benoit[1], Brenen Wynd[3], April Marie Wright[3] and Bruce Rubidge[1]

[1]Evolutionary Studies Institute, University of the Witwatersrand, Johannesburg, South Africa, [2]School of Geosciences, University of the Witwatersrand, Johannesburg, South Africa, [3]Department of Biological Sciences, Southeastern Louisiana University, Hammond, LA, United States

The Dicynodontia (Therapsida: Anomodontia) is one of the most successful Permo-Triassic terrestrial tetrapod clades and the oldest specimens are recorded from the middle Permian *Eodicynodon* Assemblage Zone of South Africa. Their fossil record is abundant and species-rich across Pangea. By contrast, the fossil record of the basal-most anomodonts, which includes non-dicynodont anomodonts and early forms of dicynodonts, is patchy and their morphology and phylogeny are deduced from relatively few specimens. Discovered in 1982 and described in 1990, the holotype of *Eodicynodon oelofseni* (NMQR 2913) is one of the better-preserved early anomodont specimens. However, it has been suggested that *E. oelofseni* does not belong to the genus *Eodicynodon*. Here, using CT-scanning and 3D modeling, the skull of *Eodicynodon oelofseni*, *Patranomodon nyaphulii* and *Eodicynodon oosthuizeni* are redescribed. In the framework of this study, the application of 3D scanning technology to describe anatomical structures which were previously inaccessible in these fossils has enabled detailed redescription of the cranial morphology of the basal anomodonts *Patranomodon*, *Eodicynodon oelofseni* and *E. oosthuizeni* and led to a greater understanding of their cranial morphology and phylogenetic relationships. Based on an anatomical comparison and phylogenetic analyses (Bayesian and cladistics) the phylogenetic relationships of basal anomodonts are reassessed and it is suggested that NMQR 2913 does not belong to the genus *Eodicynodon* but likely represents a separate genus basal to other dicynodonts. A new genus is erected for NMQR 2913. This presents one of the first applications of Bayesian Inference of phylogeny on Therapsida.

KEYWORDS

Therapsida, Dicynodontia, *Eodicynodon*, phylogeny, Bayesian Inference, *Nyaphulia*

1 Introduction

Synapsida, one of the major groups of terrestrial amniotes, comprises both living mammals and a diverse group of stem-taxa (Luo et al., 2002; Kemp, 2005; Benton, 2015; Angielczyk and Kammerer, 2018; Rougier et al., 2021). During the Permian Period, the clade Anomodontia was the most species-rich clade of non-mammalian synapsids

(Fröbisch, 2009; Angielczyk and Kammerer, 2018) and was dominant in terms of specimen abundance, geographic range, species richness, and ecological diversity (Kemp, 2005; Fröbisch and Reisz, 2008; Fröbisch, 2009; Nicolas and Rubidge, 2010; Smith et al., 2012). They survived the devastating end-Permian extinction (Ruta et al., 2013) and persisted until the end of the Triassic (Dzik et al., 2008; Sulej et al., 2010). Anomodonts also were one of the first clades of herbivorous tetrapods to undergo a major evolutionary radiation (Reisz and Sues, 2000; Reisz, 2006) and their extensive fossil record has facilitated studies on their paleobiology and functional anatomy in great detail (Ray et al., 2004; Fröbisch and Reisz, 2009; Botha-Brink and Angielczyk, 2010; Chinsamy-Turan, 2011; Ruta et al., 2013; Kammerer et al., 2014; Benoit et al., 2018; Marilao et al., 2020).

The current phylogenetic and taxonomic framework suggests that Dicynodontia is a monophyletic group that does not include basal anomodont taxa such as the "Chainosauria" (*Patranomodon*, *Galeops*, *Galechirus*, *Anomocephalus*, *Galepus*), the "Venyukovioidea" (*Otsheria*, *Suminia*, *Ulemica*) and other basal taxa, such as *Biseridens* and *Tiarajudens* (Fröbisch and Reisz, 2008; Liu et al., 2010; Angielczyk et al., 2021). In contrast to derived dicynodonts, basal anomodonts are rare in the fossil record, and are known from only Brazil, China, Russia and South Africa. All South African specimens have been found at the base of the Karoo Beaufort Group, in the lower Abrahamskraal Formation, where the fossil record is patchy (Rubidge, 1995; Rubidge and Day, 2020). Previous authors suggested that the early anomodont radiation could have been accomplished in two waves happening in Laurasia and Gondwana (Liu et al., 2010).

Amongst dicynodonts, *Eodicynodon* is considered the basal-most genus (Fröbisch and Reisz, 2008; Kammerer et al., 2011; Angielczyk et al., 2021) and comprises two species: *Eodicynodon oosthuizeni*, represented by numerous specimens, and *Eodicynodon oelofseni* represented by a single specimen, NMQR 2913 which is housed in the National Museum of Bloemfontein (Rubidge, 1990a; Rubidge, 1990b). Recent phylogenetic works suggest that *E. oelofseni*, when coded separately from *E. oosthuizeni* in phylogenetic analyses, does not form a clade with the type species of the genus, and may thus belong to a separate genus (Kammerer et al., 2011; Angielczyk et al., 2021).

The present work, for the first time, examines and describes the internal cranial anatomy of the basal anomodonts *Patranomodon* and *Eodicynodon* based on CT scanned material. This technique to study internal cranial anatomy has proven effective on other anomodonts (Castanhinha et al., 2013). In addition to complete descriptions of four basal anomodont specimens, the study leads to a taxonomic reappraisal of *Eodicynodon oelofseni* and the genus *Nyaphulia* is introduced as the earliest-diverging dicynodont.

2 Materials and methods

Specimen NMQR 3000, *Patranomodon nyaphulii*, was found by Mr. John Nyaphuli in 1986 on the farm Combrinkskraal in the Prince Albert district, Western Cape, South Africa (Rubidge and Hopson, 1996). Geologically it is from the Combrinkskraal Member of the Abrahamskraal Formation, *Eodicynodon* Assemblage Zone, Karoo Beaufort Group, South Africa (Day and Rubidge, 2014; Benoit et al., 2018). The specimen comprises a relatively complete skull with lower jaw and various postcranial remains: vertebrae, complete manus, pelvic bones and femur (Rubidge and Hopson, 1996). It was described as the holotype of *P. nyaphulii*, a monospecific genus (Rubidge and Hopson, 1990). Only the skull was CT scanned for this study.

Specimen BP/1/6230 of *E. oosthuizeni*, was found by Mr. Charlton Dube, on the farm Bloukrans in the Prince Albert district, Western Cape, South Africa (Jinnah and Rubidge, 2007) in the *Eodicynodon* Assemblage Zone of the Abrahamskraal Formation (Jinnah and Rubidge, 2007; Rubidge and Day, 2020; Smith et al., 2020). The specimen, which is dorsoventrally compressed, is identified as *E. oosthuizeni* because of the presence of "postcanine teeth lateral to the lower jaw" and a "laterally flared pterygoid processes" (Jinnah and Rubidge, 2007). Specimen BP/1/6230 comprises a complete skull with lower jaw and some postcranial material attached and articulated to the skull.

Specimen NMQR 2978 of *E. oosthuizeni*, was found on the farm Rietkuil (previously named Zwartgrond), in the Rietbron district, Eastern Cape, South Africa (Karoo collection database and Rubidge, 1990b), in the *Eodicynodon* Assemblage Zone, Karoo Beaufort Group (Benoit et al., 2018). The specimen, comprisisng a complete skull with two large tusks, was described as *E. oosthuizeni* (Rubidge, 1990b).

Specimen NMQR 2913, *Eodicynodon oelofseni* was found on the farm Botterkraal, in the Prince Albert District, Western Cape, South Africa (Rubidge, 1990a) in the *Eodicynodon* Assemblage Zone, Abrahamskraal Formation, Karoo Beaufort Group, South Africa. It was found by John Nyaphuli in October 1982 in a calcareous nodule (Rubidge, 1990a). The nodule was broken into four pieces which had weathered separately, resulting in some parts of the skull being missing. The specimen was mechanically and acid prepared by Mr. John Nyaphuli and was described as the holotype of *Eodicynodon oelofseni* (Rubidge, 1990a). Since then, the delicate specimen has been accidentally broken several times and some sections of the skull, described in the original publication, are now lost.

2.1 Scanning parameters and 3D reconstruction

All scans were performed at the Evolutionary Studies Institute using X-ray μCT with a Nikon Metrology XTH 225/320 LC. CT scans were initially performed for a separate study, so we lack exact exposure times for direct replication, but note that to our knowledge, no filters were used during scanning. Specimens NMQR 3000, BP/1/6230, NMQR 2913 and NMQR 2978 were each scanned in single sessions using the following parameters:

- NMQR 3000, holotype of *Patranomondon nyaphulii*
  A beam energy of 70 kV was used, with a flux of 80 μA at a voxel size of 35.6 μm
- BP/1/6230, referred specimen of *Eodicynodon oosthuizeni*
  A beam energy of 100 kV was used, with a flux of 140 μA at a voxel size of 64.6 μm
- NMQR 2978, referred specimen of *Eodicynodon oosthuizeni*
  A beam energy of 125 kV was used, with a flux of 135 μA at a voxel size of 73.9 μm

- NMQR 2913, holotype of *Eodicynodon oelofseni*
  A beam energy of 100 kV was used, with a flux of 140 μA at a voxel size of 42.3 μm

Three-dimensional reconstructions and visualisation of CT data of all specimens were generated using AVIZO 9.0 lite (FEI VSG, Hillsboro, OR, United States of America) and VG Studio Max (Volume Graphics GmbH). Three-dimensional renderings were obtained using manual segmentation with AVIZO 9.0 lite (FEI VSG, Hillsboro, OR, United States of America).

2.2 Matrix construction

The phylogenetic matrix used in this study is based on the discrete character matrix of Angielczyk et al. (2021) updated with some characters from Surkov and Benton (2004), personal observations and the descriptions provided in the literature (Barry, 1974; Brinkman, 1981; Rubidge, 1990a; Rubidge, 1990b; Rubidge and Hopson, 1996; Modesto et al., 1999; Ivakhnenko, 2003; Modesto et al., 2003; Sullivan and Reisz, 2005; Castanhinha et al., 2013). Mesquite v3.04 (Maddison and Maddison, 2015) was used for the analysis.

This study focuses on the cranial and endocranial anatomy of *Patranomodon* and *Eodicynodon* that are some of the most basal anomodonts. Accordingly, the matrix of Angielczyk et al. (2021) was edited to retain only cranial characters, and endocranial characters from Surkov and Benton (2004) were added. The most derived dicynodont taxa were removed from the analysis with the exception of those where braincase characters had been previously scored and referred to in the literature (Surkov and Benton, 2004), and the character list was modified accordingly.

To assess the taxonomic affiliation and phylogenetic position of NMQR 2913, the holotype of *Eodicyodon oelofseni*, all specimens described were scored separately, including the holotype of *E. oosthuizeni*. The phylogenetic matrix contains a total of 34 taxa and 151 discrete unordered morphological characters.

2.3 Phylogenetic analysis parameters

2.3.1 Parsimony

To run the cladistic analysis, TNT (Tree analysis using New Technology; Goloboff et al., 2003) version 1.5 was applied (Goloboff and Catalano, 2016). A heuristic search (New Technology Analysis) was performed to find the most parsimonious trees. The Random Sectorial Search was defined with a minimum and maximum size of the sector of 5 and 17 respectively. The Consensus-Based Sectorial Search was set for 100 rounds and the minimum size of the sector was 5. The Ratchet algorithm was limited to a total of 5,000 iterations. A hundred rounds were selected for the Tree Fusing algorithm, and the trees were obtained by the random addition of a thousand sequences. Other parameters for the algorithms used were kept as default.

2.3.2 Bayesian Inference

In addition to the TNT analysis, a Bayesian analysis was run with MrBayes v3.2.7a (Huelsenbeck and Ronquist, 2001). The software uses Markov chain Monte Carlo (MCMC, a random walk sampling method that explores the parameter and tree space to optimise their value; see Metropolis et al., 1953; Hastings, 1970; Green, 1995; Geyer, 1991; Larget and Simon, 1999; Huelsenbeck and Ronquist, 2001) to find the best parameters of an evolutionary model (Mk(v) model for a morphological dataset, see Lewis, 2001) given the morphological matrix. The gamma model was used for the substitution rate among characters (the lognormal model, specific to MrBayes and often used in vertebrate analysis, gave similar results) and an exponential distribution for the branch length. This is the first application of Bayesian Inference aimed at investigating the earliest diverging therapsids and their relationships.

Additionally, we performed a more complex set of model estimation approaches in RevBayes (Höhna et al., 2016). Sequence model is shown to strongly affect topology in molecular analyses (Brown and Lemmon, 2007). Comparatively little attention has been paid to this in morphological analyses, with most researchers using the standard Mk model (Lewis, 2001). However, more models of evolution are possible for morphological traits. We tested the Site-Heterogeneous Discrete Morphology model [SHDM] (Nylander et al., 2004; Wright et al., 2016). This model allows for asymmetrical rates of transition (such as different probabilities of gain and loss in a trait) across characters in a discrete matrix.

In testing these models in comparison with the Mk model, we employed reversible-jump Markov Chain Monte Carlo to perform model averaging (Wasserman, 2000). This technique uses MCMC to fit not just the parameters of the model of evolution, but to choose the model itself. We ran this model using two replicate runs and 1,000,000 generations. RevBayes runs multiple MCMC moves per iteration, meaning that an overall lower number of MCMC generations is needed, than other phylogenetic estimation approaches (e.g., MrBayes; Höhna et al., 2016). We assess convergence in Tracer, and judge parameter convergence based on reaching or exceeding an effective sample size of 200 (Rambaut et al., 2018).

Institutional abbreviations—BP/ESI, Evolutionary Studies Institute, Johannesburg, South Africa; NMQR, National Museum, Bloemfontein.

Cranial abbreviations—acst, anterior crus of the stapes; ang, angular; app, anterior process of the parietal; apbo, anterior process of the basioccipital; apro, anterior process of the prootic; apt, anterior process of the pterygoid; apobsh, anterior process of the orbitosphenoid; art, articular; ascc, attachment of the anterior semicircular canal; aso, anterior estension of the supraoccipital; bo, basioccipital; bot, basioccipital tubera; bsh, basisphenoid; bshw, basisphenoid wing; bptp, basipterygoid process; c, caniniform tooth; cc, crus communis; co, occipital condyle; cor, coronoid; d, dentary; da, dentary apex; dpq, dorsal plate of the quadrate; dpro, dorsal process of the prootic; dpsur, dorsal process of the surangular; ds, dorsum sellae; dsh, dentary shelf; dspt, dorsal septum of the pterygoid; dsq, dorsal process of the squamosal; dt, dentary table; ect, ectopterygoid; eo, exoccipital; f, frontal; fo, fenestra ovalis; i, incisiform tooth; icgq, intercondylar groove of the quadrate; iptv, interpterygoid vacuity; ivv, intervomerine vacuity; j, jugal; l, lacrimal; lcq, lateral condyle of the quadrate; lf, lacrimal foramen; lnq, lateral notch of the quadrate; lpro, lateral bulge of the prootic; lt, lower jaw teeth; m, maxilla; mf, mandibular fenestra;

mcq, medial condyle of the quadrate; mpqj, medial process of the quadratojugal; mxd, maxilla depression; n, nasal; npm, nasal process of the premaxilla; obsh, orbitosphenoid; op, opisthotic; opfeo, opisthotic facet of the exoccipital; p, parietal; pafeo, pro-atalas facet of the exoccipital; pal, palatine; palb, palatal boss of the palatine; palp, palatal pad of the palatine; pao, paroccipital process; part, pre-articular; pbs, parabasisphenoid; pc, postcanine; pcst, posterior crus of the stapes; pcult, processus cultriformis; pcultc, processus cultriformis crest; pcults, processus cultriformis sulcus; pf, postfrontal; pla, pila antotica; pm, premaxilla; po, postorbital; pob, postorbital bar; pp, postparietal; ppf, posterior process of the frontal; ppm, palatal process of the premaxilla; prc, precanine; prsh, presphenoid; prf, prefrontal; pro, prootic; prp, preparietal; psh, parasphenoid; pt, pterygoid; ptf, postemporal fenestra; q, quadrate; qj, quadratojugal; qpt, quadrate process of the pterygoid; rl, reflected lamina; rt, replacement tooth; smtobsh, semi tubular region of the orbitosphenoid; smx, septomaxilla; soap, supraoccipital anteriorly projected crest; so, supraoccipital; spl, splenial; st, stapes; sth, stapedial head; stfp, stapedial footplate; stu, sella turcica; sq, squamosal; srspo, skull roof section of the postorbital; sur, surangular; t, tabular; tpt, transverse process of the pterygoid; tq, trochlea of the quadrate; v, vomer; vas, vomer anterior septum; vitptp, vomer inter-pterygoid plate; vkobsh, ventral keel of the orbitosphenoid; vkp, ventral keel of the palate; vps, vomer posterior septum; vksur, ventral keel of the surangular; vs, vomerine septum; vsq, ventral process of the squamosal; zsq, zygomatic process of the squamosal.

Neuromuscular system abbreviations—cf, carotid foramen; crso, canal for the ramus supraorbitalis; csss, canal for the superior sagittal sinus; E, opening for the endolymphatic duct in the floccular cavity; ff, facial foramen; flo, floccular fossa; jf, jugular foramen; lf, lacrimal foramen; mxs, maxillary sinus; oc, olfactory cavity; lpf, lateral palatal foramen; smxf, septomaxilla foramen; stf, stapedial foramen; vest, vestibule; V, opening for the cranial nerve V, VII, foramen for the cranial nerve VII, XII, foramen for the cranial nerve XII or hypoglossal nerve.

3 Results

3.1 Description

3.1.1 *Patranomodon nyaphulii*

Systematic Paleontology
Therapsida Broom, 1905
Anomodontia Owen, 1859

Definition—The most common ancestor of *Biseridens*, *Anomocephalus*, *Patranomodon*, *Galeops*, *Eodicynodon* and *Dicynodon* and all of its descendants.

Diagnosis—after Sidor (2001), antorbital region shortened to less than 50% of total skull length; presence of a lateral mandibular fenestra; zygomatic arch elevated above the margin of upper tooth row which fully exposes the quadrate and the quadratojugal in lateral view; squamosal with long ventral ramus supporting the quadrate; preparietal is present; teeth of upper tooth row decrease in size posteriorly with upper canine barely or not at all differentiated.

Genus *Patranomodon* Rubidge and Hopson, 1990

Type species—*P. nyaphulii*.

Diagnosis—As for the species.

Patranomodon nyaphulii Rubidge and Hopson, 1990

Material—NMQR 3000, the holotype from the National Museum in Bloemfontein, South Africa. A second specimen, BP/1/8740, was found in 2021, also on the farm Combrinkskraal, and is currently undergoing preparation and study at the Evolutionary Studies Institute.

Type locality—Combrinkskraal farm, Combrinkskraal member of the Abrahamskraal Formation. *Eodicynodon* Assemblage Zone, Beaufort Group, Karoo Supergroup, South Africa.

List of figures—Figures 1–6.

Diagnosis—after Rubidge and Hopson (1996), short palatal exposure of the premaxilla; premaxilla not closely approaching palatine medial to the maxilla; tabular extending ventrally towards the level of the postemporal foramen, covering the contact with the squamosal; the interpterygoid vacuity is an elongate slit between the ventral ridges of the pterygoids; the articulation surface between the quadrate and the articular is screw-shaped, precluding fore-aft sliding movement of articular on quadrate.

Description—Specimen NMQR 3000 is a well preserved skull with lower jaw, with very little compression or distortion (Rubidge and Hopson, 1990; Rubidge and Hopson, 1996). This description of the skull is based on the CT-scan and 3D reconstruction (Figure 1). Cranial elements were fully described by Rubidge and Hopson (1990) and Rubidge and Hopson (1996). This paper brings additional information and focuses on the connections and elements revealed *via* CT scanning. The lower jaw was not scanned for this study and is described by Rubidge and Hopson (1996). The bone surface of the skull is smooth, without external ornamentation or pachyostosis (Figure 1). In lateral view, the skull of *Patranomodon* is broadly rectangular with a domed dorsal margin (Figures 1A,B, 5A,B). The orbit faces anterolaterally (Figure 1C,G) and is about 1.5 times larger than the temporal fenestra. The occiput is well preserved and its surface is perpendicular to the skull roof (Figure 1A,B,H).

The premaxilla of NMQR 3000 is a relatively small paired bone forming the anteriormost part of the skull (Figures 1, 2). The anterior-most tip of the premaxilla is broken and the internarial bar is missing. Dorsally, the nasal process of the premaxilla forms a narrow strip of bone located on the sagittal line above the external naris (Figure 1C,G). The two processes do not touch medially such that the nasals are visible from the ventral side (Figure 1G).

In ventral view, the palatal process of the premaxilla forms the anterior portion of the palate (Figure 1D, I). It contacts the maxilla laterally and the vomers posteromedially (Figure 1D). The suture with the vomer is interdigitated. As noted by Rubidge and Hopson (1996), *Patranomodon* does not have a secondary palate, unlike the condition in dicynodonts such as *Eodicynodon*. As a result, the internal choana opens immediately posterior to the incisors, at the level of the first and the second maxillary teeth (Figure 1D). In ventral view, the palatal process of the left premaxilla is pierced laterally by a small incisive foramen (Figure 2D).

The maxilla is the largest cranial bone in *Patranomodon* (Figures 1, 2) and covers about 60% of the lateral surface of the snout (Figures 1A, B, 2A, B). It forms the posterior margin of the

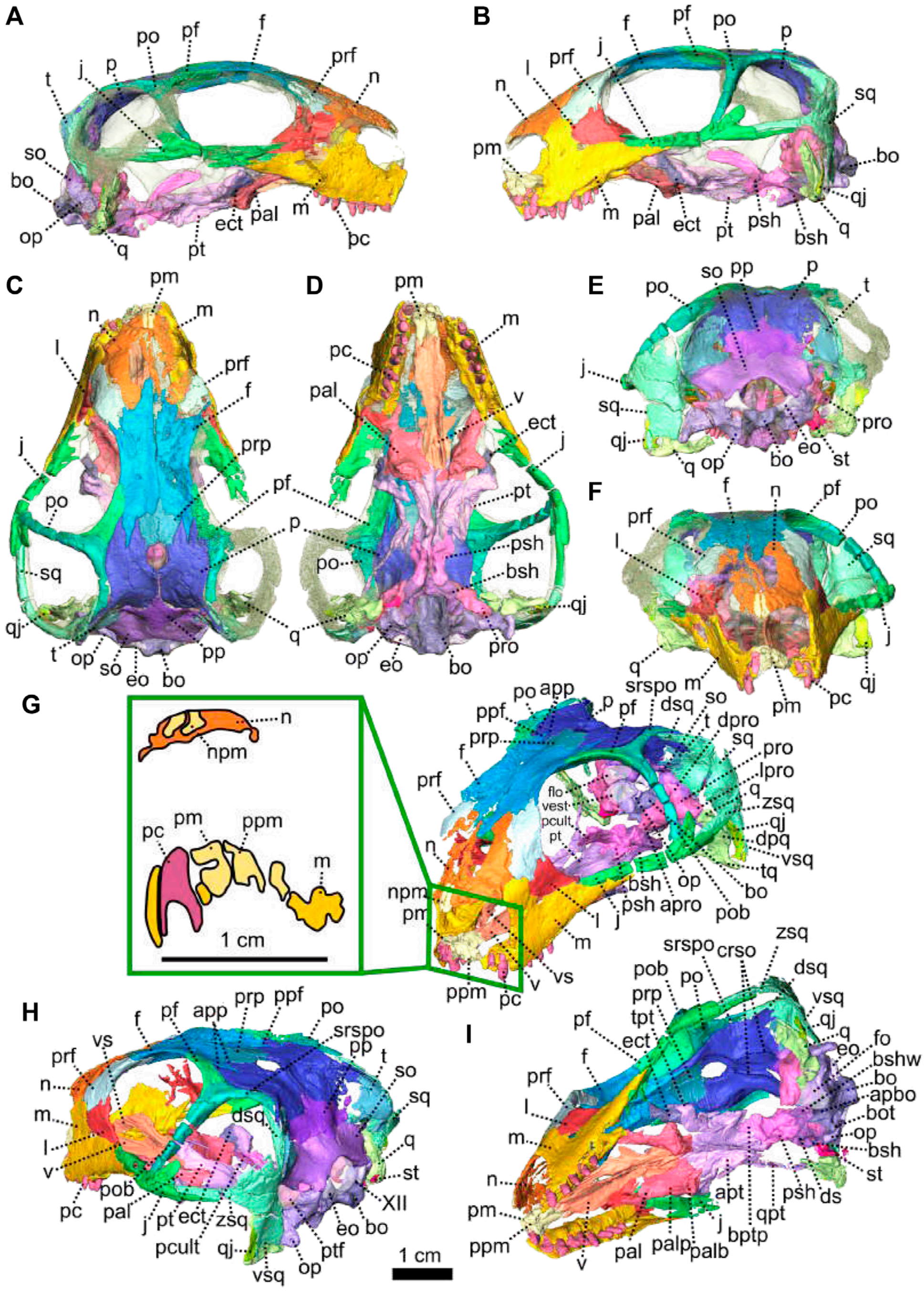

FIGURE 1
Patranomodon nyaphulii, NMQR 3000, from Combrinkskraal farm, Prince Albert district, Western Cape, South Africa; *Eodicynodon* AZ, Guadalupian, Beaufort Group, Karoo Supergroup. 3D rendering in **(A)**, right lateral view; **(B)**, left lateral view; **(C)**, dorsal view; **(D)**, ventral view; **(E)**, posterior view and **(F)**, anterior view; **(G)**, anterolateral view; **(H)**, posterolateral view and **(I)**, ventrolateral view. **(G)**, Transverse section at the level of the nasal process of the premaxilla, showing the premaxilla protruding into the nasals. Abbreviations: acst, anterior crus of the stapes; ang, angular; app, anterior process of the parietal; apobsh, anterior process of the orbitosphenoid; apt, anterior process of the pterygoid; art, articular; bo, basioccipital; bot, basioccipital tubera; bsh, basisphenoid; bshw, basisphenoid wing; bptp, basipterygoid process; c, caniniform tooth; dpq, dorsal plate of the quadrate; d, dentary; ds, dorsum sellae; dsq, dorsal process of the squamosal; ect, ectopterygoid; eo, exoccipital; f, frontal; fo, fenestra ovalis; icgq, intercondylar groove of the quadrate; ivv, intervomerine vacuity; j, jugal; l, lacrimal; lpro, lateral bulge of the prootic; m, maxilla; mcq, medial condyle of the quadrate; n, nasal; npm, nasal process of the premaxilla; op, opisthotic; p, parietal; pal, palatine; palb, palatal boss of the palatine; palp, palatal pad of the palatine; pc, postcanine; pcult, processus cultriformis; pf, postfrontal; pm, premaxilla; po, postorbital; pob, postorbital bar; pp, postparietal; ppf, posterior process of the frontal; ppm, palatal process of the premaxilla; prsh, presphenoid; prf, prefrontal; pro, prootic; prp, preparietal; psh, parasphenoid; pt, pterygoid; ptf, postemporal fenestra; q, quadrate; qj, quadratojugal; qpt, quadrate process of the pterygoid; smtobsh, semi tubular region of the orbitosphenoid; so, supraoccipital; spl, splenial; st, stapes; sth, stapedial head; stf, stapedial foramen; stfp, stapedial footplate; sq, squamosal; srspo, skull roof section of the postorbital; sur, surangular; t, tabular; tpt, transverse process of the pterygoid; v, vomer; vkobsh, ventral keel of the orbitosphenoid; vkp, ventral keel of the palate; vps, vomer posterior septum; vs., vomerine septum; vsq, ventral process of the squamosal; zsq, zygomatic process of the squamosal. Scale bar = 1 cm.

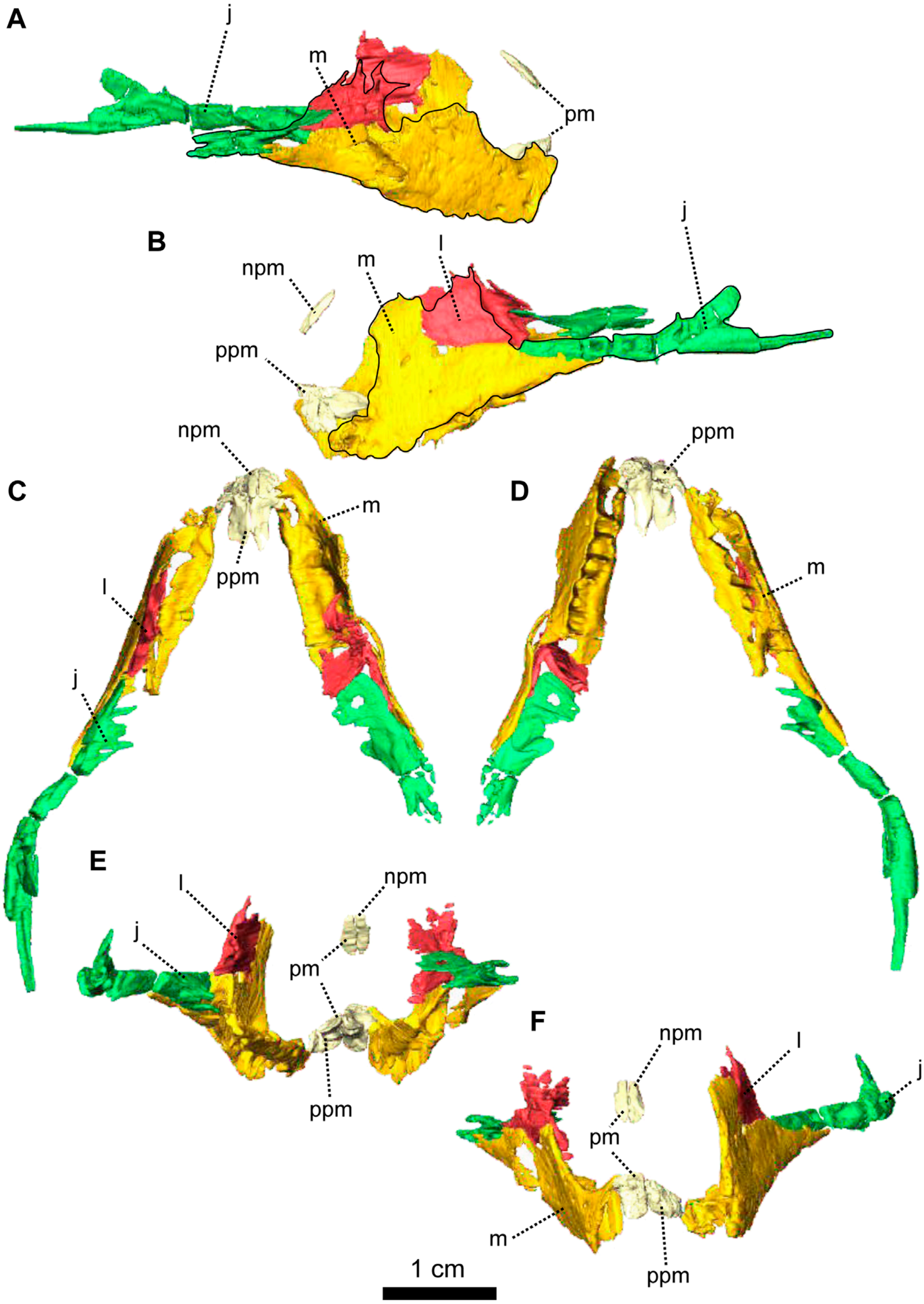

FIGURE 2
Paired maxillae and associated masticatory elements of *Patranomodon nyaphulii*, NMQR 3000, from Combrinkskraal farm, Prince Albert district, Western Cape, South Africa; *Eodicynodon* AZ, Guadalupian, Beaufort Group, Karoo Supergroup. 3D rendering in **(A)**, right lateral view; **(B)**, left lateral view; **(C)**, dorsal view; **(D)**, ventral view; **(E)**, posterior view and **(F)**, anterior view. Abbreviations: j, jugal; l, lacrimal; m, maxilla; n, nasal; npm, nasal process of the premaxilla; pm, premaxilla; ppm, palatal process of the premaxilla.

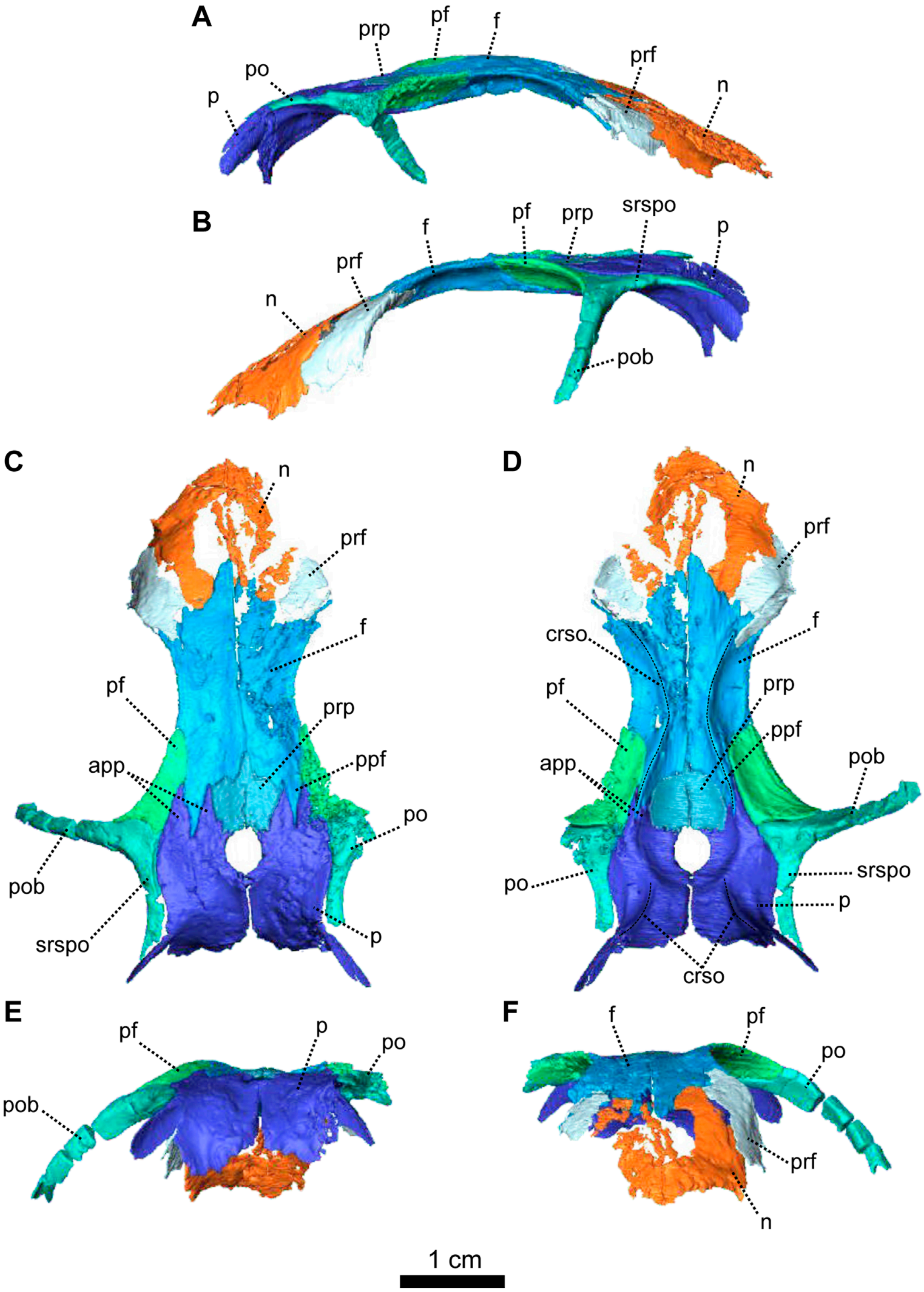

FIGURE 3
Parietal and associated dorsal elements of *Patranomodon nyaphulii*, NMQR 3000, from Combrinkskraal farm, Prince Albert district, Western Cape, South Africa; *Eodicynodon* AZ, Guadalupian, Beaufort Group, Karoo Supergroup. 3D rendering in **(A)**, right lateral view; **(B)**, left lateral view; **(C)**, dorsal view; **(D)**, ventral view; **(E)**, posterior view; **(F)**, anterior view. Abbreviations: app, anterior process of the parietal; apbo, anterior process of the basioccipital; apro, anterior process of the prootic; crso, canal for the ramus supraorbitalis; f, frontal; p, parietal; ppf, posterior process of the frontal; pf, postfrontal; po, postorbital; pob, postorbital bar; prf, prefrontal; srspo, skull roof section of the postorbital. Scale bar = 1 cm.

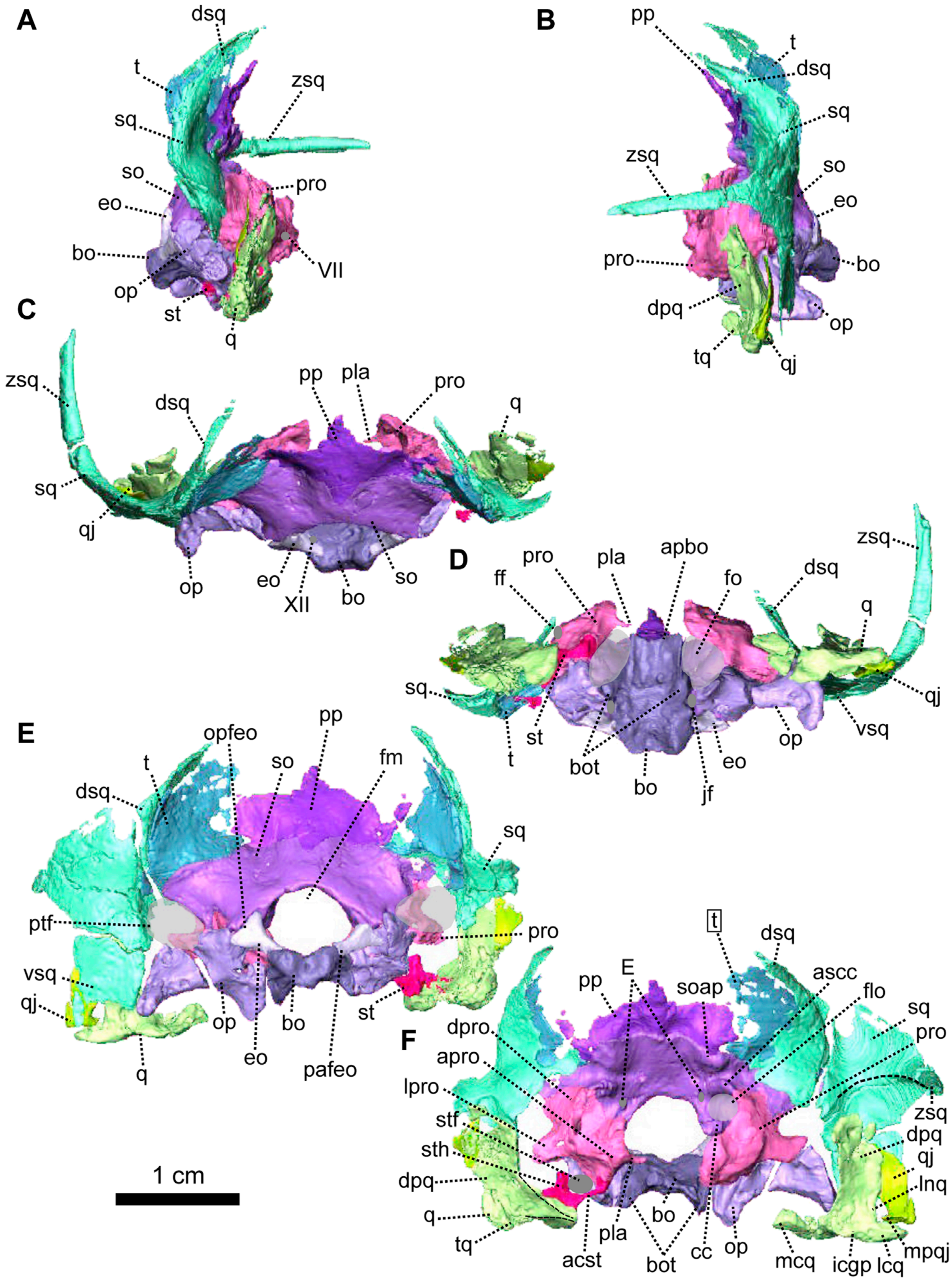

FIGURE 4
Occipital bones of *Patranomodon nyaphulii*, NMQR 3000, from Combrinkskraal farm, Prince Albert district, Western Cape, South Africa; *Eodicynodon* AZ, Guadalupian, Beaufort Group, Karoo Supergroup. 3D rendering in **(A)**, right lateral view; **(B)**, left lateral view; **(C)**, dorsal view; **(D)**, ventral view; **(E)**, posterior view and **(F)**, anterior view. Abbreviations: V, opening for the cranial nerve V, VII, foramen for the cranial nerve VII, XII, foramen for the cranial nerve XII or hypoglossal nerve; acst, anterior crus of the stapes; apbo, anterior process of the basioccipital; apro, anterior process of the prootic; ascc, attachment of the anterior semicircular canal; aso, anterior estension of the supraoccipital; bo, basioccipital; bot, basioccipital tubera; cc, crus communis; dpq, dorsal plate of the quadrate; dpro, dorsal process of the prootic; dsq, dorsal process of the squamosal; jf, jugular foramen; eo, exoccipital; fo, fenestra ovalis; icgq, intercondylar groove of the quadrate; jf, jugular foramen; lcq, lateral condyle of the quadrate; lnq, lateral notch of the quadrate; lpro, lateral bulge of the prootic; mcq, medial condyle of the quadrate; mpqj, medial process of the quadratojugal; op, opisthotic; opfeo, opisthotic facet of the exoccipital; pafeo, pro-atalas facet of the exoccipital; pla, pila antotica; pp, postparietal; pro, prootic; ptf, postemporal fenestra; q, quadrate; qj, quadratojugal; qpt, quadrate process of the pterygoid; soap, supraoccipital anteriorly projected crest; so, supraoccipital; st, stapes; sth, stapedial head; stfp, stapedial footplate; sq, squamosal; t, tabular; tq, trochlea of the quadrate; vsq, ventral process of the squamosal; zsq, zygomatic process of the squamosal. Scale bar = 1 cm.

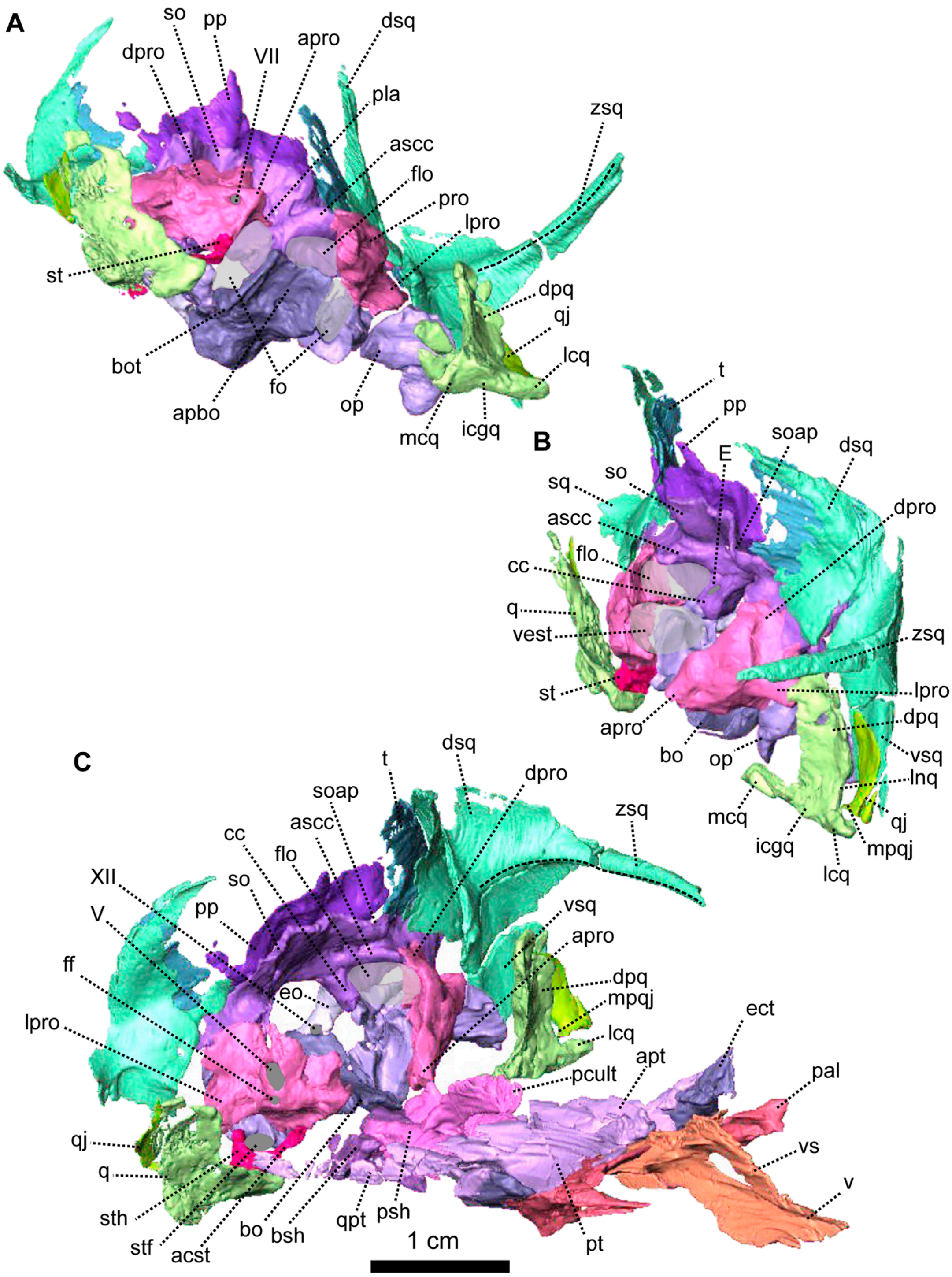

FIGURE 5
Anatomical details of *Patranomodon nyaphulii*, NMQR 3000, from Combrinkskraal farm, Prince Albert district, Western Cape, South Africa; *Eodicynodon* AZ, Guadalupian, Beaufort Group, Karoo Supergroup. 3D rendering of the posterior part of the skull in **(A)**, left ventral view; **(B)**, left medial view and **(C)**, right anterodorsal view. Scale bar = 1 cm. Abbreviations: V, opening for the cranial nerve V, VII, foramen for the cranial nerve VII, XII, foramen for the cranial nerve XII or hypoglossal nerve; acst, anterior crus of the stapes; apbo, anterior process of the basioccipital; apro, anterior process of the prootic; ascc, attachment of the anterior semicircular canal; bo, basioccipital; bot, basioccipital tubera; cc, crus communis; dpq, dorsal plate of the quadrate; dpro, dorsal process of the prootic; dsq, dorsal process of the squamosal; eo, exoccipital; fo, fenestra ovalis; icgq, intercondylar groove of the quadrate; jf, jugular foramen; lcq, lateral condyle of the quadrate; lnq, lateral notch of the quadrate; lpro, lateral bulge of the prootic; mcq, medial condyle of the quadrate; mpqj, medial process of the quadratojugal; op, opisthotic; pla, pila antotica; pp, postparietal; pro, prootic; q, quadrate; qj, quadratojugal; soap, supraoccipital anteriorly projected crest; so, supraoccipital; st, stapes; sth, stapedial head; stfp, stapedial footplate; sq, squamosal; t, tabular; vest, vestibule; vsq, ventral process of the squamosal; zsq, zygomatic process of the squamosal.

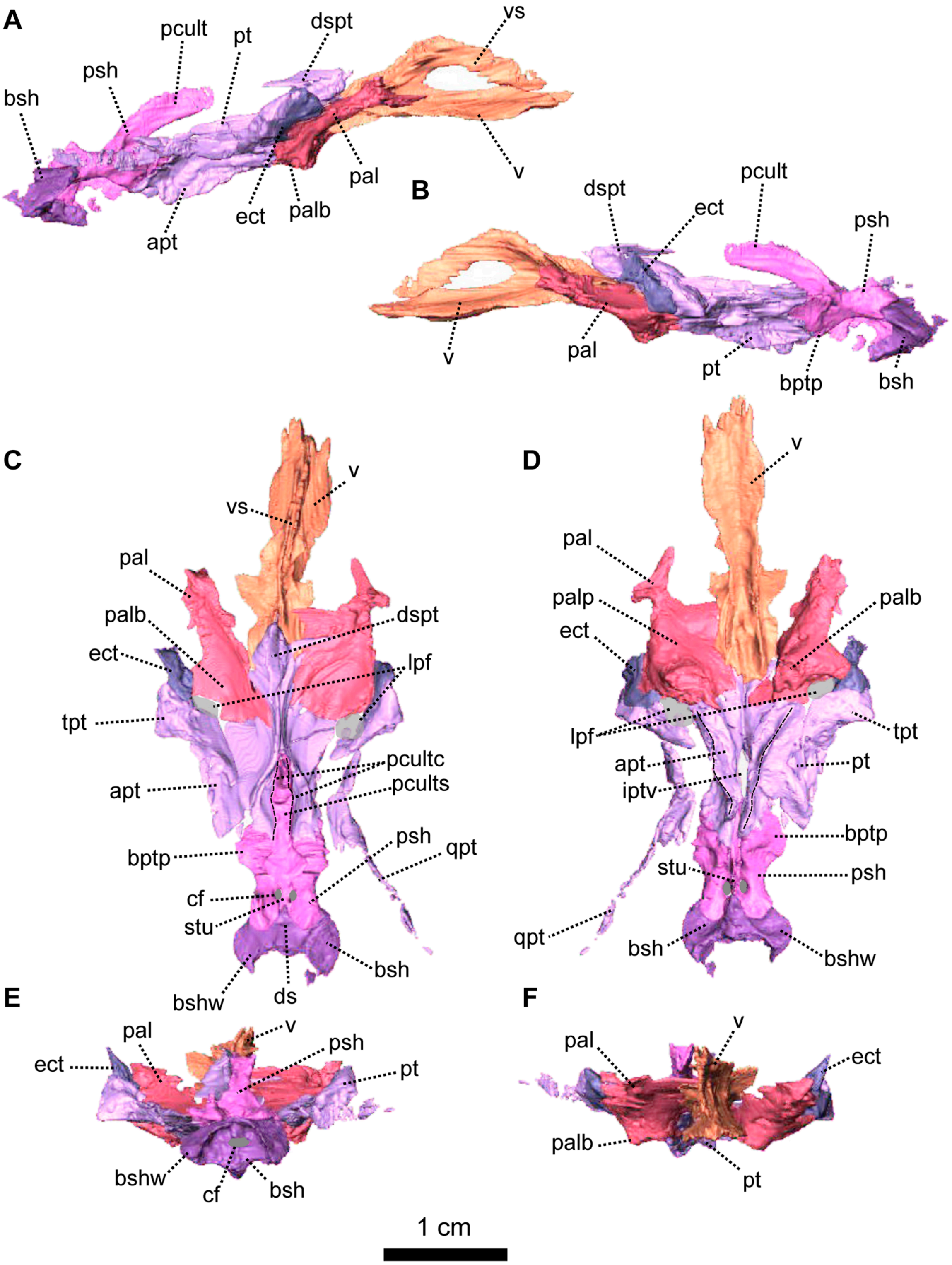

FIGURE 6
Palatal bones of *Patranomodon nyaphulii*, NMQR 3000, from Combrinkskraal farm, Prince Albert district, Western Cape, South Africa; *Eodicynodon* AZ, Guadalupian, Beaufort Group, Karoo Supergroup. 3D rendering in **(A)**, right lateral view; **(B)**, left lateral view; **(C)**, dorsal view; **(D)**, ventral view; **(E)**, posterior view and **(F)**, anterior view. Abbreviations: apt, anterior process of the pterygoid; bot, basioccipital tubera; bsh, basisphenoid; bshw, basisphenoid wing; bptp, basipterygoid process; cf, carotid foramen; ds, dorsum sellae; dspt, dorsal septum of the pterygoid; ect, ectopterygoid; iptv, interpterygoid vacuity; lpf, lateral palatal foramen; pal, palatine; palb, palatal boss of the palatine; palp, palatal pad of the palatine; pcult, processus cultriformis; pcultc, processus cultriformis crest; pcults, processus cultriformis sulcus; psh, parasphenoid; pt, pterygoid; qpt, quadrate process of the pterygoid; stu, sella turcica; tpt, transverse process of the pterygoid; v, vomer; vs., vomerine septum. Scale bar = 1 cm.

external naris (Figure 1B, G). In lateral view, the maxilla sends a dorsal process towards the nasal bone (Figures 1B) and the suture between the nasal and maxilla is slightly curved dorsally (Figure 1B). Posterodorsally, the maxilla contacts the prefrontal, and the lacrimal posteriorly (Figure 1B, 2B). Posteriorly, the zygomatic process of the maxilla forms the anteroventral margin of the suborbital bar. It extends along the ventral border of the jugal and tapers posteriorly below the middle of the orbit (Figure 1B, G). In ventral view, the maxilla comprises two processes, a short medial one toward the palatine and a longer zygomatic extension (Figures 1D, I, 2D). The maxilla does not form a secondary palate (Figure 2C, E). This suggests that the anterior portion of the palate of *Patranomodon* was likely soft. Another possibility is that *Patranomodon* did not have a palatal separation between the nasal cavity and the mouth. In medial view, the maxillary sinus is visible on the right side (Figure 1H). It is broadly triangular and located at the base of the zygomatic process of the maxilla. It is partially hidden by some broken pieces of the maxilla. Nine postcanines are preserved in the right maxilla and six in the left (Figures 1A, B, D, 2A, B, D). An additional potential empty socket is present at the back of the left maxilla. The disparity in the number of teeth between the right and left side of the maxilla could be due to preservation bias.

The left nasal bone of *Patranomodon* is almost complete, but the surface of the right nasal is weathered and fragmentary (Figures 1, 3). The nasal borders the dorsal margin of the external naris anterolaterally (Figure 1B). Posteromedially, the nasals share a W-shaped suture with the frontals (Figures 1C, G, 3). Anterolaterally, the nasal is overlapped by the maxilla, and the prefrontal on the posterolateral side (Figures 1F, 3F). Ventrally the internal surface of the nasal is slightly concave and smooth (Figure 3F).

The lacrimal is well preserved on the left side of the skull, but is incomplete on the right (Figures 1, 2). It makes up the anteroventral margin of the orbit (Figures 1B, H, 2B). In lateral view, the lacrimal has an oblique dorsal contact with the prefrontal (Figure 1B) and is bordered by the maxilla anteriorly and ventrally (Figure 2A, B). On the dorsal side of the zygomatic arch, the lacrimal extends posteriorly towards the anterior tip of the jugal bone, with which it shares a suture (Figures 1H, 2A–C). In posterior view, the intraorbital process of the lacrimal forms a vertical rectangular strip of bone (Figure 2E). The lacrimal foramen is not preserved.

The jugal is the largest bony element of the suborbital bar (Figure 1). In NMQR 3000, the left jugal is complete but the right one is missing (Figures 1, 2). It has a short contact with the lacrimal anteriorly at the level of the palatine (Figures 1B, D, 2B, D). Posteriorly, it extends below the squamosal to form the temporal portion of the zygomatic bar (Figure 1B, H) and contacts the postorbital at the base of the postorbital bar (Figure 1B). From this contact, the postorbital process of the jugal extends posterodorsally (Figures 1, 2). This process is flat and rounded dorsally in lateral view (Figure 2B). In lateral view, the jugal bears a small horizontal ridge at the level of the postorbital bar (Figures 1A, 2A). In dorsal view, the jugal appears bowed as it curves anteriorly beneath the orbit (Figure 2C) and tapers posteriorly (Figure 2C–E).

The left postorbital is complete but the right one has been damaged by weathering (Figures 1, 3, 5). The postorbital is a thin, curved bone which makes up the entire postorbital bar and a section of the skull roof (Figures 1G, H, 3). The postorbital bar separates the orbit from the temporal fenestra (Figure 1B, G, H) and forms the anterior and anterodorsal margin of the temporal fenestra (Figures 1, 3). It reaches the zygomatic arch ventrally and meets the jugal (Figure 1B, H) with an oblique suture in lateral view (Figure 1B). The postorbital bar curves dorsally to become the horizontal skull roof section of the postorbital (Figures 3B, 5B). This section contributes to the intertemporal space, where it extends to the level of the anterior margin of the pineal foramen (Figures 1H, 3C). Anterodorsally, the postorbital overlaps and intrudes into the postfrontal (Figure 1B, C). Medially, the postorbital contacts the parietal (Figures 1C, D, 3C, D) and dorsally, the postorbital tapers and contributes to the occiput wall between the squamosal and the parietal (Figure 1C).

The left squamosal of NMQR 3000 is almost complete, but the right one is badly damaged by weathering (Figures 1, 4, 5). The squamosal comprises three processes: a ventral process, a dorsal process and a zygomatic process (Figures 1, 4, 5). The ventral process occupies a large surface on the occiput (Figure 4E) and overlaps the dorsal process of the quadrate ventrally (Figures 1, 5). The dorsal process of the squamosal forms the posterodorsal margin of the temporal fenestra (Figure 1H) and extends dorsomedially towards the postorbital along the parietal (Figure 1E, H). In posterior view, the dorsal process of the squamosal is concealed by the overlapping tabular and supraoccipital (Figures 4E, F, 5B, C). It reaches the supraoccipital in anterior view (Figure 1G). The zygomatic process forms the ventral margin of the postemporal fenestra (Figure 1B, H) and tapers anteriorly to the level of the postorbital bar (Figures 1B, H, 4B). The squamosal has a long horizontal contact with the jugal anteroventrally, such that the squamosal rests on top of the posterior process of the jugal, beneath the temporal fenestra (Figure 1B, H). On its posteromedial surface, the zygomatic process of the squamosal bears a horizontal ridge (Figures 4F, 5A, C). A similar condition is found on the more derived anomodont *Niassodon* (Castanhinha et al., 2013).

As noted by Rubidge and Hopson (1996), the squamosal is not folded backward (condition seen in dicynodonts, see NMQR2978 below and *Niassodon* in Castanhinha et al. (2013)) but is rather convexly rounded dorsally. A similar condition is found in Biarmosuchia and Dinocephalia (Rubidge and Hopson, 1996; Sidor, 2003; Kruger et al., 2018; Duhamel et al., 2021) and is believed to be plesiomorphic for therapsids (Rubidge and Hopson, 1996).

Both prefrontals are preserved on NMQR 3000, but the left one is slightly larger and better preserved (Figures 1, 3). The prefrontal in NMQR 3000 borders the anterodorsal margin of the orbit (Figure 1H). In both dorsal and ventral views, the contact between the frontal and prefrontal is V-shaped posteromedially, such that the prefrontal extends posteriorly into a notch that is just medial to the anterolateral-most margins of the frontals (Figures 1B, C, D, 3B, C, D). In lateral view, the prefrontal contacts the dorsal margin of the lacrimal ventrally (Figure 1B, G). The contact is oblique anteriorly, and becomes S-shaped posteriorly; as previously recognized by Rubidge and Hopson (1996). Above the lacrimal, the prefrontal has a short anteroventral contact with the dorsal extension of the maxilla (Figure 1B, G) and has a longer oblique contact with the nasal anterodorsally (Figure 3B, D).

The frontal forms most of the dorsal margin of the orbit, between the prefrontal anteriorly and the postfrontal posteriorly (Figure 1, 3). As in most therapsids, the paired frontals constitute a large portion of the supraorbital skull roof and contact each other along the midline. The midline suture is straight and non-interdigitated (Figure 13C, D). In dorsal view, the frontal has a short contact with the prefrontal anterolaterally (Figure 3C) and meets with the nasal anteriorly (Figure 3C). Unlike most dicynodonts, in which the suture is transverse, the frontals intrude into the nasals forming a V-shaped suture, such that the anteromedial-most extension of the frontals are anterior to the posterolateral-most extensions of the nasals (see BP/1/6230, NMQR 2978 and Damiani et al., 2007; Castanhinha et al., 2013; Kammerer, 2016b; Angielczyk and Kammerer, 2017; Angielczyk et al., 2019). The frontal shares a curved suture with the postfrontal posterolaterally (Figure 3C). In both dorsal and ventral view, the frontal has a posterior process that incises the parietal (Figures 1, 3–C, D) as in other non-mammalian therapsids (van Heerden, 1972; Rubidge and Kitching, 2003; Fröbisch and Reisz, 2008; Castanhinha et al., 2013; Kammerer, 2016a; Kammerer, 2016b; Pusch et al., 2019; Pusch et al., 2020). In ventral view, the frontal bears a medially curved ridge (Figures 1I, 3D) which has its origin on the prefrontal and extends posteriorly onto the parietal. This ridge represents the external margin of the olfactory tract posteriorly and the olfactory cavity anteriorly (*ramus supraorbitalis*). No foramen could be identified on the frontal of NMQR 3000.

The postfrontal on NMQR 3000 is an elongated, roughly triangular, flat bone bordering the dorsal margin of the orbit (Figures 1, 3). It is bordered by the frontal anteromedially, the parietal posteromedially and the postorbital posteriorly (Figure 3C). The contact between the frontal and postfrontal is curved (Figure 3C). In ventral view, the postfrontal overlaps the frontal medially (Figure 3D). The contact between the postfrontal and parietal is oblique, both in dorsal and ventral views (3-C and D). Posteriorly, the postfrontal has a curved sutural contact with the postorbital (Figure 3C). In dorsal view, at the contact with the postorbital, the postfrontal projects two small triangular processes posterolaterally and posteromedially respectively. In ventral view, the suture between the postfrontal and postorbital is transverse (Figure 3D). The ventral side of the postfrontal is excavated by a shallow fossa.

In dorsal view, the preparietal is a small, trapezoidal bone, bordering the anterior margin of the pineal foramen (Figures 1, 3) and has a short triangular process extending anteriorly between the two frontals (Figure 3C). This triangular process is less pronounced and thinner in ventral view (Figures 1I, 3D). In dorsal view, the preparietal contacts the parietal laterally and posterolaterallly (Figure 3C). The contact is straight laterally and becomes interdigitated posteriorly (Figure 3C, D). Importantly, the remnant of a midline suture is visible on the posterior part of the preparietal (Figure 3C). In ventral view, the preparietal has a rounded anterolateral margin (Figures 1I, 3D).

The parietal is a large smooth paired bone forming most of the posterior part of the skull roof (Figures 1, 3) and extends posteroventrally on the occipital face (Figure 1). Both parietals suture along the midline (Figure 3) and border the lateral and posterior margins of the pineal foramen (Figures 1H, 3E). In dorsal and posterior views, the parietal shows two equal-sized triangular anterior processes: one lateral and the other medial (Figure 3C, D). The anterolateral process extends between the postfrontal and the frontal bones and the more medial process is situated between the frontal and the preparietal. The anterior suture of the parietal with the preparietal is tranversely straight in ventral view and further laterally the suture with the frontal forms a W around the olfactory ridge (Figures 1I, 3D).

On the occiput, the parietal is overlapped by both the tabular and the postparietal (Figures 1E, 3E) such that the parietal extends laterally beneath the tabular and incises the dorsal process of the squamosal (Figures 1B, C, E, 3C, E). In ventral view, the parietal has a well-formed depression around the pineal foramen (Figure 3D).

The occiput of NMQR 3000 is damaged on the right side and well preserved on the left (Figure 1). As a consequence, the following description is based mainly on the left side (Figures 1, 4, 5). The external surface is smooth and does not show any ornamentation (Figures 1, 4). The foramen magnum is large, rounded and bordered by the supraoccipital dorsally, the exoccipitals laterally, and the basioccipital ventrally (Figure 4E). The postemporal fenestra is half the size of the foramen magnum and is formed by the tabular dorsally, the squamosal laterally, the opisthotic ventrally, and the supraoccipital medially (Figures 1E, H, 4E, F).

The postparietal is a narrow unpaired bone located on the dorsal-most half of the occiput (Figures 1, 4, 5). Its external surface is flat and the internal surface slightly wrinkled (Figures 4E, F, 5B, C). In posterior view, the dorsal side of the postparietal overlaps the parietal (Figure 1E, H). In the same view, the postparietal is a transversely elongated bone with pointed dorsal and ventral processes (Figure 4E) and the dorsal process overlaps the parietal (Figure 1C, E, H). In occipital and anteromedial views it is evident that the postparietal overlaps the supraoccipital ventrally (Figure 4C, 5B). In posterior view, the postparietal contacts the tabular laterally (Figures 1E, 4E) but the contact is not well preserved. On its internal surface, the postparietal exhibits a broad and blunt vertical midline ridge (Figures 4F, 5).

The tabular, which forms the dorsolateral part of the occipital surface on NMQR 3000, is a thin bone (Figures 1E, H, 4E). The tabular overlaps the posterolateral portion of the parietal along the posteromedial border of the temporal fenestra (Figure 1C, E) and laterally overlies the medial side of the squamosal (Figure 1H, 5C). As a result, the anterior exposure of the tabular in anterior view is greatly reduced (Figures 4E, F, 5B, C). In posterior view, the tabular shares a transverse suture with the supraoccipital ventrally and forms the dorsolateral margin of the postemporal fenestra (Figure 4E).

As in other therapsids, the inner ear system of *Patranomodon* is housed by the supraoccipital, prootic, opisthotic, exoccipital, and basioccipital (Olson, 1944; Cox and Broom, 1962; Fourie, 1974; Sigogneau, 1974; Luo et al., 1995; Luo, 2001; Cifelli et al., 2004; Surkov and Benton, 2004; Araújo et al., 2017; Pusch et al., 2019). With the exception of the basioccipital, all these bones accommodate part of the semicircular canals (Pusch et al., 2019) and the auditory capsule is formed by the prootic, the opisthotic and the supraoccipital (Cluver, 1971). The supraoccipital and the prootic enclose the floccular fossa dorsally, while the prootic and the opisthotic enclose the vestibular fossa ventrally (Figure 5B, C).

The supraoccipital is the largest of the occipital bones in anomodonts (Rubidge and Hopson, 1996; Fröbisch and Reisz, 2008; Castanhinha et al., 2013). This bone is well preserved in NMQR 3000 (Figures 1, 4, 5) and makes up the rounded dorsal margin of the foramen magnum (Figure 4E, F). In posterior view, the supraoccipital bears two small symmetrical depressions that extend dorsally onto the surface of the postparietal (Figure 4E).

Dorsally, the supraoccipital is overlapped by the postparietal (Figure 4C, E, F). Dorsolaterally, it has a curved contact with the tabular (Figure 4E, F). Ventromedially, in posterior view, the supraoccipital has an oblique contact with the exoccipital and meets the opisthotic (Figure 4E). Laterally, the supraoccipital has a diagonal edge that borders the postemporal fenestra (Figure 4E). In anterior view, the supraoccipital overlaps part of the ventromedial section of the squamosal (dorsal ramus of the squamosal, Figure 5B, C). In the same view, the supraoccipital bears an anteriorly projected dorsal crest, and the anterior semicircular crests laterally (see Macungo et al. (2022); Figures 4F, 5B, C). The semicircular crest of the supraoccipital accommodates the anterior semicircular canals, at the level of the contact with the prootic (Araújo et al., 2017; Pusch et al., 2019; Macungo et al., 2022). This crest delineates the dorsal margin of the floccular fossa (Figure 5B). Ventral to the floccular fossa, the supraoccipital bears a crest that forms the attachment for the crus communis (Figures 4F, 5C).

The prootic, sometimes referred to by the mammalian term periotic (fusion of the opisthotic, the prootic, the epiotic and sometimes the supraoccipital, see Angielczyk et al., 2021) is positioned on the anterior side of the occipital wall in anomodonts (Rubidge and Hopson, 1996; Surkov and Benton, 2004; Castanhinha et al., 2013) and forms part of the sidewall of the braincase (Castanhinha et al., 2013; Laaß, 2015a; Laaß, 2015b). It comprises three parts: the prootic dorsal process, prootic lateral bulge, and prootic anterior process (Figures 4, 5). The latter extends ventromedially into the pila antotica (Figures 4D, F, 5A). The pila antotica, only preserved on the right prootic, is incomplete. It forms a slender triangular process.

The dorsal process of the prootic is triangular in anterior view (Figure 4F) and contacts the supraoccipital posteriorly at the level of the postemporal fenestra (Figure 5C). It forms the attachment of the anterior semicircular canal dorsally along with the suppraoccipital (Figures 4F, 5B, C). In medial view, the dorsal process of the prootic is curved with a dorsal and a posterior process (Figure 5B), which form the anterior margin of the floccular fossa.

The lateral process of the prootic, which is rectangular in anterior view, extends laterally toward the quadrate (Figures 4, 5B, C, F) and forms a smooth angle with the dorsal process. In ventral view, the surface of the lateral process of the prootic is concave (Figure 4D). It contacts the opisthotic posteriorly (Figures 4D, 5A).

The anterior process of the prootic is roughly triangular in lateral and lateroventral views (Figures 4A, B, 5A) and forms the curved anterior margin of the vestibular chamber (Figure 5B). In anterolateral view, the anterior process of the prootic contacts the parasphenoid anteriorly (Figure 5C) and turns into the dorsal process at the level of the foramen for the cranial nerve V (Figure 5C). The foramen is large and leads into the vestibular chamber where it contacts the opisthotic posteriorly. Below the foramen for cranial nerve V, is the small foramen for the facial nerve (Figure 5C). The foramen for the nerve VII is positioned at the anterioventral side of the anterior process of the prootic; and is visible in lateral and lateroventral views (Figures 4A, 5A). Also in ventral and in lateroventral views, the prootic has a short curved posterior contact with the stapes (Figures 4A, 5B). The anterior process of the prootic forms the anterolateral margin of the fenestra ovalis, where it bears a slight depression towards the pila antotica (Figures 4D, 5A).

The opisthotic constitutes a large part of the posterior portion of the periotic region. It is sometimes fused with the prootic (to form the periotic) and/or the exoccipitals. It forms the posterior border of the vestibular fossa (Figure 5B). Posteriorly, it forms the ventral margin of the postemporal fenestra (Figures 1, 4, 5A). In posterior view, the opisthotic has two robust triangular ventral processes, one lateral and one medial, the latter being the paroccipital process (Figure 4E). Between these two processes, the ventral margin of the opisthotic is notched by the opening of the fenestra ovalis (Figure 4E). The ventrolateral process is the longest and contacts the quadrate ventrolaterally (Figure 4E, F), and dorsolaterally has an oblique suture with the squamosal (Figure 4E). The ventromedial process shares a vertical contact with the basioccipital tubera on the medial side. In ventral view, the jugular foramen is positioned between the opisthotic and the basioccipital (Figure 4D).

In contrast with the condition in more derived therapsids (Pusch et al., 2019) and dicynodonts (Castanhinha et al., 2013; Macungo et al., 2022), the opisthotic of NMQR 3000 is not fused to the prootic. In lateral view, the suture between the opisthotic and the prootic is slightly oblique and located anterior to the opisthotic (Figure 4A). Both the prootic and the opisthotic enclose the vestibular fossa (Figure 5B). In ventral view, the left opisthotic forms a thick semicircular ridge contributing to the posterior margin of the fenestra ovalis (Figure 4D). In lateral view, the ventrolateral process of the opisthotic is excavated by a deep ventral fossa (Figure 4A). In posterior view, the opisthotic meets the squamosal laterally (Figure 4E) and is overlapped by the exoccipital dorsomedially.

The exoccipital is a small trapezoidal bone forming the ventrolateral margin of the foramen magnum (Figures 1, 4). The exoccipital of NMQR 3000 is not fused to any surrounding bones, nor to the basioccipital condyle, unlike in more derived anomodonts (Castanhinha et al., 2013). In posterior view, the exoccipital tapers medially, such that it is broader laterally than medially. Its dorsal-most margin is accommodated within a triangular notch in the supraoccipital (Figure 4E). The ventromedial suture with the basioccipital is similar (Figure 4E) and forms the proatlas facet.

The basioccipital encloses the braincase ventrally (Figures 4, 5). It is formed by the occipital condyle, two dorsal lobes, the basioccipital tubera and a saddle-shaped anterior process (Figures 1, 4, 5). The basioccipital contributes to the medial and the posteromedial margin of the fenestra ovalis (Figures 4D, 5A). In posterior view, the basioccipital forms the ventromedial margin of the foramen magnum and its two dorsolateral lobes suture with the exoccipitals (Figure 4E). The occipital condyle has a rounded occipital pit. In the same view, the basioccipital tubera are triangular (Figure 4E). They contact the opisthotic laterally and the contact is flat, vertical and at the level of the jugular foramen. In dorsal view, the basioccipital is roughly rectangular, with its longest axis oriented anteroposteriorly. On its dorsal surface, the foramen for the hypoglossal nerve (cranial nerve XII) is located on the suture between the basioccipital and exoccipital (Figures 1, 4C, 5C). The anterior process of the basioccipital bears the longitudinal intertuberal ridge (Figure 4C) and reaches the basioccipital anteriorly (Figure 1D). In ventral and lateroventral view, the surface of the basioccipital is excavated by a shallow anteroposteriorly oriented fossa that forms a concave surface (Figures 4D, 5A). The fossa is bordered by two longitudinal ridges that separate the main body of the basioccipital bone from the fenestra ovalis. In the same views, the two basioccipital tubera, that are oriented towards the opisthotic, contribute to the posteromedial margin of the fenestra ovalis (Figures 4D, 5A).

In NMQR 3000, the stapes is a small bone positioned between the dorsomedial side of the quadrate and the lateral margin of the fenestra ovalis (Figures 4D, 5A). The right stapes is missing and the left one is partially broken (Figures 4, 5). The stapes of NMQR 3000 is missing its posterior crus and the stapedial footplate. When fully preserved, it would have most likely been shaped with two crura (the bicrurate condition), a stapedial head and footplate. This differs from the condition observed in Dicynodontia, where the stapes is often hourglass-shaped (Sullivan and Reisz, 2005; Castanhinha et al., 2013). The anterior crus is thin and short (Figures 4F, 5C). Medially, it contacts the ventral margin of the anterior process of the prootic. The contact is short and curved in lateral and lateroventral views (Figures 4A, 5A). Lateroventrally, the anterior crus contacts the stapedial head (Figure 5C). In lateral and lateroventral views, the stapedial head is roughly triangular (Figures 4A, 5C) and has a posterodorsal process similar to that of the cynodont *Thrinaxodon* (Pusch et al., 2019). In anterior view, the stapedial head contacts the medial condyle of the quadrate's trochlea laterally (Figure 4F). The contact is oblique in ventral view (Figure 4D) and roughly horizontal in medial view (Figure 5B). The stapedial head and the anterior crus form the lateral and anterior margins of the stapedial foramen (Figures 4F, 5C).

The quadrate comprises a ventral trochlea and a dorsal vertical plate (Figures 1, 4, 5). The dorsal plate is a thin transverse extension (Figures 4B, 5B) and is overlapped posteriorly by both the quadratojugal and the squamosal (Figures 1, 4, 5B). The dorsal plate bears a lateral notch, that would have accommodated the medial process of the quadratojugal (Figure 5B, C). The trochlea of the quadrate is the articulation surface for the articular bone of the lower jaw (Figure 4B, F). It is formed by the rounded and well-defined lateral condyle of the quadrate, a smaller medial condyle, and a concave intercondylar groove (Figures 4F, 5A, B). In anterior view, the medial condyle of the right quadrate bears two small oblique ridges that originate respectively on the dorsal plate and lateral condyle (Figure 4F), before joining on the medial condyle of the trochlea.

In lateral view, the quadratojugal is a vertical strip of bone located between the squamosal posteriorly and the quadrate anteriorly (Figures 1G, H, 4E, F, 5B, C). Both quadratojugals are preserved in NMQR 3000. The left quadratojugal thickens ventrally to form a small flat surface (Figure 4B, D, E) that bears a small ventromedial hook (Figures 4E, F, 5B, C). This is the medial process of the quadratojugal that is accommodated by the lateral notch of the quadrate (Pusch et al., 2019).

The palate of NMQR 3000 is overall well preserved but most of the sphenethmoidal bones are missing (Figures 1, 5A, C, 6) and only the parasphenoid is preserved on the specimen (Figures 1G, I, 5C, 6). One notable anatomical feature is that the parasphenoid and the basisphenoid are two distinct bones, contra Rubidge and Hopson (1996) who considered that they were fused. In therapsids, they are usually fused to form the parabasisphenoid (Sidor and Rubidge, 2006; Pusch et al., 2019) but for them to be unfused is not uncommon among anomodonts (Castanhinha et al., 2013; Macungo et al., 2022).

The vomer comprises a ventral plate and a long and tall dorsal septum (Figures 1, 5, 6). The ventral plate reaches the premaxillary palatal process anteriorly at the level of the third maxillary tooth (Figure 1D) and the dorsal septum divides the nasal cavity medially (Figures 1H, 6). In lateral view, a large hole is present in the vomerine dorsal septum (Figures 6A, B) and is likely due to postmortem damage. However, Ivakhnenko (2008) reported the presence of a large foramen in some therapsids in the same area of the internasal septum. In ventral view, the ventral plate of the vomer is excavated by a deep midline groove bordered by two sharp lateral ridges (Figure 6D). Posterolaterally the vomer contacts the palatine and posteriorly forms the anterior margin of the interpterygoid vacuity at the level of the posterior end of the maxilla (Figures 1D, 6D). It was previously suggested that the vomer of *Patranomodon* may be a paired structure (Rubidge and Hopson, 1996), but no suture could be identified on the CT images.

In ventral view, the palatine is positioned posteromedially to the maxilla and extends posteriorly up to the anterior ramus of the pterygoid (Figures 1I, 7D). It comprises mainly the palatine pad (Castanhinha et al., 2013), which includes a well-defined and thick edentulous palatine boss (Figure 6A, B, D, F). In ventral view, the palatine pad extends anteriorly to reach the maxilla behind the last maxillary tooth (Figure 1D, I). In the same view, the palatine contacts the ectopterygoid posterolaterally, at the level of the palatine bosses. The palatine pad contacts the pterygoid posteromedially (Figure 1D, I) and forms the medial and the anterior margins of the lateral palatal foramen (Figure 6D). On its dorsal surface, the palatine bears a steep depression posteriorly, which corresponds to a negative image of the corresponding palatine boss (Figure 6C).

The pterygoid of NMQR 3000 is paired and presents the typical tripartite therapsid morphology with anterior, transverse and quadrate rami (Figures 1, 5C, 6). The interpteryoid vacuity of NMQR 3000 is narrow and diamond-shaped 6-D). *Patranomodon* does not show the pronounced ventrally oriented transverse ramus which is characteristic of *Eodicynodon* specimens. On the right, the transverse ramus is detached from the main body but the left side is intact (Figure 6C, D). In ventral view, the transverse ramus is roughly triangular (Figure 6D), forms the posterior margin of the lateral palatal foramen, and contacts the ectopterygoid anteriorly (Figures 5C, 6), with an oblique suture in lateral view (Figure 6A). The transverse ramus forms an angle of 90° with the sagittal plane of the skull (Figure 6D).

The anterior ramus comprises a ventral ridge, dorsal septum and median plate (Figures 1I, 5C, 6A–D). The median plate contacts the palatine anteriorly at the level of the palatine bosses. This contact is oblique in ventral view (Figure 6D) and transverse in dorsal view (Figure 6C). The median plates contact anteriorly, enclosing the interpterygoid vacuity anteriorly.

The ventral ridge of the anterior ramus is oblique in ventral view (Figure 6D). Both rami contact posteriorly and enclose the interpterygoid vacuity posteriorly. In lateral view, the ventral ridge becomes taller posteriorly (Figure 6A) and contacts the palatine anteriorly. This contact is oblique in ventral view (Figure 6D).

Dorsally, the anterior ramus of the pterygoid is laterally flattened, and projects into a vertical septum medially (Figure 6A–C). This septum extends between the two palatine bones to reach the vomer's septum anteriorly at the level of the ectopterygoid (Figures 5C, 18A, B). The contact is oblique in lateral and anterolateral views. In ventral view, the anterior ramus of the pterygoid meets the parasphenoid posteromedially at the level of the basipterygoid process. The contact is oblique in lateral view (Figures 1I, 6A, B) and forms the floor of the hindbrain (Castanhinha et al., 2013; Pusch et al., 2019). No medial plate, usually found in derived anomodonts at the contact with the parabasisphenoid (Castanhinha et al., 2013; Laaß and Schillinger, 2015; Laaß et al., 2017), could be identified in the specimen.

The quadrate ramus of the pterygoid is preserved only on the right side and is detached from the main body of the pterygoid (Figures 1I, 5C, 6C, D). This ramus is slender posteriorly and thickens at the level of the parasphenoid. It makes an angle of 45° with the sagittal plane of the skull.

Both ectopterygoids are present and are small elements forming the anterolateral aspect of the transverse process of the pterygoid (Figures 5C, 6). An ectopterygoid is present in most anomodont taxa (Castanhinha et al., 2013), but has been lost in derived dicynodonts such as *Lystrosaurus* (Cluver, 1971), although it is retained in some juveniles (Benoit pers. obv.). In lateral view, the ectopterygoid is roughly triangular and extends dorsally (Figure 6B) and the contact between the ectopterygoid and the pterygoid is oblique. In ventral view, the ectopterygoid contacts the palatine medially (Figure 6D). It forms the lateral margin of the lateral palatal foramen (Figure 6C, D).

The sphenethmoidal complex of NMQR 3000 is poorly preserved, and of the internal bones that support the hindbrain and the forebrain, only the parasphenoid and the basisphenoid remain (Figures 5C, 6).

The parasphenoid is unpaired and includes the processus cultriformis (often called parasphenoid rostrum (Castanhinha et al., 2013; Macungo et al., 2022)) anteriorly, two hourglass-shaped processes laterally, and the sella turcica medially (Figures 5C, 6). The two carotid foramina are present and visible in both dorsal and ventral views (Figure 6C, D). They form two separate canals. The *canalis vidii* (the palatal branch of the cranial nerve VII) is not visible on NMQR 3000.

The processus cultriformis is a rod-like structure, originating on the sella turcica and curving anterodorsally to the level of the anterior margin of the interpterygoid vacuity (Figures 5C, 6). The base of the processus is large and the processus becomes thinner anteriorly (Figure 6C). In both dorsal and lateral views, the base of the processus cultriformis is triangular (Figure 6B, C). The dorsal surface of the process bears two lateral crests and a median sulcus (Figure 6C). The base of the processus cultriformis supports the anteroventral section of the hindbrain behind the hypophysis (Castanhinha et al., 2013).

Two hourglass-shaped processes form the lateral margin of the carotid foramina (Figure 6C, D) and contact the prootic posterodorsally (Figures 1A, B, 5C). The anterior-most part of the hourglass-shaped process is formed by the basipterygoid processes, referred as the basisphenoidal tubers in Macungo et al. (2022) (Figure 6). In lateral view, the basipterygoid process is roughly triangular (Figure 6B) and bears a small ventral keel, referred to as the parasphenoid keel in Araújo et al. (2017). It has a reversed V-shaped contact anteriorly with the anterior ramus of the pterygoid. At this point, the basipterygoid process tapers to a mediolaterally thin point where it contacts the pterygoid. In lateral view, the hourglass-shaped process has a V-shape contact with the basiphenoid posteriorly (Figure 6A, B). In dorsal and ventral views, the contact between the parasphenoid and the basisphenoid is round (Figure 6C, D).

The sella turcica forms the central part of the parasphenoid (Figure 6C). It makes up the medial and posterior margin of the carotid foramina and extends ventrally in a thin septum (Figure 6A, B, D).

The basisphenoid is unpaired, lies at the base of the hindbrain and encloses posteroventrally the brain cavity in therapsids (Castanhinha et al., 2013). In NMQR 3000, the basisphenoid is bordered by the parasphenoid anteriorly and the basioccipital posteriorly (Figures 1I, 5C, 6). In dorsal view, the dorsum sellae is a thin medial triangular process (Figure 6C) that tapers between the hourglass-shaped processes of the parasphenoid and is surrounded by two laterally projecting symmetrical wings (Figures 1I, 6C, D). In ventral view, the wings form the anterior margin of the fenestra ovalis and have a depression between them (Figure 1D, I). In the same view, the basisphenoid bears a triangular process medially that differs from the sella turcica. In lateral view, this process makes an angle of 30° with the horizontal plane ventrally (Figure 6A, B). It contacts the ventral septum of the parasphenoid anterodorsally. In the same view, the basisphenoid wings make an angle of 30° dorsally and contact the parasphenoid with a reverted V-shaped suture (Figures 6A, B). In posterior view, the basisphenoid is partially hollow for the articulation with the basioccipital, and the opening of the internal carotid canal is in the centre (Figure 6E).

As in most basal anomodonts, the dentition of *Patranomodon* is homodont (Rubidge and Hopson, 1996; Rybczynski and Reisz, 2001; Kemp, 2005; Cisneros et al., 2015). Similar-shaped teeth are present in both the maxilla and premaxilla, and there is not an enlarged caniniform tooth or tusk (Figure 1G, H and see Supplementary Material). The specimen has nine maxillary teeth on the right side, all of similar sizes, except the posterior-most tooth, which is smaller. On the left side, six teeth of similar shape and size are preserved (Figure 1G, H). The difference in number on the left and right sides is possibly due to preservation. On the right, it is evident that the anterior-most tooth is rooted at the suture between the maxilla and the premaxilla (Figure 1D, I).

3.1.2 *Eodicynodon oosthuizeni*

Systematic Paleontology
Therapsida Broom, 1905
Anomodontia Owen, 1859
Dicynodontia Owen, 1859

Definition—All taxa more closely related to *Dicynodon lacerticeps* than *Galeops whaitsi* (Kammerer and Angielczyk, 2009).

Diagnosis—after Sidor (2001) and Kammerer and Angielczyk (2009), alveolar margin of the premaxilla recurved; ventral surface of the premaxilla has a median ridge with a flattened and expanded anterior area; vomerine process of the premaxilla lost so that vomer abuts the body of the premaxilla; internal narial shelf well-developed and formed primarily by the premaxilla and the maxilla; interpterygoid vacuity relatively long but does not reach the level of the palatal exposure of the palatines; lateral palatal foramen present at the level of the anterior expanded palatal exposure of the palatines; transverse flange of the pterygoid reduced and oriented longitudinally; squamosal with lateral fossa for muscle

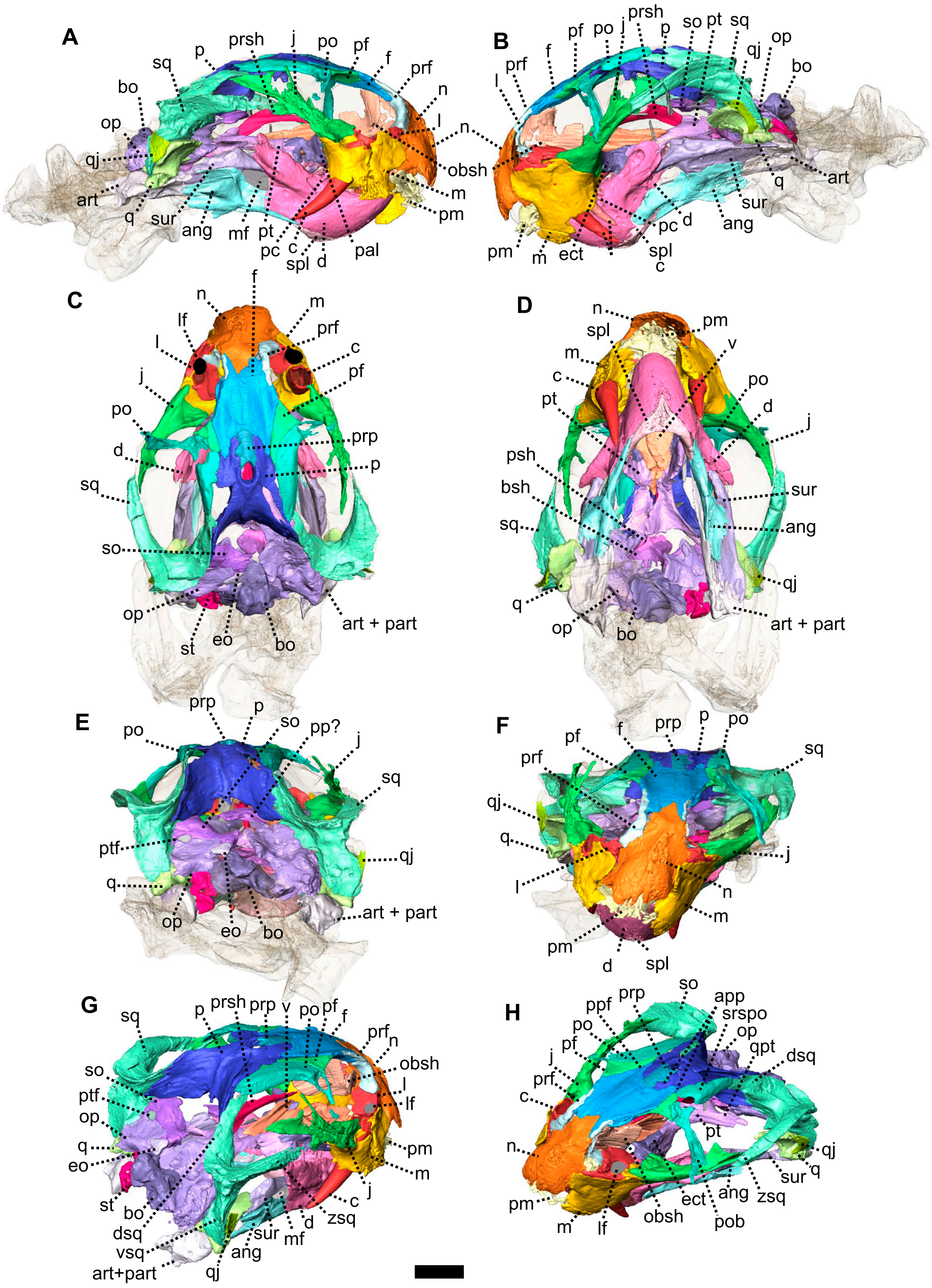

FIGURE 7

Eodicynodon oosthuizeni, BP/1/6230, from Bloukrans farm, Prince Albert district, Western Cape, South Africa; *Eodicynodon* AZ, Guadalupian, Beaufort Group, Karoo Supergroup. 3D rendering in **(A)**, right lateral view; **(B)**, left lateral view; **(C)**, dorsal view; **(D)**, ventral view; **(E)**, posterior view; **(F)**, anterior view; **(G)**, posterolateral view and **(H)**, dorsolateral view. Abbreviations: ang, angular; app, anterior process of the parietal; art, articular; bo, basioccipital; bot, basioccipital tubera; bsh, basisphenoid; c, caniniform tooth; d, dentary; dsq, dorsal process of the squamosal; ect, ectopterygoid; eo, exoccipital; f, frontal; j, jugal; l, lacrimal; lf, lacrimal foramen; m, maxilla; mf, mandibular fenestra; n, nasal; obsh, orbitosphenoid; op, opisthotic; p, parietal; pal, palatine; part, pre-articular; pc, postcanine; pf, postfrontal; pm, premaxilla; po, postorbital; pob, postorbital bar; pp, postparietal; ppf, posterior process of the frontal; ppm, palatal process of the premaxilla; prf, prefrontal; prp, preparietal; psh, parasphenoid; pt, pterygoid; ptf, postemporal fenestra; q, quadrate; qj, quadratojugal; qpt, quadrate process of the pterygoid; so, supraoccipital; sq, squamosal; srspo, skull roof section of the postorbital; st, stapes; sur, surangular; t, tabular; tpt, transverse process of the pterygoid; v, vomer; vkp, ventral keel of the palate; vsq, ventral process of the squamosal; zsq, zygomatic process of the squamosal. Scale bar = 1 cm.

origination; squamosal anterior process dorsoventrally compressed; squamosal with a distinct dorsolateral notch in posterior view; quadratojugal is plate-like distally; vomer forms the anterior margin of the interpterygoid vacuity; foramen magnum much taller than wide; splenial visible in lateral view near the jaw symphysis; medial section of the angular extends long and nearly reaches the symphysis; vertical lamina of the surangular absent; prearticular without a lateral exposure; premaxillary teeth absent; caniniforms long and tusk-like; postcanines reduced or absent; caniniform process present.

Eodicynodon Barry, 1974

Diagnosis—after Rubidge (1990a), intertemporal and interorbital regions broad with large parietal exposure; skull relatively deep and zygoma not emarginated as much as other dicynodonts; medially unfused premaxilla; anterior medial tip of premaxilla on the ventral side flattened to form a broad fan-shaped ridge which tapers posteriorly to a thin ridge which protrudes ventrally; no teeth on the anterior part of the premaxilla or dentary; postcanine teeth present, maxilla borders the lateral side of internal nares and separate the premaxillae and the palatines; vomers and premaxillae paired; stongly developed and ventrally directed lateral process of the pterygoid; palatine bulbous and rugose; median interpterygoidal crest enlarged to form a large ventral boss; squamosal separated from the maxilla by the jugal on the zygomatic arch; fully developed sliding contact between the quadrate and the articular condyle; postemporal foramen situated medially to suture between the squamosal and exoccipital; stapes often pierced by stapedial foramen; dentary with dentary shelf which has a triangular fossa on the posterodorsal side for insertion of the lateral external adductor muscle; and rounded dentary tables situated on anterodorsal side of each ramus of the lower jaw.

Eodicynodon oosthuizeni Barry, 1974

Holotype—ROZ 1, from the private collection of Mr. Roy Oosthuizeni, now curated at Iziko South African Museum in Cape Town, South Africa.

Referred Material—NMQR 2902 to 2912, NMQR 2978, NMQR 2988 to 2996, NMQR 2998 to 3003, 3005, 3007, 3014, 3026, 3094 and 3095, 3139, NMQR 3153 to 3155 to 3159, NMQR 3330, 3333, 3339, 3392, SAM-PK-011879, SAM-PK-K07914, SAM-PK-K10019, BP/1/5577, 5573, 5574, 6230, 6975, ROZ B95, ROZ 5, 7, 9 and 11.

Type locality—farm Zwartskraal, Prince Albert district, Western Cape, South Africa; *Eodicynodon* Assemblage Zone, Beaufort Group, Karoo Supergroup.

Diagnosis—after Rubidge (1990a), caniniform tusk-like teeth present; maxillary teeth commonly present and situated on lateral side of maxilla either posterior or medial to the tusk; palatal rim interrupted by a deep cleft in front of maxillary tusk; low coronoid eminence on posterodorsal surface of the dentary.

List of figures—Figures 7–19.

Description—The skull of two specimens of *E. oosthuizeni* are described in unprecedented detail thanks to CT-scanning and manual segmentation. These specimens of *E. oosthuizeni* were previously reported by Rubidge (1990b) and Jinnah and Rubidge (2007) and are from the *Eodicynodon* Assemblage Zone of the South African Karoo Beaufort Group.

Specimen BP/1/6230 is a small complete skull with lower jaw and associated postcranial elements (Figure 7). The skull is slightly distorted (Figure 7F) as the occipital bones have been flattened and shifted towards the horizontal plane by diagenesis (Figure 7E). The specimen was identified as a pathological double-tusked specimen of *E. oosthuizeni* (Jinnah and Rubidge, 2007). This interpretation has been supported by a more recent study (Olroyd et al., 2021).

Specimen NMQR 2978, comprising a complete skull without a lower jaw (Figure 8), was mentioned for the first time by Rubidge (1990b), along with other *E. oosthuizeni* specimens in a paper describing the general morphology of *E. oosthuizeni*. Preservation of the specimen is good, but the posterior left section of the skull (at the level of the postemporal fenestra) has been crushed. Part of the dorsal skull roof is damaged by an obscuring crack that made 3D reconstruction of this section difficult. As a result, a preparietal was not identified in the specimen, but is likely present. The temporal fenestra is about 1.5 times the size of the orbit. The following description is a composite of the best-preserved parts of the two specimens.

The premaxilla is an edentulous bone that forms the anteriormost part of the snout and encloses the anteroventral and anterior margin of the external naris. Ventrally, it forms a secondary palate that separates the nasal cavity from the oral cavity. The premaxilla, which is a paired bone as pointed out by Rubidge (1990b), is better preserved in NMQR 2978 than in BP/1/6230 (Figures 7, 8). In ventral view, the inter-premaxillary suture is straight and extends along the midline (Figure 9D) but does not reach the posterior margin of the premaxilla (Figures 8D, 9D) ending at the level of the anterior margin of the tusk. In anterior view, the contact between the two premaxillae is Y-shaped (Figures 8F, 9F). The premaxilla comprises the nasal and palatal processes (Figures 9, 10). The nasal process is not preserved in BP/1/6230.

The nasal process forms the anterior border of the external naris (Figures 8G, 9A, B). In anterior view, it extends dorsally into a thick internarial process that separates the two nares (Figure 9F). In anterior view, the premaxilla has an inverted U-shaped contact with the nasal dorsally (Figure 8F).

The palatal process forms the anteroventral margin of the naris (Figures 8G, H, 9A, B), is slightly concave and roughly triangular in ventral view (Figure 9D). It has an oblique contact with the maxilla posterolaterally, in both ventral and lateral views (Figure 9A, B, D).

The maxilla forms the posterior margin of the external naris (Figures 7, 8) and is triangular in ventral view (Figure 9D). In lateral view, the maxilla is roughly rectangular (Figures 10B, 9B) and has a well-formed oblique depression anterior to the tusk (Figure 9B). It contacts the nasal dorsally with an oblique suture (Figures 7A, 8A). In lateral view, the maxilla has a long horizontal posterodorsal contact with the lacrimal at the level of the tusk (Figure 8A, B) and meets the jugal posteriorly (Figure 9A). The contact is oblique in both lateral and posterior views (Figures 8H, 9B, E, 10B, E). In ventral view, the maxilla sutures with the premaxilla anteromedially (Figures 10D, 9D) and the contact is oblique in both dorsal and ventral views (Figure 9C, D).

On the ventral side, the maxilla bears a large posteromedial ovoid depression to accommodate the palatine (Figures 8D, 9D) and has a short contact with the ectopterygoid posteriorly (Figures 8D, 18G). This contact is longer and vertical in lateral view (Figure 8A, H). The maxilla bears tusks and postcanines in

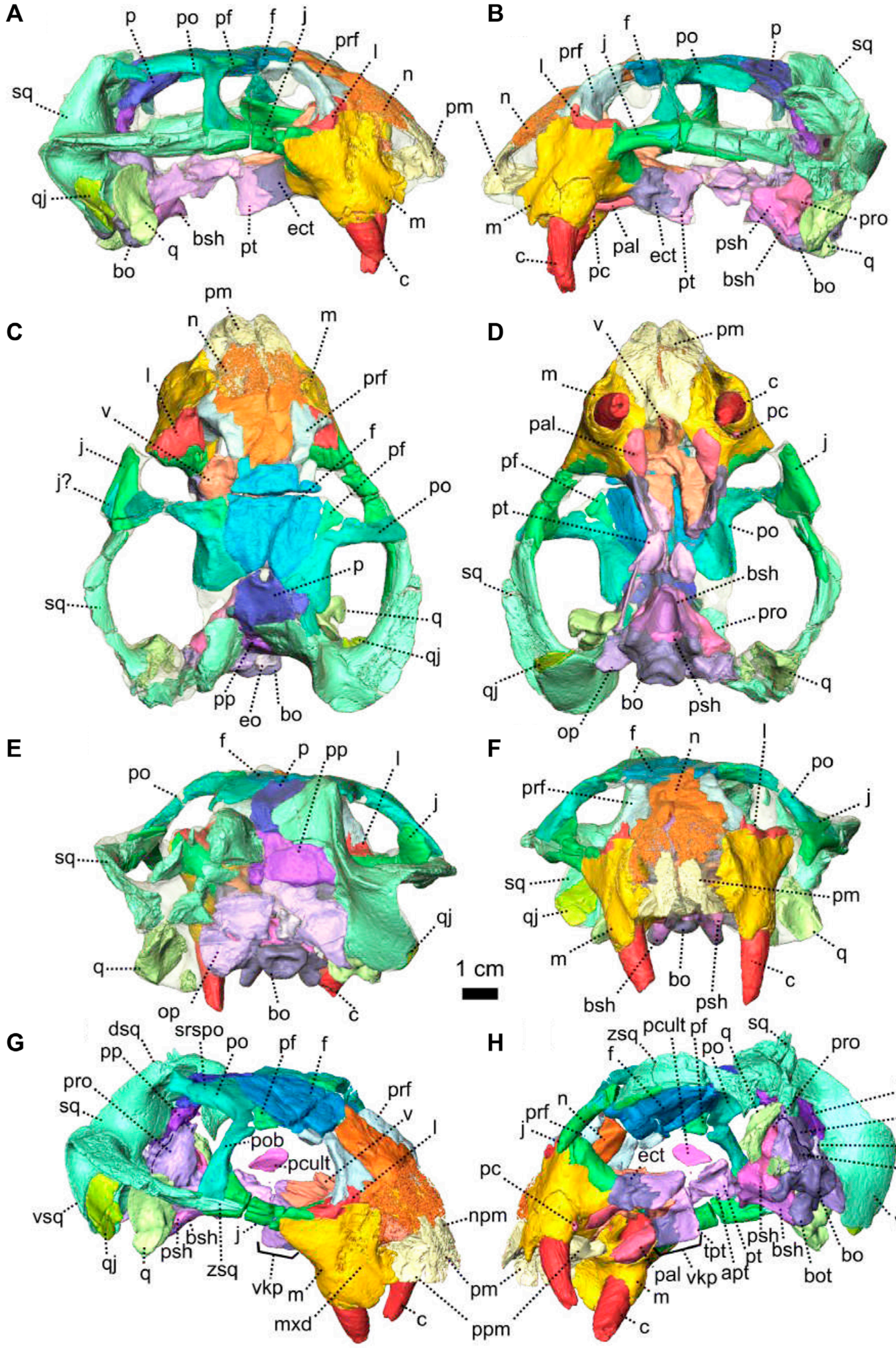

FIGURE 8
Eodicynodon oosthuizeni, NMQR 2978, farm Rietkuil (previously named Zwartgrond), Rietbron district, Eastern Cape, South Africa; *Eodicynodon* AZ, Guadalupian, Beaufort Group, Karoo Supergroup. 3D rendering in **(A)**, right lateral view; **(B)**, left lateral view; **(C)**, dorsal view; **(D)**, ventral view; **(E)**, posterior view; **(F)**, anterior view; **(G)**, anterolateral view and **(H)**, posteroventral view. Abbreviations: Abbreviations: apt, anterior process of the pterygoid; bo, basioccipital; bot, basioccipital tubera; bsh, basisphenoid; c, caniniform tooth; dsq, dorsal process of the squamosal; ect, ectopterygoid; eo, exoccipital; f, frontal; j, jugal; l, lacrimal; m, maxilla; mxd, maxilla depression; n, nasal; npm, nasal process of the premaxilla; op, opisthotic; p, parietal; pal, palatine; pc, postcanine; pcult, processus cultriformis; pf, postfrontal; pm, premaxilla; po, postorbital; pob, postorbital bar; pp, postparietal; ppm, palatal process of the premaxilla; prf, prefrontal; pro, prootic; prp, preparietal; psh, parasphenoid; pt, pterygoid; q, quadrate; qj, quadratojugal; qpt, quadrate process of the pterygoid; so, supraoccipital; sq, squamosal; srspo, skull roof section of the postorbital; sur, surangular; t, tabular; tpt, transverse process of the pterygoid; v, vomer; vkp, ventral keel of the palate; vsq, ventral process of the squamosal; zsq, zygomatic process of the squamosal. Scale bar = 1 cm.

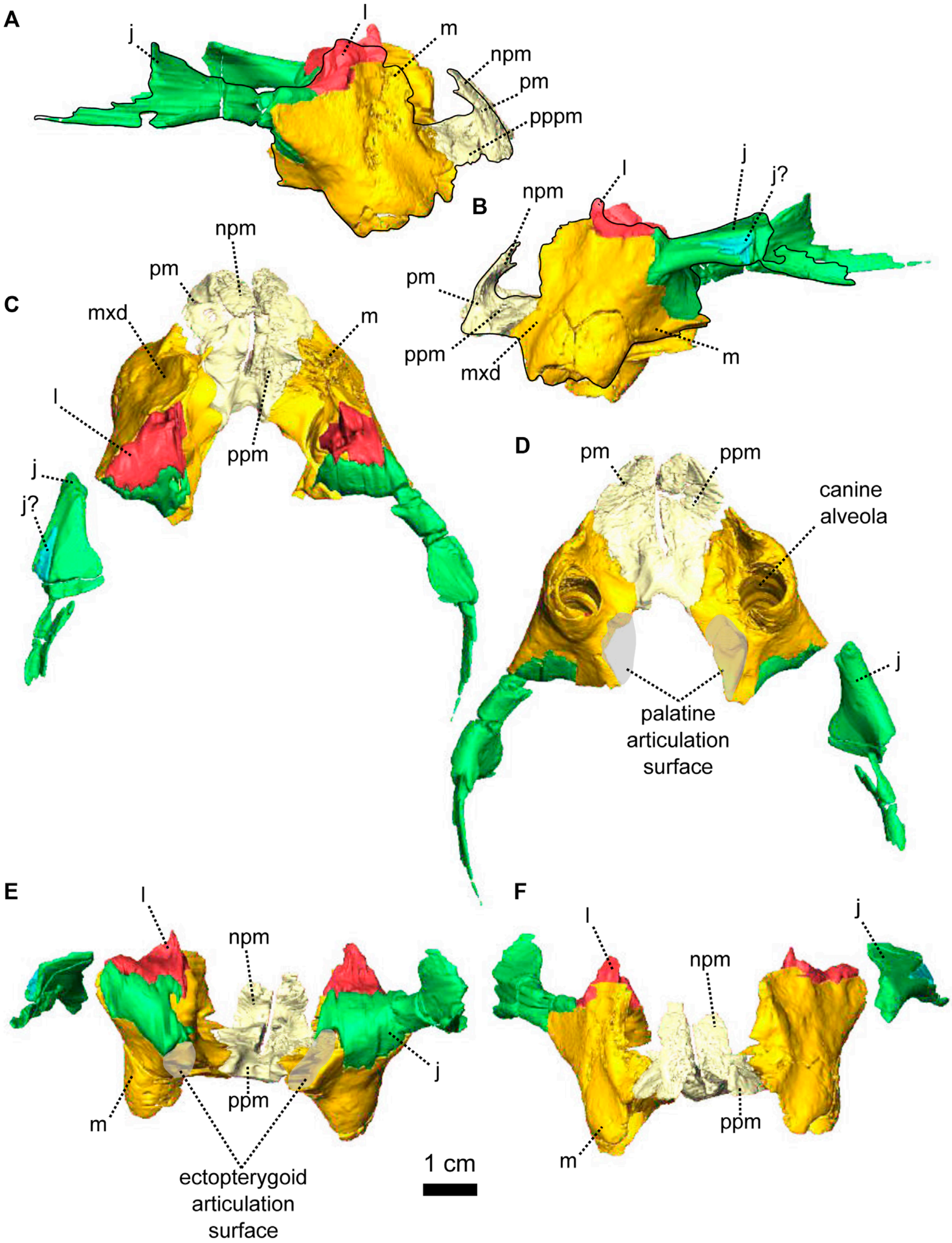

FIGURE 9
Paired maxillae and associated masticatory elements of *Eodicynodon oosthuizeni*, NMQR 2978, farm Rietkuil (previously named Zwartgrond), Rietbron district, Eastern Cape, South Africa; *Eodicynodon* AZ, Guadalupian, Beaufort Group, Karoo Supergroup. 3D rendering in **(A)**, right lateral view; **(B)**, left lateral view; **(C)**, dorsal view; **(D)**, ventral view; **(E)**, posterior view and **(F)**, anterior view. Abbreviations: j, jugal; l, lacrimal; m, maxilla; mxd, maxilla depression; n, nasal; npm, nasal process of the premaxilla; pm, premaxilla; ppm, palatal process of the premaxilla. Scale bar = 1 cm.

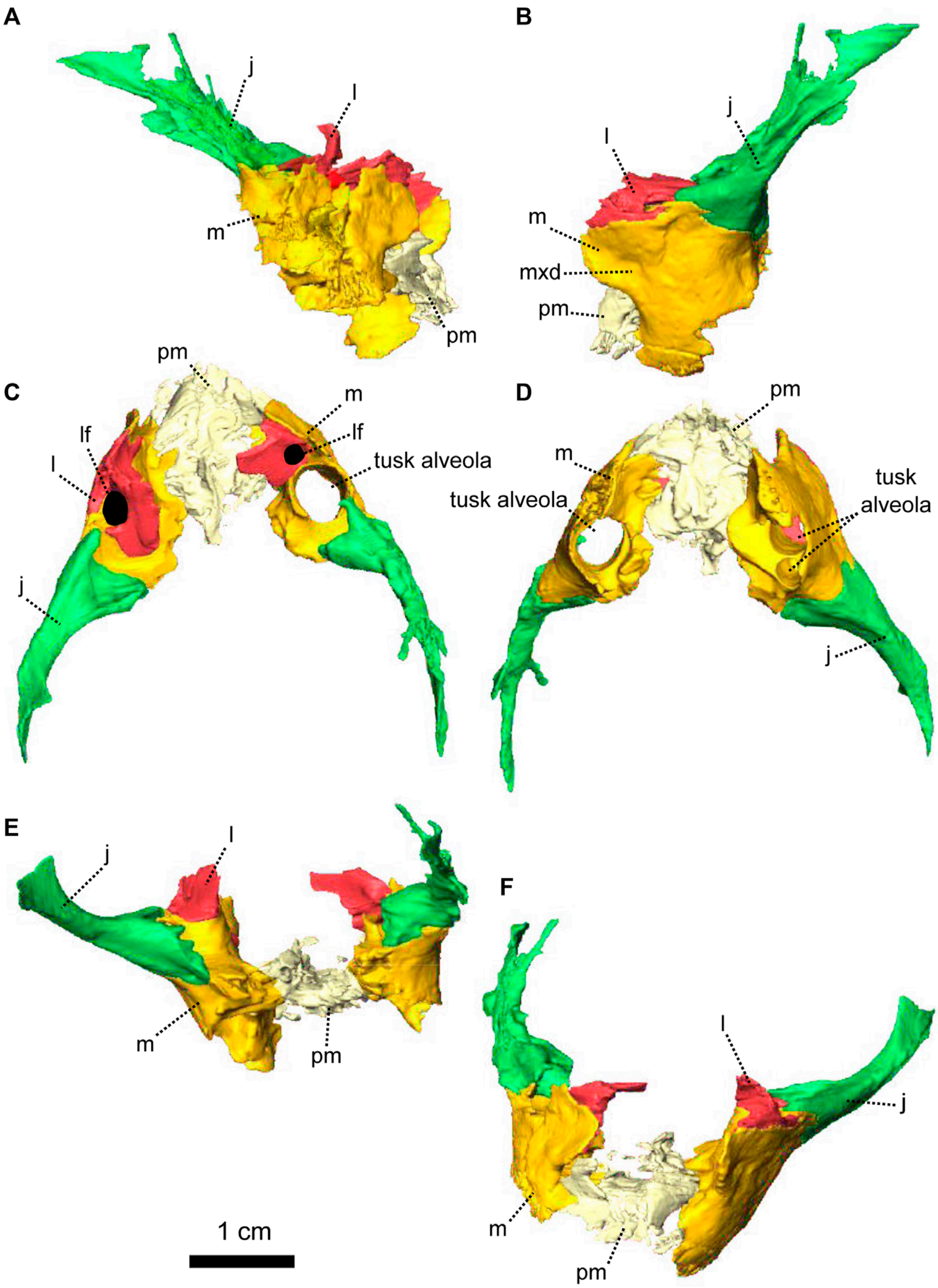

FIGURE 10
Paired maxillae and associated masticatory elements of *Eodicynodon oosthuizeni*, BP/1/6230, from Bloukrans farm, Prince Albert district, Western Cape, South Africa; *Eodicynodon* AZ, Guadalupian, Beaufort Group, Karoo Supergroup. 3D rendering in **(A)**, right lateral view; **(B)**, left lateral view; **(C)**, dorsal view; **(D)**, ventral view; **(E)**, posterior view; **(F)**, anterior view. Abbreviations: j, jugal; l, lacrimal; m, maxilla; mxd, maxilla depression; n, nasal; npm, nasal process of the premaxilla; pm, premaxilla; ppm, palatal process of the premaxilla. Scale bar = 1 cm.

both BP/1/6230 and NMQR 2978, but specimen BP/1/6230 has an additional pathological tusk on the left (Figures 7, 8).

The nasal is a paired bone that forms most of the anterodorsal part of the snout (Figures 7, 8, 13, 14) and makes up the dorsal margin of the naris (Figures 7A, B, 8A, B). In lateral view, the nasal has a small anteroventral triangular extension, posterior to the naris (Figure 9B). This extension is overlapped by the maxilla ventrally in both lateral and anterior views (Figures 8B, F, 7A, F). In dorsal view, the nasal contacts the prefrontal posterolaterally with a slightly oblique contact (Figure 13C). Posteriorly, the nasal contacts the frontal (Figure 14) and in both dorsal and anterior views, the contact forms an inverted V (Figure 14C, F).

The lacrimal is a relatively small horizontal bone in *E. oosthuizeni* and does not extend dorsally as far as in *Patranomodon* (Figures 2, 9). It forms the anteroventral margin of the orbit (Figures 7G, 9) and in lateral view, has a long horizontal ventral contact with the maxilla (Figure 9B). In posterolateral view, the nasal has a horizontal contact with the prefrontal dorsally, at the level of the lacrimal foramen (Figures 7G). In dorsal view, the lacrimal is roughly triangular and has an oblique contact with the jugal posteriorly (Figure 9C) and transverse in posterior view (Figure 9E). The lacrimal foramen is present as a large circular opening (Figure 7A).

The jugal forms the ventral margin of the orbit, the anterior-most section of the zygomatic arch (Figures 7, 8) and makes up the anteroventral margin of the temporal fenestra (Figures 7B, 8B). In lateral view, the jugal contacts the maxilla anteriorly with an oblique contact (Figure 10B). Half-way along the length of the jugal, it contacts the postorbital bar dorsally with a horizontal suture (Figure 8A, B, G). In lateral view, the jugal has a horizontal depression posteriorly to accommodate the zygomatic ramus of the squamosal (Figures 7B, 8B, 10B). In dorsal view, the jugal contacts the lacrimal anteriorly (Figure 9C) and in ventral view, the jugal contacts the maxilla at the level of the palatine bosses (Figures 9D, 10D).

The postorbital makes up part of the skull roof above the anterior end of the temporal opening and comprises the entire postorbital bar (Figures 7, 8, 13, 14). In dorsal view, it contacts the postfrontal anteromedially with a curved suture, reaches the parietal medially with a slightly oblique contact (Figure 14C) and has a short contact with the dorsal process of the squamosal posteriorly (Figures 7C, 8C). The postorbital bar separates the orbit from the temporal fenestra (Figures 7H, 8G). In lateral view, the postorbital bar thickens as it contacts the jugal ventrally with a horizontal suture (Figure 8A, B) and a marked vertical groove is present on the postorbital bar (Figure 14B). In ventral view, the skull roof section of the postorbital shows a prominent depression, with the lateral margin being thicker than the medial margin, which meets the parietal medially (Figures 13D, 14D).

The squamosal of BP/1/6230 and NMQR 2978, folds around the back of the skull, enclosing the temporal fenestra posteriorly (Figures 7, 8, 11) as in other dicynodonts (Hammer and Cosgriff, 1981; Angielczyk, 2007; Kammerer et al., 2011; Castanhinha et al., 2013; Hancox et al., 2013; Boos et al., 2016; Olroyd et al., 2018). Similar to the situation in other dicynodonts, the squamosal of *E. oosthuizeni* comprises three thin processes: the flat zygomatic, dorsal, and ventral processes (Figures 7G, 8G, H, 11, 12). The zygomatic process of the squamosal extends anteriorly and makes up the posteroventral margin of the temporal fenestra (Figures 7B, G, H, 8B, G). In dorsal view, the zygomatic process has a flat anteromedial contact with the jugal (Figure 8C). In posterior view, the dorsal process of the squamosal folds anterodorsally (Figure 8E) and is overlapped medially by the parietal-postparietal complex (Figure 7C, E). In dorsal view, the dorsal process of the squamosal has a short anterior contact with the postorbital (Figure 7C). In posterior view, the spatulate ventral process extends ventrally (Figures 12E, 11E) and contacts the supraoccipital and the opisthotic medially (Figures 12E, 11E). In lateral view, the squamosal masks both the dorsal plate of the quadrate and the quadratojugal (Figures 11, 12), and the ventral process of the squamosal slopes at an angle of 45° to the vertical plane (Figure 11A).

The orbital region of both BP/1/6230 and NMQR 2978 is well preserved (Figures 7, 8). With the exception of the sclerotic rings all the bones surrounding the orbit and eye are present. The postorbital bar, which closes the orbit posteriorly, is broken on BP/1/6230 and does not reach the zygomatic bar (Figure 7C) but for *E. oosthuizeni*, the orbit is surrounded by the jugal and lacrimal anteriorly, the prefrontal, frontal and postfrontal dorsally, and the postorbital posteriorly.

The prefrontal forms the anterior border of the orbit (Figures 7G, B, 8, 5A, 13) and is roughly triangular in lateral view (Figure 13B). The prefrontal contacts the lacrimal above the lacrimal foramen (Figure 7G, H). The contact is oblique in lateral and anterolateral view (Figure 8A, B, G). In dorsal view, the prefrontal contacts the nasal medially with an oblique contact (Figure 13C) and extends posteriorly to contact the frontal.

With the parietal, the frontal is the largest bone of the *Eodicynodon* skull (Figures 7, 8, 13, 14) and makes up the dorsal margin of the orbit (Figures 7A, B, C, H). Although the frontal is a paired bone in dicynodonts, the midline suture between the two frontals could not be determined in BP/1/6230, and the frontal of NMQR 2978 is damaged by a crack (Figures 13, 14). In dorsal view, the frontal contacts the nasal anteriorly with a V-shaped suture (Figures 14C, 13C) and has a short contact with the prefrontal anterolaterally (Figure 14A, B, C). In dorsal, lateral and ventral views, the frontal overlaps the postfrontal posterolaterally with an oblique contact in dorsal view (Figures 14A, C, D, 16C) and meets the preparietal posteriorly with a curved contact (Figure 14C). In ventral view, the contact between the frontal and the preparietal could not be determined (Figure 14D). In dorsal view, the posterior process of the frontal wedges between the postfrontal laterally and the parietal medially, with its apex bordering on the pineal foramen. This process is not visible in ventral view (Figure 14D) and implies that the posterior process of the frontal overlaps the dorsal side of the parietal (Figure 16C). In ventral view, the transverse suture between the frontal and the parietal is straight (Figure 14D) and the frontal bears a lateral ridge that extends from the nasal anteriorly, to the parietal-frontal suture posteriorly (Figure 14D). This ridge (often not preserved in dicynodonts) houses a neurovascular canal (*ramus supraorbitalis*) and borders the forebrain laterally up to the olfactory bulbs (Laaß et al., 2017; de Simão-Oliveira et al., 2019; Pusch et al., 2019).

The postfrontal forms the posterodorsal margin of the orbit between the frontal anteriorly and the postorbital posteriorly (Figures 7, 8, 13, 14). In dorsal view, it is triangular and contacts the frontal anteromedially with an oblique suture (Figure 14C).

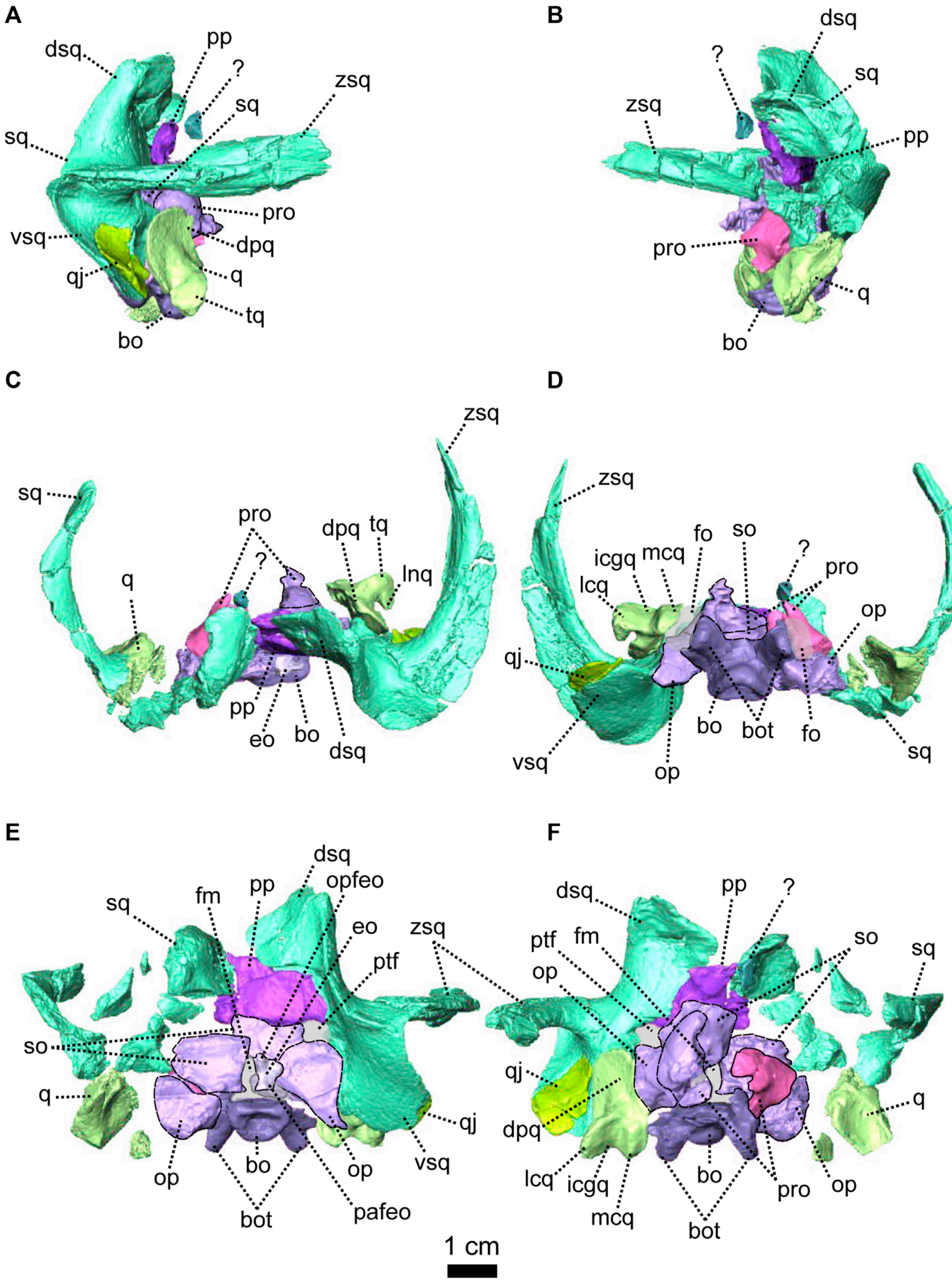

FIGURE 11
Occipital bones of *Eodicynodon oosthuizeni*, NMQR 2978, farm Rietkuil (previously named Zwartgrond), Rietbron district, Eastern Cape, South Africa; *Eodicynodon* AZ, Guadalupian, Beaufort Group, Karoo Supergroup. 3D rendering in **(A)**, right lateral view; **(B)**, left lateral view; **(C)**, dorsal view; **(D)**, ventral view; **(E)**, posterior view and **(F)**, anterior view. Abbreviations: bo, basioccipital; bot, basioccipital tubera; dpq, dorsal plate of the quadrate; dsq, dorsal process of the squamosal; eo, exoccipital; fm, foramen magnum; fo, fenestra ovalis; icgq, intercondylar groove of the quadrate; lcq, lateral condyle of the quadrate; mcq, medial condyle of the quadrate; op, opisthotic; opfeo, opisthotic facet of the exoccipital; pp, postparietal; pro, prootic; ptf, postemporal fenestra; q, quadrate; qj, quadratojugal; so, supraoccipital; sq, squamosal; vsq, ventral process of the squamosal; zsq, zygomatic process of the squamosal. Scale bar = 1 cm.

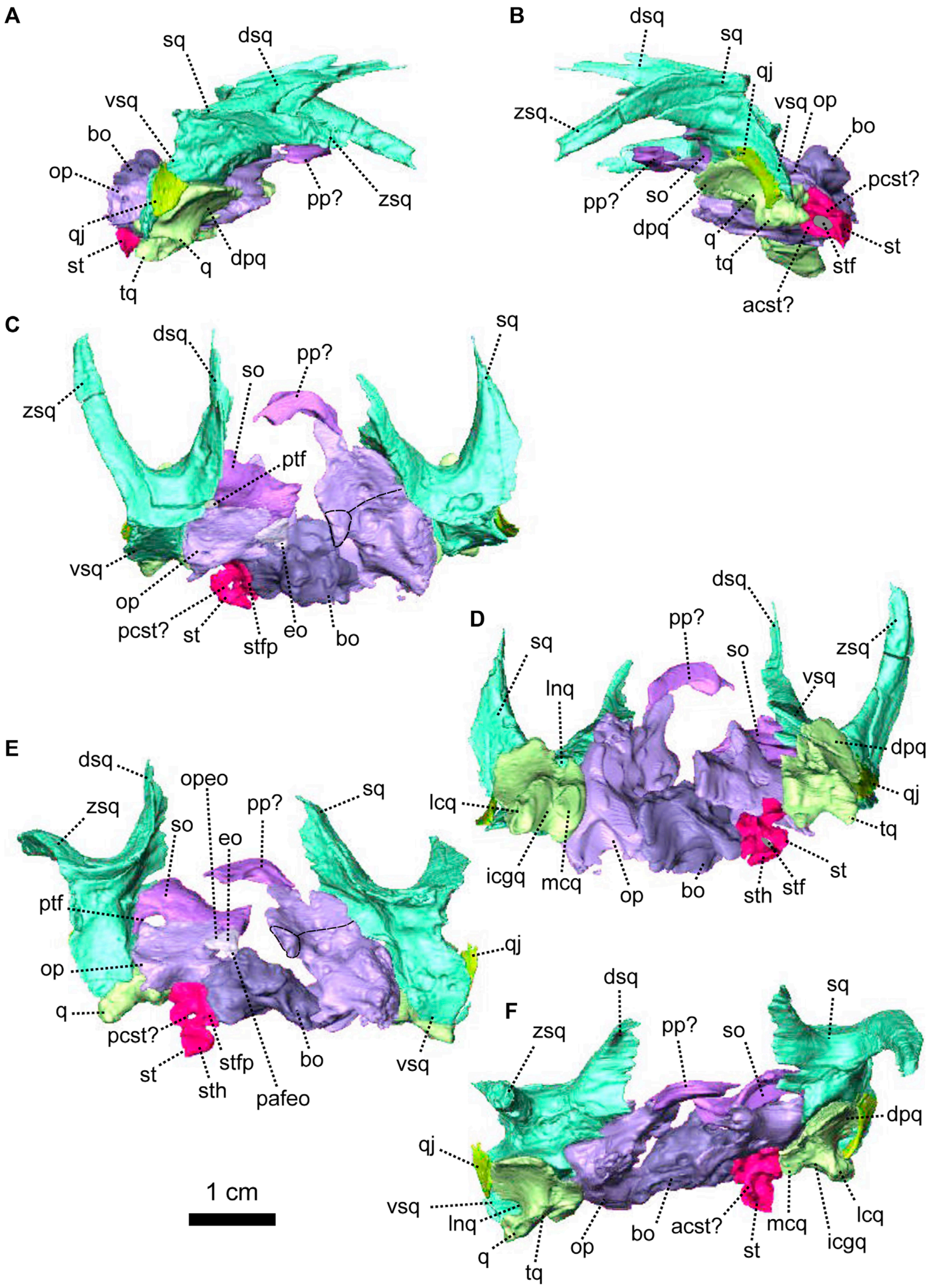

FIGURE 12
Occipital bones of *Eodicynodon oosthuizeni*, BP/1/6230, from Bloukrans farm, Prince Albert district, Western Cape, South Africa; *Eodicynodon* AZ, Guadalupian, Beaufort Group, Karoo Supergroup. 3D rendering in **(A)**, right lateral view; **(B)**, left lateral view; **(C)**, dorsal view; **(D)**, ventral view; **(E)**, posterior view and **(F)**, anterior view. Abbreviations: acst, anterior crus of the stapes; bo, basioccipital; dpq, dorsal plate of the quadrate; dsq, dorsal process of the squamosal; eo, exoccipital; icgq, intercondylar groove of the quadrate; lcq, lateral condyle of the quadrate; lnq, lateral notch of the quadrate; mcq, medial condyle of the quadrate; opfeo, opisthotic facet of the exoccipital; pafeo, pro-atalas facet of the exoccipital; pcst, posterior crus of the stapes; pp, postparietal; pro, prootic; ptf, postemporal fenestra; q, quadrate; qj, quadratojugal; so, supraoccipital; st, stapes; sth, stapedial head; stf, stapedial foramen; stfp, stapedial footplate; sq, squamosal; vsq, ventral process of the squamosal; zsq, zygomatic process of the squamosal. Scale bar = 1 cm.

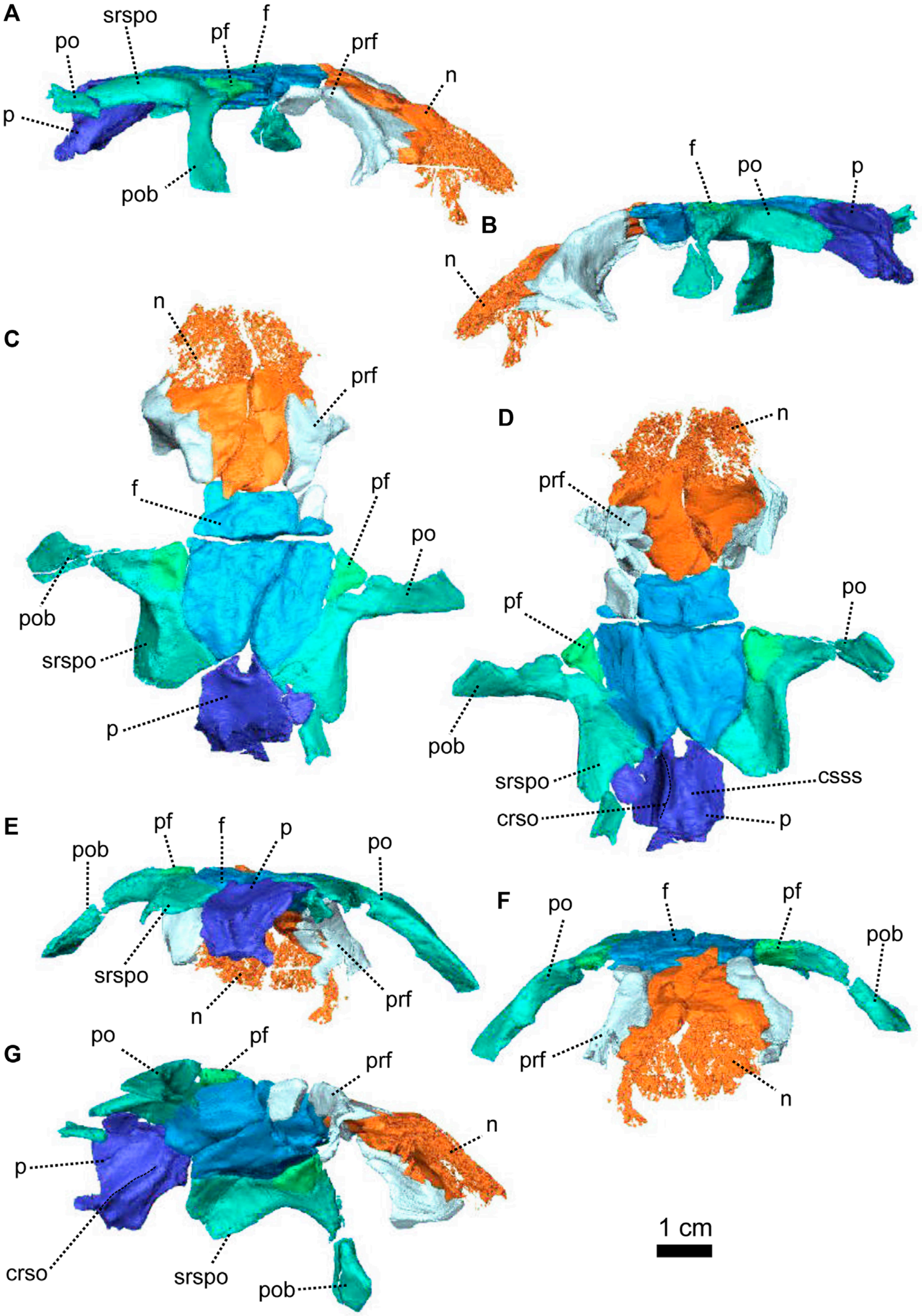

FIGURE 13
Parietal and associated dorsal elements of *Eodicynodon oosthuizeni*, NMQR 2978, farm Rietkuil (previously named Zwartgrond), Rietbron district, Eastern Cape, South Africa; *Eodicynodon* AZ, Guadalupian, Beaufort Group, Karoo Supergroup. 3D rendering in **(A)**, right lateral view; **(B)**, left lateral view; **(C)**, dorsal view; **(D)**, ventral view; **(E)**, posterior view; **(F)**, anterior view and **(G)**, anteroventral view, anteroventral view. Abbreviations: crso, canal for the ramus supraorbitalis; f, frontal; n, nasal; p, parietal; pf, postfrontal; po, postorbital; pob, postorbital bar; prf, prefrontal; srspo, skull roof section of the postorbital. Scale bar = 1 cm.

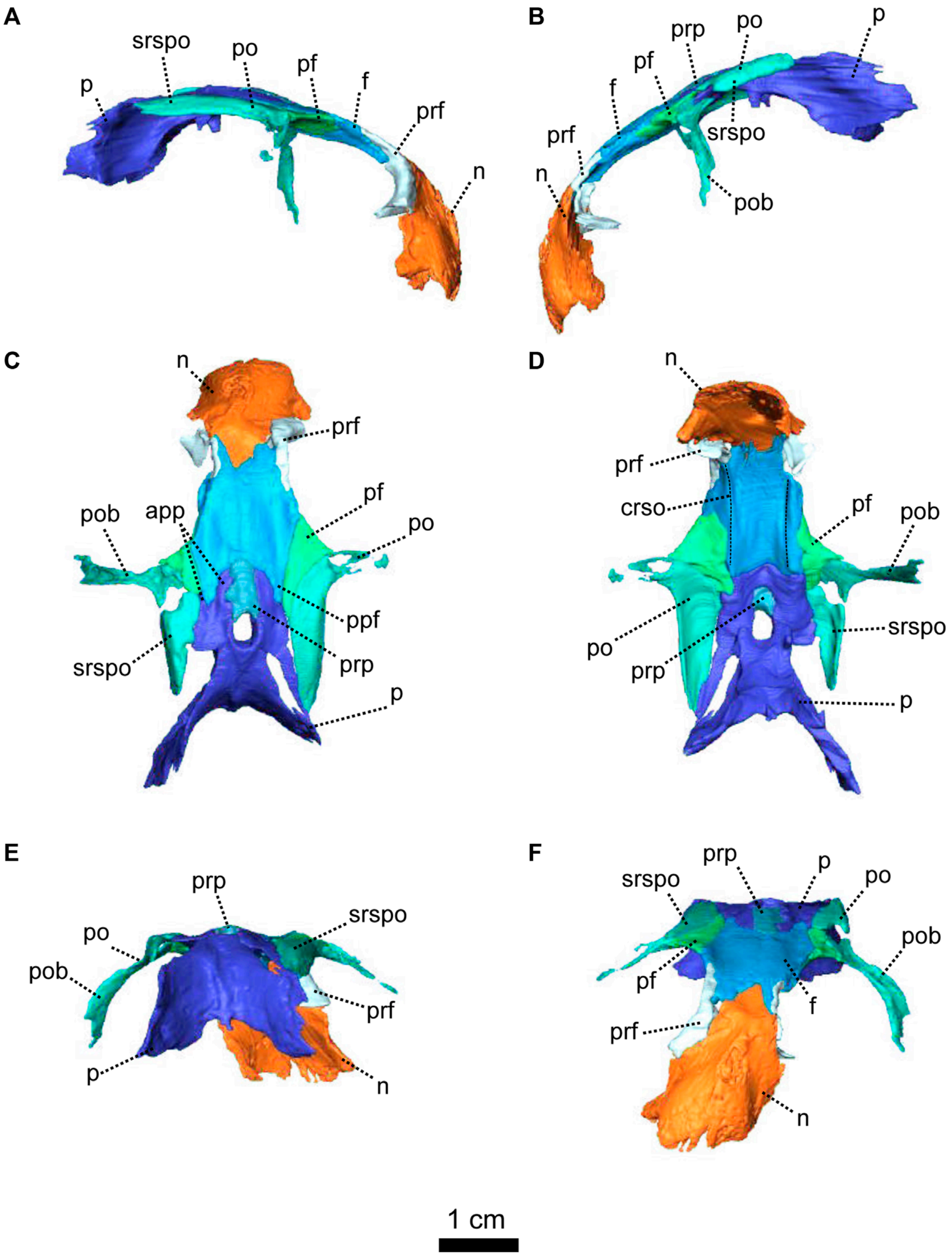

FIGURE 14
Parietal and associated dorsal elements of *Eodicynodon oosthuizeni*, BP/1/6230, from Bloukrans farm, Prince Albert district, Western Cape, South Africa; *Eodicynodon* AZ, Guadalupian, Beaufort Group, Karoo Supergroup. 3D rendering in **(A)**, right lateral view; **(B)**, left lateral view; **(C)**, dorsal view; **(D)**, ventral view; **(E)**, posterior view and **(F)**, anterior view. Abbreviations: app, anterior process of the parietal; crso, canal for the ramus supraorbitalis; f, frontal; n, nasal; p, parietal; pf, postfrontal; ppf, posterior process of the frontal; po, postorbital; pob, postorbital bar; prf, prefrontal; prp, preparietal; srspo, skull roof section of the postorbital. Scale bar = 1 cm.

Symmetrically, in dorsal view, the postfrontal has a curved posteromedial contact with the postorbital and a short contact with the parietal posteriorly (Figure 14C). In lateral and ventral views, the postfrontal is overlapped by the frontal anteromedially (Figure 14A, C).

The preparietal, positioned along the midline between the anterior processes of the paired parietals, is a narrow rectangular bone in dorsal view (Figures 7, 14) and square in ventral view (Figure 14C, D). It forms the anterior margin of the pineal foramen (Figure 14C, D). In dorsal view, the preparietal has a longitudinal contact with the parietal and meets the frontal with a curved suture (Figure 14C). In ventral view, the anterior part of the preparietal is covered by the parietal and the preparietal does not reach the frontal (Figure 14D). This may be an artefact of segmentation, as this feature is absent on other well-preserved anomodonts (see Figure 3D; Castanhinha et al., 2013).

The parietal forms the lateral and posterior margins of the pineal foramen (Figures 13, 14) and comprises most of the intertemporal region (Figure 13C). As in the case of the frontal, the midline suture is not visible and the parietal appears to be unpaired (Figures 13, 14). In BP/1/6230, no sutures between the parietal and the postparietal could be recognised on the CT-scan, so the parietal is likely to be co-ossified with the postparietal (Figure 7E). In dorsal view, the anterior process of the parietal extends anteriorly between the preparietal medially and the frontal laterally (Figure 14C) but is notably absent in ventral view (Figure 14D). In dorsal view, the parietal has a short posterior contact with the postparietal and a longer oblique contact with the postorbital (Figure 14C). In posterior view, the parietal, which has a vertical medial nuchal crest (Figures 7E, 14E), overlaps the dorsal process of the squamosal laterally (Figure 7E) and meets the postparietal ventrally (Figure 8E). In ventral view, the parietal manifests a thick rectangular process (Figures 14D, 13D). It bears the curved canals for the *ramus supraorbitalis* laterally and the groove for the superior sagittal sinus medially (Figure 13D, G). In the same view, the parietal has two small bosses that are likely to be part of the epipterygoid (Figures 14D, 16C).

The occiput of NMQR 2978 is poorly preserved, apart from the basioccipital and the prootic (Figures 8, 11). The tabular and the left exoccipital are not preserved (Figure 11E). As in most dicynodonts, the supraoccipital, opisthotic and prootic are co-ossified, and no sutures could be identified on the CT slices (Figure 11).

The occiput of BP/1/6230 is vertically crushed and compressed (Figure 7) and the tabular, postparietal, prootic and right stapes are missing and several bones have been damaged such as the supraoccipital which has been shattered (Figure 12). The right supraoccipital and opisthotic are co-ossified, and it appears that the postparietal is co-ossified with the parietal. The jaw articulation (quadrate and quadratojugal) and the squamosal are well preserved, and the left postemporal fenestra is undeformed and well preserved (Figures 7E, 12E).

The postparietal, which is poorly preserved in NMQR 2978 (Figures 11, 15), is rectangular in posterior view (Figure 11E). The bone surface is smooth in posterior view, but shattered in anterior view (Figure 11E, F). The postparietal of NMQR 2978 is displaced so that it abnormally overlaps the supraoccipital and forms the dorsal margin of the postemporal fenestra ventrally (Figures 21E, F, 15). In posterior view, the postparietal contacts the dorsal ramus of the squamosal laterally (Figure 11E). The contact is slightly oblique in both occipital and anterior views (Figure 11E, F).

The supraoccipital is poorly preserved in both *E. oosthuizeni* specimens and forms the dorsal margin of the postemporal fenestra (Figures 12E, 11E). In NMQR 2978, the supraoccipital is fused with the opisthotic and right prootic (Figure 11). In BP/1/6230, the right supraoccipital is fused with the opisthotic and the exoccipital (Figure 12). In posterior view, the supraoccipital forms the lateral margin of the triangular foramen magnum (Figure 12E) and contacts the exoccipital medioventrally (Figures 12E, 11E). It contacts the opisthotic ventrally with a horizontal suture laterally, that becomes oblique towards the exoccipital (Figure 12E). Similar to *Patranomodon*, the supraoccipital in *E. oosthuizeni* forms the posterior margin of the floccular cavity, where it contacts or fuses with the prootic (Figure 15A, B).

The walls of the floccular cavity, formed by the supraoccipital and the prootic, are relatively thicker in *E. oosthuizeni* than in *Patranomodon* and *E. oosthuizeni* it has a relatively smaller floccular cavity (Figures 4, 11, 12, 15).

Apart from the left prootic of NMQR 2978, the prootic of *E. oosthuizeni* is fused to the supraoccipital and the opisthotic (Figures 11, 12, 15). It forms the anterior walls of the floccular cavity and the vestibule (Figure 15B, D). The anterior, dorsal and lateral process of the prootic are smooth and less pronounced than in *Patranomodon* (Figures 4, 5, 11, 15). The pila antotica is not preserved and no foramina could be observed on the CT-images.

In ventral and anterior views, the prootic encloses the fenestra ovalis dorsally (Figures 11D, F, 15B). In lateral view, the prootic contacts the parasphenoid anteroventrally with an S-shaped suture (Figure 8B, G). In dorsolateral view the anterior process of the prootic contacts the parasphenoid, so that it encloses the base of the hindbrain area (Figure 15D). Also in dorsolateral view, the prootic contacts the opisthotic posteriorly, at the level of the vestibule. In anterior view, the prootic contacts the basioccipital ventrally (Figure 11F).

The opisthotic forms the ventral margin of the postemporal fenestra and is partially fused to the prootic, supraoccipital and exoccipital (Figures 11, 12, 15). Its ventral surface is curved, in between a lateroventral and a medioventral process (Figure 11D). In ventral view, the opisthotic forms the posterior border of the fenestra ovalis (Figures 11D, 15A).

In posterior view, the opisthotic supports the exoccipital medially and contacts the basioccipital ventromedially (Figures 12E, 11E) with a short and oblique suture in ventral and posterior views (Figures 12D, E, 11D, E). In the latter view, the opisthotic has a vertical lateral contact with the ventral process of the squamosal (Figures 12E, 11E). In dorsolateral view, the opisthotic forms the posterior wall of the vestibule, where it contacts the prootic (Figure 15A, D).

The exoccipital forms the lateral margin of the foramen magnum (Figures 12E, 11E). It is partially fused to the opisthotic (the right exoccipital cannot be differentiated from the opisthotic in BP/1/6230). In posterior view, the exoccipital is triangular, the proatlas facet is narrow while the opisthotic facet is broad (Figures 12E, 11E). The exoccipital has a short contact with the supraoccipital dorsally (Figure 12E). In the same view, it contacts the opisthotic laterally and the basioccipital ventrally. The contact

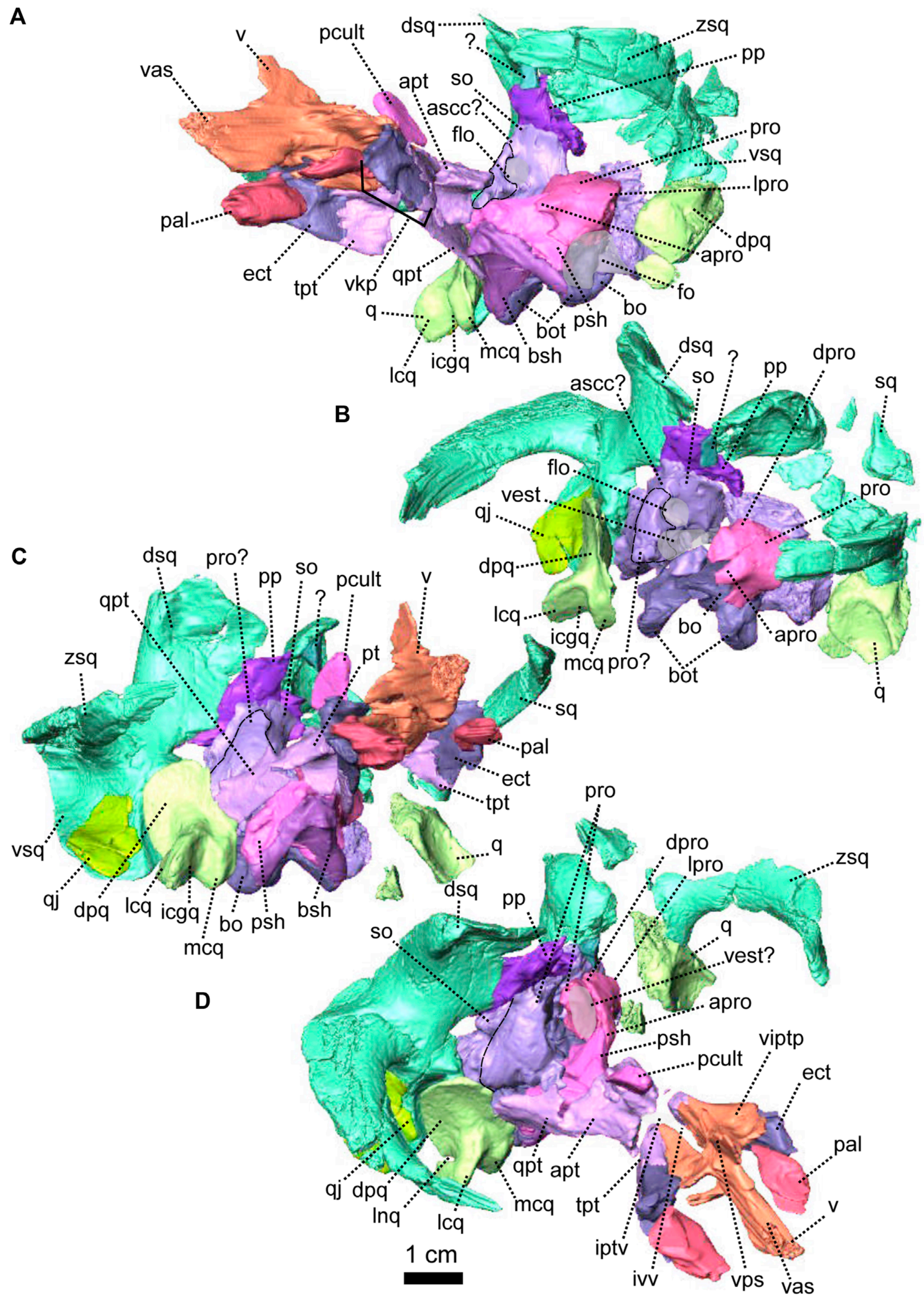

FIGURE 15
Occipital and palatal bones of *Eodicynodon oosthuizeni*, NMQR 2978, farm Rietkuil (previously named Zwartgrond), Rietbron district, Eastern Cape, South Africa; *Eodicynodon* AZ, Guadalupian, Beaufort Group, Karoo Supergroup. 3D rendering in **(A)**, left lateroventral view; **(B)**, left dorsolateral view; **(C)**, right lateroventral view and **(D)**, right laterodorsal view. Abbreviations: apro, anterior process of the prootic; apt, anterior process of the pterygoid; bo, basioccipital; bot, basioccipital tubera; bsh, basisphenoid; dpq, dorsal plate of the quadrate; dpro, dorsal process of the prootic; dsq, dorsal process of the squamosal; ect, ectopterygoid; fo, fenestra ovalis; icgq, intercondylar groove of the quadrate; iptv, interpterygoid vacuity; ivv, intervomerine vacuity; lcq, lateral condyle of the quadrate; lnq, lateral notch of the quadrate; lpro, lateral bulge of the prootic; mcq, medial condyle of the quadrate; pal, palatine; pcult, processus cultriformis; pro, prootic; psh, parasphenoid; pt, pterygoid; q, quadrate; qj, quadratojugal; qpt, quadrate process of the pterygoid; so, supraoccipital; sq, squamosal; tpt, transverse process of the pterygoid; v, vomer; vas, vomer anterior septum; vest, vestibule; vitptp, vomer inter-pterygoid plate; vkp, ventral keel of the palate; vps, vomer posterior septum; vs., vomerine septum; vsq, ventral process of the squamosal; zsq, zygomatic process of the squamosal. Scale bar = 1 cm.

with the opisthotic is oblique while the contact with the basioccipital is short.

The basioccipital forms the ventral margin of the foramen magnum and the floor of the hindbrain region (Figures 11, 15). It comprises an anterior process and three lobes: the occipital condyle, and two basioccipital tubera (Figure 11). The dorsal surface of the basioccipital has been greatly eroded on both BP/1/6230 and NMQR 2978 specimens (Figures 11C, 12C). In ventral view, the basioccipital forms the medial border of the fenestra ovalis (Figure 11D). In posterior view, the basioccipital has a short contact with the proatlas facet of the exoccipital and contacts the opisthotic dorsolaterally with a short and oblique contact (Figure 12E). Below this contact, the basioccipital reaches the stapedial footplate. In ventral view, the occipital condyle is thick and extends posteriorly and has a large and rounded occipital pit which is visible in posterior view (Figure 11D, E). In ventral view, the basioccipital tubera extends anteroventrally from the lateral side of the basioccipital (Figure 11E) and the two tubera make an angle of 20° with the frontal plane (Figure 11E). In ventral view, the basioccipital tubera reach the parasphenoid anteriorly, with a transverse contact in ventral view, while this contact is oblique in lateral view (Figure 8B, D). In anterior view, the main corpus of the basioccipital has a short contact with the prootic laterally (Figure 8F), the contact being horizontal in lateral view (Figure 11B).

The stapes is a small bone linking the quadrate (external ear) to the soft inner ear in anomodonts. It is preserved in only four *Eodicynodon* specimens: ROZ 9, NMQR 3001, NMQR 2912 and R0Z B95 (Rubidge, 1990b). The stapes is not preserved in NMQR 2978 (Figures 8, 11) and only the left stapes is preserved in BP/1/6230 (Figures 7, 12, 16). It is deformed and displaced, but has a general bicrurate shape, in contrast to derived dicynodonts that have a rod-like shaped stapes (Castanhinha et al., 2013).

In lateral view, similarly to *Patranomodon*, the stapes comprises an anterior crus, posterior crus, stapedial head and stapedial footplate (Figure 16). The posterior crus is flattened to form a thin plate (Figures 12, 16). It forms the dorsal margin of the stapedial foramen (Figures 12B, 16A) and bears an opening towards the stapedial foramen in posterior view (Figure 12E). In lateral view, the anterior crus is thin and forms the ventral margin of the stapedial foramen (Figures 12B, 16A). In posterior view, the stapedial footplate is slightly distorted (Figure 12E). It contacts the opisthotic-prootic (=periotic) complex dorsally and the basioccipital medially. The stapedial head is positioned at the posterior end of the anterior crus, and contacts the posterior crus dorsally (Figure 16). In posterior view, the stapedial head is ovoid (Figure 12E).

The quadrate of *E. oosthuizeni* comprises the trochlea and dorsal plate (Figures 5, 11, 12, 16). In anterolateral view, the dorsal plate of the quadrate is roughly rectangular (Figure 5C) and has a flat posterior contact with the ventral process of the squamosal (Figures 5D, 11A, 12A). In anterior view, the dorsal plate of the quadrate contacts the quadratojugal laterally (Figure 11F) and in dorsolateral view a notch is present between the trochlea and the dorsal plate laterally (Figure 5D); also visible in ventral and dorsal view (Figure 4C, D). This notch accommodates the medial process of the quadratojugal. In anterodorsal view, the dorsal plate has a short dorsal contact with the opisthotic-prootic complex (Figure 15B).

The trochlea comprises two condyles (one medial and one lateral) and an intercondylar grove, visible in ventral and anterior view (Figures 8D, F, 12–D, F, 15, 16). Compared to the situation in *Patranomodon*, the lateral and medial condyles of *Eodicynodon* are massive and rounded, similar to the condyles found in *Niassodon* and *Lystrosaurus* (Cluver, 1971; Castanhinha et al., 2013). In ventral view, the lateral condyle of *Eodicynodon* is ovoid and the medial one is rectangular (Figure 11D). In anterior view, the lateral condyle extends ventrolaterally, while the medial condyle extends ventrally (Figure 11F).

The quadratojugal is a small and thin plate-like bone (Figures 11, 16) which is covered posteriorly by, and is in contact with, the ventral process of the squamosal, with what it shares a flat posterior contact (Figures 5C, 11A). In lateral view, the quadratojugal hooks onto the quadrate between the trochlea ventrally and the dorsal plate of the quadrate medially (Figures 11F, 12F).

The palate of NMQR 2978 is relatively well preserved (Figures 15, 17), but apart from the basisphenoid and part of the parasphenoid, most of the sphenethmoidal complex is absent.

The palate of BP/1/6230 is also in a good state of preservation, apart from the posterior section of the basioccipital and the anterior part of the palate (Figures 16, 18). The delicate presphenoid and orbitosphenoid are preserved (Figure 16C, D), but the ectopterygoids, hyoids and epypterygoids are missing (Figures 7, 18). Three unidentified bone fragments are possibly remnants of the quadrate process of the pterygoid and/or part of a displaced hyoid (Figure 18). The anterior section of the palate, including the premaxilla, is shattered, and the suture between the premaxilla and vomers is not identifiable (Figure 7D).

The vomer is a paired bone located at the anterior-most section of the palate (Figures 7D, 8D, 15, 16), and the midline suture is visible in anterior view in BP/1/6230 (Figure 18F). In lateral view, the vomer extends anterodorsally to form the septum which divides the air passage (Figure 16C). The anterior septae are fused dorsally in NMQR 2978 (Figures 15C, 17F). In both ventral and dorsal views, the vomer forms a paired inter-pterygoidal plate which is roughly triangular in dorsal view (Figures 15C, 17C, D). In ventral view, it contacts the ectopterygoid anterolaterally, and the transverse process of the pterygoid posterolaterally (Figure 17D). The suture with the pterygoid is oblique. In ventral and dorsal views, the intervomerine vacuity is positioned between the two vomers' inter-pterygoid plates (Figures 15C, 17C, D). It is roughly rectangular in ventral view and about 1.5 times wider than the interpterygoid vacuity (Figure 17D). The intervomerine vacuity is not present in *Patranomodon*. In lateral view, the two vomer inter-pterygoid plates join dorsally to form a posterior septum (Figures 15C, 17D, 18B). The vomer posterior septum is thin and divides dorsally to form a V-shaped process, similar to that of *Patranomodon* (Figure 18B). In lateral view, this process contacts the presphenoid anterodorsally. The anterior and posterior vomer septum observed in *E. oosthuizeni* were likely to have been connected and to form the vomerine process as evident in *Patranomodon* (Figures 6, 17, 18).

The palatine forms the large palatine pads characteristic of *Eodicynodon* (Figure 8D, H) and the ventral wall of the olfactory chamber (de Simão-Oliveira et al., 2019; Pusch et al., 2019). In contrast to the condition in *Patranomodon* the palatine pad of *E. oosthuizeni* is positioned close to the maxilla rather than close to the pterygoid (Figures 8D, 6D). In ventral view, the palatine is oval

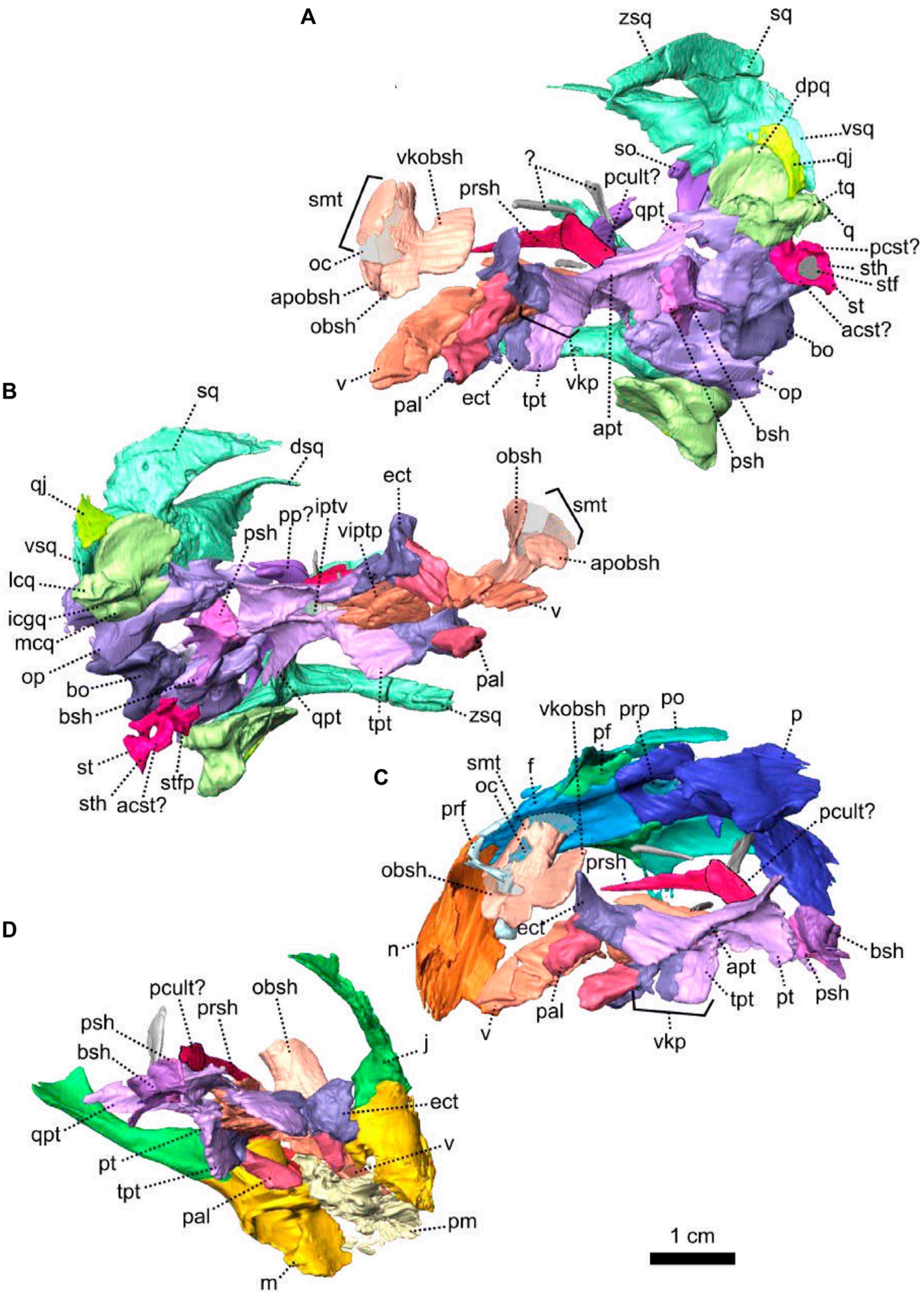

FIGURE 16
Anatomical details of *Eodicynodon oosthuizeni*, BP/1/6230, from Bloukrans farm, Prince Albert district, Western Cape, South Africa; *Eodicynodon* AZ, Guadalupian, Beaufort Group, Karoo Supergroup. 3D rendering in **(A)**, left lateroventral view; **(B)**, left right lateroventral view; **(C)**, left lateroventral view and **(D)**, right lateroventral view. Abbreviations: acst, anterior crus of the stapes; apt, anterior process of the pterygoid; apobsh, anterior process of the orbitosphenoid; bo, basioccipital; bsh, basisphenoid; dpq, dorsal plate of the quadrate; dsq, dorsal process of the squamosal; ect, ectopterygoid; icgq, intercondylar groove of the quadrate; iptv, interpterygoid vacuity; ivv, intervomerine vacuity; j, jugal; lcq, lateral condyle of the quadrate; m, maxilla; mcq, medial condyle of the quadrate; n, nasal; obsh, orbitosphenoid; oc, olfactory cavity; pal, palatine; pcst, posterior crus of the stapes; pcult, processus cultriformis; pf, postfrontal; pm, premaxilla; po, postorbital; prsh, presphenoid; prf, prefrontal; psh, parasphenoid; pt, pterygoid; q, quadrate; qj, quadratojugal; qpt, quadrate process of the pterygoid; smtobsh, semi tubular region of the orbitosphenoid; so, supraoccipital; st, stapes; sth, stapedial head; stf, stapedial foramen; stfp, stapedial footplate; sq, squamosal; tpt, transverse process of the pterygoid; v, vomer; vitptp, vomer inter-pterygoid plate; vkobsh, ventral keel of the orbitosphenoid; vkp, ventral keel of the palate; vps, vomer posterior septum; vsq, ventral process of the squamosal; zsq, zygomatic process of the squamosal. Scale bar = 1 cm.

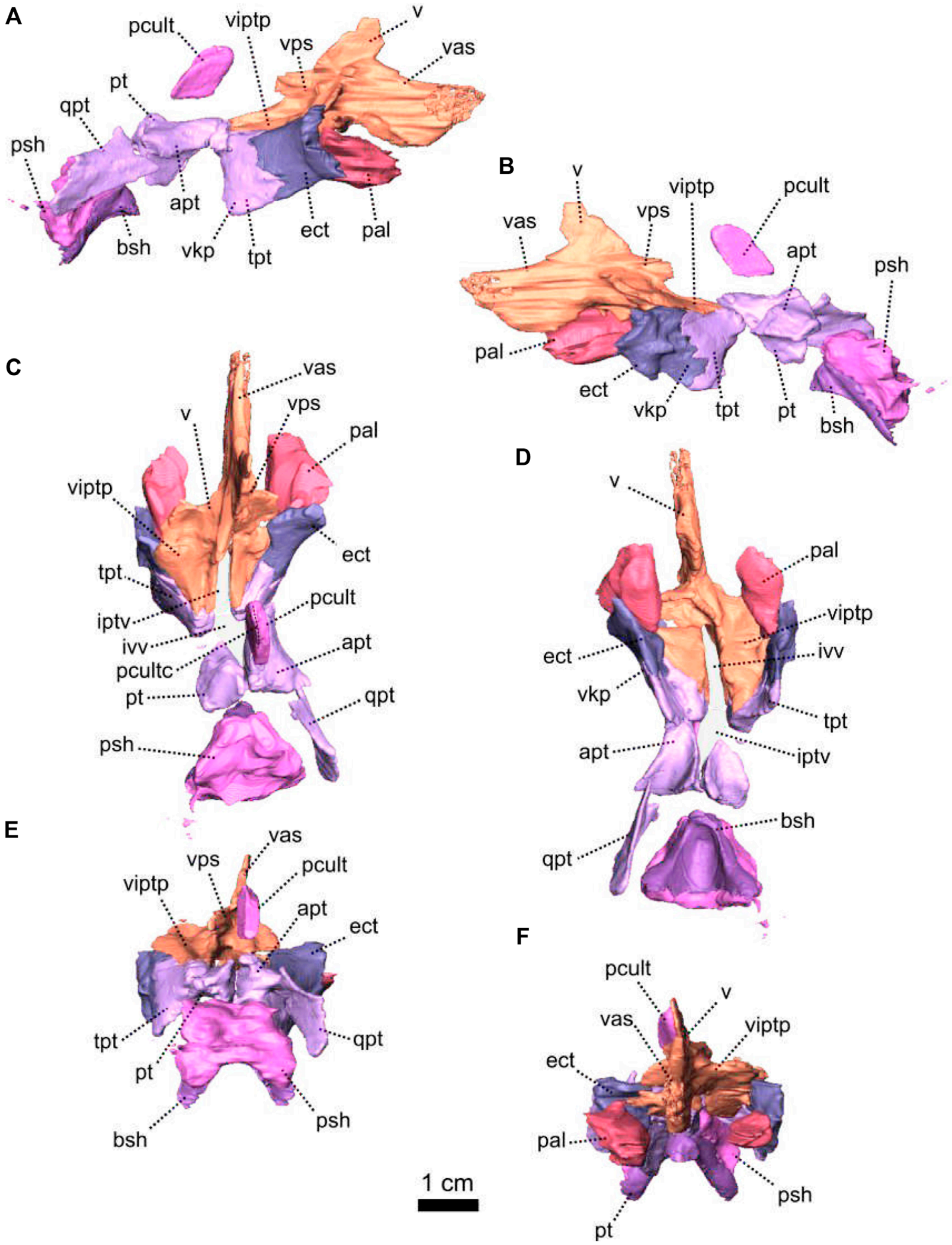

FIGURE 17
Palatal series of *Eodicynodon oosthuizeni*, NMQR 2978, farm Rietkuil (previously named Zwartground), Rietbron district, Eastern Cape, South Africa; *Eodicynodon* AZ, Guadalupian, Beaufort Group, Karoo Supergroup. 3D rendering in **(A)**, right lateral view; **(B)**, left lateral view; **(C)**, dorsal view; **(D)**, ventral view; **(E)**, posterior view and **(F)**, anterior view. Abbreviations: apt, anterior process of the pterygoid; bsh, basisphenoid; ect, ectopterygoid; iptv, interpterygoid vacuity; ivv, intervomerine vacuity; pal, palatine; pcult, processus cultriformis; pcultc, processus cultriformis crest; psh, parasphenoid; pt, pterygoid; qpt, quadrate process of the pterygoid; tpt, transverse process of the pterygoid; v, vomer; vas, vomer anterior septum; vitptp, vomer inter-pterygoid plate; vkp, ventral keel of the palate; vps, vomer posterior septum. Scale bar = 1 cm.

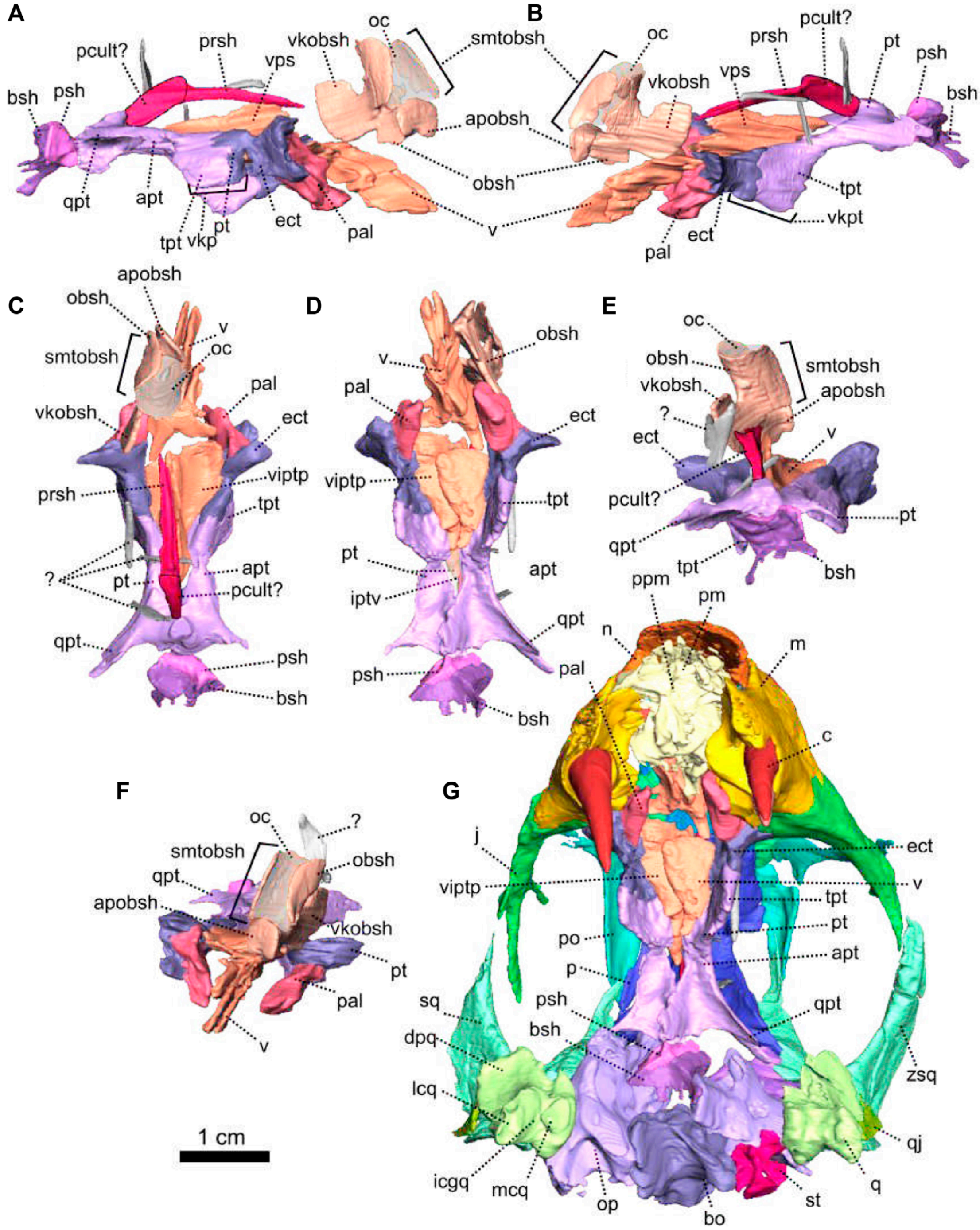

FIGURE 18
Palatal bones of *Eodicynodon oosthuizeni*, BP/1/6230, from Bloukrans farm, Prince Albert district, Western Cape, South Africa; *Eodicynodon* AZ, Guadalupian, Beaufort Group, Karoo Supergroup. 3D rendering in **(A)**, right lateral view; **(B)**, left lateral view; **(C)**, dorsal view; **(D)**, ventral view; **(E)**, posterior view; **(F)**, anterior view and **(G)**, ventral view with surrounding cranial bones. Abbreviations: apt, anterior process of the pterygoid; apobsh, anterior process of the orbitosphenoid; bo, basioccipital; bsh, basisphenoid; c, caniniform tooth; dpq, dorsal plate of the quadrate; ect, ectopterygoid; icgq, intercondylar groove of the quadrate; iptv, interpterygoid vacuity; ivv, intervomerine vacuity; j, jugal; lcq, lateral condyle of the quadrate; m, maxilla; mcq, medial condyle of the quadrate; n, nasal; obsh, orbitosphenoid; oc, olfactory cavity; op, opisthotic; pal, palatine; pcult, processus cultriformis; ppm, palatal process of the premaxilla; prsh, presphenoid; psh, parasphenoid; pt, pterygoid; q, quadrate; qj, quadratojugal; qpt, quadrate process of the pterygoid; sq, squamosal; st, stapes; smtobsh, semi tubular region of the orbitosphenoid; tpt, transverse process of the pterygoid; vitptp, vomer inter-pterygoid plate; vkobsh, ventral keel of the orbitosphenoid; vkp, ventral keel of the palate; vps, vomer posterior septum; zsq, zygomatic process of the squamosal. Scale bar = 1 cm.

(Figure 17D). It contacts the maxilla anterolaterally and anteriorly with a curved suture. Posterolaterally, the palatine contacts the ectopterygoid (Figures 8H, 17D) with an oblique suture in ventral view (Figure 17D) and vertical in medial view (Figure 8H).

Like in most non-mammalian synapsids, the pterygoid of *E. oosthuizeni* is a tripartite bone comprising the transverse flange (called palatal ramus in Cluver, 1971), anterior ramus (also called palatal ramus in Castanhinha et al., 2013) and quadrate ramus (Figures 15–18). In lateral view, the transverse flange forms, with the ectopterygoid, the ventral keel of the palate (Figures 15A, 16A, 17A, B, and 18A, B). A similar large palatal keel is found in *Prosictodon*, but is reduced in other dicynodonts (Sullivan and Reisz, 2005; Angielczyk and Rubidge, 2010; Castanhinha et al., 2013; Angielczyk et al., 2017). In posterior view, the palatal keel makes an angle of 80° with the horizontal plane. In the same view, the pterygoid contacts the ectopterygoid anteriorly (Figure 18E). In lateral view, the transverse flange of the pterygoid contacts the ectopterygoid anteriorly with an interdigitated suture (Figures 15B, 16A, 17A, B). In ventral view, the pterygoid has an oblique medial contact with the vomer (Figure 17D) and extends posteriorly to form the anterior process of the pterygoid (Figures 17D, 18D). The anterior process is triangular in both dorsal and ventral views (Figure 18C, D). In ventral view, the interpterygoid vacuity is diamond-shaped and positioned posterior to the intervomerine vacuity at the level of the contact between the transverse process and the anterior process of the pterygoid (Figures 17D, 18D). Posterior to the interpterygoid vacuity, in lateral view, the left and right anterior processes meet in the midline to form a vertical keel (Figures 16A, 17B, D, 18B, D). This keel is smaller than the transverse flange keel and contacts the parasphenoid posteriorly (Figure 16A) with an oblique suture when seen in lateral view (Figure 18B). The pterygoid expands dorsally into a conical boss which makes up the floor of the braincase. In dorsal view, this dorsal boss of the pterygoid meets with the presphenoid anteriorly (Figure 18C). The quadrate ramus is short and forms the posterolateral extension of the anterior process of the pterygoid (Figures 15–18). It curves posterolaterally toward the medial condyle of the quadrate (Figures 7D, 8D).

The ectopterygoid is positioned on the anterior side of the palatal keel (Figures 8, 15–17). In lateral view, the ectopterygoid is rectangular and contacts the pterygoid posteriorly (Figure 17A, B). In ventrolateral view, the ectopterygoid contacts the jugal anteriorly, has a short oblique contact with the maxilla anteriorly, and reaches the palatine anteroventrally (Figures 15B, 16D). In ventral view, the ectopterygoid meets the maxilla anterolaterally and the palatine anteromedially with an oblique suture on the anterior side (Figure 8D).

The sphenethmoidal complex includes internal bones that support the hindbrain anterior to the pila antotica and the forebrain up to the olfactory chamber (Benoit et al., 2017; Laaß et al., 2017; Pusch et al., 2019). It comprises the orbitosphenoid, presphenoid, epipterygoid (paired, possibly related to the mammalian alisphenoid see Crompton et al., 2018), parasphenoid, basisphenoid (called the parabasisphenoid when fused to the parasphenoid) and the paired hyoids. These bones are most often broken or not preserved in therapsids (as not fully ossified in come taxa, see Benoit et al. (2017)). With the exception of a few exceptional specimens (Barry, 1974), the hyoids have only been properly studied with the recent development of CT-scanning technologies (Laaß, 2015b; Araújo et al., 2017; Benoit et al., 2017).

The orbitosphenoid (ethmoid in Castanhinha et al., 2013) supports the olfactory bulbs in the olfactory chamber (Barry, 1974; Laaß, 2015b; Araújo et al., 2017; Benoit et al., 2017; Macungo et al., 2022). In specimen BP/1/6230, the orbitosphenoid is slightly displaced anteriorly, and would initially have had a loose articulated contact with the frontal (Figure 16C). The paired orbitosphenoid of *E. oosthuizeni* comprises a semi-tubular region, ventral keel and anterior process (Figures 16, 18). The semi-tubular region is formed by two hemicylindrical orbitosphenoids which join ventrally and encapsulate the olfactory cavity of the forebrain. In dorsal view, the semi-tubular region is U-shaped (Figure 18C). In lateral view, the orbitosphenoid projects as a posteroventrally oriented keel which is roughly rectangular and has the same surface area as the semi-tubular region (Figures 16A, C, 18B).

The orbitosphenoid also extends anteriorly to form the anterior process of the orbitosphenoid. This process is hammerhead-shaped and is roughly triangular in dorsal view (Figure 18C). The ventral keel would have sutured anteriorly with the vomers and posteroventrally with the interorbital septum of the presphenoid (Barry, 1974; Benoit et al., 2017; Crompton et al., 2018), but the contact is lost in BP/1/6230.

The presphenoid forms a thin septum-like bone (Figures 16, 18) and is possibly fused to the processus cultriformis of the parasphenoid posteriorly (Figures 16C, 18). In lateral view, the posterior section is rectangular and extends anteriorly as a thin triangular ramus (Figure 18A, B) which has a medial depression on the dorsal side (Figure 18E). In ventral view, the presphenoid has a contact with the posterior side of the pterygoid dorsal boss (Figure 18A).

The parasphenoid and the basisphenoid, which are partially preserved in BP/1/6230 and NMQR 2978, are not fused in *Eodicynodon*. The parasphenoid forms the top of the parabasisphenoid complex and the basisphenoid forms the base (Figures 15A, C, 16, 17 and 18). The anterior portion of the processus cultriformis is an isolated septum which is rounded anterodorsally (Figures 8G, H, 15, 17A, B). In lateral view, the contact between the parasphenoid and the basisphenoid is oblique (Figures 15B, 17B) and in ventral view the main corpus of the parasphenoid has a transverse posterior contact with the basioccipital (Figure 8D). In dorsal view, the parasphenoid contacts the prootic posterolaterally at the level of the vestibule (Figures 8B, D and 15D). This forms the anterior wall of the base of the hindbrain (Figure 15D). In lateral view, the contact between the prootic and the parasphenoid is oblique (Figure 8A, B). Neither the carotid foramina nor the *canalis vidii* are preserved on NMQR 2978 and BP/1/6230. In lateral and ventral view, the basisphenoid shows two ventrolateral processes that reach the basioccipital posteroventrally (Figures 8D, 15A, C). In ventral view, the basisphenoid is triangular (Figure 17D). In lateral view, it makes an angle of 45° with the transverse plane (Figure 8B). In the same view, the basisphenoid contacts the base of the basioccipital tubera posteroventrally (Figure 8B, H).

No lower jaw is preserved with NMQR 2978 (Rubidge, 1990b) but BP/1/6230 preserves an articulated mandible (Figure 7). The posterior end of the lower jaw has been distorted as the result of the deformation of the occiput (Figures 7, 19). Both lower jaw rami are preserved showing a mandibular fenestra bordered by the dentary,

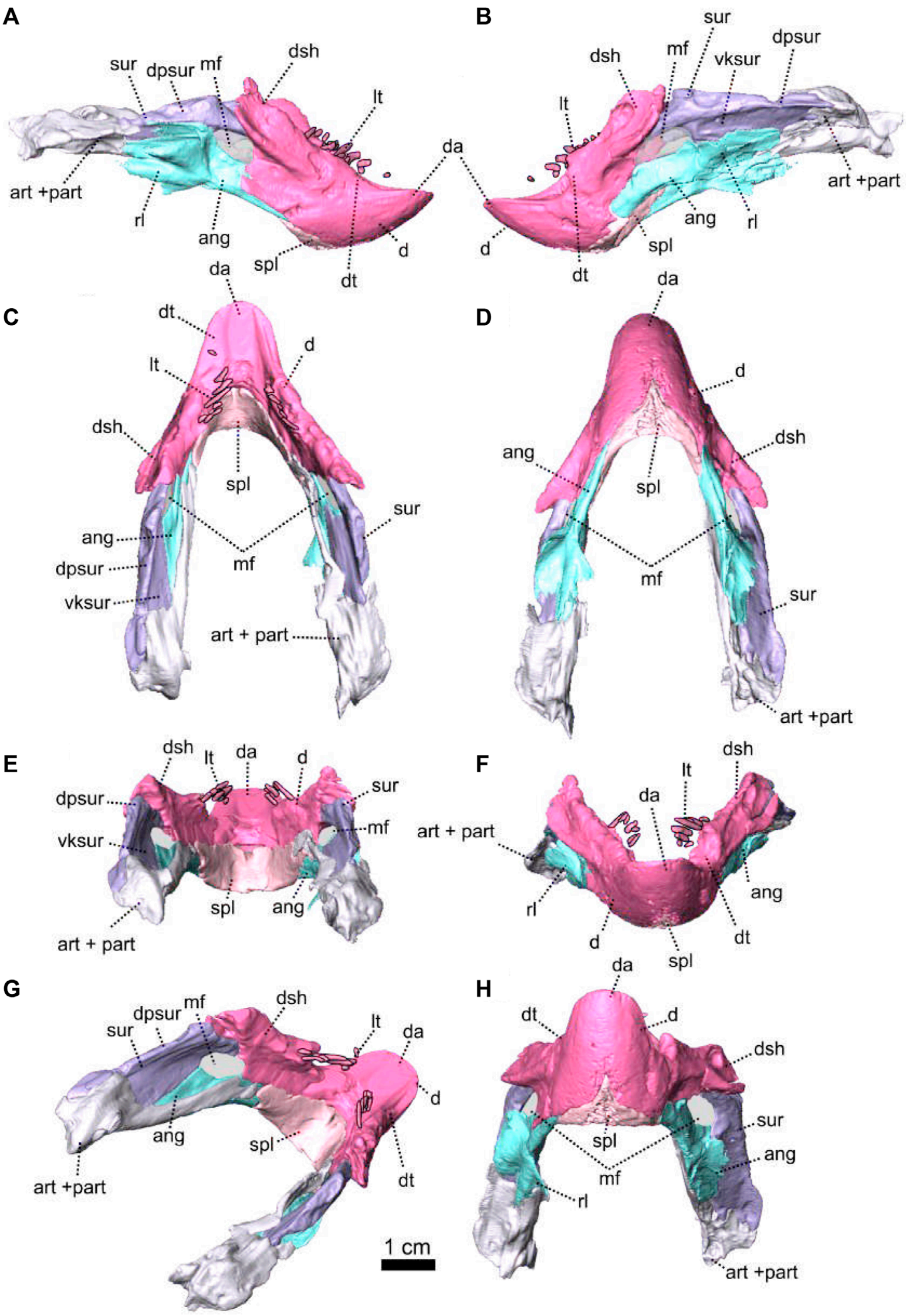

FIGURE 19
Lower jaw of *Eodicynodon oosthuizeni*, BP/1/6230, from Bloukrans farm, Prince Albert district, Western Cape, South Africa; *Eodicynodon* AZ, Guadalupian, Beaufort Group, Karoo Supergroup. 3D rendering in **(A)**, right lateral view; **(B)**, left lateral view; **(C)**, dorsal view; **(D)**, ventral view; **(E)**, posterior view; **(F)**, anterior view; **(G)**, right laterodorsal view and **(H)**, anteroventral view. Abbreviations: ang, angular; art, articular; d, dentary; da, dentary apex; dpsur, dorsal process of the surangular; dsh, dentary shelf; dt, dentary table; lt, lower jaw teeth; mf, mandibular fenestra; part, pre-articular; rl, reflected lamina; spl, splenial; sur, surangular; vksur, ventral keel of the surangular. Scale bar = 1 cm.

surangular and angular (Figure 19) as is present in all anomodonts (Modesto et al., 1999).

The dentary is well preserved as a single element (Figures 7, 19). In anterior view, the symphysis is fused dorsally (Figure 19F, H) and is triangular in ventral view (Figure 19F, H). No signs of the nutrient foramina, usually associated with the presence of a keratinous beak, are evident. In ventral view, the dentary contacts the splenial anteromedially, and the angular posteromedially (Figure 19D). The contact with the angular is long and oblique and the contact with the splenial is V-shaped (Figure 19D, H).

Overall, the dentary has a typical dicynodont morphology, with an edentulous and round anterior apex and two posterior processes, with the lateral dentary shelf and table on the dorsal side (Figure 19A). In lateral view, the posterior processes form the anterior margin of the mandibular fenestra (Figure 19A). In dorsal view, the dentary apex bears a gentle groove, bordered by the two dentulous dentary tables (Figure 19C, G). In lateral view, the anterior portion of the dentary table has a deep depression anterior to the mandibular teeth (Figure 19B). The dentary table extends posterodorsally to form the dentary shelf (Figure 19A, B) which extends onto the surangular above the mandibular fenestra where it exhibits a thick and rounded lateral margin (Figure 19E, F).

The splenial is a small and thin unpaired bone, with a short exposure on the lateral side of the jaw (Figures 7, 19). In lateral and anterior view, the splenial is overlapped by the dentary dorsally (Figure 19A, B, E, G, H) and in posterior view the splenial is broad on the medial side of the symphysis and thins posteriorly on each jaw ramus (Figure 19D, E, G). The splenial contacts the prearticular ventral to the lateral dentary shelf (Figure 7B–D, G) and meets the angular posteromedially (Figure 19D).

The angular forms the posteroventral margin of the lower jaw (Figures 7, 19) and in lateral view it makes up the ventral margin of the mandibular fenestra (Figure 19A, B). It is overlapped by the dentary anteriorly, contacts the surangular dorsally and the articular posteriorly (Figure 19A, B). In ventral view, the angular has a long contact with the prearticular on the medial side (Figure 19D). The right reflected lamina has been shattered but the left one is intact and is broad and thin (Figure 19). In lateral view, the reflected lamina extends posteriorly as three processes (Figure 19A). It contains three distinct fossae: the anteroventral, anterodorsal and posteroventral fossae (Olroyd and Sidor, 2022). The dorsal notch of the reflected lamina is V-shaped and placed at the level of the mandibular fenestra (Figure 19A and Olroyd and Sidor, 2022).

The surangular is the dorsal-most bone of the lower jaw (Figures 7, 19) and comprises a flat horizontal dorsal process and a slender ventral keel (Figure 19B, G, H). In lateral view, the anterior margin of the keel forms the posterior border of the mandibular fenestra (Figure 19B) and the dorsal process of the surangular meets up with the dentary shelf of the dentary anteriorly (Figure 19B). This dorsal process forms the dorsal margin of the mandibular fenestra. The ventral keel of the surangular contacts the angular ventrally, and posteriorly the surangular contacts the articular with an oblique suture which is visible in dorsal view (Figure 19C). On the medial side of the lower jaw, the ventral keel of the surangular contacts the prearticular posteroventrally (Figure 19G).

In BP/1/6230, the prearticular and the articular are co-ossified (Figure 19). A similar condition is found in *Niassodon* (Castanhinha et al., 2013). Posteriorly, the articular surface comprises two articular condyles, lateral and medial (Figure 19F, G). In lateral view, the articular contacts the surangular anterodorsally and the angular anteroventrally (Figure 19B). On the medial side, the prearticular is a thin and elongated rod-like process which extends along the surangular and the angular to contact the splenial anteriorly (Figure 19–D, E, G).

Specimen NMQR 2978 bears a single well-formed closed-rooted tusk on either side of the maxilla (Figure 8 and see Supplementary Material). An additional small oval postcanine is placed posteriorly to the left tusk.

Specimen BP/1/6230 manifests the usual dicynodont tusk on either side of the maxilla, and an additional tusk is present posterior to the large tusk on the left side of the maxilla (Figure 7 and see Supplementary Material). One postcanine tooth is present on the maxilla (Figures 7, 19 and see Supplementary Material). The lower jaw has five small conical teeth on the dentary.

3.1.3 NMQR 2913, holotype of *Eodicynodon oelofseni*

SYSTEMATIC PALEONTOLOGY
THERAPSIDA Broom, 1905
ANOMODONTIA Owen, 1859
DICYNODONTIA Owen, 1859
Eodicynodon Barry, 1974
Eodicynodon oelofseni Rubidge, 1990a

Material—Skull, lower jaw and indeterminate postcranial elements.

Type locality—Botterkraal farm, Abrahamskraal Formation, *Eodicynodon* Assemblage Zone, Karoo Beaufort Group, South Africa.

List of figures—Figures 20–22.

Diagnosis—after Rubidge (1990a), canine tusk-like teeth absent; laterally situated maxillary teeth which point in an anterior direction; no coronoid eminence on the posterodorsal surface of the dentary.

Description—Specimen NMQR 2913 comprises a reasonably well-preserved skull and lower jaw, and a few postcranial elements. The cranial material was published by Rubidge (1990a) as a new taxon, *Eodicynodon oelofseni*. Here NMQR 2913 is redescribed in the light of new anatomical data which has been revealed through CT scanning and has taxonomic implications. The scan of NMQR 2913 was made after the specimen had been accidentally broken into three pieces through the years of research at the National Museum and was subsequently reassembled: snout with the anterior portion of the palate and attached; occiput with the posterior part of the palate; and the lower jaw (Figures 20–22). The specimen has been deformed through postmortem damage (Rubidge, 1990a). The posterior section of the palate is crushed and twisted though 45° and the occiput has been displaced (Figure 21).

Because of poor preservation parts of the skull were inaccessible and could not be fully described in the first publication of Rubidge (1990a), but scanning has enhanced possibilities for description. The paired premaxilla forms the anterior and anteroventral margin of the naris and the tapering dorsal extension has a wedged contact with the nasal, extending to a point behind the posterior margin of the external naris (Figure 20–A,B). Ventrally, the premaxilla has a palatal extension (Figure 20). In ventral view, the short

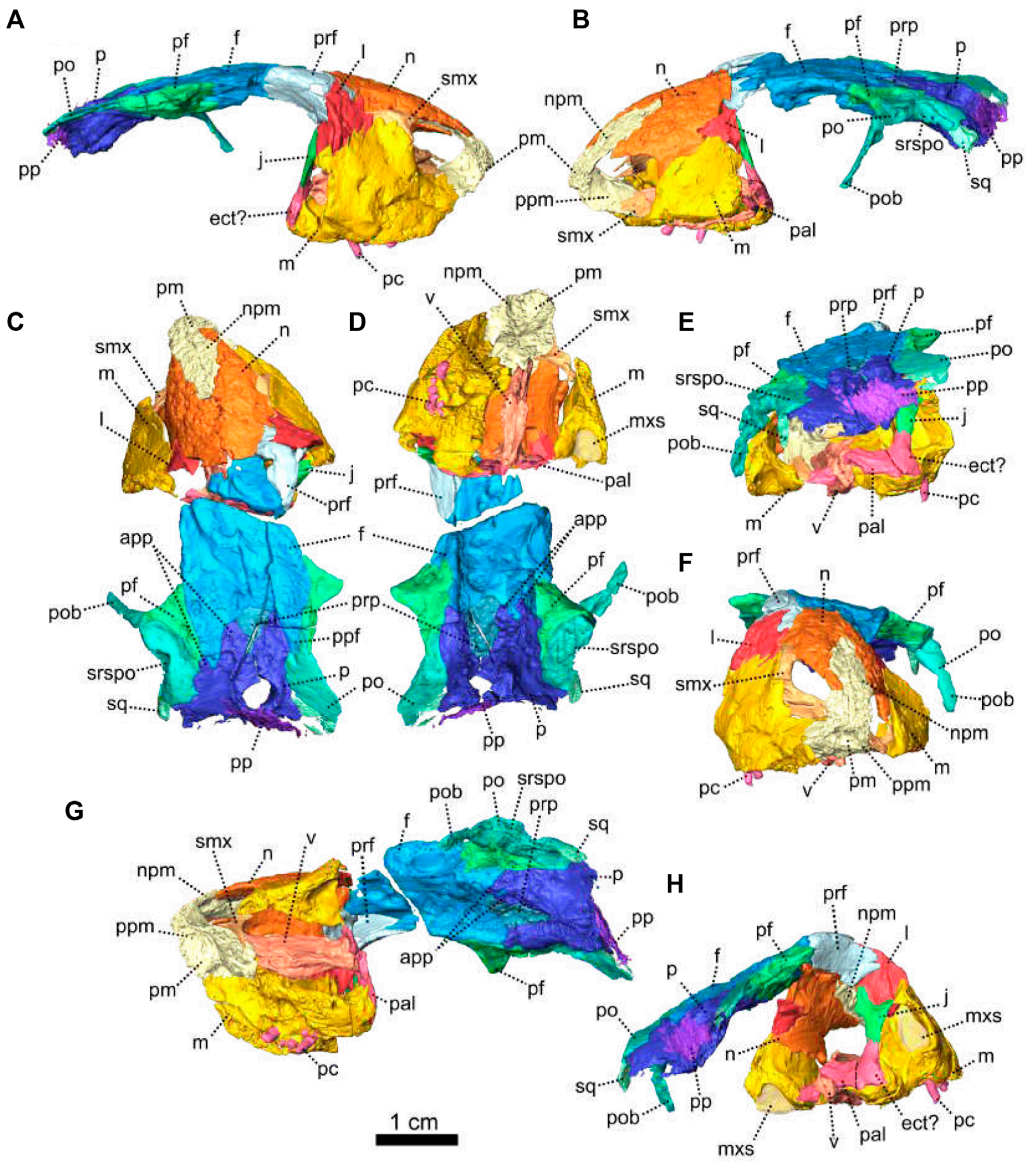

FIGURE 20
Snout and skull roof fragment of *Eodicynodon oelofseni*, NMQR 2913, farm Botterkraal, Prince Albert district, Western Cape, South Africa; *Eodicynodon* AZ, Guadalupian, Beaufort Group, Karoo Supergroup. 3D rendering in **(A)**, right lateral view; **(B)**, left lateral view; **(C)**, dorsal view; **(D)**, ventral view; **(E)**, posterior view; **(F)**, anterior view; **(G)**, left ventrolateral view and **(H)**, right posterolateral view. Abbreviations: app, anterior process of the parietal; ect, ectopterygoid; eo, exoccipital; f, frontal; j, jugal; l, lacrimal; m, maxilla; n, nasal; npm, nasal process of the premaxilla; p, parietal; pal, palatine; pc, postcanine; pf, postfrontal; pm, premaxilla; po, postorbital; pob, postorbital bar; pp, postparietal; ppf, posterior process of the frontal; ppm, palatal process of the premaxilla; prf, prefrontal; prp, preparietal; smx, septomaxilla; sq, squamosal; srspo, skull roof section of the postorbital; v, vomer. Scale bar = 1 cm.

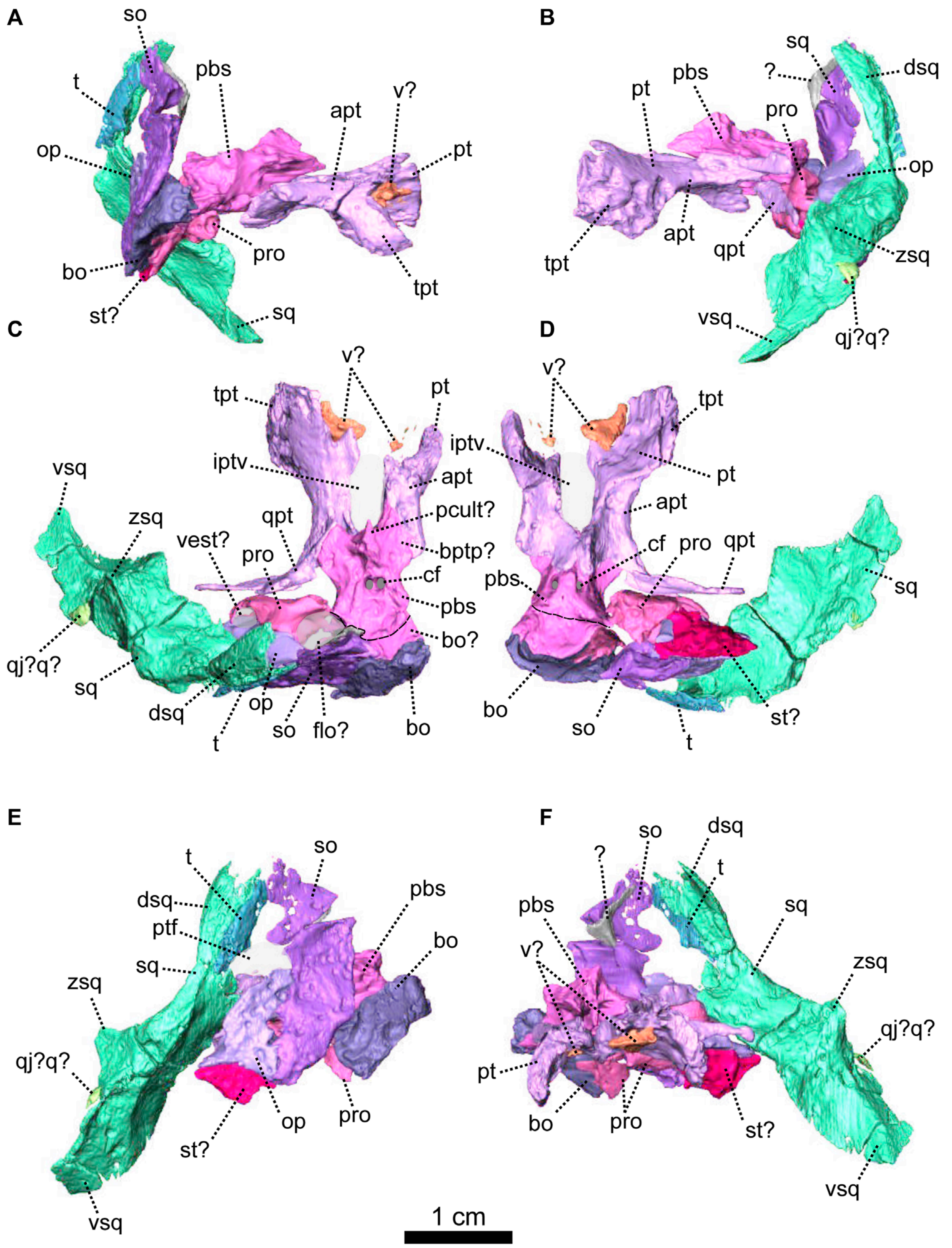

FIGURE 21
Occipital piece of *Eodicynodon oelofseni*, NMQR 2913, farm Botterkraal, Prince Albert district, Western Cape, South Africa; *Eodicynodon* AZ, Guadalupian, Beaufort Group, Karoo Supergroup. 3D rendering in **(A)**, right lateral view; **(B)**, left lateral view; **(C)**, dorsal view; **(D)**, ventral view; **(E)**, posterior view and **(F)**, anterior view. Abbreviations: apt, anterior process of the pterygoid; bo, basioccipital; bptp, basipterygoid process; cf, carotid foramen; dsq, dorsal process of the squamosal; iptv, interpterygoid vacuity; op, opisthotic; pbs, parabasisphenoid; pcult, processus cultriformis; pro, prootic; pt, pterygoid; ptf, postemporal fenestra; q, quadrate; qj, quadratojugal; qpt, quadrate process of the pterygoid; so, supraoccipital; sq, squamosal; st, stapes; t, tabular; tpt, transverse process of the pterygoid; v, vomer; vas, vomer anterior septum; vest, vestibule; vsq, ventral process of the squamosal. Scale bar = 1 cm.

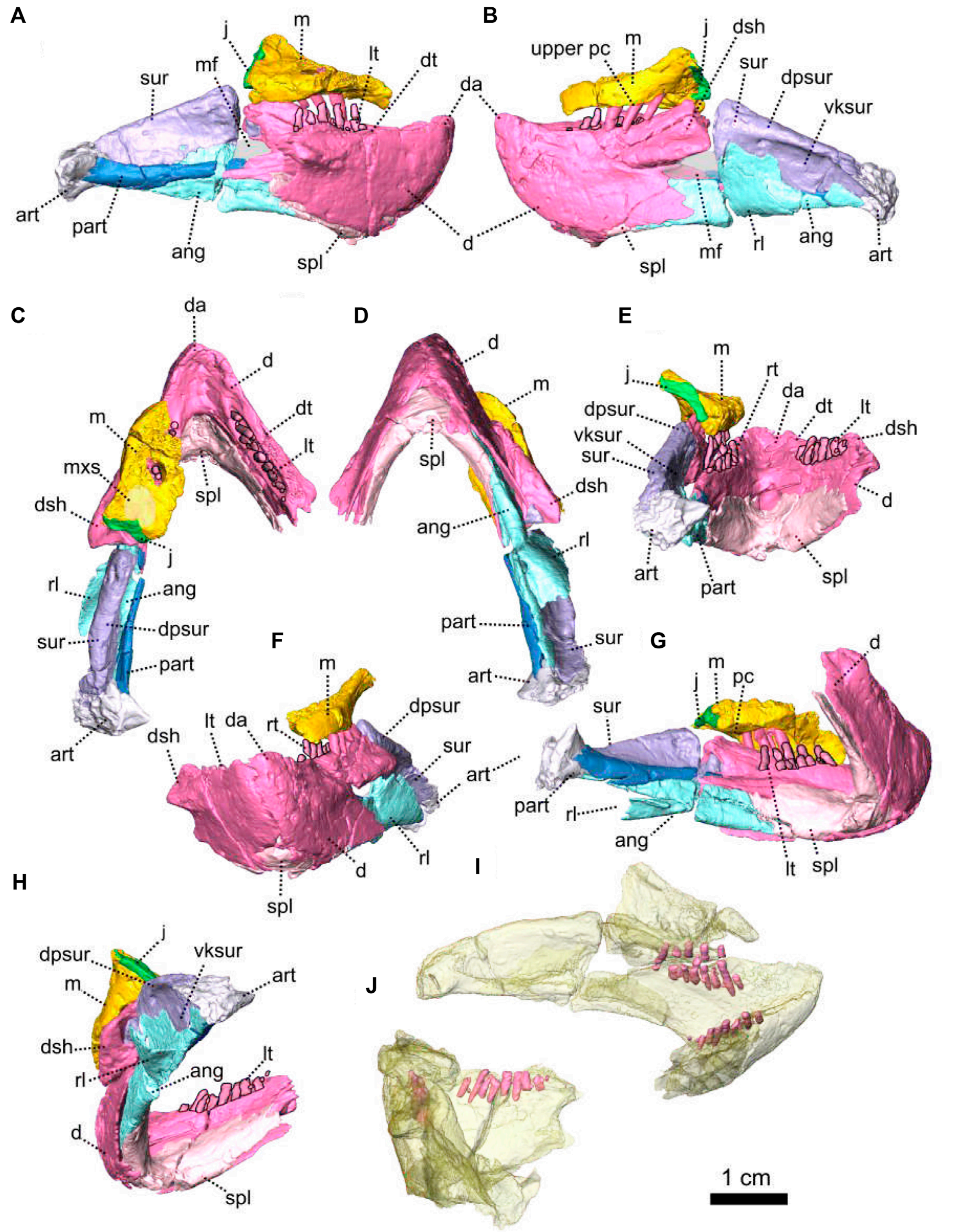

FIGURE 22
Lower jaw piece of *Eodicynodon oelofseni*, NMQR 2913, farm Botterkraal, Prince Albert district, Western Cape, South Africa; *Eodicynodon* AZ, Guadalupian, Beaufort Group, Karoo Supergroup. 3D rendering in **(A)**, right lateral view; **(B)**, left lateral view; **(C)**, dorsal view; **(D)**, ventral view; **(E)**, posterior view; **(F)**, anterior view; **(G)**, left posterolateral view and **(H)**, right lateroventral view. 3D rendering of the lower jaw teeth in **(I)**, left posteromedial view and **(J)**, right posteromedial view. Scale bar = 1 cm. Abbreviations: ang, angular; art, articular; d, dentary; da, dentary apex; dpsur, dorsal process of the surangular; dsh, dentary shelf; dt, dentary table; j, jugal; lt, lower jaw teeth; m, maxilla; mf, mandibular fenestra; mxs, maxillary sinus; part, pre-articular; pc, postcanine; rl, reflected lamina; spl, splenial; sur, surangular; vksur, ventral keel of the surangular. Scale bar = 1 cm.

premaxillary palatal extension is roughly rounded as a result of postmortem deformation (Figure 20D) and possibly has a midline suture (Rubidge, 1990a). It contacts the maxilla laterally with an oblique suture and has a short oblique contact with the septomaxilla posterolaterally (Figure 20D). Posteriorly the palatal extension of the premaxilla contacts the vomers (Figure 20D). This contact is oblique in ventrolateral view (Figure 20G).

Amongst the four basal anomodont specimens described in this paper, NMQR 2913 is the only specimen with a complete nasal process of the premaxilla which thins posteriorly on the skull roof as it wedges along the midline between the nasals. The nasal process of NMQR 2913 is visible on both the external and internal surface of the snout whereas in *Patranomodon* it intrudes the nasal and is visible only on the dorsal side (Figures 1G, 20C, H). The nasal process of NMQR 2913 is also relatively longer than those of NMQR 3000, BP/1/6230 and NMQR 2978 (Figures 1, 7, 8, 20).

Specimen NMQR 2913 is the only specimen of our sample that has the septomaxilla preserved (Figure 20). This bone, as evident from the right side of the skull, comprises two processes: an intranarial section and a lateral facial extension (Figure 20A, D). In lateral view, the lateral facial extension is triangular with the base forming the round posterodorsal margin of the naris and tapers posteriorly toward the lacrimal (Figure 20A). It has a long curved dorsal sutural contact with the nasal as evident in lateral view (Figure 20A). The septomaxilla is overlapped by the lacrimal posteroventrally and by the maxilla ventrally (Figure 20A, F). In ventral view, the intranarial section is triangular and reaches the premaxilla anteriorly with a curved contact (Figure 20D). On the left side of the skull, the lateral facial extension of the septomaxilla is not evident in the reconstruction (Figure 20B), but as the sutures are not clear on this part of the skull, it is likely to be present but was not recognised.

The maxilla forms the posteroventral border of the snout and is best preserved on the left (Figure 20). Here the maxilla is preserved in two parts: a dorsal section which is present on the snout fragment and a ventral fragment which is attached to the lower jaw fragment (Figures 20, 22). In lateral view, the maxilla is broadly triangular with the apex extending dorsally to meet the lacrimal with a rounded contact (Figure 20A, B). It has a short contact with the jugal posteriorly (Figure 22B), and an oblique suture with the nasal anterodorsally (Figure 20B). The dorsal contact with the lacrimal is shorter on the left side of the snout (Figure 20A, B). The maxilla meets the septomaxilla dorsally with a curved contact (Figure 20A). In ventral view, the left maxilla is triangular and a large maxillary sinus is present at the posterior end (Figure 20D) and is also evident in posterior view (Figure 20H). The left maxilla has three teeth while the right bears six (Figures 20, 22).

The paired nasal forms a large part of the anterior section of the snout (Figure 20) and is triangular in dorsal view with the apex pointing anteriorly (Figure 20C). In lateral view, the nasal forms the posterodorsal margin of the naris (Figure 20A, B). In dorsal view, the nasal has a straight transverse sutural contact with the frontal, but this shape is likely due to preservation (Figure 20C). Anterodorsally the nasal has a long contact with the nasal process of the premaxilla (Figure 20C). The contact is oblique in both lateral and dorsal views (Figure 20B, C). In lateral view, the nasal contacts the lacrimal posteroventrally (Figure 20A, B) but the nature of the contact is uncertain because of poor lacrimal preservation. Ventrally, the nasal is overlapped by the maxilla (Figure 20F). This contact is oblique in lateral view and horizontal on the medial side of the skull (Figure 20H).

On both sides of the skull the lacrimal is poorly preserved (Figure 20) and typically makes up the anterodorsal border of the orbit (Figure 20A, B). In lateral view, it has a short posterodorsal contact with the prefrontal, an oblique suture with the nasal anterodorsally, touches the septomaxilla anteriorly, and contacts the maxilla anteroventrally (Figure 20A). The lacrimal foramen could not be determined because of poor preservation.

Most of the jugal is missing and this bone is present only as a thin slither, mostly on the lower jaw fragment (Figures 20, 22). It is rectangular in posterior view (Figure 20E). In lateral view, the jugal contacts the maxilla anteriorly as the maxilla surrounds the edges of the jugal (Figure 22A). In posterior view, the jugal possibly contacts the ectopterygoid ventrally (Figure 20E).

The postorbital, as preserved on the left side of the skull, is relatively small (Figure 20) and forms a small section of the skull roof on the anterodorsal margin of the temporal fenestra and the entire postorbital bar (Figure 20B). The postorbital bar is missing on the right side of the skull (Figure 20A). In lateral view, the postorbital overlaps the postfrontal anteriorly, and the parietal posteromedially (Figure 20B). In dorsal view, the contact of the postorbital with the postfrontal is curved, and oblique with the parietal (Figure 20C). The postorbital has a short contact with the squamosal posteriorly, which is evident in dorsal view (Figure 20C). In ventral view, unlike *E. oosthuizeni* specimens BP/1/6230 and NMQR 2978, the surface of the postorbital is smooth and does not show any ornamentation (Figures 13, 14, 20D). In lateral view, the postorbital bar forms the posterior margin of the orbit, and the anterior margin of the temporal fenestra (Figure 20B). It is thin and originates dorsally at the contact between the postorbital and the postfrontal.

The squamosal of NMQR 2913 is preserved as two separate pieces (Figures 20, 21). The small anterior fragment contacts the postorbital anterodorsally on the margin of the temporal fenestra (Figure 20). The posterior fragment forms the posterior and posteroventral margins of the temporal fenestra, and curves anteroventrally. On the posterior fragment, in lateral view, the squamosal is bent anteroventrally (Figure 21B). It does not fold backwards as in other dicynodonts and is rather straight, similar to the situation in *Patranomodon* (Figure 1). The zygomatic process of the squamosal is missing, and only the ventral and the dorsal processes are preserved (Figure 21). In posterior view, the ventral process is thin and rounded ventrally and bears a vertical ridge (Figure 21E). The dorsal process is broken dorsally. It is overlapped by the tabular dorsally and contacts the supraoccipital dorsomedially. In anterior view, the dorsal process has a lateral ridge (Figure 21F), and a curved ridge originates medially at the base of the dorsal process and terminates laterally at the base of the broken zygomatic process.

The orbital region of NMQR 2913 is poorly preserved and the zygomatic arches are missing (Figure 20). The jugal is damaged on both sides, the left prefrontal is missing, and the zygomatic process of the squamosal is not preserved. The postorbital bar is preserved only on the left side of the skull.

The prefrontal, preserved only on the right side (Figure 20), forms the anterodorsal margin of the orbit in lateral view (Figure 20A). It contacts the lacrimal anteroventrally. In dorsal view, the prefrontal reaches the nasal anteromedially with a V-shaped suture, and has an oblique posteromedial sutural contact with the frontal (Figure 20C).

The frontal is a paired bone (Figure 20) with a straight midline suture which is visible only on the posterior part of the skull roof (Figure 20C). In dorsal view, the frontal covers the skull roof from the nasal to the level of the centre of the temporal fenestra (Figure 20C) and makes up the dorsal margin of the orbit between the prefrontal and the postfrontal (Figure 20A, B). It has a straight transverse contact with the nasal anteriorly, in both dorsal and ventral view (Figure 20C, D). In dorsal view, the frontal meets the prefrontal anterolaterally with an oblique contact and posteromedially the frontal overlaps the preparietal (Figure 20C, D). The posterior process of the frontal is triangular in dorsal view (Figure 20C) and extends posterolaterally as a wedge between the parietal and the postorbital in both dorsal and ventral views (Figure 20C, D). Posterolaterally, the frontal contacts the postfrontal (Figure 20) with a straight and longitudinal contact evident from the dorsal view (Figure 20C). In ventral view, the frontal bears a longitudinal ridge that reaches the parietal posteriorly (Figure 20D). In the same view, the postfrontal overlaps the frontal ridge.

In lateral view, the postfrontal forms the posterodorsal margin of the orbit (Figure 20B). It is triangular in dorsal view and is present as a wedge between the postorbital laterally, the frontal medially and its apex touches the parietal posteriorly (Figure 20C). In ventral view, the postfrontal slightly overlaps the frontal anteromedially (Figure 20D). In dorsal view, the postfrontal contacts the postorbital posterolaterally. The contact is curved in both dorsal and ventral views (Figure 20C, D).

The preparietal of NMQR 2913 is unpaired ovoid bone positioned between the parietals and the frontals (Figure 20) but does not border on the pineal foramen unlike the situation in *Patranomodon* and specimen BP/1/6230 (Figures 3C, 14C, 20C). The preparietal contacts the frontals anteriorly with a semilunate suture (Figure 20C). In ventral view, the preparietal is also ovoid, overlapping the frontals anteriorly and the parietals laterally (Figure 20D).

The parietal is a paired bone present on the skull roof and on the dorsal section of the occiput (Figure 20). In dorsal view, the parietal surrounds the pineal foramen and the medial anterior process tapers between the frontal laterally and the preparietal medially (Figure 20C). A smaller lateral anterior process is present between the frontal and the postfrontal. In dorsal view, the parietal has a long lateral contact with the postorbital (Figure 20C). In dorsal, ventral and posterior views, this contact is curved (Figure 20C, D, E). In dorsal and posterior views, the parietal sutures with the squamosal posterolaterally (Figure 20C, E) and extends onto the occiput where it is overlapped by the postparietal (Figure 20E).

The occiput of NMQR 2913 is poorly preserved and has been displaced dorsolaterally (Figure 21). Both exoccipitals are missing as well as all the occipital bones on the right side of the skull. Preserved bones on the left are incomplete and greatly deformed (Figures 20, 21). The identification of the supraoccipital and the opisthotic is uncertain.

The postparietal of NMQR 2913 is unpaired and diamond-shaped, similar to that in *Patranomodon* (Figures 4, 20). In posterior view, it is displaced dorsolaterally and as a result, overlaps the occipital section of the parietal (Figure 20E). It does not show any sutural contacts.

A small part of the tabular is preserved on the left side of the occiput (Figure 21B, E). In posterior view, the tabular is a thin and oval bone that overlaps the dorsal process of the squamosal (Figure 21E).

The supraocipital and the opisthotic of NMQR 2913 are very badly preserved and are probably fused, as the sutures are extremely difficult to distinguish on the specimen and CT images (Figure 21). The supraoccipital of NMQR 2913 is partially preserved on the left in two pieces around the postemporal fenestra (Figure 21). In posterior view, the dorsal-most part of the supraoccipital is flat and it has a S-shaped ventrolateral margin (Figure 21E). It forms the dorsal margin of the postemporal fenestra and contacts the tabular laterally. A second piece of supraoccipital forms the medial margin of the temporal fenestra in posterior view (Figure 21E). Its dorsal and lateral borders are straight and the ventral margin is curved (Figure 21E). The supraoccipital has a short contact with the basioccipital medially and, in posterior view, contacts the opisthotic laterally. No distinct sulci for the semicircular canals are evident.

Part of the left prootic is preserved on the left side of the occiput and reaches the opisthotic posteriorly (Figure 21). In ventral view, the prootic is roughly triangular. It has a short contact with the parabasisphenoid medially. The prootic contacts the basioccipital posteromedially with a horizontal suture, and the stapes laterally (Figure 21D). In dorsal view, the prootic contacts the opisthotic posteriorly (Figure 21C). In the same view, the prootic extends into a small curved process laterally (Figure 21C). This would have possibly accommodated the vestibule, and symmetrically on the medial side, the floccular fossa.

The opisthotic is rectangular in posterior view and forms the lateral border of the postemporal fenestra (Figure 21C). It contacts the stapes ventrally. In dorsal view, it has a short contact with the opisthotic anteriorly (Figure 21C). No sulci for the semicircular canals are preserved.

The basioccipital is only partially preserved on specimen NMQR 2913, without its tubera (Figure 21). In posterior view, the basioccipital is rectangular, displaced dorsolaterally and the surface is smooth (Figure 21E). It contacts the supraoccipital ventromedially. In both ventral and dorsal views, the basioccipital outline is semicircular (Figure 21C, D). In ventral view, it meets with the prootic laterally (Figure 21D) and contacts the parabasisphenoid anteriorly with a curved contact. By comparing NMQR 2913 with *Patranomodon* and *E. oosthuizeni*, the placement of the basioccipital-parabasisphenoid suture might have been mistakenly placed on the CT reconstruction of NMQR 2913 and could be actually located more anteriorly, as indicated by the dotted lines on Figure 21.

A possible remnant of the stapes is preserved on NMQR 2913 (Figure 21). The identification is however uncertain, due to the poor preservation of the occiput. In posterior view, the stapes contacts the opisthotic dorsally (Figure 21E). In ventral view, the stapes is triangular (Figure 21D) and tapers laterally towards the squamosal. In the same view, it contacts the prootic anteromedially. In anterior view, the stapes bears a lateral vertical ridge (Figure 21F).

The palate of NMQR 2913 is preserved in two pieces (Figures 20, 21). The vomers, part of the palatine and possibly the ectopterygoid are preserved on the anterior piece (Figure 20). The pterygoid and the parabasisphenoid are preserved on the posterior fragment (Figure 21).

The vomer of NMQR 2913 is a paired bone mainly preserved on the anterior fragment (Figure 20) with possible small pieces of the posterior part of the vomers present on the other fragment (Figure 21). In posterior view, the vomer extends dorsally as a thin septum (Figure 20E) and in ventral view, it is slender and broadly rectangular It contacts the palatine extension of the premaxilla anteriorly and the palatine posteriorly (Figure 20D). In lateroventral view, this contact is oblique and the vomer overlaps the premaxilla anteriorly. In ventral view, the left vomer has a short anterolateral contact with the septomaxilla (Figure 20D).

The palatine is incomplete (Figure 20). The anterior-most portion is preserved on the anterior fragment and a small portion is likely preserved on the posterior fragment (Figures 20, 21). In ventral view, the preserved section of the palatine is a small rectangular bone which has a short contact with the vomer medially (Figure 20D). In posterior view, it possibly reaches the ectopterygoid laterally (Figure 20E).

The pterygoid is a paired bone (Figure 21). As in *Patranomodon* and *E. oosthuizeni* it comprises a transverse process, an anterior ramus, and a quadrate ramus (Figure 21D). The left pterygoid is complete, but the right pterygoid is missing its quadrate ramus. In lateral view, the ventral keel of the palate bears a large transverse ramus (Figure 21A,B) which makes an angle of 20° with the frontal plane (Figure 21F). The anterior process bears a small posteroventral keel (Figure 21A, B). In ventral view, the anterior ramus encloses the oval interpterygoid vacuity and a curved ridge links the two ventral keels (Figure 21D). In lateral view, the posterior portion of the anterior ramus is overlapped by the parabasisphenoid and the quadrate ramus extends posterolaterally. This ramus makes an angle of 85° with the sagittal plane (Figure 21A, B).

The parabasisphenoid of NMQR 2913 is a co-ossification of the parasphenoid and the basisphenoid (Figure 21) and has two well-defined carotid foramina which are visible in both ventral and dorsal views (Figure 21C, D). Anteriorly, the parabasisphenoid forms two lateral flat extensions that overlap the pterygoids (Figure 21A–C). These extensions are similar to the basisphenoid wings observed in *Patranomodon*. In lateral view, above the posteroventral keel of the pterygoid, the parabasisphenoid forms a conical dorsal process (Figure 21A, B). Posteriorly, in ventral and dorsal views, the parabasisphenoid broadens and contacts the basioccipital posteromedially and the prootic posterolaterally (Figure 21C, D).

As reported in Rubidge (1990a), the lower jaw of NMQR 2913 is incomplete as the posterior section of the right ramus is not preserved (Figure 22G, H). The left ramus has a crack at the level of the prominent mandibular fenestra, which is surrounded by the dentary, surangular, angular and prearticular bones (Figure 22A, B). Rubidge (1990a) could not determine the presence of a symphysial suture and our reconstruction confirms that the symphysis is fused. The left dentary shows a posterodorsal lateral dentary shelf similar to that of BP/1/6230 (Figures 19, 22), but this section is not preserved on the right dentary.

The dentary covers about 50% of the lower jaw ramus and, in lateral view, forms its anterior-most portion (Figure 22). As in BP/1/6230, the dentary of NMQR 2913 comprises a dentary table, dentary shelf, and a thin posteroventral process (Figures 19, 22G, H). The dorsal edge of the dentary is curved, with the anterior tip and the shelf being higher than the median part of the dentary. In lateral view, the dentary shelf forms the dorsal margin of the mandibular fenestra (Figure 22B). A dorsal fossa of the dentary accommodates the surangular posteriorly. The dentary extends posteroventrally into a thin triangular process below the mandibular fenestra. In ventral view, this process contacts the angular posteromedially (Figure 22D) and the dentary contacts the splenial anteromedially. The left dentary accommodates six teeth with alternating replacement teeth (Figure 22A) and the right dentary bears eight teeth, with four small replacement teeth (Figure 22C, E). The replacement teeth are placed lingually to the main tooth row.

The splenial is an unpaired bone which forms the anteroventral margin of the lower jaw (Figure 22). Morphologically it is similar to that of BP/1/6230: a thin bone with small anterior and lateral exposure (Figure 22A, B, F). In ventral view, the splenial contacts the dentary laterally and it has a short contact with the angular on the posterior end (Figure 22D). In posterior view, the splenial is roughly triangular and the anterodorsal margin of the splenial is hooked (Figure 22E), similar to that of BP/1/6230 (Figure 19E).

In lateral view, the angular forms the ventral and the posteroventral margin of the mandibular fenestra and of the lower jaw (Figure 22B). Posterior to the mandibular fenestra, the angular extends into a dorsomedial process and the reflected lamina (Figure 22B, G, H). The dorsomedial process overlaps the surangular up to the level of the dorsal margin of the mandibular fenestra (Figure 22B). The reflected lamina is a thin sheet of bone which is broadly triangular in lateral view (Figure 22B, G). In posterior view, the reflected lamina curves ventromedially to join the angular (Figure 22E, G). In lateral view, the angular extends posteriorly into a thin rectangular process, has a long dorsal contact with the surangular and touches the articular posteriorly (Figure 22B). In ventral view, the angular tapers in between the dentary laterally and the splenial medially (Figure 22D). In medial view, the angular has a flat long contact with the prearticular (Figure 22A, C, D, G).

The surangular forms the dorsal-most section of the lower jaw (Figure 22) and makes up the posterolateral and dorsomedial margin of the mandibular fenestra (Figure 22A, B). As in BP/1/6230, the surangular of NMQR 2913 comprises a thick dorsal section and a thin ventral keel (Figures 19, 22), but the keel of NMQR 2913 is less pronounced than that of *E. oosthuizeni* (BP/1/6230). In lateral view, the dorsal section bears a thick horizontal ridge dorsally (Figure 22B), also visible in posterolateral view (Figure 22G). In medial and lateral views, the dorsal section of the surangular extends anteriorly to the dentary shelf (Figure 22A, B) and the ventral keel is overlain by the angular laterally (Figure 22A, B, H). In lateral view, the surangular has a short contact with the articular posteroventrally (Figure 19B) and in medial view, the ventral keel of the surangular contacts the prearticular ventrally (Figure 22A, H).

The prearticular and the articular of NMQR 2913 are not fused, unlike the situation in BP/1/6230 (Figure 22). The prearticular is a long horizontal strip of bone, visible on the medial side of the lower jaw ramus (Figure 22A, H). It extends from the articular to the level of the mandibular fenestra (Figure 22A, C, D, H) and forms medially the posteroventral corner of the mandibular fenestra while reaching the articular posteriorly (Figure 22A). In medial and ventral views, the contact between the prearticular and the articular is oblique (Figure 22A, D). In medial view only, the prearticular contacts the angular ventrally and the surangular dorsally (Figure 22A, H).

The articular forms the posterior part of the lower jaw and would have accommodated the quadrate to form the mandibular articulation (Figure 22). In posterior view, the articular extends medially in a triangular process (Figure 22E). In lateral view, the articulation surface is oblique and the articular bears an oblique ridge that extends from the surangular anteriorly to the posterior tip of the lower jaw (Figure 22B). In lateral and ventral views, the articular has a short anterior contact with the angular (Figure 22B, D). In medial and ventral views, the articular has an oblique contact with the prearticular anteromedially (Figure 22A, D, H).

Unlike *E. oosthuizeni* specimens, NMQR 2913, the holotype of *Eodicynodon oelofseni*, does not have a tusk-like caniniform (Figure 20). Its upper dentition comprises homodont cylindrical teeth located only on the maxilla. In contrast, *Patranomodon* has its anterior-most tooth positioned at the suture between the maxilla and the premaxilla. The right maxilla of NMQR 2913 bears six teeth, two of which are located posteromedially and may be replacement teeth (Figure 20D). The left maxilla bears only three teeth (Figure 22B). On the lower jaw, NMQR 2913 has eight cylindrical teeth (Figure 22I, J). The left dentary shows a pattern of continuous replacement similar to that described by Olroyd et al. (2021). The right dentary has smaller teeth alongside the main eight teeth, which might be remnants of an earlier stage of replacement teeth (Figure 22C, J).

3.2 Phylogenetic results

3.2.1 Cladistics: Heuristic analysis using TNT

The Cladistic analysis was run with TNT version 1.5 (Goloboff and Catalano, 2016). It retained 58 trees and 147 223 106 672 rearrangements were examined for the Sectorial Search, Ratchet and Tree Fusing algorithm. The minimum length is 167 steps, the maximum length is 877 steps and the length of the consensus tree is 383 steps. Then $RI = 0,70$ $CI = 0,44$ and $HI = 0.56$. The strict consensus tree is relatively well-resolved except for early-diverging anomodonts (Figure 23). Specimen NMQR 2913 is retrieved as the basal-most dicynodont and the clade is supported by the following synapomorphies:

- The premaxilla does not have teeth (character 8)
- The septomaxilla posterodorsal extension is long and separates the maxilla and nasal (character 19)
- The contact between the premaxilla and maxilla is absent (character 32)
- The preparietal is present (character 50)
- The contribution of the parietal to the skull table is transversely as broad as long (character 53)
- The squamosal bears a lateral fossa above the quadrate-quadratojugal complex (character 63)
- The squamosal has a dorsolateral notch below the zygomatic arch (character 65)
- The posteroventral process of the squamosal is short, such that there is a relative extensive exposure of the quadrate and quadratojugal in posterior view (character 66)
- The zygomatic process of the squamosal is transversely expanded (character 68)
- The pterygoids are separated by the vomers anteriorly, so that the vomers contribute to the interpterygoid vacuity (character 90)
- The tranverse flange of the pterygoid does not project laterally (character 91)
- The pterygoid keels are present (character 92)
- The dentary table is present (character 126)
- The coronoid is absent (character 136)
- The angular has an anterolateral trough for the posterior process of the dentary (character 137)

The analysis gave the following autapomorphies for specimen NMQR 2913:

- The lacrimal contacts the septomaxilla (character 43)
- The zygomatic process of the squamosal is narrowly based and in line with the occipital condyle (character 69)
- The exposure of the internal carotid is directed medially (character 104)
- The height of the dorsum sellae is moderate, clearly distinct but does not reach the height of the pila antotica

Other dicynodonts (node A, see Figure 23) are supported by the following synapomorphies:

- The posterior median ridge on the palatal surface of the premaxilla is present (character 5)
- The posterodorsal spur of the septomaxilla is absent (character 18)
- The caniniform tooth is present on the maxilla (tusk, character 25)
- The caniniform process of the maxilla is present (character 33)
- The parasphenoid is excluded from the interpterygoid vacuity (character 101)
- The exit of the carotid canals on the sella turcica is a single foramen (character 145)

3.2.2 Bayesian analysis using MrBayes

In the Bayesian Inference analysis utilising MrBayes, a total of 4,506 trees were sampled and examined, with 8 chains, 6 runs and 4 swaps, and the relburnin option was set to 0.25. The gamma model was used for the substitution rate among characters that follows an exponential distribution. The branch length also follows an exponential distribution. The statistical results for the parameters are presented in Supplementary Material.

The Bayesian analysis using MrBayes provided good values for the clade credibility (ie. the Bayesian support and posterior probability value for the node), and extra phylogenetic resolution compared to the cladistic analysis (Figures 23, 24). The Dicynodontia node has a posterior probability support of 1, with NMQR 2913 as the basal-most taxon (Figure 24). Specimens BP/1/6230, NMQR 2978 and ROZ 1 are placed in a polytomy at the base of the dicynodont clade. Specimens BP/1/6230 and ROZ 1 are branching together with a low probability of 0.60. Posterior probability values for other nodes are figured in Figure 24.

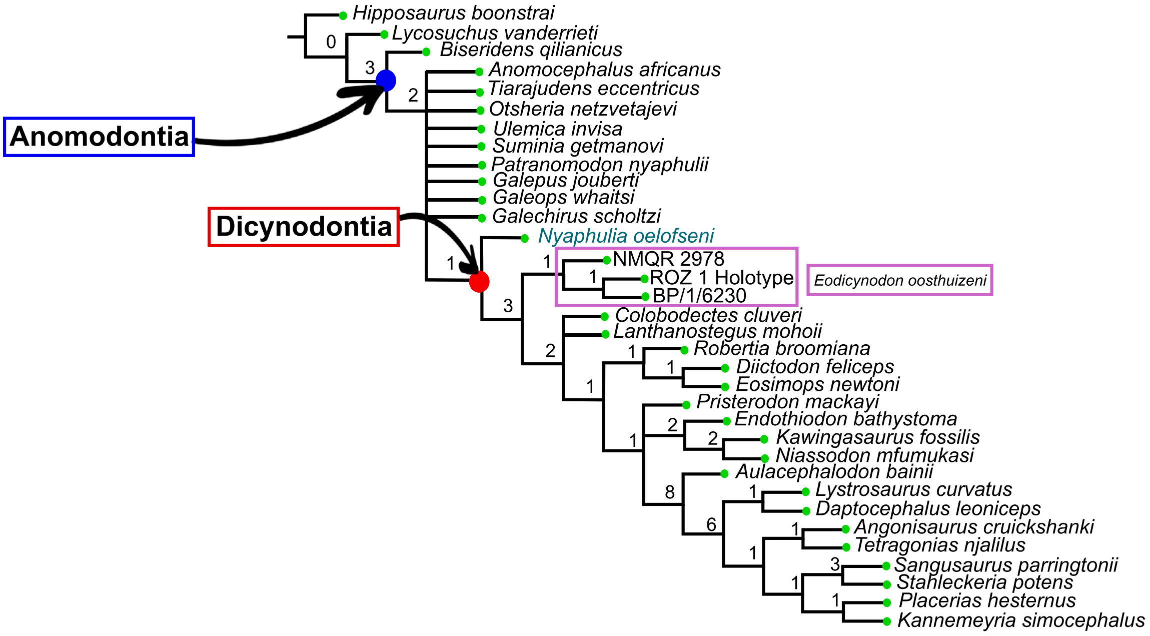

FIGURE 23
Cladistic analysis of the Anomodontia. Strict consensus of 58 trees obtained with a Heuristic Search. The numbers at the nodes are Bremer indices.

3.2.3 Bayesian analysis using RevBayes

The analysis from RevBayes provided a complete resolution of the phylogenetic analysis (Figure 25). *Patranomodon* is placed as the sister taxon to the "Dromasauria" with a good posterior probability of 0.8. Specimen NMQR 2913 also places as the earliest diverging dicynodont, with an excellent posterior probability of 1. The phylogenetic result from RevBayes also supports specimens BP/1/6230 and ROZ 1 being sister taxa with 0.78 posterior probability. NMQR 2978 is within Dicynodontia with a low posterior probability of 0.29. When a more complex model (SHDM) is used, BP/1/6230 and ROZ 1 are supported as sisters with posterior support of 0.983, and NMQR 2978 is within Dicynodontia with posterior probability of 0.653.

3.2.4 Description of the phylogenetic results

The cladistic analysis provided a well-resolved tree, apart from the relationship between the basal anomodonts, including *Patranomodon* (Figure 23). Derived dicynodonts are well-resolved, and similar topology to that of previous work was obtained (Fröbisch and Reisz, 2008; Kammerer et al., 2011; Castanhinha et al., 2013; Boos et al., 2016; Kammerer and Smith, 2017; Angielczyk et al., 2021; Macungo et al., 2022), with the cistecephalids *Niassodon*, *Kawingasaurus* and *Endothiodon* branching together; as well as *Robertia*, *Diictodon* and *Eosimops* (Pylaecephalidea) being closely related.

The Bayesian Inference analysis using MrBayes provided a relatively well-resolved tree, and partially elucidated the relationship amongst basal anomodonts whereas the Cladistics shows an irresolution (Figures 23, 24). The relationship of early-diverging anomodonts is fully resolved in the RevBayes analysis (Figure 25).

MrBayes and RevBayes returned trees with similar phylogenetic topologies and support values. The main phylogenetic result was extremely robust to both the software and the model choice. When a different model of character evolution was used with RevBayes (SHDM), some aspects of the crown topology changed, but the placement of the BP/1/6230, ROZ 1, and NMQR 2978 specimens remained the same with similar support. The preferred model found three unique SHDM rate categories, with the majority of characters showing a preference for a Mk-like q-matrix, in which the forward rates (0 -> 1) are roughly equivalent to the backward rates (1 -> 0). The other two SHDM categories suggest that a smaller proportion of characters are presented that more frequently transition forward (4:1), and an even smaller proportion that favors almost exclusively forward transitions. This means that characters that are poorly-described by the Mk model will be biased towards gains rather than losses.

The clade Anomodontia is supported by a Bremer index of 3 and an excellent posterior probability of 0.97 in both Bayesian analyses (Figures 23–25). The following synapomorphies support the clade:

- On the palate, the posterior exposure of the premaxilla is present (character 10)
- The palatine has a shelf ventral to the naris (character 12)
- The maxilla has a caniniform tooth (character 25)
- The posterolateral process of the parietal is short (character 54)
- The zygomatic process of the squamosal is widely based and flares posteriorly beyond the occipital condyle (character 68)
- The level of the palatine flush with surrounding bones and does not have any elevated portions (character 79)
- The pterygoid does not have teeth (character 96)

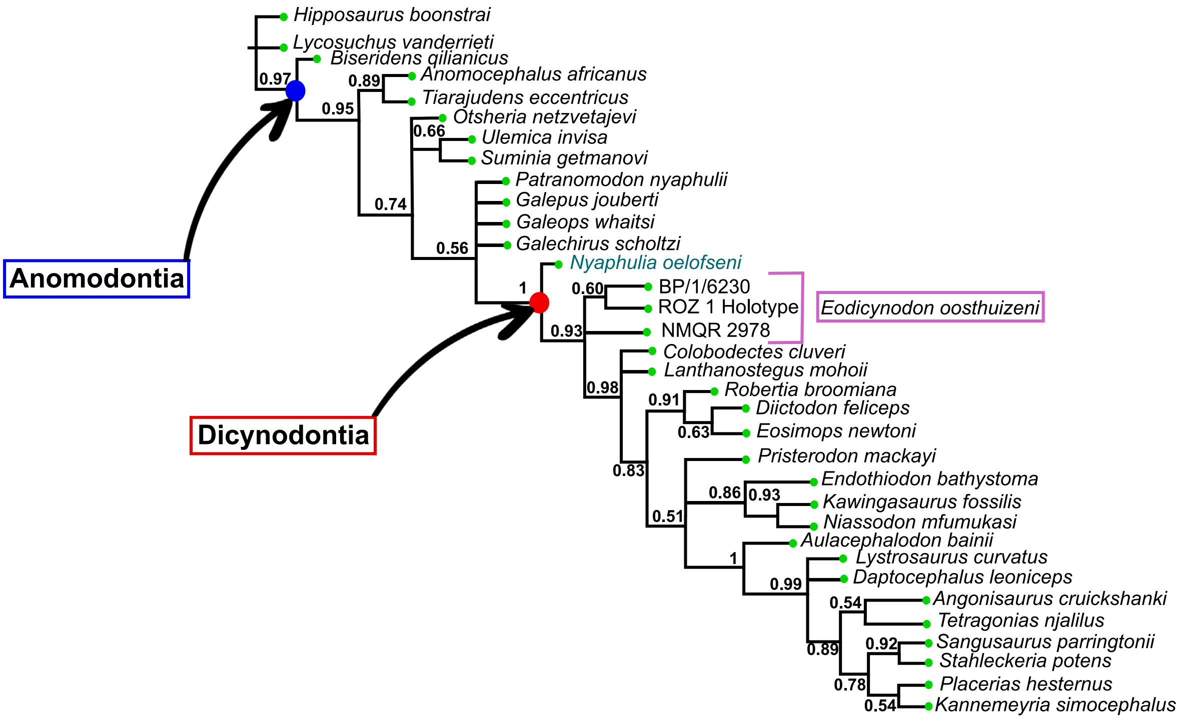

FIGURE 24
Bayesian phylogenetic analysis of the Anomodontia with MrBayes. Values at nodes indicate the posterior probability of the node.

- The tabular is separated from the opisthotic by the squamosal (character 110)
- The lower jaw has a mandibular fenestra (character 116)
- The dentary does not have an enlarged canine (character 141)

In both the cladistic and Bayesian analyses, *Biseridens* is placed as the most basal anomodont (Figures 23–25), as previously argued by Liu et al. (2010) and supported by Cisneros et al. (2011), Kammerer et al. (2011) and Angielczyk et al. (2021). As already proposed by Cisneros et al. (2011), the Anomocephaloidea *Tiarajudens* and *Anomocephalus* form a clade that is the sister group to other anomodonts in both Bayesian analyses with a posterior probability of 0.89 in MrBayes and 0.92 in RevBayes (Figures 24, 25). Before the relatively recent description of *Tiarajudens* in 2011, *Anomocephalus* was considered as the second most basal anomodont (Modesto et al., 1999; Fröbisch and Reisz, 2008; Liu et al., 2010; Kammerer et al., 2011). Angielczyk and Kammerer (2017) and Angielczyk et al. (2021) however suggested a more derived position for the Anomocephaloidea, more derived than *Galepus* but more basal than *Patranomodon*.

The Russian venyukovioids *Otsheria*, *Ulemica* and *Suminia* are left unresolved in both the cladistic and the MrBayes analyses (Figures 23, 24). The MrBayes analysis suggests that *Ulemica* and *Suminia* branch with a moderate posterior probability of 0.66 (Figure 24). The RevBayes analysis supports the monophyly of the venyukovioids with a strong posterior probability of 0.96, supporting previous phylogenetic works (Liu et al., 2010; Kammerer et al., 2011; Boos et al., 2016; Angielczyk et al., 2021). Similarly to the MrBayes analysis, *Suminia* and *Ulemica* form a clade with a strong posterior probability of 0.99 (Figure 25).

In both the cladistic and MrBayes analyses, the phylogenetic relationship of *Patranomodon* with the dromasaurs (non monophyletic group including *Galeops*, *Galechirus* and *Galepus*) is left unresolved (Figures 23, 24 and see Kammerer and Angielczyk, 2009). The RevBayes analysis retrieves the dromasaurs as a clade, with a moderate support of 0.69 (Figure 25). *Patranomodon* places as the sister taxon and the node is supported by a good posterior probability of 0.8. This phylogenetic position is not supported by recent phylogenetic work, that retrieved the dromasaurs as non-monophyletic (Boos et al., 2016; Angielczyk and Kammerer, 2017; Angielczyk et al., 2021).

In Angielczyk and Kammerer (2017) and Angielczyk et al. (2021), *Patranomodon* is in a more basal postion than *Galechirus* and *Galeops*, but more derived than *Galepus* and the Anomocephaloidea. In Boos et al. (2016) and Kammerer and Smith (2017), *Patranomodon* holds a very basal position, between the Anomocephaloidea and the Venyukovioidea, *Galepus* and *Galechirus* branch together but are more basal than *Galeops*. Most previous phylogenetic works place *Galeops* as the sister group to the Dicynodontia (Cisneros et al., 2011; Kammerer et al., 2011; Boos et al., 2016) whereas Fröbisch and Reisz (2008) suggested the placement of *Galeops* as the sister taxon to the Venyukovioidea.

In both the cladistic and Bayesian analyses, NMQR 2913 is placed as the basal-most dicynodont, following the definition of Kammerer and Angielczyk (2009) (Figures 23–25). This was

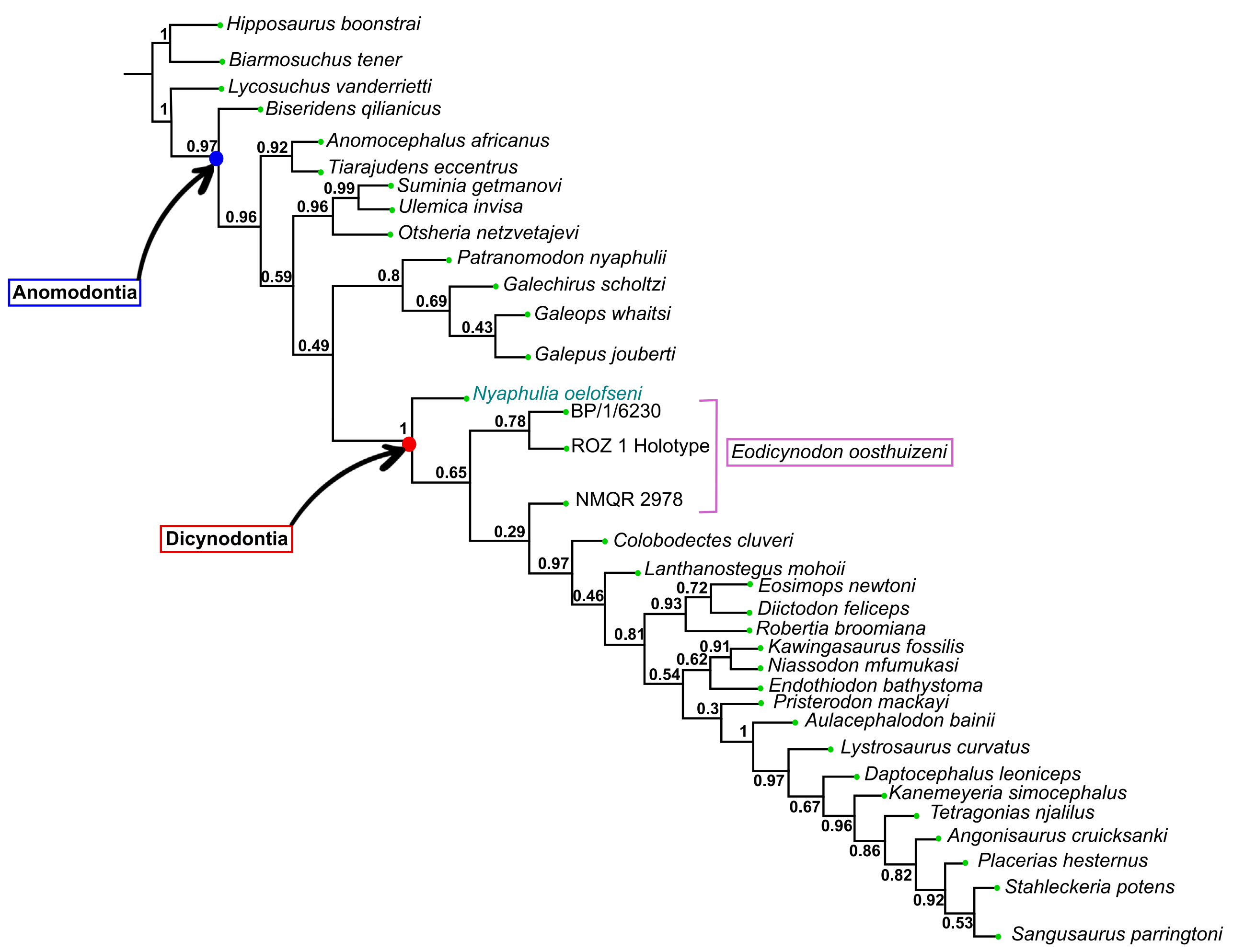

FIGURE 25
Bayesian phylogenetic analysis of the Anomodontia with RevBayes. Values at nodes indicate the posterior probability of the node.

previously suggested by several authors and it is discussed below. The clade Dicynodontia is supported by a low Bremer index of 1, but a strong posterior probability of 1 with both Bayesian softwares (Figures 23–25).

The phylogenetic position of *Lanthanostegus* and *Colobodectes* is left unresolved at the base of the dicynodont clade in both cladistic and MrBayes analyses (Figures 23, 24). The RevBayes analysis elucidates their position and places *Colobodectes* as early diverging (Figure 25).

The pylaecephalids *Eosimops*, *Diictodon* and *Robertia* are retrieved as a clade in the three analyses, with a low Bremer index of 1 but good posterior probabilies of 0.9 and 0.93 (Figures 23–25).

Endothiodon and the emydopoids *Niassodon* and *Kawingasaurus* form a clade in the three analyses, with a Bremer index of 2 and posterior probabilities of 0.86 and 0.62 (Figures 23, 24). The position of that clade in relation to *Pristerodon* and later diverging dicynodonts is left unresolved in the cladistic and MrBayes analysis (Figures 23, 24). The RevBayes analysis gives a full resolution, with *Pristerodon* placed in a more derived position, but the posterior probabilities are low (Figure 25). *Pristerodon* is retrieved one step after the pylaecephalids in Kammerer and Angielczyk (2009).

The Dicynodontoidea are undersampled in the analyses but place as a terminal clade in both the Bayesian and the cladistic analyses with a similar topology, with a Bremer index of 1 and a Bayesian posterior probabilities of 0.99 and 1 (Figures 23–25). Among them, the relation between *Lystrosaurus* and *Daptocephalus* is unresolved in the MrBayes analysis, whereas they branch together in the cladistic analysis (Figures 23, 24). The RevBayes analysis gives a third topology, with *Lystrosaurus* forming the sister taxon to all other dicynodontoids (Figure 25).

4 Discussion

Described and named by Rubidge (1990a), NMQR 2913 was previously assigned to a new species of the genus *Eodicynodon*, *Eodicynodon oelofseni*. It was later scored in a phylogenetic analysis as *Eodicynodon* along with the type of *E. oosthuizeni* (Fröbisch and Reisz, 2008). Later, It was suggested that NMQR 2913, the holotype of *Eodicynodon oelofseni*, does not form a clade with *E. oosthuizeni* and therefore, should be assigned to a different genus (Modesto et al., 2003; Abdala et al., 2008). This hypothesis was supported by recent studies in which NMQR 2913 and *E. oosthuizeni* were scored separately in phylogenetic analyses (Boos et al., 2016; Angielczyk and Kammerer, 2017; Kammerer and Smith, 2017; Angielczyk et al., 2021). They consistently resulted in the placement of NMQR 2913 in a more basal position than *E. oosthuizeni* (Modesto et al., 2003; Abdala et al., 2008; Kammerer et al., 2011; Angielczyk et al., 2021). The current work addresses these phylogenetic hypotheses.

4.1 Identity of NMQR 2913: anatomical comparisons and phylogeny

As in *Patranomodon*, NMQR 2913 does not bear tusks, and has homodont conical maxillary and dentary teeth. A similar condition is present in most other non-dicynodont anomodonts, with the exception of *Tiarajudens* and *Biseridens* which both have a well-formed caniniform (Liu et al., 2010; Cisneros et al., 2011). *Suminia* has homodont teeth but, in contrast to those of NMQR 2913, they are massive and have a talon-and-heel morphology, similar to tapinocephalid dinocephalians (Rybczynski, 2000; Ivakhnenko, 2003).

All basal dicynodonts, including *E. oosthuizeni*, have a well-formed tusk-like caniniform while NMQR 2913 does not (Figures 7, 8, 20, and Kammerer et al., 2011). The presence of a well-formed caniniform tusk is a synapomorphy to all the dicynodonts more derived than NMQR 2913 (Rubidge and Sidor, 2001).

Specimen NMQR 2913 and *E. oosthuizeni* do not possess premaxillary teeth, *Patranomodon*, specimen NMQR 3000 has a tooth at the suture between the maxilla and premaxilla (Figures 1D, 8D, 20D and Modesto et al., 1999; Liu et al., 2010), which supports that it had premaxillary teeth, as in most non-dicynodont anomodonts. A newly discovered, but yet unprepared, specimen with a complete snout supports the idea that *Patranomodon* has premaxillary teeth (pers. obv.). Early-diverging anomodonts including *Tiarajudens* and *Anomocephalus* (Anomocephaloidea), the Venyukovioidea (*Otsheria*, *Suminia* and *Ulemica*) and "Dromasauria" (*Galeops* (?), *Galepus* and *Galechirus*) all have incisiform teeth on the premaxilla (Olson, 1962; Brinkman, 1981; Modesto et al., 1999; Rybczynski, 2000; Ivakhnenko, 2003; Cisneros et al., 2011). The Anomocephaloidea bear premaxillary teeth with a unique spade-like morphology, which is not found in any other anomodont (Cisneros et al., 2015). The relatively slender maxillary and dentary teeth of NMQR 2913 more closely resemble those of *Galeops* and *Eodicynodon* than those of *Biseridens*, *Suminia*, *Ulemica*, *Tiarajudens* and *Anomocephalus* that are mediolaterally broad (Brinkman, 1981; Modesto et al., 1999; Ivakhnenko, 2003; Liu et al., 2010; Cisneros et al., 2011).

The general shape and morphology of the skull in NMQR 2913 more closely resemble that of *Patranomodon* and *Galeops* rather than *Eodicynodon* (Figures 1, 8, 20). The snout in NMQR 2913, does not slope anteriorly gently as in dicynodonts or *Suminia*, but slopes more abruptly, as in *Patranomodon* or *Ulemica*. The snout in *Tiarajudens*, *Anomocephalus* and *Otsheria* steeply slopes upwards whereas that of NMQR 2913 slopes more gently (Modesto et al., 1999; Cisneros et al., 2011; 2015). The snout of NMQR 2913 resembles that of *Patranomodon*, but the nasal process of the premaxilla in *Patranomodon* intrudes into the nasal (Figure 1G) whereas it does not in NMQR 2913 (Figure 20C, D). The squamosal is unfolded and slender as in most other non-dicynodont anomodonts (with the exception of *Ulemica* and *Galeops*, see Ivakhnenko (2003); Brinkman (1981)). In contrast *Eodicynodon* has a robust and folded squamosal, like that of all dicynodonts (Figures 7, 8).

Otsheria and *Biseridens* have a pachyostotic skull whereas that of NMQR 2913 and other anomodonts is gracile (Brinkman, 1981; Rubidge and Hopson, 1996; Ivakhnenko, 2003; Liu et al., 2010; Cisneros et al., 2015). The general shape of the lower jaw of NMQR 2913 is close to that of *Galeops* and *Eodicynodon*. It differs from *Ulemica* in the absence of an anteroventral notch on the dentary (Ivakhnenko, 2003), and is more gracile than the lower jaw of *Biseridens* (Liu et al., 2010).

The anterior margin of the orbit in NMQR 2913 and *Patranomodon* is relatively vertical, whereas it is rounded in the *E. oosthuizeni* specimens NMQR 2978 and BP/1/6230 (Figures 7B, 8B and 20B). In lateral view, NMQR 2913 has an exposed septomaxilla. This bone is absent in *Patranomodon* and *Eodicynodon*. The septomaxilla is not exposed laterally in most dicynodonts (with the exception of some derived taxa such as *Sangusaurus*, see Angielczyk et al., 2017). On the other hand, the septomaxilla is present and laterally exposed in most basal therapsids and in all basal anomodonts (Brinkman, 1981; Ivakhnenko, 2003; Liu et al., 2009; Liu et al., 2010; Day et al., 2018). It borders the posteroventral margin of the naris and is relatively reduced in *Otsheria*, *Ulemica*, *Tiarajudens*, *Biseridens* and *Galeops* (Olson, 1962; Ivakhnenko, 2003; Liu et al., 2010; Cisneros et al., 2011). In *Suminia*, it extends posteriorly (Rybczynski, 2000; Ivakhnenko, 2003) and resembles that of NMQR 2913 but is likely incomplete (Figure 20A).

Patranomodon does not have a secondary palate (Figure 1D). A similar condition is found in NMQR 2913, *Ulemica*, *Otsheria* and *Biseridens* where the choanae open directly at the level of the first maxillary teeth (Figure 20D). In contrast, *E. oosthuizeni* and other dicynodonts have a secondary palate comprising mainly the premaxilla and choanae opening behind the level of the tusk (Figures 8D, 1G; see Modesto et al., 2003; Fröbisch and Reisz, 2008; Kammerer et al., 2011).

On the palate, the posterior section of the parabasisphenoid in NMQR 2913 has a similar morphology to the parabasisphenoid wings in *Patranomodon* (Figures 6, 21). However, the general morphology of the pterygoids in NMQR 2913 resembles that of *Eodicynodon*, with pronounced posterior and anterior ventral keels (=transverse flange of the pterygoid). The interpterygoid vacuity is wider in NMQR 2913 and *Eodicynodon* than in *Patranomodon*, which has a very narrow interpterygoid vacuity (Figures 6, 18, 21).

The parasphenoid reaches the interpterygoid vacuity in *Suminia*, *Ulemica* and NMQR 2913, while it is excluded from it in *Patranomodon* and all dicynodonts; including *Eodicynodon* (Figures 6, 17, 21). On the dorsal side of the parasphenoid of *Patranomodon*, the two carotid foramina are widely separated; while they are close to each other in NMQR 2913.

Co-ossification of cranial and jaw bones can occur in Anomodontia and is documented in different taxa. On the lower jaw, the articular and prearticular are sometimes fused, as in *E. oosthuizeni* or *Niassodon* (see Figure 19 and Castanhinha et al., 2013). In NMQR 2913, on the medial side of the lower jaw, there is a clear suture between the articular and prearticular (Figure 22). A similar condition is found in the lower jaw of *Patranomodon* and likely in *Galeops* (Brinkman, 1981; Rubidge and Hopson, 1996). On the occiput, some co-ossification can occur, especially in the bones of the periotic region (Castanhinha et al., 2013; Pusch et al., 2019; Macungo et al., 2022). In some cases, the fusion of the opisthotic and prootic forms a periotic bone in therapsids. In *Eodicynodon*, the periotic region is partly co-ossified, as some sutures between the supraoccipital, opisthotic and prootic are unclear (Figures 11, 12). In *Patranomodon*, all sutures of the periotic region are clearly defined, indicating that the bones in this area are not fused (Figures 4, 5). Lastly, at the base of the hindbrain, the parabasisphenoid results from the co-ossification of the parasphenoid and basisphenoid in most basal anomodonts (*Suminia*, *Ulemica*, *Otsheria*…), in NMQR 2913, in therapsids as a whole and in “pelycosaurs” (Romer and Price, 1940; Cluver, 1971; Rubidge, 1990a; Modesto et al., 2003; Sidor and Rubidge, 2006; Day et al., 2018; Pusch et al., 2019). However, in *Patranomodon*, NMQR 2978 and BP/1/6230, the parabasisphenoid is divided between the parasphenoid and basisphenoid (Figures 1, 7, 8). This has been observed in *Niassodon*, some cistecephalids and *Pristerodon* (Castanhinha et al., 2013; Macungo et al., 2022).

To sum up, in addition to the autapomorphic characters presented in the phylogenetic results section, specimen NMQR 2913 possesses a combination of anatomical features and is different from other early-diverging anomodonts. It is closer to *Patranomodon* or *Galeops* (and other dromasaurians) in overall morphology, by being gracile and not heavily pachyostotic like *Otsheria* or *Suminia*. Specimen NMQR 2913 has non-gomphodont, peg-like, maxillary and dentary teeth, unlike *Anomocephalus*, *Tiarajudens* and *Suminia*. It does not have a tusk-like caniniform tooth, unlike *Tiarajudens* and *Eodicynodon* and most other dicynodonts. Its lower jaw is slender as in *Patranomodon* and *Eodicynodon*, while the lower jaw of *Ulemica* is robust with an anteroventral notch on the dentary. This suggests that NMQR 2913 differs from every other basal anomodont, including *Eodicynodon*, and as suggested by previous authors (Modesto et al., 2003; Abdala et al., 2008; Angielczyk et al., 2021), should be distinguished at generic level.

In their latest review, Kammerer and Angielczyk (2009) (page 5) stated that dicynodonts are “all taxa more closely related to *Dicynodon lacerticeps* than *G. whaitsi*”. From a taxonomic point of view, in both Bayesian and cladistic analyses (Figures 23, 24), NMQR 2913 is thus a dicynodont. If NMQR 2913 is considered as a Dicynodontia, the presence of tusks and secondary palate can no longer be considered synapomorphies of the Dicynodontia clade. This taxon thus represents an important transitional stage in the development of dicynodont synapomorphies.

Modesto et al. (2003) (page 211) were the first to question the taxonomic affiliation of NMQR 2913 to the genus *Eodicynodon* and stated that there is “little basis for recognizing *Eodicynodon oelofseni* as the closest relative of *E. oosthuizeni*”. Their analysis placed NMQR 2913 as the sister taxon to Dicynodontia. Later, the analysis of Kammerer et al. (2011) retrieved this phylogenetic topology with strong cladistic support. Some phylogenies have retrieved NMQR 2913 as the earliest diverging member of Dicynodontia (Abdala et al., 2008; Angielczyk et al., 2017; Angielczyk et al., 2021; Macungo et al., 2022). Others did not score NMQR 2913 separately from *E. oosthuizeni* (Angielczyk, 2007; Fröbisch and Reisz, 2008; Cisneros et al., 2011). Boos et al. (2016) retrieved NMQR 2913 as a non-dicynodont anomodont. In the cladistic analysis proposed here (Figure 23), the strict consensus suggests that NMQR 2913 does not form a clade with *E. oosthuizeni* and is the sister taxon to the clade gathering *E. oosthuizeni* and all other dicynodonts. All specimens attributed to *E. oosthuizeni* form a clade sister to all other derived dicynodonts in the cladistic analysis but not in the Bayesian analyses. The latter supports the exclusion of NMQR 2913 from the genus *Eodicynodon* and gives a posterior probability support of 1 for the clade Dicynodontia with NMQR 2913 as the basal-most taxon (Figure 24).

4.2 Taxonomy and updated systematic paleontology of NMQR 2913

Following the results obtained from the parsimony analysis with TNT presented above, NMQR 2913 can be distinguished from the genus *Eodicynodon* by the following features:

- The absence of canine-like tusks
- The absence of contact between the prefrontal and maxilla
- The base of the zygomatic process of the squamosal is narrow
- The internal carotid foramen (dorsal surface of the parasphenoid) is directed medially
- The height of the dorsum sellae is moderate, as clearly distinct but does not reach the height of the pila antotica

Specimen NMQR 2913 differs from early-diverging anomodonts in the absence of premaxillary teeth (Character 8, state 1), presence of a transverse process of the pterygoid that does not project laterally (Character 91, state 2), the presence of a pterygoid keel (Character 92, state 1), a well-developed dentary shelf (Character 129, state 1), and a surangular without a vertical lamina (Character 139, state 1). It differs from other dicynodonts in the presence of a lateral exposure of the septomaxilla (Character 18, state 0), the absence of a secondary palate, the absence of a canine-like tusk (Character 25 and 26, state 1 and “-” respectively), a parasphenoid that reaches the interpterygoid vacuity (Character 101, state 1; present in all basal anomodonts except *Patranomodon*).

Based on the updated descriptions and comparisons presented above, the phylogenetic analyses produced and literature (Modesto et al., 2003; Abdala et al., 2008; Fröbisch and Reisz, 2008; Kammerer et al., 2011; Boos et al., 2016; Angielczyk et al., 2021), all evidence indicates that NMQR 2913 is a distinct genus from *Eodicynodon* and is the most basal dicynodont. A new taxonomic unit, *Nyaphulia olofseni*, is introduced and refers specimen NMQR 2913 as the holotype.

SYSTEMATIC PALEONTOLOGY
THERAPSIDA Broom, 1905

ANOMODONTIA Owen, 1859
DICYNODONTIA Owen, 1859
Nyaphulia gen. nov.

urn:lsid:zoobank.org:act:A1873A91-F8FE-4A35-9FB4-4A13BF35066B

Type species—*oelofseni*.

Diagnosis—As for the species.

Etymology—The name refers to John Nyaphuli, a former employee of the National Museum of Bloemfontein, that extensively contributed to South African paleontology with his numerous fossil finds, particularly of the most basal therapsids from South Africa. He additionally discovered specimen NMQR 2913 in 1982.

Nyaphulia oelofseni gen. nov.

Holotype—NMQR 2913.

Material—Skull, lower jaw and postcranial elements.

Type locality—Botterkraal farm, Abrahamskraal Formation, *Eodicynodon* Assemblage Zone, Beaufort Group, Karoo Supergroup, South Africa.

Diagnosis—Anomodont that uniquely combines the absence of a tusk-like caniniform tooth and secondary palate, with the absence of premaxillary and anterior dentary teeth (osseous beak present). Also comprises the following unique combination of characters: laterally situated maxillary teeth that point in an anterior direction; absence of contact between the maxilla and the prefrontal; septomaxilla with a lateral projection present; a narrowly based zygomatic process of the squamosal; internal carotid foramina directed medially on the dorsal surface of the parabasisphenoid; a moderate height of the dorsum sellae that does not reach the level of the pila antotica and no coronoid eminence on posterodorsal surface of the dentary.

Description—See the Description above.

5 Conclusion

We describe in detail four early-diverging anomodont specimens from the *Eodicynodon* Assemblage Zone of the Karoo Supergroup, to feed an updated revision of basal anomodont phylogenetic relationships. The ultimate goal is to address the taxonomic attribution of NMQR 2913 to the genus *Eodicynodon*.

The detailed redescription of *Patranomodon nyaphuli*, two specimens of *E. oosthuizeni* and NMQR 2913 using CT-data provides crucial data on the external and endocranial anatomy of basal anomodonts. This supports that NMQR 2913 differs at the generic level from *E. oosthuizeni* in the structure of its braincase floor (parasphenoid, basisphenoid), anatomy of the interpterygoid vacuity, sutural contacts of the snout bones, presence of a septomaxilla, absence of a tusk and secondary palate, and morphology of the dentition and general shape of the skull and skull roof. Overall, NMQR 2913 appears anatomically dissimilar to *E. oosthuizeni*. Fully resolved phylogenetic analyses with TNT, MrBayes and RevBayes indicate that NMQR 2913 is better interpreted as a new genus, here named *Nyaphulia oelofseni*, and supports that it is the earliest diverging dicynodont.

Data availability statement

The original contributions presented in the study are included in the article/Supplementary Material, further inquiries can be directed to the corresponding author.

Author contributions

AD conceived the study, produced the 3D models, created the figures and wrote the manuscript. JB and BR supervised the study, provided input on the cranial morphology of basal anomodonts and undertook extensive reviews of the manuscript. BW and AW reviewed the Bayesian Inference method, produced the RevBayes analysis and made extensive comments and reviews on the manuscript. All authors contributed to the article and approved the submitted version.

Funding

This study was funded by the University of the Witwatersrand, the South African National Research Foundation (NRF) and GENUS (DST-NRF Centre of Excellence in Palaeosciences). AW and BW were funded on NSF-DEB 2045842. JB was funded by DSI-NRF African Origins Platform (AOP210218587003; UID: 136505).

Acknowledgments

We acknowledge the financial help of the University of the Witwatersrand, the NRF and GENUS. We are grateful for the help of Dr. Kudakwashe Jakata for the scan of the specimens at the Evolutionary Studies Institute. We are grateful to Dr. Jennifer Botha and Elize Butler for all their assistance with the loan of specimens from the National Museum. We thank the handling editor Dr. Shinya Iwasaki and the reviewers Prof. Jörg Fröbisch and Dr. Saverio Bartolini Lucenti for their helpful comments on the manuscript. Lastly, we are grateful to Dr. Stergios Zarkogiannis for his assistance with administrative matters; to Giorgia Aprile, Amy Tighe, and Stephen Breese, who supported us throughout the production process; and to Dr. Pauline Guenser who invited us for this publication.

Conflict of interest

The authors declare that the research was conducted in the absence of any commercial or financial relationships that could be construed as a potential conflict of interest.

Publisher's note

Supplementary material

The Supplementary Material for this article can be found online at: https://www.frontiersin.org/articles/10.3389/feart.2023.1220341/full#supplementary-material

References

Abdala, F., Rubidge, B. S., and van den Heever, J. (2008). The oldest therocephalians (Therapsida, Eutheriodontia) and the early diversification of Therapsida. *Palaeontology* 51, 1011–1024. doi:10.1111/j.1475-4983.2008.00784.x

Angielczyk, K., Benoit, J., and Rubidge, B. S. (2019). A new tusked cistecephalid dicynodont (Therapsida, Anomodontia) from the upper Permian upper Madumabisa Mudstone formation, Luangwa Basin, Zambia. *Pap. Palaeontol.* 7, 405–446. doi:10.1002/spp2.1285

Angielczyk, K., and Kammerer, C. (2018). *Non-mammalian synapsids: the deep roots of the mammalian family tree*. Berlin: De Gruyter, 117–198.

Angielczyk, K. D. (2007). New specimens of the Tanzanian dicynodont *Cryptocynodon parringtoni* von Huene, 1942 (Therapsida, Anomodontia), with an expanded analysis of Permian dicynodont phylogeny. *J. Vertebrate Paleontology* 27, 116–131. doi:10.1671/0272-4634(2007)27[116:nsottd]2.0.co;2

Angielczyk, K. D., Hancox, P., and Nabavizadeh, A. (2017). A redescription of the Triassic kannemeyeriiform dicynodont *Sangusaurus* (Therapsida, Anomodontia), with an analysis of its feeding system. *J. Vertebrate Paleontology* 37, 189–227. doi:10.1080/02724634.2017.1395885

Angielczyk, K. D., and Kammerer, C. F. (2017). The cranial morphology, phylogenetic position and biogeography of the upper Permian dicynodont *Compsodon helmoedi* van Hoepen (Therapsida, Anomodontia). *Pap. Palaeontol.* 3, 513–545. doi:10.1002/spp2.1087

Angielczyk, K. D., Liu, J., and Yang, W. (2021). A redescription of *Kunpania scopulusa*, a bidentalian dicynodont (Therapsida, Anomodontia) from the Guadalupian of Northwestern China. *J. Vertebrate Paleontology* 41, e1922428. doi:10.1080/02724634.2021.1922428

Angielczyk, K. D., and Rubidge, B. S. (2010). A new pylaecephalid dicynodont (Therapsida, Anomodontia) from the *Tapinocephalus* Assemblage Zone, Karoo basin, Middle Permian of South Africa. *J. Vertebrate Paleontology* 30, 1396–1409. doi:10.1080/02724634.2010.501447

Araújo, R. M. N., Fernandez, V., Polcyn, M. J., Fröbisch, J., and Martins, R. M. S. (2017). Aspects of gorgonopsian paleobiology and evolution: insights from the basicranium, occiput, osseous labyrinth, vasculature, and neuroanatomy. *PeerJ* 5, e3119. doi:10.7717/peerj.3119

Barry, T. (1974). A new dicynodont ancestor from the Upper Ecca (lower middle Permian) of South Africa. *Ann. South Afr. Mus.* 64, 117–136.

Benoit, J., Angielczyk, K. D., Miyamae, J. A., Manger, P., Fernandez, V., and Rubidge, B. (2018). Evolution of facial innervation in anomodont therapsids (Synapsida): insights from X-ray computerized microtomography. *J. Morphol.* 279, 673–701. doi:10.1002/jmor.20804

Benoit, J., Jasinoski, S. C., Fernandez, V., and Abdala, F. (2017). The mystery of a missing bone: revealing the orbitosphenoid in basal Epicynodontia (Cynodontia, Therapsida) through computed tomography. *Sci. Nat.* 104, 66–10. doi:10.1007/s00114-017-1487-z

Benton, M. (2015). *Vertebrate palaeontology*. John Wiley & Sons.

Boos, A. D. S., Kammerer, C. F., Schultz, C. L., Soares, M. B., and Iiha, A. L. R. (2016). A new dicynodont (Therapsida: Anomodontia) from the Permian of Southern Brazil and its implications for bidentalian origins. *PLoS ONE* 11, e0155000. doi:10.1371/journal.pone.0155000

Botha-Brink, J., and Angielczyk, K. D. (2010). Do extraordinarily high growth rates in Permo-Triassic dicynodonts (Therapsida, Anomodontia) explain their success before and after the end-Permian extinction? *Zoological J. Linn. Soc.* 160, 341–365. doi:10.1111/j.1096-3642.2009.00601.x

Brinkman, D. (1981). The structure and relationships of the dromasaurs (Cambridge: Therapsida). *Breviora* 465, 1–34.

Broom, R. (1905). On the use of the term Anomodontia. *Rec. Albany Mus.* 1, 266–269.

Brown, J. M., and Lemmon, A. R. (2007). The importance of data partitioning and the utility of Bayes factors in Bayesian phylogenetics. *Syst. Biol.* 56, 643–655. doi:10.1080/10635150701546249

Castanhinha, R., Araújo, R. M. N., Júnior, L. C., Angielczyk, K. D., Martins, G. G., Martins, R. M. S., et al. (2013). Bringing dicynodonts back to life: paleobiology and anatomy of a new emydopoid genus from the Upper Permian of Mozambique. *PLoS ONE* 8, e80974. doi:10.1371/journal.pone.0080974

Chinsamy-Turan, A. (2011). *Forerunners of mammals: radiation, histology, biology*. Indiana University Press.

Cifelli, R., Luo, Z.-X., and Kielan-Jaworowska, Z. (2004). *Mammals from the age of dinosaurs: origins, evolution, and structure*. Columbia University Press.

Cisneros, J. C., Abdala, F., Jashashvili, T., de Oliveira Bueno, A., and Dentzien-Dias, P. (2015). *Tiarajudens eccentricus* and *Anomocephalus africanus*, two bizarre anomodonts (Synapsida, Therapsida) with dental occlusion from the Permian of Gondwana. *Open Sci.* 2, 150090. doi:10.1098/rsos.150090

Cisneros, J. C., Abdala, F., Rubidge, B. S., Dentzien-Dias, P. C., and de Oliveira Bueno, A. (2011). Dental occlusion in a 260-million-year-old therapsid with saber canines from the Permian of Brazil. *Science* 331, 1603–1605. doi:10.1126/science.1200305

Cluver, M. A. (1971). The cranial morphology of the dicynodont genus *Lystrosaurus*. Ph.D. thesis. Stellenbosch: Stellenbosch University.

Cox, C. B., and Broom, R. (1962). A natural cast of the inner ear of a dicynodont. *Am. Mus. novitates* 2116, 1–6.

Crompton, A., Musinsky, C., Rougier, G., Bhullar, B.-A., and Miyamae, J. (2018). Origin of the lateral wall of the mammalian skull: fossils, monotremes and therians revisited. *J. Mammalian Evol.* 25, 301–313. doi:10.1007/s10914-017-9388-7

Damiani, R., Vasconcelos, C., Renaut, A., Hancox, J., and Yates, A. (2007). *Dolichuranus primaevus* (Therapsida: Anomodontia) from the Middle Triassic of Namibia and its phylogenetic relationships. *Palaeontology* 50, 1531–1546. doi:10.1111/j.1475-4983.2007.00727.x

Day, M. O., and Rubidge, B. S. (2014). A brief lithostratigraphic review of the Abrahamskraal and Koonap Formations of the Beaufort Group, South Africa: towards a basin-wide stratigraphic scheme for the middle Permian Karoo. *J. Afr. Earth Sci.* 100, 227–242. doi:10.1016/j.jafrearsci.2014.07.001

Day, M. O., Smith, R. M. H., Benoit, J., Fernandez, V., and Rubidge, B. S. (2018). A new species of burnetiid (Therapsida, Burnetiamorpha) from the early Wuchiapingian of South Africa and implications for the evolutionary ecology of the family Burnetiidae. *Pap. Palaeontol.* 4, 453–475. doi:10.1002/spp2.1114

de Simão-Oliveira, D., Kerber, L., and L Pinheiro, F. (2019). Endocranial morphology of the Brazilian Permian dicynodont *Rastodon procurvidens* (Therapsida: Anomodontia). *J. Anat.* 236, 384–397. doi:10.1111/joa.13107

Duhamel, A., Benoit, J., Day, M. O., Rubidge, B. S., and Fernandez, V. (2021). Computed tomography elucidates ontogeny within the basal therapsid clade Biarmosuchia. *PeerJ* 9, e11866. doi:10.7717/peerj.11866

Dzik, J., Sulej, T., and Niedźwiedzki, G. (2008). A dicynodont-theropod association in the latest Triassic of Poland. *Acta Palaeontol. Pol.* 53, 733–738. doi:10.4202/app.2008.0415

Fourie, S. (1974). The cranial morphology of *Thrinaxodon liorhinus* Seeley. *Ann. South Afr. Mus.* 65, 337–400.

Fröbisch, J. (2009). Composition and similarity of global anomodont-bearing tetrapod faunas. *Earth-Science Rev.* 95, 119–157. doi:10.1016/j.earscirev.2009.04.001

Fröbisch, J., and Reisz, R. R. (2008). A new species of *Emydops* (Synapsida, Anomodontia) and a discussion of dental variability and pathology in dicynodonts. *J. Vertebrate Paleontology* 28, 770–787. doi:10.1671/0272-4634(2008)28[770:ansoes]2.0.co;2

Fröbisch, J., and Reisz, R. R. (2009). The late Permian herbivore *Suminia* and the early evolution of arboreality in terrestrial vertebrate ecosystems. *Proc. R. Soc. B Biol. Sci.* 276, 3611–3618. doi:10.1098/rspb.2009.0911

Geyer, C. J. (1991). "Markov chain Monte Carlo maximum likelihood," in Proceedings of the 23rd Symposium on the Interface (Interface Foundation of North America), 156–163.

Goloboff, P. A., and Catalano, S. A. (2016). TNT version 1.5, including a full implementation of phylogenetic morphometrics. *Cladistics* 32, 221–238. doi:10.1111/cla.12160

Goloboff, P. A., Farris, J. S., and Nixon, K. (2003). TNT: tree analysis using new technology. *Syst. Biol.* 54, 176–178. doi:10.1080/10635150590905830

Green, P. J. (1995). Reversible jump Markov chain Monte Carlo computation and Bayesian model determination. *Biometrika* 82, 711–732. doi:10.1093/biomet/82.4.711

Hammer, W., and Cosgriff, J. (1981). *Myosaurus gracilis*, an anomodont reptile from the Lower Triassic of Antarctica and South Africa. *J. Paleontology* 55, 410–424.

Hancox, P. J., Angielczyk, K. D., and Rubidge, B. S. (2013). *Angonisaurus* and *Shansiodon*, dicynodonts (Therapsida, Anomodontia) from Subzone C of the *Cynognathus* Assemblage Zone (Middle Triassic) of South Africa. *J. Vertebrate Paleontology* 33, 655–676. doi:10.1080/02724634.2013.723551

Hastings, W. K. (1970). Monte Carlo sampling methods using Markov chains and their applications. *Biometrika* 57, 97–109. doi:10.1093/biomet/57.1.97

Höhna, S., Landis, M. J., Heath, T. A., Boussau, B., Lartillot, N., Moore, B. R., et al. (2016). RevBayes: Bayesian phylogenetic inference using graphical models and an interactive model-specification language. *Syst. Biol.* 65, 726–736. doi:10.1093/sysbio/syw021

Huelsenbeck, J. P., and Ronquist, F. (2001). MRBAYES: Bayesian inference of phylogenetic trees. *Bioinformatics* 17, 754–755. doi:10.1093/bioinformatics/17.8.754

Ivakhnenko, M. F. (2003). Eotherapsids from the east European placket (late Permian). *Paleontological J.* 37, 339–465.

Ivakhnenko, M. F. (2008). Cranial morphology and evolution of Permian dinomorpha (Eotherapsida) of Eastern Europe. *Paleontological J.* 42, 859–995. doi:10.1134/s0031030108090013

Jinnah, Z. A., and Rubidge, B. (2007). A double-tusked dicynodont and its biostratigraphic significance. *South Afr. J. Sci.* 103, 51–53.

Kammerer, C. F. (2016a). Systematics of the Rubidgeinae (Therapsida: Gorgonopsia). *PeerJ* 4, e1608. doi:10.7717/peerj.1608

Kammerer, C. F. (2016b). Two unrecognised burnetiamorph specimens from historic Karoo collections. *Palaeontol. Afr.* 50, 64–75.

Kammerer, C. F., Angielczyk, K., and Fröbisch, J. (2014). *Early evolutionary history of the Synapsida*. Netherlands: Springer.

Kammerer, C. F., and Angielczyk, K. D. (2009). A proposed higher taxonomy of anomodont therapsids. *Zootaxa* 2018, 1–24. doi:10.11646/zootaxa.2018.1.1

Kammerer, C. F., Angielczyk, K. D., and Fröbisch, J. (2011). A comprehensive taxonomic revision of *Dicynodon* (Therapsida, Anomodontia) and its implications for dicynodont phylogeny, biogeography, and biostratigraphy. *J. Vertebrate Paleontology* 31, 1–158. doi:10.1080/02724634.2011.627074

Kammerer, C. F., and Smith, R. M. H. (2017). An early geikiid dicynodont from the *Tropidostoma* Assemblage Zone (late Permian) of South Africa. *PeerJ* 5, e2913. doi:10.7717/peerj.2913

Kemp, T. S. (2005). *The origin and evolution of mammals*. Oxford: Oxford University.

Kruger, A., Rubidge, B. S., and Abdala, F. (2018). A juvenile specimen of *Anteosaurus magnificus* Watson, 1921 (Therapsida: Dinocephalia) from the South African Karoo, and its implications for understanding dinocephalian ontogeny. *J. Syst. Palaeontol.* 16, 139–158. doi:10.1080/14772019.2016.1276106

Laaß, M. (2015a). Bone-conduction hearing and seismic sensitivity of the Late Permian anomodont *Kawingasaurus fossilis*. *J. Morphol.* 276, 121–143. doi:10.1002/jmor.20325

Laaß, M. (2015b). Virtual reconstruction and description of the cranial endocast of *Pristerodon mackayi* (Therapsida, Anomodontia). *J. Morphol.* 276, 1089–1099. doi:10.1002/jmor.20397

Laaß, M., and Schillinger, B. (2015). Reconstructing the auditory apparatus of therapsids by means of neutron tomography. *Phys. Procedia* 69, 628–635. doi:10.1016/j.phpro.2015.07.089

Laaß, M., Schillinger, B., and Kaestner, A. (2017). What did the "Unossified zone" of the non-mammalian therapsid braincase house? *J. Morphol.* 278, 1020–1032. doi:10.1002/jmor.20583

Larget, B., and Simon, D. L. (1999). Markov chain Monte Carlo algorithms for the Bayesian analysis of phylogenetic trees. *Mol. Biol. Evol.* 16, 750–759. doi:10.1093/oxfordjournals.molbev.a026160

Lewis, P. O. (2001). A likelihood approach to estimating phylogeny from discrete morphological character data. *Syst. Biol.* 50, 913–925. doi:10.1080/106351501753462876

Liu, J., Rubidge, B., and Li, J. (2009). New basal synapsid supports Laurasian origin for therapsids. *Acta Palaeontol. Pol.* 54, 393–400. doi:10.4202/app.2008.0071

Liu, J., Rubidge, B., and Li, J. (2010). A new specimen of *Biseridens qilianicus* indicates its phylogenetic position as the most basal anomodont. *Proc. R. Soc. Lond. B Biol. Sci.* 277, 285–292. doi:10.1098/rspb.2009.0883

Luo, Z., Crompton, A. W., and Lucas, S. G. (1995). Evolutionary origins of the mammalian promontorium and cochlea. *J. Vertebrate Paleontology* 15, 113–121. doi:10.1080/02724634.1995.10011211

Luo, Z.-X. (2001). The inner ear and its bony housing in tritylodontids and implications for evolution of the mammalian ear. *Bull. Mus. Comp. Zoology* 156, 81–97.

Luo, Z.-X., Kielan-Jaworowska, Z., and Cifelli, R. L. (2002). In quest for a phylogeny of Mesozoic mammals. *Acta Palaeontol. Pol.* 47, 113–121.

Macungo, Z., Benoit, J., Fernandez, V., and Araújo, R. M. N. (2022). X-ray microcomputed and synchrotron tomographic analysis of the basicranial axis of emydopoid dicynodonts: implications for fossoriality and phylogeny. *Zoological J. Linn. Soc.* 198, 1–46. doi:10.1093/zoolinnean/zlac033

Maddison, W. P., and Maddison, D. R. (2015). *Mesquite: a modular system for evolutionary analysis*. Version 3.04.

Marilao, L. M., Kulik, Z. T., and Sidor, C. A. (2020). Histology of the preparietal: a neomorphic cranial element in dicynodont therapsids. *J. Vertebrate Paleontology* 40, e1770775. doi:10.1080/02724634.2020.1770775

Metropolis, N., Rosenbluth, A. W., Rosenbluth, M. N., Teller, A. H., and Teller, E. (1953). Equation of state calculations by fast computing machines. *J. Chem. Phys.* 21, 1087–1092. doi:10.1063/1.1699114

Modesto, S., Rubidge, B. S., Visser, I., and Welman, J. (2003). A new basal dicynodont from the Upper Permian of South Africa. *Palaeontology* 46, 211–223. doi:10.1111/1475-4983.00295

Modesto, S., Rubidge, B. S., and Welman, J. (1999). The most basal anomodont therapsid and the primacy of Gondwana in the evolution of the anomodonts. *Proc. R. Soc. B Biol. Sci.* 266, 331–337. doi:10.1098/rspb.1999.0642

Nicolas, M., and Rubidge, B. S. (2010). Changes in Permo-Triassic terrestrial tetrapod ecological representation in the Beaufort Group (Karoo Supergroup) of South Africa. *Lethaia* 43, 45–59. doi:10.1111/j.1502-3931.2009.00171.x

Nylander, J. A., Ronquist, F., Huelsenbeck, J. P., and Nieves-Aldrey, J. (2004). Bayesian phylogenetic analysis of combined data. *Syst. Biol.* 53, 47–67. doi:10.1080/10635150490264699

Olroyd, S. L., LeBlanc, A. R., Araújo, R., Angielczyk, K. D., Duhamel, A., Benoit, J., et al. (2021). Histology and μCT reveal the unique evolution and development of multiple tooth rows in the synapsid *Endothiodon*. *Sci. Rep.* 11, 16875–16923. doi:10.1038/s41598-021-95993-6

Olroyd, S. L., and Sidor, C. A. (2022). Nomenclature, comparative anatomy, and evolution of the reflected lamina of the angular in non-mammalian synapsids. *J. Vertebrate Paleontology* 42, e2101923. doi:10.1080/02724634.2022.2101923

Olroyd, S. L., Sidor, C. A., and Angielczyk, K. D. (2018). New materials of the enigmatic dicynodont *Abajudon kaayai* (Therapsida, Anomodontia) from the lower Madumabisa Mudstone Formation, middle Permian of Zambia. *J. Vertebrate Paleontology* 37, e1403442. doi:10.1080/02724634.2017.1403442

Olson, E. C. (1944). *Origin of mammals based upon cranial morphology of the therapsid suborders*. Geological Society of America Special Papers 55, 1–137.

Olson, E. C. (1962). Late Permian terrestrial vertebrates, USA and USSR. *Trans. Am. Philosophical Soc.* 52, 1–224. doi:10.2307/1005904

Owen, R. (1859). On the orders of fossil and recent Reptilia and their distribution in time. *Rep. Br. Asociation Adv. Sci.* 1859, 153–166.

Pusch, L. C., Kammerer, C. F., and Fröbisch, J. (2019). Cranial anatomy of the early cynodont *Galesaurus planiceps* and the origin of mammalian endocranial characters. *J. Anat.* 234, 592–621. doi:10.1111/joa.12958

Pusch, L. C., Ponstein, J., Kammerer, C. F., and Fröbisch, J. (2020). Novel endocranial data on the early therocephalian *Lycosuchus vanderrieti* underpin high character variability in early theriodont evolution. *Front. Ecol. Evol.* 7, 464. doi:10.3389/fevo.2019.00464

Rambaut, A., Drummond, A. J., Xie, D., Baele, G., and Suchard, M. A. (2018). Posterior summarization in Bayesian phylogenetics using tracer 1.7. *Syst. Biol.* 67, 901–904. doi:10.1093/sysbio/syy032

Ray, S., Botha, J., and Chinsamy, A. (2004). Bone histology and growth patterns of some nonmammalian therapsids. *J. Vertebrate Paleontology* 24, 634–648. doi:10.1671/0272-4634(2004)024[0634:bhagpo]2.0.co;2

Reisz, R. R. (2006). Origin of dental occlusion in tetrapods: signal for terrestrial vertebrate evolution? *J. Exp. Zoology Part B Mol. Dev. Evol.* 306, 261–277. doi:10.1002/jez.b.21115

Reisz, R. R., and Sues, H.-D. (2000). Herbivory in late Paleozoic and Triassic terrestrial vertebrates. *Evol. herbivory Terr. vertebrates* 9–41, 9–41. doi:10.1017/cbo9780511549717.003

Romer, A. S., and Price, L. W. (1940). Review of the Pelycosauria. *Geol. Soc. Am. Special Pap.* 28, 1–534. doi:10.1130/spe28-p1

Rougier, G. W., Martinelli, A. G., and Forasiepi, A. M. (2021). *Mesozoic mammals from South America and their forerunners*. Springer.

Rubidge, B. S. (1990a). The cranial morphology of a new species of the genus *Eodicynodon* (Therapsida, Dicynodontia). *Navorsinge Nas. Mus.* 7, 38–39.

Rubidge, B. S. (1990b). Redescription of the cranial morphology of *Eodicynodon oosthuizeni* (Therapsida; Dicynodontia). *Navorsinge Nas. Mus.* 7.

Rubidge, B. S. (1995). Biostratigraphy of the Beaufort Group (Karoo, Supergroup). South African committee for stratigraphy. *Biostratigraphic Series No. 1, Council for Geosciences, Pretoria*, 1–7.

Rubidge, B. S., and Day, M. O. (2020). Biostratigraphy of the *Eodicynodon* Assemblage Zone (Beaufort Group, Karoo Supergroup), South Africa. *South Afr. J. Geol.* 123, 141–148. doi:10.25131/sajg.123.0010

Rubidge, B. S., and Hopson, J. A. (1990). A new anomodont therapsid from South Africa and its bearing on the ancestry of Dicynodontia. *South Afr. J. Sci.* 86, 43–45.

Rubidge, B. S., and Hopson, J. A. (1996). A primitive anomodont therapsid from the base of the Beaufort Group (Upper Permian) of South Africa. *Zoological J. Linn. Soc.* 117, 115–139. doi:10.1111/j.1096-3642.1996.tb02152.x

Rubidge, B. S., and Kitching, J. W. (2003). A new burnetiamorph (Therapsida: Biarmosuchia) from the lower Beaufort Group of South Africa. *Palaeontology* 46, 199–210. doi:10.1111/1475-4983.00294

Rubidge, B. S., and Sidor, C. A. (2001). Evolutionary patterns among Permo-Triassic therapsids. *Annu. Rev. Ecol. Syst.* 32, 449–480. doi:10.1146/annurev.ecolsys.32.081501.114113

Ruta, M., Angielczyk, K. D., Fröbisch, J., and Benton, M. J. (2013). Decoupling of morphological disparity and taxic diversity during the adaptive radiation of anomodont therapsids. *Proc. R. Soc. B Biol. Sci.* 280, 20131071. doi:10.1098/rspb.2013.1071

Rybczynski, N. (2000). Cranial anatomy and phylogenetic position of *Suminia getmanovi*, a basal anomodont (Amniota: Therapsida) from the Late Permian of Eastern Europe. *Zoological J. Linn. Soc.* 130, 329–373. doi:10.1111/j.1096-3642.2000.tb01634.x

Rybczynski, N., and Reisz, R. R. (2001). Earliest evidence for efficient oral processing in a terrestrial herbivore. *Nature* 411, 684–687. doi:10.1038/35079567

Sidor, C. A. (2001). *Evolutionary trends and relationships within the Synapsida*. Ph.D. thesis. The University of Chicago.

Sidor, C. A. (2003). The naris and palate of *Lycaenodon longiceps* (Therapsida: Biarmosuchia), with comments on their early evolution in the Therapsida. *J. Paleontology* 77, 977–984. doi:10.1666/0022-3360(2003)077<0977:tnapol>2.0.co;2

Sidor, C. A., and Rubidge, B. S. (2006). *Herpetoskylax hopsoni, a new biarmosuchian (Therapsida: Biarmosuchia) from the Beaufort Group of South Africa*. University of Chicago Press, 76–113.

Sigogneau, D. (1974). The inner ear of *Gorgonops* (Reptilia, Therapsida, Gorgonopsia). *Ann. South Afr. Mus.* 64, 53–69.

Smith, R. M. H., Rubidge, B. S., Day, M. O., and Botha, J. (2020). Introduction to the tetrapod biozonation of the Karoo Supergroup. *South Afr. J. Geol.* 123, 131–140. doi:10.25131/sajg.123.0009

Smith, R. M. H., Rubidge, B. S., and Van der Walt, M. (2012). *Therapsid biodiversity patterns and paleoenvironments of the Karoo Basin, South Africa*. Bloomington, Indiana: Indiana University Press, 30–62. chap.

Sulej, T., Bronowicz, R., Tałanda, M., and Niedźwiedzki, G. (2010). A new dicynodont–archosaur assemblage from the Late Triassic (Carnian) of Poland. *Earth Environ. Sci. Trans. R. Soc. Edinb.* 101, 261–269. doi:10.1017/s1755691011020123

Sullivan, C., and Reisz, R. R. (2005). Cranial anatomy and taxonomy of the late Permian dicynodont *Diictodon*. *Ann. Carnegie Mus.* 74, 45–75. doi:10.2992/0097-4463(2005)74[45:caatot]2.0.co;2

Surkov, M. V., and Benton, M. J. (2004). The basicranium of dicynodonts (Synapsida) and its use in phylogenetic analysis. *Palaeontology* 47, 619–638. doi:10.1111/j.0031-0239.2004.00382.x

van Heerden, J. (1972). Interspecific variation and growth changes in the cynodont reptile *Thrinaxodon liorhinus*. *Navorsinge Nas. Mus. Bloemfontein* 2, 307–347.

Wasserman, L. (2000). Bayesian model selection and model averaging. *J. Math. Psychol.* 44, 92–107. doi:10.1006/jmps.1999.1278

Wright, A. M., Lloyd, G. T., and Hillis, D. M. (2016). Modeling character change heterogeneity in phylogenetic analyses of morphology through the use of priors. *Syst. Biol.* 65, 602–611. doi:10.1093/sysbio/syv122

Frontiers in
Earth Science

Investigates the processes operating within the major spheres of our planet

Advances our understanding across the earth sciences, providing a theoretical background for better use of our planet's resources and equipping us to face major environmental challenges.

Discover the latest Research Topics

See more →

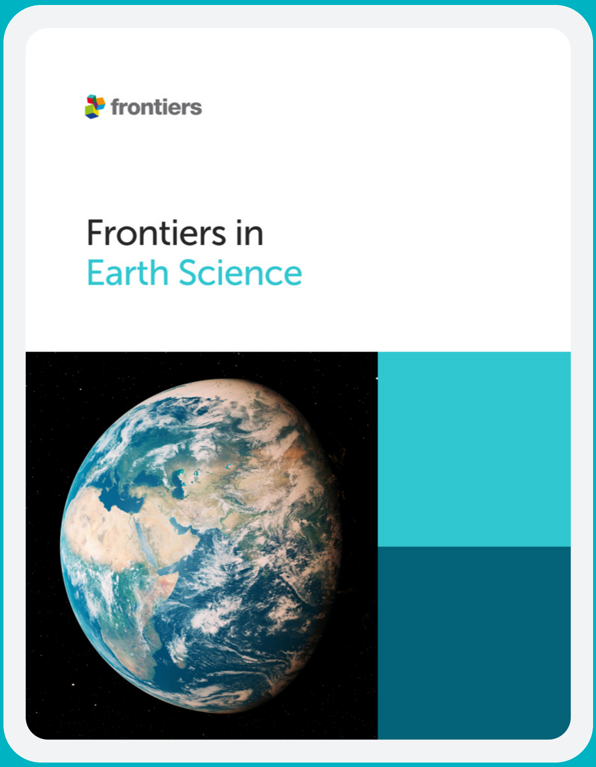

frontiers

Frontiers in
Earth Science

Frontiers

Avenue du Tribunal-Fédéral 34
1005 Lausanne, Switzerland
frontiersin.org

Contact us

+41 (0)21 510 17 00
frontiersin.org/about/contact